A new aerodynamic phenomenon and its effects on the design of ultra-high cylindrical towers

by
Francesca Lupi
born 21 April 1984
from Prato, Italy

Dissertation submitted to and approved by the Department of Architecture, Civil Engineering and Environmental Sciences of the University of Braunschweig - Institute of Technology and the Department of Civil and Environmental Engineering of the University of Florence in candidacy for the degree of a Doktor-Ingenieurin (Dr.-Ing.) / Dottore di Ricerca in Mitigation of Risk due to Natural Hazards on Structures and Infrastructures*)

Submitted on	6 March 2013
Oral examination on	23 April 2013
Professorial advisors	Prof. Claudio Borri
	Prof. Udo Peil
	Prof. Hans-Jürgen Niemann

*) Either the German or the Italian form of the title may be used.

Berichte aus dem Bauwesen

Francesca Lupi

A new aerodynamic phenomenon and its effects on the design of ultra-high cylindrical towers

Shaker Verlag
Aachen 2013

Bibliographic information published by the Deutsche Nationalbibliothek
The Deutsche Nationalbibliothek lists this publication in the Deutsche Nationalbibliografie; detailed bibliographic data are available in the Internet at http://dnb.d-nb.de.

Zugl.: Braunschweig, Techn. Univ. and Univ. of Florence , Diss., 2013

Printed in Germany.

ISBN 978-3-8440-2441-8
ISSN 0945-067X

Shaker Verlag GmbH • P.O. BOX 101818 • D-52018 Aachen
Phone: 0049/2407/9596-0 • Telefax: 0049/2407/9596-9
Internet: www.shaker.de • e-mail: info@shaker.de

Acknowledgments

First of all, I would like to thank my advisors, Prof. Claudio Borri, Prof. Udo Peil and Prof. Hans-Jürgen Niemann. A special thanks to Prof. Borri, for his continuous support and interest in this work and for his many ideas, which have suggested further new hints of research. All my gratitude to Prof. Peil, because his advice motivated me to pursue the original contributions of this work. I will always be grateful to Prof. Niemann for the time and the constancy he dedicated to our discussions. The strong motivation he transmitted has been during these years my encouragement and support to always go deeper and deeper in this research.

I would also like to acknowledge Prof. Borri and Prof. Peil for the efforts they made for the success of our International Doctoral Course. This International PhD has been an intensive sequence of many different experiences which have really enriched me.

I am grateful to my colleagues in Florence for their support and discussions during these years. I would like to thank Prof. Luca Facchini for the ideas he exchanged with me and the interesting new studies which could develop from this research.

I express my gratitude to all the colleagues at the TU Braunschweig for their kind hospitality and exchange of ideas. I especially thank Dr. Mathias Clobes for the fruitful discussions we had.

I acknowledge Mrs Serena Cartei and Mrs Yvonne Wissmann for their kind support and many efforts in the organization.

I will never forget the support and the friendly atmosphere I experienced at WiSt Ruhr University Bochum, where I spent many months during this work. First of all, I would like to thank Prof. Rüdiger Höffer for his kind hospitality at the Institute and the opportunity he gave me to work in the wind tunnel. Mrs Christa Hoogterp and Mr Volkmar Görnandt have always been so kind and helpful in the organization of my stay in Bochum, I appreciated it so much. A special thanks is for Mr Reinhard Elke and Mr Uwe Wagner, for their indispensable guidance and kind support during the wind tunnel experiments at WiSt. I would also like to express my gratitude to all the colleagues I met there, their company has been so important during the hardest periods of this work.

I express my gratitude to Lorenzo Procino and Alessandra Borsani for the support during the wind tunnel tests at CRIACIV.

I deeply acknowledge Simone Salvadori and Alessandro Mattana of Prof. Martelli's research group at the University of Florence for their cooperation in the numerical simulations. I also thank Gabriele Barbanti and Giulio Vita for their kind help.

I owe very much to my family, that I always felt close even living abroad and encouraged me in every moment of my life to purse my goals.

Abstract

The dissertation addresses the design of ultra-high towers in the atmospheric boundary layer under the wind action and has a special application for Solar Updraft Power Plants (SUPPs). They represent a highly sustainable natural resource for electric power generation, based on a combined sun-wind energy solution.

The object of the investigation is a 1-km tall solar updraft tower, made of reinforced concrete and stiffened along the height by stiffening rings. Stiffening rings are usually introduced in the design of solar updraft towers in order to reduce their structural vulnerability to the wind action by enhancing a beam-like behaviour. However, wind tunnel experiments – which were performed for the first time on such a structure within this research – showed that the presence of ring beams along the height of the tower modifies the aerodynamics of the flow around the circular cylinder and creates a bi-stable and asymmetric load condition, which does not disappear even at moderately high Reynolds numbers. This phenomenon is new and unknown. Similar effects were observed around circular cylinders (without rings) in the critical range of the Reynolds number and around two side-by-side cylinders, but the conditions of occurrence and the physical reasons were profoundly different.

The discovery of the existence of such a bi-stable and asymmetric load condition induced by ring beams along the height of a finite length circular cylinder, its interpretation, as well as the cross-checked experimental evidence in different wind-tunnel laboratories confirmed also by numerical simulations, are the original contributions of this work. Then, the effect is quantified on the structural response. The bi-stable asymmetric load on the structure did not result to be a prohibitive load condition for solar updraft towers and the magnitude of the effect depends on the number and/or on the size of the rings. Mitigation strategies are then proposed in the work. Furthermore, the dissertation evaluates the shell response to the stochastic wind loading process, especially in the vicinity of the ring beams, and provides to the designer a general unified simple tool to define design wind loads for quasi-static calculations of ultra-high towers in any atmospheric boundary layer flow.

Sommario

La tesi riguarda il progetto di torri di altezza straordinaria nello strato limite atmosferico, soggette all'azione del vento. Un particolare campo di applicazione è quello degli impianti di torri solari ad aspirazione, "Solar Updraft Power Plants" (SUPPs). Questi rappresentano una nuova e sostenibile risorsa di energia rinnovabile, basata sullo sfruttamento combinato di energia solare ed eolica.

L'oggetto dello studio è una torre solare ad aspirazione in calcestruzzo armato alta 1 km e irrigidita lungo l'altezza da travi ad anello. Queste sono normalmente utilizzate nel progetto di torri solari per ridurre la vulnerabilità all'azione del vento, in quanto la loro presenza garantisce un comportamento strutturale predominante a trave. Tuttavia, gli esperimenti in galleria del vento – effettuati per la prima volta su una struttura di questo tipo nell'ambito del presente lavoro – hanno mostrato che gli anelli lungo l'altezza della torre modificano l'aerodinamica del flusso e creano attorno al cilindro una condizione di carico bistabile e non simmetrico. L'effetto non scompare a numeri di Reynolds moderatamente elevati ed il fenomeno è nuovo e sconosciuto. Effetti simili sono stati osservati attorno a cilindri circolari (senza anelli) nell'intervallo critico del numero di Reynolds e attorno a due cilindri affiancati. Tuttavia, le condizioni in cui si verificano e il principio fisico sono profondamente diversi.

La scoperta dell'esistenza di una tale condizione di carico bistabile e non simmetrica indotta da anelli disposti lungo l'altezza di un cilindro circolare di altezza finita, la sua interpretazione, così come l'evidenza sperimentale in gallerie del vento diverse e la sua conferma numerica, sono i contributi originali di questo lavoro. L'effetto è poi quantificato in termini di risposta strutturale. La condizione di carico bistabile e non simmetrica non risulta proibitiva per il progetto di torri solari e la sua incidenza dipende dal numero e/o dalla dimensione degli anelli. Strategie di mitigazione dell'effetto sono proposte nel lavoro. Inoltre, la tesi studia la risposta della torre al carico del vento, specialmente vicino agli anelli di irrigidimento. Infine, la tesi fornisce al progettista uno strumento semplice e di validità generale per definire i carichi di progetto dell'azione del vento, utilizzabili nel calcolo quasi-statico della risposta di torri di altezza elevata nello strato limite atmosferico.

Zusammenfassung

Die hiermit vorgelegte Doktorarbeit befasst sich mit der Einwirkung des natürlichen Windes auf ultra-hohe Turmbauwerke, die weit in die atmosphärische Grenzschichtströmung hineinreichen. Die Türme von Aufwindkraftwerken stehen hierbei im Vordergrund. Derartige Kraftwerke ermöglichen eine schadstofffreie Erzeugung elektrischer Energie. Sie stellen eine sehr nachhaltige Technologie dar, die thermische Energie der Sonne in Strömungsenergie umwandelt, die ihrerseits mit Hilfe von Turbinen als elektrische Energie nutzbar gemacht wird.

Als Untersuchungsgegenstand der Arbeit dient beispielhaft ein 1 km hoher Aufwindturm. Das Tragwerk ist als Stahlbetonschale, die durch Aussteifungsringe verstärkt ist, konzipiert. Die Versteifung vermindert die durch die Einwirkung von Winddrücken erzeugten Beanspruchungen, indem sie ein stabartiges Tragverhalten bewirkt. Erstmalig wurden im Rahmen dieser Forschungen Windkanalversuche an Aufwindtürmen durchgeführt. Sie zeigten, dass die außenliegenden Versteifungsringe die aerodynamischen Eigenschaften des Turmes im Vergleich zu einem endlichen Kreiszylinder ohne Ringe erheblich verändern: Zwischen den Ringen entsteht abschnittsweise ein unsymmetrischer, bi-stabiler Strömungs- und Belastungszustand, der bis zu den höchsten untersuchten Reynoldszahlen zu beobachten ist. Ähnliche Effekte sind zwar auch bei einem Zylinder ohne Ringe bekannt, sie sind dort jedoch auf einen schmalen Bereich kritischer Reynoldszahlen beschränkt. Ebenfalls zeigen sich derartige Strömungszustände bei 2 nebeneinanderliegenden Zylindern bei bestimmten Abstandsverhältnissen. Die physikalischen Ursachen des hier bei Zylindern mit Ringen erstmalig beobachteten Phänomens sind jedoch grundsätzlich unterschiedlich.

Originäre Beiträge der Arbeit sind die Entdeckung der abschnittsweise unsymmetrischen, bi-stabilen Windbelastung, die Bestätigung des experimentellen Befundes durch Versuche in einem zweiten Windkanallaboratorium und durch numerische Simulationen, sowie schließlich die Deutung des Phänomens. Weiterhin wird die Auswirkung der zusätzlichen Windbelastung auf die Strukturbeanspruchungen untersucht. Es wird gezeigt, dass Anzahl und Breite der Ringbalken die Größe des Lasteffekts bestimmen; Maßnahmen zu seiner Minderung werden entwickelt. Insgesamt bleiben die Zusatzbeanspruchungen beherrschbar. Abschließend befasst sich die Arbeit mit den Tragwerksbeanspruchungen infolge des stochastischen Windlastprozesses, insbesondere mit den Störungen des Membranzustands in der Umgebung der Ringsteifen. Für die Tragwerksplanung werden verallgemeinerte Wind-Ersatzlasten entwickelt, die geeignet sind, als Grundlage zur Berechnung der statischen und quasi-statischen Beanspruchungen ultrahoher Türme in beliebiger atmosphärischer Grenzschichtströmung zu dienen.

Table of Contents

List of Figures

List of Tables

List of Symbols

A_c = area of the chimney

A_{coll} = area of the collector

C_D = drag coefficient

$C_{D,m}$ = mean drag coefficient

$C_{D,\ peak}$ = peak drag coefficient

$C_{D,\ \sigma}$ = standard deviation of the drag coefficient

C_L = lift coefficient

$C_{L,m}$ = mean lift coefficient

$C_{L,\ \sigma}$ = standard deviation lift coefficient

Co = co-spectrum

C_p = pressure coefficient (external)

$C_{p,air}$ = specific heat capacity of air

$C_{p,b}$ = base pressure coefficient

$C_{p,h}$ = pressure coefficient at φ_h

$C_{p,i}$ = internal pressure coefficient

$C_{p,m}$ = mean pressure coefficient

$C_{p,max}$ = maximum pressure coefficient

$C_{p,min}$ = minimum pressure coefficient

C_{pp} = decay coefficient of ρ_p

C_{uu} = decay coefficient of ρ_u

$C_{p,\sigma}$ = standard deviation of pressure coefficient

$C_{p,\sigma,BI}$ = standard deviation of pressure coefficient, body-induced part

$C_{p,\sigma,TI}$ = standard deviation of pressure coefficient, turbulence-induced part

D = diameter

$\mathbf{D}$ = damping matrix

D_{coll} = diameter of the collector

E = voltage measured by hot-wire anemometers (either E_a or E_{corr})

E_a = voltage measured by hot-wire anemometers, without temperature correction

E_{corr} = voltage measured by hot-wire anemometers, with temperature correction

EaR = element at risk

F_m = mean (drag) force

$\mathbf{F}_r$ = friction force (vector)
F_x = friction force along x-axis
F_y = friction force along y-axis
F_z = friction force along z-axis
F_σ = rms (drag) force
G = 1) solar radiation (Chapter 1); 2) gradient wind speed (Chapter 2)
H = height of the tower = 1000 m
H/D = aspect ratio
H&D = Harris and Deaves model
I_F = intensity of force (standard deviation / mean value)
I_p = intensity of pressure (standard deviation / mean value)
$I_{p,TI}$ = intensity of pressure (standard deviation / mean value), turbulence-induced part
I_u = turbulence intensity (along wind component)
$\mathbf{K}$ = stiffness matrix
K_0 = Kolmogorov parameter
L = 1) mixing length; 2) length scale of mid-latitude synoptic systems
L_f = eddy formation region in the wake of a cylinder
L_{LIFT} = correlation length of C_L
L_{pz} = pressure correlation length (z direction)
L_{ux}, L_{uy}, L_{uz} = integral length scales of the along-wind velocity component
L_{VS} = correlation length of vortex shedding lift
L_{vx}, L_{vy}, L_{vz} = integral length scales of the across-wind velocity component
L_{wx}, L_{wy}, L_{wz} = integral length scales of the vertical component of wind velocity
$\mathbf{M}$ = mass matrix
M_D = bending moment in the along-wind direction
$M_{D,m}$ = mean bending moment in the along-wind direction
$M_{D,peak}$ = peak bending moment in the along-wind direction
$M_{D,\sigma}$ = rms bending moment in the along-wind direction
M_{D,σ_B^2} = variance of M_D, quasi-static part (resonance not included)
$M_{D,\sigma_B^2+\sigma_R^2}$ = variance of M_D, including resonance
M_L = bending moment in the across-wind direction
$M_{L,m}$ = mean bending moment in the across-wind direction
$M_{L,peak}$ = peak bending moment in the across-wind direction
$M_{L,\sigma}$ = rms bending moment in the across-wind direction
M_{L,σ_B^2} = variance of M_L, quasi-static part (resonance not included)

$M_{L,}\sigma_B^2 + \sigma_R^2$ = variance of M_L, including resonance
$M_{res,m}$ = mean resultant bending moment
$M_{res,peak}$ = peak resultant bending moment
$M_{res,\sigma}$ = rms resultant bending moment
$M_{res,}\sigma_B^2$ = variance of M_{res}, quasi-static part (resonance not included)
$M_{res,}\sigma_B^2 + \sigma_R^2$ = variance of M_{res}, including resonance
N = number of time steps
P_{el} = electric output
P_{tot} = power of the power plant
Qu = quad-spectrum
$\dot{Q}$ = heat increase in the collector
R = radius
Re = Reynolds number
Re_{cr} = critical Reynolds number
Re_e = effective Reynolds number
Ro = Rossby number
R_u = autocovariance function of u
S = 1) power spectral density function; 2) generic effect in the tower response (either n_{11}, n_{22}, …)
S_{cr} = Scrouton number
S_t = Strouhal number
SUPP = Solar Updraft Power Plant
T_0 = ambient temperature
T_a = ambient temperature during acquisition of hot-wire signals
T_{ux} = integral time scale
T_w = hot-wire operational temperature = 250°
T/D = centre-to-centre transverse pitch ratio in side-by-side cylinders
U = wind velocity in the along wind direction
U_{cr} = critical velocity
U_{FS} = full-scale velocity
U_g = gradient wind, component along x-axis (reference system as specified in the context)
U_m = mean along wind component
$U_{m,\infty}$ = mean along wind component in the undisturbed flow
U_{pra} = Prandtl velocity, i.e. wind tunnel velocity at the Prandtl tube
U_{ref} = reference wind velocity

U_{WT} = wind tunnel velocity
$\mathbf{V}$ = velocity vector
V_b = basic wind velocity at 10 m height (code denomination)
V_c = flow speed in the chimney
$V_{c,max}$ = maximum flow speed in the chimney
V_g = gradient wind, component along y-axis (reference system as specified in the context)

c = ratio between L_{uz} and L_{pz}
cov_D = covariance matrix of drag force
f_c = Coriolis parameter
f_{sz} = correction factor on C_D for boundary layer flow (ESDU)
g = gravitational acceleration
h = gradient height
k = von Karman constant ($k = 0.4$)
k_F = peak factor of the force ($k_F = 3.5$)
ks = thickness of ribs on the wind tunnel model
k_P = peak factor of the velocity ($k_P = 3.5$)
k_{pw} = pressure withdrawal factor for the turbines
$\dot{m}$ = mass flow rate
$m_{i,e}$ = equivalent mass of the structure per unit length, i^{th} vibration mode
m_{11} = bending moment in the circumferential direction per unit length ($m_{11,m}$, $m_{11,\sigma}$, $m_{11,peak}$, see $n_{11,...}$)
m_{22} = bending moment in the meridional direction per unit length ($m_{22,m}$, $m_{22,\sigma}$, $m_{22,peak}$, see $n_{11,...}$)
n = frequency
n_s = vortex shedding frequency
n_1 = first eigenfrequency
n_{11} = internal force in the circumferential direction per unit length
$n_{11,m}$ = mean value of n_{11}
$n_{11,\sigma}$ = mean value of n_{11}
$n_{11,peak}$ = peak value of n_{11}
n_{22} = internal force in the meridional direction per unit length ($n_{22,m}$, $n_{22,\sigma}$, $n_{22,peak}$, see $n_{11,...}$)
p = pressure
p_m = mean pressure

p_σ = standard deviation of the pressure p

$p_{\sigma,BI}$ = standard deviation of the pressure p, body-induced part

$p_{\sigma,TI}$ = standard deviation of the pressure p, turbulence-induced part

q_m = mean velocity pressure

q_{peak} = peak velocity pressure

t = time

u = along-wind component

u_* = friction velocity

v = across-wind component

w = $^{1)}$ vertical wind component; $^{2)}$ width of the ring beams

x = along-wind direction in the wind tunnel

y = across-wind direction in the wind tunnel

z_0 = roughness length

z = vertical coordinate

z' = downwards vertical coordinate with origin at $z = H$ (tower top)

z_{ref} = reference height

ΔC_p = pressure recovery

Δp_d = pressure difference, dynamic component

Δp_s = pressure difference, static component

Δp_{tot} = pressure difference, static + dynamic

ΔT = temperature increase/decrease

Ω = angular velocity of Earth rotation, magnitude

$\boldsymbol{\Omega}$ = angular velocity of Earth rotation, vector

α = exponent of mean wind profile by using power law

δ = $^{1)}$ thickness of the boundary layer; $^{2)}$ logarithmic decrement

ε = dissipation

ξ = modal damping ratio

η = $^{1)}$ efficiency of the power plant (Chapter 1); $^{2)}$ influence coefficient (Chapter 7)

η_c = efficiency of the chimney

η_{coll} = efficiency of the collector

η_{turb} = efficiency of the turbines

θ = phase angle

ϑ_0 = maximum angle of turn due to Ekman spiral

λ_F = frequency scale factor (wind tunnel and full scale)
λ_L = length scale factor (wind tunnel and full scale)
λ_R = roughness factor in the definition of Re_e
λ_T = 1) time scale factor (wind tunnel and full scale); 2) turbulence factor in the definition of Re_e
λ_V = velocity scale factor (wind tunnel and full scale)
μ = dynamic viscosity
ν = kinematic viscosity
ρ = 1) mass density of air; 2) cross-correlation coefficient
ρ_0 = mass density of air at 20°
ρ_a = mass density of air outisde the chimney
ρ_c = mass density of air inside the chimney
ρ_{coll} = mass density of air inside the collector
ρ_D = correlation matrix of drag force
ρ_p = cross-correlations of p
ρ_u = cross-correlations of u
σ = standard deviation
σ^2 = variance
σ_B = standard deviation of background response
σ_u = standard deviation of u
$\sigma_{u,\infty}$ = standard deviation of along wind component in the undisturbed flow
σ_v = standard deviation of v
σ_w = standard deviation of w
τ = shear stresses
ϕ = latitude
φ = circumferential angle
φ_h = angle of separation
φ_{min} = angle of $C_{p,min}$
ω = circular frequency

^{EXP} = experimental result
^{LM} = loading model
‘ = fluctuating component

Chapter 1. **Introduction**

The design of ultra-high structures in the atmospheric boundary layer is a pioneering field of study, where research and application complement each other. The recent construction of super-tall skyscrapers – more than 800 m in height – represents today the highest synthesis of these efforts. This thesis proposes and investigates a new context of application – the Solar Updraft Power Plant Technology – a highly sustainable natural resource for electric power generation. This chapter introduces the technology, the working principle and the aim of the research.

1.1 The Solar Updraft Power Plants technology

The Solar Updraft Power Plants technology (SUPPs) produces renewable energy by sun-wind energy harvesting. Solar radiation is an inexhaustible input, which is converted into electric power through the natural updraft of heated air in a very high chimney.

Peculiar characteristics of this technology are its long lifetime (more than 100 years), its very low costs of operation, the no-need of water for power generation and the absence of pollutant emissions (if one incorporates the CO_2 emissions during construction, one ends up with a few grams of CO_2 per kWh of produced electricity (Backström et al., 2008)).

A SUPP consists of three elements (Figure 1.2): the collector, the turbine(s) with coupled generators as power conversion unit and the solar tower. The collector is a large glass-covered area where the visible and the ultraviolet wavelengths of the solar radiation heat the ground and consequently warm up the air under the roof, through the mechanism of natural convection. Meanwhile, the infrared wavelengths warm up the energy storage layer made of the soil itself, stones or, in case, water. Such an energy storage allows night operation. Then, the heated, less dense air rises up into the chimney of the plant, thereby drawing in more air at the collector perimeter and thus initiating forced convection. The driving force or potential that causes air to flow through the solar tower is the pressure difference between a column of cold air outside and a column of hot air inside the chimney. The stream of warm air turns the turbines at the chimney foot and in the power conversion unit the kinetic energy of the flow is transformed into electric power.

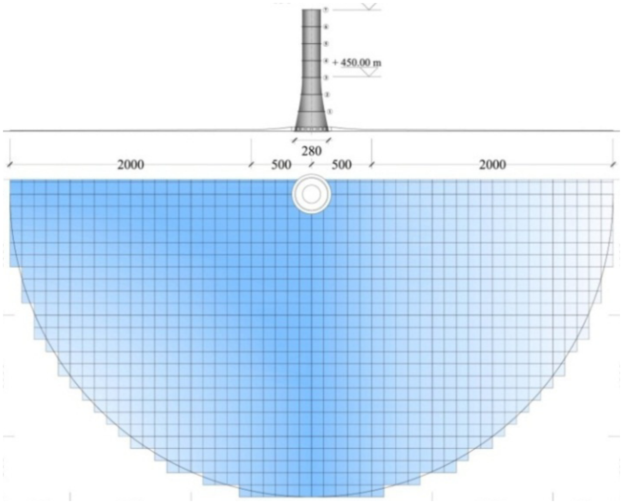

Figure 1.1 View of a Solar Updraft Power Plant

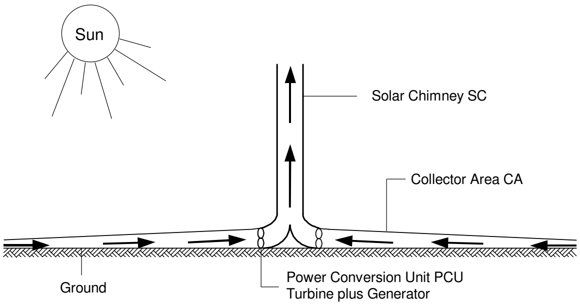

Figure 1.2 Working principle

The production of energy is proportional to the volume of the cylinder with the height of the tower and the diameter of the collector (Schlaich et al., 2005). For this reason, provided sufficiently high solar radiation input (e.g. 2000 kWh/m^2 or even more), very good efficiency of the power plant can be reached with extra-large dimensions of the tower and/or the collector.

A map of the yearly solar radiation distribution is shown in Figure 1.3. It suggests the most suitable locations for SUPPs around the world (Pretorius, 2007). In those areas, a plant with a collector diameter of 7 km and with solar tower height of 1500 m is estimated to deliver a maximum (peak) electricity power of 400 MW (Pretorius&Kröger, 2006). This assumption has been also assessed, both experimentally and theoretically for a wide range of plant geometries, as a reasonable global assumption (Fluri, 2008).

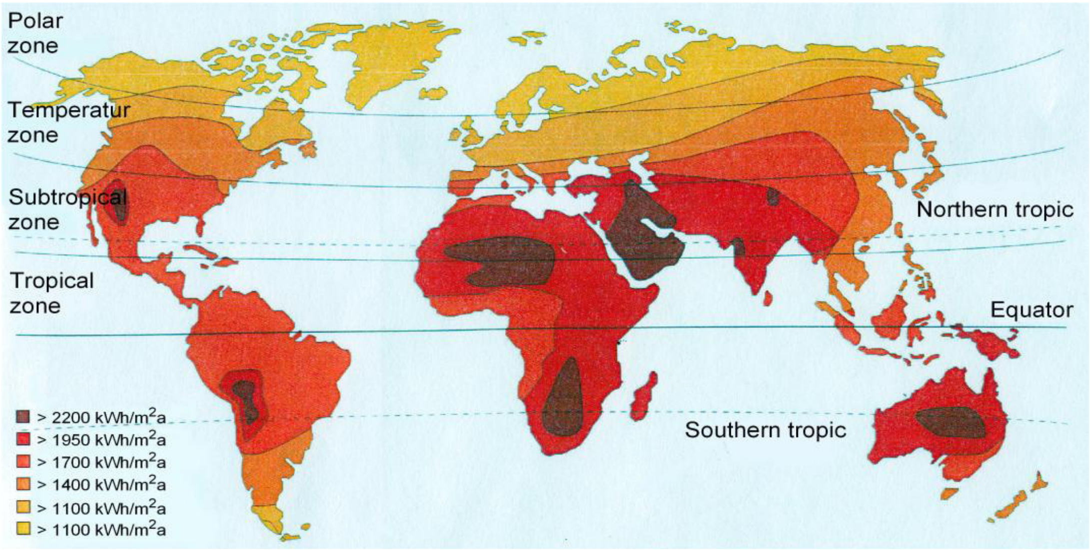

Figure 1.3 Solar radiation input (Pretorius, 2007)

1.2 Historical review

The paternity of the SUPPs idea is commonly attributed to the Spanish army colonel I. Cabanyes (Cabanyes, 1903), although a patent for “an improved temperature differential air motor” was invented even earlier – in 1896 – by A. R. Bennett (Bennett, 1896), a prototype of which is shown at the Science Museum in London.

The apparatus proposed by Cabanyes consisted of an air-heater attached to a house with a chimney. Inside the house, there was a wind propeller for electricity production (Figure 1.4).

Another early description of the SUPP principle can be found in the work of the German author Hanns Günther (Günther, 1931). The idea of the author was a solar chimney on the slope of a mountain (Figure 1.5). The very high air speed could deliver an enormous amount of energy, which could be extracted by means of wind turbines.

AÑO V.—Tomo 8. 25 de Agosto de 1903. Núm. 4

La Energía Eléctrica

REVISTA GENERAL DE ELECTRICIDAD Y SUS APLICACIONES

PUBLICACIÓN QUINCENAL ILUSTRADA

SUMARIO

Proyecto de motor solar (continuará), por Isidoro Cabanyes.—Algo de electricidad práctica. —Instalación eléctrica del tranvía de Bilbao á Durango y Arratia (continuación), por S. C.—¿Qué es el potencial? (continuará), por Nicolás de Ugarte.—Estaciones transportables para telegrafía sin conductores, sistema del profesor Braun y Siemens y Halske, y su empleo en el ejército alemán (continuará), por C. Ferrero. Teorías y explicaciones sobre el papel que en la propagación de las ondulaciones eléctricas, en la Telegrafía sin conductores, parecen desempeñar la tierra, la antena y la atmósfera (conclusión), por Carlos Dorrien.—*Crónica científica:* Radio-actividad del agua.—La resistencia eléctrica de los aceites.—*Información.—Ofertas y demandas.—Correspondencia particular.*

PROYECTO DE MOTOR SOLAR

Concibamos una gran caja de cristal herméticamente cerrada; bajo la caja transparente, otra de hierro pintada de negro, y dentro de esta última caja, aire ó agua, medios que, una vez elevados á alta temperatura pasen á cualquiera de las máquinas ya conocidas de aire caliente ó de vapor de agua y en ella funcionen; y todo ello, caja

Figure 1.4 Article of Isidoro Cabanyes, published on “La Energia Electrica” (Cabanyes, 1903).

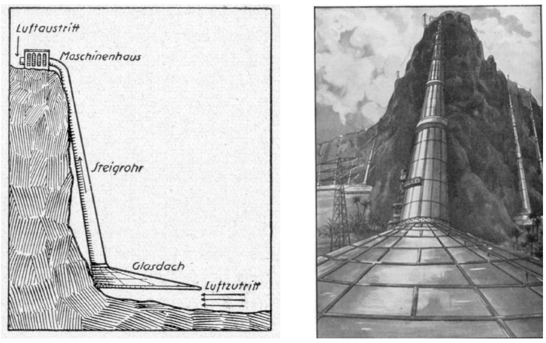

Figure 1.5 A solar chimney on the slope of a high mountain. (Günther, 1931)

Around 1975, a series of patents were granted to the US engineer R.E. Lucier in countries with deserts suitable for SUPPs, like Australia, Canada, Israel and the US. These patents concerned: "Apparatus for converting Solar to Electrical Energy", "Utilization of Solar Energy", "System and Apparatus for Converting Solar Heat to Electrical Energy", "System for converting solar heat to electrical energy".

Jörg Schlaich, Rudolf Bergermann and their team have been very active in developing and spreading the Solar Updraft Power Technology. Their first idea – as reported in (Schlaich, 2010) – goes back to 1972, when they were invited by the power industry to develop a large scale cooling tower for dry cooling. A new question arose among them, whether the natural updraft which is produced in such chimney tubes could not be utilized to produce electricity, provided an additional “fire” at the base of the chimney tube. And why not to use solar radiation and collect solar warm air by means of a large greenhouse roof? All of that resulted, in 1979, in what they called the “Solar Chimney” (Schlaich, 2010). As they said, Schlaich and his team developed the whole idea on their own, and only some years later they got hold of the paper written in 1931 by Günther, describing the similar basic principle of the solar updraft tower. In 1980, thanks to a grant by the German Ministry for Research and Technology, J. Schlaich built a solar tower prototype with a maximum power output of 50 kW in Manzanares (Spain), in order to test the new technology and confirm analytical results through experimental data (Figure 1.6). “The aim of this research project was to verify, through field measurements, the performance projected from calculations based on theory, and to examine the influence of individual components on the plant’ output and efficiency under realistic engineering and meteorological conditions” (Schlaich, 1995). The chimney was a cylindrical tube of 195 m in height and 10 m in diameter. It was surrounded by a collector of 240 m in diameter. The design was only made for experimental purposes, i.e. to collect measurements for a period of three years. The plant was intended to be removed without trace after that. Being a temporary structure, the chimney was made of a corrugated metal sheeting, whose thickness was only 1.25 mm and which could be used again after the experiment. In fact, the original plan was to take measurements in 1981 and 1982 and dismantle the structure in 1983, after three years from the construction, since the grant did not permit regular corrosion protection especially for the stay-cables. Anyway, years passed away permitting them to take more measurements. The chimney lasted for eight years, until spring 1989, when the cables broke in a storm and the chimney fell down. When it happened, the necessary measurements had largely been completed. Experimental results were very promising, a detailed analysis can be found in (Schlaich, 1995).

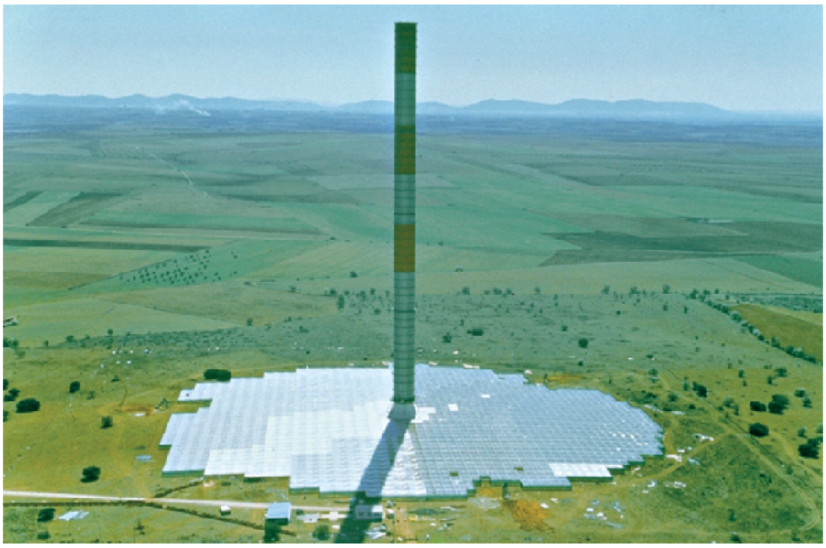

Figure 1.6 J. Schlaich’s prototype in Manzanares/Spain (Schlaich, 1995)

In 1987, Pasumarthi and Sherif erected a small prototype installation in California and published the first thermo-mechanical plant model (Pasumarthi&Sherif, 1997).

A recent experimental investigation of the solar collector temperature field on a 9 m tall prototype with sloped collector is currently being performed by Kalash et others, 2012. A complete up-to-date bibliography of the latest worldwide studies can be found in the Proceedings of both the 2nd and the 3rd International Conferences on SUPPs (STPT2010, SUTPT 2012).

Up to now, several projects of large SUPPs have been developed in arid zones all over the world, but none of them has come to realization. In 2008, the Namibian government approved a proposal for the construction of a 400 MW solar chimney called the 'Greentower'. The tower was planned to be 1.5 kilometres tall and 280 m in diameter, and the base consisted of a 37 square kilometres greenhouse. In recent years EnviroMission (Australia) proposed a 200 MW power plant in the US deserts. Such a power plant could provide enough electricity to power around 100000 households (www.enviromission.com).

In October 2010 a so-called Solar Heated Wind Updraft Tower Power System became operational in the Wuhai desert, Inner Mongolia (China). It is a medium size power plant with a 53 m tall tower and a collector area of 6300 m^2. There are 5 turbines, each one having a capacity of 40 kW (Wei&Wu, 2012). In October 2010 the generating electricity system was combined to the grid and since then monitoring devices have been controlling the thermodynamic behaviour. Some pictures of the power plant, taken during a visit in October 2012, are reported in the following (Figure 1.7, Figure 1.8).

Figure 1.7 Solar Heated Wind Updraft Tower Power in Wuhai desert, Inner Mongolia (China). Visit to the prototype in October 2012, during the 3rd Int. Conf. on Solar Updraft Tower Power Technology.

a)

b)

c)

Figure 1.8 Solar Heated Wind Updraft Tower Power in Wuhai desert, Inner Mongolia (China). a) View of the tower under the glass collector, b) Tower, c) Turbine

1.3 Production of energy

The thermo- and fluid-dynamic behaviour of the power plant and the efficiency of energy production are crucial aspects for the development of the technology. However, they are not addressed in this work and only a simplified approach – resulting from documentation in literature – is presented now. For further details, the first wide studies of the multi-physics of solar updraft power plants can be found in Weinrebe (2000) and Bernades (2004). Then, Pretorius (2007) presents another milestone work. Recent studies are presented in Krätzig (2012a,b).

A simple theory to understand the mechanism of SUPPs is outlined in Schlaich (1995) and briefly addressed here. According to that, the efficiency of the power plant is the product of the individual component efficiencies, i.e. the collector roof, the solar tower and the turbines:

$$\eta = \eta_{coll} * \eta_{c} * \eta_{turb} \tag{1.1}$$

The efficiency of the collector (η_{coll}) describes the effectiveness with which solar radiation is converted into heat. The efficiency of the chimney (η_{c}) describes the effectiveness with which the quantity of heat delivered by the collector is converted into flow energy. η_{turb} is the efficiency of the wind turbines.

The collector

The collector converts solar radiation G (W/m^2) on the collector surface A$_{coll}$ (m^2) into heat increase in the collector airflow $\dot{Q}$ (W). Thus, the efficiency of the collector is defined by the ratio:

$$\eta_{coll} = \frac{\dot{Q}}{A_{coll} * G} \tag{1.2}$$

In recent publications, Krätzig (2012a,b) applies one-dimensional flow-tube theory and prosecutes a mass of air on its way through the collector, the turbines and the chimney. The efficiency of the collector is estimated successively and iteratively for each one-dimensional collector element with a characteristic finite volume of air. The thermo-fluidmechanics in the collector is described by fluid equations (conservation of mass, conservation of momentum and Bernoulli's energy equation to connect the ambient atmosphere around the plant at the collector rim with its interior) and thermodynamic conditions (conservation of energy). Fluid equations and thermodynamic conditions are coupled by the equation of state of air, as an ideal gas.
The heat output $\dot{Q}$ under steady conditions is expressed as the product of the mass flow rate $\dot{m}$ (kg/s), the specific heat capacity of the air C$_{p,air}$ (J/kgK) and the temperature difference between the collector inflow and outflow (a typical value is ΔT ≈ 30°K):

$$\dot{Q} = \dot{m} C_{p,air} \Delta T \tag{1.3}$$

According to Pretorius (2007) the efficiency of the collector η_{coll} can be approximated by the following interpolation relation, in which the diameter of the collector D_{coll} is measured in km:

$$\eta_{coll} = 0.680 * \left(1 - 0.229\sqrt{D_{coll} - 2}\right) \tag{1.4}$$

In order to model the physical processes of transformation of solar radiation G into heat increase ΔT of the air flux, the specific design of the collector comes into play. In fact, the manifold exchanges of convective and radiation heat power that exist in the different components of the collector – single or double glass panels, air flow, water heat storage or soil absorber – must be considered in the heat power balance conditions (Krätzig, 2012a,b).

The chimney

The chimney converts the heat flow $\dot{Q}$ produced by the collector into kinetic energy. The pressure difference Δp_{tot} between a column of cold air outside and a column of hot air inside the chimney is the driving force that causes air to flow through the Solar Updraft Power Plant.

$$\Delta p_{tot} = g \int_0^H \{\rho_a(z) - \rho_c(z)\} dz \tag{1.5}$$

$\rho_a(z)$ and $\rho_c(z)$ stand for the height-depending mass density (kg/m^3) of the air outside and inside the chimney, while g is the gravitational acceleration (m/s^2).
With the barometric pressure dependence from height, air as an ideal gas and ΔT constant over h, the pressure difference can be evaluated by solving analytically equation (1.5) over the tower height:

$$\Delta p_{tot} = g \rho_{coll} H \frac{\Delta T}{T_0} \tag{1.6}$$

being ρ_{coll} the density of air at temperature $T_0 + \Delta T$ at collector outflow and T_0 the ambient temperature at ground level.
The pressure difference can be divided into a static and a dynamic component (neglecting friction losses):

$$\Delta p_{tot} = \Delta p_s + \Delta p_d \tag{1.7}$$

Such a division is due to the energy taken by the turbines: the static pressure difference drops at the turbines, while the dynamic component describes the kinetic energy of the airflow. If the turbines are left out ($\Delta p_s = 0$), the maximum flow speed $V_{c,max}$ is achieved and the whole pressure difference is used to accelerate the air.

From Bernoulli's equation we calculate the maximum air velocity at the chimney's entrance:

$$V_{c,\max} = \sqrt{2gH\frac{\Delta T}{T_0}} \tag{1.8}$$

The whole pressure difference is then converted into kinetic energy. Therefore, the total power contained in the flow is:

$$P_{tot} = \Delta p_{tot}\frac{\dot{m}}{\rho} = \Delta p_{tot} V_{c,\max} A_c = \frac{1}{2}\dot{m} V_{c,\max}^2 \tag{1.9}$$

V$_{c,max}$ and A$_c$ are the maximum flow speed and the cross-section of the chimney, respectively.

The efficiency of the chimney can be calculated by combining equations (1.3), (1.8), (1.9):

$$\eta_c = \frac{P_{tot}}{\dot{Q}} = \frac{gH}{C_{p,air} T_0} \tag{1.10}$$

All of that is a simplified representation, but it highlights that the efficiency of the chimney is fundamentally dependent on its height. Pretorius (2007) also proposes an approximated expression to consider the influence of the mean chimney diameter D.

The turbines

The turbines at the base of the chimney convert free convection flow into rotational energy. The pressure drop at the turbines can be expressed, in a first approximation, by the Bernoulli equation:

$$\Delta p_s = \Delta p_{tot} - \frac{1}{2}\rho_c V_c^2 \tag{1.11}$$

being ρ_c and V$_c$ the air density and the flow speed in the chimney, respectively.

Thus, the theoretically useful power at the turbines becomes, in analogy to equation (1.9):

$$P_{tot} = \Delta p_s \frac{\dot{m}}{\rho} = \Delta p_s V_c A_c = \frac{1}{2} \dot{m} V_c^2 \tag{1.12}$$

By introducing η_{turb} for the turbine efficiency and the pressure withdrawal factor k_{pw} (so that $\Delta p_s = k_{pw} \Delta p_{tot}$)), the effective electrical power generated by the power plant can be finally expressed as:

$$P_{el} = k_{pw} \eta_{turb} \eta_{coll} \eta_c A_{coll} G \tag{1.13}$$

The power is maximized if the pressure drop $\Delta p_s = k_{pw} \Delta p_{tot}$ is about two thirds of the total pressure difference available, i.e $k_{pw} = 2/3$ (Schlaich, 1995). By substitution, it results:

$$P_{el} = \frac{2}{3} \eta_{turb} \eta_{coll} \frac{gH}{C_{p,air} T_0} A_{coll} G \tag{1.14}$$

The electrical output of the Solar Updraft Power Plant is then proportional to the product HA_{coll}, i.e. to the volume included within the chimney height and the collector area, as it was stated in section 1.1. Further detailed and updated studies can be found in Proc. SUTPT 2012.

Electric power and electricity costs

Despite the high initial cost of the SUPPs, the estimated leveled electricity costs LECs (due to IEA-guidelines) of the harvested energy are very low.

Krätzig (2012b) estimates a maximum electric power of 75 MW for a power plant with a 750 m tall chimney and 3500 m collector diameter, by assuming solar radiation G = 2.2 MWh/m^2. If the capacity factor (i.e. full load hours/24*365 hours in one year) is considered about 34%, - it means that the full load hours in one year are around 3000 - then the total annual energy harvest is around 75/0.34 = 220 GWh/a. The same paper provides an estimation of investment costs (around 340 M€, 60% of which due to the collector, 20% due to the chimney and 15% due to the turbines, plus extra costs). By considering a depreciation period of 33 years, it results in LECs equal to 9.9 €cent/kWh.

A similar value of LECs also resulted in other previous studies (Bergermann&Weinrebe, 2010). They estimated for a 200MW Solar Updraft Tower a total investment of 750 M€ and an average yearly production for a North African location of 650 GWh. It resulted, by assuming a depreciation period of 30 years, in LECs equal to 10.3 €cent/kWh.

Further studies about economic aspects can be found in (Breuer&Hüwe, 2010).

1.4 Main components of the power plant

1.4.1 The tower

Solar Updraft Towers (SUTs) are slender and extremely thin shells, usually made of reinforced concrete. In Europe, two main German schools are leading the structural design of Solar Updraft Towers, headed by J. Schlaich and W.B. Krätzig, respectively. J. Schlaich proposes tubes of cylindrical shape, usually stiffened along the height by spoke wheels. Various alternatives and non-linear structural analyses are reported in (Goldack, 2004, 2011). A double-wall tower is also presented in (Goldack, 2004). Two examples are shown in Figure 1.9 and Figure 1.10.

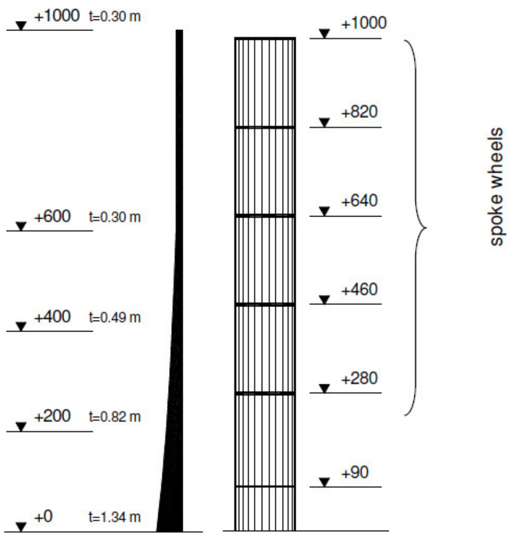

Figure 1.9 1-km tower (Goldack, 2004, 2011)

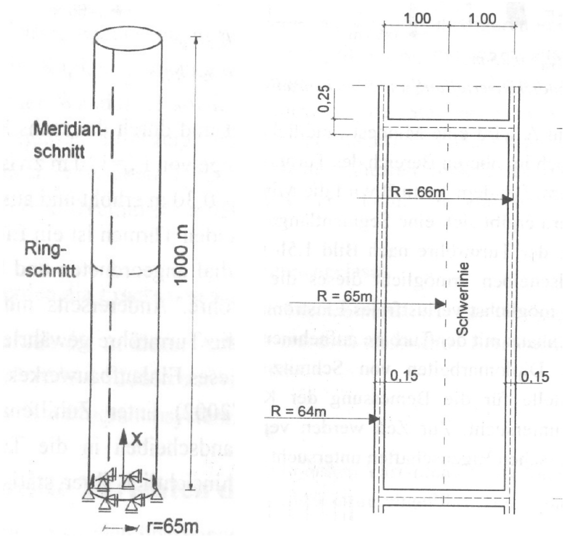

Figure 1.10 Double-wall tower (Goldack, 2004)

W.B. Krätzig transfers insights from designs of natural draft cooling towers' projects to solar chimneys. Figure 1.11 gives an overview over these attempts, demonstrating the way from cooling towers to chimneys of SUPPs up to an elevation of 1500 m (Krätzig et al., 2008-2009a,b).

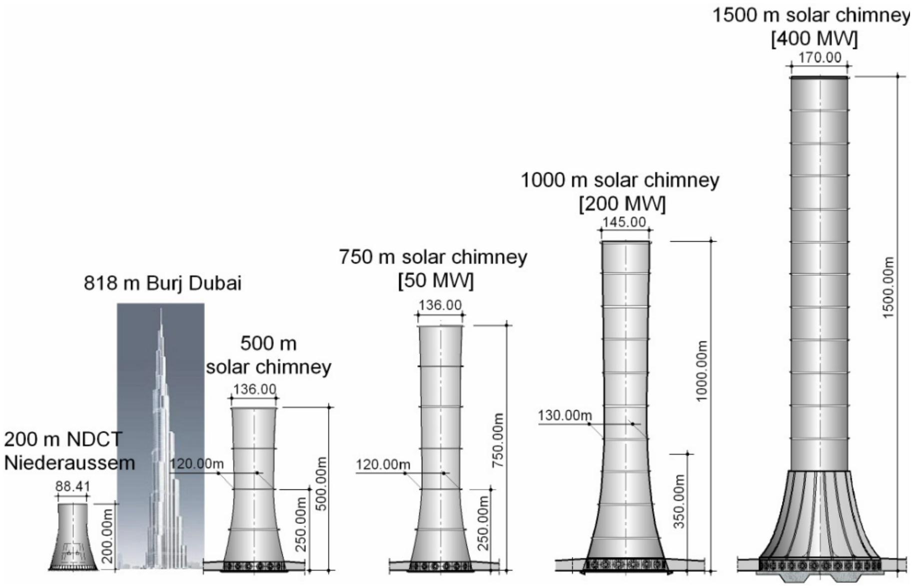

Figure 1.11 From cooling towers to chimneys of Solar Updraft Power Plants (Krätzig et al., 2008-2009a,b)

The distinctive feature is that the lower part of the tower turns into a hyperboloid. Thanks to the use of a double curvature surface, the structure applies the benefits of shape strengthening. Two recent pre-designs of a 1000 m high reinforced concrete solar tower are shown in Figure 1.12 and Figure 1.13 (Krätzig et al., 2008-2009a,b; Harte et al., 2010). With a collector size of 6000 m of diameter they shall produce a peak power of 200 MW_p (annual work of 600 GWh). In Figure 1.12, shortly above the throat at 400 m of height, the shell diameter is 130 m wide, while at the upper ring it is 145 m. Below 400 m the tower shell widens in strength-optimized hyperbolic shape up to a foot-diameter of 260 m. The wall thickness of high-performance reinforced concrete (C70/85) varies from 0.25 m to 0.65 m. In addition to the upper edge member, nine intermediate reinforced concrete ring-stiffeners are applied, fixed on the outer shell face. 16 turbo-generators deliver the mentioned plant capacity, see (Backström et al, 2008). In Figure 1.13 the upper part of the tower has a constant diameter of 150 m and the maximum shell thickness at the base is 0.60 m. This one drawn in Figure 1.13 is the reference structure which is always considered in this work.

From the structural viewpoint it is important to construct the solar tower as thin as possible. This can be achieved by using high-strength concrete and/or by installing stiffening rings along the chimney height and on top. Stiffening rings can be realized in several ways, e.g. classical reinforced concrete beams (Figure 1.14), composite steel-concrete, spoken wheels with carbon fiber strings (Figure 1.15). In order not to reduce the efficiency of production, the interference between stiffening rings and internal efflux in the chimney has to be minimized. For this reason, it is preferable that stiffening rings are fixed on the outer surface.

Firstly, the intermediate stiffeners enhance a beam-like distribution of the meridional forces under wind loading. The second important contribution of the rings is the increase in the stability safety by localization of the buckling modes. For tower designs without ring-stiffeners one would recognize that instability modes dominate the entire shell, so that the concrete quality for this alternative had to be increased to a high performance reinforced concrete (e.g. C90/105), (Krätzig et al., 2008-2009a,b). Moreover, the vulnerability to vortex shedding would be strongly increased if the shell-like behaviour predominated at the first eigenmode.

Provided a very good soil, the foundation of 1 km tower may only consist of a reinforced concrete circular ring beam (Krätzig et al., 2008-2009a,b).

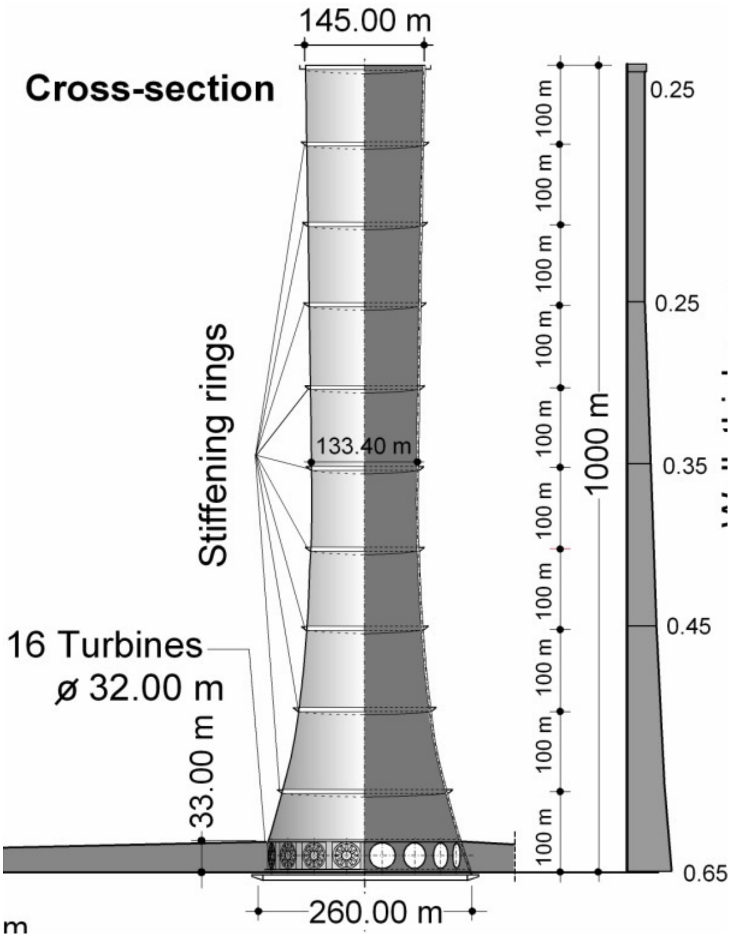

Figure 1.12 Example n.1 of 1-km tall solar tower (Krätzig et al., 2008-2009a,b; Harte et al. 2010)

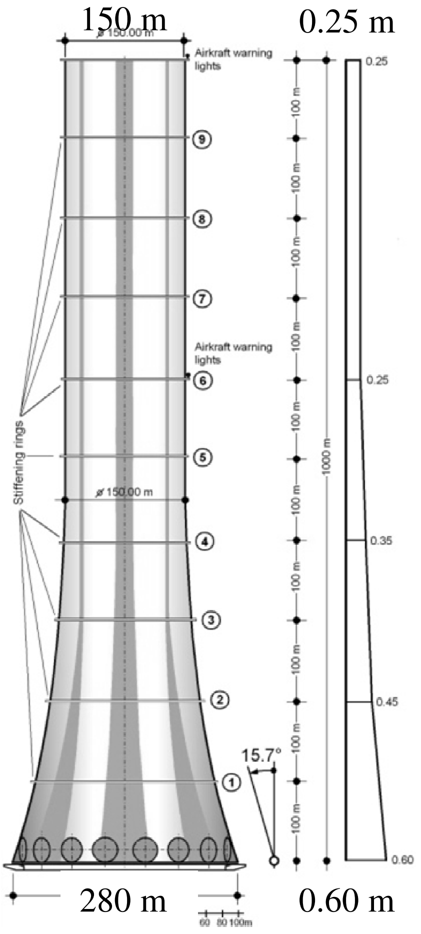

Figure 1.13 Example n.2 of 1-km tall solar tower (Krätzig et al., 2008-2009a,b; Harte et al. 2010)

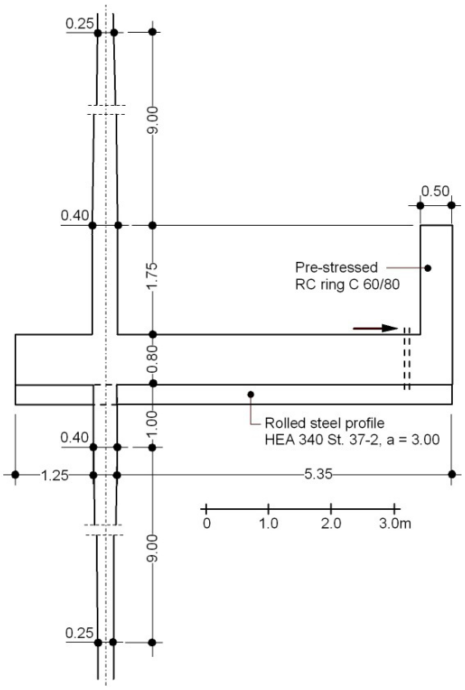

Figure 1.14 Reinforced concrete stiffening ring (Krätzig et al., 2008-2009a,b)

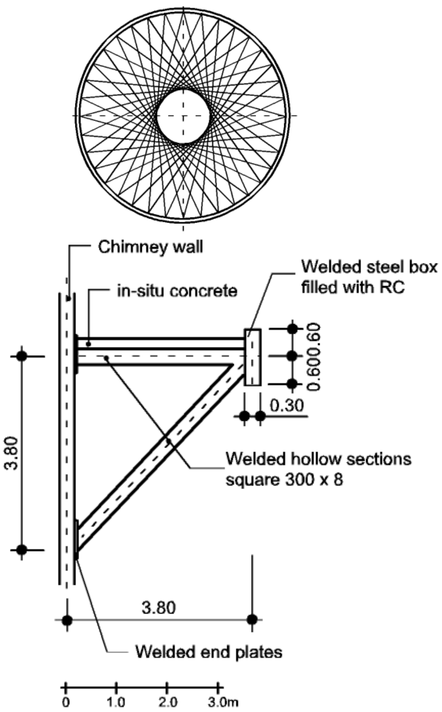

Figure 1.15 Spoke wheels with carbon fiber strings (Krätzig et al., 2008-2009a,b)

1.4.2 The collector

The collector area is not investigated within this work. However, the collector is one of the main components of the power plant. In fact, as previously mentioned, the power output of Solar Updraft Towers is proportional to the collector area (1.14). The diameter of the collector ranges from 1 up to 7 km, depending on the required energy output, it is usually made of glass and it could also take the secondary function of being a greenhouse for agricultural purposes. Its cost is a high percentage (between 40% and 60%) of the entire power plant, as reported in several publications (e.g. Krätzig , 2012b; Bergermann&Weinrebe, 2010). Thus, the collector plays a key role and the performances of the SUPP, in terms of energy production, can be significantly increased by improving the collector glass quality. In particular, the optical glass quality is of the greatest importance. The transmittance and absorptivity of glass depend on the solar radiation incident angle, the refractive index of the glass, the thickness of the glass and its extinction coefficient. The latter determines the amount of radiation absorbed and consequently transmitted by the medium (Pretorius, 2007). Moreover, a better quality of the glass implies a better transparency, allowing more solar radiation to penetrate it.

Several studies and on-going researches about the collector can be found in literature. For example, numerical simulations are performed in (Pretorius, 2007), referring to a SUPP located in South Africa, with a 5000 m collector diameter and a 1000 m high, 210 m diameter chimney. These simulations show that through the modification of the collector roof reflectance, collector roof emissivity, ground surface absorptivity and ground surface emissivity, major improvements on plant performance are possible. An improved plant performance can also be reached by introducing thermal insulation and double glazing of the collector roof. The better is the insulation of the warm collector air from the environment, the smaller are the heat losses through the roof. It is also predicted a notable sensitivity to the ground surface absorptivity value.

Techniques to control the power output of a SUPP according to specific demand patterns are investigated in (Pretorius, 2007). Without any control, SUPPs deliver electricity simultaneously to sun radiation and are designed neither for base load power generation nor for peak load. The introduction of a secondary collector roof beneath the main one is a strategy proposed by Pretorius to regulate the air-flow, and thus the energy production, according to specific demand patterns. Another strategy to control the power production of SUPPs is the incorporation of water tanks under the collector roof, so that the energy (heat) storage capability increases significantly thanks to the high specific heat capacity of water. In this way, the production during the day-time is lower, but the night-time production is much higher.

Recent studies about heat storage and heat transfer have been presented at the International conference SUTPT 2012 (e.g. Bernardes (2012) and Fasel (2012)).

1.4.3 The turbines

Milestones studies regarding the layout of the turbines of solar updraft towers belong to the University of Stellenbosch (Backström&Fluri, 2006; Fluri, 2008; Fluri&Backström, 2008; Backström&Fluri, 2010).

The two typical solar tower configurations are one with vertical axis (used in a single turbine layout) and one with horizontal axis (used in multiple turbine layout). Backström&Fluri (2010) explain that the vertical axis layout with horizontal entrance is favoured for layouts where there is one turbine per chimney, while the horizontal layout for many turbines per chimney. In Fluri (2008) it is stated that many smaller generators replacing a large one weigh and cost less than a huge one. Fluri investigated the optimum number of turbines for solar chimney power plants of various output. He found that for large plans with nominal power of 200 MW the optimal number of turbines is about 30, and the turbine diameter is about 30 m. Each turbine will then have a rating of about 6.7 MW.

The turbine layout is not considered in this work. However, the reference structure of this Thesis, depicted in Figure 1.13 presents 16 turbines of 32 m in diameter.

1.5 Aim of the research

The dissertation investigates the Aeolian risk scenario on ultra-high structures, like solar updraft towers. For such structures, the wind action represents the main natural hazard.

At first, the dissertation aims to revise the knowledge about the nature of strong winds in the atmospheric boundary layer. The usual wind engineering applications are limited to the lowest 200-300 m of the atmosphere, where codified wind profiles can be applied. The coupling between wind engineering and meteorology allows to investigate higher levels. The problem is addressed in the thesis on theoretical bases, because experimental data at large heights in strong winds are, so far, inexistent. Several issues still remain unsolved and their uncertainty increases the structural risk of ultra-high towers. However, this should not prevent the design, provided that the vulnerability of the structure to the wind action is low.

The structural vulnerability of solar towers to the wind action is especially addressed in the dissertation. In fact, so far it was known that stiffening rings applied along the height of the tower reduce the vulnerability of the structure, because they enhance a beam-like behaviour. However, their effect on the load had never been investigated before. Moreover, no load model is so far available to the designer to calculate the structural response of a solar updraft tower to a stochastic wind loading process. Without that, the actual damage of such a structure due to the wind action could not be really estimated.

Thus, the main purpose of this research is to investigate – by means of wind tunnel experiments – the aerodynamics of the flow around circular cylinders, like solar towers. Beside the traditional case of study, i.e. a circular cylinder with a free-end (which is addressed in literature but not in all its aspects) the dissertation also investigates the effect of rings along the height of the tower. This case is not treated in literature. The dissertation aims at investigating the new phenomenon created by spanwise rings, both from the fluid dynamic point of view – by means of wind tunnel experiments and numerical simulations – and from the structural point of view.

The experimental investigation is performed in two wind tunnels, at WiSt Ruhr-University Bochum and at CRIACIV University of Florence. The comparative study aims to cross-check results. In view of that, numerical simulations represent a further support. However, the wind pressures depend on atmospheric boundary layer characteristics. Since the boundary layers in two different wind tunnels are necessarily different, the experiments also aim to investigate such a dependency. So, as a further result of this work, the designer will benefit of a quasi-static stochastic load model which is not referred to a pre-defined boundary layer, but it can be generalized to any atmospheric boundary layer flow. This tool allows to evaluate the structural damage even in the vicinity of the stiffening rings, where the shell-like behaviour predominates and no load model was available before.

The tower structure which is used as reference in the dissertation is the one in Figure 1.13. The height is 1-km, the diameter at the base is 280 m and at the top it is 150 m. However, the wind tunnel model has a simpler and more general shape. It is a circular cylinder with aspect ratio H/D = 1000/150 = 6.7.

Chapter 2. **Risk scenario for SUPPs technology**

This chapter describes the risk scenario of the apparently most economic and sustainable technology for renewable energy harvesting, with focus on the Aeolian risk. The theory of the atmospheric boundary layer at large heights – resulting from coupling wind engineering with boundary layer meteorology – is presented as the basis for a deeper knowledge of the natural hazard. Moreover, so far it is known that the structural vulnerability of the tower to the wind action can be reduced by introducing stiffening rings along the height.

2.1 Aeolian risk

Many studies around the world (SCPT, 2010; SUTPT, 2012) proved that Solar Updraft Power Plants would be the most economic technology for renewable energy harvesting in the world, as reported in section 1.3. The leveled electricity costs of the energy (according to the definition in the IEA-guidelines) would be of a few €cent/kWh, considerably lower than those for other competitive renewable energy concepts. So, why have big power plants not come to realization, yet? It is not only a matter of the high initial cost, because it would be retrieved after the amortization period, including depreciation. In fact, SUPPs are considered a highly risky technology. The high risk concerns especially two main aspects: the production of energy and the structural feasibility. Some projects stopped before being completed because it was realized that the production of energy of the power plant would have resulted lower than expectations, for which investors were gained. The structural aspect is another challenge, since 1 km tower would be the highest structure in the world.

The present work focuses on the structural aspect; the wind action on the tower is selected among all natural hazards. Thus, the focus is on the Aeolian risk scenario, which is first introduced in the next section within a general framework. In particular, the following issues are discussed in the dissertation:

NATURAL HAZARD

The state of knowledge of the nature of wind at high altitudes results from coupling boundary layer meteorology with wind engineering. Theoretical models like the Harris and Deaves (H&D) one (Harris&Deaves, 1980) describe the mean wind profile, the turbulence intensity and the integral length scale of turbulence in strong wind conditions up to the boundary layer height, on the basis of order of magnitude analyses of the equations of motion. The Coriolis force is included. However, a further question is whether such mid-latitudes models could be applied at small latitudes, where the Coriolis force becomes smaller and smaller in the geostrophic balance. Moreover, to which extent can full-scale measurements at large heights (e.g. 1 km height) be used to study the turbulent properties of wind, for engineering purposes? These issues are addressed in section 2.3. Tropical cyclones and tornadoes are only mentioned but not included in this work.

Wind tunnel experiments performed in different boundary layers (and different wind tunnels) allowed to study the effect of certain boundary layer properties on wind forces and pressures. A simplified model of wind pressures on the tower shell, with regard to the turbulent properties of the incoming flow, is proposed in Chapter 7. It can be applied by the designer in any boundary layer flow to calculate the quasi-static response of the tower (resonance not included).

EXPOSURE

The tower is considered exposed to strong wind conditions (exposure factor E = 1).

VULNERABILITY

The main part of the dissertation studies the effect of stiffening rings applied along the height of the tower, like those reported in Figure 1.14 and Figure 1.15. They were originally introduced in the design in order to reduce the vulnerability of the structure, as explained in section 2.4, but their effect on the flow had never been investigated before. The thesis discovers and proves that this strategy for the reduction of structural vulnerability might induce an even more severe load condition, if improperly used.

2.2 Risk management framework

The risk scenario of the Solar Updraft Power Plants Technology can be described within the general approach of the risk management framework. The latter is outlined as a unified methodology throughout different disciplines in Pliefke (2010).

The risk management framework is organized in three main steps (see Figure 2.1), that are risk identification, risk assessment and risk treatment. They are performed sequentially and accompanied by a risk review step and a continuous risk monitoring.

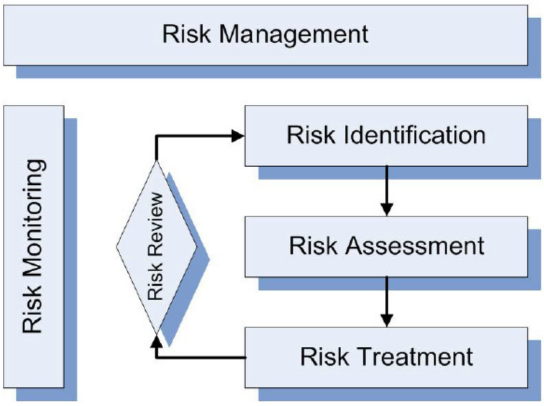

Figure 2.1 The general risk management framework (Pliefke, 2010)

As outlined in Pliefke (2010), the risk identification phase consists in the definition of the system under analysis and of the hazards that could endanger it. In the present work, the system is the solar tower and the natural hazard under investigation is the wind action.

The risk assessment phase is divided in two sub-steps (Figure 2.2): the risk analysis and the risk evaluation. The risk analysis (Figure 2.3) consists in a quantification of the risk. To do that, the hazard must be defined, for a certain return period, in term of its intensity and frequency parameters. Then, for each element at risk (EaR) of the system, i.e. for each element with a non-zero exposure to the hazard, the impact of the hazard is converted into hazard load. Depending on the structural response of the element at risk to the hazard load, the damage can be identified. The relation between the hazard load and the resulting damage is the structural vulnerability. It indicates “the degree of physical susceptibility towards the impact of the hazard”. The expected damage per year can be interpreted as the structural risk. By definition, the structural risk is “the product of the annual probability of occurrence of damage multiplied by the potential damage that goes in line with it”. Then, direct and indirect consequences, both tangible and intangible, are estimated in order to calculate the total risk, i.e. the expected loss per year, which is “the product of the annual probability of occurrence of the loss and the loss that goes in line with it”. Tangible consequences are measured in monetary value. Intangible consequences must be converted in monetary values, otherwise no comparison of risks is possible. After that, the risk evaluation sub-step aims to find adequate risk measures, so that the risk under investigation can be compared to other risks for the system.

The last phase in Figure 2.1, that is the risk treatment, creates a rational basis to handle the risk and, if necessary, reduce it by risk mitigation initiatives. Then, for those risks that have already run through the whole process at least once, a risk review process can be performed.

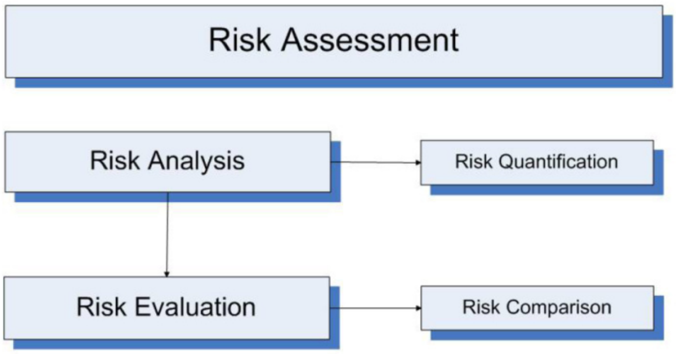

Figure 2.2 The risk assessment phase (Pliefke, 2010)

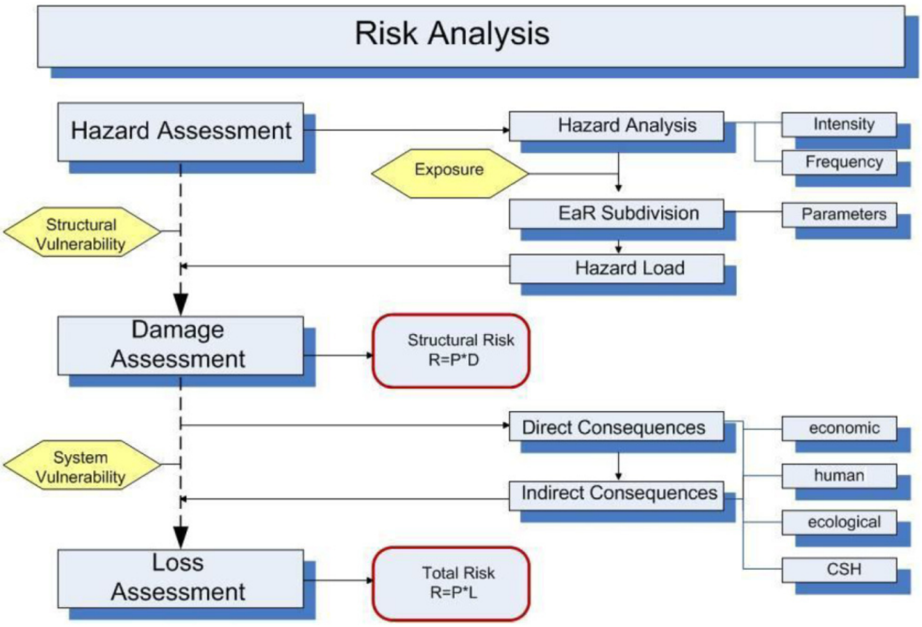

Figure 2.3 The risk analysis (Pliefke, 2010)

The risk management framework proposed by Pliefke is consistent with other definitions of risk in literature. In particular, Augusti et al., (2001) define the damage risk as “the risk associated with physical damage to constructed facilities”. The probability of a negative consequence caused by a potentially dangerous event is “the product of three factors, namely: 1) hazard, i.e. the probability of occurrence of a dangerous event (the action); 2) exposition, i.e. the probability that the action finds something that can be damaged; 3) vulnerability, i.e. the (conditional) probability that the facility is damaged when hit by the dangerous action.” The damage is associated to its consequences (“losses”). The latter can be considered as a measure of the damage itself, so that the three-factor formulation yields directly the risk as “expected cost of damage”. Alternatively, the “expected cost of damage” can be split up into the product of the “probability of damage” times the “cost of damage”. In this case, the cost of damage is the fourth factor to be included in the probabilistic definition of risk.

2.3 Natural hazard – the wind action

Solar Towers are subjected to loads and other actions that are typical for high reinforced concrete towers:

- dead load of the shell wall, the ring beams, the turbine houses, and the foundation ring;
- wind loading acting both on the external and the internal surfaces of the shell
- temperature effects, operational ones from the action of the heated air, axisymmetrical ones due to ambient air temperature, non-axisymmetrical ones due to solar irradiation on the tower shell;
- seismic action if the location of the Solar Updraft Power Plant exhibits sufficiently important seismicity;
- shrinkage effects;
- pre-stressing if applicable;
- construction loads, e.g. anchor forces from pre-stressed guys of the central crane;
- differential soil settlements of external origin.

Wind and seismic activity are the main natural hazards to be considered in the tower design. However, the very high first natural period of the tower (beam-like bending mode, like a soft cantilever), makes it isolated against strong earthquake excitations. Therefore, even in case of seismic hazard, the vulnerability of the structure to earthquake loading is not high. The seismic risk is thus neglected in this work. Instead, the main risk in the solar tower design is due to the wind action.

The wind hazard for strong winds in “well-behaved” wind climates (i.e. excluding tropical cyclones and tornadoes) is related to the design wind velocity. This is the 10-min-average velocity that has a 2% yearly probability of exceedance, which roughly corresponds to a 50-year-return period (Eurocode1). Tropical cyclones and tornadoes are not covered in this dissertation (they are only mentioned in section 2.3.4), as well as occurrence of low-level jets in the deserts.

The height of solar updraft towers (up to 1500m) exceeds by far the main definition domain of up to 300 m for established and codified wind profiles and wind load models. In this domain, the concept of the turbulent Prandtl layer with constant shear is a useful approximation. Above the Prandtl layer, in the Ekman layer, the shear turbulence decreases while the Coriolis force increases and tends to align the flow in the direction of the isobars according to the Ekman spiral.

The knowledge of the nature of the wind is a pre-requisite for investigating the wind load on solar towers. However, experimental data are scarce at large heights, and accurate measurements of wind turbulence are currently not available above 300 m. This section addresses the state of knowledge of the structure of strong winds at high altitudes and to which extent it can be enhanced by means of field measurements. The modelling of the wind action with regard to turbulent properties of the flow (Chapter 7) by means of wind tunnel experiments in different boundary layer flows is the way which is proposed in this work to approach the open problem concerning the nature of wind at large heights.

2.3.1 The structure of strong winds in the atmospheric boundary layer

Five equations form the foundation of boundary layer meteorology (Stull, 1988): 1) equation of state (ideal gas law), 2) conservation of mass (continuity equation), 3) conservation of momentum (Newton's second law), 4) conservation of moisture, 5) conservation of heat (first law of thermodynamics). In addition, there are equations for conservation of scalar quantities, e.g. a tracer in the atmosphere.

In strong winds, it can be assumed that the ambient temperature gradient is adiabatic (neutrally stable atmosphere), so that only the mechanical stirring and not the convective action of buoyancy forces will generate turbulence. Essentially, the conservation of momentum and the continuity equation govern the motion of strong atmospheric winds. The latter leads to the incompressibility approximation if typical velocity and length scales of the boundary layer are used. In a rotating Cartesian frame of reference the former equation is (Stull, 1988):

$$\underset{\text{I}}{\frac{\partial U_i}{\partial t}} + \underset{\text{II}}{U_j \frac{\partial U_i}{\partial x_j}} = \underset{\text{III}}{-\delta_{i3} g} + \underset{\text{IV}}{f_c \varepsilon_{ij3} U_j} \underset{\text{V}}{- \frac{1}{\rho}\frac{\partial p}{\partial x_i}} + \underset{\text{VI}}{\frac{1}{\rho}\frac{\partial \tau_{ij}}{\partial x_j}} \tag{2.1}$$

where i,j = 1,2,3 and $\varepsilon_{ij3} = +1$ if ij3 = 123 and = -1 if ij3 = 213; $\varepsilon_{ij3} = 0$ if i = j (alternating unit tensor) and $\delta_{i3} = +1$ if i = 3, otherwise it is 0 (Kronecker delta). The terms on the left-hand side represent the time rate of change of the wind velocity (i.e. acceleration) following a moving fluid element: the first contribution (term I) is the time rate of change at a fixed point (local derivative), while the second term (term II, advection) is the time rate of change due to the movement of the fluid element from one location to another in a flow field where the flow properties are spatially different. The terms on the right-hand side represent the sum of forces (per unit mass) acting on a fluid particle. They are body forces (term III, due to gravity and acting only vertically), Coriolis force (term IV, an apparent force due to the earth rotation, f_c is the Coriolis parameter), pressure-gradient forces (term V) and viscous forces (terms VI).

To a close approximation, air in the atmosphere behaves like a Newtonian fluid (viscous stresses are proportional to the velocity gradients), so that, by assuming incompressibility, the term VI reduces to:

$$\text{Term VI} = \frac{1}{\rho}\frac{\partial \tau_{ij}}{\partial x_j} \rightarrow \nu \frac{\partial^2 U_i}{\partial x_j^2} \tag{2.2}$$

$$\text{being: } \nu = \frac{\mu}{\rho} \text{ the kinematic viscosity and } \tau_{ij} = \mu\left(\frac{\partial U_i}{\partial x_j} + \frac{\partial U_j}{\partial x_i}\right) \tag{2.3}$$

The horizontal pressure gradient term (V) can be expressed by using the definition of geostrophic wind:

$$f_c U_g = -\frac{1}{\rho}\frac{\partial p}{\partial y} \quad \text{and} \quad f_c V_g = +\frac{1}{\rho}\frac{\partial p}{\partial x} \tag{2.4}$$

So that the horizontal equations of motion can be written as:

$$\underbrace{\frac{dU}{dt}}_{\text{I+II}} = \underbrace{-f_c\left(V_g - V\right)}_{\text{IV+V}} + \underbrace{\nu\frac{\partial^2 U}{\partial x_j^2}}_{\text{VI}} \tag{2.5}$$

$$\underbrace{\frac{dV}{dt}}_{\text{I+II}} = \underbrace{+f_c\left(U_g - U\right)}_{\text{IV+V}} + \underbrace{\nu\frac{\partial^2 V}{\partial x_j^2}}_{\text{VI}} \tag{2.6}$$

where the terms IV+V are sometimes called the geostrophic departure terms because they are zero when the actual winds are geostrophic.

Then, the wind velocity can be expanded into mean and fluctuating components. It is remarkable that, due to the non-linearity of the equations, unknown terms arise even in the equations of the mean fluid motion (equations (2.7)). They are the Reynolds stresses. Physically, this implication means that turbulence must be considered in making forecasts in the turbulent boundary layer, even if only mean quantities are of interest. The following forecast equation for mean wind is formally very similar to the basic conservation equation (2.1) except for the addition of the turbulence term at the end (VII):

$$\underset{\text{I}}{\frac{\partial \overline{U_i}}{\partial t}} + \underset{\text{II}}{\overline{U_j}\frac{\partial \overline{U_i}}{\partial x_j}} = \underset{\text{III}}{-\delta_{i3} g} + \underset{\text{IV}}{f_c \varepsilon_{ij3} \overline{U_j}} - \underset{\text{V}}{\frac{1}{\rho}\frac{\partial \overline{p}}{\partial x_i}} + \underset{\text{VI}}{\nu \frac{\partial^2 \overline{U_i}}{\partial x_j^2}} - \underset{\text{VII}}{\frac{\partial \left(\overline{u_i' u_j'}\right)}{\partial x_j}} \tag{2.7}$$

In order to solve the problem, the unknown Reynolds stresses must be somehow specified (closure problem).

Mean wind profile

Some simplifying assumptions are introduced in meteorology, in order to develop analytical expressions of the mean wind profile throughout the whole depth of the boundary layer, including the Coriolis force (Stull, 1988):

- steady state (→ $\partial\overline{(\ )}/\partial t = 0$, i.e. no time-dependence);
- horizontal homogeneous flow, as it happens in large-scale storms, on a horizontal site of uniform roughness over a sufficiently large fetch (→ $\partial\overline{(\ )}/\partial x = 0, \partial\overline{(\ )}/\partial y = 0$, i.e. no advection);
- barotropic flow, i.e. negligible horizontal density gradient (→ constant geostrophic wind);
- geostrophic approximation (→ the curvature of the isobars is negligible);
- no subsidence (→ the mean vertical wind component is zero).

In these conditions, the equations of mean motion reduce to (Stull, 1988):

$$0 = f_c \overline{V} - \frac{1}{\rho}\frac{\partial p}{\partial x} + \frac{1}{\rho}\frac{\partial \tau_x}{\partial z} \quad \rightarrow \quad 0 = -f_c\left(\overline{V_g} - \overline{V}\right) + \frac{1}{\rho}\frac{\partial \tau_x}{\partial z} \tag{2.8}$$

$$0=-f_c\overline{U}-\frac{1}{\rho}\frac{\partial p}{\partial y}+\frac{1}{\rho}\frac{\partial\tau_y}{\partial z} \quad\rightarrow\quad 0=+f_c\left(\overline{U_g}-\overline{U}\right)+\frac{1}{\rho}\frac{\partial\tau_y}{\partial z} \tag{2.9}$$

where τ_x and τ_y are the horizontal shear stresses, including both contributions from viscous forces and Reynolds stresses. $\overline{U}$ and $\overline{V}$ are the components of the mean wind. For convenience, it is chosen a reference system with the x-axis aligned with the direction of gradient wind G:

$$-\overline{V}f_c=+\frac{1}{\rho}\frac{\partial\tau_x}{\partial z} \tag{2.10}$$

$$f_c\left(\overline{U}-G\right)=\frac{1}{\rho}\frac{\partial\tau_y}{\partial z} \tag{2.11}$$

where:

$$G=\sqrt{U_g^2+V_g^2} \tag{2.12}$$

The boundary conditions are:

$$z=0 \quad\rightarrow\quad \overline{U}=\overline{V}=0 \tag{2.13}$$

$$z\rightarrow\infty \quad\rightarrow\quad \overline{U}\rightarrow G,\ \overline{V}\rightarrow 0 \ \text{ and } \ \tau_x,\ \tau_y,\ \frac{\partial\tau_x}{\partial z},\ \frac{\partial\tau_y}{\partial z}\rightarrow 0 \tag{2.14}$$

Meteorologists have attempted to solve equations (2.8) and (2.9) by introducing phenomenological relations to describe the shear stresses τ_x and τ_y.

A well-known assumption (Schlichting, 1960) is that an eddy viscosity K and a mixing length L may be defined, so that (first-order local closure K-theory):

$$\frac{\tau_x}{\rho}=-K\frac{\partial\overline{U}}{\partial z} \ \text{ and } \ \frac{\tau_y}{\rho}=-K\frac{\partial\overline{V}}{\partial z} \tag{2.15}$$

where:

$$K(x,y,z)=L^2(x,y,z)\left[\left(\frac{\partial U}{\partial z}\right)^2+\left(\frac{\partial V}{\partial z}\right)^2\right]^{1/2} \tag{2.16}$$

Either the eddy viscosity K or the mixing length L must be specified. An analytical solution of the equations (2.8) and (2.9) can be obtained under the assumption of a constant eddy viscosity (Ekman, 1905). That is the Ekman spiral model:

$$\overline{U}(z)=G\left[1-e^{-\gamma_E z}\cos\left(\gamma_E z\right)\right] \tag{2.17}$$

$$\overline{V}(z)=G\left[e^{-\gamma_E z}\sin\left(\gamma_E z\right)\right] \tag{2.18}$$

where $\gamma_E = (f_c/2K)^{1/2}$, and $f_c = 2\Omega\sin\phi$ is the Coriolis parameter (ϕ = latitude, Ω = angular velocity of Earth rotation). The wind speed is geostrophic at height $z = \pi/\gamma_E$. This height is used as an estimate of the depth of the neutral boundary layer. Hence, the Ekman layer depth can be defined as $h = \pi/\gamma_E$.

A different type of approach, based on the asymptotic similarity theory, is developed in Csanady (1967). The boundary layer is divided in two regions: a surface layer and an outer layer. The theory is based on the attempt to express the profile of wind velocity as a function of height in non-dimensional form. This poses the problem of finding appropriate velocity and length scale parameters. It turns out that for the velocity, anywhere in the height range considered, the velocity scale parameter is the friction velocity u_*. In the case of the height scale, in the lower layer, close to the ground, the appropriate parameter is the roughness length z_0, while in the upper layer it is the gradient height h. The law of the wall describes the flow in the surface layer, while a velocity defect law applies in the outer layer.

The key to solve the problem lies in the assumption that a region of overlap exists, in which both laws are valid. It results in a logarithmic solution. Out of it, the gradient wind velocity can be calculated (Gill, 1968; Monin&Yaglom, 1971). It depends on two universal constants A and B:

$$G = \left[B^2 + \left(\ln \frac{u_*}{f_c z_0} - A \right)^2 \right]^{1/2} \frac{u_*}{k} \tag{2.19}$$

Several authors proposed values for A and B, as listed in Simiu&Scanlan (1996). It can be considered 0 < A < 2.8 and 4.3 < B < 5.3.

A similar approach, based on a modified version of the asymptotic similarity theory, was developed by Harris&Deaves (1980). The peculiar feature of the so-called H&D model is the closure assumption to solve the equations of motion (2.8) and (2.9): the shear stresses are assumed to decrease parabolically with height (equation (2.20)). Some justification for this assumption was found by the authors in full-scale data, but it is also justifiable on theoretical grounds, on the basis of an order of magnitude analysis between production, diffusion and dissipation of turbulent energy (Deaves, 1981).

$$\tau(z) = \rho u_*^2 \left(1 - \frac{z}{h} \right)^2 \tag{2.20}$$

This expression is adopted by the ESDU Data Items (ESDU 85020).

Accordingly, the velocity defect law is parabolic for a substantial part of the boundary layer, so that:

$$\overline{U}(z) = \frac{1}{k} u_* \left\{ \ln \frac{z}{z_0} + a_1 \frac{z}{h} + a_2 \left(\frac{z}{h} \right)^2 + a_3 \left(\frac{z}{h} \right)^3 + a_4 \left(\frac{z}{h} \right)^4 \right\} \tag{2.21}$$

where z_0 is the roughness length, h is the atmospheric boundary layer thickness, u_* is the friction velocity and *k* the Von Karman constant ($k = 0.4$). The coefficients a_i, i = 1, ..., 4 are universal constants whose values are determined theoretically, in terms of two experimental parameters: β and A. From fitting a number of good quality wind profiles, it resulted $\beta = 6$ and $A = -1$ (Harris&Deaves, 1980). So that:

$$a_1 = 2(\ln \beta - A) + \frac{1}{6} \approx 5.750 \quad a_2 = 1 - \frac{a_1}{2} = -1.875 \quad a_3 = -\frac{4}{3} \quad a_4 = \frac{1}{4} \tag{2.22}$$

The H&D model thus extends the log-law (which fits good near the surface) through the Ekman layer, in order to blend into the gradient wind velocity at the gradient height. Indeed, if compared to both the well-known logarithmic and power laws, the Harris and Deaves model is the only one which recognizes the top of the atmospheric boundary layer.

It is known that the boundary layer height (h) in neutral atmosphere is proportional to the ratio between the friction velocity and the Coriolis coefficient (Csanady, 1967). In the H&D model such proportionality is expressed by the coefficient 1/β:

$$h = \frac{1}{\beta}\frac{u_*}{f_c} \tag{2.23}$$

In order to give an idea of the boundary layer height, at a latitude ϕ = 30° it results h ≈ 4300 m, being $z_0 = 0.05$ m, $V_b = 25$ m/s (at 10 m). Thus, the Deaves and Harris model has three scaling parameters: z0 and u* – inherited from the log-law model – and the additional length parameter, h, which is the atmospheric boundary layer height. It is a function of the wind speed, the surface roughness and also the latitude.
Then, by evaluating the H&D wind profile at z = h, the gradient wind speed is given by:

$$G = \frac{1}{k} u_* \left\{ \ln \frac{u_*}{f_c z_0} - A \right\} \tag{2.24}$$

This expression is comparable with equation (2.19), but the universal constants have different values. The same letter A is used in expressions (2.19) and (2.24), because this is the traditional nomenclature reported in the literature on this topic. This should not create confusion. Finally, by using the closure assumption (2.20) and by applying the boundary conditions to the equations of motion, the H&D model derives the following relationship involving ϑ_0, the total (maximum) angle of turn of the wind throughout the boundary layer:

$$\frac{G \sin \vartheta_0}{u_*} = 2\beta = 12 \tag{2.25}$$

The model also suggests to use above the Prandtl layer a linear variation with height of the wind rotation angle. In fact, the variation of the wind angle would result from the solution of partial differential equations, but a linear approximation can be accepted.
In conclusion, relying on the closure assumption (2.20) – derived by an order-of-magnitude analysis – on the boundary conditions, on theoretical considerations and two constants (A and β) determined empirically, the H&D model gives a complete description of the mean flow in the atmospheric boundary layer (equation (2.21))[1]. However, this is valid at mid-latitudes, where a state of dynamic equilibrium establishes in strong wind conditions, so that the energy subtracted by the mean flow exactly balances that absorbed by the work done against surface friction and dissipated by the viscosity of air (Harris&Deaves, 1980). At tropical latitudes, strong winds are associated with large scale storms, but these may contain intense components of thermal origin. Moreover, the geostrophic assumption is more approximated as the Coriolis force becomes small. To which extent the H&D model is valid at small latitudes is addressed in section 2.3.3.

Standard deviation of the along-wind component σ_u

The H&D model also provides an analytical expression of the standard deviation σ_u of the along-wind component of turbulence at any height in the atmospheric boundary layer, that is valid over uniform flat terrain. On theoretical grounds, it has been seen that for a flow – which is fully in equilibrium with the surface – σ_u / u_* starts from a constant value near the surface and approximately constant within the inner layer, then it achieves a maximum before decreasing linearly with height. At large heights, it is (Harris&Deaves, 1980):

$$\frac{\sigma_u(z)}{u_*} \propto 1 - \frac{z}{h} \tag{2.26}$$

An empirical expression proposed in the H&D model, which matched the data set available to the authors, is:

---

[1] In the following, the horizontal superscript which distinguishes the mean velocity component $\overline{U}$ from the total velocity in the along wind direction $U = \overline{U} + u'$ is neglected, in order not to burden the treatment. Therefore, in the following it is normally referred to U_m as the mean wind velocity.

$$\frac{\sigma_u(z)}{u_*} = \frac{7.5\left[1-\frac{z}{h}\right]\left\{0.538+0.09\ln\left(\frac{z}{z_0}\right)\right\}^{\left[1-\frac{z}{h}\right]^{16}}}{1+0.156\ln\left(6\frac{h}{z_0}\right)} \tag{2.27}$$

This expression is adopted by the ESDU Data Items (ESDU 85020).

Integral length scales of turbulence

Harris and Deaves also propose an expression for the integral length scale of the longitudinal component of turbulence L_{ux}, which is adopted by the ESDU Data Items (ESDU 85020 and 86010). The length scale increases with increasing height above the ground up to a maximum value. Also, for a given height, it increases with increasing wind speed and surface roughness. As the wind strength increases, the boundary layer height increases and the eddies within the boundary layer are stretched accordingly. Moreover, apart from low levels close to the ground, the longitudinal length scale in the boundary layer is generally twice the value of the lateral scale.

The starting point to develop the H&D model of L_{ux} is to match the well-established Kolmogorov and Von Karman spectrum formulas (Harris and Deaves, 1980). For turbulent flows in which an equilibrium range exists (i.e. at high Re), the Kolmogorov formula for the high frequency range of the spectrum is:

$$nS(z,n) = K_0(\varepsilon U)^{2/3} n^{-2/3} \tag{2.28}$$

being K_o the Kolmogorv parameter.

The Von Karman form of the spectrum for the longitudinal component of turbulence is:

$$\frac{nS(z,n)}{\sigma_u^2} = \frac{4\frac{L_{ux}n}{U}}{\left(1+70.8\left(\frac{L_{ux}n}{U}\right)^2\right)^{5/6}} \tag{2.29}$$

At high frequencies, it reduces to:

$$\frac{nS(z,n)}{\sigma_u^2} = A\left(\frac{L_{ux}n}{U}\right)^{-2/3} \tag{2.30}$$

being A = 0.115.

By combining the Von Karman spectrum at high frequencies and the Kolmogorov formula, it is obtained:

$$L_{ux} = \left(\frac{A}{K_o}\right)^{3/2} \frac{\sigma_u^3}{\varepsilon} \tag{2.31}$$

This result is completely independent of the H&D model, which only becomes involved when the variation with height of the standard deviation σ_u (according to equation (2.27)) and the dissipation ε (using equation (2.32)) are introduced. The dissipation can be approximated by:

$$\varepsilon \cong \frac{\tau}{\rho}\frac{dU}{dz} \tag{2.32}$$

Moreover, two further questions are discussed in the H&D model, through the investigation of experimental data:

1. If autocorrelations and spectra are both derived from field measurements, the length scales derived by the integration of the autocorrelation functions are generally greater than the length scales required in the Von Karman formula to fit the measured spectral density data. It is due to the inadequacy of the Von Karman spectrum to represent the characteristic of turbulence closely at all frequencies. The disparity between length scales is a factor of around 1.4, but it decreases with height. A modification to the coefficient A = 0.115 in the formula of the spectrum is then suggested and adopted in (ESDU, 85020):

$$A = 0.115\left[1 + 0.315\,(1 - z/h)^6\right]^{2/3} \tag{2.33}$$

2. Due to anisotropy of turbulence near the ground, the Kolmogorov parameter should vary with height up to a constant value at sufficiently high altitude. An empirical relationship, based on a re-analysis of data by (Thompson, 1990), is defined by equation (2.34) (ESDU, 85020):

$$K_0(z) = 0.19 - \left(0.19 - \frac{0.39}{Ro^{0.11}}\right)\exp\left[-24Ro^{0.155}\left(\frac{z}{h}\right)^{1.24Ro^{0.008}}\right] \tag{2.34}$$

where Ro is the Rossby number ($Ro = u_* / f_c z_0$). By combining equations from (2.31) to (2.34), the expression of the integral length scale of turbulence L_{ux} is thus obtained. Even though the H&D model of L_{ux} is adopted by the ESDU Data Items, it leads to values of the integral length scale which are larger than those recommended in other Codes of practice (e.g. Eurocodes). As a consequence, if the H&D model of L_{ux} is used in the calculations in place of the expressions recommended by other Codes (in case extrapolated at high altitudes), it results that the quasi-static loading is slightly increased, while dynamic loading is decreased.

Cross-correlation functions and cross-spectral densities of wind turbulence

The cross-correlations functions characterize the relationship between fluctuating velocity components at two points in space and in the general case at different times (time lag τ). The zero-lag cross correlations are especially important since they describe how the instantaneous fluctuating component of wind velocity varies in space. Because changes in the gust velocity at one point are not necessarily reflected immediately by similar changes in the gust velocity at another point, the cross-correlation functions are, in general, not symmetrical functions of τ. They can be considered to be composed of two components, the larger one being a symmetrical function of τ and the other being an anti-symmetrical function of τ. Once they are split up in the frequency domain, they are the Fourier transforms of the real (in-phase) and the imaginary (out-of-phase) components of the cross-spectral density. These are the co-spectral density and the quad-spectral density functions, respectively, and are related by the phase-lag angle. The latter is sometimes expressed in terms of an “eddy slope” (ESDU 86010). For most cases, the quad-spectra are small and often neglected, so that the coherence equals the co-coherence. Moreover, the out-of-phase component integrates to zero.

For points having a spatial separation Δx in the along-wind direction, if the assumption of frozen turbulence applies (Taylor's hypothesis), Δx can be converted into an equivalent time lag Δx/U, being U the mean velocity of the flow. In this case, the coherence function would be 1 and the phase angle $\theta = 2\pi n \Delta x / U$. In practice, Taylor's hypothesis is not always strictly applicable (particularly near the ground, when U/n is greater than 300 m, according to an ESDU 86010 recommendation).

The phase angle for separations normal to the wind direction can be taken as zero in the horizontal plane (lateral direction). Instead, for separations in the vertical directions the eddies are inclined with the mean wind shear, so that changes in the gust component higher up are followed by similar changes lower down at some time later. Thus, in general, the phase angles θ_{uu} and θ_{vv} (for the u- and v- wind components) are not zero. They are zero, no matter the value of z and Δz, only in case of isotropic turbulence. This applies to the high frequency range when, even near the ground, turbulent exhibits isotropic properties. However, θ_{uu} and θ_{vv} tend to zero as z increases and dU/dz tends to zero. Because of that, the ESDU 86010 provides the following formulas for the phase angles θ_{uu} and θ_{vv}:

$$\theta_{uu}\{\Delta z\} = \left(1.3\Delta z / z_m\right)(c-1)^{0.7}\left(2\pi n \Delta z / U_m\right) \tag{2.35}$$

$$\theta_{vv}\{\Delta z\} = \left(3\Delta z / z_m\right)(c-1)^{0.7}\left(2\pi n \Delta z / U_m\right) \tag{2.36}$$

where c is a frequency-dependent coefficient defined in the code, that varies between 2 (low frequencies) and 1 (high frequencies). The factors $1.3\Delta z/z_m$ and $3\Delta z/z_m$ are estimations – on the basis of different sources of data up to about 80 m – of the eddy slope for the u and v components.

The H&D model (ESDU Data Items) and other codes: comparison of wind profiles

For purpose of comparison, the H&D model – adopted by the ESDU Data Items and applicable throughout the whole height of the boundary layer – is compared to the extrapolations of the log- and power- law models, adopted by Eurocode and DIN. Rigorously, these would be limited to 200 m and 300 m, respectively. The dependence on latitude is included in the H&D model.

The following case studies are selected:

- terrain category II (z_0 = 0.05 m)

- $V_b(10\text{m}) = 25$ m/s
- Latitude $\phi = 30°, 23°$.

In these conditions, according to the Eurocode (up to 200 m), it is:

$$U_m(z) = V_b\, 0.19 \ln\left(\frac{z}{z_0}\right) \tag{2.37}$$

$$I_u(z) = \frac{1}{\ln\left(\frac{z}{z_0}\right)} \tag{2.38}$$

$$L_{ux}(z) = 300\left(\frac{z}{200}\right)^{0.67 + 0.05\ln(z_0)} \tag{2.39}$$

According to the DIN-EN (up to 300 m), it is:

$$U_m(z) = V_b\left(\frac{z}{10}\right)^{0.16} \qquad I_u(z) = \left(\frac{z}{10}\right)^{-0.16} \qquad L_{ux}(z) = 300\left(\frac{z}{300}\right)^{0.26} \tag{2.40}$$

All the previous models neglect the variation of air density with height. In Backström et al. (2008) the following expression is proposed:

$$\rho(z) = \rho_0 \frac{22000 - z}{22000 + z} \tag{2.41}$$

where $\rho_0 = 1.25$ kg/m^3.

As shown in Figure 2.4, the profiles of mean wind and turbulence intensity recommended by the Codes do not differ significantly at low heights. The H&D model predicts much larger integral scales. This issue is further commented by Harris (1986), because the large values imply, from the structural point of view, an increase in the quasi-static response and a decrease in the dynamic response. The question about the representativeness of such large values is still open today.

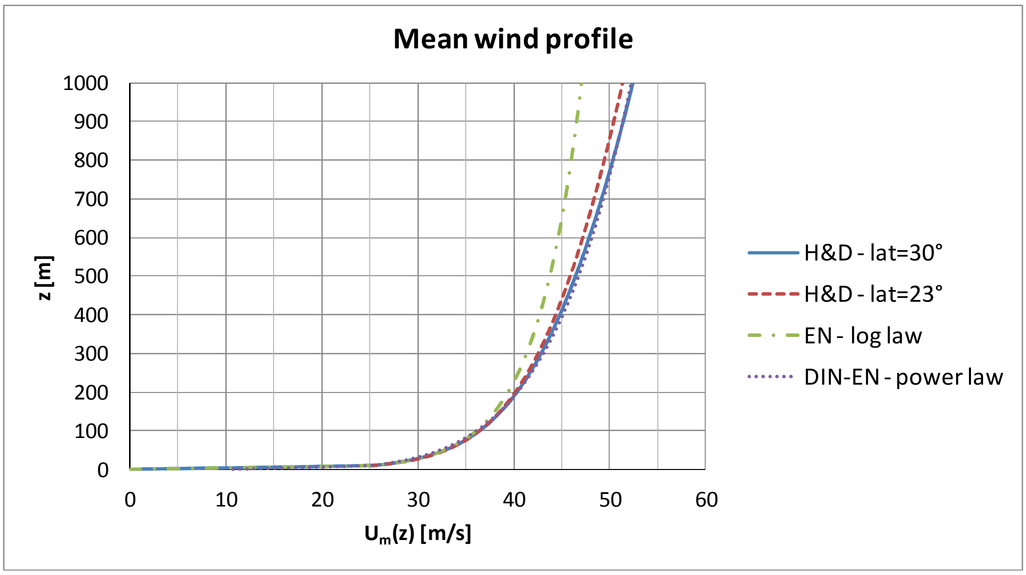

Figure 2.4 Mean wind profile: ESDU, EN, DIN-EN

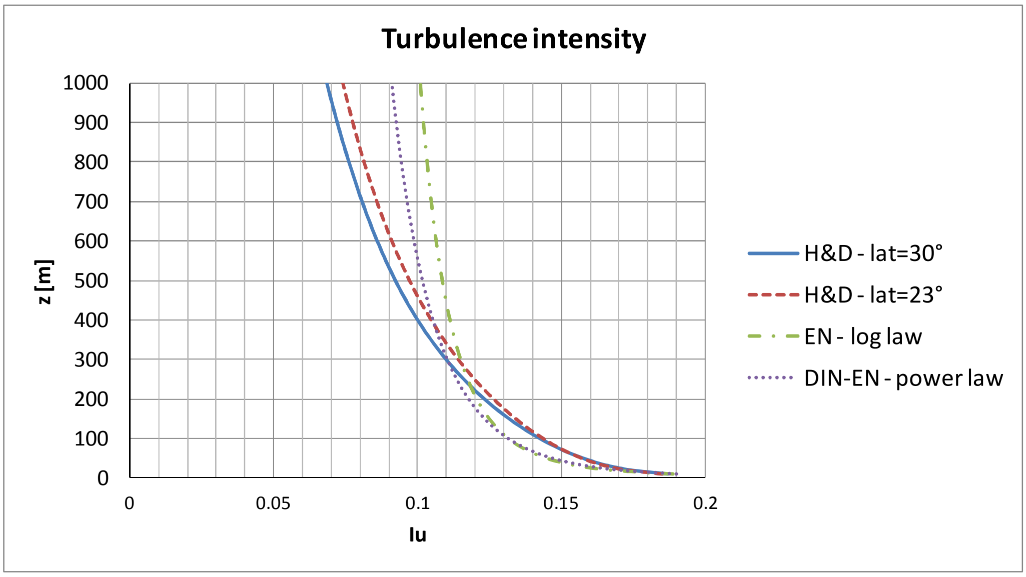

Figure 2.5 Turbulence intensity: ESDU, EN, DIN-EN

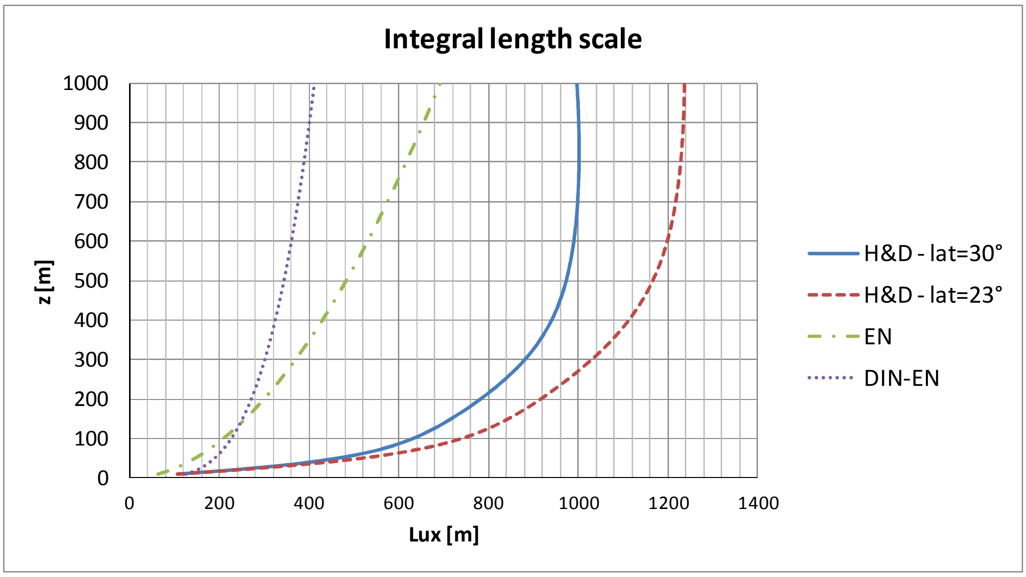

Figure 2.6 Integral length scale: ESDU, EN, DIN-EN

2.3.2 Experimental and numerical investigation of the ABL

Up to around 300 m, wind velocities can be accurately measured at sufficiently high frequency resolution (for example by means of anemometers on high towers, Figure 2.7). Therefore, the structure of wind turbulence up to that level is deeply investigated in literature (Peil et al., 1990, 1992, 1996; Clobes et al., 2009; Clobes&Willecke, 2009).

Figure 2.7 Gartow tower (344 m) equipped with anemometers (picture from http://www.is.tu-braunschweig.de/)

As briefly mentioned in the previous section concerning strong wind conditions, there are still many open problems in the nature of wind at large heights. Recommendations of the Codes of practice are usually limited to 200-300 m. The ESDU Data Items provide profiles which are valid up to the boundary layer height, but there is considerable uncertainty in many parameters, for example the integral length scales of turbulence. Moreover, in light wind conditions the mean wind profile can assume different shapes and no information is currently codified for the designer of super-tall structures. Further investigation in the Ekman layer is thus needed. This section aims at providing an overview of the technologies which are available nowadays to investigate the atmospheric boundary layer at large heights.

Field experiments at large heights

Above 300 m, no experimental evidence is currently available for the purpose of structural wind engineering. It does not mean that no experimental evidence is available at all. In fact, measurements are usually performed at large heights (1000-1500 m) by meteorologists. However, for structural design, specific requirements should be fulfilled:

- sufficiently high frequency resolution, in order to measure turbulence fluctuations;
- spatial averages over big volumes should be avoided;
- relatively small distance between simultaneous measuring points, to calculate cross-correlations.

With regard to the design in the ultimate limit state, only the shear production of turbulence (due to surface friction) and not the buoyancy forces arising from convective motions and thermal stratification of the atmosphere should be considered. It corresponds to neutral stratification of the atmosphere. In these conditions, the scatter of data due to the thermal effects is much reduced, so that a more defined pattern can be evaluated (e.g. power- or log- law for the mean wind profile). Moreover, in the ideal condition of neutral atmosphere, wind is a stationary random process, in the sense that statistics are invariant with time. Instead, thermal effects, convective motions of the atmosphere and buoyancy production of turbulence play a role in light wind conditions. This is a wide field of research in meteorology. For this reason, the instruments that have been used since long time ago to measure wind at large heights are normally required to work only in light wind conditions.

For example, measurements with balloons and aircrafts are possible even at high altitudes. Examples of airborne measurements are reported in Figure 2.8 and Figure 2.9. Such aircrafts do not fly if the wind speed is higher than 10 m/s. In fact, accuracy of these measurements depends on the relative velocity of the aircraft and the wind speed, and it is much affected if they are of the same order.

Balloons represent a less expensive technique than aircrafts for atmospheric investigation. They can be tethered or free balloons. Measurements can be performed either along the vertical while the balloons are flying up, at a fixed point if they are tethered or in the mean wind direction, as they are transported by the flow. Kites are another choice. Again, the use of these instruments by meteorologists is only limited to light wind speeds.

Figure 2.8 Aircraft measurement during the field campaign in Emden, Germany, 2008 (Kroonenberg v.d., 2009)

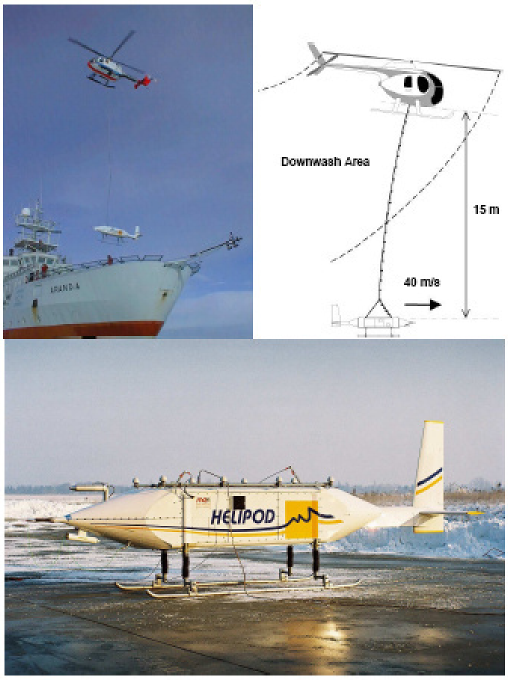

Figure 2.9 Turbulence probe Helipod, field campaign in the Baltic sea (Bange, 2007)

The type of measurements described above fall in the broad category of in-situ sensors, because the sensing instrument (mounted either on towers, aircraft or balloons) lies in the probe volume. Another category is that one of remote sensing instruments. They can be mounted at ground level, on aircrafts or even on satellites. Their peculiarity is that they do not have a sensing element within or around the volume of interest. They infer atmospheric properties through their effects on acoustic, microwave and optical signals propagation through the air. They can be classified into three main groups:

- acoustic waves are used by SODARs (Sonic Detecting And Ranging)
- light waves are used by LIDARs (Light Detecting and Ranging)
- radio waves are used by RADARs (RAdio Detecting And Ranging)

The wind speed is measured through the doppler effects (in fact, the proper names of the instruments would be doppler-SODAR, doppler-LIDAR, doppler-RADAR). The doppler effect consists in the change of frequency between the emitted signal (known and fixed) and the returned signal. The latter depends on the velocity of the air particles which scatter the signal back. This shift in phase is the necessary information to calculate the velocity of air particles, that is the wind velocity.

Figure 2.10. Movable mono-static Doppler SODAR with three antennas for the measurements of mean wind and turbulence profiles (Emeis, 2010)

Some SODAR campaigns have been recently performed (e.g. Tamura et al., 2007), but results are only available for the mean wind up to 500 m. In fact, the main limit of SODARs is that they measure over an averaging time of several minutes (e.g. 30) and the resolution of measurements decreases with height. Thus, it is not possible to have good results above 400-600 m. This height decreases as the wind speed increases, because the backscattered signal tends to be displaced away from the receiver by the wind itself.

RADARs are not addressed in this context since their resolution of wind measurements is low for the scopes of structural engineers. The reason is that the radio wave is not so well aligned. Instead, conceptually similar but much more focused and precise is the light wave used by LIDARs. High frequency measurements are possible with these instruments, thanks to the high speed of light. Moreover, atmosphere can be investigated up to some kilometers, even if with a decreasing resolution as height increases.

Turbulence measurements using lidars are still a subject of research and the method of analysis of data is not fully established, yet. An attempt to answer the question “Can the available wind lidars measure turbulence?” has been recently presented in Sathe et al. (2011).

Conical scanning is the usual mode of operation of a wind LIDAR (see Figure 2.11), in order to measure vertical profiles of the three-dimensional wind vector. In fact, as the signal sweeps around the conical surface, at each altitude several measurements around the circumference are available. They are all needed to provide information about the wind speed at the circumference centre. However, as the height increases, the radius of the circumference increases, so that big horizontal distances are swept at high altitudes, providing information for wind speed only at the circumference centre.

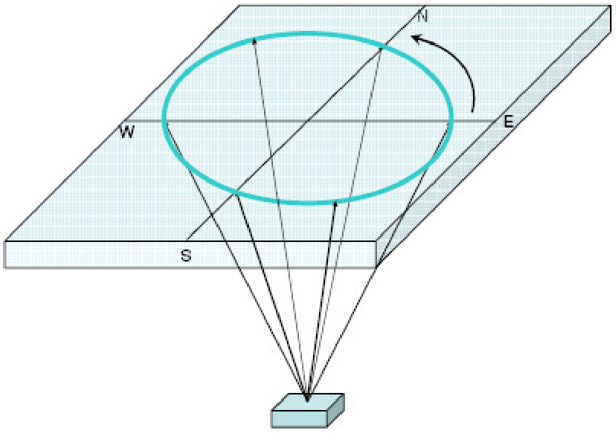

Figure 2.11 Conical scanning pattern of a wind LIDAR in order to measure profiles of the three-dimensional wind vector (Emeis, 2010)

Usually, the signal is transmitted in pulses (Range-resolved remote sensing systems), which are then scattered by atmospheric inhomogeneities or suspensions (e.g., aerosol, droplets), sending a small fraction of the transmitted energy back to the receiver. Distance to the measurement volume is determined by the time of flight of the signal pulse. The state of the art of LIDAR techniques for wind and turbulence measurements by using signal delay for range determination is given by Hardesty & Darby (2005) and Davies et al. (2003). An important point is the spatial resolution, i.e. the volume on which the measured wind speed is averaged. If the signal is sent in pulses in a certain direction, the spatial resolution is related to the distance swept by the pulse in the time interval. Due to the high speed of light, it is in the order of tens of meters (see Figure 2.12). Such a spatial average over big volumes is sometimes useful, for example for applications in the field of wind turbines (Emeis et al., 2007; Mikkelsen et al., 2008). In fact, the average volume is in the order of the volume swept by a blade of a wind turbine, thus it is some good information to design the rotor.

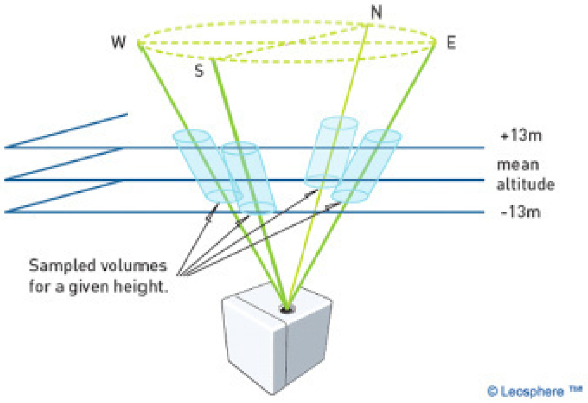

Figure 2.12 Sketch of the operation principle of the Leosphere Windcube (Waechter et al., 2009)

A transportable continuous-wave wind LIDAR (Figure 2.14) has been recently designed and built (Emeis, 2010). The system emits a continuous-wave beam, so that detection of the wind speed at a given range is achieved by focusing, rather than by the time-of-flight method of pulsed systems (range determination by beam focusing). The system cannot distinguish between air motion towards and away from the LIDAR, and this leads to an ambiguity of 180° in the derived value of wind direction. This is easily resolved, however, by making reference to a simple wind direction measurement at a height of a few meters. The profile of the three-dimensional wind vector is yielded by scanning a cone with a 30° half angle once per second (Banakh et al. 1995, Emeis et al. 2007a, Kindler et al. 2007). Hence the diameter of the measured volume is 173 m at a height of 150 m. The probe length increases roughly as the square of the height. As an example, the vertical resolution is ~ ± 10 m at a height of 100 m. Strong reflections from particles and other moving objects outside the focal range (e.g. due to smoke, fog or birds) can lead to spurious Doppler returns (Harris et al. 2001), but these effects can be recognized and mitigated by signal processing techniques.

Figure 2.13 Small pulsed Doppler wind LIDAR for measurement of wind profiles in a height range between 40 and 200 m. Distance determination by pulse travel time (Emeis, 2010)

Figure 2.14 Small continuous-wave Doppler wind LIDAR for measurement of wind profiles in a height range between 10 and 200 m. Distance determination by beam focusing (Emeis, 2010)

Within the context of this dissertation, field measurements have not been available. Moreover, the concern in the Thesis is mainly on strong wind conditions, which so far have never been investigated in any experiment. However, the field of research on full-scale wind measurements at large heights is currently very active and in rapid development. For example, sophisticated mathematical models are being developed to manage the major and unavoidable problem of spatial average as the height increases (see Emeis, 2010).

Numerical simulations of the atmospheric boundary layer

Numerical simulations of the atmospheric boundary layer are an alternative and a support to field measurements. For example, Canadillas (2010) presents the investigation of the marine boundary layer by means of a PArallelized Large eddy simulation Model (PALM Code), developed at the Institute of Meteorology and Climatology of the Leibniz University of Hannover (Raasch&Etling 1991, 1998 and Raasch&Schröter, 2001). Examples of results achievable with LES are reported in Figure 2.15 and compared to field data (Canadillas, 2010). In this case, the simulation is performed in neutrally stratified conditions of atmosphere. Such conditions are often achieved in the marine boundary layer even at low wind speeds (the ocean surface and the air flowing above it nearly have the same temperature), so that a comparison with field data can be made. However, these well-defined meteorological conditions (no large-scale advection, homogeneous surface, stationary conditions), like over the sea, should not be easily expected over land on heterogeneous terrain, so that such a comparison with observations is generally extremely difficult.

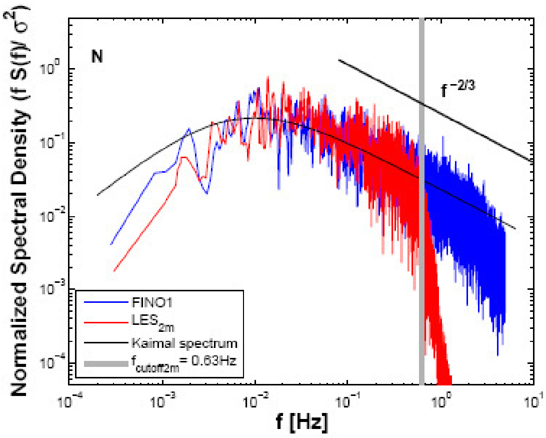

Figure 2.15 Normalized one-dimensional spectra of the horizontal wind velocity fluctuations: comparison between LES simulation of the marine boundary layer (red) and field data (blue) (Canadillas, 2010)

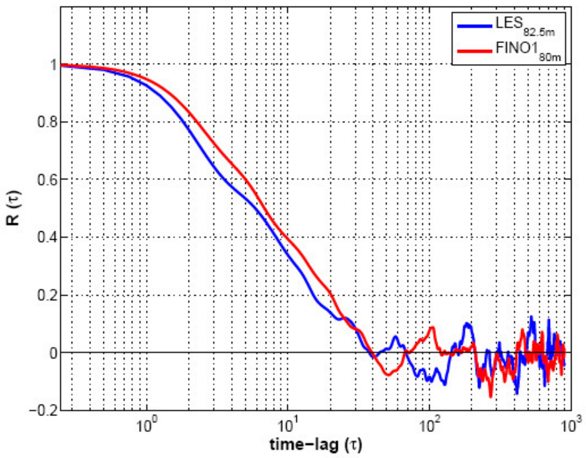

Figure 2.16 Autocorrelation function for the horizontal wind velocity fluctuations: comparison between LES simulation of the marine boundary layer (red) and field data (blue) (Canadillas, 2010)

2.3.3 The Coriolis force

An analytical expression of the Ekman spiral was previously described (equation (2.17)) and a useful approximation to define angle of turn of the mean wind profile is included in the H&D model (equation (2.25)). However, two further questions need some attention:

1) which is the effect of the Coriolis force on turbulence;
2) which model should be used in tropical regions, where the Coriolis force is small (and becomes zero at the equator). In fact, the H&D model is a mid-latitude model.

These questions are addressed in the following.

The Coriolis force in the equations for turbulent departures

Equations for mean variables in turbulent flow have been previously introduced. In particular, equation (2.7) expresses the conservation of momentum. Turbulent departures of the variables are the deviations from their respective means. The equations for the variance of the wind speed are obtained by expansion of the momentum conservation equation and subtraction of the mean part. Such equations contain the local storage of variance, the advection of variance by the mean wind, the buoyancy production, the shear production, the turbulent transport term describing how variance is moved around by the turbulent eddies, the pressure redistribution term describing how variance is redistributed by pressure perturbations and the viscous dissipation term. The Coriolis term, instead, is identically zero for velocity variances (Stull, 1988).

Phisically, this means that Coriolis force cannot generate turbulence kinetic energy. The Coriolis term merely redistributes energy from one horizontal direction to another. Furthermore, the magnitude of the redistribution term is about three orders of magnitude smaller than other terms. For this reason, the Coriolis terms can be neglected in the turbulence equations, even for the cases where they are not identically zero (Stull, 1988).

The Coriolis force in tropical regions

The equations of motion, which describe all types and scales of atmospheric motions, are derived by the second Newton’s law: “the rate of change of momentum of an object referred to coordinates fixed in space equals the sum of all the forces acting”. Such forces are: the pressure gradient force, the gravitational force and friction. Moreover, since the motion in the atmosphere is usually referred to a coordinate system rotating with the Earth, the Newton’s second law can still be applied provided certain apparent forces: the centrifugal force and the Coriolis force.

The centrifugal force is the force that an object at rest experiences in a rotating system. Usually, its effects are combined with those of the gravitational force, by defining a gravity force which is everywhere directed normal to the local level. The Coriolis force is the force that a moving object (e.g. an air particle) experiences in a rotating system. Therefore, the Newton's second law for motions relative to a rotating coordinate frame – written in the notation used by Holton (1979) – is:

$$\frac{d\mathbf{V}}{dt} = -2\mathbf{\Omega}\times\mathbf{V} - \frac{1}{\rho}\nabla p + \mathbf{F}_r \tag{2.42}$$

The left-hand side represents the substantial derivative of wind flow (local + advective acceleration), while the terms on the right-hand side represent the Coriolis force, the pressure gradient force and the friction force. This is consistent with what has been described before. However, a deeper analysis is required to better understand the flow movements even at low latitudes.

If such an equation is written in spherical coordinates, being x the westward direction, y the northward direction and z the upward direction, it is (Holton, 1979):

$$\frac{du}{dt} - \frac{uv\tan\phi}{a} + \frac{uw}{a} = -\frac{1}{\rho}\frac{\partial p}{\partial x} + 2\Omega v\sin\phi - 2\Omega w\cos\phi + F_x \tag{2.43}$$

$$\frac{dv}{dt} + \frac{u^2\tan\phi}{a} + \frac{vw}{a} = -\frac{1}{\rho}\frac{\partial p}{\partial y} - 2\Omega u\sin\phi + F_y \tag{2.44}$$

$$\frac{dw}{dt} - \frac{u^2 + v^2}{a} = -\frac{1}{\rho}\frac{\partial p}{\partial z} - g + 2\Omega u\cos\phi + F_z \tag{2.45}$$

where ϕ is the latitude and a the radius of Earth.

They are the complete equations for all motions in the atmosphere. Now, let us consider the synoptic scale motions, i.e. those systems of typically several hundred kilometers in horizontal direction. Characteristic scales of the field variables based on observed values for mid-latitude synoptic systems are (Holton, 1979):

- $U \sim 10$ m/s = horizontal velocity scale
- $W \sim 10^{-2}$ m/s = vertical velocity scale
- $L \sim 10^{6}$ m = length scale
- $D \sim 10^{4}$ m = depth scale

- $\Delta p/\rho \sim 10^3$ m^2/s^2 = horizontal pressure fluctuation scale
- $L/U \sim 10^5$ s = time scale

In the free atmosphere, i.e. by neglecting friction, an order-of-magnitude analysis of the equations shows that at mid-latitude the pressure gradient force and the Coriolis force are of the same order of magnitude (10^{-3} m/s^2) and approximately in balance, while all the other terms are one or more orders of magnitude smaller. Thus, the geostrophic approximation – which describes the familiar situation in which the wind blows parallel to the isobars and the Coriolis force balances the pressure gradient force – turns to be confirmed. In other words, being U_g and V_g the horizontal components of the gradient wind, it is:

$$-f_c V_g \cong -\frac{1}{\rho}\frac{\partial p}{\partial x} \tag{2.46}$$

$$+f_c U_g \cong -\frac{1}{\rho}\frac{\partial p}{\partial y} \tag{2.47}$$

At lower altitudes, i.e. within the atmospheric boundary layer (ABL), the equations of motion are approximately a tree-way balance between the pressure gradient force, the Coriolis force and friction (see Figure 2.17 and Figure 2.18).

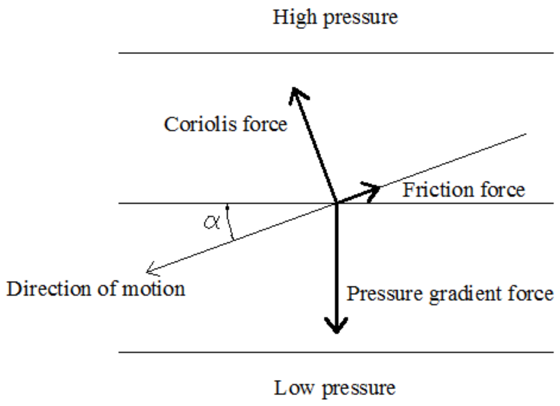

Figure 2.17 Balance of forces within the ABL at mid-latitudes

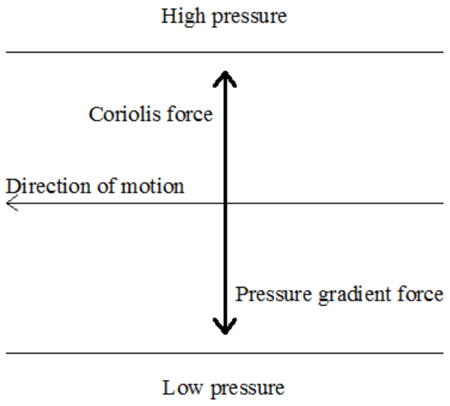

Figure 2.18 Balance of forces in the free atmosphere at mid-latitudes

If the same scale analysis of momentum equations is repeated in tropical regions, it turns out that it is not appropriate to assume that the Coriolis force term balances the pressure gradient. As the Coriolis force becomes smaller, the pressure gradient must be balanced by the inertial acceleration term. As a consequence, in order to satisfy such a balance, for synoptic scale systems in tropical regions characterized by the same horizontal length and velocity scales as in mid-latitudes, the pressure gradient force is an order of magnitude smaller than at mid-latitudes (Holton, 1979).

Although it is only a rough calculation, it is apparent that large scale motions on the so-called equatorial beta-plane, i.e. in the tropical region including the effect of variation of the Coriolis force with latitude, are much more complicated and result in wave motions involving the balance between pressure gradient forces, inertial forces and a varying Coriolis force (latitude-dependent). Unfortunately, there is not as yet a single unifying theory for tropical motions comparable to the quasi-geostrophic theory for mid-latitude motions. This matter, which was firstly posed by Matsuno in 1966 (“is there quasi-geostrophic motion even at the equator?”), is still of relevance even today in Physics of the Atmosphere (e.g. Verkley&Velde, 2010).

Therefore, for wind engineering purposes, there is no other theory available which includes the effect of the Coriolis force on the mean wind by solving the equations of motion, apart from those proposed for mid-latitude models (e.g. Ekman, 1905 or Harris and Deaves, 1980) and addressed in section 2.3.1. They assume the geostrophic approximation in the free atmosphere, i.e. the balance between the Coriolis and the pressure gradient force. Therefore, the question is: to which extent, in terms of latitude, can we assume that these theories are approximately valid? The answer to this question is as follows: the horizontal frictionless flow can be approximated like geostrophic flow if the inertial acceleration term is sufficiently smaller than the Coriolis force. A convenient measure of the acceleration magnitude compared to the Coriolis force may be obtained by forming the ratio of the characteristic scales for the acceleration and the Coriolis force terms:

$$\frac{U^2/L}{f_c U}=\frac{U}{f_c L}=Ro \qquad (2.48)$$

This ratio is a non-dimensional number called the Rossby number (Ro). Thus, the smallness of the Rossby number is a measure of the validity of the geostrophic approximation. At mid-latitudes (being $U \approx 10$ m/s, $f = 2\Omega\sin\varphi \approx 10^{-4}$ m/s, $L = 10^6$ m), it results $Ro \approx 0.1$. At lower latitude, e.g. 10°, $Ro \approx 0.4$, but only at 4° Ro changes its order of magnitude (≈ 1.0). For this reason, it can be assumed that the geostrophic approximation can be accepted up to a latitude of about 4°. Being on the safe side, the lower limit for latitude can be set at 10° (Houghton, 1977). In view of the solar updraft tower design, such a limit encloses most of the possible locations for solar towers (see Figure 1.3). It means that the models based on the (frictionless) geostrophic balance can be applied, within an acceptable range of approximation.

However, even if the H&D model approximation is still acceptable at relatively low latitudes, the failure of the model is physically motivated by the different type of storms creating strong winds near the equator, which should be reflected in the design. This issue is addressed by Irwin (2009). The types of storms near the equator tend to be local, e.g. thunderstorms, and in these storms the boundary layer depth is limited by the small scale of the storm and not by Coriolis effects.

2.3.4 Tropical cyclones and tornadoes

Tropical cyclones and tornadoes are not included in this work. In these motions the Coriolis force is always of secondary importance with respect to the acceleration term in the equations of motion.

Tropical cyclones (called hurricanes in the Atlantic and typhoons in the Pacific) are intense vertical storms which develop over tropical oceans in regions of very warm surface water. They are characterized by a horizontal scale of the region where convection is strong of about 100 km in radius. Maximum tangential wind speeds in these storms range typically from 50 to 100 m/s. For such high velocities and relatively small scales, the centrifugal force term cannot be neglected compared to the Coriolis force. It means that, to a first approximation, the radial force balance in a steady-state hurricane satisfies the gradient wind relationship (equation (2.49)), but not the geostrophic balance.

$$\frac{U^2}{R} + f_c U = -\frac{1}{\rho}\frac{\partial p}{\partial n} \tag{2.49}$$

Anyway, tropical cyclones rapidly degenerate when they move on land and, as can be seen in Figure 2.19, they do not affect possible locations for solar towers.

Besides tropical cyclones, tornadoes are not considered in this Thesis as well. In fact, a methodology to design structures against tornadoes does not exist. Haan et al. (2008) designed a large tornado simulator for wind engineering applications, but physical model testing in wind tunnels is still in need of further development (Irwin, 2009). Usually, tornadoes are only treated in terms of their probability of occurrence (Goliger&Milford, 1998) and the great majority of structures (with exclusion of nuclear reactors and other critical facilities) is not designed to withstand them.

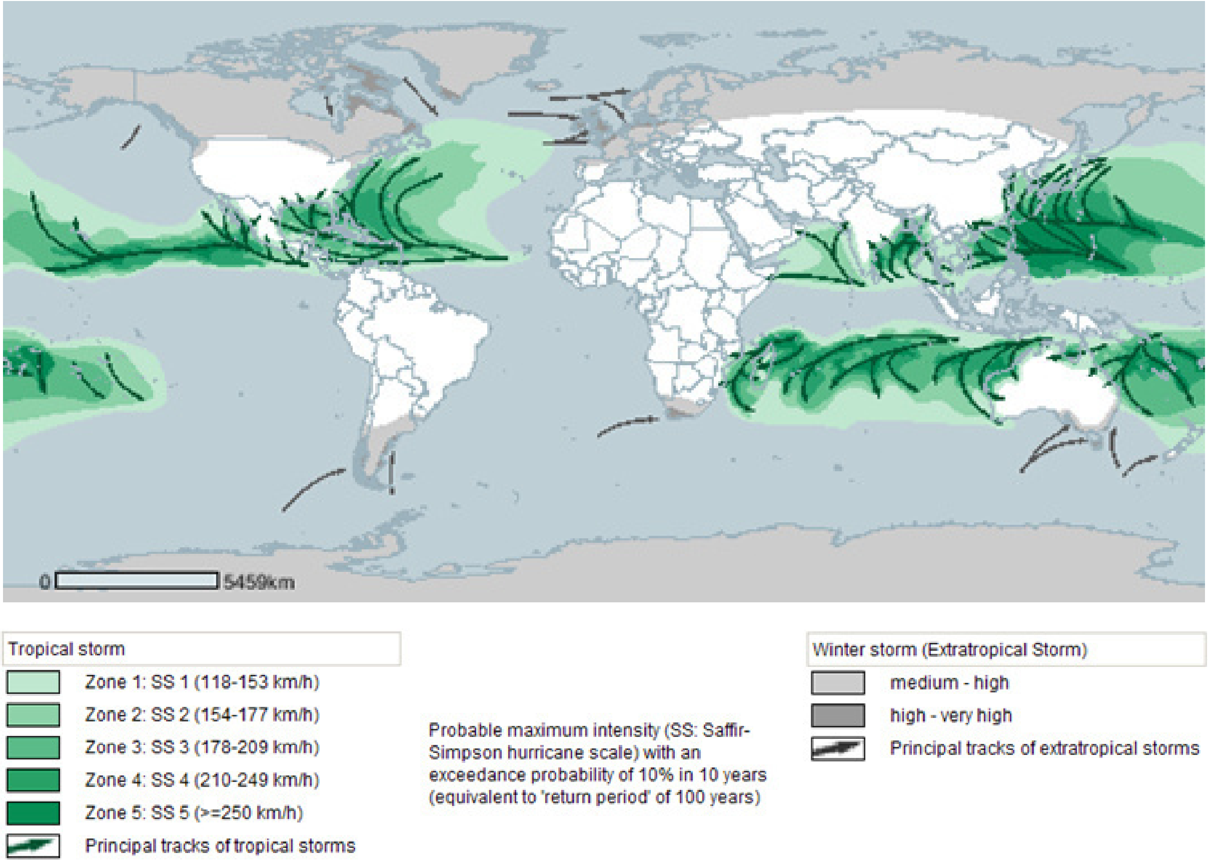

Figure 2.19 Principle tracks and intensities of tropical cyclonic storms

2.4 Structural vulnerability of the tower to the wind action

So far, it is known that the structural vulnerability of the solar tower to the wind action can be significantly reduced by applying stiffening rings along the height (Figure 1.9, Figure 1.12, Figure 1.13). As explained in several publications about solar towers (Goldack, 2004; Backström et al., 2008; Krätzig et al., 2008-2009a,b; Lupi, 2009, 2011; Niemann et al., 2009; Harte et al. 2010; Borri et al., 2010), the stiffening rings guarantee a beam like behaviour at the first eigenmode, reduce ovalling deformations of the shell, increase buckling safety and improve the distribution of internal forces. This is the same concept as for steel chimneys, which was first investigated by Peil&Nölle (1988) and constitutes the basis of the rule in the German Standard DIN 4133.

Figure 2.20 shows the natural vibration modes of the tower depicted in Figure 1.13, that is the reference structure in the Dissertation. The calculation on the left-hand side is done in absence of stiffening rings. The shell-like behaviour (modes with three and two waves, respectively) definitely predominates. Instead, in case of ten stiffening rings (like those in Figure 1.14), the first vibration mode is a bending mode, with an eigenfrequency of about 0.17 Hz, and the second mode shape is a shell-like one, with two waves and no inversion along the meridian. A wider study about the influence of stiffening rings on the vibration modes can be found in Lupi (2009). It was seen that at least five rings would be necessary along the height, in order to promote a beam-like mode.

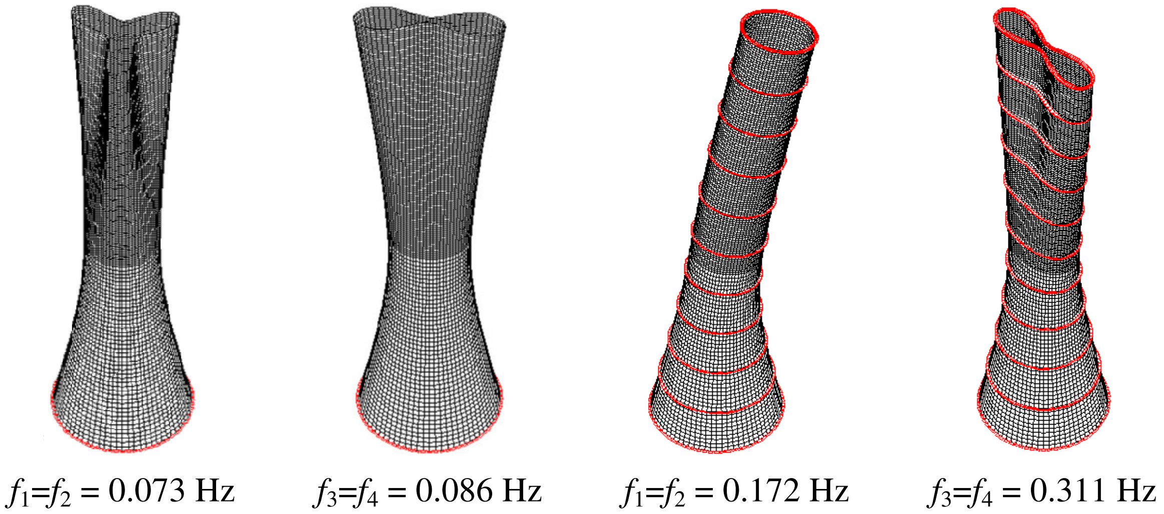

Figure 2.20 Natural vibration modes of 1000 m tower (Borri et al., 2010)
without stiffening rings *with 10 stiffening rings*

The reduction of shell-like deformations significantly improves the distribution of internal forces. This diminishes the structural vulnerability, especially to the wind action, because the peaks of tension at the windward side are reduced. Ideally, the internal distribution of forces tends to a beam-like distribution, which is linear in the cross-section and crosses zero at 90°. In presence of ten stiffening rings like those in Figure 1.14, this ideal response distribution is achieved at about middle height of the tower, as shown in Chapter 7 (Figure 7.57). As the peaks of tension due to the wind action are reduced at the windward side, tensile stresses can even be completely balanced by the compressive stresses due to self-weight. Consequently, the amount of steel reinforcement is significantly reduced and if needed it can be restricted to the minimum percentage that is required by the Codes. It was calculated in Niemann et al. (2009) that even at the base of the tower and even at the ultimate limit states, the tensile stresses due to the wind action can be completely balanced by self-weight. This also means that the risk of an overturning of the tower is prevented and pales against overturning are not necessary in the foundations. It explains the relatively small foundation ring, which is depicted below the tower in Figure 1.12 and Figure 1.13.

However, even if the predominant behaviour of the solar tower is a beam-like bending mode, relevant shell stresses still arise, especially in the vicinity of the stiffening rings and in the tip region. The local effects in the vicinity of the stiffening rings are evaluated in Chapter 7. In the tip region, the ovalization of the shell is evident in Figure 7.57, where at high levels compressive forces arise at stagnation and lateral tension is present at the flanges. Therefore, even if the beam-like calculation of the structure provides a good estimation of global effects, it would not be sufficiently representative in view of the design. This is confirmed by Peil&Nölle (1988), who investigated the stress distribution in steel chimneys and proposed a simple formula (introduced in the Eurocodes) to identify the admissible shell geometries, i.e. those geometries that can be calculated by the beam theory. It depends on geometric parameters like H/R and R/t, being H, R and t the height of the tower, the radius and the wall thickness, respectively. The equation for allowable shell geometries is given by Peil&Nölle (1988):

$$\frac{H}{R} \geq 0.14 * \frac{R}{t} + 10 \tag{2.50}$$

In the case of the solar tower, it results (measures are in m):

$$\frac{1000}{75} \geq 0.14 * \frac{75}{0.25} + 10 \quad \rightarrow \quad 13.3 \geq 52 \quad \rightarrow \quad FALSE \tag{2.51}$$

It is then clear that the enhancement of the beam-like behaviour by introducing stiffening rings is a strategy of risk mitigation, because it reduces the structural vulnerability (especially to the wind action), but the design cannot neglect the shell-like behaviour.

In addition, the presence of rings is crucial in order to reduce the structural vulnerability to vortex shedding. The frequency of shedding (n_s) is conveniently represented in non-dimensional form by the Strouhal number:

$$S_t = \frac{n_s D}{U} \tag{2.52}$$

where D is the diameter of the cylinder and U is the wind speed. For circular cylinders, S_t is of the order of 0.18-0.2 (but it varies with the Reynolds number). As wind speed increases, the dominant frequency of vortex shedding n_s increases, until the critical flow velocity U_{cr} is reached. It happens when n_s is close to a natural frequency of vibration of the body. At the critical flow speed, a significant amplification of the across-flow forces occurs and large amplitude of across-flow oscillations can result.

The amplitude of the induced oscillations depends on the Scruton number:

$$S_{cr} = \frac{4\pi m_{i,e}\xi_i}{\rho D^2} \tag{2.53}$$

where $m_{i,e}$ is the equivalent mass of the structure per unit length corresponding to the i^{th} mode of vibration and ξ_i is the damping ratio corresponding to the i^{th} mode of vibration. If the Scruton number is large, the motion induced by the vortex shedding will not exceed a few per cent of the diameter, although fluctuating forces induced by vortex shedding will still be present. Instead, if the Scruton number is small, the motion of the body has a significant influence on the strength of the vortices shed and the forces induced by them, which in turn affect the oscillation amplitude. It is an aeroelastic effect.

When the amplitudes of oscillation are small, the fluctuating forces are generally random in nature, with significant energy distributed over a relatively broad band of frequencies centered on n_s. In this case, the distribution of the vortex-induced fluctuating forces along the length of the cylinder is also disorganized, which means that the maximum value of the fluctuating force does not occur simultaneously at all positions along the cylinder. The resulting response is a broad-band response of random amplitude nature at approximately the body frequency. For larger amplitudes of oscillation, the local forces due to vortex shedding are amplified. In such cases, the motion of the structure tends to cause the shedding frequency n_s to “lock-in” to the body frequency n_j over a range of local flow velocities. The fluctuating forces at various sections along the structure in the lock-in region are in phase with the body motion and thus completely correlated with each other, further enhancing the response. These forces are nearly periodic in nature, with significant energy confined to a relatively narrow band of frequencies centered on the body frequency n_j. The resulting response is a narrow-band response of an almost constant amplitude of sinusoidal nature at approximately the frequency n_j.

Solar towers are characterized by small Scruton numbers, therefore the lock-in phenomenon may be dangerous. However, the critical wind speed at which it would occur is so high that, in practice, it cannot be reached. It is primarily due to the aspect ratio of solar towers, which is generally not too high. It reduces the sensitivity to vortex-induced oscillations. In addition, the presence of the ring beams along the height is very important, because the beam-like behaviour at the first eigenmode increases the critical velocity, as calculated in the following.
The critical wind speed for 1-kilometer tall tower with ten stiffening rings (n_1 = 0.17 Hz), corresponding to a beam-like bending mode, is calculated as (by assuming D = 150 m, like in Figure 1.13 at the tower top):

$$U_{cr} = \frac{n_1 D}{S_t} = \frac{0.17*150}{0.20} = 127.5 \text{ m/s} \qquad (2.54)$$

As regards the ovalling modes of vibration, the critical wind speed corresponding to the second mode, characterized by two waves around the cross-section (n_1 = 0.31 Hz), can be calculated as:

$$U_{cr} = \frac{n_2 D}{2S_t} = \frac{0.31*150}{2*0.20} = 116.25 \text{ m/s} \qquad (2.55)$$

The Codes require that the critical wind speed is at least 25% higher than the design wind speed, assumed for a period of 50 years. Such requests are largely satisfied. However, in absence of rings (or with a few rings, like one or two, see Lupi (2009)), the critical velocity would be much lower. For example, if n_1 = 0.073 Hz and there are three waves, like in Figure 2.20, the critical velocity would have been only 18 m/s. In this case, the amount of steel reinforcement and width of cracks are secondary aspects, because the collapse of the structure would likely be produced by aeroelastic effects due to the lock-in.

Chapter 3. **Flow around circular cylinders: state of the art**

This chapter describes the current state of knowledge of the flow around smooth and rough circular cylinders. The Reynolds number is the single governing parameter in disturbance-free flow around a two dimensional circular cylinder. Real flows are affected by a wide variety of disturbances, classified as influencing parameters. In particular, three dimensional effects have to be considered in view of the design of structures. They can be enhanced in atmospheric flow and depend on the aspect ratio.

3.1 The boundary layer and its separation

A body is classified as aerodynamically bluff – in opposite to streamlined – “when the flow streamlines do not follow the surface of the body, but detach from it leaving regions of separated flow and a wide trailing wake” (Cook, 1985). Circular cylinders belong to the class of bluff bodies with rounded shape, characterized by a separation point which can move and adjust itself in response to the flow structure in the separated region. In particular, separation will generally be delayed when transition from laminar to turbulent boundary layer occurs (Buresti, 2012). According to Zdravkovich (1997), the disturbed flow field around a circular cylinder can be divided into four regions: 1) one narrow region of retarded flow close to stagnation; 2) two boundary layers attached to the surface of the cylinder; 3) two sidewise regions of displaced and accelerated flow; 4) a wide downstream region of separated flow, called the wake. The near wake is initially bordered by the separated boundary layers which continue to develop downstream as free-shear layers. The concept of a thin boundary layer which develops around a body as a result of viscous friction was first presented by Prandtl in 1904. He evaluated the boundary layer thickness (δ) around circular cylinders at high Re as:

$$\delta \propto \frac{D}{\sqrt{\mathrm{Re}}} \tag{3.1}$$

The boundary layer has only a small thickness near the stagnation point and generally increases with distance along the surface. Zdravkovich (1997) uses a factor of proportionality equal to 5 at φ = 60°.

In the boundary layer, the velocity varies from the free stream value to zero at the wall, where fluid adheres to the boundary (no-slip condition). Therefore, a large velocity gradient exists normal to the surface and the shearing forces (which arise from the tangential shearing flow of the fluid along the surface of the body) are transmitted through the fluid shear layers adjacent to the surface. In the forward facing part of a circular cylinder, the flow accelerates and the boundary layers around the cylinder are subjected to a favorable (negative) pressure gradient. The region of accelerated flow is then followed by a small region of adverse (positive) pressure gradient before separation. In this decelerating flow region – over the rearward facing part of the body – the velocity at the edge of the boundary layer decreases. Due to the no-slip condition at the surface, at each value of z within the boundary layer the reduction of velocity in passing downstream varies from zero at the wall to a certain value at the edge of the boundary. There often comes a point at which the velocity gradient normal to the surface, at the surface, becomes zero. At this point, the viscous shear force must also be zero, which means that the boundary layer can no longer progress along the surface and thus separates. For this reason, the positive pressure gradient in the decelerating flow region is regarded as an adverse pressure gradient (ESDU 71012).

Downstream of the separation of the boundary layer, there is a region of reversed flow close to the surface. In fact, the region between the separated boundary layer and the surface is filled with an eddying flow in which the velocity and direction vary with time in an almost random manner and it has little or no relation to that of the free stream.

3.2 The state of the flow as a function of the Reynolds number

The state of the flow around a circular cylinder can be either fully laminar (at very low Re), fully turbulent (at very high Re, theoretically Re $\rightarrow \infty$, in practice it is limited by occurrence of compressibility effects in air) or there can be a transition from laminar to turbulent state either in the wake, in the free shear layers or in the boundary layers. In laminar flow, the adjacent fluid layers in the flow slide over each other and only friction forces act between them, without macroscopic mixing. Transition from laminar to turbulent flow was first discovered by Reynolds (1883) in a smooth pipe and then the concept was applied by Rayleigh (1896, 1915) to the flow around spheres and cylinders. In this case, the external diameter of the sphere or the circular cylinder was taken as the characteristic length. The Reynolds number is thus the governing parameter of the state of the flow. However, as stressed by Zdravkovich (1997), it is the single governing parameter only in disturbance-free flow. Real flows around circular cylinders in most practical applications are affected by a wide variety of disturbances, which are classified as influencing parameters. Turbulence of the incoming flow, surface roughness, aspect ratio, end-effects (ground-wall effects and free-end effects), oscillations and wall-blockage are the most common influencing parameters. Transition is very sensitive to small disturbances, which may initiate transition at lower Re and in case become themselves governing parameters.

In this section, it is referred to an idealized disturbance-free flow, so that it is allowed to classify the flow regimes on the only basis of the Reynolds number (the aspect ratio is an ever-present influencing parameter, but – as clarified by Zdravkovich – it becomes a governing one only for a short cylinder with a free end).

The adverse pressure gradient reduces the skin friction to zero and at that instant the separation of the flow from the surface takes place. The capability of the boundary layer to sustain higher adverse pressure gradients before separation depends on the state of the flow and thus on the Reynolds number. The effect of mixing of fluid elements in a turbulent boundary layer promotes a greater interchange of momentum between layers which in turn increases the thickness δ of the boundary layer. Furthermore, the mixing process produces an effective shear stress which is additive to the shear stress produced by the viscosity of the fluid. As a consequence, the retarded fluid layers adjacent to the surface can be pulled further along the surface into regions of higher pressure. Because of that, the thick turbulent boundary layer is able to progress further against an unfavorable pressure gradient and it separates at a point further along a surface. Instead, in free-disturbance conditions, fully laminar boundary layers can only exist when the external pressure gradient is favorable. This is the reason for the early occurrence of laminar separation. As it will be showed in the following, a useful parameter which quantifies the capability of the flow to sustain the adverse pressure gradients prior to separation around a circular cylinder is the adverse pressure recovery. Its magnitude can be expressed by $C_{p,b} - C_{p,min}$, being $C_{p,b}$ and $C_{p,min}$ the base pressure coefficient (at $\varphi = 180°$) and the minimum pressure coefficient.

A first classification of the states of the flow around a smooth cylinder is proposed by Roshko (1961). Four regimes are defined: subcritical, critical, supercritical and transcritical. Later, Achenbach (1971) also referred to this classification for rough cylinders (section 3.3). In the subcritical state, there is an early laminar separation (angle of separation ≈ 70°-80°) and the drag is independent on Re. The critical regime is a range of transition between laminar and turbulent separation. It begins with the initial fall of the drag coefficient and ends with the formation of two laminar separation bubbles at $Re = Re_{cr}$, which corresponds to the minimum drag. The supercritical range on smooth cylinders is still characterized by the two bubbles (rather constant low drag coefficient and narrow wake, with separation around 140°). After this first stable stage, the supercritical regime becomes unstable, with disruption of bubbles and suppression of vortex shedding. Roshko suggests that the disappearance of the bubbles marks the transition from supercritical to transcritical range, where the separation is purely turbulent and it occurs at lower angles (≈ 110°). Vortex shedding reappears in the transcritical range, it was discovered by Roshko and published for the first time in 1961.

According to Zdravkovich (1997), the position of the separation point (with regard to the position of transition from laminar to turbulent boundary layer) is the key feature to classify a particular state of the flow around a circular cylinder. He proposes a detailed classification based on occurrence of transition in different regions around the circular cylinder. It is reported in Table 3.1 and briefly explained in the following.

Table 3.1 Epitome of disturbance-free flow regimes (Zdravkovich, 1997)

STATE		REGIME		Re RANGES
L	LAMINAR	1	No-separation	0 to 4-5
		2	Closed wake	4-5 to 30-38
		3	Periodic wake	30-48 to 180-200
TrW	TRANSITION IN WAKE	1	Lower transition regime	180-200 to 220-250
		2	Upper transition regime	220-250 to 350-400
TrSL	TRANSITION IN SHEAR LAYERS	1	Lower subcritical	350-400 to $1*10^{3}$-$2*10^{3}$
		2	Intermediate subcritical	$1*10^{3}$-$2*10^{3}$ to $2*10^{4}$-$4*10^{4}$
		3	Upper subcritical	$2*10^{4}$-$4*10^{4}$ to $1*10^{5}$-$2*10^{5}$
TrBL	TRANSITION IN BOUNDARY LAYERS	0	Pre-critical	$1*10^{5}$-$2*10^{5}$ to $3*10^{5}$-$3.4*10^{5}$
		1	Single bubble	$3*10^{5}$-$3.4*10^{5}$ to $3.8*10^{5}$-$4*10^{5}$
		2	Two-bubble	$3.8*10^{5}$-$4*10^{5}$ to $5*10^{5}$-10^{6}
		3	Supercritical	$5*10^{5}$-10^{6} to $3.5*10^{6}$-$6*10^{6}$
		4	Post-critical	$3.5*10^{6}$-$6*10^{6}$ to (?)
T	FULLY TURBULENT	1	Invariable	(?) to ∞
		2	Ultimate	

3.2.1 Fully laminar state

The fully laminar state (L, $Re < 200$) is characterized by three basic flow regimes. In the first one, the creeping flow regime (L1), separation does not occur because the cylinder at extremely low Re (Re < 5) is dominated by viscous forces. Then, the magnitude of viscous forces decreases at higher Re and a steady separation initiates; the free shear layers meet at the end of the near-wake at the so-called confluence point. Thus, a laminar, closed, steady near-wake is formed behind the cylinder (L2). The well-known Von Karman eddy street starts with the instability of such an elongated closed near-wake which commences a sinusoidal oscillation for Re > 30-48. As Reynolds increases, the amplitude of the trail oscillations increases and the shear layers start to roll up at crests and troughs. That is, according to the nomenclature chosen by Zdravkovich, the flow regime L3. In such a shedding mode, initiated by the instability of the laminar wake, the laminar eddies are not shed starting from the cylinder, but they are formed gradually as they are carried downstream. Kovasznay (1949) writes: “it is remarkable that the fluctuations close to the cylinder are very small and that they develop the maximum intensity only in the vicinity of X/D = 7. Thus, the eddies are not shed starting from the cylinder at this low Re, but develop several diameters downstream”. This mode is also identified as the low-speed mode, as opposite to the high-speed shedding mode of turbulent eddies which are shed starting from the cylinder itself at higher Re. Karman (1912) derived the first theoretical model by considering the stability of staggered vortices in two parallel rows. However, it was Bénard in 1908 the first who sketched the alternate procession of eddies observed in water.

3.2.2 Transitional states

All laminar flows undergo transition to turbulence above a certain Re. Around circular cylinders, it is interesting to describe the succession of transitions in various regions of the disturbed flow as Re increases. Zdravkovich (1997) identifies three different transitional stages of flow, based on the fact that transition may occur in the wake (TrW), in the shear layers (TrSL) and in the boundary layers (TrBL). Gerrard (1978) noted that all transition states are characterized by the appearance, development and disappearance of an entirely new flow structure. As it will be explained later, such flow structures are called fingers in TrW, transition waves in TrSL and separation bubbles in TrBL.

Transition in the wake

As Reynolds number increases, the laminar wake undergoes transition to turbulence (TrW, Re from 180-200 until 350-400), due to random initiation and growth of irregularities. The progressive distortion of laminar eddy filaments is described by Gerrard (1978) as the onset of “fingers” at randomly disposed spanwise positions. The name “fingers” describes the fact that such a distortion of filaments always points toward the cylinder.

In the so-called lower transition regime (TrW1), the eddies are formed laminar and become turbulent further downstream. Then, transition spreads gradually upstream with increasing Re, until the eddies become turbulent during its formation (TrW2). According to Gerrard (1978), it is the mixing with the free stream around the eddies that promotes the formation of turbulent eddies.

The key feature of this transitional state is the change of the shedding mode from low-speed mode (which characterizes L3 and TrW1) to high-speed mode, which appears in TrW2. This change – that represents the boundary between TrW1 and TrW2 – is marked by a jump in the Strouhal number. It has been measured at Re $\approx$ 250 by Roshko, (1954) and it distinguishes two different S_t-versus-Re curves, for the two shedding modes, respectively: while in L3 and TrW1 (low-speed mode) S_t increases with Re, later on S_t is almost constant with rising Re. Anyway, the transition from low- to high-speed mode of eddy shedding is not smooth and an overlapping of the two modes of shedding (two peaks in the frequency spectra) has also been argued (Zdravkovich, 1992).

The characteristic feature of the high-speed mode (Gerrard, 1966) is that the growth of an eddy on one side of the cylinder (in an almost stationary position) induces transverse flow across the wake, which is responsible for the cut-off of the subsequent eddy from a further supply of circulation. It is at this stage, and because of the shear layer crossing the wake, that the eddy is shed from the cylinder.

Transition in the shear layer

After transition in the wake, at higher Re, transition occurs in the shear-layer, TrSL (Re from 350-400 until $1\text{-}2*10^5$). Basically, it is the usually called subcritical flow state, meaning that the boundary layer remains laminar up to and beyond separation. In this state, the free shear layers which surround the near-wake are initially laminar but they become turbulent before rolling up into turbulent eddies.

More precisely, the TrSL is divided by Zdravkovich (1997) in three stages: the lower-, intermediate- and upper-subcritical regime. The typical flow structures of the TrSL state are the so-called transition eddies.

At first, undulations of both free shear layers develop from the separation lines in TrSL1. They are called Gerrard-Bloor transition waves and were first described by Gerrard (1978). Such waves are symmetric on the two sides of the cylinder and in-phase, therefore they are not related to the alternating eddy shedding. Zdravkovich (1997) describes an analogy between the onset of instability and oscillation of the laminar Karman-Bénard street (L3) and the onset of these undulations in the free-shear layers (TrSL1).

In TrSL2, the transition eddies appear before transition to turbulence. They were firstly sketched by Couregelongue (1929) during outdoor experiments in a river and appeared as “chains” of small eddies along the free shear layers. As Re increseas, there is a progressive movement of transition towards separation and it is accompanied by a shortening of the eddy formation region (L_f), so that the eddies are brought closer to the base of the cylinder. A reduction in L_f is always reflected in a decrease in $C_{p,b}$ (higher suction in the wake, thus higher drag) and an increase in C'_L (higher lift fluctuations), because the eddies form closer to the body. However, the S_t number does not change significantly from TrSL1 (elongation of the formation region) to TrSL2 (shortening of the formation region). Because of that, Gerrard (1966) suggested that the shedding frequency is primarily related to the distance between the two free shear layers, which varies through TrSL but not so largely as the variation of L_f. In particular, according to Gerrard (1966) and Bloor and Gerrard (1966), two opposite tendencies seem to cancel each other in order to keep the same strength of the turbulent eddies in TrSL2, thus an almost constant S_t: the shortening of the formation region and the widening of the turbulent shear layers. In addition, in the TrSL2 regime the shortening of L_f counteracts the increase in the shear layer thickness, since thick turbulent shear layers need more time for a roll up to be carried across the wake.

As the shortening of the eddy formation region is completed, at the end of TrSL2, the transition eddies disappear and TrSL3 begins. It is characterized by a wide near-wake (small angle of separation), high suction in the wake, high drag and high lift fluctuations due to the very short length of the formation region L_f. Zdravkovich (1997) describes the transition to turbulence as a sudden burst in the free shear layers close to the cylinder. Three-dimensional flow structures develop in the near-wake, responsible for a significant reduction of the correlation length along the span. The interesting feature of TrSL3 is the stabilizing effect produced on the transition in the free shear layers in this range of Re, so that the upper subcritical regime is defined as a quasi-invariable flow. The reason is that the wide near-wake (produced by short L_f) displaces the free shear layers into the free stream and causes the acceleration of the stream adjacent to the near-wake. This has a stabilizing effect, so that the transition region does not progress upstream with increasing Re. As a consequence, TrSL3 is characterized by almost constant $C_{p,b}$, C_D (the horizontal stretch before the critical fall in the drag), C'_D and C'_L (see Figure 3.3) and S_t number as well.

Transition in the boundary layer

The stabilizing effect, which characterizes the quasi-invariable nature of the flow in the subcritical range - due to the accelerated free stream that squeezes the separated shear layers that surround the wide wake - gradually weakens with rising Re, as the free-shear layers become more aligned with the adjacent free stream. Transition to turbulence advances in the free shear layers towards separation until it reaches the separation line. It starts then a complex interaction between transition and separation, which was first observed by Taylor (1916) and better investigated by Fage in 1928. Zdravkovich (1997) names this regime transition in the boundary layer TrBL (Re from 10^5-$2*10^5$ – according to Zdravkovich, but generally somewhat arbitrary in literature – to an undefined upper limit, in the order of 10^6, which marks the entering in fully turbulent conditions).

The beginning of TrBL is marked, according to Zdravkovich, by the initial fall of the drag coefficient (Re = 10^5-$2*10^5$), due to a reward movement of the separation point. Instead, according to Schewe, 1983 the key feature which denotes such a boundary between subcritical and critical regimes is the onset of randomization of lift fluctuations, at a slightly higher Re (in Schewe's results, Re = $2.8*10^5$ marked the onset of random lift fluctuation, while Re = $1.4*10^5$ was at the initial fall of the drag).

This initial stage (TrBL0), which Zdravkovich includes in the critical regime, is named pre-critical. The decrease in the drag coefficient is the result of the narrowing of the wake and a gradual displacement of separation downstream with rising Re (Achenbach&Heinecke, 1981). The length of the eddy formation region L_f, which was short in TrSL3, elongates and the roll up of the free shear layers is displaced downstream. This reduces the negative base pressure and weakens the alternate pressure fluctuations on the two sides of the cylinder. The small suction in the wake is associated to high maximum lateral suction and this is the reason for the fall in the drag coefficient and the rise of the pressure recovery. Bearman (1969) noticed that the S_t number remains constant in TrBL0. Again, the constancy of S_t is related to two opposite tendencies: on one hand the free shear layers tends to get closer, but the elongation of L_f leads to a slight widening.

The state TrBL1 is named by Zdravkovich single bubble regime, followed by TrBL2 that is the two-bubble regime.

Eisner (1925) was the first who measured stable asymmetric mean pressure distributions around a circular cylinder in a certain range of Re. He concluded, correctly, that transition occurred on one side only of the cylinder. Only at slightly higher Re, transition could complete on the two sides. When this happens, C_D reaches the minimum value (at Re = Re_{cr}). However, the state of flow in this particular range of Re was deeply investigated only several years later (Achenbach, 1968; Bearman, 1969; Farell and Blessmann, 1983; Schewe, 1983). The key feature is the formation of laminar separation bubbles, either on one side only or on two sides of the cylinder.

The formation of laminar separation bubbles on two sides of a cylinder (at Re ≈ Re_{cr}) was identified by Achenbach (1968) through measurements of skin friction. He found that at Re = 10^5, at $\phi = 105°$ ($\phi = 255°$) there was not a final separation. In fact, there was a region between laminar separation and turbulent reattachment in which the wall shear stresses theoretically vanished. Downstream, there was an intensive rise of the skin friction, showing that the boundary layer was turbulent. Turbulent separation occurred finally at $\phi = 147°$ ($\phi = 220°$).

In 1969, Bearman identified a bistability of the flow in a sub-range of Re before symmetric twin bubbles appeared by experimental evidence of discontinuous changes in $C_{p,b}$ and S_t at Re = $3.4*10^5$ and $3.8*10^5$. He found the cause in the formation of a laminar separation bubble on one side only of the cylinder. The $C_{p,b}$ distribution along the height showed that the bubble took place along the complete length of the cylinder. He also noted that the asymmetric pressure distribution was accompanied by the displacement of the stagnation point away from the bubble.

Further studies on the formation of only one bubble are reported by Farell and Blessmann (1983). Contrary to the results of Bearman (1969), who found the single-bubble regime to occur always with the bubble consistently on the same side of the cylinder, in Farell and Blessmann's experiments no preference was detected for the bubble to form on either side of the cylinder.

Schewe (1983) described in detail the physical phenomenon of a laminar separation bubble on one side only of the cylinder. A discontinuity in the drag coefficient and a sudden jump of S_t (up to 0.33) mark the onset of a bistable flow condition (Figure 3.1, letter c). The name explains that there are two stable states, corresponding to the two possible signs of the lift force. The asymmetric stable state persists for a very small range of Re. Then, a second discontinuity in the drag, as well as another sudden jump in S_t (up to 0.48 that is the highest value, letter f in Figure 3.1) marks the abrupt disappearance of the steady lift and the attainment of the minimum drag, corresponding to the critical Re. The bistable flow condition is preceded and followed by two unstable ranges (corresponding to $S_t = 0.2$ and 0.31 respectively, according to Figure 3.4). Such unstable ranges correspond to the letters a, b and d, e in Figure 3.1.

“The explanation for the phenomena”, Schewe writes, “lies in the behaviour of the boundary layer. The asymmetric flow and thus the steady lift in the critical range is caused by the fact that the boundary layer transition from laminar to turbulent has occurred on one side only of the cylinder. Thus a laminar separation bubble is formed as follows: the transition from laminar to turbulent flow occurs in the detached boundary layer just downstream from the separation point. After reattachment of the boundary layer on the back of the cylinder, the separation is turbulent.” Figure 3.2 shows the asymmetry of laminar and turbulent separations on the two sides of the cylinder. Figure 3.6 reports a clear representation made by Basu (1985) of the flow field near the point of separation in transitional range of Re, with formation of a laminar separation bubble.

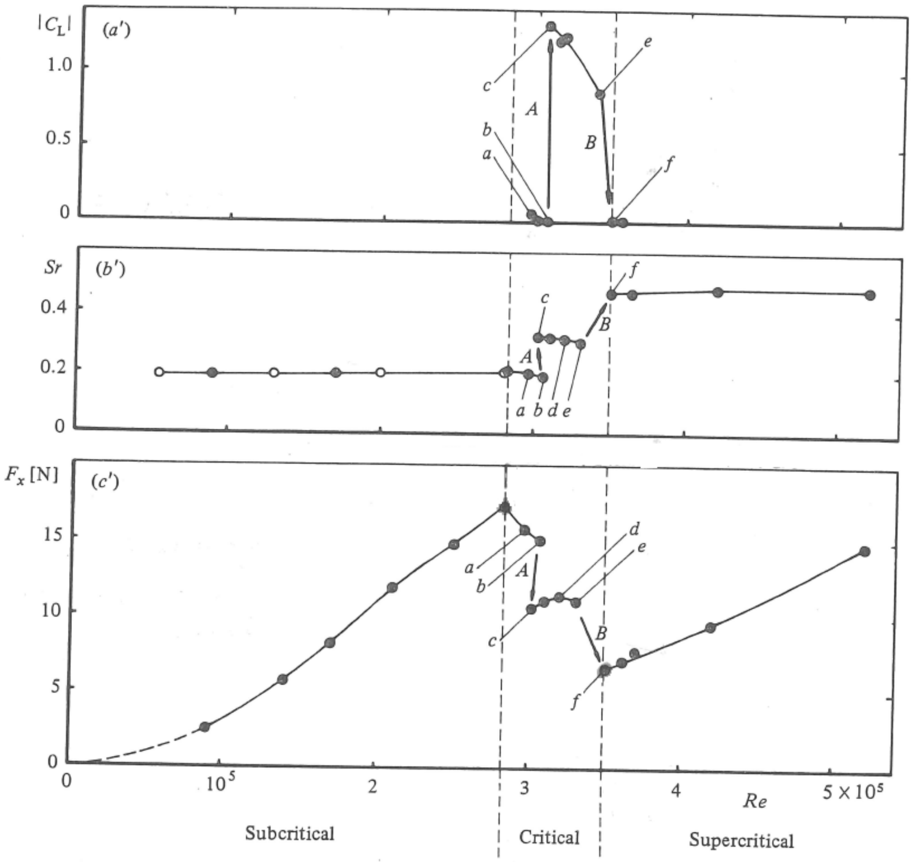

Figure 3.1 Steady lift, Strouhal number and drag force. Asymmetric bistable flow indicated by letter c (Schewe, 1983)

The reason for which transition in the detached boundary layer is initiated on one side only of the cylinder and not simultaneously on both sides is the occurrence on that side of perturbations or fluctuations, which are inherent in the boundary layer and in the free stream. Then, once transition and then reattachment have occurred on one side, there is an acceleration of the fluid on that side and deceleration on the other side. Since deceleration delays transition in the free shear layer (it reduces Re), the formation of the bubble also on the other side is delayed. According to Schewe (1983) this is the reason which stabilizes and fixes the asymmetric flow state. Of course, such a bistable flow condition is extremely sensitive to Re and is possible only if there is a very low probability for simultaneous occurrence of perturbation on both sides. In fact, the bistable flow disappears on rough cylinders as well as in turbulent flow.

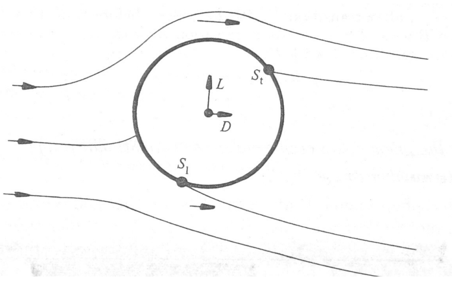

Figure 3.2 Asymmetric flow state in the critical regime of Re (Schewe, 1983)

As soon as the flow also reattaches on the other side of the cylinder, symmetric conditions are again achieved with two bubbles on the two sides of the cylinder: the drag is then minimum and that is the critical Re. Zdravkovich defines this symmetric state of the flow as two-bubble regime (TrBL2) and it precedes the supercritical (TrBL3) regime. The latter begins with the fragmentation and disruption of bubbles and it is characterized by large scatter of results and suppression of vortex shedding, due to high three-dimensionality of the flow. Slightly different in the nomenclature and in the subdivision of the flow regime, is the classification proposed by Roshko (1961) and Achenbach (1971): the supercritical regime starts immediately after the critical drop and for the smooth cylinder it is at first stable, with two separation bubbles and narrow band lift fluctuations, i.e. regular vortex shedding. According to this classification, vortex shedding is rather evident in the first stage of supercritical flow, with the highest Strouhal value ($S_t = 0.48$ according to Schewe, 1983). Then, the upper transition range is an unstable state, characterized by suppression of vortex shedding, which marks the transition to the transcritical regime.

Until the surprising discovery made by Roshko in 1961, it was believed that once the boundary layer becomes turbulent upstream of the separation the periodic eddy shedding should cease due to the irregular and chaotic state of the free shear layers. Instead, Roshko discovered that the periodic eddy shedding reappears in what he called transcritical regime. That is, referring to Zdravkovich's nomenclature, TrBL4 or post-critical regime. In this regime, all the C_D curves by different authors show the same trend: they rise up to a certain Re in the TrBL3 and level out in the TrBL4 regime. It means that the separation point is essentially fixed. According to Achenbach's classification, the more or less constant position of the separation point is the boundary between what he defined supercritical and transcritical regimes, at about Re = $5*10^6$.

3.2.3 Fully turbulent state

Above TrBL4, Zdravkovich concludes the classification with the fully turbulent state (T). Theoretically, it is reached when all the three disturbed regions (wake, free shear and boundary layers) are fully turbulent, i.e. transition is very close to stagnation. In practice, it is not defined, in terms of Re, neither the beginning of T (i.e. the end of TrBL4) nor the end. Transition should reach the stagnation point when Re → ∞, so that the final regime is called ultimate. However, compressibility effects in air appear at high Re and they become the governing parameters. Anyway, what is accepted for sure, is that (Roshko, 1961) “it seems unlikely that there will be any further transitions once all disturbed regions around the cylinder are turbulent”. The invariance of the flow pattern implies that all coefficients remain constant as Re increases.

3.2.4 Summary

Figure 3.3 (Zdravkovich, 1990) summarizes the behaviour of the mean drag and rms value of the lift coefficients for the whole range of Re.

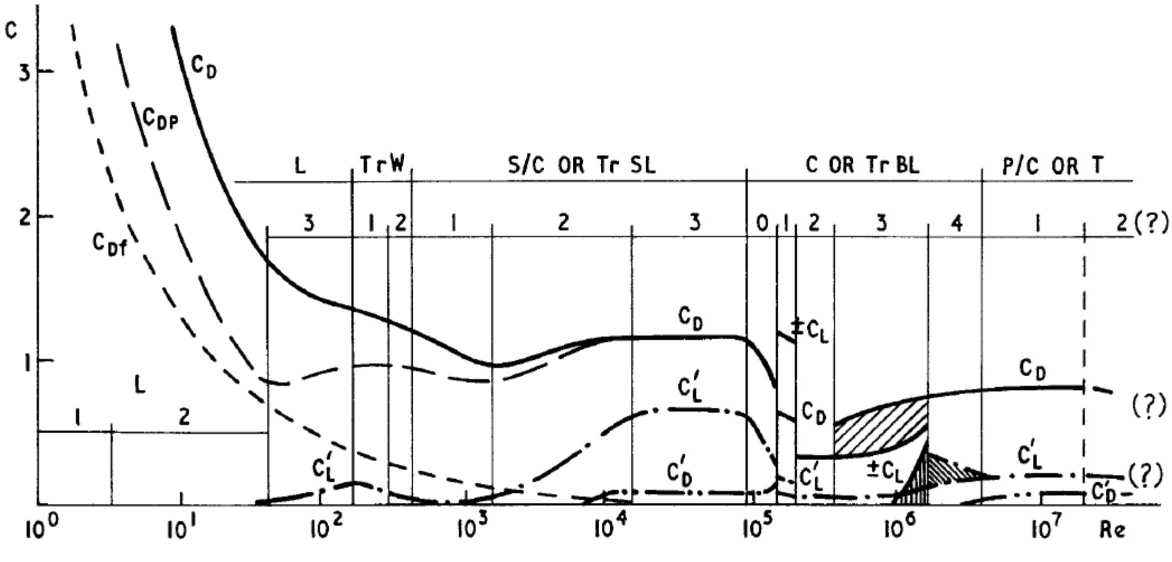

FIG. 2 Force Coefficients versus Reynolds Number; C_D - mean drag, C_{Df} - friction drag, C_{DP} - pressure drag, $C_D{}^1$ - fluctuating drag, C_L - mean lift $C_L{}^1$ - fluctuating lift.

Figure 3.3 Force coefficients versus Reynolds number (Zdravkovich, 1990)

Relying on Schewe (1983)’s results and in accordance with Roshko and Achenbach’s classification of the regimes of flow, Niemann&Hölscher (1990) suggest, for the smooth cylinder, the following review (Figure 3.8):

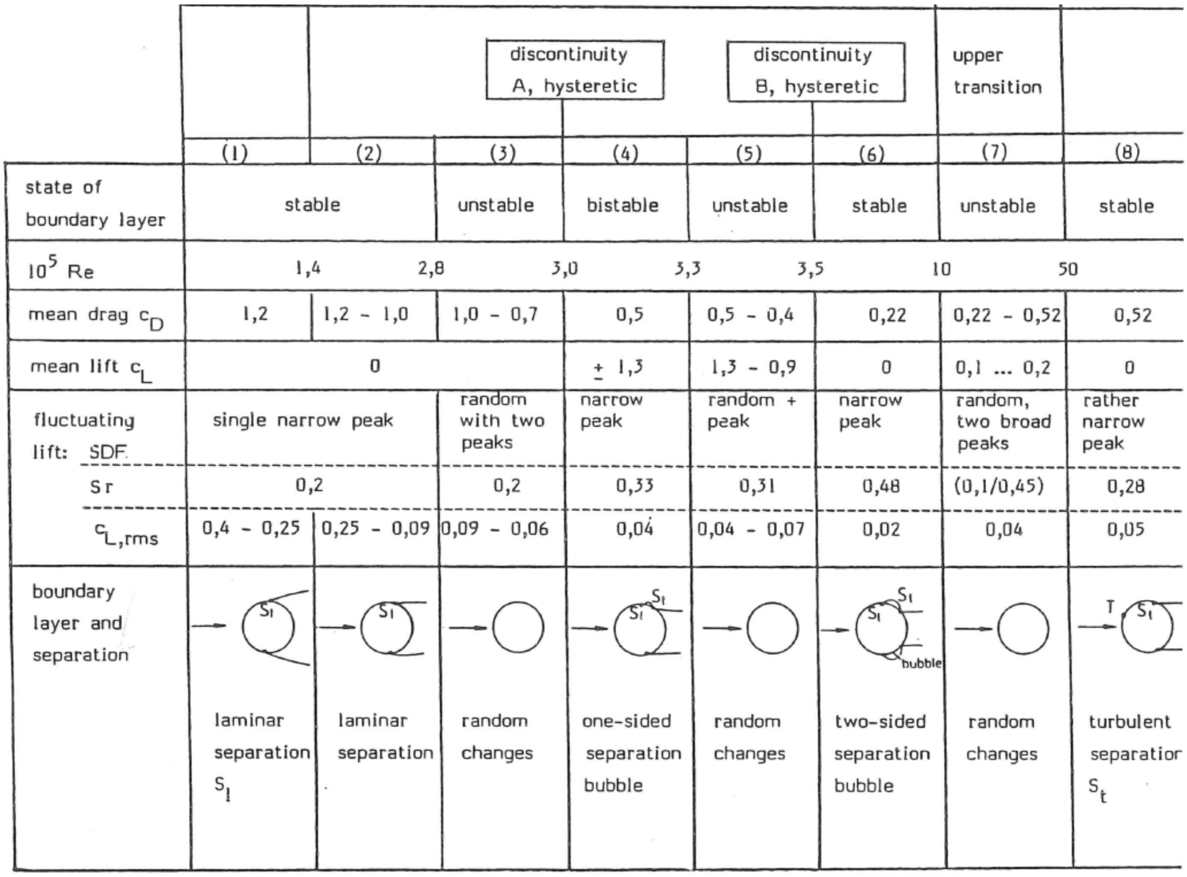

			discontinuity A, hysteretic		discontinuity B, hysteretic		upper transition	
	(1)	(2)	(3)	(4)	(5)	(6)	(7)	(8)
state of boundary layer	stable		unstable	bistable	unstable	stable	unstable	stable
10^5 Re	1,4	2,8	3,0	3,3	3,5	10	50	
mean drag c_D	1,2	1,2 - 1,0	1,0 - 0,7	0,5	0,5 - 0,4	0,22	0,22 - 0,52	0,52
mean lift c_L	0			± 1,3	1,3 - 0,9	0	0,1 ... 0,2	0
fluctuating lift: SDF	single narrow peak		random with two peaks	narrow peak	random + peak	narrow peak	random, two broad peaks	rather narrow peak
Sr	0,2		0,2	0,33	0,31	0,48	(0,1/0,45)	0,28
$c_{L,rms}$	0,4 - 0,25	0,25 - 0,09	0,09 - 0,06	0,04	0,04 - 0,07	0,02	0,04	0,05
boundary layer and separation	laminar separation S_l	laminar separation	random changes	one-sided separation bubble	random changes	two-sided separation bubble	random changes	turbulent separatior S_t

Figure 3.4 Smooth circular cylinder – review (Niemann&Hölscher, 1990)

The flow field near the point of separation in different Re regimes is well depicted by Basu (1985). It is reported in Figure 3.5 (at subcritical Re), in Figure 3.6 (in the transitional range, with formation of a laminar separation bubble) and in Figure 3.7 (at transcritical Re).

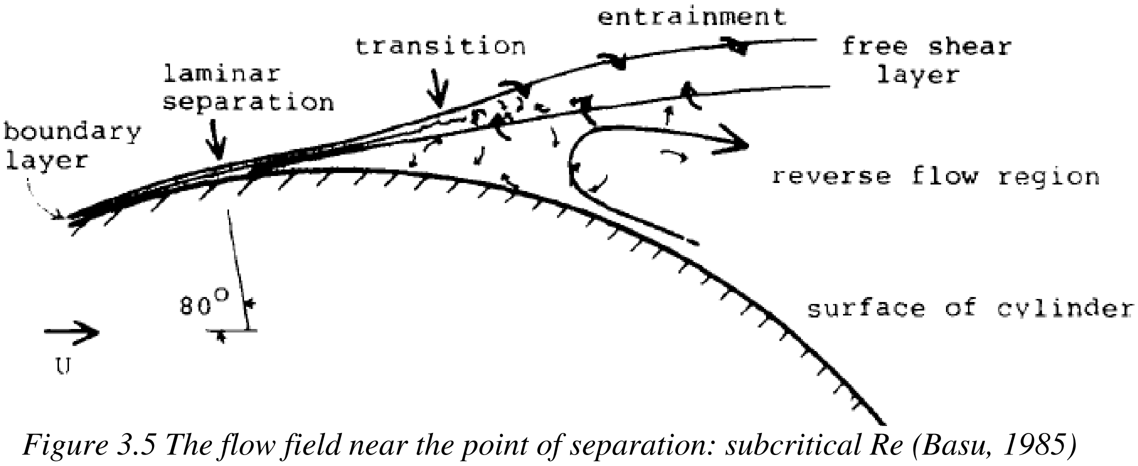

Figure 3.5 The flow field near the point of separation: subcritical Re (Basu, 1985)

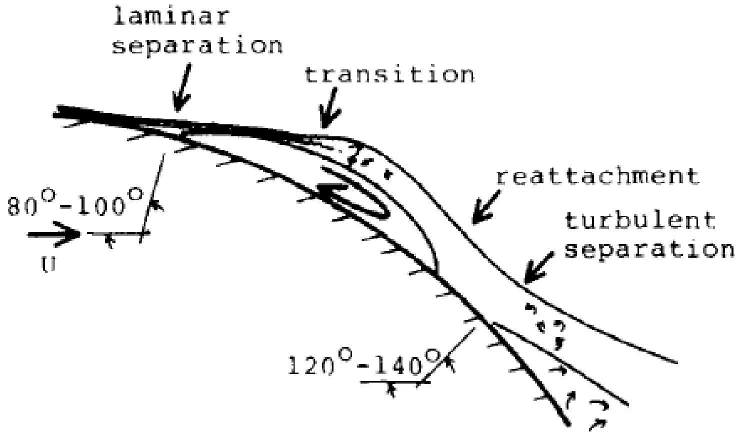

Figure 3.6 The flow field near the point of separation: transitional Re (Basu, 1985)

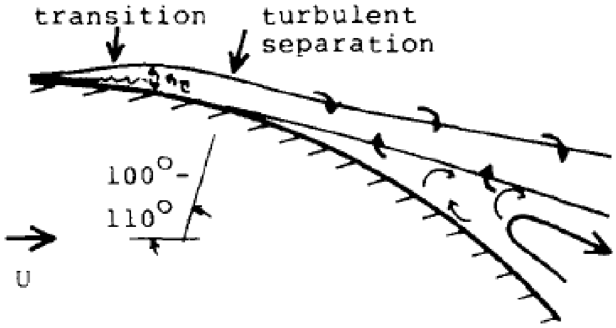

Figure 3.7 The flow field near the point of separation: transcritical Re (Basu, 1985)

3.3 Effect of surface roughness

The flow pattern around a circular cylinder is primarily determined by the position of the separation point. Such a location is governed by the Reynolds number and strongly influenced by the roughness of the cylinder surface and to some extent also by the turbulence characteristics of the approaching flow. Surface roughness is often used in wind tunnel tests as a simulation technique of high Reynolds numbers.

A practical approach to quantify this effect is proposed in the ESDU 74030 and results in the calculation of the so-called effective Reynolds number (Re_e). This is a modified Re, which incorporates a factor λ_R depending on surface roughness, and a factor λ_T depending on incoming turbulence. Re_e reproduces, at lower Reynolds numbers, the same effects in the flow that would occur at higher Reynolds numbers. It is then a useful tool in wind tunnel tests on scale models.

$$\mathrm{Re}_e = \mathrm{Re}\,\lambda_R \lambda_T \tag{3.2}$$

Increasing surface roughness and/or turbulence of the incoming flow has the effect of increasing the boundary layer thickness and enhancing transition from laminar to turbulent flow, so that transition occurs at progressively lower Re. This explains the decrease in the critical Re. In addition, increasing surface roughness increases the value of C_D at Re_{cr}, while increasing incoming turbulence does not change the value of C_D at Re_{cr} significantly. The effect of incoming turbulence will be addressed in the next section, while this section addresses the effect of surface roughness. Surface roughness is especially effective in triggering transition in TrBL and the effectiveness depends on the height of roughness elements with respect to the thickness of the boundary layer. Pioneering experiments on the effect of surface roughness were carried out by Fage and Warsap (1929). They showed that the steep drop in the steady drag occurs at progressively smaller Reynolds numbers with increasing surface roughness.

Milestone studies on the influence of surface roughness on circular cylinders at high Re (up to $3*10^6$), obtained in atmospheric and high-pressure wind tunnel, have been published by Achenbach (1971) and Achenbach&Heinecke (1981). Similarly to what Roshko (1961) proposes for a smooth cylinder, the curve representing the drag coefficient as a function of Reynolds number for a rough cylinder (Achenbach, 1971) is divided into four parts (Figure 3.8). Each range – subcritical, critical, supercritical, transcritical, respectively – is characterized by a special boundary layer behaviour. According to Achenbach, “the subcritical flow regime is not yet influenced by the surface roughness. In a large range of Reynolds number the drag coefficient is nearly constant. Increasing the Reynolds number the drag coefficient suddenly drops. This range, the lower limit of which is dependent upon the roughness conditions, is denoted the critical flow regime. Exceeding the Reynolds number of minimum C_D the drag coefficient grows up again (supercritical range) and reaches a nearly constant value in the transcritical range. This transcritical drag coefficient increases with rising roughness parameter”.

Achenbach studied the behaviour of the boundary layer by measuring local pressures and skin friction. In subcritical flow regime the boundary layer separates laminarly. At immediately higher Re, the disturbances produced by surface roughness “support the boundary layer with energy from outside”. Thus, the boundary layer can remain adjacent to the wall over a larger distance. The separation point shifts to the back of the cylinder and this reduces the drag coefficient, although the separation is still laminar (critical range). At minimum C_D, laminar separation and turbulent reattachment occur. This is the phenomenon of the separation bubbles, as previously described on smooth cylinders. However, it is remarkable that this phenomenon – clearly visible in the horizontal plateau at $C_{D,min}$ for smooth cylinders (Figure 3.9) – is restricted to a very narrow flow range if the surface of the cylinder is rough. In fact, as proved by Buresti (1981) and stated in the review by Niemann&Hoelscher (1990), the extension of the critical and supercritical range is diminished on a rough cylinder. The critical range basically consists in a shift downstream of separation (without the unstable and bistable flow ranges observed on smooth cylinders) and then the drag increases to its transcritical value due to an upstream shift of the transition point. Moreover, as previously said, with increasing roughness the minimum of C_D at the critical Reynolds number increases.

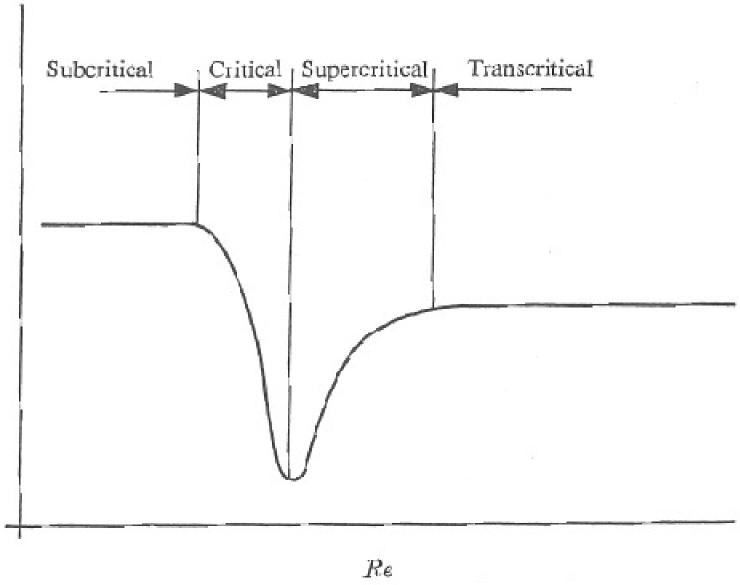

Figure 3.8 Definition of four ranges for the flow past a rough circular cylinder (Achenbach, 1971)

Figure 3.9 reports the different behaviour of the Strouhal-versus-Re curve on a rough cylinder. In particular, on a rough cylinder the Strouhal number exhibits an increase in the critical flow regime, but with growing roughness parameter the step in the curve becomes smaller (Achenbach&Heinecke, 1981). In any case, this is much smaller than the constant value of the Strouhal number due to the formation of laminar separation bubbles on a smooth cylinder (range 6 in Figure 3.9). The smaller S_t and the higher $C_{D,min}$ at critical Re on a rough cylinder, with respect to a smooth cylinder, are due to the upstream shift of the location of boundary layer separation. In other words, higher roughness produces earlier separation. This is confirmed by Achenbach (1971): “with increasing roughness parameter, the angle of separation becomes smaller (≈110°) compared with that of the smooth cylinder (≈140°) at critical flow conditions”.

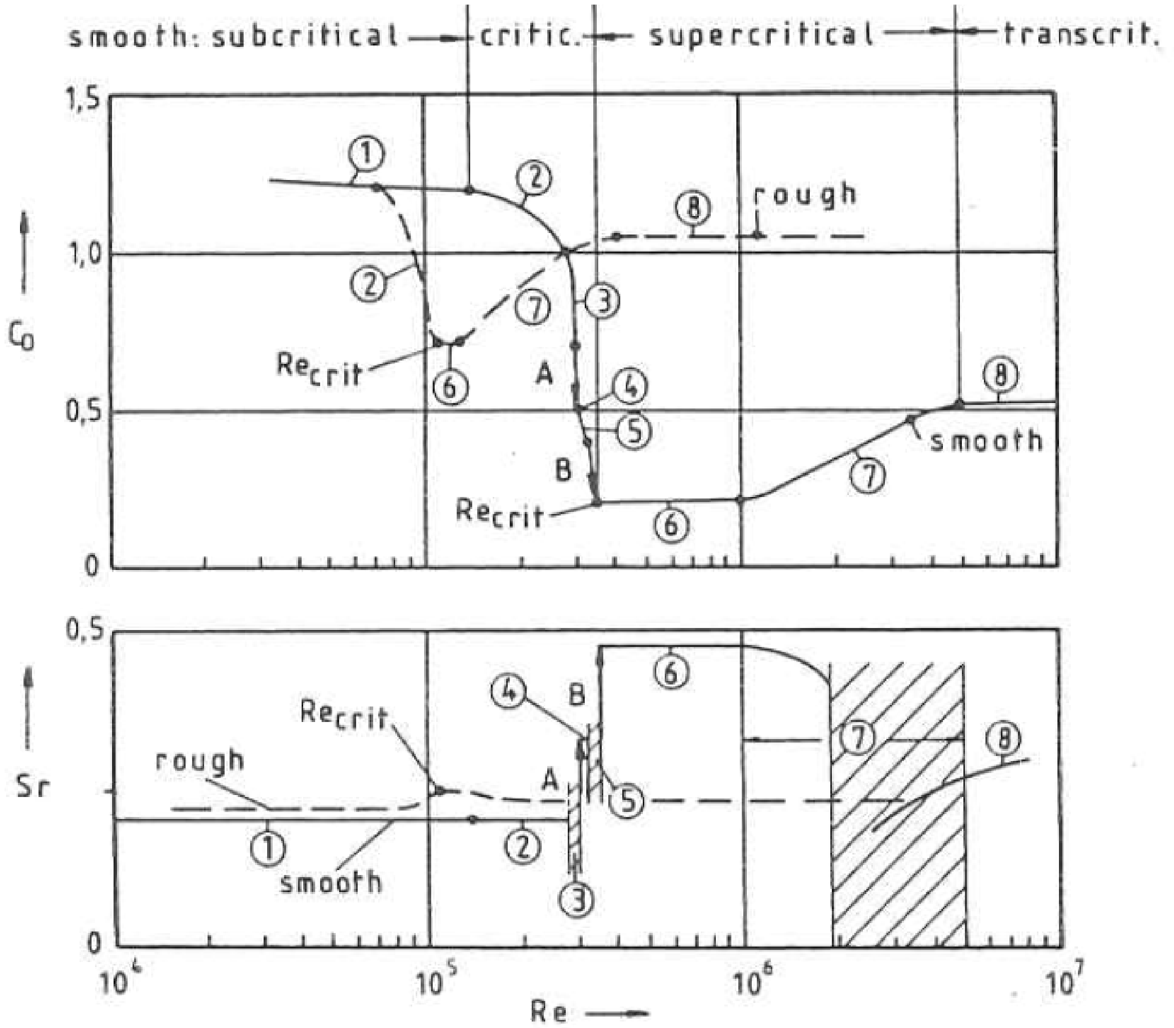

Figure 3.9 Flow regimes for smooth and rough cylinders. The corresponding flow regime description is counted in Figure 3.4 – review (Niemann&Hölscher, 1990)

Various surface roughness types are investigated by Achenbach&Heinecke (1981). Despite the differences in the curves (in terms, for example, of C_D and S_t), the fundamental boundary layer phenomena are the same for all roughness types. However, “the boundaries between the various regimes, as well the supercritical and post-critical drag coefficients and Strouhal numbers are a function of both the size and the type of surface roughness” (Buresti, 1981). In the same years, Güven et al. (1980) measures the effects on the mean flow past circular cylinders due to five different sizes of distributed sandpaper roughness. In particular, the pressure rise to separation results to be closely related to the characteristics of the boundary layer; smaller pressure rise is associated to thicker boundary layers. Larger roughness gives rise to a thicker and more retarded boundary layer which separates earlier and with a smaller pressure recovery. The influence of meridional ribs on the development of the boundary layer around a circular cylinder is calculated by an analytical method in Güven et al. (1983). Ribeiro (1991) investigates “which types of surface roughness are more efficient in triggering a transition of the flow so as to simulate the mean and fluctuating pressures occurring at ultra-critical Reynolds numbers”. Among sand paper, wire mesh screen and ribs, he finds that “all the roughness types were efficient in triggering regime transitions and in allowing the establishment of the ultra-critical regime with relatively low Reynolds numbers”. However, “an increase in relative roughness progressively distorts the mean pressure distribution results (distorts in the sense of deviating from what is observed with smooth circular cylinders)”. Therefore, he suggests that “the smallest relative roughness to establish ultracritical conditions should be chosen for simulation problems of cylindrical structures with circular cross-section and smooth surface”. Moreover, Ribeiro also observed that “the mean values of the force and pressure coefficients obtained with the ribs model were closer than any of the others to the values observed on smooth circular cylinders. The behaviour was such that, with regard to mean values, the rib roughness type seems the most appropriate to be employed in simulation problems of cylindrical structures of circular cross-section and smooth surface, because of its efficiency in establishing the ultra-critical condition and because it does not interfere excessively with the mean force and pressure coefficients”. According to Ribeiro, the same conclusion regarding the use of ribs also holds regarding the fluctuating loads, although the fluctuating values measured on the rough circular cylinders (at relatively low Re values) were larger than those observed on the smooth cylinder at high Re values.

Other important contributors on the topic are for example Batham (1973), who measured pressure distributions on smooth and rough cylinders at critical Reynolds numbers in uniform and turbulent flows; Szechenyi (1974, 1975), who performed supercritical Reynolds number simulations for two-dimensional flow over circular cylinders; Nakamura&Tomonari (1982), who studied the effect of different types of surface roughness at high Reynolds numbers; Basu (1985), who gathered data from a large number of experiments in order to describe the behaviour of the mean drag coefficient, the Strouhal number and the rms lift coefficient as functions of Re and relative roughness. In recent years, the effect of surface roughness on lift forces has been investigated by Eaddy (2004).

Last but not least, the effect of surface roughness is not only a simulation technique of high Reynolds numbers, but it is utilized for example on cooling towers to reduce wind-induced stresses in shell structures, by reduction of high lateral peaks of suction (VGB, 2010). However, this is not the case of solar towers, which should be smooth in full-scale in order to be subjected to lower drag forces (Figure 3.10b).

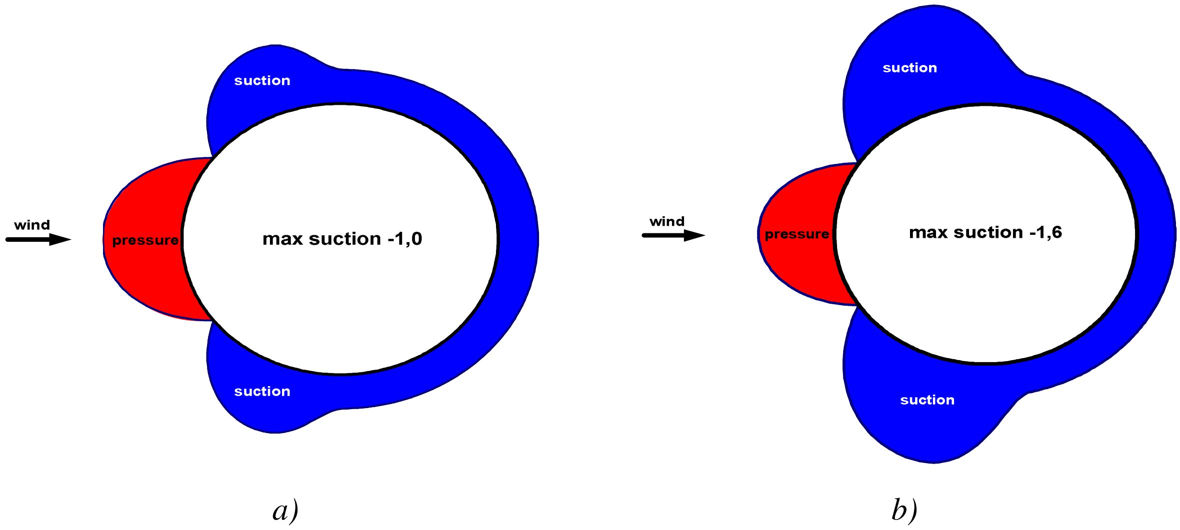

Figure 3.10 Mean pressure distribution at transcritical Re
a) rough surface, $C_{D,m} = 0.66$; *b) smooth surface,* $C_{D,m} = 0.46$ *(Niemann, 2009).*

3.4 Effect of free-stream turbulence

Free stream turbulence is basically characterized by two parameters: the turbulence intensity σ_U/U_m and the integral length scale of the longitudinal component L_{ux}. For very large ratios L_{ux}/D, longitudinal velocity fluctuations are perceived as slow changes in the mean wind speed and lateral fluctuations as slow changes in wind speed direction. Under these conditions, the quasi-steady approximation can be used to evaluate pressure fluctuations, by applying equation (3.3) (Basu, 1986). Instead, when L_{ux}/D ratios are small, further complication arises because turbulence is distorted by the presence of the body.

$$Cp_{\sigma}(\varphi) = \left\{ \left[\left(\frac{2\sigma_u}{U_m} \right) Cp_m(\varphi) \right]^2 + \left(\frac{dCp_m(\varphi)}{d\varphi} \right) \left(\frac{\sigma_v}{U_m} \right)^2 \right\}^{1/2} \tag{3.3}$$

Incoming turbulence modifies mean pressures and forces on a circular cylinder because it induces earlier transition to turbulence in the cylinder boundary layers or in the separated shear layers than would occur in smooth flow. Since small-scale turbulence is better able to interact with the cylinder boundary layers and shear layers than large-scale turbulence, at large turbulence scale-to-diameter ratios the interaction between free-stream turbulence and the cylinder boundary layers and wake is reduced, so that premature transitions are less likely to occur (Basu, 1986). Moreover, depending on the intensity of turbulence, two mechanisms play a major role: at low levels of turbulence the main effect is to disrupt the coherence of vortex shedding; at higher levels of turbulence the enhanced entrainment from the near wake into the shear layers dominates. Because of this last mechanism, while the influence of incoming turbulence on the fluctuating pressures in the stagnation region is direct, in the wake region it is more subtle. In fact, the wake region is separated from the external flow by the presence of the free-shear layers and only at sufficiently high intensity the small-scale turbulence is able to penetrate. Since the principal influence of free-stream turbulence is in the stagnation region, while the influence on the wake is quite weak, it is often assumed that the pressure fluctuations at the rear of the cylinder are independent on the incident turbulence.

As previously mentioned, further complication arises from the distortion that the turbulence experiences as the flow approaches and passes the cylinder. Hunt (1972) developed a theory, namely rapid distortion theory, to predict the modification of turbulence near a structure, and how these changes depend on the shape of the structure and on the scale of the turbulence relative to the structure. Once the disturbed flow field near the structure is mathematically described, the pressure fluctuations on the body surface can be predicted. This is the core of the theory, which aims to identify the effects of the incident turbulent on the unsteady velocities near a bluff body invested by wind and on the fluctuating pressures on its surface.

The effects of the incident turbulence should be distinguished from the effects of the self-induced unsteady velocities and surface pressures, which are induced near a structure when a completely steady wind blows around it. They are due to separated flows at the sides and rear of the obstacle and to instability of the flow at the ground or at the tip. The theory assumes that the intensity of the upwind turbulence is weak and it does not interact with the velocity fluctuations induced by the wake. In this way, the velocity fluctuations outside the wake caused by eddies shed at the wake boundaries are statistically independent on the velocity fluctuations caused by the upwind turbulence. Therefore, the two types of velocity fluctuations can be analyzed separately (Hunt, 1975). This assumption is only approximately true. In fact, fluctuations of the incident wind can strongly effect the fluctuations caused by eddy shedding. For example, if there is a significant amount of energy in the velocity fluctuations of the incident wind at frequencies close to the eddy shedding in the wake, the eddy shedding may be amplified. Experiments by Britter et al. (1979) showed that the vortex shedding peak is altered by the incident turbulence, because it may occur at a slightly lower frequency and be more broad. In general, problems to the applicability of the theory arise if there is an appreciable correlation between wake induced fluctuations and velocity fluctuations in the incident turbulence. The correlation results from the modification of the self-induced fluctuation due to incoming turbulence. However, this should not be significant if $\sigma_{u,\infty} << U_{m,\infty}$, i.e. the turbulence of the incoming (undisturbed) flow is weak. Moreover, it is interesting to note that the addition of a splitter plate, which is able to suppress vortex shedding, improves the agreement between the theory and the experiments.

The core of the theory – which allows to consider the self-induced velocity fluctuations in the external region (resulting by the unsteady wake) as statistically independent on the velocity fluctuations produced by upwind turbulence – is the rapid distortion of turbulence by changes in the mean velocity produced by the body. In other words, turbulence is disturbed so rapidly by changes in the mean velocities close to the body, that each wave number (or eddy) is distorted separately before it can exchange energy non-linearly with other wave numbers. Therefore, a limitation of the theory is that it is linear. In fact, non-linear effects can be important, especially at high frequencies, where non-linear terms do not decay as rapidly as the linear terms. In any case, a good applicability of the theory is guaranteed if the time scale for the non-linear interaction between energy-containing eddies (L_{ux}/σ_u) is large compared with the time required for the fluid to flow round the obstacle (a/U_m where "a" is used in Figure 3.11 to indicate the cylinder radius). In other words, if $(\sigma_u/U_m)(a/L_{ux}) << 1$, then the turbulence is primarily distorted by the mean velocity field before it can be modified significantly by non-linear interactions: the distortion is rapid. This criterion for linearization – suggested by Hunt (1973) – is considered even too restrictive in Durbin&Hunt (1980) and re-formulated in that paper.

The changes in the turbulent velocity field in the disturbed region near the structure have a simple physical explanation. Two phenomena explain qualitatively the amplification or reduction of the turbulent components: $^{1)}$ distortion by the mean flow of the turbulent vorticity; $^{2)}$ blocking or source effect caused by turbulence impinging on the cylinder surface. Near the stagnation point the vortex lines in the x-direction are decreased while those in the y-direction are stretched and those in the z-direction are unaffected (two dimensional case, far from end conditions). So, at stagnation, the eddies which are small compared to the structure are piled up and stretched out. Instead, if the turbulence scale is much larger than the radius of the cylinder there is no effect of vortex stretching, only a blocking effect of the cylinder (Hunt, 1975).

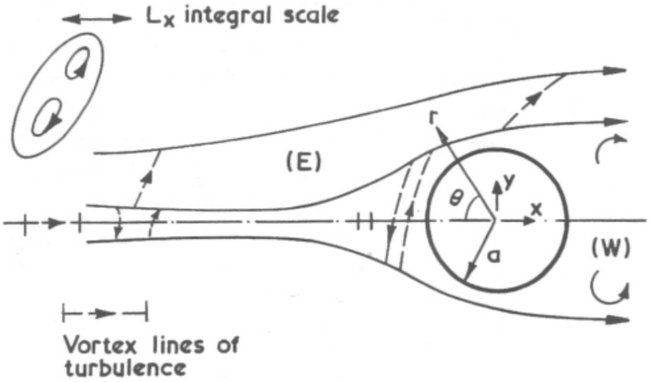

Figure 3.11 Mean streamlines around a circular cylinder showing compression and stretching of vortex lines (E stands for external region, W stands for wake region) (Hunt, 1975)

By assuming a rapid distortion, the movement of vortex elements can be described by the movement of line elements (Figure 3.11) and the movement of line elements is known if the mean velocity field near the body is known. The field of mean velocity will stretch and rotate vortex lines, altering the distribution of turbulent vorticity and thus changing the turbulent velocities. This stretching and rotating of vortex lines will take place over a distance in which the mean velocity field is significantly altered by the bluff body, i.e. over a distance a few times the radius of the cylinder (Britter et al., 1979). Instead, the blocking effect produces a change in the turbulence over a distance comparable to the scale of turbulence L_{ux} or the cylinder radius a, whichever is smaller. The relative importance of the distortion effect over the blocking one increases as a/L_{ux} increases or the distance from the cylinder increases. The effect of turbulence scale with respect to the diameter of the cylinder is demonstrated in (Hunt, 1973) by measuring the ratio between the rms values of the u-components in the undisturbed flow and in the disturbed flow near the structure ($\sigma_{u,\infty}/\sigma_u$) as a function of the ratio between cylinder radius and L_{ux} (a/L_{ux}). The issue is further addressed in Britter et al. (1979). Figure 3.12 (Britter et al., 1979) summarizes these results. If turbulent eddies are small with respect to the cylinder diameter (small scales, $a/L_{ux} >> 1$), on the stagnation line σ_u increases and σ_v decreases. However, close to the surface where both vorticity distortion and the source effect are significant, the amplification of σ_u decreases and σ_v increases. For large scales ($a/L_{ux} << 1$) the source effect dominates, turbulence is blocked by the cylinder and consequently σ_u decreases and σ_v increases. At the flanges of the cylinder (90°) the opposite occurs. The vortex lines of small scale eddies are stretched in the x-direction, but reduced in the y-direction, so that σ_u is reduced (x-direction) and σ_v is increased (y-direction), while the blocking effect acts in the cross-wind direction.

Hunt's theory predicts results for the two asymptotic limits $L_{ux}/a >> 1$ and $L_{ux}/a << 1$. The large scale limit is described by the well-known quasi-steady theory (equation (3.3)), while the small-scale limit is introduced by Hunt as a quasi-homogeneous or slowly varying approximation, where the turbulence vorticity around the body is given in terms of the upwind fluctuating vorticity and the mean velocity field. The latter is given by the standard potential-flow solution for a circular cylinder, as if separation does not take place. The quasi-steady theory for large scales is simpler than the small scale theory, because the incident vorticity is not distorted by the obstacle, which only blocks the flow. For intermediate scales, it is not practical to apply the rapid distortion theory, but reasonable extrapolation formulas (e.g. for the stagnation point) are proposed in Durbin&Hunt, 1980. In any case, whatever the value of L_{ux}/a, if the frequency is sufficiently high the results for spectra tend to the limiting situation where $L_{ux}/a << 1$.

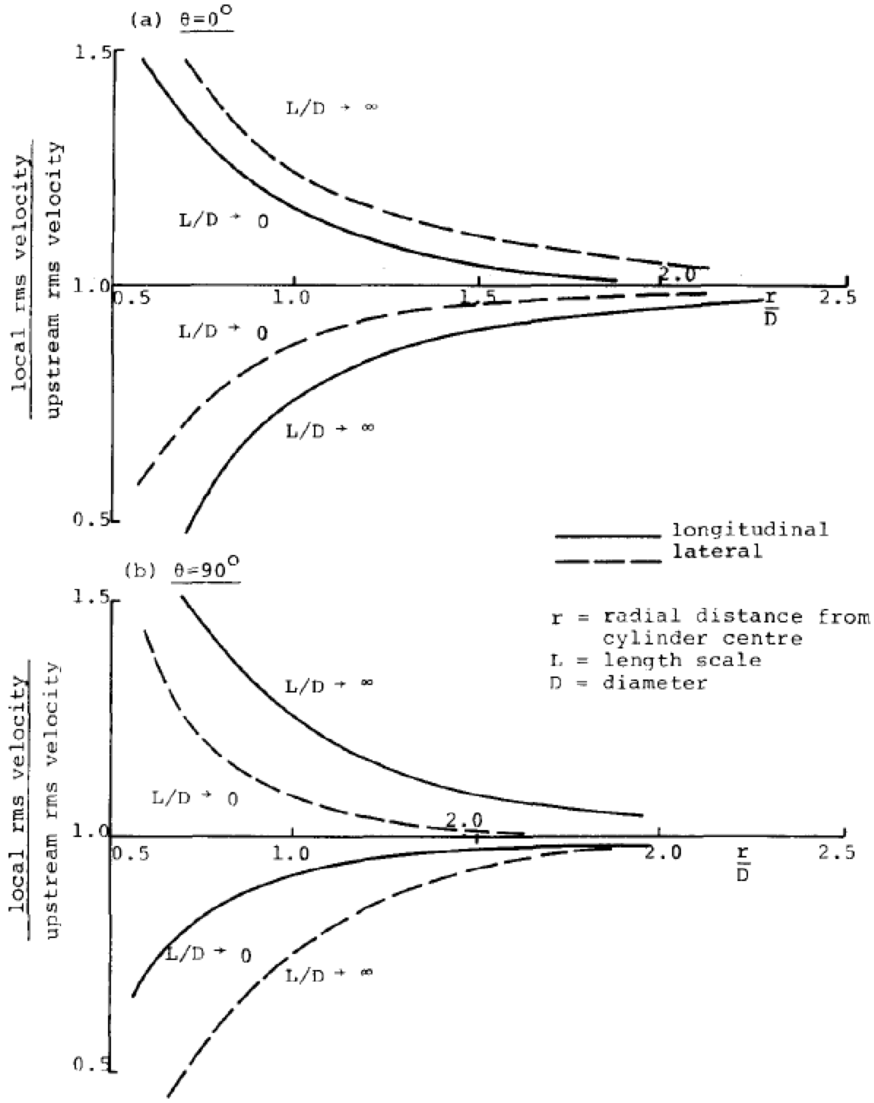

Figure 3.12 Modification of fluctuating velocities near the cylinder in small- and large-scale turbulence (Britter et al., 1979)

This Dissertation does not go further into the mathematical model behind Hunt’s theory (Hunt, 1972, 1973). However, the physical principles represented the basis to develop the wind load model in Chapter 7. Such physical principles have been applied to experimental data measured in two wind tunnels (WiSt and CRIACIV) in order to separate turbulence-induced and body-induced pressure fluctuations (section 7.1.3).

3.5 Three dimensional effects

This section addresses the aerodynamic of the flow around finite-length circular cylinders of high aspect ratio, characterized by Karman vortex shedding, where end-effects still dominate for large part of the height. Solar updraft towers are represented at best by this category. Three dimensional effects arise at the top due to the free end and at the bottom due to the ground surface. They depend on the aspect ratio, on the boundary layer conditions (uniform or shear layer) and on Re. Literature at high Re is scarce, therefore most of the experiments and simulations mentioned in the following are performed in sub-critical conditions.

In the ground-wall region, a three dimensional separation of the boundary layer occurs upstream of an obstacle and a so-called horseshoe (or necklace) vortex system develops at the base of the body. In fact, the cylinder end is submerged in a retarded wall boundary layer and an adverse pressure gradient is created. This causes the three dimensional boundary layer separation at some distance upstream of the body, followed by a roll-up of the separated boundary layers into a system of swirls. The swirl system is swept around the base of the cylinder and assumes a characteristic shape, which is responsible for the name “horseshoe vortex”.

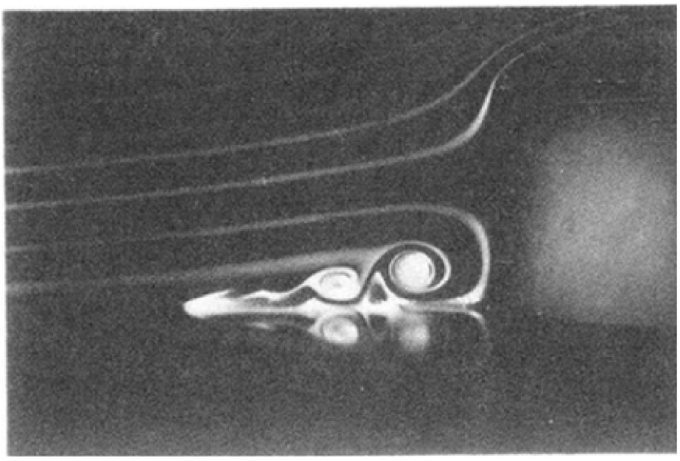

Figure 3.13 Horseshoe vortex system: experiment by Sutton (1960) in laminar boundary layer, reported in Baker (1991)

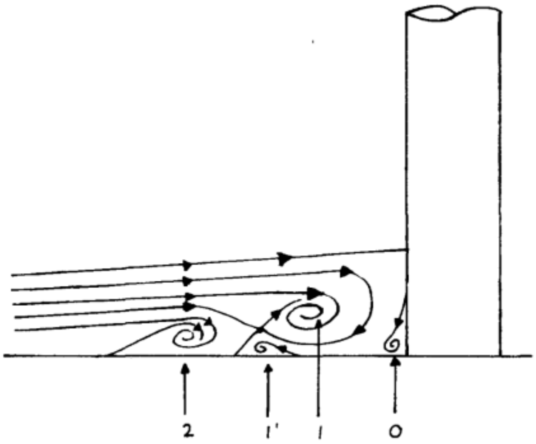

Figure 3.14 Turbulent horseshoe vortex system: sketch by Baker (1980)

As explained by Zdravkovich (2003), the physical parameters governing the horseshoe vortex system and the number of swirls are the thickness of the wall boundary layer and the cylinder diameter. The wall boundary layer may be laminar or turbulent, depending on the Re of the boundary layer, which includes the flow velocity and viscosity and – as characteristic length – the thickness of the boundary layer. If the upstream boundary layer on the wall is laminar, then the flow pattern results in steady laminar horseshoe vortices, as those shown in Figure 3.13. This is an early photograph taken by Sutton (1960) and reported in Baker (1991). There are three clockwise and three anticlockwise rotating vortices on the plane of symmetry upstream of the cylinder.

A literature review about laminar and turbulent vortex systems is presented in Baker, (1978, 1980). In particular, Figure 3.14 (Baker, 1980) shows the flow pattern of a turbulent horseshoe vortex upstream of a cylinder at low Re ($4*10^3 < Re < 9*10^4$). Four vortices (0, 1, 1' and 2) are detected in the figure. Vortex 1 is the main or primary vortex, vortex 1' is caused by separation of the boundary layer beneath vortex 1. Vortex 0 is caused by separation of the boundary layer on the upstream face of the cylinder. Baker (1990) studies the oscillatory behavior of horseshoe vortices in the transitional regime, between the steady laminar horseshoe vortices which occur at low Reynolds number and the fully turbulent horseshoe vortices that occur at higher Reynolds numbers.

The distance from the boundary layer separation to the cylinder depends on the height and diameter of the cylinder. When the height is greater than the wall boundary layer thickness, the separation is independent on the height of the cylinder. According to Belik (1973), such a distance lies between 0.45D and 0.65D. Baker (1991) also measured that for $H/D > 1$ the separation length tends to 1.1D, independent on H/D.

The size of the horseshoe vortices, relative to the height of the cylinder, decreases as the height of the cylinder increases (Okamoto&Sunabashiri, 1992). Zdravkovich (2003) estimates that the mean pressure distribution along the cylinder, at the cylinder foot, is modified by the horseshoe vortex system for a spanwise distance of about only one third of the diameter.

Hölscher (1993) measured the pressure distribution on the ground plane around a finite circular cylinder of low aspect ratio ($H/D = 2$). Roughly, the circumferential pressure on the cylinder surface is reflected on the ground plate. Positive pressures on the windward surface of the cylinder also act on the ground plate in the region upwind of the body. This study indicates that the extension is about one diameter upwind of the junction for a body totally immersed in a turbulent boundary layer. It is directly correlated to the size of the horseshoe vortex system. As the surface pressures on the cylinder decrease with the circumference, negative pressures arise on the ground plate. However, maximum suction appears in the near wake in the plane of symmetry and not at the side of the cylinder. The unsteadiness of the wake flow generates significant pressure fluctuations. They even exceed the pressure fluctuations on the windward side, which are on the other hand directly determined by the turbulence intensity of the approaching flow. Due to the free-end effect, the base pressure in the wake of a short cylinder is higher than in the case of a tall cylinder. Taniguchi (1981) and Okamoto&Sunabashiri (1992) provide comparisons of surface pressure distribution on the ground plane for cylinders of different aspect ratios.

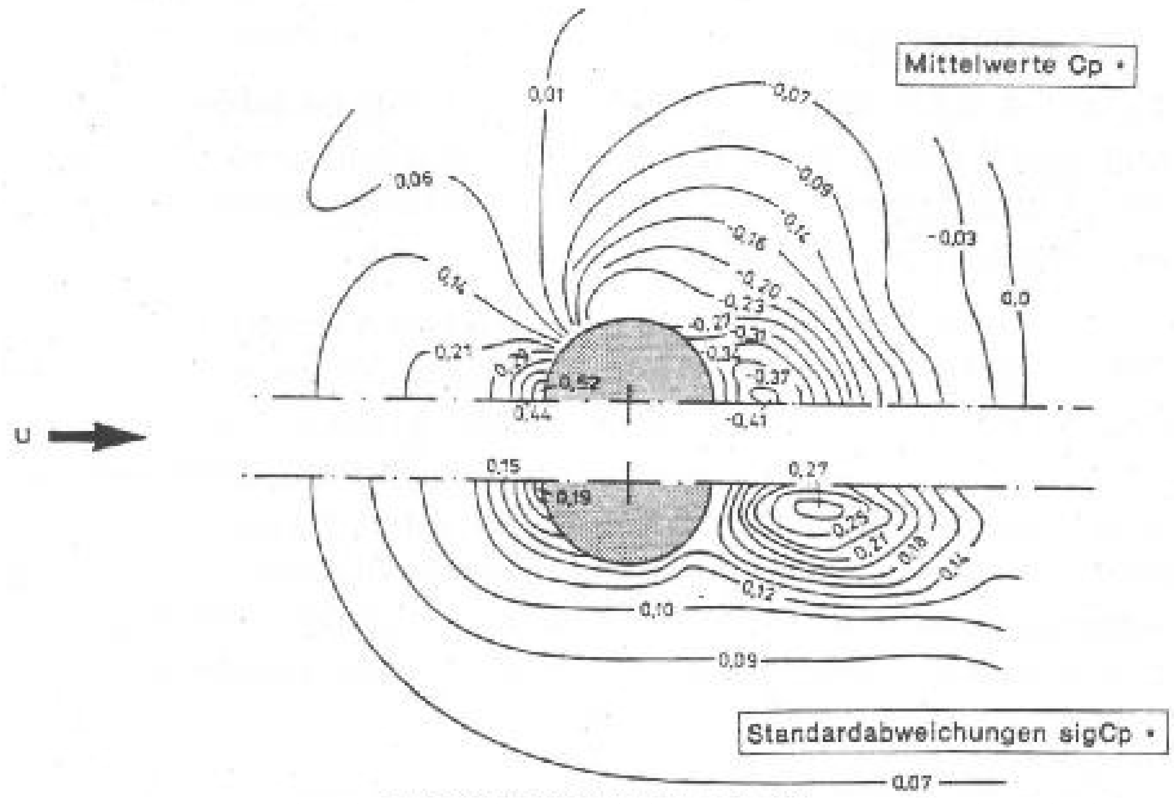

Figure 3.15 Pressure distribution on the ground plane around a finite circular cylinder. Top: mean pressure coefficient, bottom: rms-value of pressure fluctuations. H/D = 2, Re = $3.1*10^5$ (Hölscher, 1993)

In the wake, the surface pressures on the ground plane are the result of a time-averaged recirculation region behind the cylinder and depend on the aspect ratio. For small aspect ratios, the streamlines over the top of the cylinder reattach to the ground plane downstream. Okamoto&Sunabashiri (1992) identified the size of such a recirculation region for cylinders of different aspect ratio. Tests were performed in uniform flow at

Re = 2.5-4.7*10^4. According to those results, the recirculation region enlarges with an increase in H/D, as long as H/D ≤ 4. But the recirculation region decreases in the case H/D ≥ 7, because the end effect is limited to the portion near the free-end. The steady recirculation region observed in the experiments by Palau-Salvador et al. (2010) on a H/D = 5 circular cylinder at Re = 2.2*10^4 is instead somewhat smaller (Figure 3.17).

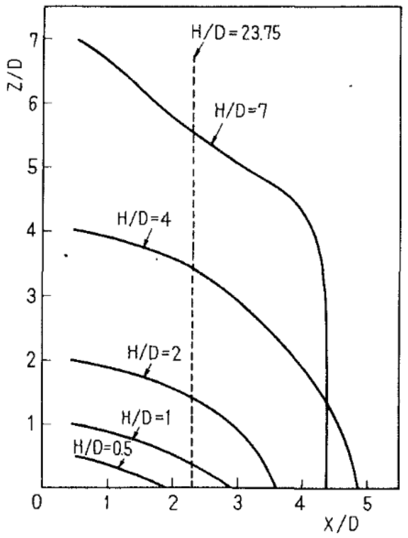

*Figure 3.16 Wake recirculation, Re= 2.5-4.7*10^4 (Okamoto&Sunabashiri, 1992)*

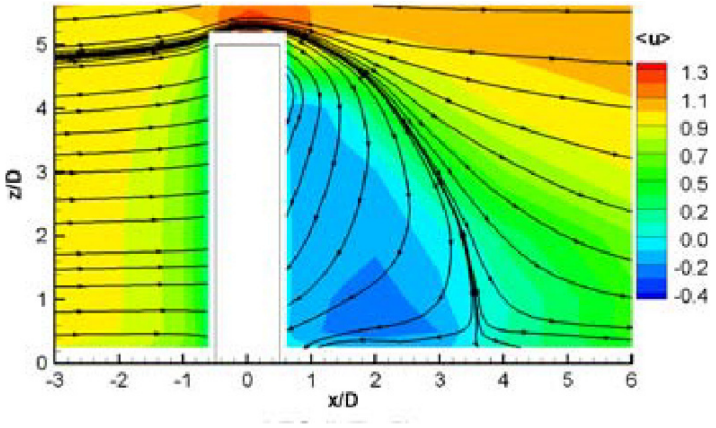

*Figure 3.17 Recirculation region in the wake, H/D = 5, Re = 2.2*10^4 (Palau-Salvador et al., 2010)*

A recent investigation on the influence of the aspect ratio on the wake structure is presented in Rostamy et al. (2012) and summarized in Figure 3.18. The study, based on a PIV visualization, is performed in flat-plate turbulent boundary layer on cylinders of aspect ratio H/D = 9, 7, 5, 3 and at Re = 4.2*10^4. The cylinders have a close end. The study highlights the strong downwash in the near-wake region, which originates near the free-end and descends in the central portion of the wake. The large recirculation zone is marked by the "dividing streamline"; the flow above it moves away from the cylinder. Within the recirculation zone, a small vortex forms immediately below the free-end. The size of this vortex varies with the aspect ratio; the largest vortex occurs for the smallest aspect ratio (H/D = 3). Depending on the size of this vortex, the flow in the tip region can move upwards along the cylinder wall toward the free-end, as it happens in Figure 3.18 c and d (H/D = 5 and 3, respectively). Near the ground, a weak upwash flow can be seen for H/D > 3, which moves towards the central region of the wake. This creates a vortex, namely base vortex, near the cylinder wall-junction. For H/D = 3 the base vortex and the upwash are absent. This is not surprising, because the wake structure of a low aspect ratio circular cylinder is completely different (for example symmetric arch-type vortices develop), as it will be explained in the following. For all the aspect ratios, a saddle point (black point in the figure) is identified between the two vortices near the free-end and near the cylinder-wall junction. This point marks the streamwise extension of the recirculation zone, as previously identified by Okamoto&Sunabashiri (1992). Accordingly, the saddle point moves downstream as H/D increases, below H/D = 7 up to x/D = 3.8. Results are not too far from Palau-Salvador et al. (2010). For H/D = 9 the saddle point moves closer to the cylinder at x/D = 3.

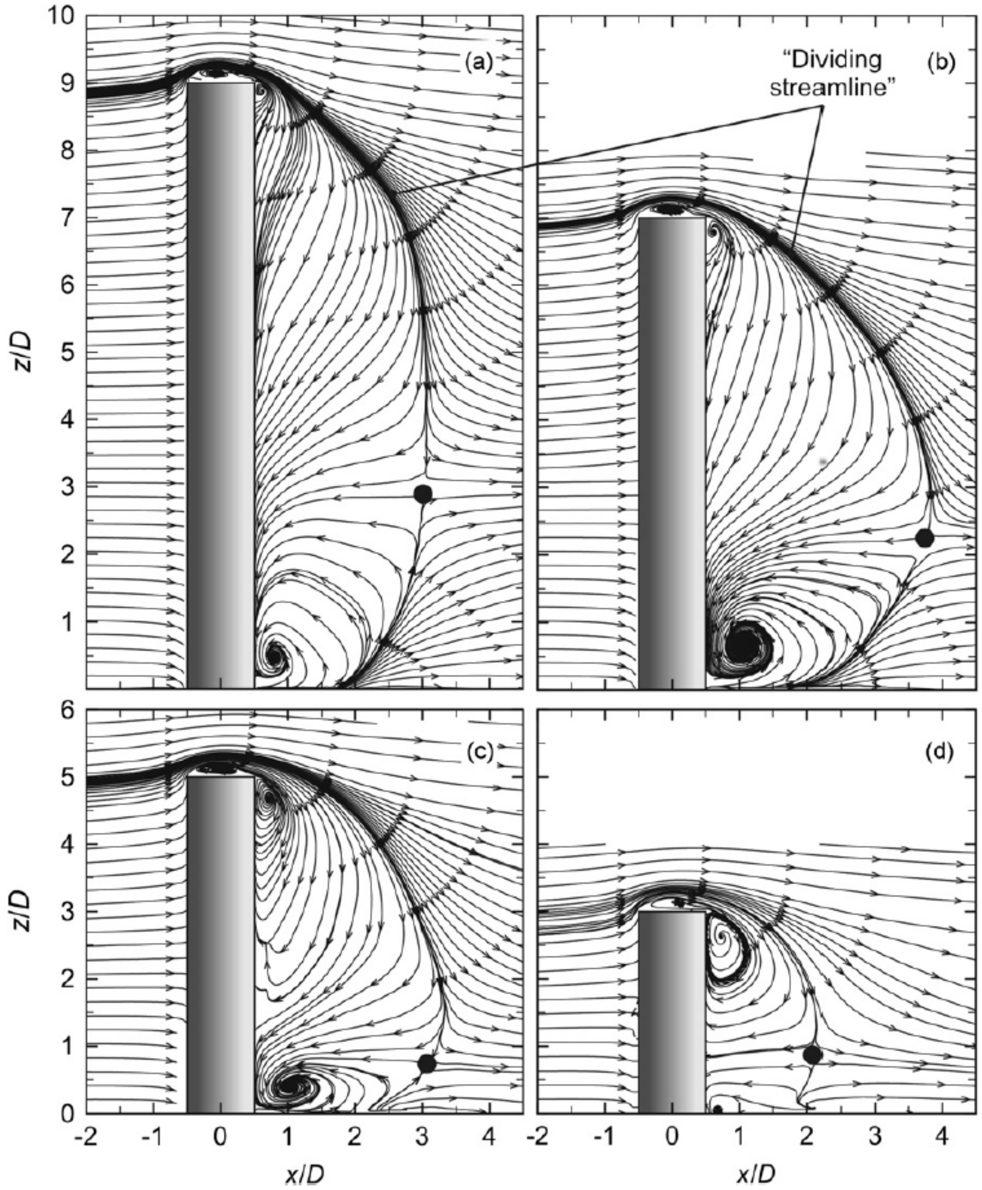

*Figure 3.18 Mean streamline field in a vertical plane on the wake centreline for: a) H/D = 9; b) H/D = 7; c) H/D = 5; d) H/D = 3; Re = 4.2*10⁴, flat-plate turbulent boundary layer (Rostamy et al., 2012)*

A clear visualization of the near-wake flow behind a H/D = 6 circular cylinder at Re = $2*10^4$ is described by using LES in Krajnovic (2011). Particular attention is paid to the upwash flow and the base vortices in uniform flow, namely N_w in the paper (with left and right legs N_{wl} and N_{wr}). “As seen in Figure 3.19, the flow in the symmetry plane moves towards the cylinder near the ground and bends down after the stagnation point, forming the N_w vortex. While the lower part of the near wake is dominated by the downwash very close to the cylinder, the upwash dominates further downstream. This is a result of the two legs, N_{wl} and N_{wr}, rotating in counter-clockwise and clockwise directions, respectively (Figure 3.19 high right-hand side corner)”. In the symmetry plane downstream of vortex N_w (Figure 3.19 low right-hand side corner), a focus F_{nw} and a saddle point S_{nw} are visible. They indicate the closure of the separation region in the near wake”.

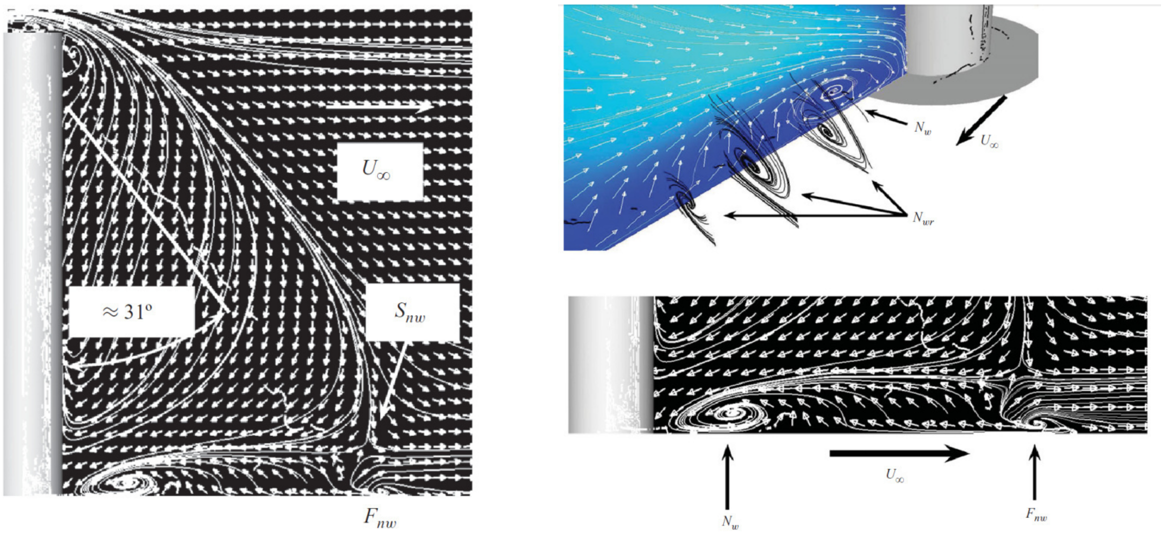

Figure 3.19 Near wake visualized with vortex cores, streamlines and velocity vectors H/D = 6, Re = $2*10^4$, uniform flow (Krajnovic, 2011)

An analogous simulation, but in boundary layer flow (Sumner&Heseltine, 2008, H/D = 3 to 9, Re = $6*10^4$) showed a similar base vortex pair (distinct from the horseshoe vortex) close to the ground. However, probably due to the boundary layer, the vortices are of different size and at higher position if compared to those in Figure 3.19. Figure 3.20 shows the strong downwash behind the cylinder and the weak upwash near the ground plane, which is associated to the base vortices. It is confirmed in this paper, that for low aspect ratios (e.g. H/D = 3) the downwash extends almost to the wall, while the base vortices and so the upwash are absent: the wake structure is then completely different. A further proof is observed by using PIV in Rostamy et al. (2012).

A flow visualization of the surface flow pattern at the base of a circular cylinder at high Re is also published by Gould et al. (1968) and shown in Figure 3.21. It refers to uniform flow conditions, but a certain boundary layer is naturally developed at the tunnel floor. The figure clearly shows the downstream movement of the separation line at the ground. The importance of these experiments, is that they are performed on a smooth cylinder in a pressurized wind tunnel up to Re = $5.4*10^6$. Therefore, they represent one of the few tests available in literature in transcritical conditions. Because of that, they will be often used as reference in the following.

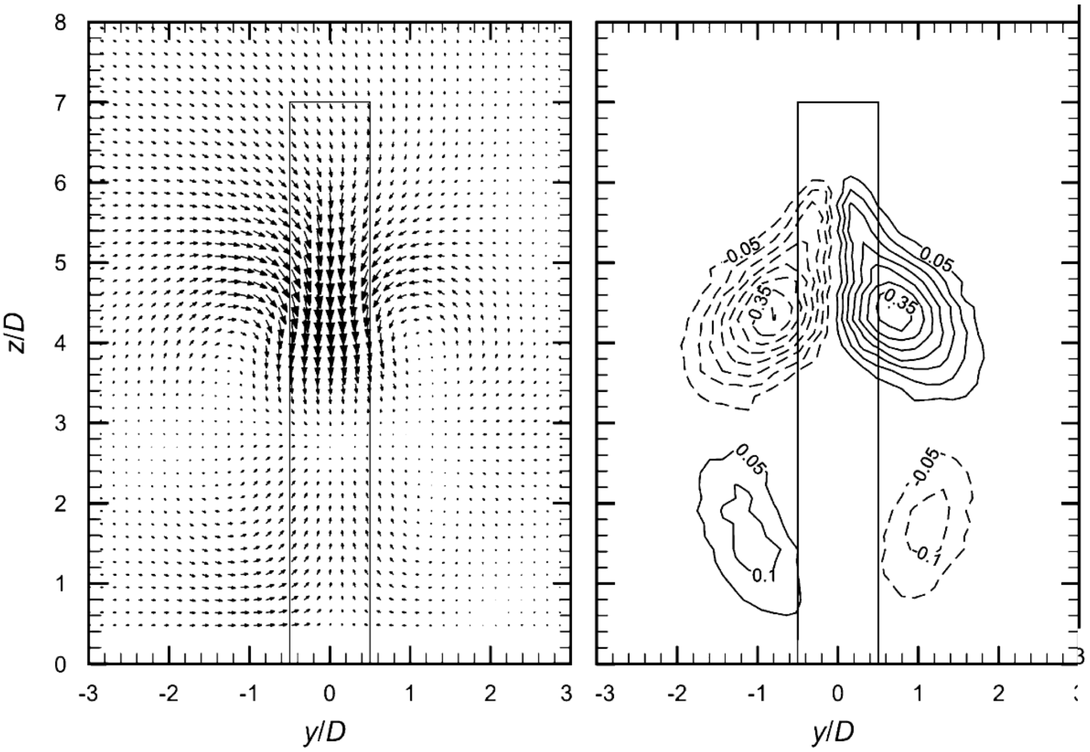

Figure 3.20 Time-averaged wake structure: in-plane velocity field and streamwise vorticity field behind the cylinder (dimensionless vorticity contour increment 0.05, minimum vorticity contour ±0.05, solid line represent counter clockwise vorticity, dashed lines represent clockwise vorticity). H/D = 7, Re = $6*10^4$, boundary layer flow (Sumner&Heseltine, 2008)

In the tip region (Figure 3.22), because the pressure induced by the flow on the forward facing surface is significantly higher than that on the rearward facing surface, a flow is induced over the tip of the cylinder from front to rear. The separated flow over the tip creates a region of very low pressure, which induces a spanwise flow towards the tip of the cylinder. This flow sweeps up the separated shear layers from intermediate heights. At short distance below the free-end (about D/2), vortex sheets roll up into a pair of trailing (tip) vortices, which form because of the interaction between the upward-directed separated flow at the sides of the cylinder and the downward-directed flow over the tip. The tip vortices are counter-rotating open vortex loops with their axis perpendicular to both the free-stream direction and the longitudinal axis of the cylinder. The tip effect is governed by the difference of pressure between the front and the rear surfaces of the cylinder and it extends for the upper two or three diameters. In sub-critical flow conditions the wake suction is high (thus high drag), therefore it is expected that the tip effect in sub-critical conditions is more vigorous than in transcritical conditions, being the latter accompanied by a smaller wake with a lower base suction (ESDU 96030).

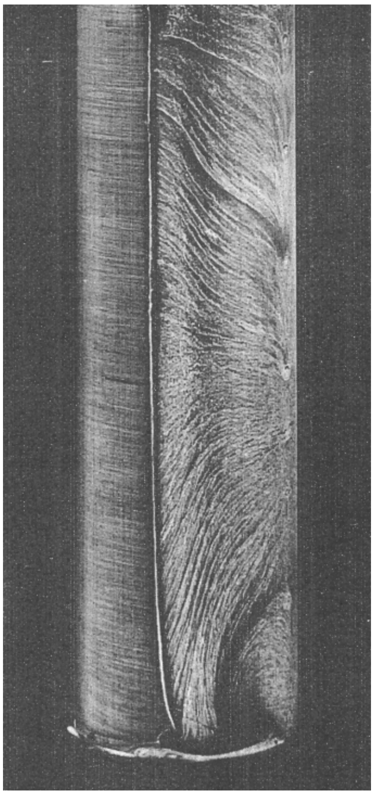

Figure 3.21 Flow pattern in the bottom region at high Re (Gould et al., 1968)

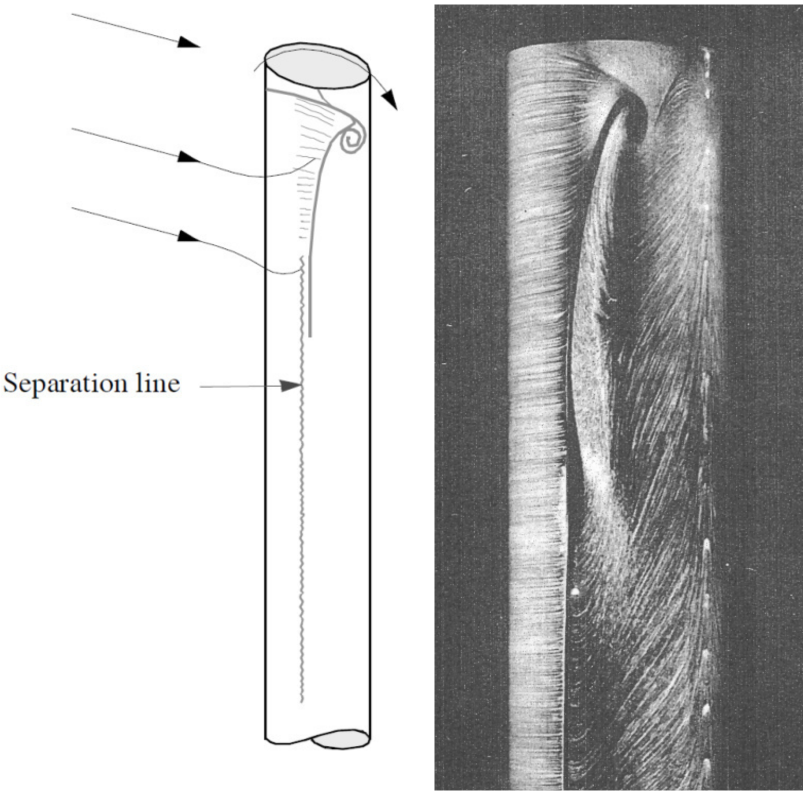

Figure 3.22 Flow pattern in the tip region:
a) Sketch of tip trailing vortices (ESDU 96030);
b) Flow visualization at high Re (Gould et al., 1968);

In presence of an efflux from a chimney, wind tunnel tests show that, at sub-critical Reynolds numbers ($Re < 10^5$), the effect of the efflux is to increase the response. However, at higher Reynolds number (as it is for solar towers) the effect is likely to be reversed (ESDU 96030).

Gould et el. (1968) also investigated the effect of efflux. In their experiments without efflux, it is confirmed the presence of tip vortices originating from the top of tower, within the plane where the local drag coefficient is maximum (i.e. at D/3 from the top, where D stands for diameter), as shown in Figure 3.22. In presence of efflux, it is noticed that there is a distortion of such a pattern. As a result, the vortices can be seen at one diameter from the top (instead of D/3). Gould et al. suggested that the effluent plume generates another pair of vortices just above the top of the chimney. These are opposite in sign to the original pair present in the absence of efflux. As the velocity of the efflux increases, the upper pair of vortices increases in strength and causes a displacement and weakening of the original pair. The apparent effect of an efflux is thus to raise the height at which the peak loading is experienced to a level closer to the top of the chimney. In such a way, there is an extension of the quasi-two dimensional region (out of the influence of the tip effect), where the drag and lift coefficients are smaller. Moreover, it is also observed in practice that if a chimney is seen to oscillate, then increasing the efflux by opening the flues will generally reduce the oscillation amplitude. Thus, at high Reynolds numbers, it is likely to be conservative to assume that the no-efflux condition presents the more critical design case (for both the along and the across wind response). The ESDU Data Items (ESDU 81017) give the same recommendation. In particular, when H/D is greater than 4 the drag coefficient is larger when the free-end is not closed, but if there is an efflux from the open end the drag coefficient is reduced approximately to the value it would have with a closed end. It is then common practice (at least for what concerns the mean load) to design a stack with the top open and no-efflux.

In summary, the three-dimensional flow pattern around a slender finite length circular cylinder, is characterized by the horseshoe vortices forming upstream at the cylinder-wall junction, a recirculation region in the near-wake, with a small vortex below the free-end and base vortices near the ground plate. The latter develop strongly in boundary layer flows as a result of an upwash near the ground. In the tip region, there are counter rotating open vortex loops, named tip vortices. As regards the fluctuating field, there is the familiar Karman vortex shedding from the sides of the cylinder. This may present, along the height, a variation of the Strouhal number, as it will be explained afterwards. Now, the mean and rms loading pattern on the cylinder surface is analyzed.

In literature, one of the first studies of the spanwise distribution of mean force and pressure coefficients in uniform and shear flow for different aspect ratios has been carried out by Okamoto and Yagita (1973, 1984) at $Re = 1.3*10^4$. The mean iso-pressures lines for a slender circular cylinder (H/D = 9) in uniform flow and shear flow (uniform shear flow) are reported inFigure 3.23 and Figure 3.24, respectively. The velocity profile for the uniform shear flow of those experiments has a non-dimensional velocity gradient of 0.4 and it is expressed by the relation: $U(z)/U(H/2) = 1 + 0.4*(z/H – 1/2)$.
Figure 3.23 and Figure 3.24 show that the free-end effect is limited to the upper three diameters and it is not affected by the boundary layer conditions. Only for smaller

aspect ratios (H/D ≤ 5 according to Okamoto&Yagita, 1984) the end effect would reach the root of the cylinder.

A typical feature of the mean surface pressure distribution in the tip region is the minimum pressure around $\phi \approx 70°$ at $z' \approx 2/3D$ from the free-end. It is due to the displacement of the separation to higher angles. Then, a second islet of minimum pressure appears at $\phi \approx 135°$ and $z'/D \approx 1/3$ from the free-end. This second $C_{p,min}$ arises considerably the local drag near the free-end. In fact, the $C_{D,max}$ is more pronounced on slender cylinders (H/D ≥ 7) and it is followed by a decrease at lower levels. $C_{D,max}$ exceeds the value of the nominal drag for two-dimensional circular cylinders (Figure 3.27 and Figure 3.28)

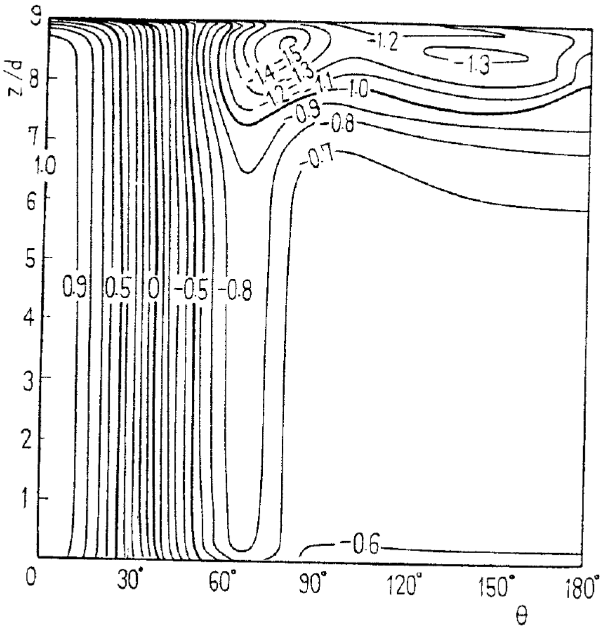

Figure 3.23 $C_{p,m}$ in uniform flow. H/D = 9, Re = $1.3*10^4$ (Okamoto&Yagita, 1984)

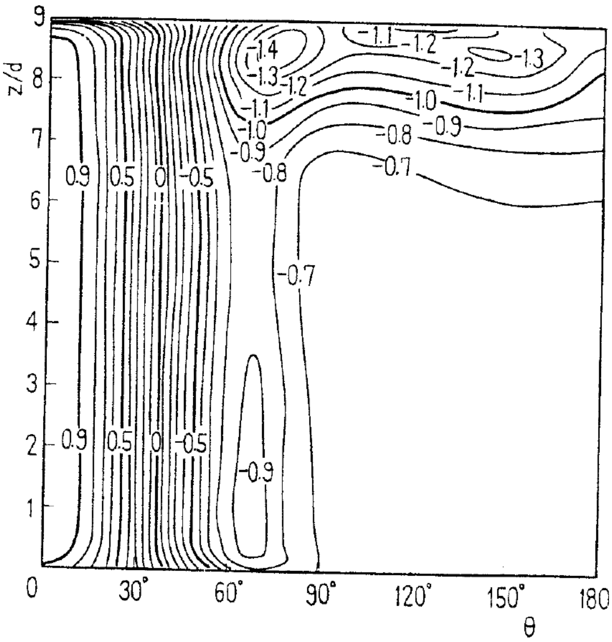

Figure 3.24 $C_{p,m}$ in uniform shear flow. H/D = 9, Re = $1.3*10^4$ (Okamoto&Yagita, 1984)

The bottom region of the cylinder in figure Figure 3.24 is influenced by the shear flow condition, but the effect is not so strong. In the low region, at the stagnation line, the C_p distribution tends to deviate from the unitary value due to the downflow produced by the horseshoe vortices. This effect is enhanced by the velocity gradient in shear flow. In shear flow there is also an increase in lateral suction at the base of the cylinder. It has, however, little effect on the drag, which results to be uniform along the height below the tip region for H/D = 9, both in uniform and in shear flow (Figure 3.27 and Figure 3.28).

At higher aspect ratios, e.g. H/D = 12, and in shear flow, the region of low pressures at the rear side gradually extends towards the root of the cylinder (Figure 3.25). The increase in wake suction at the bottom (see Figure 3.26 at high aspect ratios) implies higher drag in the low region of the cylinder. It is remarkable that this occurs for sufficiently high aspect ratios and only in shear flow, as confirmed by Figure 3.28.

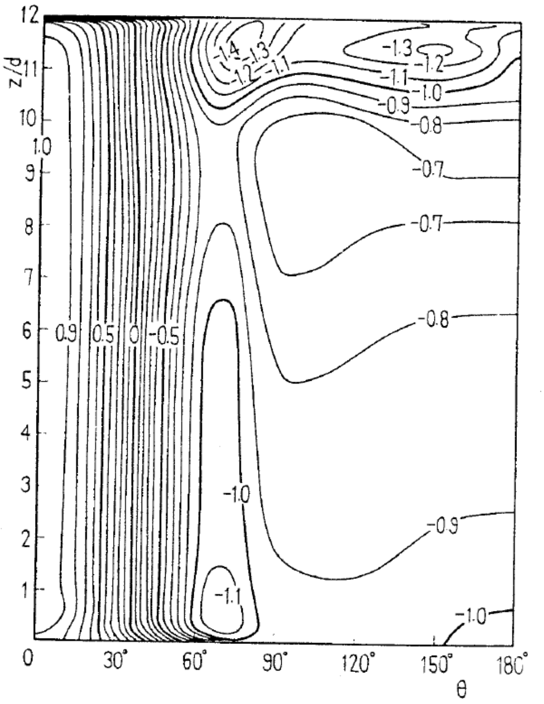

Figure 3.25 $C_{p,m}$ in uniform shear flow.
H/D = 12, Re = $1.3*10^4$
(Okamoto&Yagita, 1984)

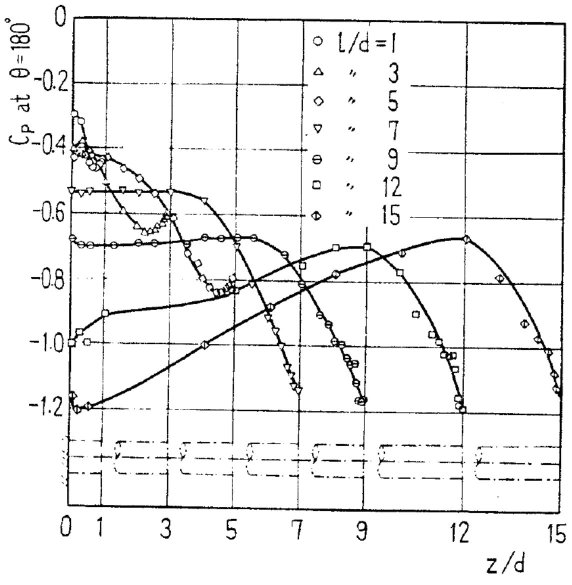

Figure 3.26 $C_{p,m}$(180°) in uniform shear flow.
H/D from 1 to 15, Re=$1.3*10^4$
(Okamoto&Yagita, 1984)

It is remarkable to further comment the comparison of local drag coefficients in uniform and shear flows in Figure 3.27 and Figure 3.28: the mean drag at low levels is constant in uniform flow, while it rises in shear flow when the aspect ratio is sufficiently high. The authors mention the existence of a secondary flow in the rear of the cylinder, which does not appear in the uniform stream. They conclude that "the pressure at the rear side of the cylinder of H/D $\geq$ 12 gradually decreases and the local drag coefficient increases as the root of the cylinder in a uniform shear stream is approached, while the pressure at the rear side of the cylinder of H/D $\geq$ 7 is nearly constant in the lower portion free from the end effect in a uniform stream".

With this regard, Farivar (1981) confirmed that in uniform flow (Re = $7*10^4$) the base pressure coefficient is independent on height in the range 0.39 $\leq$ z/H $\leq$ 0.81. At z/H $\leq$ 0.39 the variation of the base pressure was attributed to the boundary layer at the tunnel floor. Luo et al., 1996 showed that in uniform flow (at Re = $3.33*10^4$) the pressure in the stagnation region is relatively insensitive to variation of both H/D and spanwise location, with exception near the free-end. Instead, the pressure in the wake shows strong aspect ratio and spanwise position dependence. This is mainly due to tip effects, while the spanwise dependence is greatly reduced at $z/H \leq 0.5$. This is in agreement with other results in uniform flow.

In boundary layer flows, Garg&Niemann (1995) observed that on a smooth cylinder of $H/D = 8.5$ at $Re = 6.7*10^4$, the spanwise mean drag distribution is comparable to the ones in Figure 3.28, characterized by increasing values at the top (due to the tip effect) and also the bottom. The results in this Dissertation (Chapter 4) confirm this trend on a rough cylinder in atmospheric boundary layer, although this peculiar distribution is ignored in many Codes (e.g. Eurocodes).

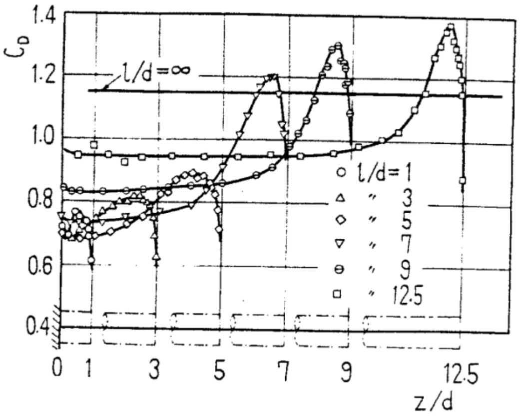

Figure 3.27 Local drag coeff. $C_{D,m}$ *in uniform flow,* $Re=1.3*10^4$ *(Okamoto&Yagita, 1984)*

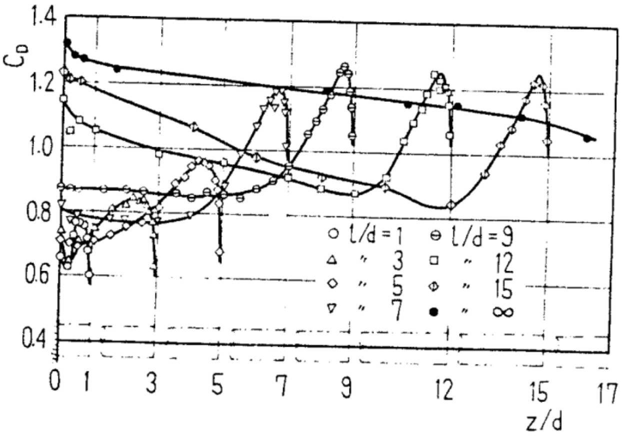

Figure 3.28 Local drag coeff. $C_{D,m}$ *in uniform shear flow,* $Re=1.3*10^4$*. (Okamoto&Yagita, 1984)*

The non-uniformity of the drag coefficient along the height of the cylinder below the tip region (i.e. apart from tip effects) in boundary layer flow – which primarily depends on higher suction in the near wake at low levels – can also find an explanation by looking at Figure 3.19 compared to Figure 3.20 (Krajnovic, 2011 and Sumner&Heseltine, 2008, respectively): the position of the base vortex pair in the time-averaged wake structure rises significantly in boundary layer flow. On low aspect ratio cylinder ($H/D < 3$), instead, base vortices are absent.

Consistently with what has been said about the non-uniformity of the mean drag in the low region in boundary layer flows, the ESDU Data Items (ESDU 81017) suggest to apply – in boundary layer flows – a correction factor, which allows to calculate the value of the local mean drag coefficient in the specific boundary layer flow condition by amplifying the C_D value in uniform flow. The extent and the magnitude of the correction depend on the local shear flow gradient.

The reason provided by the ESDU for such a correction factor, namely f_{sz}, is that in boundary layer flows stronger spanwise velocity gradients enhance the flow movement from regions of relatively high pressure to regions of relatively low pressure. This produces higher local drag coefficients at the base of the structure. In particular – as explained by the ESDU – on the front face of the cylinder in boundary layers flow the pressure decreases as z becomes smaller, because the free-stream velocity decreases. This pressure gradient induces a spanwise flow directed away from the tip. Thus, there is a flow down the front face which interacts with the free-stream flow and produces a net deflection towards the ground plane. This interaction reinforces the bound vortex system which is swept around the cylinder and downstream. The result of this three dimensional effect is to increase considerably the local drag coefficient over that occurring in uniform flow as z/H → 0. Moreover, compared to uniform flow, the bound vortex system tends to delay separation and assist the flow to attain a lower minimum pressure coefficient before separating. The larger lateral suction is accompanied by an increase in the wake suction, which is responsible for higher local drag coefficients at the base. As said, the extent of this modification depends on the local shear flow gradient. For shear flow profiles of the boundary layer type, the ESDU provides – on the basis of H/D and the profile exponent α – a correction factor to the value of the drag coefficient in uniform flow. As z/H → 0, the correction factor increases significantly the local drag coefficient, especially for high slenderness ratios. The expression for such a correction factor, namely f_{sz} in the ESDU, is as follows:

$$f_{sz} = a + b\left(\frac{z}{H} - 0.7\right)^2 \tag{3.4}$$

where:

$$a = 0.8 + 0.2 * \exp\left(-1000\alpha^3\right) \tag{3.5}$$

$$\frac{b}{b_1} = 1.5(1 - \exp(-5.5\alpha)) \quad \textit{and} \quad b_1 = 2.222\left(1 - \exp\left(-0.00303\left(\frac{H}{D}\right)^4\right)\right) \tag{3.6}$$

If H/D ≥ 6 and α = 0.16, $f_{sz}(z=0) = 2.4$, meaning that the drag coefficient at the base in shear flow is more than twice the corresponding value in uniform flow, due to a bound vortex system enhanced by vertical pressure gradients. The ESDU recommends to use such a correction factor even at transcritical Re, although most of the experiments have been carried out at lower Re.

Kawamura et al. (1984) carried out experiments on circular cylinders of different aspect ratios (H/D = 1, 2, 4, 6, 8) in turbulent boundary layer flows at Re = $3.2*10^4$. The mean surface pressure distribution for the most slender case (H/D = 8) is reported in Figure 3.29. Close to the ground, the down-wash flow at stagnation decreases $C_p(0°)$ and the horseshoe vortices increase lateral suction and move downstream the separation line. All of that is in agreement with the ESDU recommendation. The tip effect, accompanied by high suction and downstream movement of the separation line, is evident at high levels.

According to Kawamura, the second islet of minimum pressure coefficient in the tip region, which is responsible for the high drag at about 1/3D (1/2D) from the top, is due to the attachment of trailing swirls, depicted in Figure 3.30 while they move downstream. As previously explained, longitudinal trailing vortices result from a coupling of the blow-down flow from the free-end and the separated up-wash flow along the side wall. The upward-directed flow sweeps the separated shear layers from intermediate heights towards the tip and rolls up in intense tip vortices with horizontal axis – counter rotating vortices – before passing downstream in a trailing vortex street (ESDU 96030).

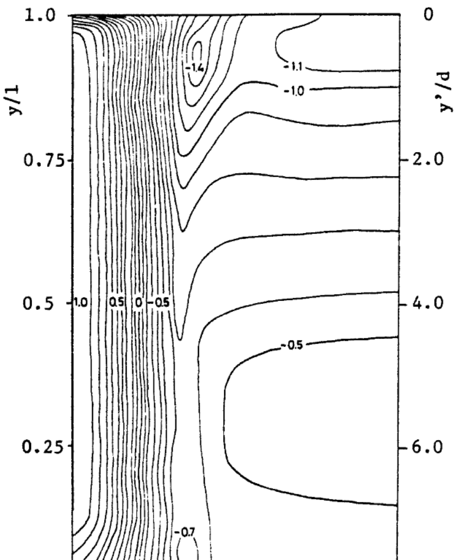

Figure 3.29 Surface pressure coefficients on a finite length circular cylinder H/D = 8 in turbulent boundary layer flow, Re = $3.2*10^4$. (Kawamura et al., 1984)

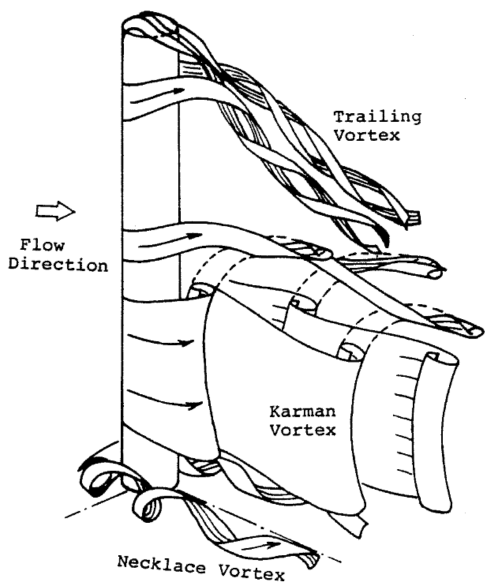

Figure 3.30 Model of the flow around a finite length circular cylinder H/D ≥ 2.5. (Kawamura et el., 1984)

Kawamura did not observe Karman vortex shedding near the free-end, because the free-end was dominated by the downwash. This issue, which will be addressed in the following, is questionable and it is contradicted by other authors.

The trailing vortices were observed by Kawamura even at low aspect ratios, while the formation of Karman vortex streets is suppressed below a critical H/D, which increases as the boundary layer grows thicker.

In contrast with Kawamura, Fox&West (1993) found that for low aspect ratios ($H/D \leq 4$) longitudinal trailing vortices do not form. Consistently, there is no evidence of trailing vortices in the results by Uematsu et al. (1994) on cantilevers with aspect ratio in the range 1 to 4.

Sakamoto&Arie (1983) found a completely different flow structure, characterized by symmetric arch-type vortices at aspect ratios below 2.5. This is considered by the authors as the “critical” H/D value where the type of vortex shedding behind a circular cylinder changes from the Karman-type vortex to the arch-type vortex. However, the overall effect of changing the boundary layer height as well as the cylinder height or diameter is still not well understood and among different authors the critical aspect ratio varies in the range 1 to 7.

Below the tip region – which usually extends for two or three diameters and is characterized by high drag due to the high vorticity – the downwash flow leads to an increase in the wake pressure and then a reduced drag coefficient with respect to the two-dimensional situation (infinite cylinder). Therefore, the introduction of additional fluid from over the top relieves some of the negative base pressure. Consequently, the mean and fluctuating pressures below the tip region are lower than those obtained on a circular cylinder between two end plates and the mean drag coefficient decreases as H/D decreases (Okamoto&Sunabashiri, 1992).

As the distance from the tip increases, the strength of the downwash is reduced. This is consistent with what has been previously said about the size of the recirculation region in the wake. Because of that, Fox&West (1993) justified that, if the cantilever is sufficiently long (the value $H/D \geq 13$ is chosen as reference to define a long cantilever), the C_D at low levels rises towards the infinite cylinder value. In their experiments they observed that such an infinite cylinder value (relatively high) is fully achieved at spanwise distance higher than 20 diameters from the top. Therefore, for longer circular cylinders, it is sufficient to consider that beyond 20 diameters from the top the conditions associated with the infinitely long circular cylinder are established. Only 3.5 diameters from the ground (Fox&West, 1990), the interference effect with the end-plate becomes significant and it is expressed by an increase in C_D.

Experiments by Fox&West are performed at subcritical Re ($Re = 4.4*10^4$). The ESDU Data Items (ESDU 96030) observe that, at higher Re ($Re > 10^6$) the tip flow is weaker and two-dimensional conditions are reached at smaller distance from the top than 20 diameters. Moreover, in presence of vertical velocity gradients and turbulence intensity due to a boundary layer, it can be supposed that the downwash is further weakened, so that the spanwise drag distribution at low levels tends to the high value of the two-dimensional drag coefficient, even at lower aspect ratios. This is a further explanation to the rise of C_D in Figure 3.28.

The weaker downwash in the wake in boundary layer flows compared to uniform flows is evident in Park&Lee' flow visualizations (2002). As a consequence of the weaker downwash, the recirculation bubble which normally develops on the rear side of the cylinder is smaller in boundary layer flows than in uniform flow. Therefore, at about middle height, the vortex formation region can move upstream, so that in boundary layer flows the vortices are formed closer to the cylinder, as shown by Figure 3.36.

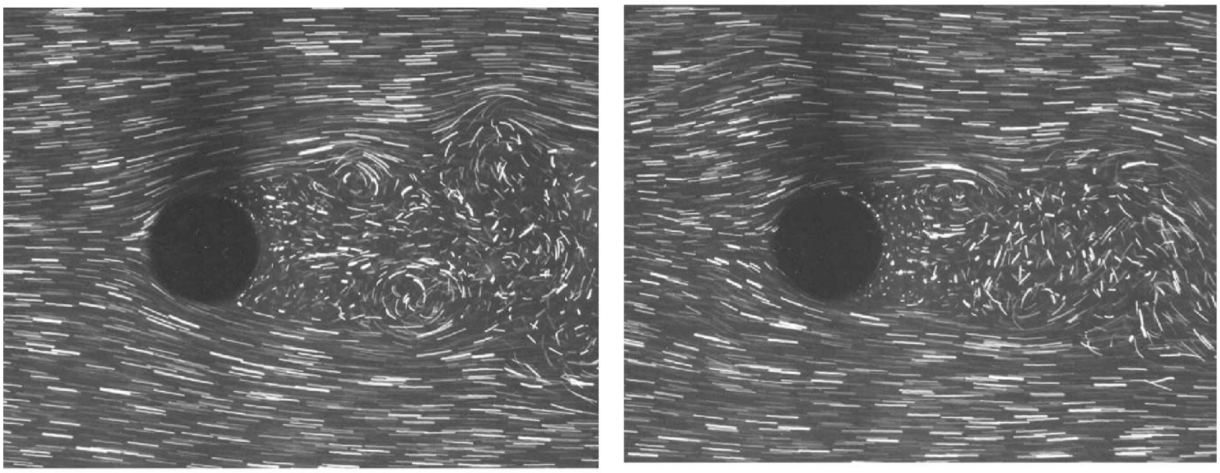

a) uniform flow *b) boundary layer flow*

Figure 3.31 Top view of wake at middle height of the finite cylinder H/D = 6, Re = $2*10^4$ (Park&Lee, 2002)

The free-end condition, allowed by the absence of a physical boundary between the free stream pressure and the base pressure in the wake, has also an effect on eddy shedding. In particular, as explained by Zdravkovich (2003), the secondary flow over the tip is responsible for: 1) elongation of the eddy formation region, widening of the near-wake, decrease in Strouhal number; 2) displacement downstream of eddy shedding; 3) suppression of eddy shedding for small aspect ratios, so that the secondary flow becomes the primary flow.

A spanwise variation of the Strouhal number has been observed at first by Farivar (1981) at Re = $7*10^4$ in uniform flow (Figure 3.32a). He found a cellular shedding with three distinctive regions: a small top region (z/H ≥ 0.9) characterized by low frequency of vortex shedding ($S_t \approx 0.08$), a middle region (0.6 < z/H < 0.9) characterized by higher frequency, but still lower than that for a classical wake flow ($S_t \approx 0.165$), and a lower region (z/H ≤ 0.6) characterized by a Strouhal number equal to that for the classical wake flow ($S_t \approx 0.19$). On the basis of Roshko's experiments with a splitter plate placed in the wake of a cylinder parallel to the stream – which proved a decreases of the Strouhal number depending on the position of the splitter plate in the wake (Roshko, 1959) – and on the basis of Gerrard's theory on the length of the eddy formation region related to the frequency of vortex shedding (Gerrard, 1966), Farivar gathered the following explanation: the decrease in the Strouhal number in the tip region is due to a lengthening of the formation region, as it can be produced by a splitter plate; in the case of a cylinder with a free-end, the flow over the top enters the wake region and this entrainment causes a blockage in the wake preventing the interaction between vortices. Because of that, the formation region elongates and the frequency of vortex shedding is reduced. However, this does not explain the cellular shedding along the height.

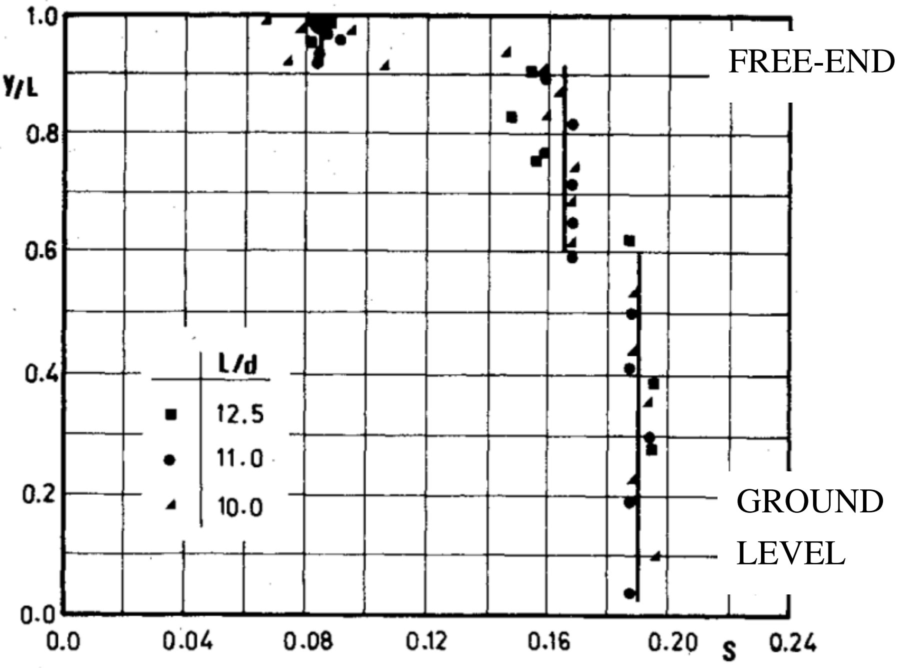

*Figure 3.32 Variation of the Strouhal number with height along a finite circular cylinder. Uniform flow, Re = Re = 7*104, H/D = 10, 11, 12.5 (Farivar, 1981)*

A decrease in the Strouhal number in the tip region of a finite length circular cylinder is also confirmed by Fox et al. (1993) and reported in Figure 3.32b. Cell-like structures were also detected in the wake by Ayoub&Karamcheti (1982), with vortex shedding occurring up to a short distance from the free-end.

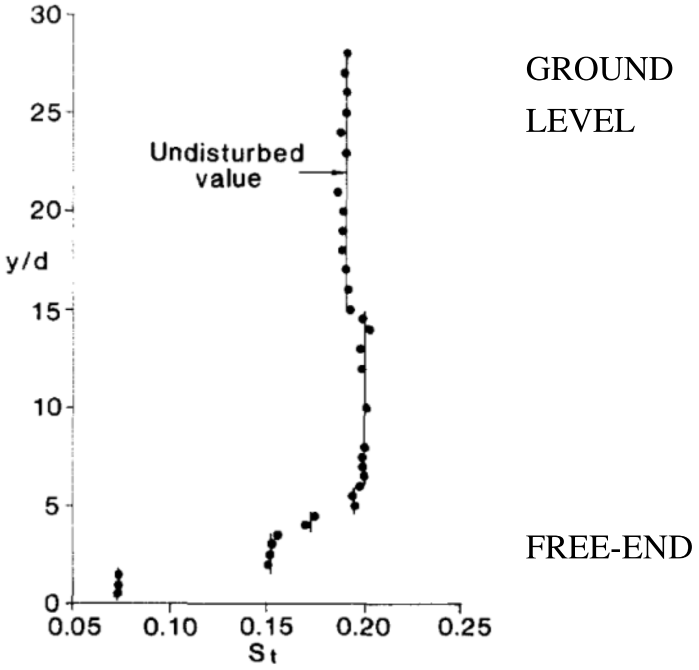

Figure 3.33 Variation of the Strouhal number with height along a finite circular cylinder. Uniform flow, Re = Re = $4.4*10^4$, H/D = 30 (Fox et al., 1993)

Park and Lee (2000) deeply investigated the shedding frequency at the free-end, in comparison with Karman vortex frequency along the height. They tested three finite circular cylinders with aspect ratios 6, 10 and 13 respectively, in uniform flow at Re = $2*10^4$. Near the free-end a peculiar spectral peak occurred at 24 Hz, which in the conditions of those tests corresponds to a reduced frequency nD/U = 24Hz*0.03m/10m/s = 0.072. At middle height the vortex shedding frequency depended on the aspect ratios and the following values were achieved: nD/U = 60*0.03/10 = 0.18 for H/D = 13; 0.16 for H/D = 10 and 0.14 for H/D = 6[2]. In the 2D conditions it resulted nD/U = 0.20, almost three times the reduced frequency in the tip region. The difference in the vortex shedding at middle height is attributed to the downwash flow along the central region of the wake. The strength of the downwash flow depends on the aspect ratio. It is interesting to note, instead, that the 24 Hz component is not modified by the different aspect ratio. However, several spanwise cells as those reported in Figure 3.32 are not observed by these authors. In agreement with Park&Lee's results, Luo et al. (1996) observed Strouhal numbers equal to 0.08 and 0.191 on their H/D = 8 cylinder at z/H = 0.95 and z/H $\leq$ 0.5 respectively, in uniform flow at Re = $3.33*10^4$.

---

[2] In Park&Lee (2002) the same tests are repeated in atmospheric boundary layers and the vortex shedding frequencies and the vortex formation regions are lower.

Another wide study in uniform flow regarding the existence of big vortices generated around the free-end of a finite circular cylinder, whose frequency is much lower than the Karman vortex shedding frequency, is documented by Kitagawa et al. (1999, 2001, 2002) at Re = $2.5*10^4$ (Figure 3.34, Figure 3.35). Such vortices are called tip-associated vortices (TAV) and tend to vanish if the end conditions are modified, for example by a sufficiently large end disk. Kitagawa et al. (1999) found that with a circular disk over the free-end, with a diameter which is 20% more than the cylinder diameter, the tip-associated vortices are weakened; with an increase in the disk diameter up to 60% more than the cylinder diameter , the tip-associated vortices are almost vanished.

The tip-associated vortices are something different from the previously mentioned counter rotating vortices with horizontal axis – usually called tip vortices – which are produced by the interaction between the upward flow at the side of the cylinder and the downward flow over the tip and the rear and pass downstream in a steady street of longitudinal trailing vortices (Figure 3.30). The shedding frequency of tip-associated-vortices measured by Kitagawa is about 1/3 of the Karman vortex shedding frequency. The tip-associated-vortices possibly correspond to one of the cells detected by Farivar (1981) and others close to the tip of the circular cylinder. Detection of vortex shedding near the top is in contrast with the results, previously mentioned, by Okamoto&Yagita (1973, 1984) and Kawamura et al. (1984). They did not observe vortex shedding near the top, but only stationary longitudinal trailing vortices (Figure 3.30).

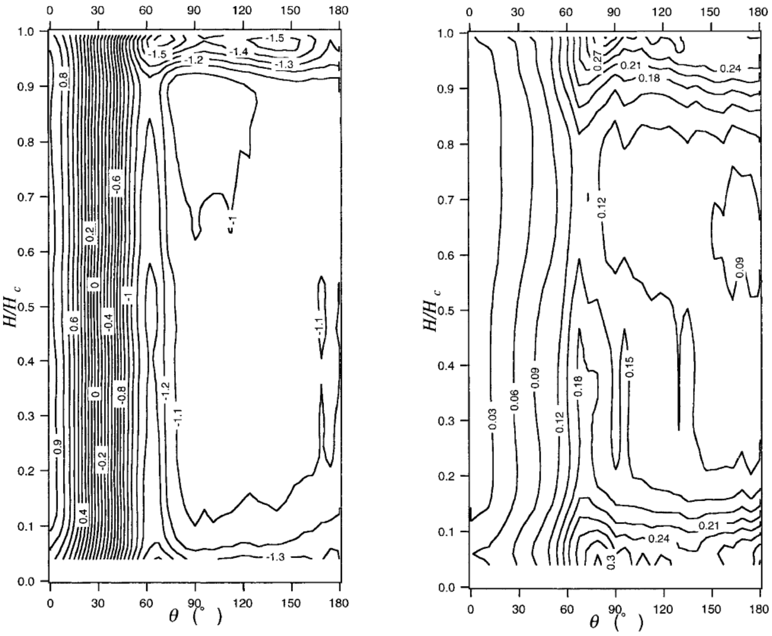

a) *b)*

Figure 3.34 Pressures on a finite cylinder, uniform flow, H/D = 25, Re = $2.5*10^4$
a) $C_{p,m}$; b) $C_{p,\sigma}$; (Kitagawa et al., 2001)

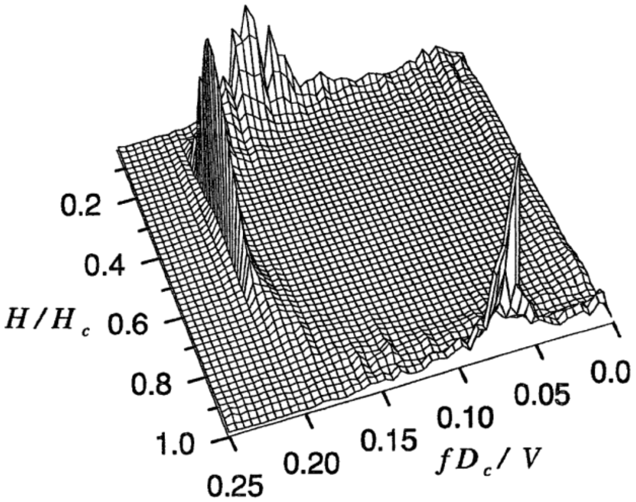

*Figure 3.35 Power spectra of fluctuating pressures at 90°: existence of tip-associated-vortices, uniform flow, H/D = 25, Re = 2.5*10^4 (Kitagawa et al., 2001).*

Aeroelastic tests by Kitagawa et al. (1999) studied the so-called end-cell-induced-vibrations (ECIV), which are similar to the vortex-induced-vibration (VIV), but they occur at a wind speed a few times higher than the threshold wind speed of VIV. Tip-associated-vortices are found to be the cause of ECIV. In fact, according to Kitagawa, ECIV could not be generated by sub-harmonic oscillations of the Karman vortex shedding, although they also occur at a flow velocity a few times higher than that for VIV. The difference is that ECIV tend to vanish with modification of the flow around the free-end, for example by using a disk plate. This would not happen if ECIV were generated by sub-harmonic oscillations and not by the tip-associated vortices.

Three dimensional effects on the flow around circular cylinders have been studied in recent years by numerical simulations. A few of them have been mentioned before. Some important ones are cited in the following. However, many of them are only for short aspect ratio cylinders. In particular, a large eddy simulation of a finite cylinder H/D = 2.5 at Re = 4.3*10^4 was performed by Fröhlich&Rodi (2004), who demonstrated the existence of tip vortices and an arch vortex in the average flow downstream of the free end. Similar results were obtained by Lee et al. (2007). Afgan et al. (2006) presented LES of the flows studied by Park&Lee (2000), i.e. circular cylinder with H/D = 6 in uniform flow at Re = 2.0*10^4. Palau-Salvador et al. (2010) made LES of their own experimental cases with H/D = 2.5 at Re = 4.3*10^4 and H/D = 5 at Re = 2.2*10^4. Krajnovic (2011), previously mentioned in the description of the near-wake flow, used LES to explore both the instantaneous and the time-averaged flows around a relatively tall cylinder (H/D = 6) in uniform flow at Re = 2*10^4.

3.6 Bi-stable flows in literature

Bistable flow conditions around isolated circular cylinders in the critical range of Re (section 3.2) represent a well-known and interesting fluid-dynamic phenomenon, but without any relevant application in the design of structures. As previously explained, the physical reason lies in the transition from laminar to turbulent boundary layer, which occurs on one side only of the cylinder. The transition to turbulent conditions is governed by the Reynolds number. The bistable regime occurs in a very small range of Re, just before Re_{cr}. Most of the structures are far beyond this regime. Moreover, the bistable phenomenon is extremely sensitive not only to Re, but also to any flow disturbance such as turbulence of the incoming flow and cylinder surface roughness.

Bistable flow conditions around circular cylinders are much more common in side-by-side configurations of cylinders in pair. In this case, the bi-stability is regarded as a phenomenon of interaction between cylinders and it can be of importance in the structural design. The fluid behaviour is primarily a function of the centre-to-centre transverse pitch ratio (T/D). Reynolds effects for the side-by-side configuration exist, but they are less prominent than, for example, the tandem configuration. Depending on T/D, three different flow patterns are possible for the side-by-side configuration (Zdravkovich, 2003):

- single-bluff-body behaviour at small pitch ratios (approximately 1.0 < T/D < 1.1-1.2, Figure 3.36a): the single eddy street is formed behind both cylinders, which appear as a single bluff body with a weak flow through the gap;
- a biased flow pattern at intermediate pitch ratios (approximately 1.1-1.2 < T/D < 2.0-2.2, Figure 3.36b): narrow and wide wakes are formed behind two identical cylinders. The gap flow forms a jet biased towards the narrow wake. The biased gap flow is bistable, and may intermittently switch to either side;
- coupled, parallel vortex streets at high pitch ratios (approximately T/D > 2.0-2.5, Figure 3.36c): both wakes are equal in size and eddy shedding is synchronized in frequency and phase. The predominant out-of-phase coupling produces two eddy streets, which mirror each other relative to the gap axis.

A recent review paper by Sumner (2010) further describes the asymmetrical or biased flow pattern at intermediate values of T/D for two side-by-side circular cylinders: the asymmetrical flow pattern is characterized by a gap flow biased towards one of the two cylinders. The cylinder towards which the flow is biased has a narrow near-wake, higher-frequency vortex shedding, and a higher drag coefficient, while the other cylinder has a wider near-wake, lower-frequency vortex shedding, and a lower drag coefficient. Because of that, the two modes "narrow wake" and "wide wake" can be identified. The deflection of the biased gap flow varies with T/D. The trend is toward a smaller degree of deflection with increasing T/D. In some cases, the biased flow pattern switches intermittently from being directed towards one cylinder to the other, and the flow pattern is termed bistable. This ‘‘flip-flopping’’ of the gap flow direction and wake sizes occurs spontaneously and irregularly, but between switchovers the flow remains stably biased to one of the cylinders for long durations (perhaps a few orders of magnitude larger than the vortex shedding period). The bistable characteristic is not caused by misalignment of the cylinders or other extraneous influences, but is an intrinsic property of the flow.

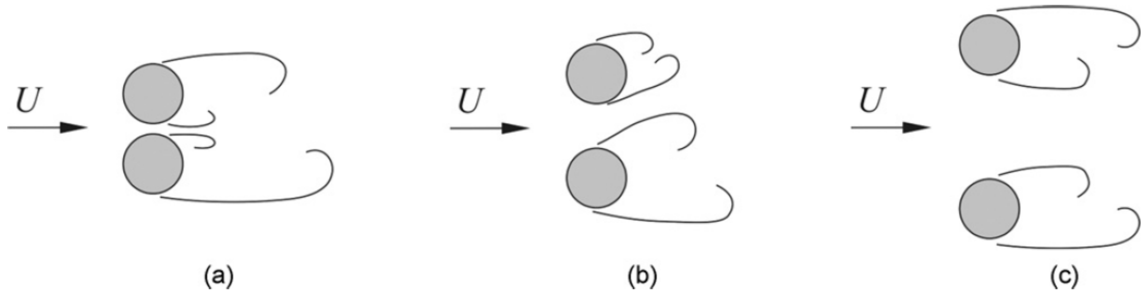

Figure 3.36 Flow patterns for two side-by-side circular cylinders: a) single-bluff-body behaviour; b) biased flow pattern; c) parallel vortex streets (Sumner, 2010);

Mahbub Alam et al. (2003) applied a wavelet analysis in order to detect the frequency of vortex shedding in the two modes (narrow wake, wide wake) and the switching phenomenon.

Three modes of flow, associated with wider wake, symmetric wake and narrow wake are described by Mahbub Alam&Meyer (2011) and sketched in Figure 3.37. The formation and burst of a separation bubble when the gap flow is biased towards one of the two cylinders can even produce a quadri-stable flip-flopping flow regime. A typical lift force signal is shown in Figure 3.38.

Zdravkovich (2003) stresses the paradox of Figure 3.36b, which shows the bistable biased gap flow. The paradox is due to two special features: the first is that an entirely symmetrical oncoming flow leads to the asymmetric narrow and wide wakes behind the two identical side-by-side cylinders. The second is that a uniform and stable flow induces a non-uniform and random bistable flow. The origin of bistable biased flow has been attributed to various causes, but still remains unresolved.

Ishigai et al. (1972) suggested that the Coanda effect is responsible for the biased gap flow. The Coanda effect is observed when a jet tangentially attached to a curved surface becomes deflected by following the surface. According to this definition, it is essential to have a rounded surface. Because of that, Bearman&Wadcock (1973) proved that the Coanda effect could not be the reason; the biased gap flow also appeared by using side-by-side flat plates.

Zdravkovich&Pridden (1977) and Zdravkovich (1987) also observed stable narrow and wide wakes on the upstream and downstream cylinders in staggered arrangement, respectively. As the side-by-side arrangement is approached, the distinction persists so that one cylinder remained upstream with a narrow wake, and the other downstream, with a wide wake. In a side-by-side configuration the asymmetric flow structure is preserved, but it becomes bistable because neither of the side-by-side cylinders is upstream nor downstream. Zdravkovich (2003) concludes that the flow structure consisting of two identical wakes appears to be intrinsically unstable and hence impossible.

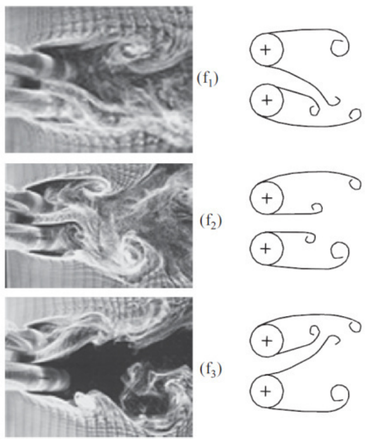

Figure 3.37 Tri-stable flow (T/D = 0.4) (Mahbub Alam&Meyer, 2011)

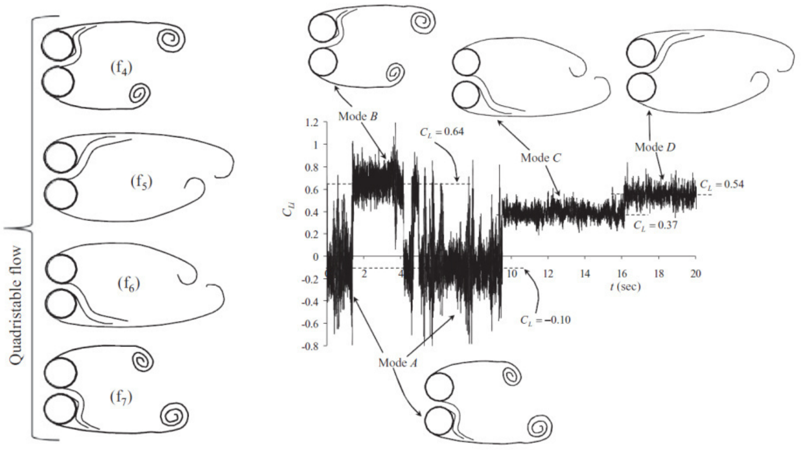

Figure 3.38 Quadri-stable flow due to formation and burst of a separation bubble (T/D = 0.13) (Mahbub Alam&Meyer, 2011)

This Dissertation addresses the case of only one isolated circular cylinder. However, a similar bistable phenomenon of interaction like the one previously described occurs in the wake between different compartments of the single cylinder, which are separated by stiffening rings. This effect is addressed in Chapter 5.

Chapter 4. **Experimental set-up for wind tunnel tests**

This chapter describes the boundary layer wind tunnel at the Ruhr-University Bochum, the model of the Solar Updraft Tower and an outline of the tests. Moreover, the preliminary results on the circular cylinder (without rings) are presented. Issues like the influence of the Reynolds number and the choice of surface roughness are also addressed in this chapter.

4.1 WiSt wind tunnel (Ruhr-University Bochum)

4.1.1 Geometry of the boundary layer wind tunnel

WiSt laboratory at Ruhr-University Bochum (Windingenieurwesen und Strömungsmechanik http://www.ruhr-uni-bochum.de/wist) is an open circuit wind tunnel with a total length of about 17 m. The tunnel itself has a length of 9.3 m. The test section is 1.8 m in width and 1.6 m in height. In case of need, the upper ceiling of the tunnel can be raised until 1.9 m. A turntable in the test section allows to test different wind directions, if necessary. A honeycomb grid is located at the inlet of the tunnel.

Figure 4.1 WiSt boundary layer wind tunnel at Ruhr-University Bochum

The turbulent boundary layer develops over a length of about 7.6 m. After a castellated barrier having a maximum height of 425 mm, there are three turbulent generators of 1.5 m in height. They are built according to Counihan's specifications (Counihan, 1969), as reported in the following sketch (Figure 4.2). The roughness field consists of six panels with 36*36*36 mm^3 cubes alternated to 36*36*18 mm^3 square prisms. It creates the lowest and most important part of the boundary layer, which undergoes a natural evolution along the wind tunnel and the largest eddy reaches approximately the thickness of this surface layer, i.e. 30-40 cm. The turbulence in the upper layer is created by turbulence generators. At a distance of about 3.5 times the height of the turbulent generators, the two layers merge and continue to grow together. The castellated barrier acts as an adjustment element. All these facilities (castellated barrier, turbulence generators and roughness field) are removed in case of low-turbulence tests in empty tunnel and approximately uniform flow. The boundary layer at each wall affects a distance of about 30 cm.

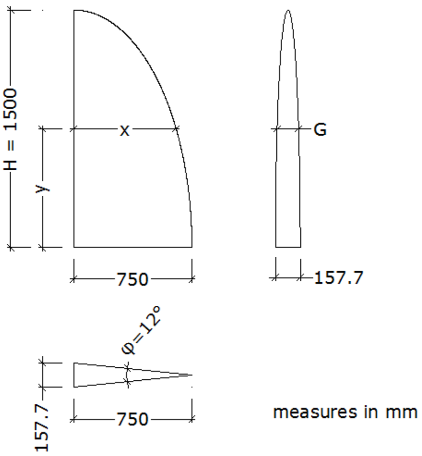

$$x = \frac{H}{2}\sqrt{1 - \frac{y^2}{H^2}}$$

$$G = 2x \tan\frac{\varphi}{2}$$

Figure 4.2 Turbulent generators of Counihan type

The diffusor and the centrifugal fan are placed at the end of the wind tunnel. The engine allows to attain a maximum wind speed of about 28-30 m/s with 1500 turns per minute of the fan. A Prandtl tube allows to measure the dynamic pressure of the incoming flow. Temperature sensors acquire temperature during the measurements. It allows to calculate the air density and therefore the mean wind speed by applying Bernoulli equation. The Prandtl tube is normally placed at 1.3 m in height – out of the influence of the wall of the wind tunnel – but its position may change depending on the tests.

Figure 4.3 View of the model in the wind tunnel with turbulent facilities

DRAWING n.1 WiSt Boundary layer wind tunnel Ruhr-University Bochum

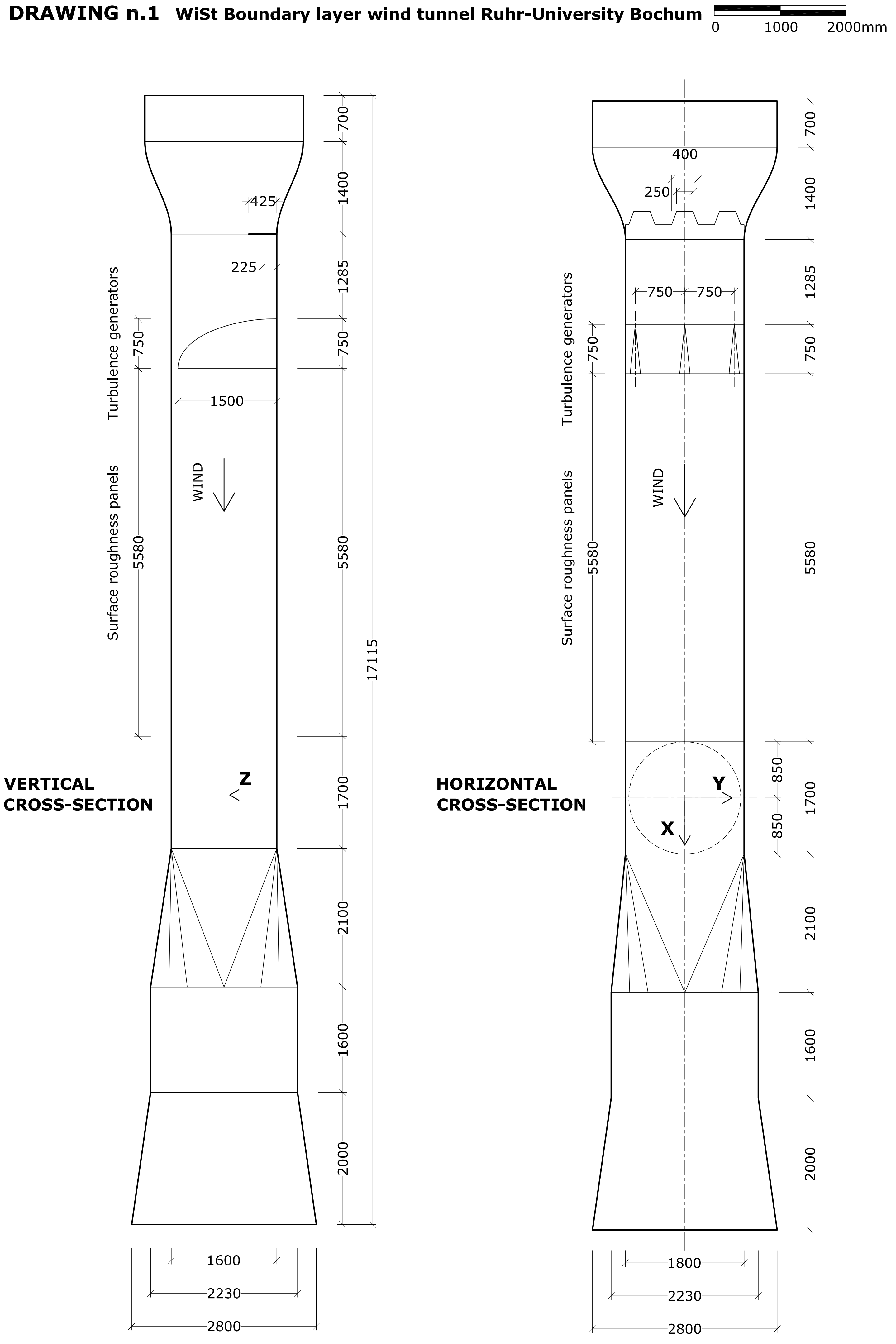

4.1.2 Flow characteristics

The castellated barrier, the turbulent generators and the roughness field, previously described, produce a certain boundary layer namely RAU8. For the wind tunnel tests on the solar tower, however, a slightly modified version of RAU8 is adopted, due to the presence of the collector. It is named RAU8+collector (Figure 4.1). The collector, i.e. a smooth panel of 4 m in length, centered at the tower position, was introduced with the aim of creating a two-phase profile, as it should be expected in full-scale. Due to the presence of the collector, the last roughness panel (the shortest one, 0.33 m in length) had to be removed. The final set-up of the wind tunnel resulted like that:

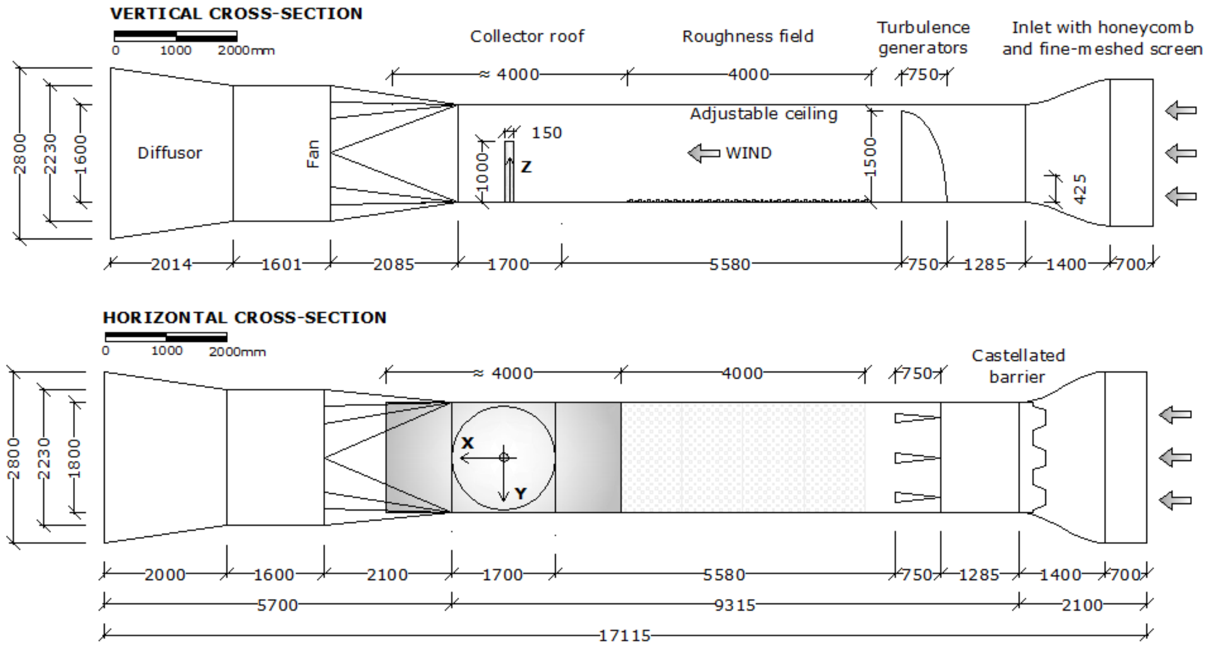

Figure 4.4 View of the Solar Tower in the wind tunnel at the Ruhr-University Bochum

The ESDU Data Items 82026 allow to estimate the height of the internal layer which develops after a roughness change, as that produced by the smooth collector roof. $z_{0,1}$ and $z_{0,2}$ are the roughness lengths corresponding to the upwind and downwind conditions, respectively. U_{z1} and U_{z2} are the resulting wind profiles. At a certain distance x from the step change in roughness, it can be assumed that the wind speed profile consists of a lower portion (internal layer), where the velocity is dependent on x and it is given by K_xU_{z2}, and an upper portion where the profile is the same as upwind. The height of the internal layer, at which the two portions intersect, can be estimated according to the ESDU procedure. If it is assumed that the smooth collector has a surface roughness $z_{0,2} = 0.005$ m, while the upwind conditions are those described in chapter 2 for the H&D model ($U_{z1}(10m) = 25$ m/s, $z_{0,1} = 0.05$ m, latitude = 23°), an internal layer of approximately 200 m can be calculated in the full-scale condition at a distance equal to the radius of the collector Rcoll (Table 4.1).

Table 4.1 Effect of a step change in roughness according to ESDU 82026 at the tower position

Upwind conditions (full-scale)			**Downwind conditions (full-scale)**		
z_{01}	0.05	m	z_{02}	0.005	m
u_{*1}	1.898	m/s	u_{*2}	1.638	m/s
Internal layer height in m (full-scale)				h_i	201
K_x factor at x = R_{coll} = 2000 m after the roughness change					0.9070

Instruments for velocity measurements

The velocity profile is measured with hot-wires anemometers. Cross wires allow to measure two wind components (either u and v, or u and w). More than one probe can record simultaneously in the wind tunnel; the Multichannel CTA 54N80 by Dantec is an amplifier which allows to measure up to 16 channels. In the experiments, however, only two cross-wire probes were used (four channels) plus temperature and Prandtl velocity (two other channels). The A/D converter is the same as for pressure measurements (see section 4.1.3) and it is set to a sampling frequency of 2 kHz.

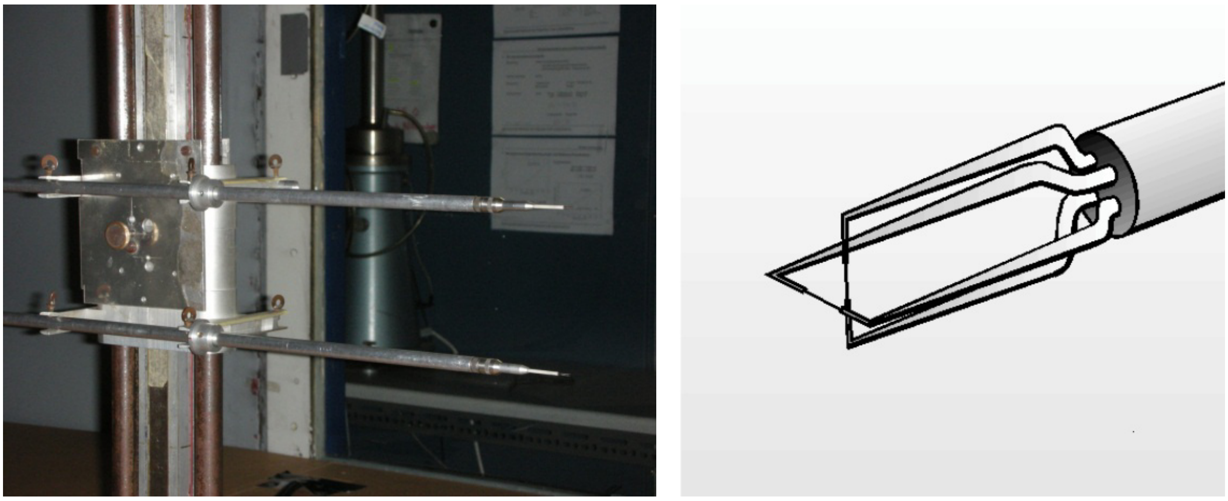

a) *b)*

Figure 4.5 Miniature wires (X-array): a) during experiments; b) zoom

The multichannel CTA is designed for use with miniature wire probes (type 55P61-64) in combination with 4m probe cables. Each channel of the CTA can be set to a certain "decade resistance", defined as twenty times the operating resistance. The latter depends on the resistances of the sensor, of the probe support and of the probe cable. The wires are 5 μm in diameter and 1.2 mm long. They are suspended between two needle-shaped prongs. The frequency bandwidth is 10 kHz and filters can be applied.

The anemometers are calibrated in laminar flow in the calibration tunnel. The calibration establishes a relation between the CTA output (voltages) and the flow velocity. It is performed by exposing the probe to a set of known velocities, U, and the corresponding voltages E are recorded. A fitting curve through the points (E,U) represents the transfer function to be used when converting data records from voltages into velocities. The fitting curve which is adopted is a polynomial curve of 4th order (equation (4.1)). The coefficients are calculated by fitting the data in the least-squares sense. An example reported is in Figure 4.6.

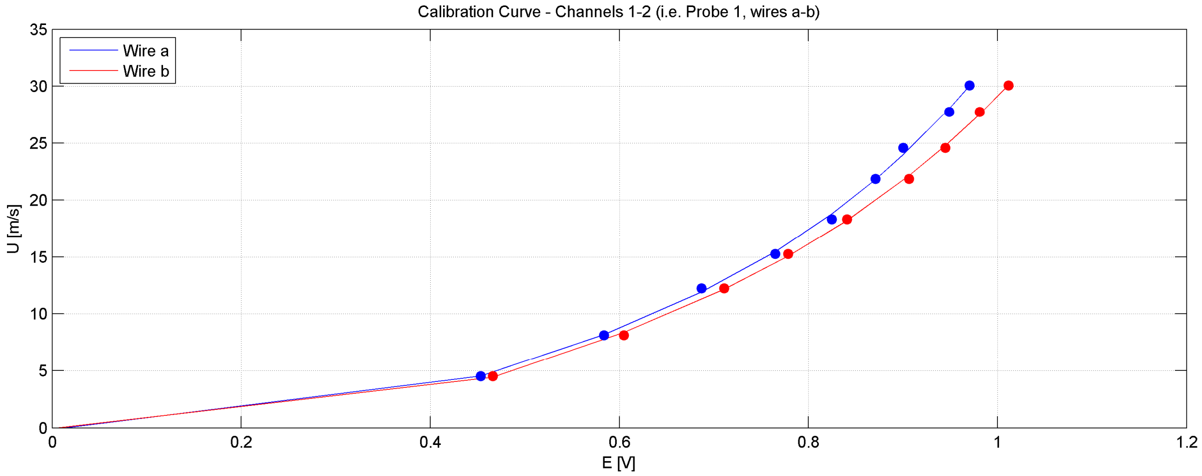

Figure 4.6 Calibration curve – wires a and b of one probe (experiment 24.10.2011)

$$U = C_0 + C_1 E + C_2 E^2 + C_3 E^3 + C_4 E^4 \tag{4.1}$$

If the temperature varies during calibration and the experiment, the recorded voltages must be corrected (E_{corr}) with the formula:

$$E_{corr} = \left(\frac{T_w - T_0}{T_w - T_a} \right)^{0.5} E_a \tag{4.2}$$

where: E_a = acquired voltage; T_w = sensor hot temperature = 250°; T_0 = ambient reference temperature (during calibration); T_a = ambient temperature during acquisition. The expression can be used for moderate temperature changes in air (± 5°C). The useful range may be expanded (Jørgensen Finn E., 2002) by reducing the exponent from 0.5 to 0.4 or 0.3.

This formula is suggested by the practical guide of Dantec, but it was checked by measurements at several different temperatures before being applied in the experiments.

Results of velocity measurements

Mean wind profile, turbulence intensity, integral length scales and spectra are evaluated by hot-wires anemometers measurements. The mean wind profile is defined by using a power law according to formula (4.3).

$$\frac{U_m(z)}{U_{ref}} = \left(\frac{z}{z_{ref}} \right)^{\alpha} \tag{4.3}$$

The reference velocity is the velocity of the Prandtl tube U_{pra}. Unfortunately, during the tests, the mean level of the velocity measured by one of the two anemometers shifted to lower values. It is probably due to a sensible modification of the calibration curve. The mean values of that anemometer could not be used. Instead, the fluctuations did not result to be affected. The results of the available data for the mean wind profile are reported in Figure 4.7 and confirmed that the influence of the collector extends up to z = 200 mm. This fits very well the ESDU recommendation mentioned before (Table 4.1).

The turbulence intensity of the u-component is calculated according to the definition (4.4). The same applies to the components in the other directions, by using either σ_v or σ_w.

$$I_u(z) = \frac{\sigma_u(z)}{U_m(z)} \tag{4.4}$$

The integral length scales of turbulence represent an average size of the vortices associated to longitudinal, transversal and vertical turbulence in the x, y and z directions, respectively. Nine integral scales of turbulence can be defined: L_{ux}, L_{uy}, L_{uz}, L_{vx}, L_{vy}, L_{vz}, L_{wx}, L_{wy}, L_{wz}. They are calculated by integration from zero to infinite of the zero-lag covariance functions divided by the variance, i.e. the cross-correlation coefficients. For example, for the u-component they are:

$$L_{ux} = \frac{1}{\sigma_u^2} \int_0^{+\infty} R_u(\Delta x, 0) d\Delta x = \int_0^{+\infty} \rho_u(\Delta x, 0) d\Delta x \tag{4.5}$$

$$L_{uy} = \frac{1}{\sigma_u^2} \int_0^{+\infty} R_u(\Delta y, 0) d\Delta y = \int_0^{+\infty} \rho_u(\Delta y, 0) d\Delta y \tag{4.6}$$

$$L_{uz} = \frac{1}{\sigma_u^2} \int_0^{+\infty} R_u(\Delta z, 0) d\Delta z = \int_0^{+\infty} \rho_u(\Delta z, 0) d\Delta z \tag{4.7}$$

The integral length scale L_{ux} can be easily calculated by Taylor's hypothesis, which allows to use only one signal measured in one position, by assuming that the vortices move in the along-wind direction at the mean wind speed:

$$L_{ux} = U_m T_{ux} \tag{4.8}$$

T_{ux} is the integral time scale, i.e. the integral of the auto-correlation function from zero until infinite (equation (4.9)). In practical terms, the integration can be extended until the first zero crossing, because all the following ondulations of the auto-correlation coefficient approximately average to zero. Also other methods exist, for example the exponential method, which assumes that the auto-correlation function has an exponential decay (Schrader, 1993). Alternately, T_{ux} can also be calculated by fitting the spectrum of the signal with an analytical expression of the velocity spectrum (e.g. von Karman spectrum in isotropic flow).

$$T_{ux} = \int_0^{\infty} \rho_{ux}(\tau) d\tau \tag{4.9}$$

Besides L_{ux}, for the purpose of this work it is especially important to investigate the integral length scale of the u-component in the z direction, i.e. L_{uz}. Approximately, in the atmospheric boundary layer flow, it is one half of L_{ux}, apart from very close to the ground. In this work, L_{uz} is calculated at each height by integration of the cross-correlation coefficients from zero until infinite (equation (4.10)). This requires simultaneous measurements of wind velocity in at least two points (Figure 4.5).

$$L_{u_z}\left(z_{ref},\Delta z\right)=\int_0^{\infty}\rho_u\left(z_{ref},\Delta z\right)d\Delta z \tag{4.10}$$

Vertical cross-correlations of the u-component in the undisturbed flow are measured both upwards and downwards at the following reference heights: 100-300-500-700-900-1100 mm. They are fitted with a negative exponential function, from which L_{uz} is easily derived:

$$\rho_u(\Delta z)=e^{-\frac{\Delta z}{Luz}} \tag{4.11}$$

The spectra of the u and v components are reported in Figure 4.11 and Figure 4.12. In particular, the investigation of the cross-wind component (v) of the wind velocity is important for a deeper study of pressure fluctuations at the flanges of the cylinder and for transversal oscillations of the structure in a dynamic calculation. The spectrum of the v-component, compared to the spectrum of the u-component, appears to be shifted (Figure 4.13). It implies higher energy in the cross-wind direction at relatively high frequency, i.e. in the frequency range of most of structures sensitive to wind.

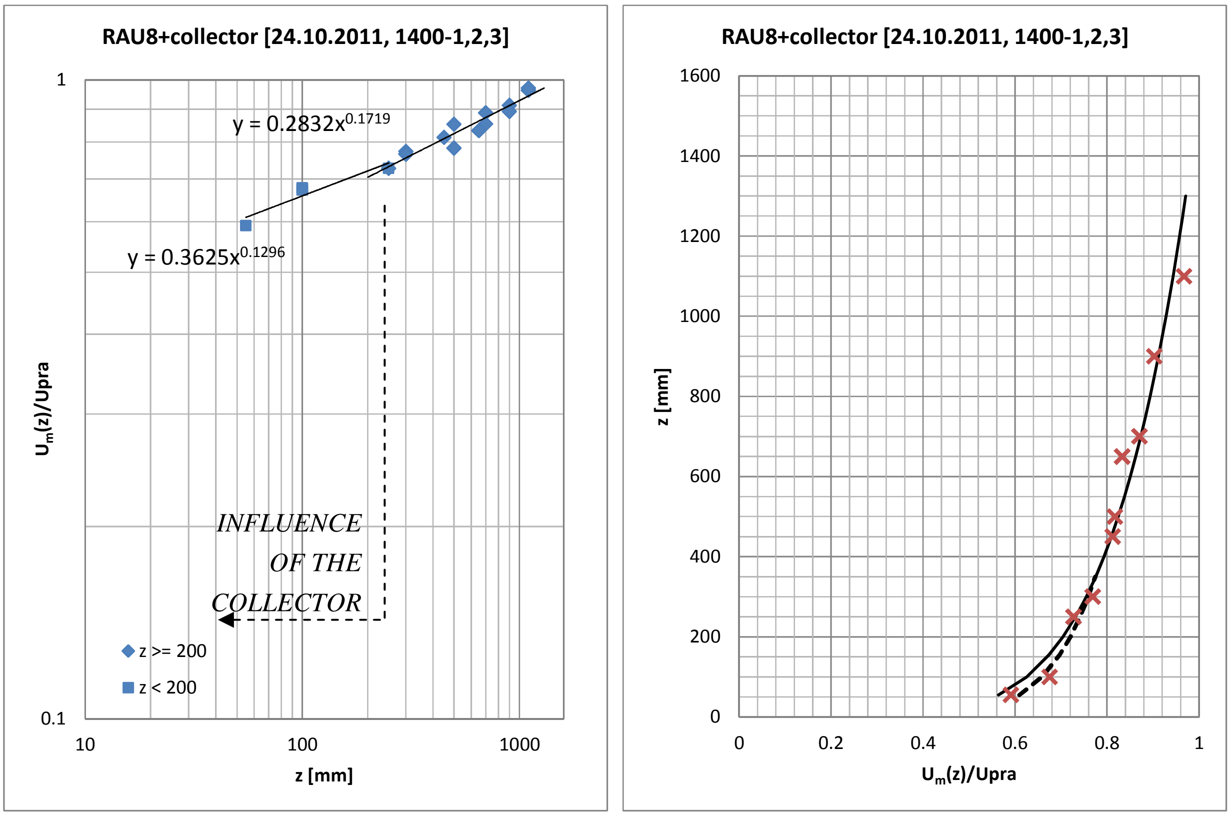

Figure 4.7 Mean wind profile (RAU8+collector)

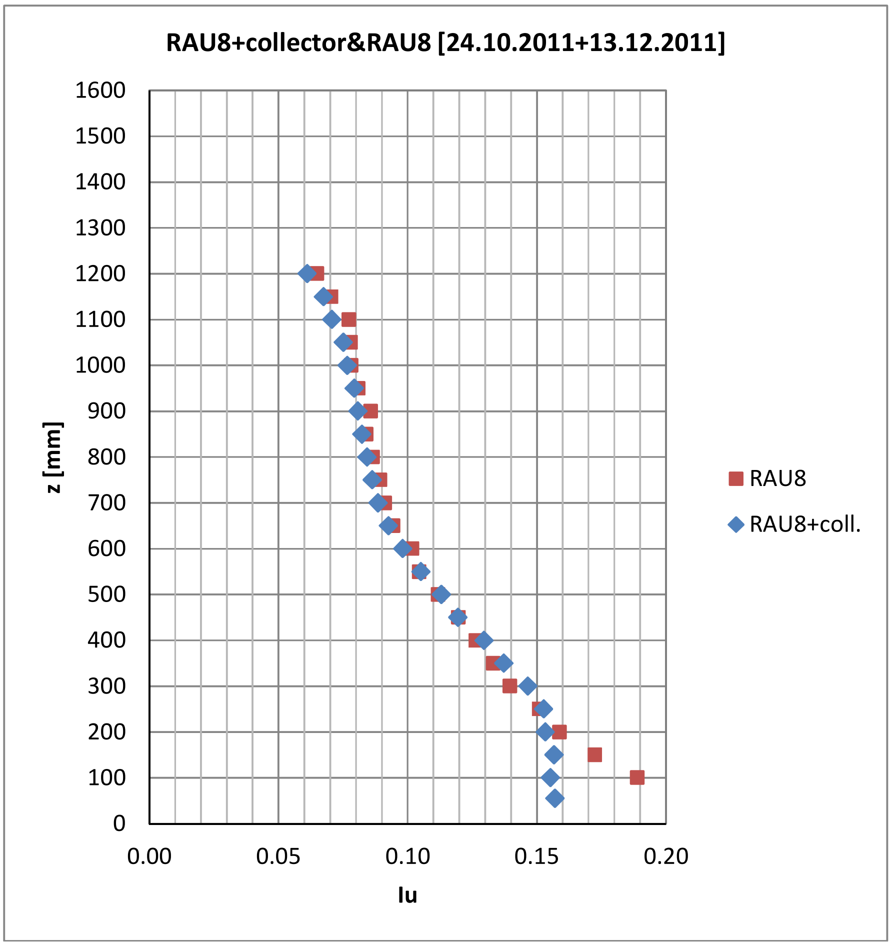

Figure 4.8 Turbulence intensity (RAU8+collector and RAU8)

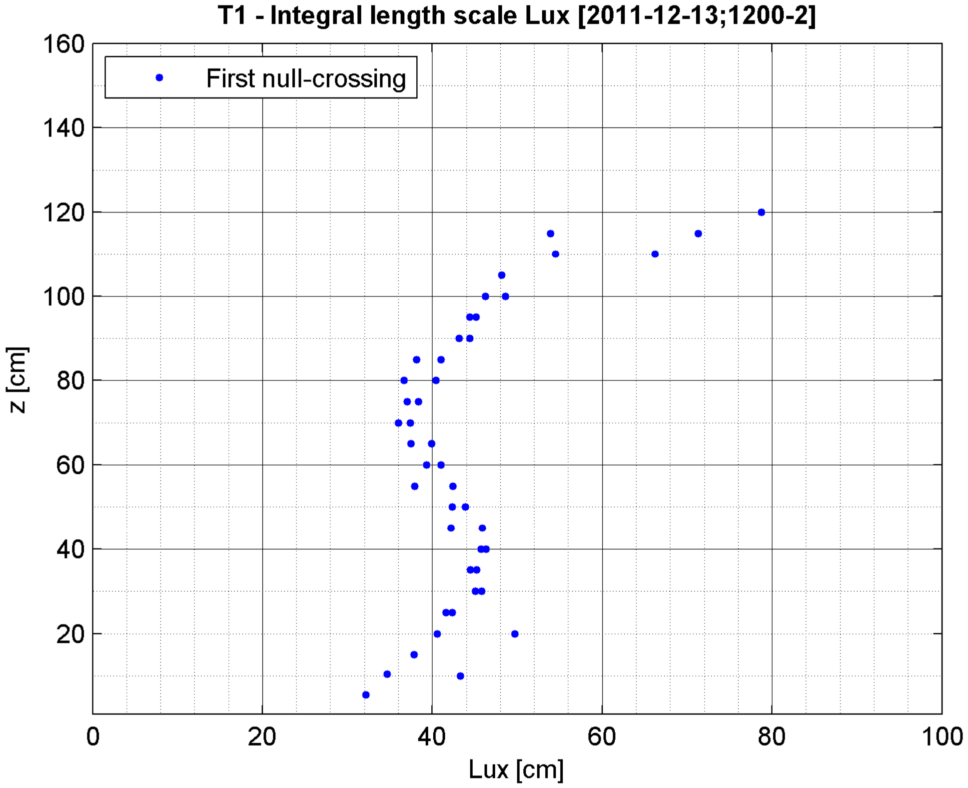

Figure 4.9 Integral length scale, L_{ux} (RAU8+collector) in the figure: first zero-crossing

Upwards **Downwards**

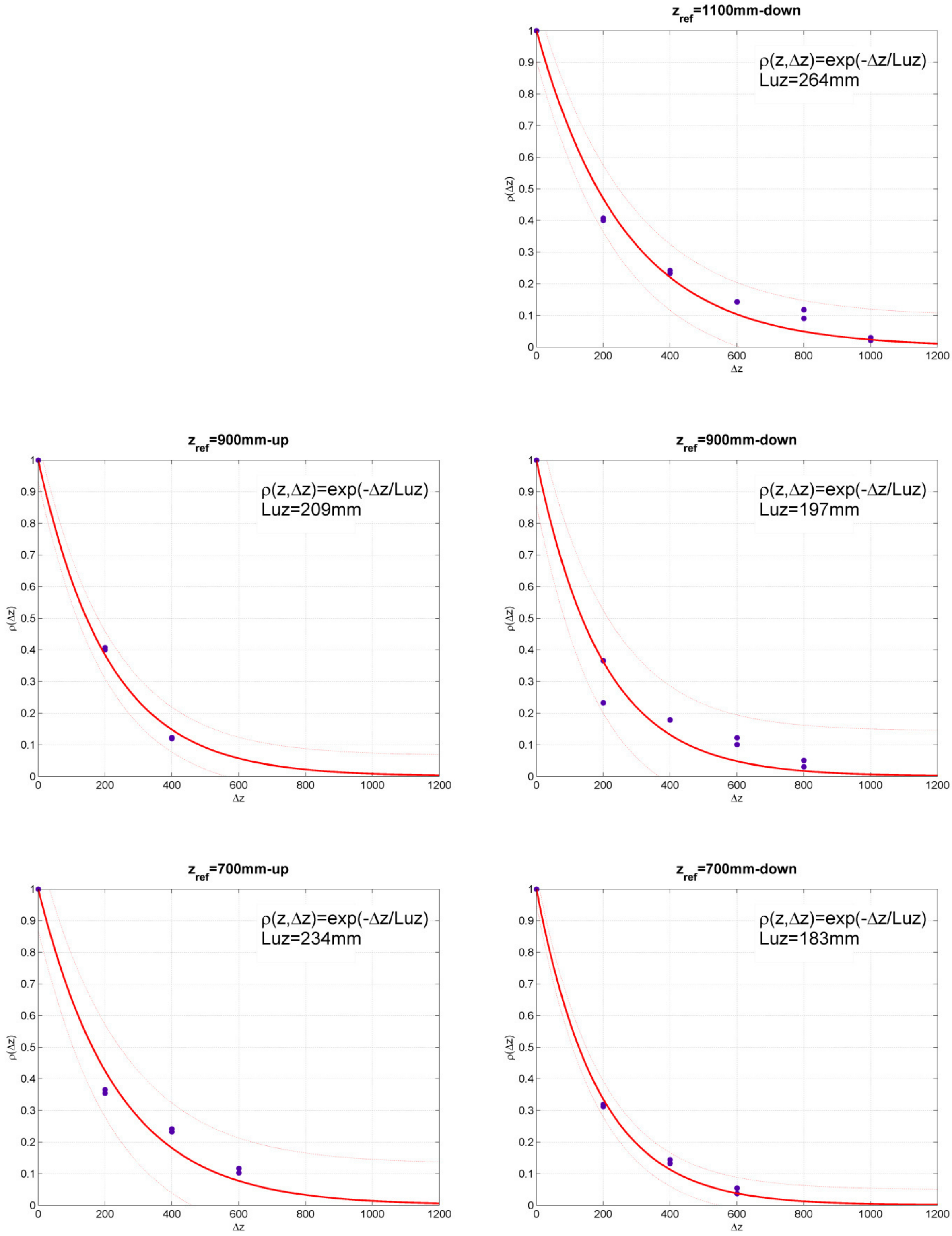

Figure 4.10 Cross-correlation coefficients $\rho_u(z,\Delta z)$ (RAU8+collector)
(continued in the next page)

Upwards **Downwards**

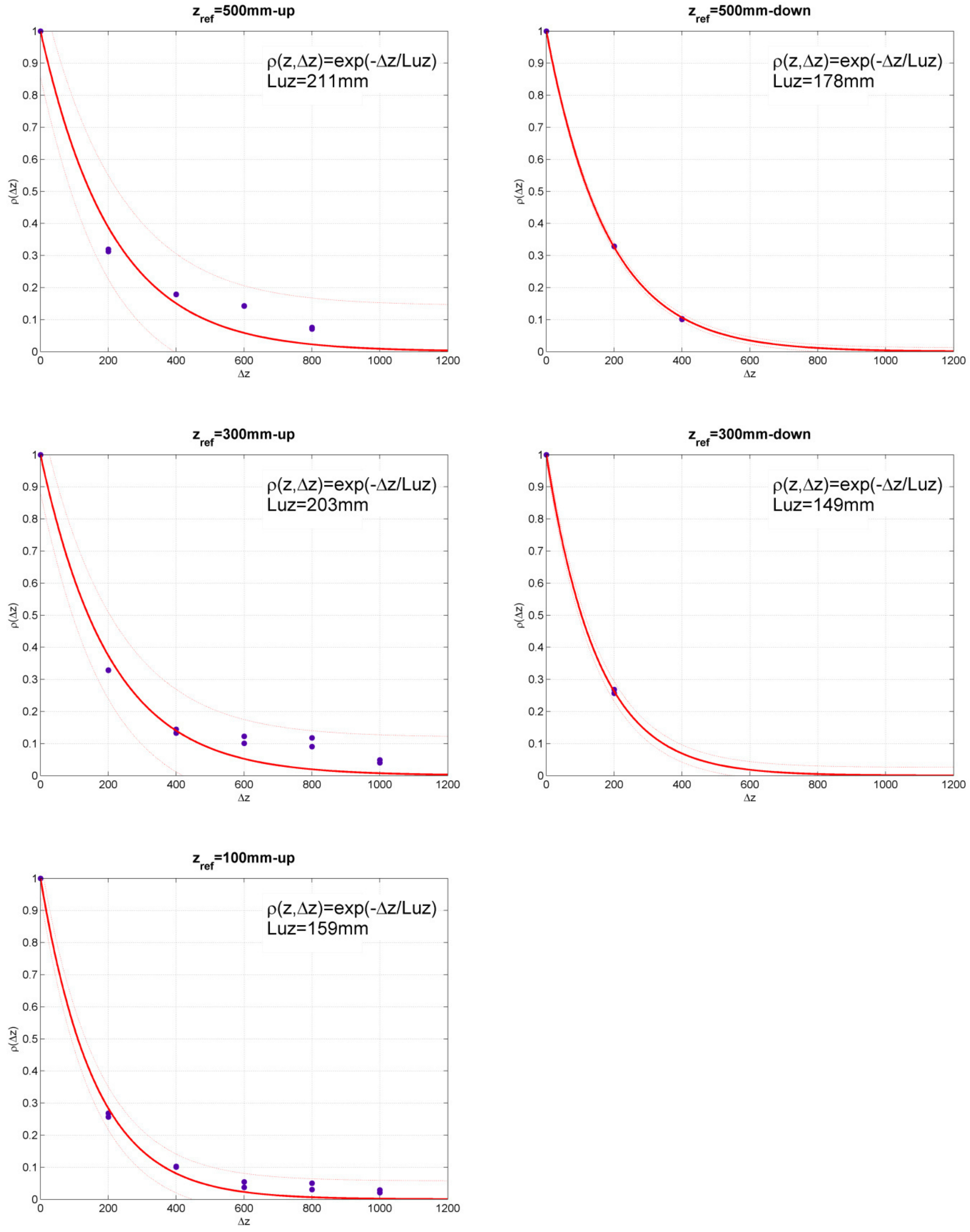

Figure 4.10 Cross-correlation coefficients $\rho_u(z,\Delta z)$ (RAU8+collector) (continued)

The vertical scale of the u-component L_{uz} will be compared in Chapter 7 to the correlation length of pressures L_{pz}. In view of that, a representative value of L_{uz} is chosen at each level as the average of the values in the upward and downward directions. The final result is:

Table 4.2 L_{uz} (average between upward and downward directions), RAU8+collector

z [mm]	100	300	500	700	900	1100	mean
L_{uz} [mm]	159	176	194	209	203	264	200

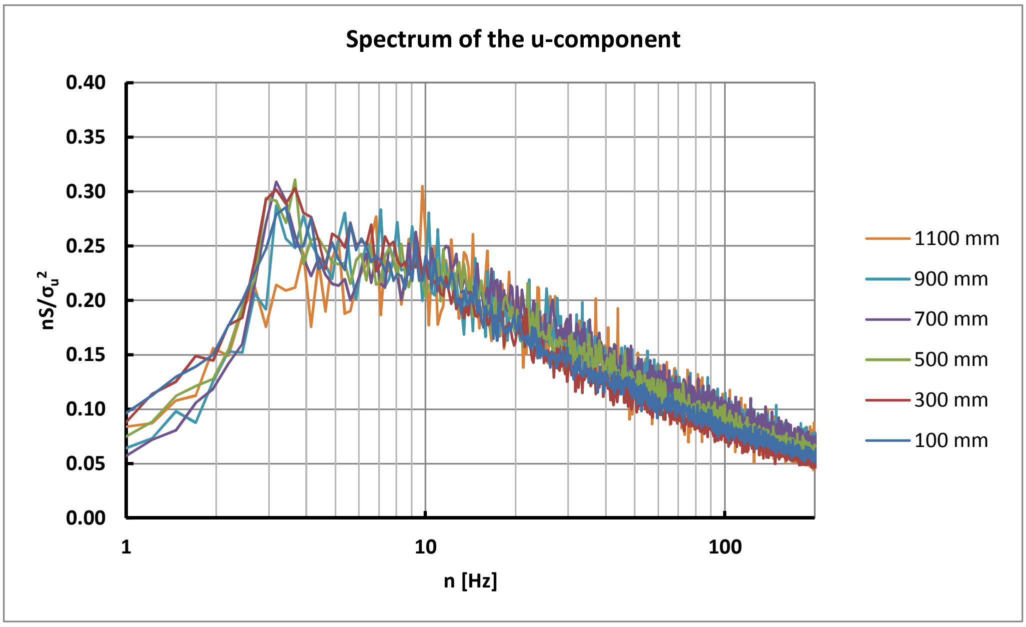

Figure 4.11 Spectra of wind fluctuations in the along-wind direction (u-component) at several levels (RAU8+collector)

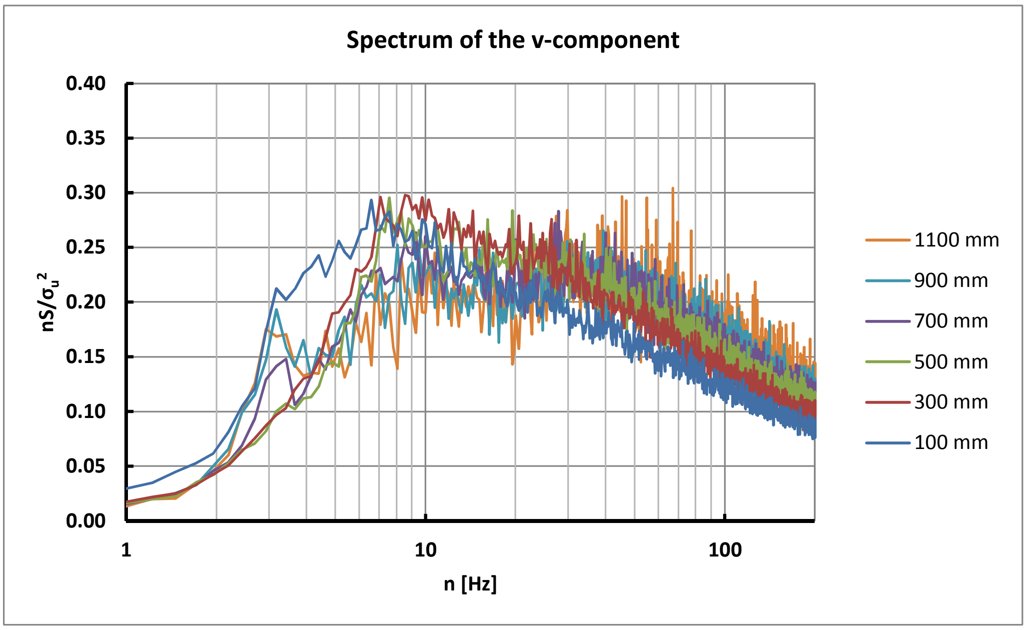

Figure 4.12 Spectra of wind fluctuations in the across-wind direction (v-component) at several levels (RAU8+collector)

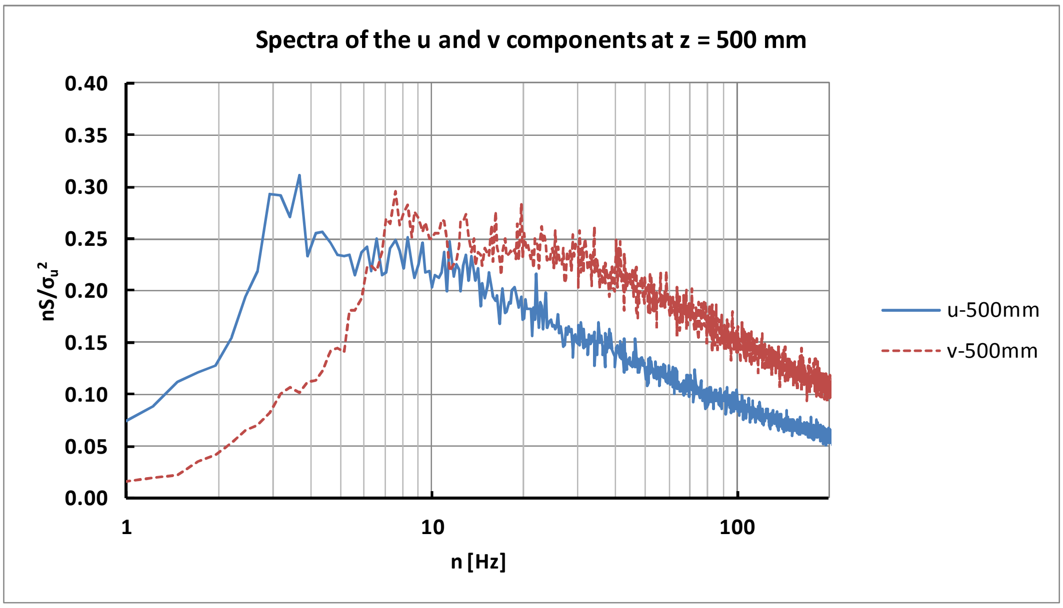

Figure 4.13 Spectra of wind fluctuations in the along-wind (u-component) and across-wind (v-component) directions at 500 mm (RAU8+collector)

The unusual peak at about 3-4 Hz in the u-spectrum in Figure 4.13 (detectable at higher frequencies also in the v-spectrum) is not produced by the slight modification of RAU8 by including the collector. It is difficult to find its precise cause. By the way, it is also recorded in pressure measurements. Once pressures are integrated along the circumference, for example to calculate the lift force, such a peak disappears in the lift spectrum because the two half lifts have negative correlation in that range of frequencies.

In any case, flow disturbances are not surprising in a wind tunnel. They can be produced by the rotor blades, the motor itself, the vibrations of the ground surface and of the wind tunnel walls or they can be electrical disturbances.

The similarity criteria between wind tunnel and full-scale require that the dimensionless parameters (e.g. S_t, Re, I_u,…) assume the same value in the wind tunnel and in full-scale. All the quantities which have the same dimension (for example, length, velocity or time) should be scaled according to the length scale λ_L, λ_V, λ_T, respectively. They represent the ratios between the values in the wind tunnel and the values in full-scale.

Due to the scale of the model, it is not possible in this work to reproduce in the wind tunnel the same Re as in full-scale. Its effects and the use of surface roughness in order to overcome the mismatch are discussed in section 4.4. The similarity of S_t requires that: $\lambda_L = \lambda_V * \lambda_T$.

$$S_t = \left(\frac{nD}{U}\right)_{WT} = \left(\frac{nD}{U}\right)_{FS} \quad \rightarrow \quad \lambda_L = \lambda_V * \lambda_T \tag{4.12}$$

If λ_L is equal to the scale of the model, i.e. 1:1000, the turbulence (in particular L_{ux}) and the boundary layer should be scaled accordingly. In fact, the full-scale value of L_{ux} is an uncertain parameter in itself. Chapter 2 proved that different codes and calculation methods provide more or less similar results in the surface layer, but very different ones in the Ekman layer. Similarly, T_{ux} can be directly calculated from wind tunnel data by equation (4.9); in full-scale it can be derived by Taylor hypothesis. The comparison between L_{ux} (T_{ux}) in the wind tunnel and in full-scale provides an estimation of the approximation, in case the data are used in a structural calculation on 1-km prototype. In any case, Figure 4.14 shows that the turbulence scale reproduced in the wind tunnel, multiplied by the scale factor 1000 (λ_L = 1:1000) is not too far from the Code predictions (even extrapolated at large heights). Instead, the H&D model would suggest much larger integral length scales, which cannot be reproduced in the wind tunnel. This partial simulation of turbulence implies, with regard to the H&D model, a smaller background response and higher dynamic amplification.

In conclusion, by assuming λ_L = 1:1000 and having λ_V = 1:2.05 (U_{FS}(z=H) = 51.31 m/s; U_{WT} (z=H) = 25.07 m/s), it results λ_F = 1/488; λ_T = 488. By looking at Figure 4.14 it can be inferred that it is not too far from the time scale that would be obtained by comparing T_{ux} in the wind tunnel and T_{ux} in full-scale.

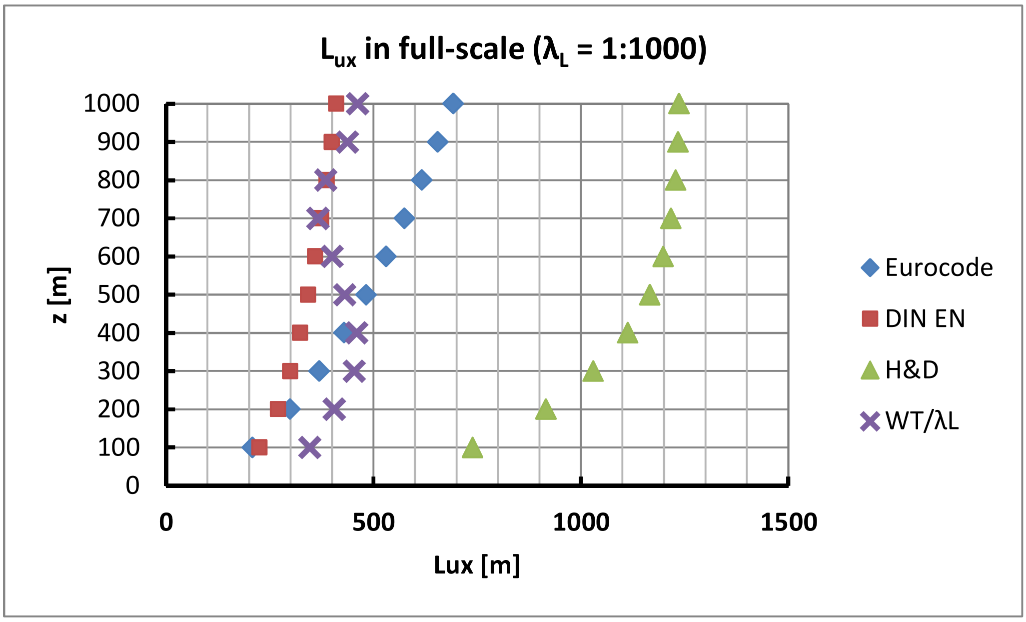

Figure 4.14 Integral length scale of turbulence L_{ux} in full-scale. The violet marks represent L_{ux} in the wind tunnel divided by the length scale factor 1:1000.

The following table summarizes the boundary layer characteristics (RAU8+collector). They are interpolated at levels of pressure measurements for further use.

z [mm]	**$U_m(z)/U_{pra}$**	**$I_u(z)$**	**L_{ux} [mm]**
990	0.927	0.077	459
950	0.920	0.079	448
910	0.914	0.081	440
890	0.910	0.081	429
850	0.903	0.082	396
750	0.884	0.086	377
650	0.862	0.093	387
550	0.838	0.105	402
520	0.830	0.110	425
505	0.826	0.112	429
495	0.823	0.114	432
480	0.818	0.116	437
450	0.809	0.119	440
350	0.775	0.137	448
250	0.741	0.153	419
150	0.694	0.157	379
50	0.602	0.157	322

Table 4.3 Summary: flow characteristics, RAU8+collector

Figure 4.15 RAU8+collector (WiSt wind tunnel)

Last but not least, some measurements are also done in empty tunnel. These are the characteristics of the flow:

- $U(z) \approx U_{pra}$ (uniform flow, apart from wall effects);
- $I_u \approx 5\%$
- $L_{ux} \approx$ 3-4 cm (isotropic turbulence), by fitting Von Karman spectrum.

4.1.3 **Pressure measurement technique**

The wind tunnel facilities allow to measure 92 pressures simultaneously. The measurement chain consists of pressure sensors, amplifiers and analogic-digital (A/D) converters. The pressure sensors are four-active-element piezoresistive bridges. When a pressure is applied, a differential output voltage, proportional to that pressure, is produced. Differential sensors provide a differential voltage proportional to the pressure differential between two ports. One port measures the wind pressure on the model, the other one is connected to the static pressure of the Prandtl tube. Two different pressure sensors are used:

- Type 1: Honeywell 170 PC
  Measurement range ± 35 mbar
- Type 2: AMSYS 5812-0001-D-B
  Measurement range ± 10.34 mbar

They are calibrated by using different factors, so that 5 mbar corresponds to 5 V for the type 1 (the most sensitive) and 5 mbar corresponds to 1 volt for type 2. A static calibration is performed to find pressure to voltage relations for each pressure sensor by using a Betz manometer, which allows to load the system with a known pressure.

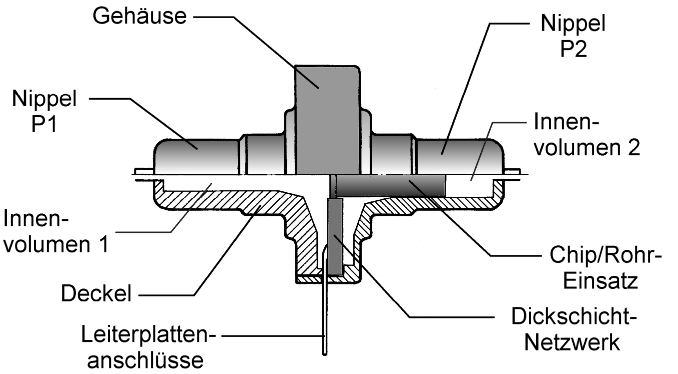

Figure 4.16 Pressure sensor Honeywell 170PC

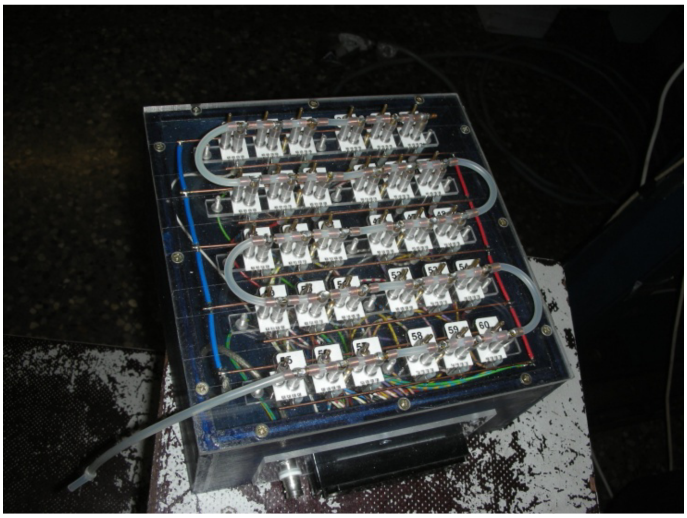

Figure 4.17 Pressure cell AMSYS

The pressure cells AMSYS also incorporate the amplifiers. Instead, the amplifiers for the type 1 are external and independent from one another (Figure 4.18). Then, all the analogic signals are converted into a digital signal by the A/D converters. Eight cards with sixteen A/D each are available in the laboratory. The pressures are scanned in a sample-and-hold modus, which produces simultaneous sampling of the measurements. A sampling frequency of 2 kHz was selected for the measurements. The software used for recording is SBench 5.0.

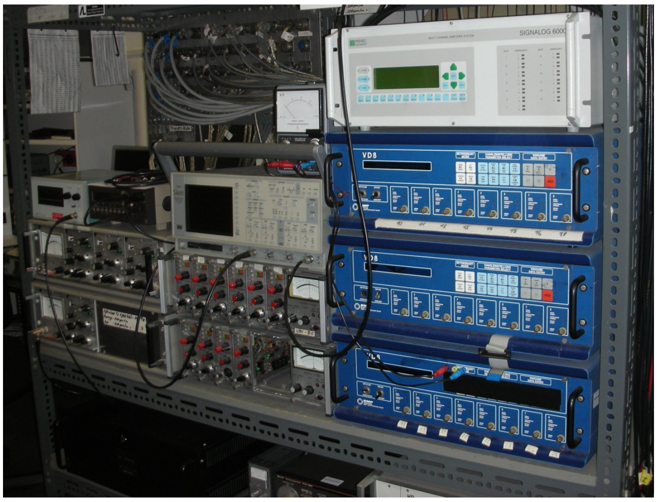

Figure 4.18 External amplifiers for pressure sensors type 1

The pressure taps on the model surface are connected to the pressure sensor by a plastic tube. Special 1.5 m long tubes are used in this work, due to the dimension of the model (see section 4.2). The usual, optimized tubes of the laboratory are 60 cm in length, so they could not be used. The 1.5 m long tubes were used in previous work by Neuhaus (2009). The recorded pressures with the long tubes are corrected by a transfer function, in order to remove the dynamic effect produced by the tubes. Neuhaus (2010) explains how it is calculated. The response spectrum of the signal by using the long tube is compared to the response spectrum obtained by applying the sensor directly on the surface of a model. The latter is considered the right measurement. In fact, the transfer function is not evaluated in absolute terms, but relatively to the right measurement of the signal. The comparison shows that the tube tends to amplify the frequencies lower than 65 Hz (with maximum at about 30 Hz) and damps the frequencies higher than 65 Hz. At 200 Hz there is a damping of 50%. Therefore, the transfer function for the amplitude could be derived in the frequency domain. As regards the phase shift, it resulted to be a linear function of the frequency. Being k the slope of this linear function, the output of the pressure tubes has a constant time delay equal to $k/2\pi$. It is about 0.005 s and it is constant for each frequency, therefore no correction to the phase is applied.

The effective range in which the digital filter applied to the pressure corrects the signal is up to 200 Hz. Therefore, even if the sampling frequency is 2000 Hz, 200 Hz is the cut-off frequency. After that, the frequencies are damped. The reason for which such a high sampling frequency was chosen, despite the relatively lower cut-off frequency, is the higher accuracy in the time domain even for high-frequency (e.g. 200 Hz) fluctuations.

The time histories of pressures are acquired for a duration of $N/f_{sampl} = 2^{18}/2000 = 131.072$ s. 2^{18} is the number of time steps (N) in each recorded signal.

4.2 Model of the solar updraft tower

The model of the Solar Updraft Tower for wind tunnel tests is a circular cylinder of 1 m in height and 15 cm in diameter, made of plexiglass. The aspect ratio is about 1:7 (H/D = 6.7). The dimensions of the model are chosen in order not to have a too high blockage ratio. On the transversal plane the model occupies an area of 1*0.15m = 0.15 m^2, while the wind tunnel cross-section is 1.8*1.6m = 2.88 m^2. The ratio between the two values gives a blockage of 5%, which can be accepted without any correction of results. In scale 1:1000, the model represents a 1-km tall prototype.

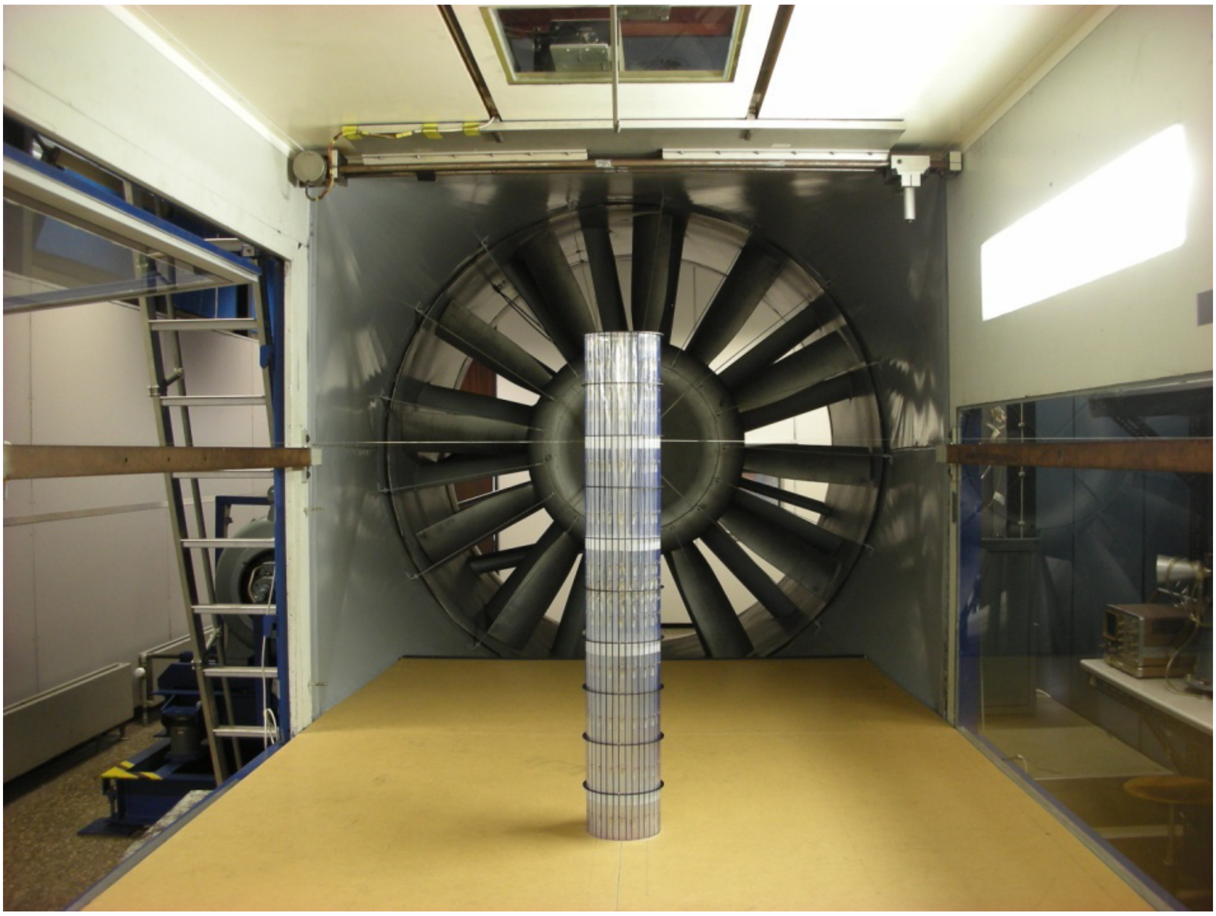

Figure 4.19 Wind tunnel model of the Solar Tower

Even though the real shape of the tower, according to the pre-designs mentioned in Chapter 1, may turn into a hyperboloid at lower levels, the wind tunnel model is a circular cylinder. This shape, which simplified the manufacturing, allows to evaluate the aerodynamic effects without any loss in generality. Moreover, the model is rigid and in order to avoid vibrations two wires[3] at 800 mm fix it at the wall of the wind tunnel.The tower model is equipped with 342 pressure taps, placed at several levels along the height and in the circumferential direction, in order to investigate vertical and horizontal cross-correlations. Both external and internal pressures are measured at each level. The external pressure taps are placed at 17 levels (990-950-910-890-850-750-650-550-520-505-495-480-450-350-250-150-50 mm) at an angular distance of 20° ($\approx$ 26 mm) at each level. The internal pressure taps in the tip region are 9 per level (angular distance = 45°) at 990 and 950 mm. Along the height (at 850-750-650-550-520-450-350-250-150-50 mm) they are 2 per level, at 0° and 180°. This is better shown in the drawing of the model (Drawing 2 on page 125).

The wind tunnel scale of the model and of the boundary layer properties reduces by around three orders of magnitude the Reynolds number from full-scale to wind tunnel conditions ($Re = UD/\nu$; $Re,_{FS} \approx 50*150/1.5*10^{-5} = 5*10^{8}$; $Re,_{WT} \approx 30*0.15/1.5*10^{-5} = 3*10^{5}$). Because of that, surface roughness (ribs) is applied along the model, in order to reproduce the same state of the flow as in full-scale. The target condition is described in the VGB guideline for cooling towers (curves K1.5-1.6). The final choice for the surface roughness – as it will be proved in section 4.4 – is $ks/D = 0.25mm/150mm$, being k the thickness of the ribs. The ribs are at an angular distance of 20°, i.e. in between two pressure taps (Figure 4.20). In any case, ribs are only applied in the scaled wind tunnel model because of Re effects, while the surface of the tower in full-scale conditions must be smooth in order to reduce the drag (Figure 3.10, Niemann,2009) .

The collector roof (4 km in diameter in full-scale) is also modeled in the wind tunnel. It is a very smooth panel in HDF, ideally representing the smooth glass surface encountered by the incoming wind (Figure 4.4). Its function in the wind tunnel is only the creation of a two-phase wind profile. The efflux inside the tower is not reproduced by means of the collector, but artificially by using the pressure difference outside-inside the wind tunnel. In fact, one of the major difficulties in the design of the model was the creation of the efflux inside the tower, due to the presence of 342 tubes inside the cylinder, which connect each measuring point on the shell to the pressure

---

[3] The wires are too thin to modify the flow condition and disturb the measurements.

transducers. The presence of such a large number of tubes inside the tower would affect the internal flow. Moreover, the efflux had to be created somehow.

After having discussed several possibilities, it was decided to use a second circular cylinder, having a smaller diameter, to be placed inside the main cylinder representing the tower. This configuration of a pipe in a pipe allows placing all the tubes for measuring the pressures in the small cavity between the two cylinders. The two cylinders are glued together at the top through a union ring, as it can be seen in Figure 4.20.

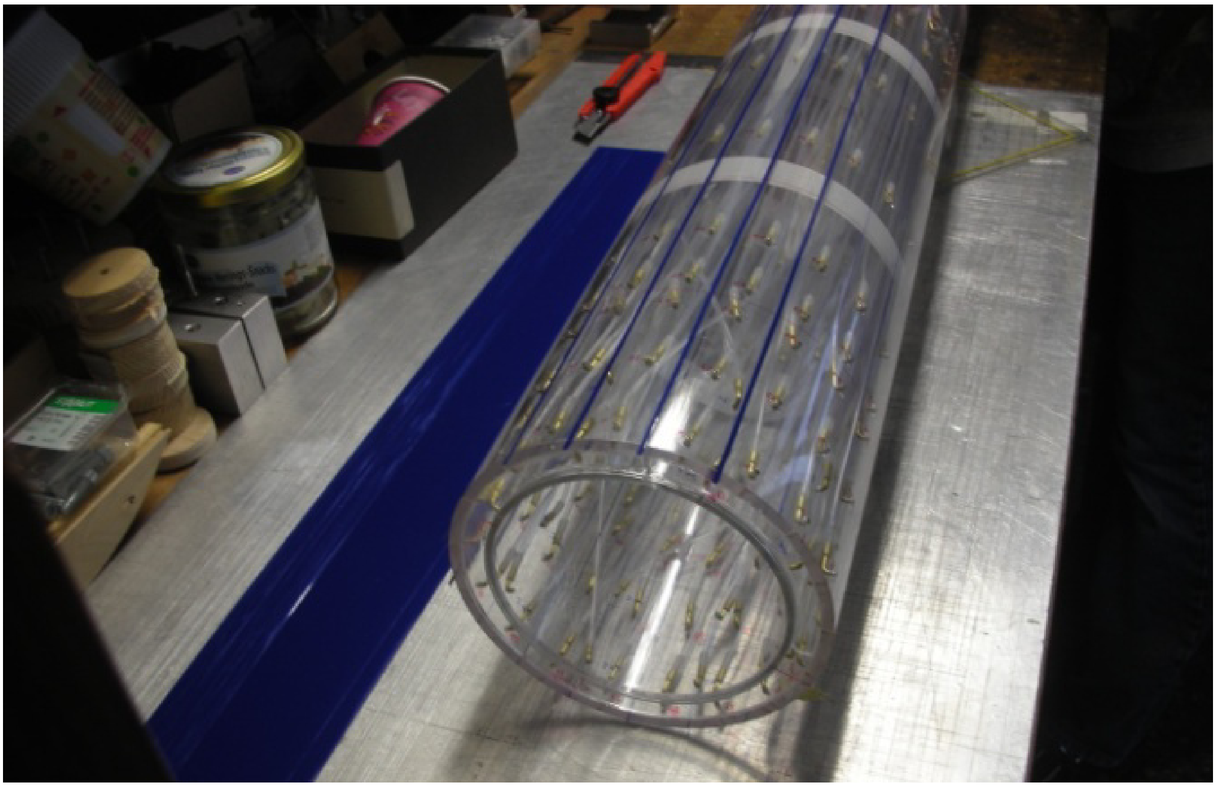

Figure 4.20 Tube-in-a-tube solution.

The outer cylinder is shorter in length than the inner one, so that the pressure tubes can come out of the model (below the wind tunnel) when the outer cylinder ends. As said, the efflux inside the tower is created by the pressure difference inside-outside the wind tunnel. In addition, a ventilator is placed below the model - at the opening of the inner cylinder - in order to achieve higher efflux velocities, if needed. Below the ventilator there is a moving plate which allows to regulate the opening, so to achieve the desired air capacity for the efflux. In addition, tests are also made in no-efflux conditions (outage condition), by closing the opening below the ventilator. Even though in reality the value of the efflux velocity during operation of the power plant depends on several conditions (e.g. the temperature rise in the collector, the pressure drop at the turbines etc.), a quite realistic condition for the design is achieved in the wind tunnel when the velocity of the efflux inside the tower is around one half of the wind tunnel velocity. The peculiarity of the model is the presence of circular ring beams applied along the height (Figure 4.21). Tests are performed both without and with rings. The size and the number of the rings resulted to be influencing parameters of the flow around the tower. Ring beams of two sizes are tested, they are identified by the prefix SR and KR as follows:

- SR = big rings (usually called simply rings in the following): external diameter 164 mm, internal diameter 150 mm, width (w) = 7 mm → w/D = 7/150 = $4.67*10^{-2}$;
- KR = small rings: external diameter 157 mm, internal diameter 150 mm, width = 3.5 mm→ w/D = 3.5/150 = $2.33*10^{-2}$;

They represent the highest and one of the lowest limits in the design of a solar tower. They are placed along the height at the reference distance of 10 cm in the wind tunnel scale (10 rings). Due to their strong effect on the flow, tests have also been repeated with 5 rings at a distance of 20 cm and 7 rings at a distance of about 14 cm (see section 4.3).

Figure 4.21 Ring beams along the height of the cylinder.

Figure 4.22 The support system for installation

Figure 4.23 Complete installation

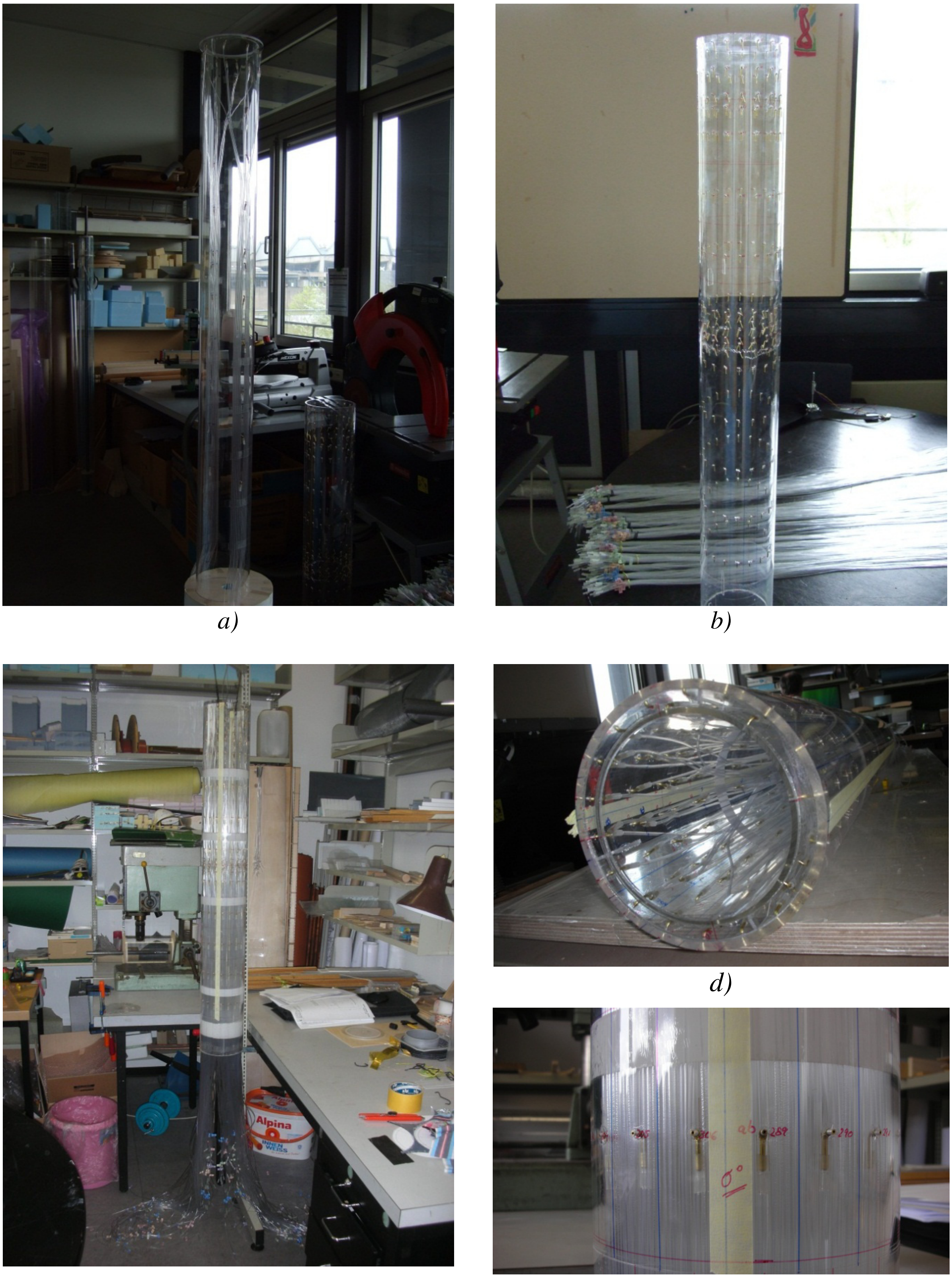

a) b)

c) d) e)

Figure 4.24 Model under construction: a) inner cylinder; b) outer cylinder; c) outer cylinder during application of pressure tubes; d) detail of the tip: the two cylinders are glued together; e) pressure taps and references on the outer cylinder

DRAWING n.2 Wind tunnel model of the solar updraft tower

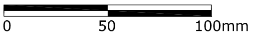

TIP REGION

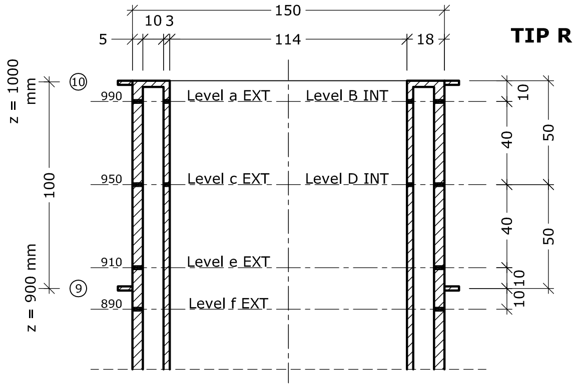

HORIZONTAL DISTRIBUTION OF PRESSURE TAPS

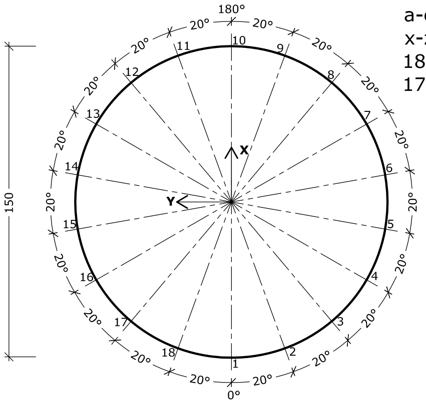

EXTERNAL PRESSURES:
Levels:
a-c-e-f-g-i-k-m-o-q-r-s-t-v
x-z-ab
18 pressure taps for each level
17 x 18 = 306

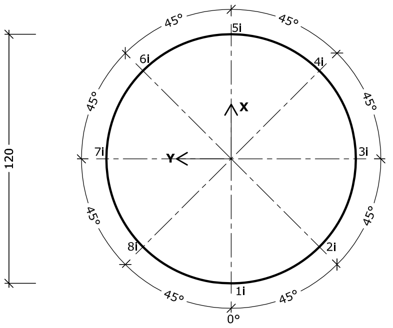

INTERNAL PRESSURES:
Levels: B-D
8 pressure taps for each level
2 x 8 = 16

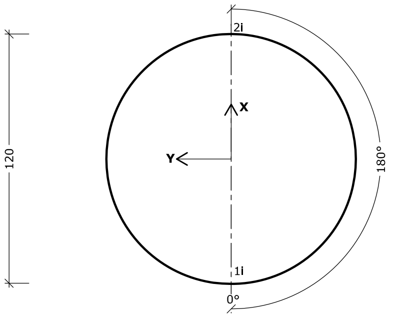

INTERNAL PRESSURES:
Levels: H-J-L-N-P-U-W-Y-AA-AC
2 pressure taps for each level
10 x 2 = 20

DETAIL OF THE STIFFENING RING

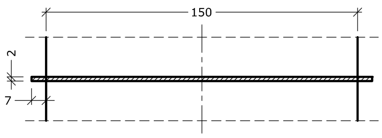

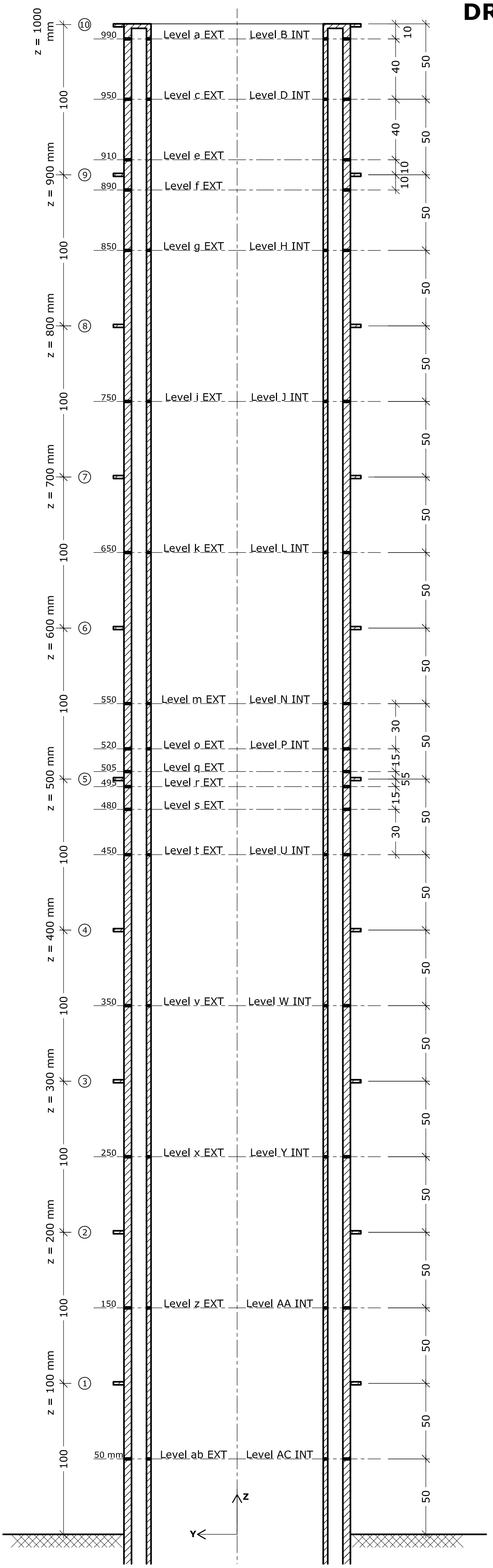

VERTICAL DISTRIBUTION OF PRESSURE TAPS

DRAWING n.3 Installation of the model and creation of efflux

Details about the model

Tower:

Height = 1 m

Outer cylinder: plexiglass, Øext = 150 mm, Øint = 140 mm

Inner cylinder: plexiglass, Øext = 120 mm, Øint = 114 mm

External pressure taps: 17 levels, 18 taps at each level (spacing 20°)

Internal pressure taps: 12 levels, 2 or 8 taps at each level

Total: 342 pressure taps

Surface roughness: ribs, spacing 20°, height = 0.25 mm

Collector:

Plate in HDF, thickness = 6 mm, width = 1.8 m, length ≈ 4 m

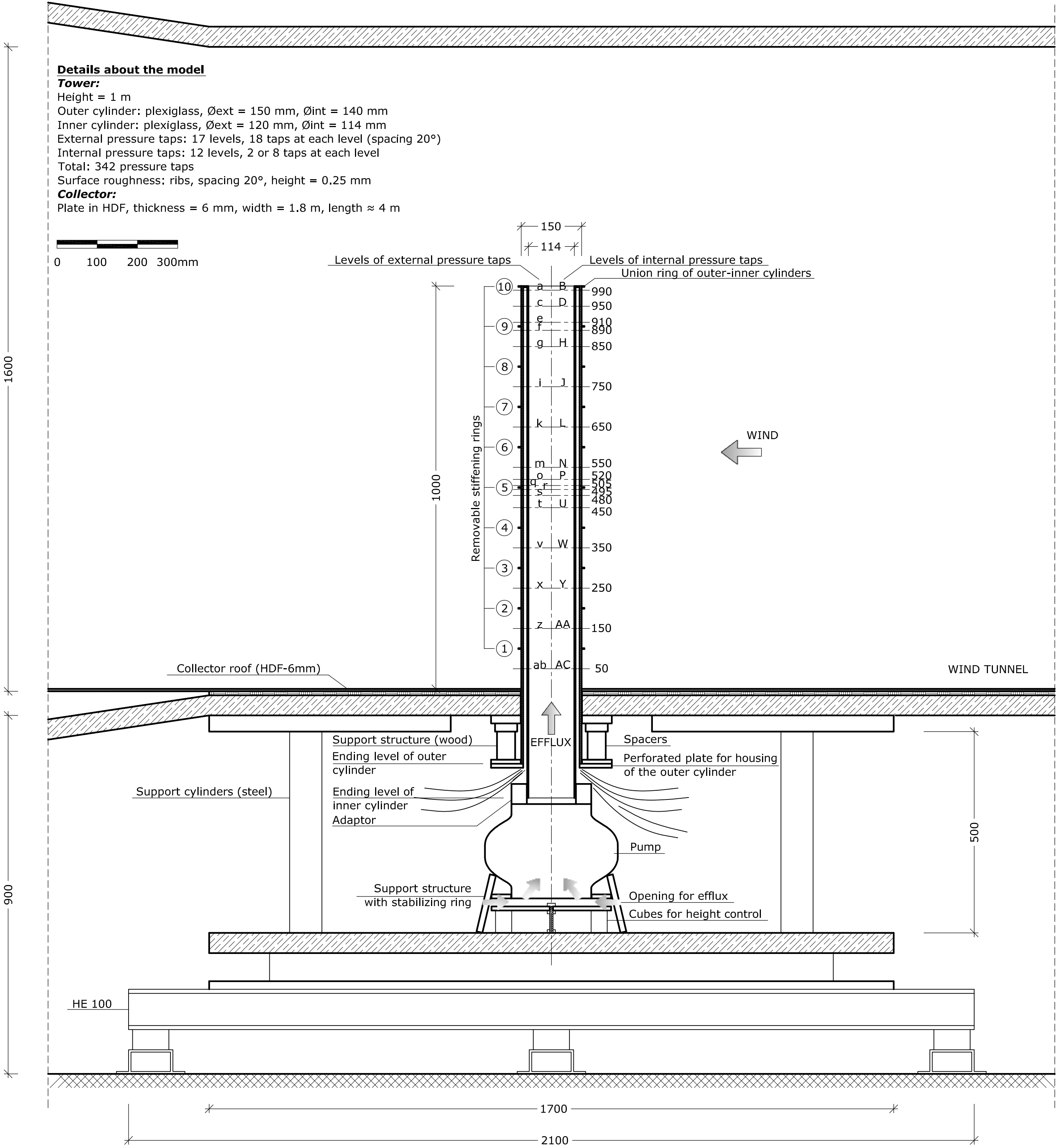

WiSt
Boundary layer wind tunnel
Ruhr-University Bochum

4.3 Outline of the experiments

The model of the tower without rings is the reference case to identify the flow condition and study the aerodynamic of the flow around a circular cylinder H/D = 7, immersed in boundary layer flow. Most of the studies in literature refer to sub-critical Re; in addition, the aspect ratio and the characteristics of the boundary layer influence the results (Chapter 3). Therefore, before investigating the effect of the ring beams, it is necessary to have a deep knowledge of the flow around the circular cylinder without ring beams. Because of that, each test is always made twice: once with the rings, once without them. In addition, several conditions, in terms of surface roughness, flow velocity, boundary layer, efflux, number of rings, size of rings are tested. The nomenclature used in the campaign is described in the following:

1. Boundary layer:
    - T1 = boundary layer flow RAU8 + collector;
    - T3 = uniform flow (empty tunnel);

2. Surface roughness conditions on the outer surface of the model:
    - R0 = smooth cylinder;
    - R1 = ribs at a spacing of 20°, ks = 0.250 mm ($ks/D = 1.67*10^{-3}$);
    - R2 = ribs at a spacing of 10°, ks = 0.250 mm ($ks/D = 1.67*10^{-3}$);
    - R3 = ribs at a spacing of 20°, ks = 0.375 mm ($ks/D = 2.50*10^{-3}$);
    - R4 = ribs at a spacing of 10°, ks = 0.375 mm ($ks/D = 2.50*10^{-3}$);
    - R5 = ribs at a spacing of 20°, ks = 0.500 mm ($ks/D = 3.33*10^{-3}$);

    The surface roughness is always made of ribs. This choice is motivated by simplicity of manufacturing and consolidated experience on cooling towers (VGB, 2010).

3. Wind tunnel velocity: for practical reasons, the wind tunnel velocity to be used in each test is identified by the number of rounds per minute (rpm) of the fan. Depending on the static pressure and on the temperature during measurements, the density of air and consequently the velocity may change. A small difference in the measured velocity corresponding to the same rpm is also noted in presence or absence of boundary layer (RAU8 or empty tunnel) and in presence or absence of efflux in the chimney. Approximately, it results:
    - 100 rpm; $U_{pra} \approx 3$ m/s
    - 200 rpm; $U_{pra} \approx 5$ m/s

- 400 rpm; $U_{pra} \approx 8$ m/s
- 600 rpm; $U_{pra} \approx 12$ m/s
- 800 rpm; $U_{pra} \approx 16$ m/s
- 1000 rpm; $U_{pra} \approx 20$ m/s
- 1250 rpm; $U_{pra} \approx 25$ m/s
- 1400 rpm; $U_{pra} \approx 27$ m/s

1400 rpm is the highest velocity which was used, although the capacity of the wind tunnel was even higher, up to 1500 rpm. However, the resulting pressure at higher wind speed would have exceeded the sensitivity range of the pressure transducers type 2, which could not be regulated.
The low velocity range 100-200-400 rpm is tested only on the smooth cylinder, in the hope to reach subcritical conditions (laminar separation). However, at very low speed the wind tunnel velocity was not always stable.

4. Efflux condition:
    - EF0 = no efflux;
    - EF1 = efflux;

The velocity of the efflux is regulated at about one half of the wind tunnel velocity (section 4.4.1).

5. Effect of ring beams:
    - SR0 = no rings;
    - SR1 = ten big rings along the height, equally spaced at a distance of 10 cm;
    - SR7 = seven big rings along the height, equally spaced at a distance of 14 cm (15 cm in the two lowest compartment);
    - SR5 = five big rings along the height, equally spaced at a distance of 20 cm;
    - KR1 = ten small rings along the height, equally spaced at a distance of 10 cm;
    - KR7 = seven small rings along the height, equally spaced at a distance of 14 cm (15 cm in the two lowest compartment);
    - KR5 = five small rings along the height, equally spaced at a distance of 20 cm;

The wind tunnel equipment allows to measure maximum 92 pressures simultaneously. However, some sensors where out of use at the time of the tests, therefore no more than four levels (with 18 pressure taps each, on the external surface) could be measured at the same time, plus other positions at proper convenience. In the first plan of the experiments, it was decided to measure all the correlations of the 342 pressure taps in the basic conditions: T1(&T3)-SR0&SR1-EF0(&EF1)-R1, where the nomenclature out of brackets had the priority. In order to measure all the cross-correlation, the pressures had to be divided into groups and each group had to be measured with all the other ones. However, due to the appearance of the new phenomenon described in Chapter 5 – during the second set of measurements (May 2011) – the original plan of experiments was revised. Different experimental conditions had to be tested for a deeper understanding of the phenomenon: not only SR0 and SR1, but also SR5, SR7, KR1, KR5, KR7; not only R1, but also R0-R2-R3-R4-R5. Consequently, the complete correlation field could not be measured, but only the most important pressures were measured simultaneously.

In summary, the following series of measurements were defined (only pressures on external surface and complete circumference are mentioned):

- MS01: levels z = 990-950-910-890 mm;
- MS02: levels z = 910-890-850-750 mm;
- MS03: levels z = 750-650-550 mm;
- MS04: levels z = 550-520-505-495 mm;
- MS05: levels z = 505-495-480-450 mm;
- MS06: levels z = 450-350-250-150 mm;
- MS07: levels z = 250-150-50 mm + vertical at 0°;
- MS08: levels z = 990-950-750 mm;
- MS09: levels z = 550-450 mm;
- MS10: levels z = 450-50 mm + vertical at 80°;
- MS28: verticals at 20°, 120°, 180°, 300°;
- MS30/MS32: levels z = 950-850-750-650 mm;
- MS31: levels z = 950, 890, 750, 650 mm;
- MS33: levels z = 950-910-890-850 mm;
- MS34: levels z = 650-550-520-480 mm;

The experimental campaign was articulated in the following four sets, which became necessary as the investigation was proceeding:

Set n.1 (April 2011):

Turbulence setting: T1
Rings: SR0
Efflux: EF0/EF1
Surface roughness: R1
Wind tunnel velocity (rpm): 600/800/1000/1250/1400
Measurement series: MS01/02/03/04/05/06/07/08/09/10/28;

Set n.2 (May 2011):

Turbulence setting: T3
Rings: SR0/SR1
Efflux: EF0/EF1
Surface roughness: R1
Wind tunnel velocity (rpm): 0600/0800/1000/1100/1250/1400
Measurement series: MS01/02/04/05/08/09;

Set n.3 (October 2011):

Turbulence setting: T1
Rings: SR0/SR1/SR7/SR5/KR1/KR7/KR5
Efflux: EF0/EF1
Surface roughness: R0/R1/R2/R3/R4/R5
Wind tunnel velocity (rpm): 0600/0800/1000/1250/1400
Measurement series: MS30/31;

Set n.4 (December 2011):

Turbulence setting: T1
Rings: SR0/SR1
Efflux: EF0/EF1
Surface roughness: R1/R3
Wind tunnel velocity (rpm): 0600/0800/1000/1250/1400
Measurement series: MS32/33/34;

4.4 Preliminary results on the circular cylinder

In this section, preliminary results on the cylinder without rings are presented.

4.4.1 Velocity of efflux

The tests are performed in two conditions: open efflux (EF1) and closed efflux (EF0). The latter represents the condition of out of use of the power plant. For many aspects, EF0 is more dangerous than EF1. In particular, the tip effect in EF0 is stronger. In the condition of open efflux, the tests are performed with only one efflux velocity. The influence of different efflux velocities on the pressures is not investigated. The efflux velocity which acts in EF1 is around one half of the undisturbed flow velocity (U_{pra}). This is achieved in the experiments by defining a proper opening below the model, through the position of the wooden plate under the ventilator (Figure 4.23).

The efflux velocity was measured during a preliminary test by a second Prandtl tube placed inside the chimney close to the tip. Figure 4.25 shows the ratio between the Prandtl velocity U_{pra} and the efflux velocity at different U_{pra}, corresponding to a certain position of the wooden plate used in all the experiments.

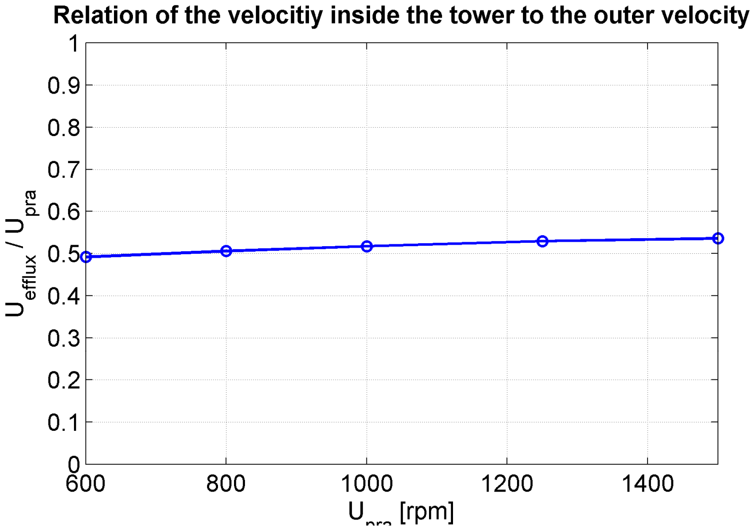

Figure 4.25 Efflux velocity

The effect of the efflux on the pressures is evident in the tip region, while it is not influent at lower levels. Figure 4.26 shows the modification of the external pressures at z/H = 0.95 due to the efflux. In EF1 the lateral suction is reduced and the separation point is shifted downstream. Moreover, the increase in suction in the wake of the cylinder, around $\varphi = 150°$ in EF0, due to tip vortices as explained in Chapter 3, is missing EF1. It is then confirmed (Gould et al., 1968) that the efflux displaces the tip vortices. The peak of pressure in the wake due to the entrainment of the flow is also leveled out in EF1, as expected.

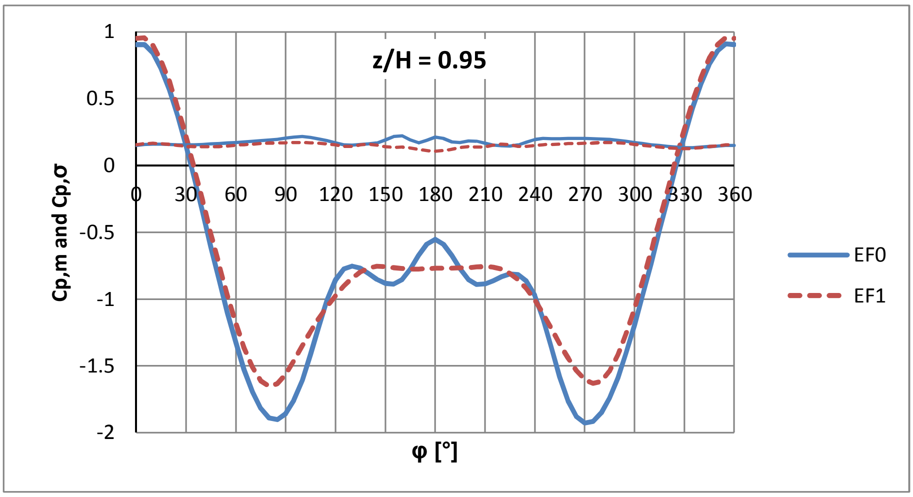

Figure 4.26 $C_{p,m}$ and $C_{p,\sigma}$ in the tip region (z/H = 0.95): influence of efflux.

4.4.2 Internal pressure

The internal pressure coefficient C_{pi} is calculated with reference to the velocity pressure at z = H. The pressure coefficient is higher is case of efflux, both in the mean as well as in the rms. Its value is approximately constant along the height and along the circumference. Only close to the tip it exhibits some variation. In any case, the value of C_{pi} is lower than the typical value for cooling towers (C_{pi} = -0.5 in VGB, 2010).

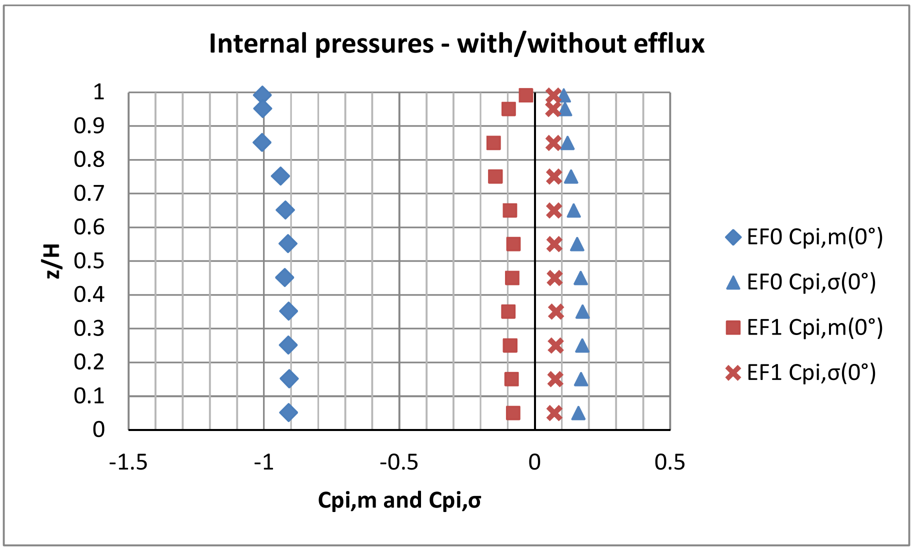

Figure 4.27 Internal pressures – spanwise varation

In absence of efflux, the internal pressure is somewhat higher at z/H = 0.99, φ = 180°, probably due to an entrainment of fluid inside the cylinder (Figure 4.28). However, the level z/H = 0.95 is already unaffected and the internal pressure does not show any circumferential variation.

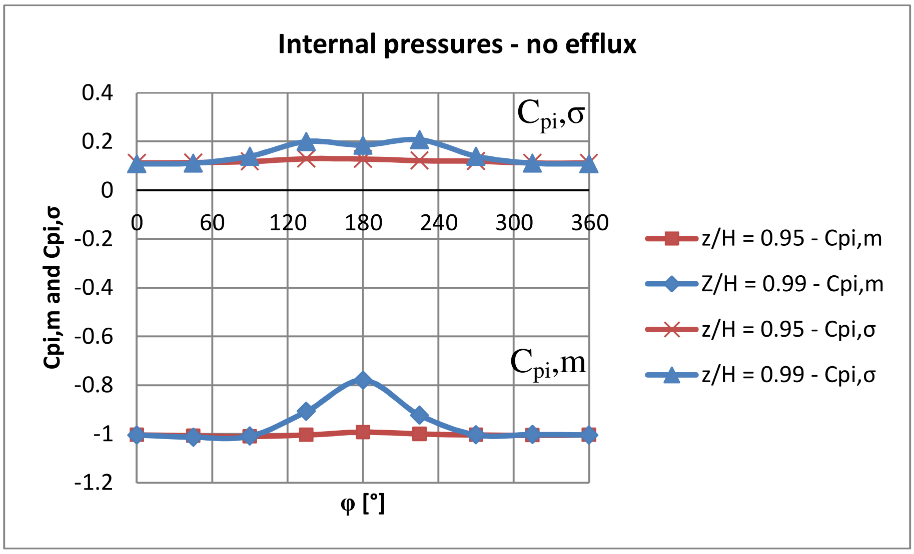

Figure 4.28 Internal pressures – circumferential varation

4.4.3 Reynolds effects on the smooth and rough cylinder

As mentioned before, due to the reduced scale of the model in the wind tunnel, the Reynolds number is around three orders of magnitude lower than in full-scale ($Re = UD/\nu$; $Re_{,FS} \approx 50*150/1.5*10^{-5} = 5*10^{8}$; $Re_{,WT} \approx 30*0.15/1.5*10^{-5} = 3*10^{5}$). Because of that, surface roughness (consisting of ribs) is applied to the model. The effect of surface roughness on the circular cylinder in the wind tunnel is studied with regard to the following key parameters:

- $C_{D,m}$ = mean value of the drag coefficient;
- $C_{D,\sigma}$ and $C_{L,\sigma}$ = rms values of the drag and lift coefficients;
- $C_{p,min}$ = minimum pressure (lateral suction);
- $C_{p,b}$ = base pressure;
- $C_{p,b}$-$C_{p,min}$ = pressure rise to separation or pressure recovery;

Further comments concern the Strouhal number (S_t) and the angle of separation.

At first, the results are presented for the level z/H = 0.65, which is out of the tip region, approximately in the two-dimensional normal range and available in most of the tests. Then, the spanwise variation is considered. The tests are in turbulent boundary layer (T1), unless differently specified, and only results in EF0 are reported. The Reynolds number is uniquely defined with respect to the local velocity at the tower top (at z = H). The dependency of air viscosity on the temperature is neglected; the value $\nu = 1.5*10^{-5}$ at 20°C is used.

Figure 4.29 plots the drag coefficient distribution at z/H = 0.65 for different Reynolds numbers (i.e. different wind tunnel velocities) and for different surface roughness conditions. The blue curve (R0) refers to the smooth cylinder (according to the nomenclature in section 4.3). It can be seen that the flow around the smooth cylinder is at first in the critical state, characterized by the fall of C_D until the minimum at $Re_{cr} \approx 1.9*10^5$. After that, the horizontal plateau is typical of the supercritical range for smooth cylinders, according to Roshko's classification (Chapter 3). On the rough cylinder in turbulent boundary layer flow (T1), for any type of surface roughness (R1-R5) the state of the flow is already beyond the critical Re. This is not only due to the surface roughness, but it is also enhanced by the turbulence of the flow. In fact, it is interesting to compare these results to the black dashed line in the figure, which is the only one referring to uniform flow and lower I_u (empty tunnel). However, due to lack of data, it is at z/H = 0.55. In any case, it can be seen that at high (effective) Re the effect of turbulence on the drag coefficient is limited, while it is stronger at low Re: in empty tunnel the flow around the rough cylinder R1 undergoes the critical state at Re $\approx 1.5*10^5$. Moreover, the figure shows a certain similarity between the curves R2-R3 and R4-R5 for the whole range of Reynolds numbers. R2 and R4 have, with respect to R3 and R5, a double number of ribs with smaller height. Therefore, within a certain limit, the height of the rib and their distance act in the same manner.

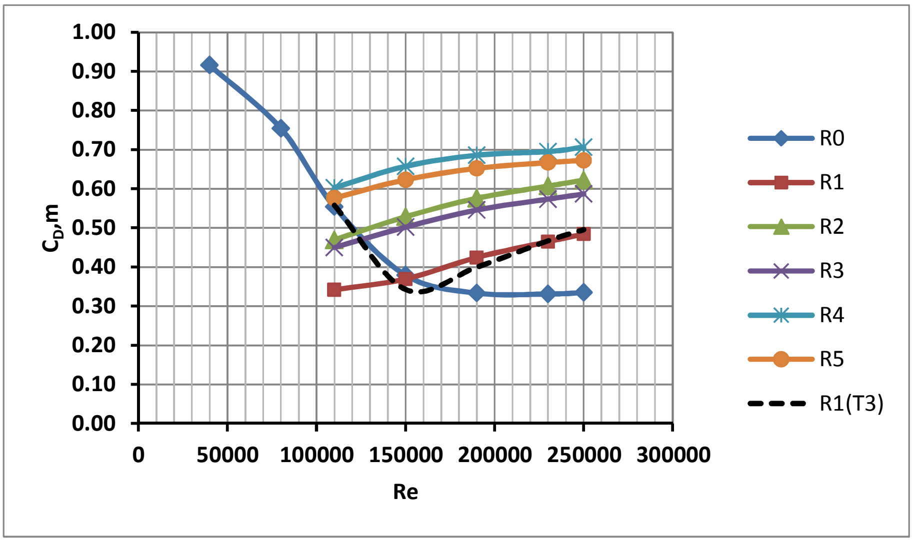

Figure 4.29 Drag coefficient vs Re (z/H = 0.65, R0-R5, T1 unless differently specified)

The rms values of both drag and lift coefficients on the rough cylinder do not show a large variability with Re (Figure 4.30 and Figure 4.31). The along wind fluctuations tend to increase with higher roughness. It is not surprising that in empty tunnel (black dashed line) the force fluctuations, especially in the along wind direction ($C_{D,\sigma}$), are lower, because turbulence is lower.

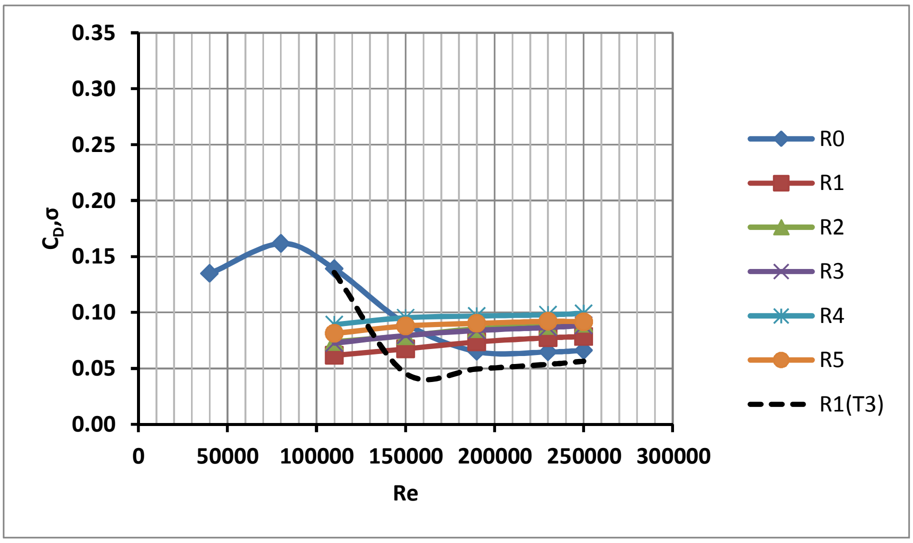

Figure 4.30 Rms drag coefficient vs Re (z/H = 0.65, R0-R5, T1 unless differently specified)

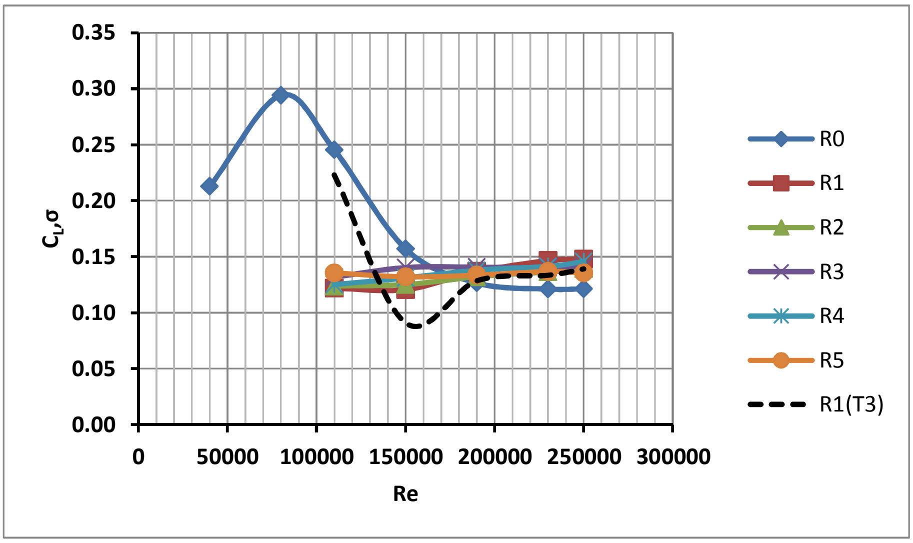

Figure 4.31 Rms lift coefficient vs Re (z/H = 0.65, R0-R5, T1 unless differently specified)

Figure 4.32, Figure 4.33 and Figure 4.34 complete the set of information by plotting the pressure recovery, the wake pressure and the minimum pressure, respectively.

On the smooth cylinder (R0) at $Re_{cr} \approx 1.9*10^5$, the blue curve reaches the maximum base pressure (the lowest wake suction) and the minimum pressure at the flanges. This corresponds to the largest value of pressure recovery, which is associated to the minimum drag. After that, the horizontal plateau in the supercritical range is confirmed. All of that is in accordance to literature (Chapter 3).

On the rough cylinder, the positive rise in terms of $C_{D,m}$ (Figure 4.29) corresponds to a decrease in the pressure recovery. It is due to the progressive increase in wake suction (which rises the drag) and decrease in lateral suction. In fact, according to Güven et al. (1980), the overall effect of surface roughness on the pressure distribution is best seen in the behaviour of the pressure rise to separation or pressure recovery $C_{p,b}$-$Cp_{,min}$. Such a parameter, which includes both variations of the base and minimum pressures and shows opposite trend with respect to the drag, is especially important because it is almost insensitive to the effects of influencing parameters such as tunnel blockage, aspect ratio and even free-end effects. Furthermore, as explained by Güven et al. (1980), in the supercritical Reynolds number range, $C_{p,b}$-$Cp_{,min}$ decreases with increasing Re for a given relative roughness and decreases with increasing relative roughness for a given Re number. The incremental changes in $C_{p,b}$-$Cp_{,min}$ decrease with increasing roughness. Such a pressure difference is closely related to the characteristic of the boundary layer prior to separation and it is the reason for its strong dependence on surface roughness. All of that is confirmed by Figure 4.32.

The black curves of the rough cylinder in empty tunnel (R1-T3) confirm the critical Re at ≈ $1.5*10^5$. This represents a point of maximum of the pressure recovery. In fact, in the critical range before Re_{cr} the pressure recovery is a small value due to the early laminar separation. At high Re, the turbulence intensity has a negligible effect on the state of the flow, as it was shown by C_D.

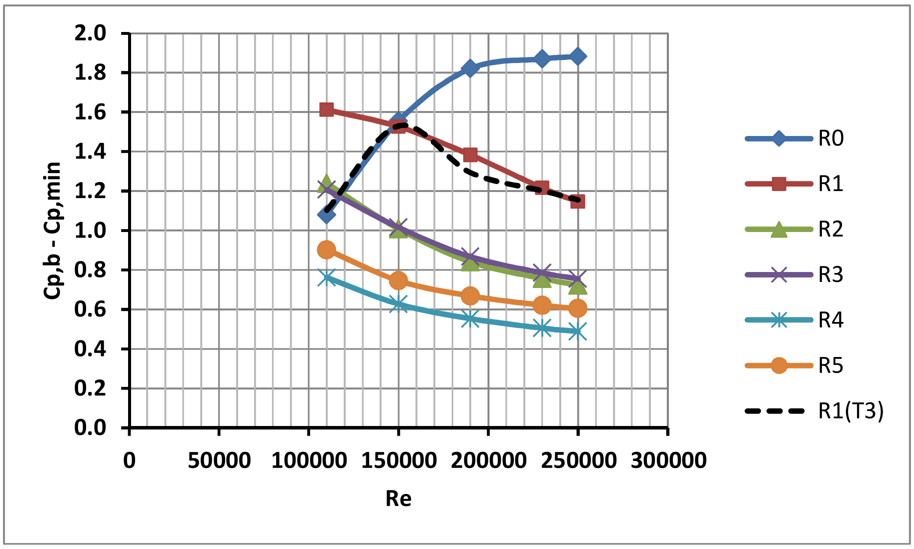

Figure 4.32 Pressure recovery (z/H = 0.65, R0-R5, T1 unless differently specified)

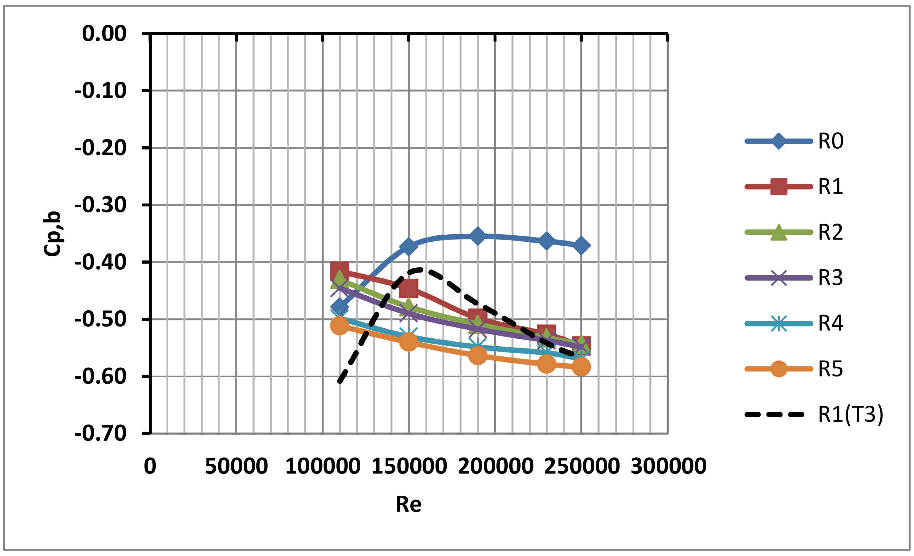

Figure 4.33 Base pressure (z/H = 0.65, R0-R5, T1 unless differently specified)

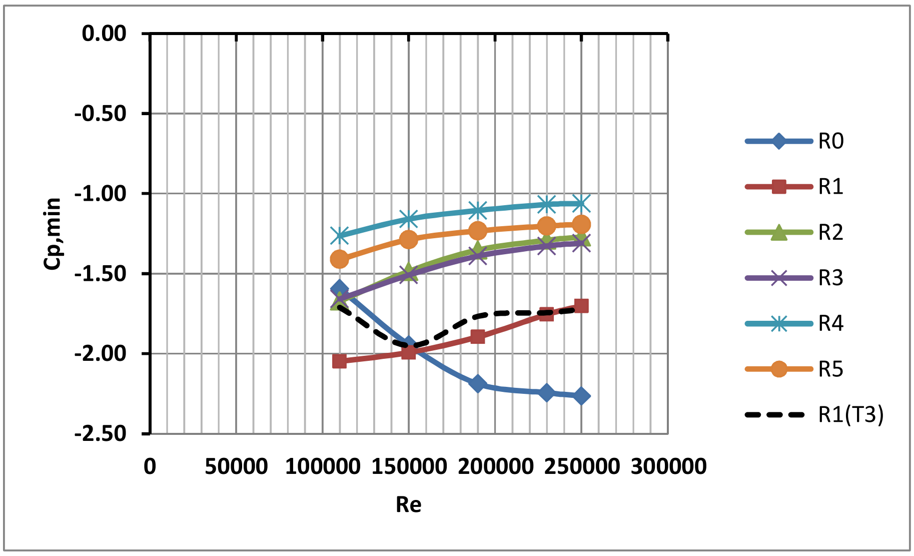

Figure 4.34 Minimum pressure at the flanges (z/H = 0.65, R0-R5, T1 unless differently specified)

The following figures show an overview of the variation of the mean pressure distribution with Re and surface roughness. On the smooth cylinder (R0) in Figure 4.35, it is clear that the increase in wind tunnel velocity progressively increases lateral suction and decreases wake suction. The blue and the red curves in the figure lie in the critical range (which is characterized by the fall in the drag). The critical condition is reached at first by the green curve (Re = $1.9*10^5$) and all the other curves collapse on that one, due to the horizontal plateau in the supercritical range. On the rough cylinder R1 (Figure 4.36), instead, the progressive increase in the Re is marked by decrease in lateral suction, accompanied by upstream movement of the separation point and increase in wake suction.

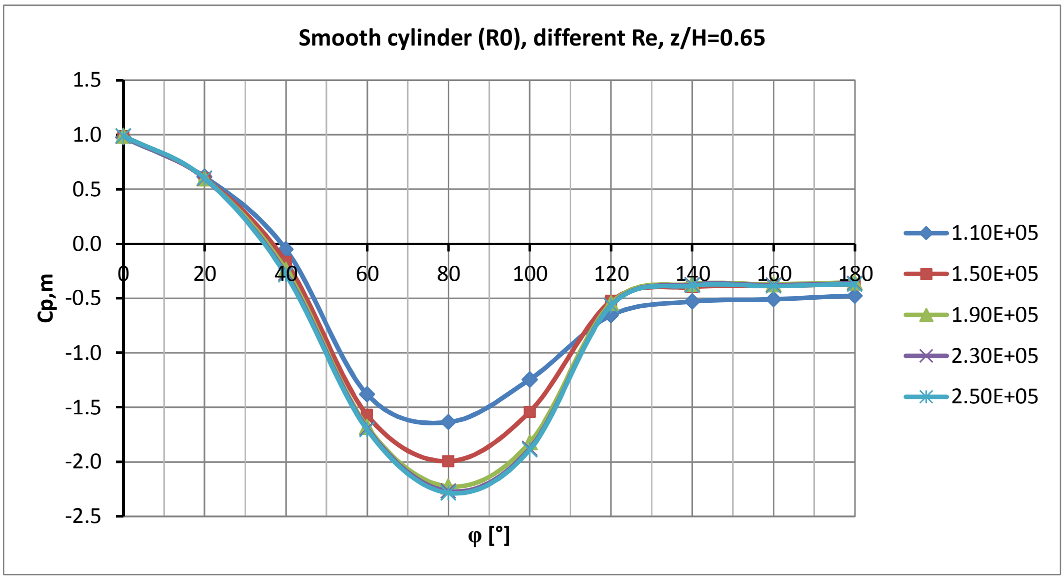

Figure 4.35 Mean pressure distribution as a function of Re on the smooth cylinder (z/H = 0.65)

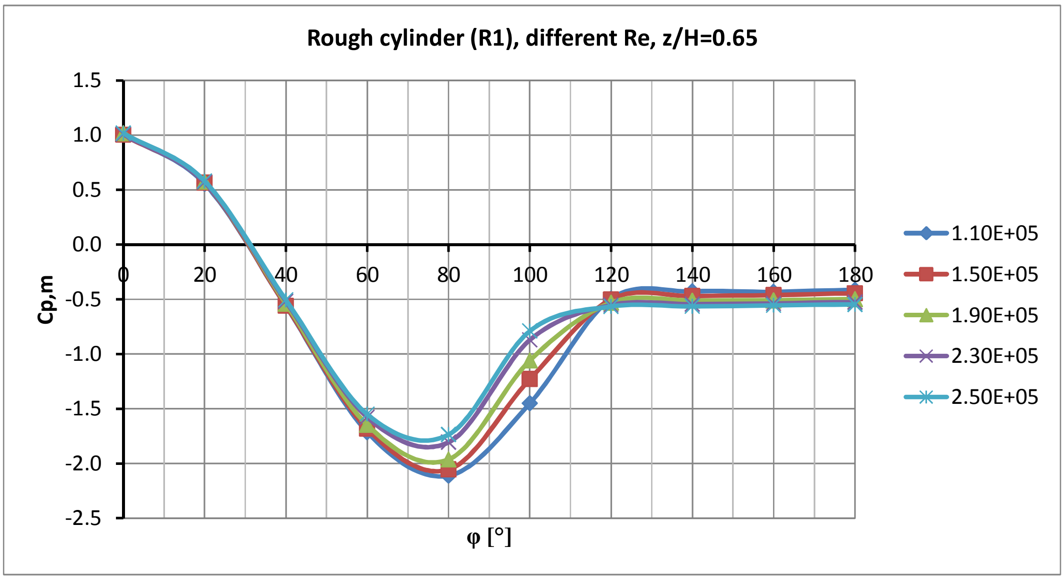

Figure 4.36 Mean pressure distribution as a function of Re on the rough cylinder (z/H = 0.65)

In time, the position of the separation point is not stationary, but it fluctuates around the average position, in full-scale as well as in the wind tunnel. The function of the ribs should not be to force the separation at precise locations, but to promote turbulent transition of the boundary layer. A turbulent boundary layer is able to overcome larger adverse pressure gradients and therefore separation is retarded. However, it can be argued whether such oscillations of separation are forced or prevented by the presence of the ribs on the wind tunnel model. Figure 4.37 clarifies that with small surface roughness (e.g. R1) the position of separation is not particularly fixed by the presence (and the specific distribution) of the ribs. The figure highlights the spatial oscillation of the separation point in a short time window. The roughness conditions R4 and R5 resulted, from this point of view, more invasive. In fact, it is not recommended to force the Reynolds regime by using high surface roughness. Ribeiro (1991) wrote: “the larger the relative roughness, the lower the Reynolds number with which the ultra-critical regime is established, but the greater the differences observed in this regime, between the parameters measured on the rough circular cylinder and those observed on smooth circular cylinders”. For this reason, the surface roughnesses R4 and R5 are discarded for further studies on the tower.

The Strouhal number decreases on the rough cylinder (R1) from 0.22 to 0.20 as the transcritical conditions are approached (Figure 4.38) and the peak becomes narrower. Such a decrease in the Strouhal number is related to the upstream movement of the separation point. The lowest S_t on the rough cylinder (R1) at the highest Re ($2.5*10^5$) is associated to the a wider wake, as shown in Figure 4.36. This is consistent with Roshko’s concept of universal Strouhal number, which is related not to the cylinder dimension but to the width of the wake (Roshko, 1955).

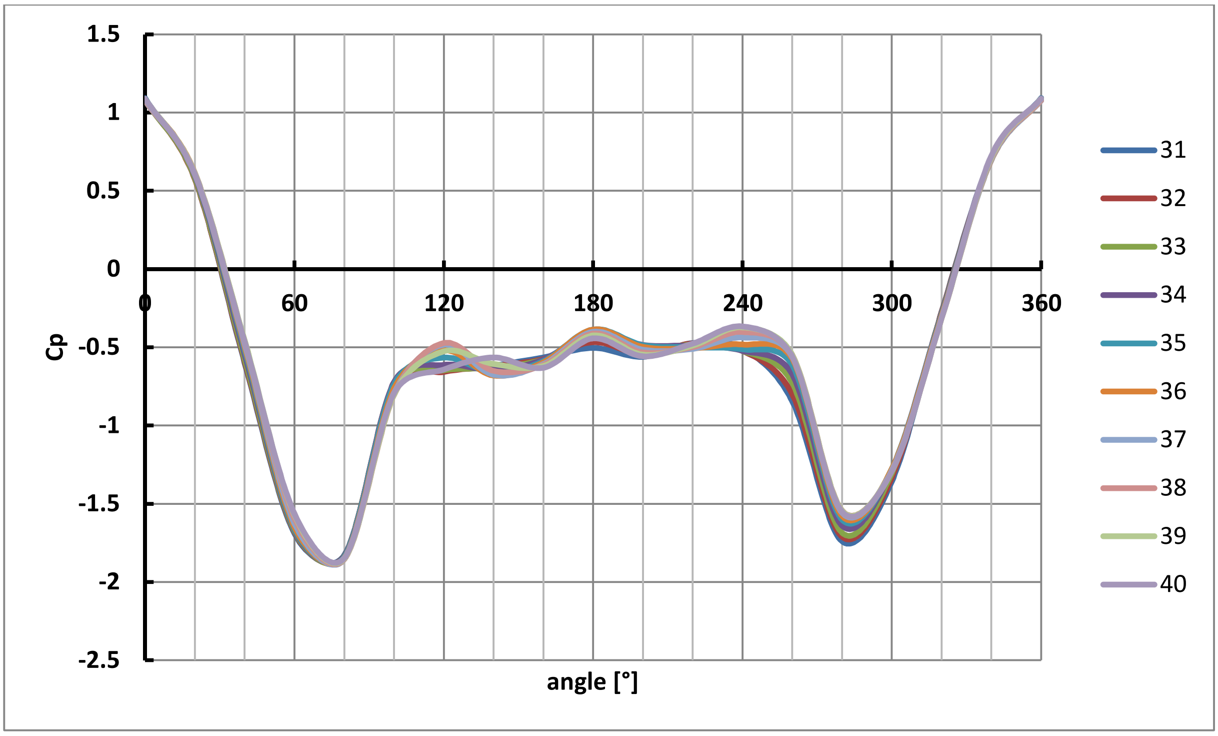

Figure 4.37 Momentary pressure distribution (z/H = 0.65, T1-R1, time steps 2897:2906)

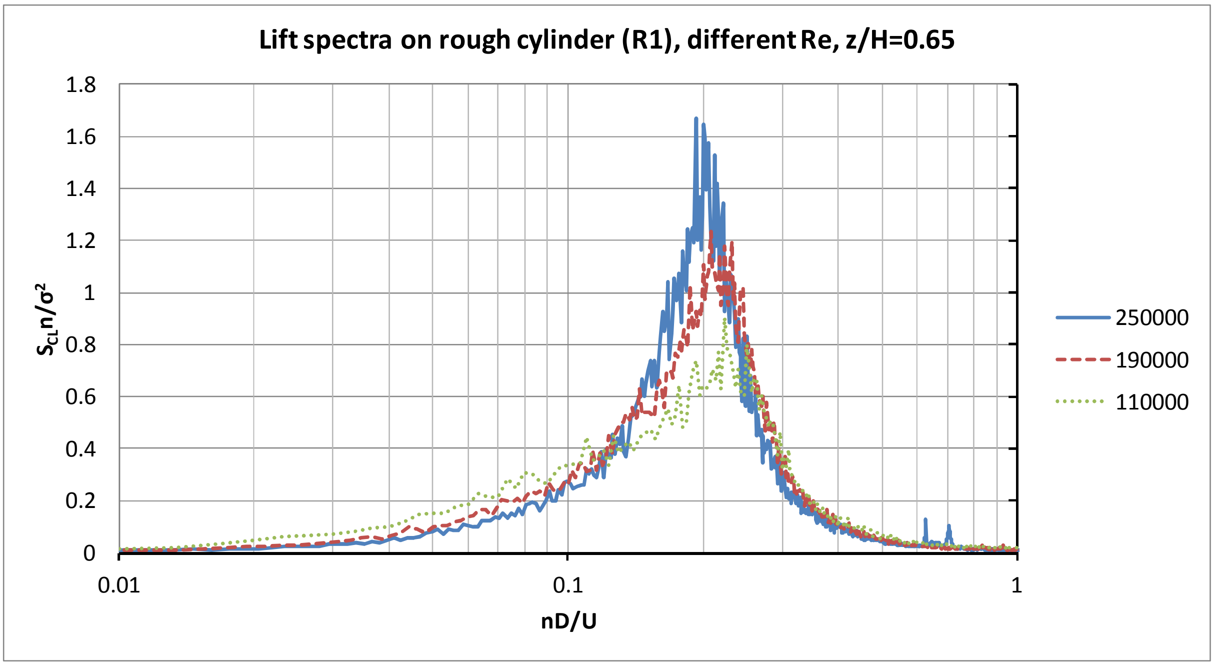

Figure 4.38 Spectra of the lift coefficient vs n [Hz] on the rough cylinder as a function of Re

The skewness of the spectra at z/H=0.65 in Figure 4.38, which is more evident at the lowest Re (green curve) but still present at the highest Re, is due to fluctuations produced at low frequencies by tip-associated-vortices. They are free-end effects, as mentioned in Chapter 3 and better investigated in Chapter 5.

So far, the discussion has been focused on the behaviour at middle height.

Figure 4.39 and Figure 4.40 describe the spanwise variation of the mean drag coefficient and of the pressure recovery at Re = $2.5*10^5$. The tip effect is influenced by the surface roughness, because the rougher is the cylinder, the lower is the wake pressure (Figure 4.33). This enhances the flow over the tip of the body. For the same reason, the tip effect on the smooth cylinder is weaker: the smooth cylinder at Re = $2.5*10^5$ is in supercritical conditions, characterized by minimum drag (horizontal plateau) due to small wake suction and very high pressure recovery due to large suction at the flanges. Moreover, in uniform flow (black curve) the tip effect is weaker than in boundary layer flow. It is in contradiction with Gould's conclusion (Gould et al., 1968) that the free-end effect is independent on the type of boundary layer. It is confirmed, instead, that the tip effect produces an increase in the lift fluctuations at about one diameter from the top, probably due to tip vortices, while the spanwise variation of drag fluctuations are less pronounced.

Another important feature in Figure 4.39 and Figure 4.40 is the ground effect, which extends up to z/H = 0.5. It is not only confined to the very low region. The higher drag at the base of the tower is probably enhanced by the presence of a boundary layer and thus vertical pressure gradients, as mentioned in Chapter 3. Unfortunately there are not so many measurements at low levels in uniform flow (T3). In this case, a significant variation of $C_{D,m}$ would not be expected. In the presence of atmospheric boundary layer, the ESDU Data Items (ESDU 81017) confirm the existence of higher wake suction and lower pressure at the flanges. The high wake suction is responsible for an increase in drag. The even larger lateral suction produces the increase in pressure recovery as $z \rightarrow 0$. In fact, the correction factor proposed by the ESDU Data Items to account for the atmospheric boundary layer profile (ESDU 81017, figure 5) shows the same trend as the red curve in Figure 4.39. A similar behaviour of the drag curve at low levels is confirmed in literature e.g. by Garg's results (1995) at sub-critical Re, but a systematic study does not exist. The blue curve in Figure 4.39 (smooth cylinder) would suggest an even higher three-dimensionality of the phenomenon. However, there are not measurements in the lower half to confirm it.

The choice of an appropriate surface roughness for the wind tunnel tests, in view of the evaluation of design wind loads, depends on the full-scale condition which one would like to achieve. For solar towers, the target full-scale condition is given by a smooth circular cylinder in transcritical Re. Codified data for smooth and rough surfaces at transcritical Re are available in the VGB guideline (2010). Further full-scale data on chimneys and TV towers are collected in (Niemann&Schräder, 1981).

Relying on the recommendation of the VGB guideline, the target value of the drag coefficient for a smooth surface is in the range 0.46-0.49. The value of the minimum lateral suction (1.5-1.6 for curves K1.5 and K1.6, respectively) should not be considered alone, rather, the difference $C_{p,b} - C_{p,min}$ is a much more significant parameter, since the base pressure depends on slenderness while the pressure recovery is not so influenced by the aspect ratio. Therefore, referring to cooling towers, for solar towers it should be expected $C_{p,b} - C_{p,min}$ in the range 1.0-1.1.

On the basis of these recommendations, three different alternatives in terms of rib height and rib distance seem to be equivalent. The highest surface roughness (R4-R5) is discarded, as previously said. By choosing an appropriate value for the wind tunnel velocity, R1, R2 and R3 may be used. Remarkable is also the similarity between R2 and R3 for the whole range of Re. In this work, in view of the design wind loads, the condition R1 at 1400 rpm (Re = $2.5*10^5$) is selected and it will be used in the next chapters.

The pressure results of the experiments, shown in terms of $C_{p,min}$, $C_{p,h}$ - $C_{p,min}$ and $C_{p,h}$, are compared with literature (Figure 4.41). Wind tunnel tests in literature at transcritical Re on smooth circular cylinders, providing pressure distributions and not only force measurements, are rare. An investigation is contributed by Gould et al. (1968), who measured pressures on smooth cylinders having different aspect ratio in a pressurized wind tunnel (Re = $2.7\text{-}5.4*10^6$). This paper is used here as reference, also in order to prove the effectiveness of surface roughness in the experiments. However, Gould's experiments are in uniform flow and this should explain the departure of results at low levels, as previously mentioned.

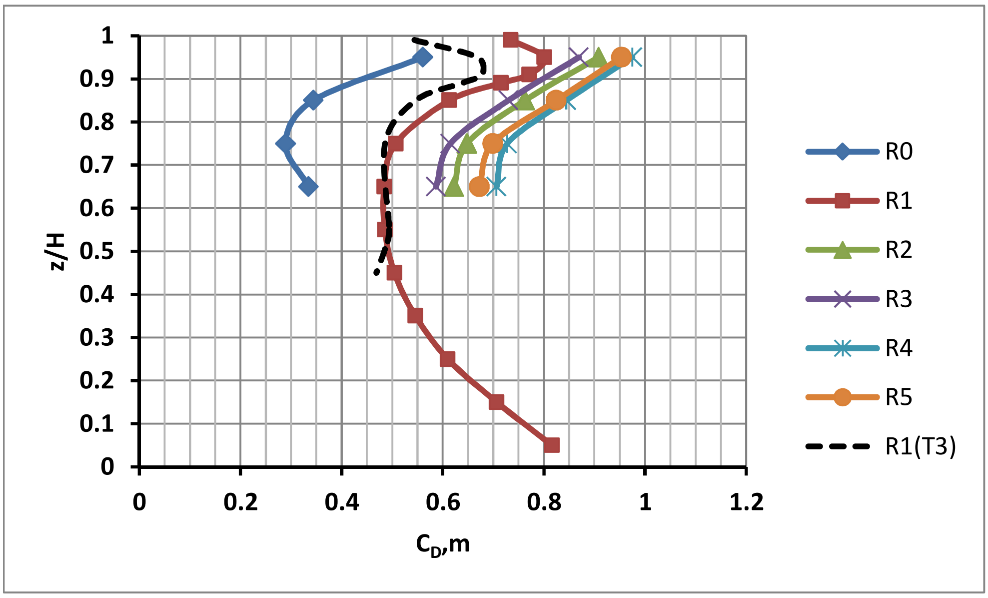

*Figure 4.39 Mean drag coefficient along the height on the smooth cylinder and for different roughness conditions at U_H≈25 m/s, Re = 2.5*105 (R0-R5, T1 unless differently specified)*

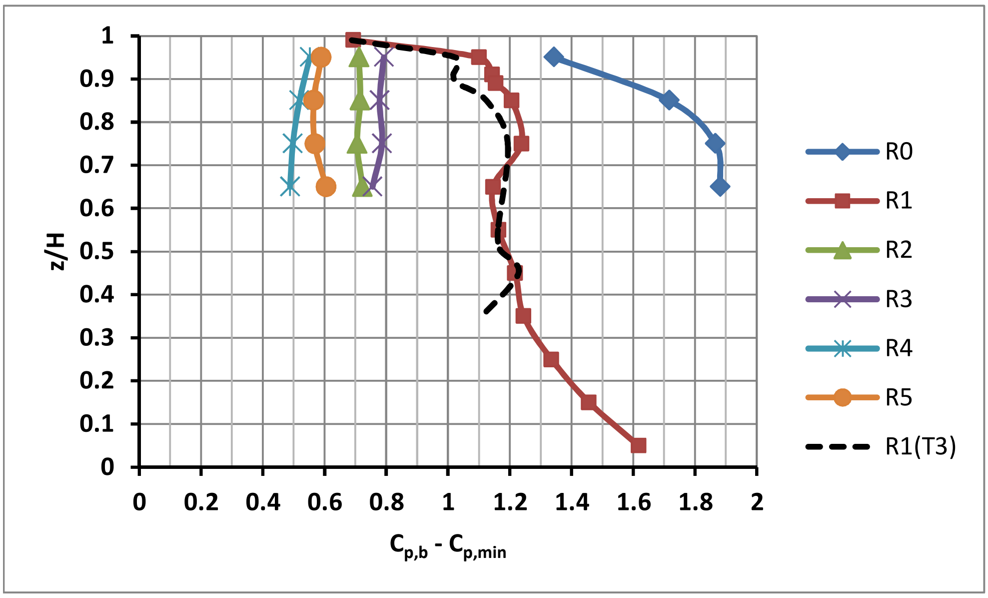

Figure 4.40 Pressure recovery along the height on the smooth cylinder and for different roughness conditions at $U_H \approx 25$ *m/s,* $Re = 2.5*10^5$ *(R0-R5, T1 unless differently specified)*

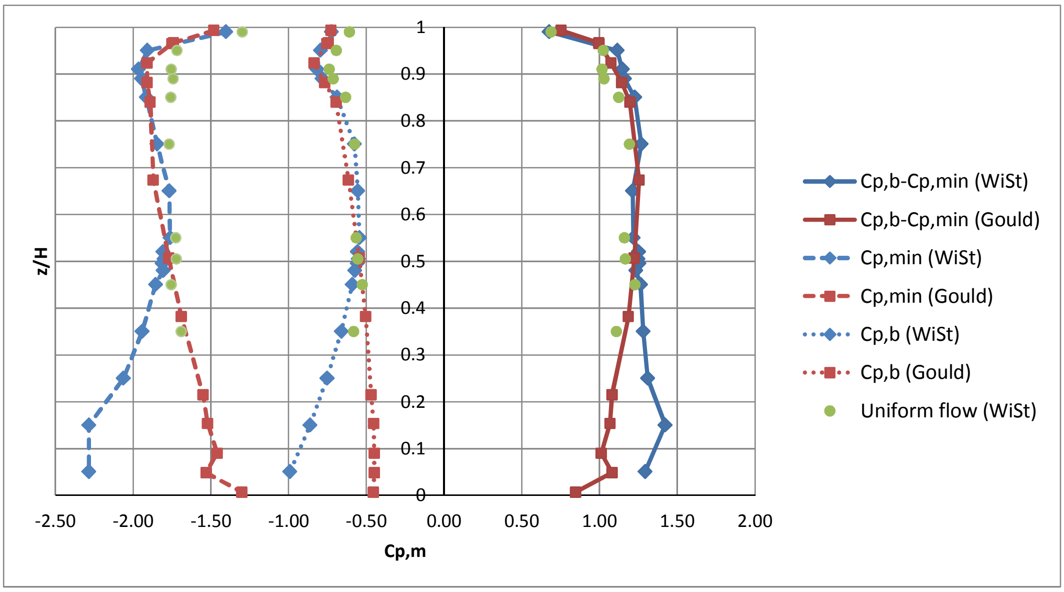

Figure 4.41 Mean pressure coefficients ($C_{p,min}$*,* $C_{p,b} - C_{p,min}$*,* $C_{p,b}$*): red = results by Gould et al., 1968 (H/D = 6,* $Re = 5.4*10^6$*, uniform flow); blue = WiSt (R1-T1). Green = WiSt (R1-T3, i.e. uniform flow)*

Chapter 5. A new phenomenon around circular cylinders

This chapter discusses the experimental evidence at WiSt wind tunnel of a new phenomenon around circular cylinders with a free-end. The peculiar feature is the presence of ring beams along the height of the cylinder. The physical interpretation proposed in this chapter is based on the investigation of pressure measurements through wind tunnel tests.

5.1 Experimental observation

The results of the first set of experiments (April 2011) on the rough circular cylinder without rings in turbulent boundary layer flow (T1-SR0-R1) at several wind tunnel velocities (and thus different Re) represented a good starting point for a deeper investigation (section 4.4). The tests were then repeated by adding 10 equally spaced ring beams along the height of the cylinder in both empty tunnel and turbulent atmospheric boundary layer flow.

Although a certain effect of the ring beams on the flow was expected, it was really surprising to see – immediately, during the first wind tunnel test on the tower with rings – a very interesting phenomenon, which was not just a local effect in the vicinity of the rings. During the experiments, the measurements at WiSt are usually checked and monitored by an oscilloscope, which plots the analogic signal coming out from the amplifiers, and by the computer, which plots on the screen the digitalized raw data. Unusual jumps in the time histories were immediately noted (Figure 5.1).

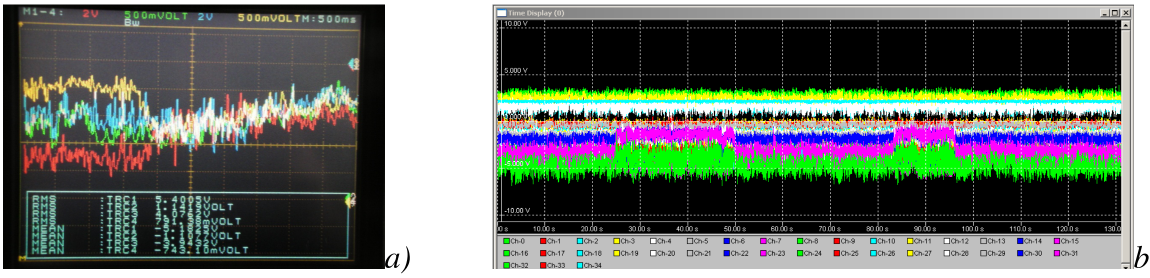
a) b)

Figure 5.1 Wind tunnel experiments on the circular cylinder with rings: appearance of jumps in the analogic signals (fig. a. oscilloscope) and digital signals (fig. b. computer screen)

The post-processing of the time histories confirmed the presence of jumps at certain points around the circumference. An error during the measurements was at first hypothesized. An error could have occurred at every step in the measurement chain.

However, since the jumps occurred both in the analogic and in the digital signal, if there was an error it could not be in the A/D converter, but before it. Moreover, while the pressure cells AMSYS (type 2) also include the amplifiers, the amplifiers to the pressure sensors Honeywell (type 1) are completely independent from one another (Figure 4.18). Therefore, if there was an error in one of these amplifiers, the others would not be affected. Then, the first check was just to connect a pressure sensor showing the jump to another of these independent amplifiers. This check was repeated several times with different pressure sensors and different amplifiers, but the result did not change. Similarly, it did not seem to be a problem of the connections and of the plastic tubes, because the same test without rings did not show the jump. Therefore, it was decided to go ahead with the measurements because no experimental error could be detected. In addition, the jumps were more evident at angles around 100°-120°, i.e. around separation, so it could have been then reasonable that they were due to a physical cause.

A further proof of validity of the experiments resulted from a closer data inspection. In fact, the jumps were coordinated around the circumference and along the height; they occurred in opposite directions on the two sides of the cylinder and in neighbouring compartments. Furthermore, since the jumps in the time histories occurred mainly at the flanges of the cylinder, they produced jumps in the time histories of the lift, but not in the drag coefficient.

The phenomenon needed to be investigated more deeply and other sets of experiments were planned (section 4.3). This chapter comments on the experimental evidence and reports results of the complete wind tunnel investigation at WiSt laboratory.

The presence of efflux out of the chimney tends to destroy the phenomenon, therefore the undisturbed effect is described in section 5.2 with only reference to the no-efflux condition. The effect of efflux will be mentioned among “other conditions” in section 5.3.5. Moreover, the phenomenon seems to be more related to geometric characteristics of the body rather than to turbulent properties of the flow. In fact, the bistable flow occurs both in empty tunnel (uniform flow) and in atmospheric boundary layer flow. Section 5.2 refers to atmospheric boundary layer flow conditions, the most important ones for the design. A comparative study of uniform and shear flow is addressed in section 5.3.3. A further comparison between different atmospheric boundary layer flows results from the cross-checked investigation at WiSt and CRIACIV wind tunnels (Chapter 6). In fact, the dependency of the bistable flow on the type of atmospheric boundary layer is one of the important issues to be considered in view of the design. First, because the design situation can refer to a different type of atmospheric boundary layer; secondly, because full-scale properties of strong winds like I_u, shear stresses, integral length scales might be not faithfully reproduced in the wind tunnel. Furthermore, the full-scale condition is associated to higher Re. This is likely the most important point, which is addressed in this chapter as well. The three-dimensionality of the cylinder with a the free-end, the spanwise distance from the tip and the distance between rings - related to the tower diameter - resulted to be key influencing parameters. The slenderness ratio, which was chosen as a fixed parameter in these experiments, should play a role as well (section 5.4), but the investigation of cylinders with different aspect ratios was not possible within this work (Chapter 8).

5.2 Description of a new cross-wind phenomenon

The phenomenon is described in this section with regard to the following condition of experiments: T1-SR1-R1-EF0. Re is $2.5*10^5$ (i.e. tests at 1400 rpm). Further conditions are introduced in the following sections.

5.2.1 Three main features

The occurrence of jumps in the time histories is only one aspect of the phenomenon – perhaps the most evident one – but the analysis of data suggested that three main features describe the flow condition around the circular cylinder with ten rings (Figure 5.3 and Figure 5.4):

1. Bi-stability of the flow: in time, the side pressures jump between two magnitudes;
2. Asymmetric flow around a symmetric structure: on opposite sides of the cylinder, the side pressures jump in opposite directions, so that a lower suction level on one side (e.g. $C_p(100°) \approx -1$) corresponds to a higher suction level on the other side (e.g. $C_p(260°) \approx -1.6$);
3. Spanwise inversion: in adjacent compartments the side pressures jump as well, in opposite directions. For example, if z_1 and z_2 belong to different compartments (e.g. $z_1 = 950$ mm and $z_2 = 850$ mm), then $C_p(z_1, 100°) \approx -1$ and $C_p(z_2, 100°) \approx -1.6$ and $C_p(z_1, 260°) \approx -1.6$ and $C_p(z_2, 260°) \approx -1$.

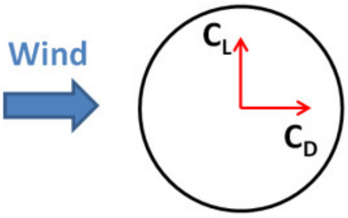

Figure 5.2 Definition of drag and lift coefficients

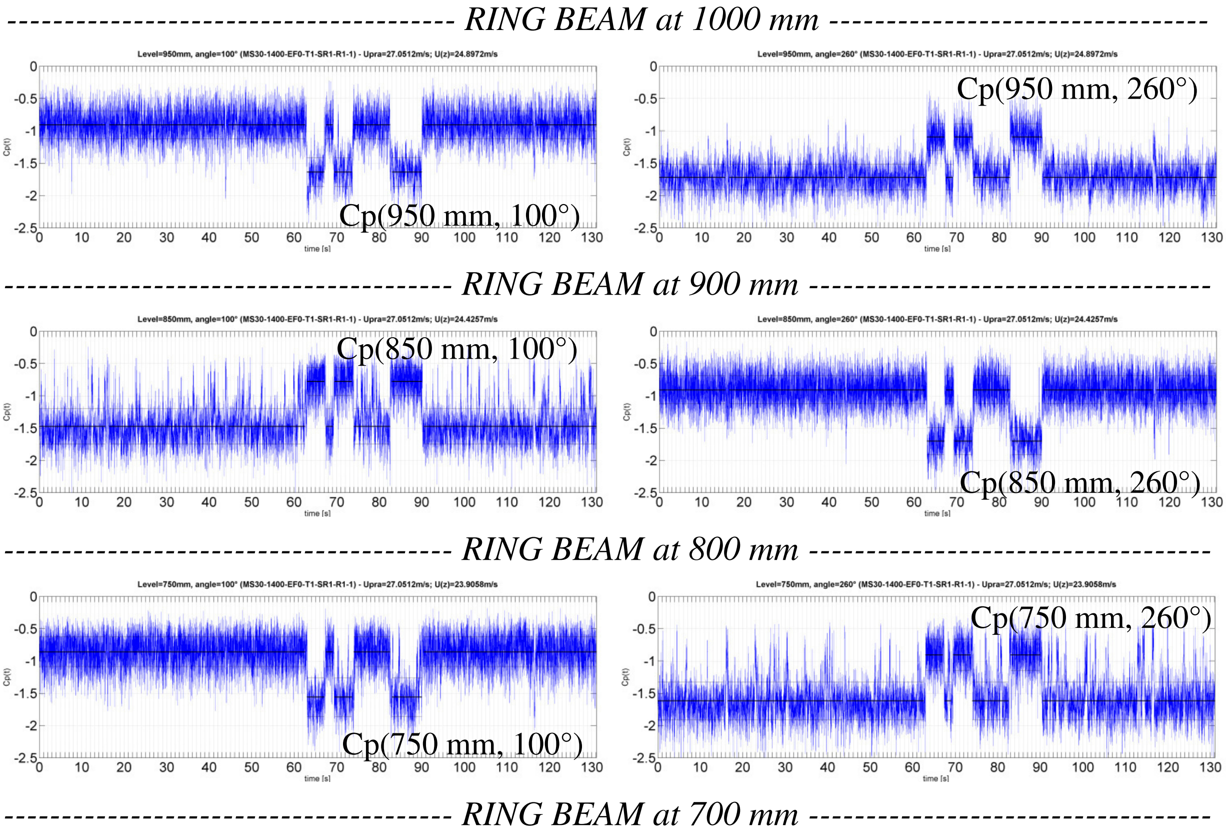

Figure 5.3 Bistable and asymmetric flow with spanwise inversion. Time histories of C_p at: 950-850-750 mm, 100° and 260° (WiSt, T1-SR1-EF0-R1, Re = $2.5*10^5$)

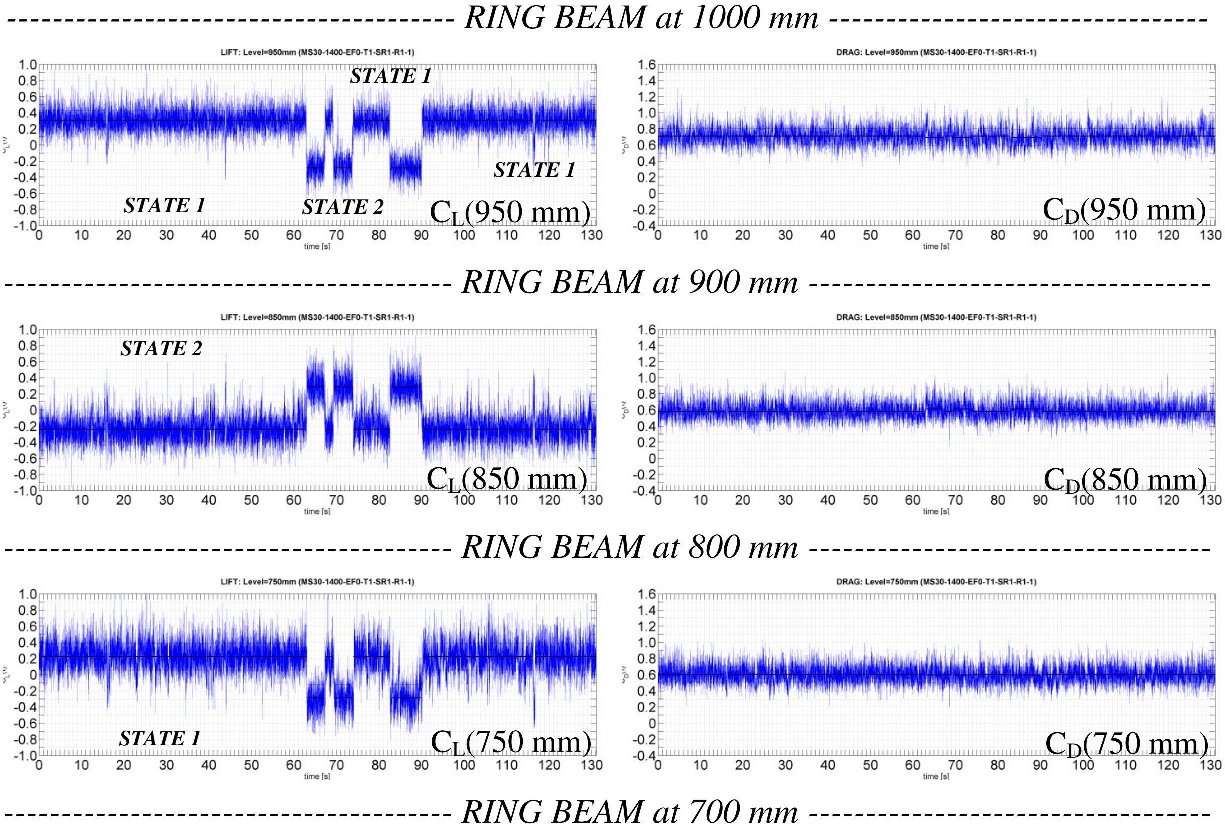

Figure 5.4 Time histories of C_L and C_D at 950-850-750 mm (WiSt, T1-SR1-EF0-R1, Re = $2.5*10^5$)

The phenomenon continues along the height of the tower, but at low levels (z < 0.6H) the mixture between the two states is more pronounced. The progressive disruption of the bistable flow along the height, as the distance from the tip increases, is an issue addressed in Chapter 6.

The mean and the rms values of the time histories are calculated separately for each interval of time before and after a jump; their circumferential distribution proves that two states can be detected. They are asymmetric but identical, just mirrored (Figure 5.5 and Figure 5.6, z/H = 0.75). Because of that, the flow is called bi-stable. As a consequence of the asymmetry, that is created by higher suction on one side of the cylinder, the mean lift coefficient is not zero (Figure 5.4). Depending on the interval of time which is considered, the mean lift can be either positive or negative. For convention, the “state 1” identifies the intervals of time associated to positive mean lift and the “state 2” is associated to negative mean lift. In the reference system of the wind tunnel, being the x-axis along the wind tunnel and the y-axis in the across wind direction (see the Drawing 1 on page 103), the state 1 has the high-suction side between 180° and 360°.

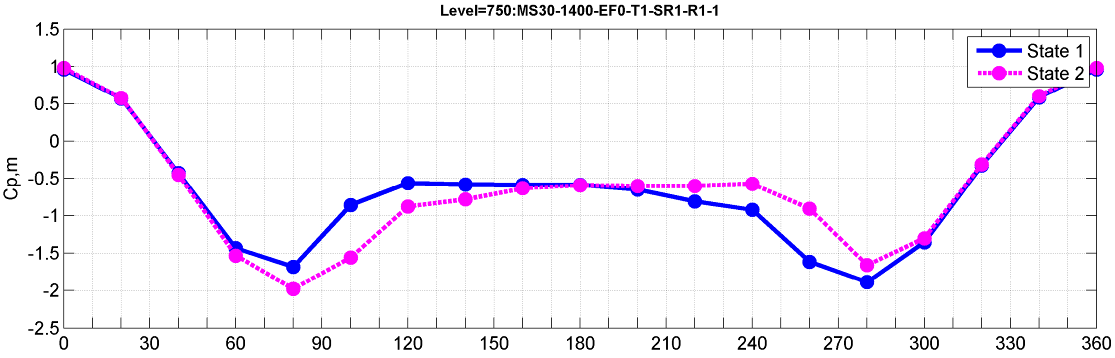

*Figure 5.5 Cp,m at 750 mm (WiSt, T1-SR1-EF0-R1, Re = 2.5*10^{5})*

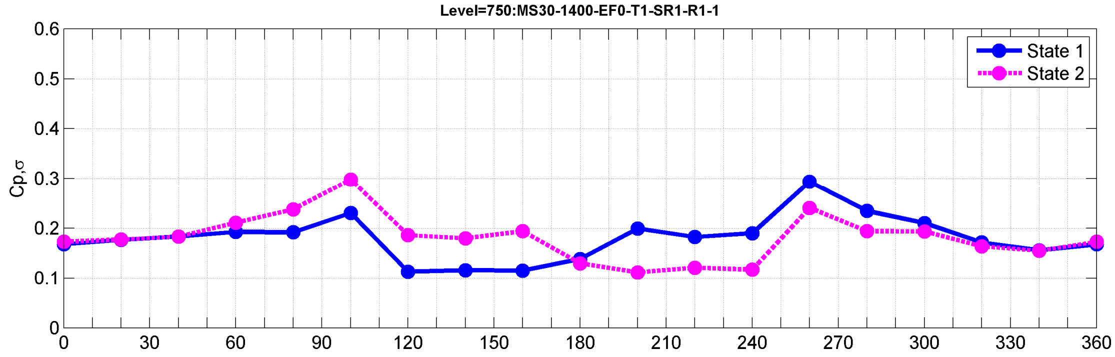

*Figure 5.6 Cp,σ at 750 mm (WiSt, T1-SR1-EF0-R1, Re = 2.5*10^{5})*

The state 1 at z/H = 0.75 is now analyzed in more detail in Figure 5.7 ($C_{p,m}$) and Figure 5.8 ($C_{p,\sigma}$). The asymmetric pressure distributions are fitted with spline curves. It can be seen that the higher suction on one side only of the cylinder is associated to a rearward movement of the separation point ($\varphi_N \approx 240°$ in Figure 5.7) and a complicated flow structure in the wake. Usually, the recirculation region in the wake of a cylinder between the separated shear layers is characterized by random fluctuations; they are not relevant for the structural design, but the wake structure is of great interest from the fluid-dynamic point of view. In particular, in presence of 10 ring beams along the tower, a recirculation bubble can be detected in the mean and rms pressure distributions. In fact, between 240° and 200°, i.e. after separation on the high-suction side, the mean pressure distribution presents a horizontal step at the constant value ≈-0.8 and then it rises again until ≈-0.6, which remains constant in the rest of the wake, also on the other side of the cylinder (low-suction side). The presence of such a horizontal step after separation can be attributed to a reattachment of the separated shear layer and further separation (Zdravkovich, 1997, page 166), i.e. the formation of a separation bubble. In the range 240° and 200° the rms values undergo a horizontal step as well, at a rather high value (Figure 5.8): the value is, in fact, comparable to the fluctuations at stagnation, while fluctuations in the wake should normally have a standard deviation about one half of the ones at stagnation (as it is in the wake on the low-suction side of the cylinder). Because of that, in case of rings the two sides of the cylinder are named "normal side" and "bubble side", i.e. "low-suction side" and "high-suction side", respectively.

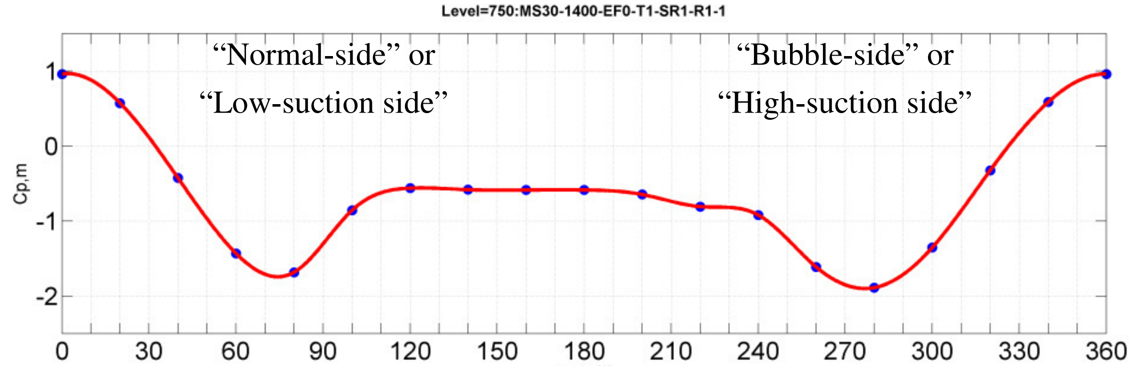

Figure 5.7 $C_{p,m}$ at 750 mm. State 1, spline fitting (WiSt, T1-SR1-EF0-R1, Re = $2.5*10^5$)

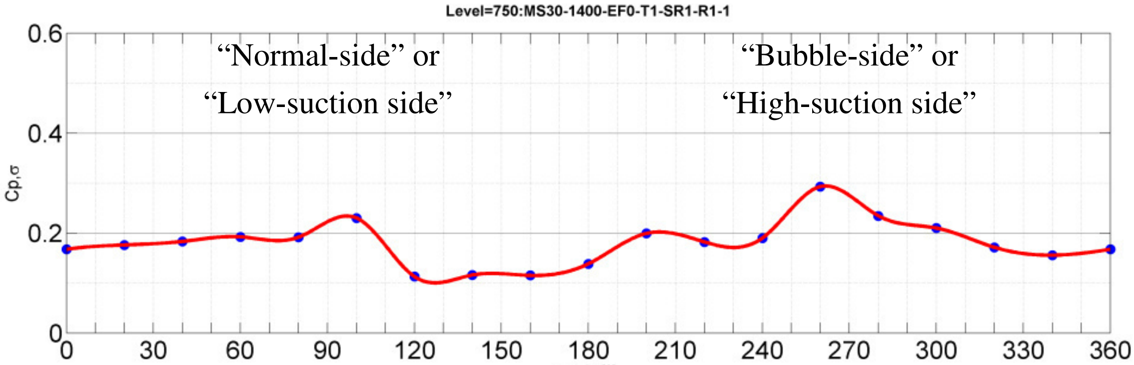

Figure 5.8 $C_{p,\sigma}$ at 750 mm. State 1, spline fitting (WiSt, T1-SR1-EF0-R1, Re = $2.5*10^5$)

Another peculiar feature is the spanwise inversion along the height of the cylinder, which means that the state of the flow is alternated in neighboring compartments. In fact, Figure 5.4 proves that during each stable interval of time the mean lift coefficient changes its sign in neighboring compartments, so that the steady cross-wind force changes its versus along the height of the cylinder. This is due to the vertical alternation of high- and low-suction sides of the cylinder, as shown in a transversal view in Figure 5.9.

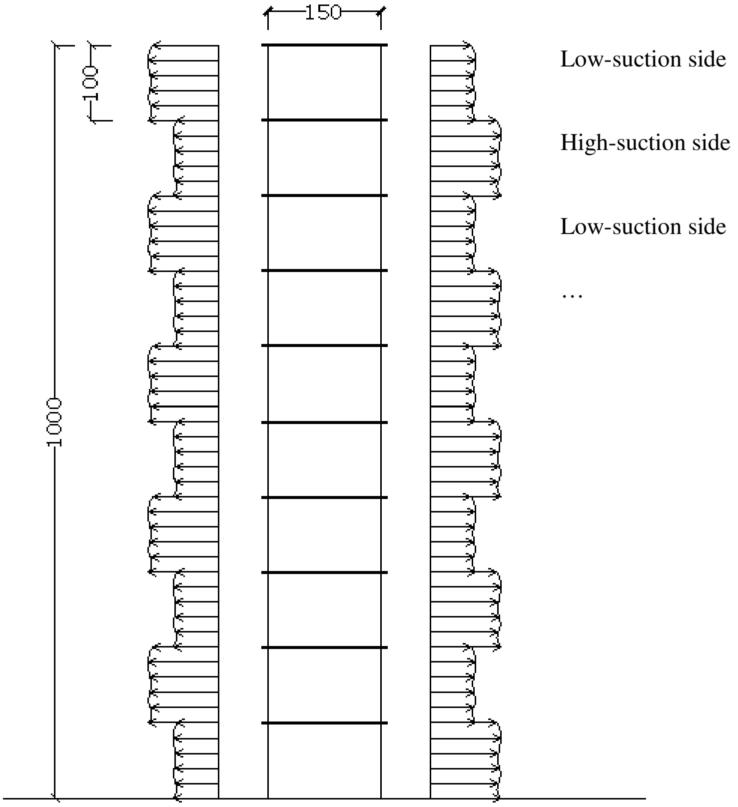

Figure 5.9 Spanwise inversion: high-suction and low-suction sides, transversal view.

5.2.2 Step by step through a jump between two states

The jump between the two states of the bistable flow is accompanied by a significant displacement of the stagnation point and the formation of a bigger separation bubble, which suddenly seems to move in the wake on the other side of the cylinder. This can be seen in a sequence of instantaneous pressure distributions within a jump. In particular, 8 significant time steps are highlighted in Figure 5.10, when the lift is either maximum or minimum in the vortex shedding cycle and crossing zero before changing state. The x-axis in the figure plots the number of time steps, it is remembered that the sampling frequency is 2000 Hz, therefore the figure plots a time window of 2 seconds.

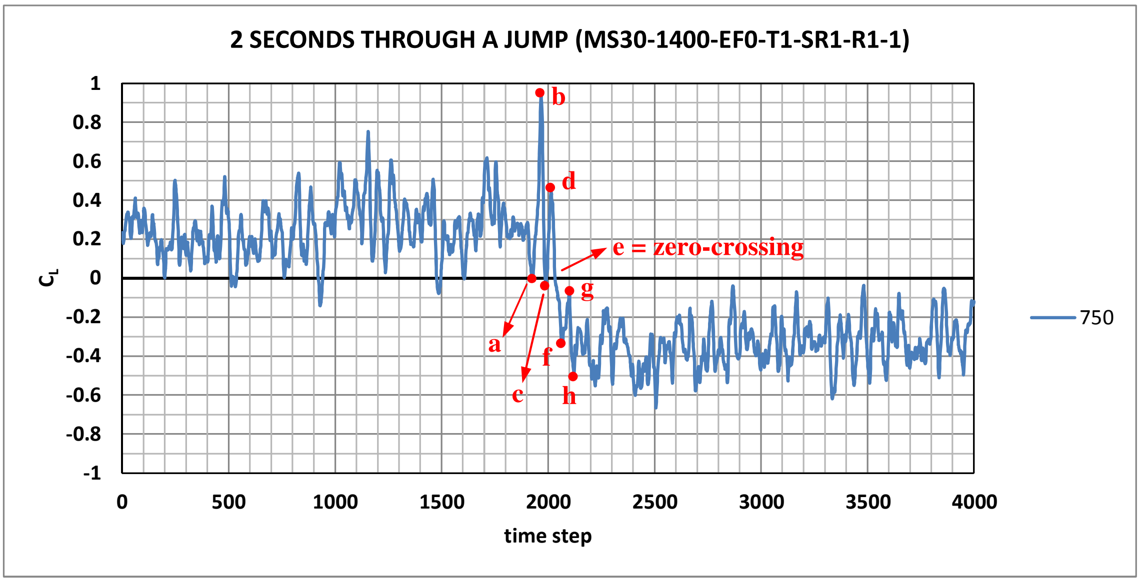

Figure 5.10 2s-time history at 750 mm ($n_{sampling}$ = 2000 Hz) : transition from state 1 to state 2 (WiSt, T1-SR1, Re = $2.5*10^5$)

Figure 5.11 (a-d) plots instantaneous distributions in the state 1, i.e. the state of positive mean lift. Then, in figure e) the flow is changing state and after that the instantaneous distributions belong to the state 2 (figures f-g-h).

In the state 1, during a shedding cycle the lift oscillates between a minimum value which is close to zero and a maximum positive value which corresponds to a von Karman vortex shed on the bubble side. For example, in Figure 5.11a) the instantaneous pressure distribution results to be almost symmetric. In fact, the lift at those instants is around the minimum value because the vortex is shed on the normal side, where the mean lateral suction is lower than on the bubble side. Thus, the growth of the vortex on the normal side reduces the asymmetry. Instead, when the vortex is shed on the bubble side, the lift assumes an extreme value, which is either positive (state 1) or negative (state 2). In the compartment below the ring the situation is simultaneously reversed.

At some time, there might be the formation of a bigger bubble (Figure 5.11d), which is anticipated by a displacement of the stagnation point. Such a displacement occurs on the same side of the cylinder at diffetent levels (despite the spanwise inversion of lift) and it is sligthly anticipated at higher levels, so that the transition of state at 950 mm appears to be about 0.11 seconds (in the wind tunnel time scale) earlier than 20 cm below. This is a very short time in the wind tunnel, but it is remembered that the vortex shedding period is more than three times shorter $(S_tU/D) \approx 0.2*25/0.15 = 0.03$s.

After the zero crossing (Figure 5.11e) the state has changed and a separation bubble of smaller size (comparable with the one in the mean distribution, plotted in Figure 5.11) develops on the other side of the cylinder.

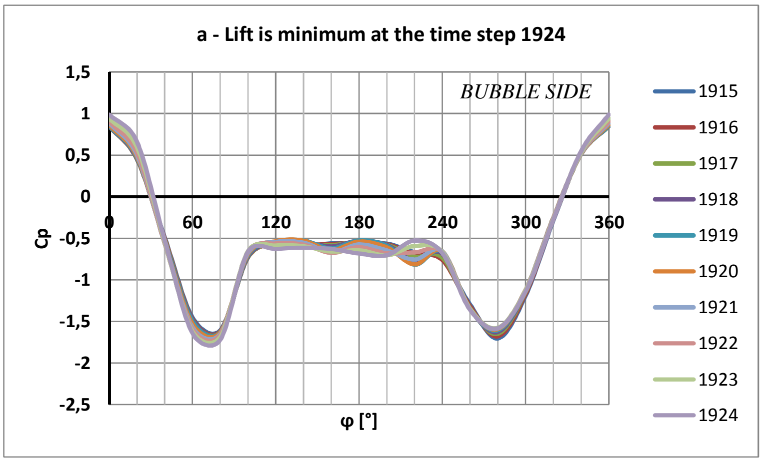

Figure 5.11 a) State 1; n. 1924 in the legend is the time step "a" in Figure 5.10

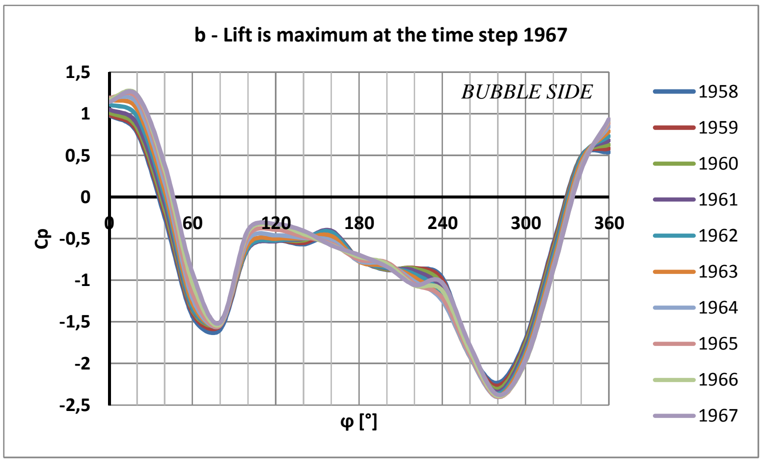

Figure 5.11 b) State 1; n. 1967 in the legend is the time step "b" in Figure 5.10

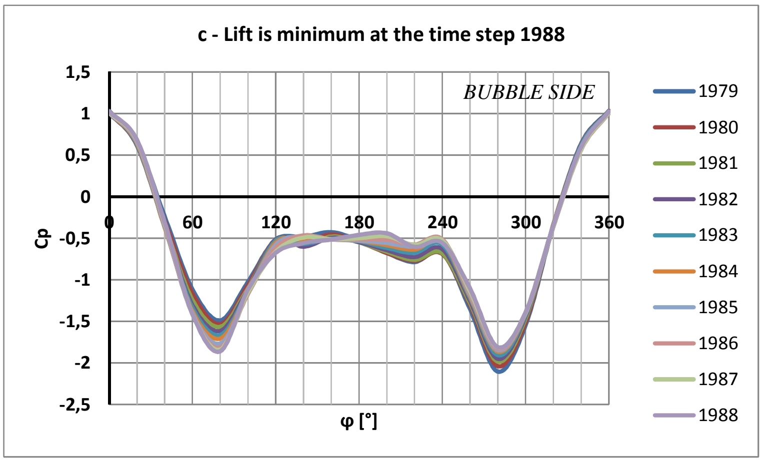

Figure 5.11 c) State 1; n. 1988 in the legend is the time step "c" in Figure 5.10

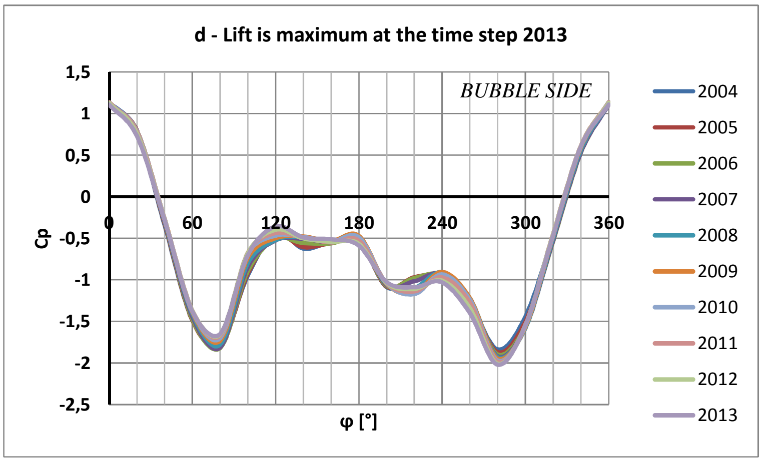

Figure 5.11 d) State 1; n. 2013 in the legend is the time step "d" in Figure 5.10

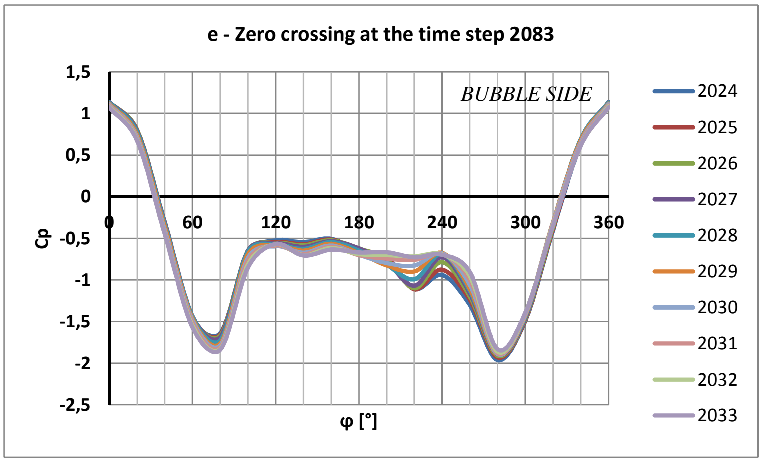

Figure 5.11 e) Change of state; n. 2033 in the legend is the time step "e" in Figure 5.10

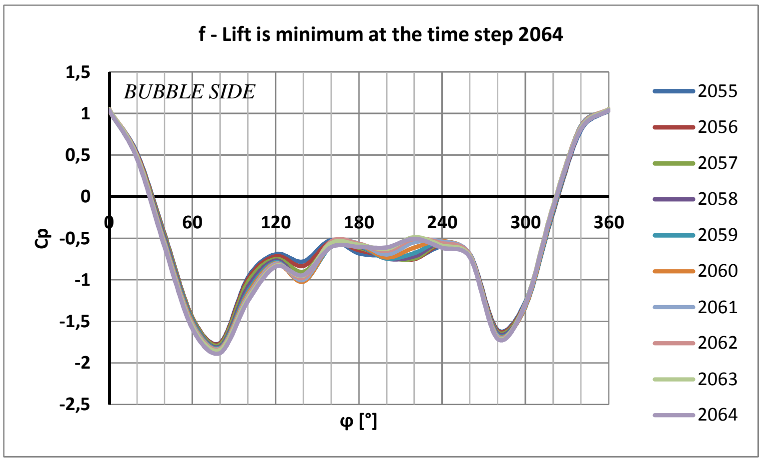

Figure 5.11 f) State 2; n. 2064 in the legend is the time step "f" in Figure 5.10

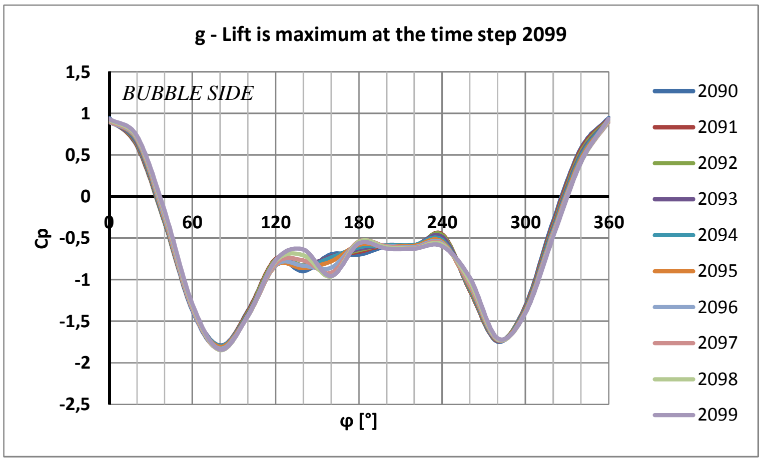

Figure 5.11 g) State 2; n. 2099 in the legend is the time step "g" in Figure 5.10

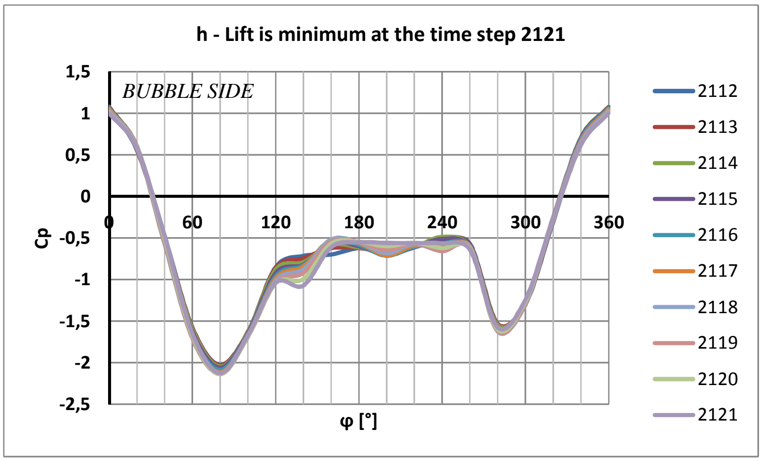

Figure 5.11 h) State 2; n. 2121 in the legend is the time step "h" in Figure 5.10

*Figure 5.11 a-h) Momentary distributions during a jump (10 time steps = 10/2000 s), Re = 2.5*10*^{5}

5.2.3 Literature and novelty

The asymmetry of the pressure distribution created by the rings is associated to higher suction and formation of a separation bubble on one side only of the cylinder. This phenomenon might be - in itself - not new. A similar effect is well-known around circular cylinders (without rings) in the critical range of Re, as mentioned in Chapter 3. However, the conditions of occurrence (further discussed in section 5.3) of the bistable phenomenon evidenced in this Dissertation make it original and physically unique.

The similar case reported in literature (Figure 3.2) is very sensitive to Re and occurs in a small range of Re just before the critical value. Moreover, it is also sensitive to disturbances and perturbations in the flow (such as turbulence). The phenomenon is thus observed only in smooth flow on smooth cylinders. It is also very difficult to catch it. The physical reason which produces the separation bubble is strictly related to the Reynolds number, because it governs the transition from laminar to turbulent flow. In particular, the flow is asymmetric because such a transition has occurred in the shear layer after separation (laminar separation) on one side only of the cylinder. On that side where transition occurred the turbulent flow gets more energy and is able to reattach. The second separation is then turbulent. In between, there is the formation of a separation bubble, namely laminar separation bubble. Transition from laminar to turbulent flow, which occurs after the first laminar separation, is due to some random perturbations on that side of the cylinder. Therefore, in ideal conditions, the side on which it may occur is completely random. Moreover, it can occur on one side only of the cylinder only if there is a low probability that there are perturbations on the two sides able to initiate a transition to turbulent flow. Because of that, the asymmetric phenomenon disappears in turbulent flow and/or on a rough cylinder: perturbations and laminar separation bubbles likely develop on the two sides of the cylinder and that is the critical (symmetric) state.

In the present case of study, the incoming flow is turbulent and the cylinder is rough. In the pictures shown up to now the wind tunnel is at full-speed (Re $\approx 2.5*10^5$, effective Re about one order of magnitude higher). In these conditions, laminar separation can be absolutely excluded. In fact, transition from laminar to turbulent boundary layer should occur very close to stagnation and certainly before separation. Consequently, even though the higher suction on one side of the cylinder may suggest the existence of a separation bubble, like in the well-known bistable flow in the critical range of Re, it cannot be a separation bubble in the classical sense, i.e. a laminar separation bubble. A laminar separation bubble is caused by a physical reason, that is transition to turbulent conditions in the free-shear layer after separation and consequent reattachment. As the formation of the laminar separation bubble is excluded in the conditions of the experiments, the corresponding physical explanation fails. For the same reason, the high sensitivity of the laminar separation bubble to Re, to the surface roughness of the cylinder and to the turbulence of the incoming flow should not necessarily be confirmed in the present phenomenon. In fact, it is not. It should also be remembered that the result shown up to now in this chapter occurs in a state of the flow far beyond the critical drop ($Re = 2.5*10^5$, surface roughness R1), as confirmed by Figure 4.29. Thus, although the dependency on Re is an issue which deserves particular attention, it is clear that it cannot be just an effect of Re_{cr}.

What is completely new is also the spanwise variation of the asymmetry. In the well-known case of literature, Bearman (1961) observed that "the distribution of base pressure along the span suggested that the establishment of a bubble on one side takes place along the complete length of the cylinder and this was later confirmed by surface oil flow patterns". In absence of ring beams along the height, in fact, there is no reason for a spanwise inversion. It is a peculiar effect of the compartments created by the rings. In particular, it must be a result of the interaction between compartments. The alternation along the height of higher and lower side pressures determines vertical pressure gradients and thus flow movements between different levels. It is believed that the key is in the recirculation bubbles in the near wake of the cylinder.

The occurrence of jumps between the two states does not present regularity. The random nature is, in any case, not surprising. It is typical, for example, of side-by-side cylinders. It reflects the random nature of the turbulent flow. Also the bistable flow in the critical range of Re presents the same characteristic: a random perturbation in the flow, on either side of the cylinder, may initiate the phenomenon.

What is interesting, moreover, is the stable nature within each state. After being initiated, a certain state establishes. This is completely different from the unsteadiness of vortex shedding, where cross-wind oscillations of the lift force average to zero. From the experiments, it was not straightforward to infer that symmetric conditions can be achieved by averaging on an infinitely long period. In any case, an infinitely long period cannot be justified in the design of a structure during a wind storm. But it must be remembered that the stable nature of the asymmetric condition is a peculiar feature of the well-known bistable flow of literature, too. The name itself, bi-stable flow, highlights that we are dealing with two conditions of stability, not with instability. In the case of literature, Schewe (1983) wrote "the immediate formation of a one-sided bubble leads to steady circulation around the cylinder. This effect results in acceleration of the fluid on the side where the boundary layer transition has occurred and in deceleration at the other side of the cylinder. Deceleration of the fluid delays the transition in this detached boundary layer and hence the formation of the bubble. This coupled occurrence of the development of a bubble on one side with the deceleration of the fluid on the other side (i.e. decrease in the Reynolds number of this boundary layer) probably causes stabilizing and fixing of the asymmetric flow state". Acceleration of the flow on the bubble side is related, in a phenomenon which is highly sensitive to Reynolds effects, to the Reynolds number. Again, the reason here must be profoundly different, but the effect is the same.

The interesting debate between known and unknown, literature and novelty, motivated further investigation of the phenomenon and a proper revision of the wind tunnel experiments. It seemed worthwhile to go deeper in the study by testing different situations. The crucial question is not only the physical reason which produces the asymmetric and bistable effect, but also the systematic investigation of the conditions of occurrence and their dependency on the Re, i.e. on the wind tunnel scale. The two wind tunnels available for the experiments allowed to test only a limited range of Re, so that surface roughness was introduced to increase the effective range. Several different combinations of wind velocities and rib height and distributions were tested. Section 5.3 explains the details, but it is now anticipated the surprising result that the phenomenon seems to stabilize even more as Re increases. Further experiments at higher Re (like full-scale conditions) would require higher velocities and bigger wind tunnels (or pressurized flow); they would be much more expensive, but rather decisive. Fluid dynamic simulations (section 6.3) were performed in parallel to the last part of the experimental work (in CRIACIV) also with the aim to explore higher Re.

5.3 Conditions of occurrence

In order to accept and be convinced of the new experimental phenomenon, it has been tested with regard to the following conditions of occurrence: $^{1)}$ different wind tunnel velocities (thus different Reynolds numbers); $^{2)}$ different surface roughness on the model, in terms of height and distribution of ribs; $^{3)}$ different boundary layers (uniform and shear flow); $^{4)}$ removal of hypothesized experimental unintentional disturbances. The tests were also repeated in presence of $^{5)}$ efflux. Then, a further question that was addressed regarded the sensitivity of the phenomenon to $^{6)}$ different design choices, for example with a different number of ring beams (5 or 7) and with smaller rings (whose width is halved).

This sensitivity analysis has been performed in only one wind tunnel (WiSt laboratory) and mostly in turbulent boundary layer flow. Only the most representative tests were repeated at CRIACIV for further validation in a different laboratory (Chapter 6). The results in WiSt tunnel are reported in the following. However, the sensitivity analysis with 10 rings did not suggest any reason for which the phenomenon should not be expected. The phenomenon is in any case mitigated by the presence of efflux and by using fewer and/or smaller rings.

Although the sensitivity analysis was carried out with the purpose of being as much general as possible, the tower model and the experimental set-up limited the experimental investigation to the 3D condition (cylinder of finite length with a free-end) and H/D = 6.7, as well as to a certain range of Re. Tests in two-dimensional flow and with different slenderness ratios would be recommended for future investigation, as well as tests with a different distribution of rings (Chapter 8). The load and response calculation (Chapter 7) should give an indication about the importance of additional experimental investigation in the structural design of Solar Updraft Towers. It basically depends on the level of structural optimization one wants to achieve.

5.3.1 Dependency on the Reynolds number

The dependency of the phenomenon on the Reynolds number is at first studied for a certain surface roughness by varying the wind tunnel velocity. The preliminary investigation described in section 4.4.3 showed that the best target condition, in terms of effective Reynolds number, is achieved by using the surface roughness condition R1. It is then the reference condition through the whole dissertation and also in this sub-section 5.3.1. In any case, the tests were also repeated with different surface roughness, in order to study its effect. The most representative results are reported in section 5.3.2.

As described in Chapter 4, five levels of wind velocity in the working range of the wind tunnel at WiSt were selected for most tests: 600-800-1000-1250-1400 rpm (corresponding to $U_{pra} \approx$ 12-16-20-25-27 m/s, respectively). Lower wind speeds (up to 3 m/s) were only tested on the smooth cylinder to reach the subcritical range (section 4.4.3).

Figure 5.12 plots the results versus Re at z = 950 mm in the two states, which can be considered reasonably equal. The dependency of the drag coefficient on Re is less pronounced than in SR0, at Re_{cr} there is only a small drop. The interesting and peculiar feature of the phenomenon is the presence of a mean steady lift throughout the whole tested range of Re. It does not show any tendency to disappear at higher Re. Because of that, so far (on the basis of these experiments) it is not expected any disappearance of the phenomenon at higher Re. The rms values in the two states do not show a significant dependence on Re.

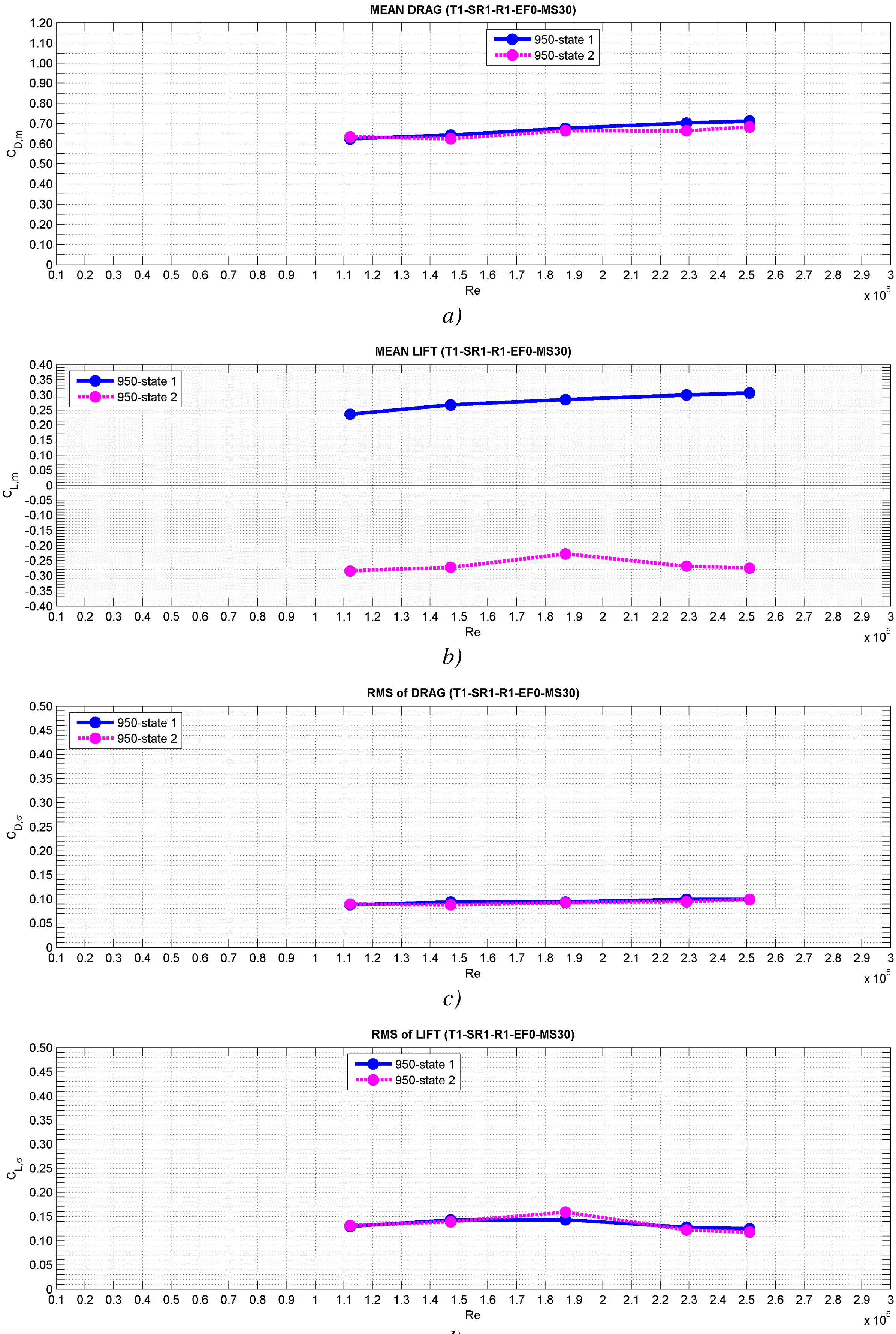

a)

b)

c)

d)

Figure 5.12 a-d) Bistable and asymmetric flow within one state as a function of Re at 950 mm: a) $C_{D,m}$; b) $C_{L,m}$; c) $C_{D,\sigma}$; d) $C_{L,\sigma}$ (WiSt, T1-SR1-R1-EF0)

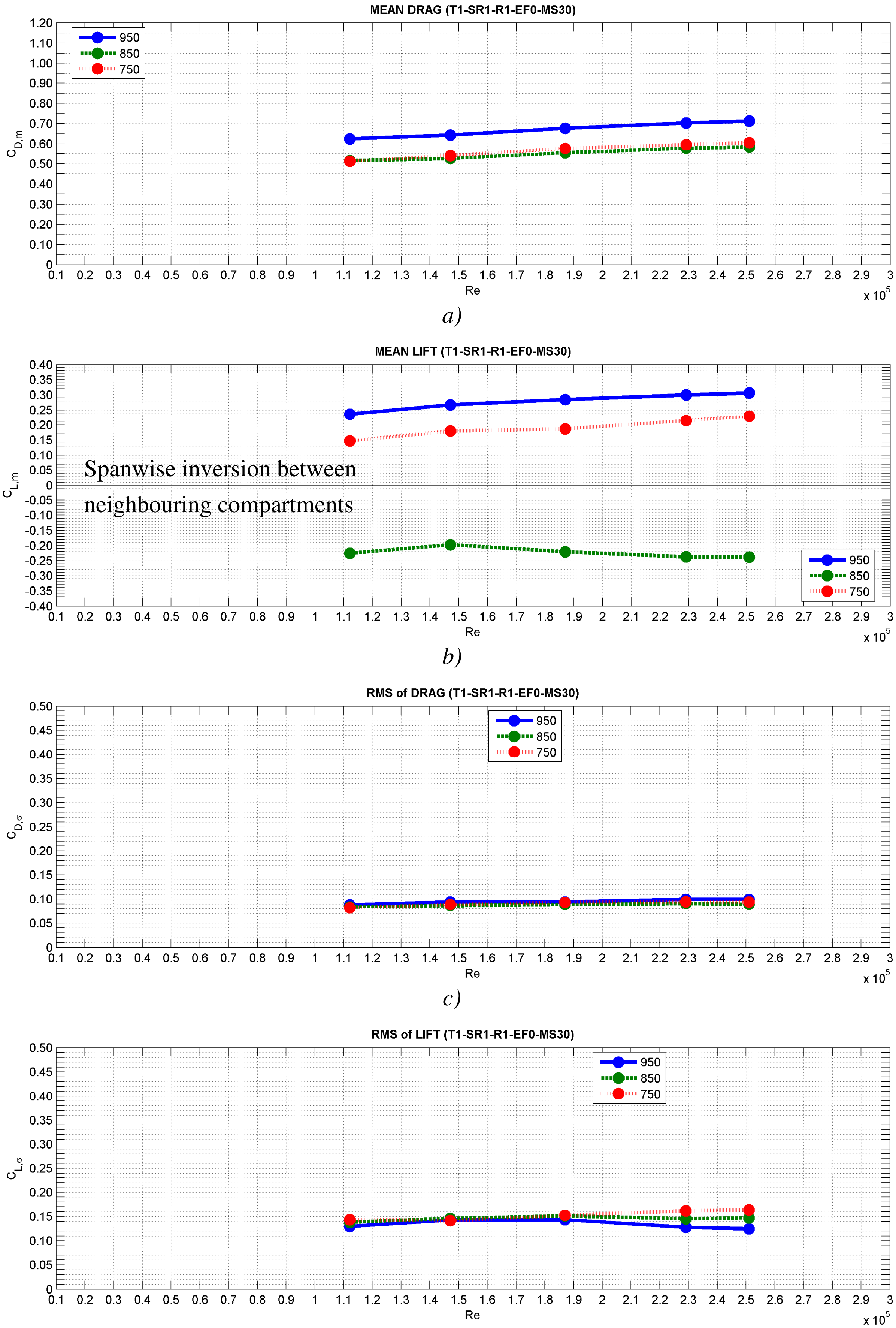

a)

b)

c)

d)

Figure 5.13 a-d) Bistable and asymmetric flow within one state as a function of Re at 950-850-750 mm: $C_{D,m}$, $C_{L,m}$, $C_{D,\sigma}$, $C_{L,\sigma}$ *(WiSt, T1-SR1-R1-EF0)*

Figure 5.13 shows the dependency of the phenomenon on the height in the tip region (the situation at lower levels is explained in Chapter 6). Only one of the two states is considered. Due to the spanwise inversion, the mean steady lift alternates in sign between different compartments. This is a very peculiar feature of the phenomenon. It can also be observed that the tip effect is not so pronounced and, apart from the highest level (950 mm), the mean drag stabilizes on the same value. The rms values do not show significant dependency on height.

Figure 5.14 plots the mean pressure coefficients distributions at different Re and explains the weak dependency of the force coefficients on Re. On the normal side of the cylinder (0-180°), as the wind velocity increases, the lateral suction decreases and the separation point moves upstream (such a movement is maybe concealed by the linear interpolation in the figure). This is typical of the supercritical range on a rough cylinder (Figure 3.8). The suction in the wake tends to increase, but this is especially appreciable on the bubble side, where lateral suction remains high. Because of that, as Re increases, the asymmetric condition tends to stabilize.

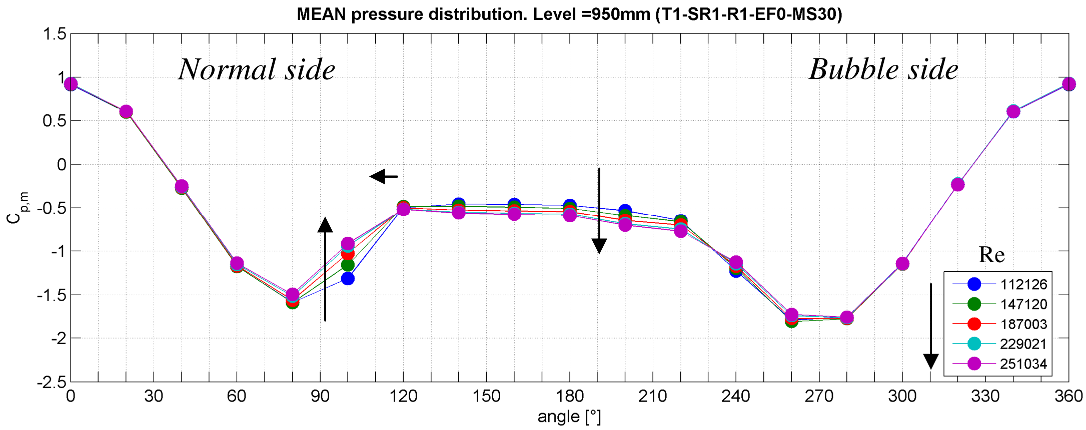

Figure 5.14 Bistable and asymmetric flow as a function of Re at 950 mm: $C_{p,m}$ in state 1 (WiSt, T1-SR1-R1-EF0)

5.3.2 Effect of surface roughness

Surface roughness, consisting of ribs, has a very strong effect on the flow because it changes the effective Reynolds number. As a consequence, it has an effect on the pressures, both with and without rings.

The most suitable flow condition for the design of the solar tower is achieved in the wind tunnel by using surface roughness R1, as already discussed in Chapter 4, whose result have been already presented (also in presence of rings, see section 5.2).

It is not in the purpose of this section to discuss the effect of a different state of the flow (produced by a different flow velocity and/or a different type of surface roughness) on the bistable phenomenon, because it would not be relevant for the design of solar updraft towers. The aim of this section is to exclude that the occurrence of the bistable phenomenon may only be a matter of a certain choice – for experimental purposes – of surface roughness for the wind tunnel model. Thus, some tests were done by applying 10 rings in the following conditions: surface roughness R1, R2, R3, R4, R5 at 600, 800, 1000, 1250, 1400 rpm and on the smooth cylinder (R0) at 100, 200, 400, 600, 800, 1000, 1250, 1400.

Out of all the tests, the main result that can exclude that the ribs are responsible for creating the bistable flow is plotted in Figure 5.15. It has been measured on the smooth cylinder at low velocity (200 rpm, ≈ 5 m/s) in turbulent boundary layer flow. The state of the flow is at the very end of the subcritical state. The figure shows that the jumps in the time histories still occur and the histogram of the pressure coefficient highlights the bistability, even without ribs, even in a different state of the flow. The angle 100° at 950 mm is chosen as representative in the picture.

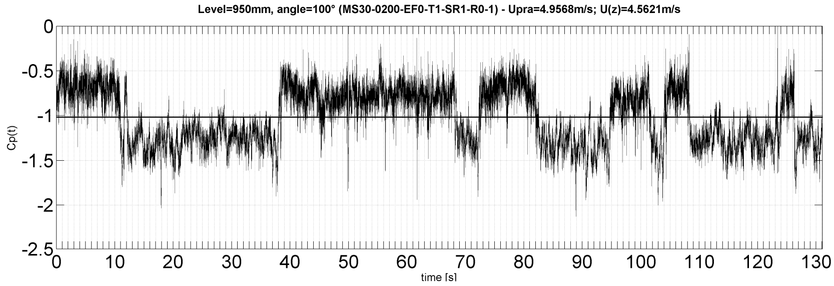

Figure 5.15 Bistable flow on the smooth cylinder (R0) with 10 rings (U_{pra} ≈ 5 m/s = 200 rpm): C_p(950m,100°) (WiSt, T1-SR1-R0-EF0)

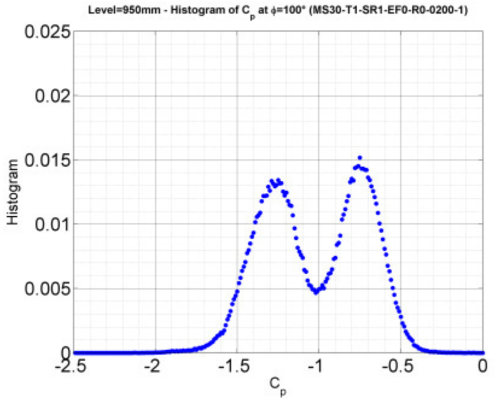

Figure 5.16 Histogram of C_p (time history in Figure 5.15)

Figure 5.17 is an example which shows that jumps in the time history also occur in a different surface roughness condition. In this example, higher roughness (R3) has been applied and the wind tunnel velocity is 800 rpm. This condition presents the same $C_{D,m}$ and pressure recovery as R1-1400rpm (section 4.4.3).

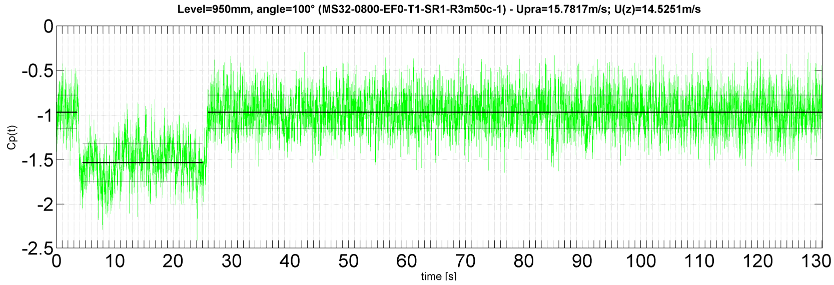

Figure 5.17 Bistable flow on a rougher (R3) cylinder with 10 rings ($U_{pra} \approx 16$ m/s = 800 rpm): C_p(950m,100°), (WiSt, T1-SR1-R3-EF0)

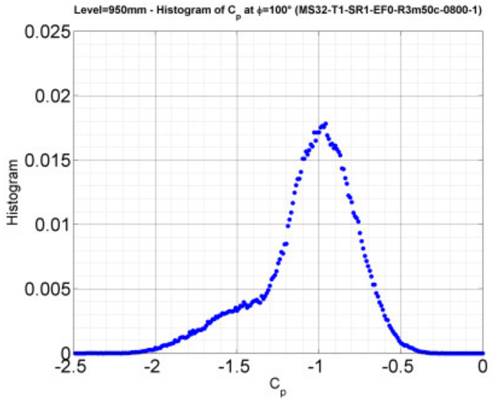

Figure 5.18 Histogram of C_p (time history in Figure 5.17)

5.3.3 Influence of boundary layer

The bistable flow occurs both in shear and in uniform flow. The values of the turbulence intensity and of the integral scales are not the governing parameter of the phenomenon, because the uniform and the shear boundary layer flow in WiSt (T1 and T3), as well as shear boundary layer in CRIACIV, are characterized by very different parameters (sections 4.1 and 6.1) and this does not prevent the occurrence of the phenomenon in the tip region. In fact, the phenomenon appears in the three cases. However, as it will be better explained in Chapter 6, the bistable flow tends to become a mixture of the two states at lower levels and there is a height at which the asymmetric flow starts to vanish. In particular, this disruption of the phenomenon starts at a certain level along the tower as a more rapid alternation of jumps on one side of the cylinder, that is the bubble side at that level.

Being the bistable flow a three-dimensional effect, it is basically governed by the free-end and the highest compartment, therefore it should not be surprising that the effect tends to disappear as the distance from the top increases. However, the experiments proved that the boundary layer influences the height at which the disruption starts. In fact, in the three boundary layers of the experiments it always starts at different levels. This will be better addressed in Chapter 6, once the CRIACIV results have been introduced. But it is now anticipated that: $^{a)}$ in the shear flow in WiSt the disruption is observed in the pressures at 650 mm (Figure 6.9); b) in the uniform flow in WiSt it is observed at 450 mm (Figure 6.13); c) in the shear flow in CRIACIV it is observed already at 750 mm (Figure 6.9 and Figure 6.12). However, a direct relationship between this height and a certain behaviour of a boundary layer property (such as I_u, L_{ux}, L_{uz} or σ_u) has not been detected.

5.3.4 Removal of experimental (unintentional) disturbances

The peculiarity of the observed phenomenon and the lack of a direct comparison with literature arose many questions and several doubts. Therefore, during the campaign some tests were repeated in order to verify that some experimental conditions should not have appreciably influenced the occurrence of the phenomenon.

For example, since separation bubbles develop in the wake of the cylinder, it was hypothesized that the ribs in the wake might have had a disturbing effect. Therefore, a few tests were repeated by removing the ribs in the separated region, which do not have any effect on the state of the flow. In the reference condition R1 the result did not change. In case of higher roughness (e.g. R3) the asymmetric condition could stabilize even better. Therefore, ribs in the wake were not responsible at all for creating the effect.

In order to allow the ribs to adhere to the model all along the cylinder without interruption, very small cuts were done in the ring beams for passage of the ribs. Although such cuts were very small, about 1 mm, they might have acted as holes in the rings. Therefore, the tests were repeated by accurately closing all these “holes” with tesa film. The result did not change significantly, but the removal of this disturbance allowed to the asymmetric flow to stabilize better. This enhanced the idea that the design of ring beams with some holes inside would have reduced the bistable effect on the structure. In fact, the asymmetry and the inversion in different compartments create pressure differences above and below the rings. The rings prevent the vertical flow along the tower surface and enhance the interaction between compartments due to gradients of pressure. Some holes inside the rings would reduce the pressure gradients. However, this mitigation proposal has not been extensively tested and validated. The experiments available before closing the cuts in the rings did not show a disappearance of the bistable flow, just a slight disturbance (i.e. more frequent jumps).

5.3.5 The effect of the efflux

The efflux suppresses the bistable phenomenon, even with 10 rings. It is easily seen in the histograms of the lift coefficients, which are approximately symmetric and centered in zero in presence of efflux (Figure 5.19, right column).

5.3.6 The effect of number and size of rings

The number and the size of the rings play a key role. So far, the reference condition with ten big rings at a distance of 10 cm in the wind tunnel scale (100 m in full-scale if λ_L = 1:1000) has been considered. This is just one design condition, and the bistable flow depends strongly on the distribution of rings and to some extent on the size of the rings. Therefore, once the bistable phenomena were ascertained in the previously described sensitivity analysis (influence of Re, influence of surface roughness, removal of disturbances), different design cases were studied. The main results (in the no-efflux condition) are presented here and a physical explanation will be proposed in section 5.4. Then, a conclusion and a proposed recommendation will be explained in section 5.6. Figure 5.20 plots the histograms of the lift coefficients in two situations:

1) 10 small rings (KR1) on the left column;
2) 5 big rings (SR5) on the right column.

On the left column, as well as in Figure 5.19, the distance between rings is 10 cm, i.e. 2/3 of the diameter; on the left column it is 4/3 of the diameter (20 cm). A first conclusion which can be drawn from the graphs is that the flow is bistable only in case of 10 big rings and no efflux (Figure 5.19, left column). In other words, the flow is able to undergo a jump, i.e. the bubble is able to pass on the other side of the cylinder, only if the rings are sufficiently big. As it was shown in Figure 5.11, a bigger bubble develops shortly before a jump, accompanied by a stronger deviation of the stagnation angle. This bubble is the result of 3D secondary vortices in the wake due to the flow over the tip which enters the wake. The spanwise inversion is a sort of cascade effect from the highest compartment. The trigger occurs randomly in time, according to the random nature of the flow. Apparently, smaller rings do not offer enough horizontal excrescence so that sufficiently big bubbles can develop. As long as the bubbles are small they produce asymmetric flow (because they are on one side only), but they do not pass on the other side. The size of the separation bubbles, related to the size of the rings should then explain the bistability of the flow.

However, in view of the design, the bi-stability (i.e. the jump) might not be the leading feature, because it is rapid in the wind tunnel but slower in full-scale (λ_T = 488, section 4.1.2). Instead, additional stresses in the shell may arise from the stable asymmetric condition. This is still present even with 10 small rings. Therefore, more than the size of rings, it is the distribution of rings which influences the design. In any case, if the rings are small, the asymmetry is limited to a smaller range (only two compartments in Figure 5.20a). When the distance between rings is large, e.g. 20 cm on the 1 m model (whose diameter is 15 cm), both the bi-stability and the asymmetry vanish (Figure 5.20 right column). Increasing the distance between rings is then a safe mitigation strategy.

SR1-EF0: 10 big rings - without efflux (C_L) *SR1-EF1: 10 big rings - with efflux (C_L)*

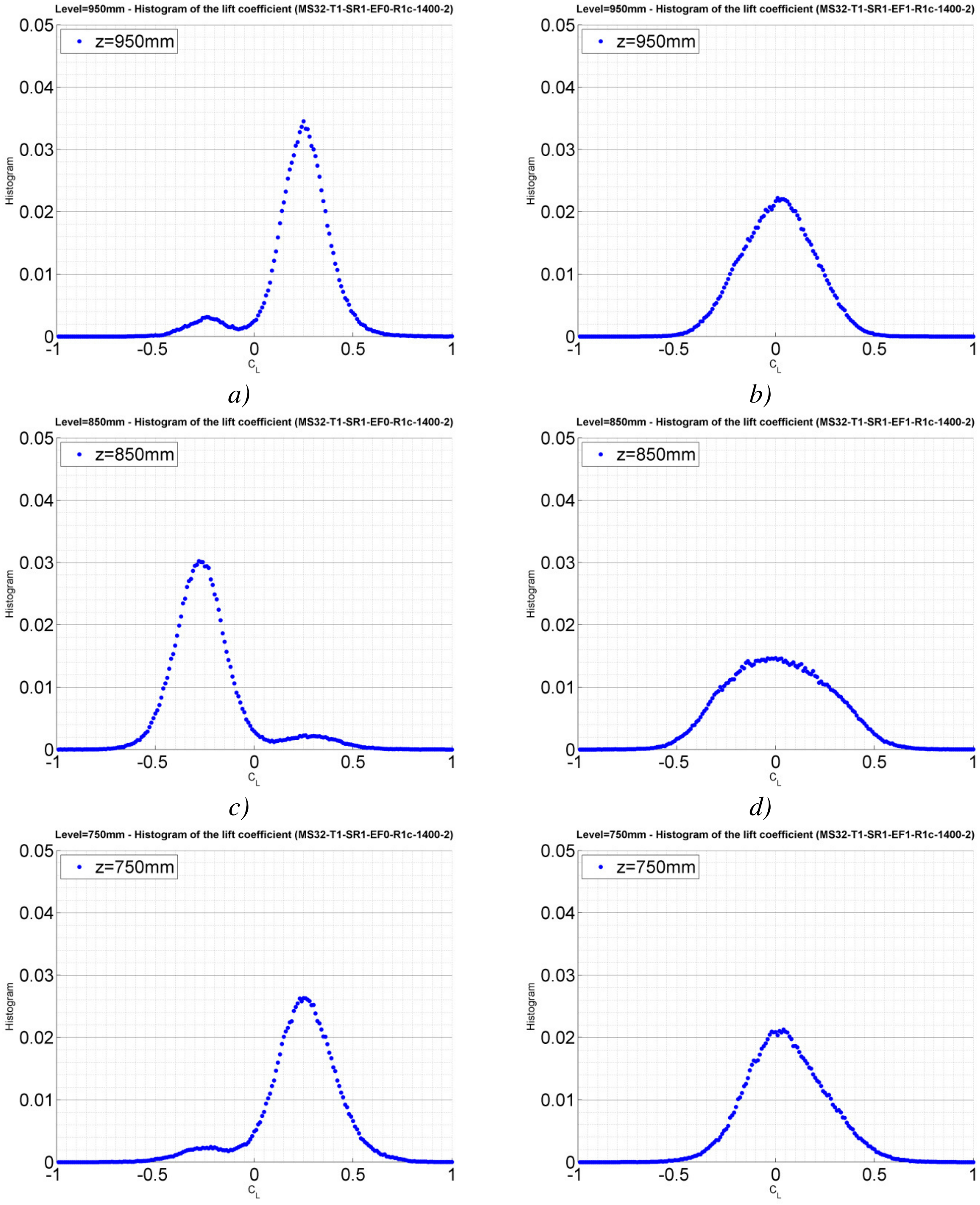

a) *b)* *c)* *d)* *e)* *f)*

Figure 5.19 Effect of efflux on the bistable flow with 10 rings, histograms of C_L: a) level 950 mm (EF0); b) level 950 mm (EF1); c) level 850 mm (EF0); d) level 850 mm (EF1); e) level 750 mm (EF0); f) level 750 mm (EF1); (WiSt, T1-SR1-R1-EF0/EF1)

KR1-EF0: 10 small rings - without efflux (C_L)   *SR5-EF0: 5 big rings - without efflux (C_L)*

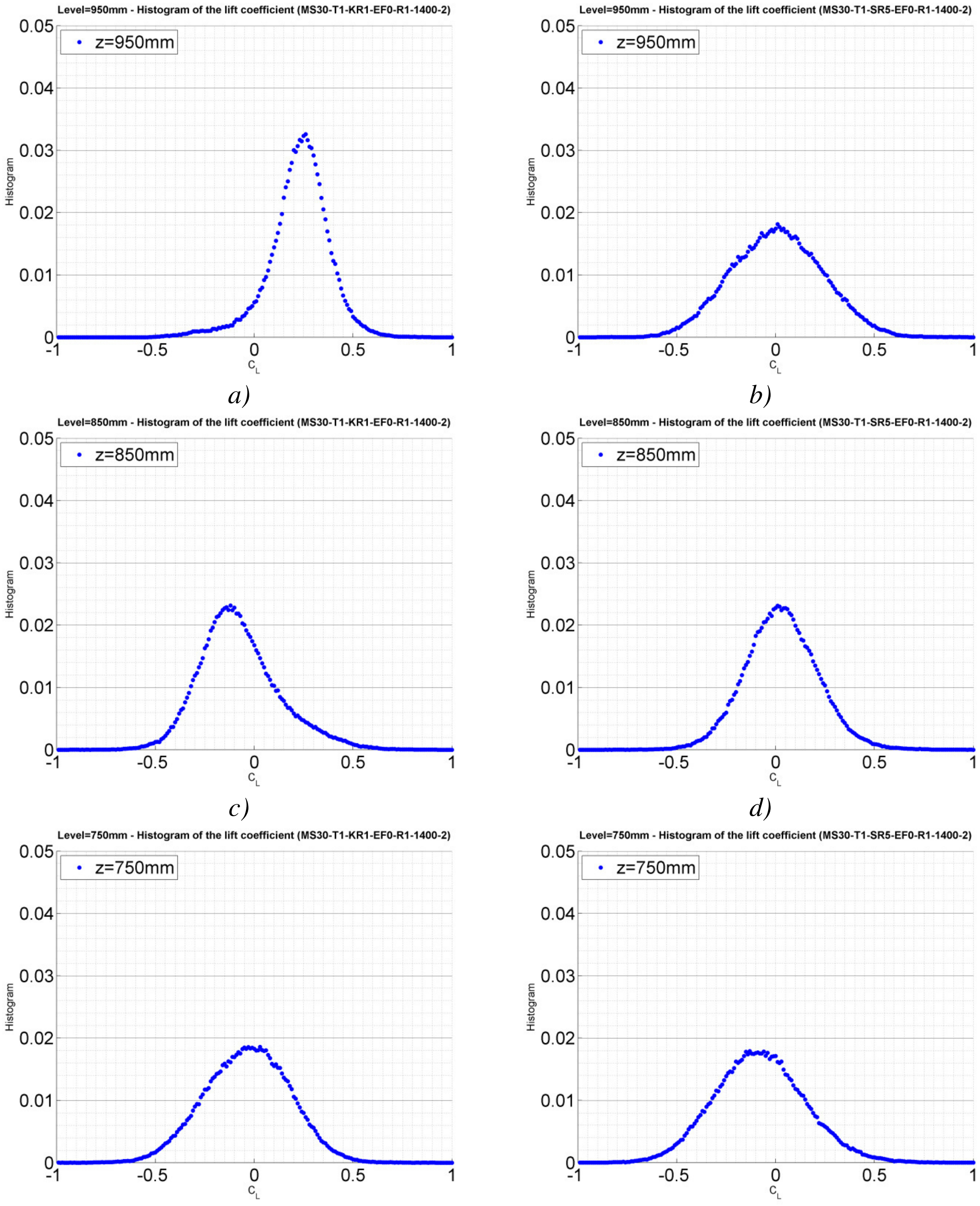

a)   *b)*

c)   *d)*

e)   *f)*

Figure 5.20 Effect of size and number of rings on the bistable asymmetric flow, histograms of C_L: a) level 950 mm (KR1); b) level 950 mm (SR5); c) level 850 mm (KR1); d) level 850 mm (SR5); e) level 750 mm (KR1); f) level 750 mm (SR5); (WiSt, T1-KR1/SR5-R1-EF0)

5.4 A physical interpretation

The key points of the cross-wind phenomenon described so far are first remembered in a brief summary.

Pressure measurements on 1 m circular cylinder with 10 rings of 7 mm in width at spacing of 100 mm (scale 1:1000 to the prototype) have shown:

1. two steady asymmetric states (namely “state 1” and “state 2”);
2. a bi-stability of the flow, i.e. a change of state in time;
3. a spanwise inversion, i.e. a change of state in space.

It was not found, at increasing Re, any tendency for this phenomenon to disappear. Instead, the phenomenon is cancelled out by the efflux and the effect is mitigated by using fewer and/or smaller rings.

The phenomenon is more evident in the upper part of the tower, this would support the thesis that it is a 3D effect, related to the free-end. The occurrence of the phenomenon does not depend significantly on the atmospheric boundary layer. The characteristics of the atmospheric boundary layer are not governing parameters, they only influence the development – or the disruption – of the phenomenon along the height. The spanwise inversion may be interpreted as a cascade effect in the neighbouring compartments, starting from the highest one. The change of state in time, i.e. the jump, appears randomly: no periodicity has been found. This random nature of the bi-stability reflects the random nature of turbulent flow. Relying on the wind tunnel measurements, it is not straightforward to state that a symmetric state can be obtained if an infinitely long period is considered. In fact, the asymmetric conditions, once formed, tend to establish. Each state is intrinsically stable. The change of state must then receive some stronger input from the flow in order to initiate and take place. It is not astonishing, therefore, that sometimes this input is not found in the time window of a measurement. In any case, asymmetric states generally persist so long that the design of the structure should necessarily include the asymmetric interval, even though the structure is symmetric.

Secondary vortices like separation bubbles develop in the wake on one side only of the cylinder, that is called in this work “bubble side”. A key role, from the fluid-dynamic point of view, is the near-wake structure. In fact, the structural design is not directly governed by wake fluctuations, but the development of a certain wake structure and a vortex street are responsible for cross-wind loads and body-induced fluctuations in the attached boundary layer before separation.

An in-depth examination of the cross-wind phenomenon introduced in section 5.2 has led to the physical interpretation proposed in the following. The focus is not in the jump between two states, rather on the asymmetric steady condition within each state.
Von Karman vortex separation produces an oscillation of the separation point. Instantaneously, the pressure distribution is not symmetric, but the lateral suction increases on the side of the cylinder where the vortex is growing, before being shed. However, the phenomenon described in section 5.2 is not dealing with an instantaneous asymmetry of pressures, which produces an oscillating cross-wind force. This would be the well-known phenomenon of vortex separation. Instead, section 5.2 describes a steady asymmetric state, which produces a mean lift. This is a first fundamental characteristic. Therefore, the asymmetry must be sought at first in the averaged position of the separation point in the mean pressure distribution. Separation angles are identified at z/H = 0.95 in Figure 5.21, referring to the state 1.

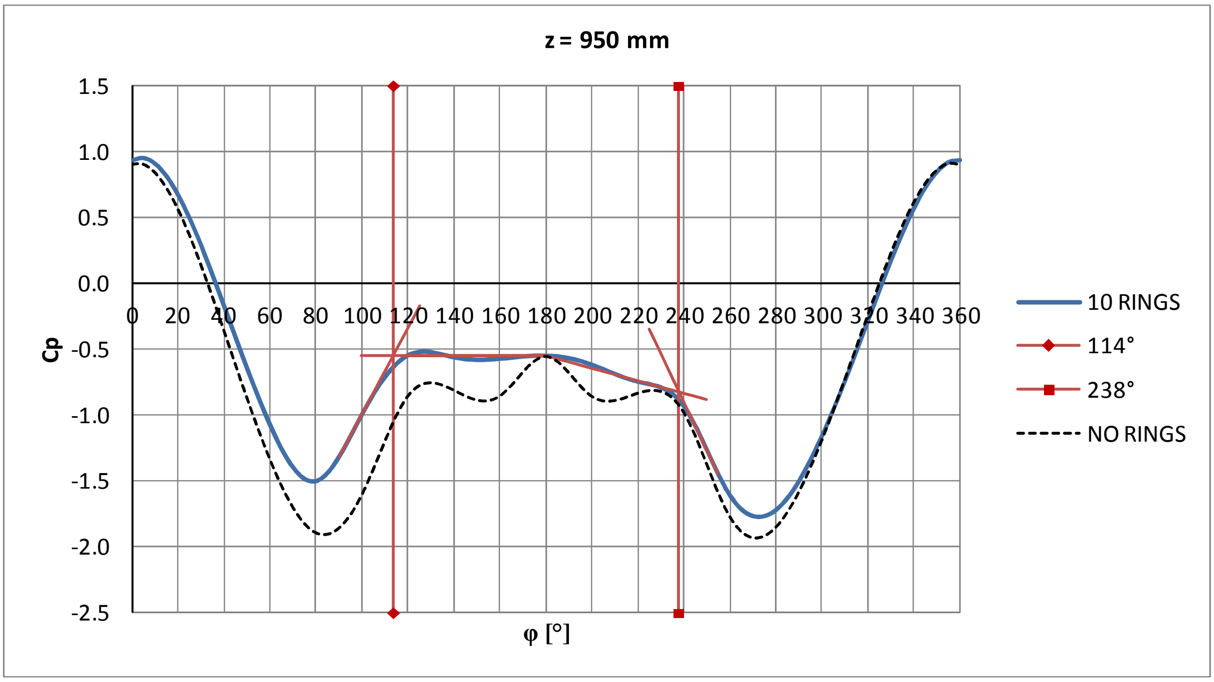

Figure 5.21 Mean pressure distribution and separation angles (WiSt, T1-SR1/SR0-R1-EF0)

Figure 5.21 describes the horizontal distribution and the strong asymmetry at a certain cross-section (z = 950 mm), but it cannot say anything about the three-dimensionality of the effect within the compartment and between different compartments. This issue is better addressed – in a first stage – by the cross-correlation coefficients; then they will be split up in the frequency domain. Since the phenomenon is a sort of cascade effect from the highest compartment (i.e. compartment number 10), the cross-correlations within this compartment and between it and the neighbouring one are investigated, both far from the rings and close to them. One state is considered alone.

Figure 5.22 shows the circumferential cross-correlations within compartment number 10, i.e. between levels z_1 = 950 mm and z_2 = 910 mm. The continuous line refers to the case with 10 rings (SR1), while the dashed line refers to the case without rings (SR0). At stagnation and for a certain region downstream the presence of rings does not modify the cross-correlations within the compartment: the ring beam is like not-existing. Then, at a certain angle, the cross-correlations SR1 drop down significantly. The asymmetry of the mean pressure distribution is also confirmed in the cross-correlations, because such a drop starts earlier on one side of the cylinder (0°-180° in this case). By looking at Figure 5.21, it can be seen that the drop starts earlier on the normal side. The earlier drop in the correlations likely reflects an anticipated separation of the boundary layer on the normal side of the cylinder, with respect to SR0, where separation is normally at large angles due to the tip effect. Since the cross-correlation is between two levels (z_1 = 950 mm, z_2 = 850 mm), the earlier separation may occur either at the level z_1, or at the level z_2, or on both levels.

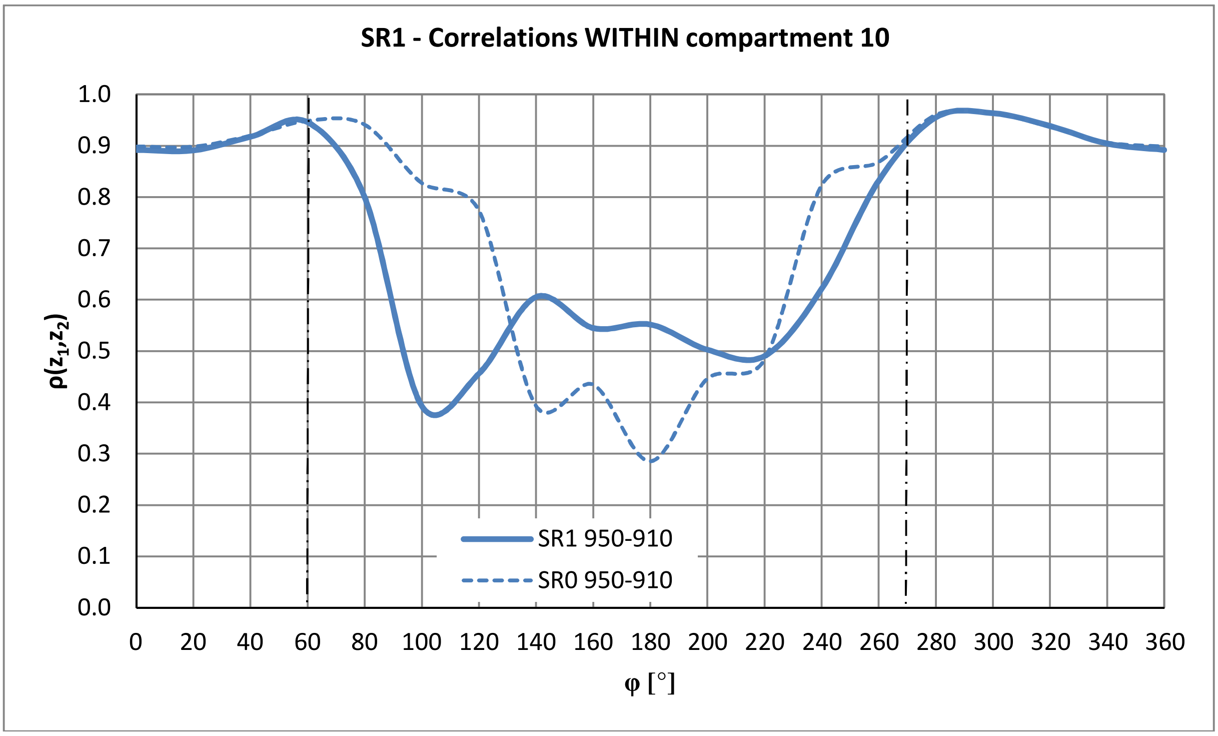

Figure 5.22 Cross-correlations of C_p between two levels
10 rings (continuous line SR1), without rings (dashed line SR0)
z_1 = 950 mm, z_2 = 910 mm (WiSt, T1-SR1/SR0-R1-EF0)

Let us consider the reference height z_1 = 950 mm, as before. Figure 5.22 described the cross-correlations of this level within the compartment. Now, the cross-correlations with the neighbouring compartment are added (Figure 5.23 and Figure 5.24). In particular, Figure 5.23 shows the cross-correlations of z_1 = 950 mm with a level close to the ring n.9 (below it, z_2 = 890 mm) and Figure 5.24 shows the cross-correlations with a level in the middle of the compartment below (z_2 = 850 mm). It must be remembered, from Figure 5.22, that ρ(950,910) drops early on one side at about 60° due to the effect of the ring. It is now remarkable to see that such an earlier drop on the same side of the cylinder, i.e. at 60°, does not appear neither in Figure 5.23 nor in Figure 5.24. In fact, ρ(950,890) and ρ(950,850) are not affected by the rings until about 90°-100°. Instead, perfectly consistent with the inversed mirrored condition previously described in terms of $C_{p,m}$ and $C_{p,\sigma}$, an earlier drop at 300° (i.e. -60°) occurs in ρ(950,890). Even more remarkable, is that the correlation between middle levels in different compartments (950 and 850 mm) does not perceive the earlier drop (Figure 5.24). This suggests that the effect of the ring is an earlier separation that develops within the compartment on one side only of the cylinder, as we move closer to the ring. The cross-correlations between middle levels remain unaffected much longer downstream.

In Figure 5.22, the movement towards the ring is from above (because $z_1 > z_2$) and the earlier drop is at 60°. Figure 5.25 (ρ(850,890)) is like Figure 5.22 – i.e. it shows the cross-correlations within the compartment – but in the compartment below. The reference level is z_1 = 850 mm and the movement towards the ring is from below (z_1 = 850 mm < z_2 = 890 mm). The cross-correlations confirm not only the asymmetry of the pressures, but also the inversion between different compartments, because the earlier drop in the cross-correlations ρ(850,890) occurs mirrored with respect to Figure 5.22, i.e. at 300°.

Therefore, the earlier drop of the correlation coefficient on one side only of the cylinder (normal side) and close to the ring (either above or below it) is explained by an earlier separation of the boundary layer at the ring (earlier than in absence of rings). On the other side of the cylinder, as well as in the neighbouring compartment on the same side, instead, the flow remains longer attached (separation is delayed). That is the bubble side. This movement of the mean separation line induced by the rings is confirmed by the mean pressure distributions calculated during only one state: the separation line is not at a symmetric position on the two sides of the cylinder (thus the steady asymmetry results, as shown in Figure 5.26 and Figure 5.27) and presents a discontinuity at the ring. In other words, the wake is not aligned in the rear of the cylinder.

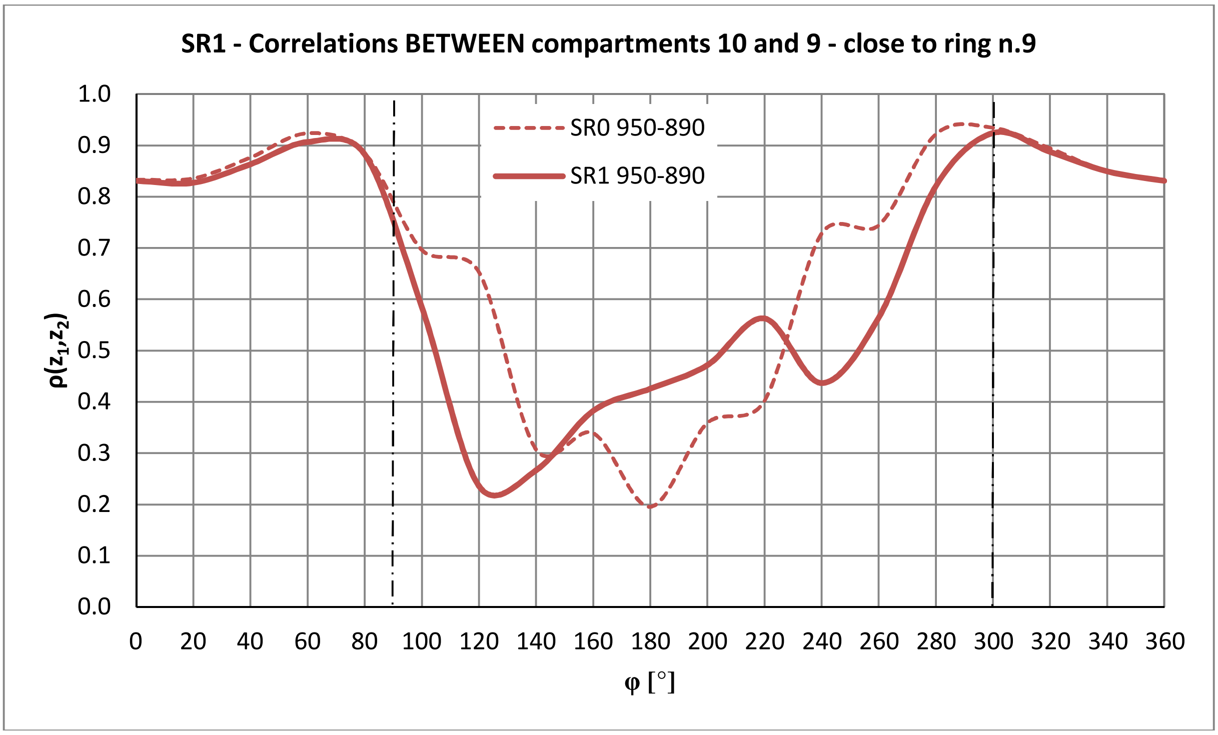

Figure 5.23 Cross-correlations of C_p between two levels
10 rings (continuos line SR1), without rings (dashed line SR0)
$z_1 = 950$ *mm*, $z_2 = 890$ *mm (WiSt, T1-SR1/SR0-R1-EF0)*

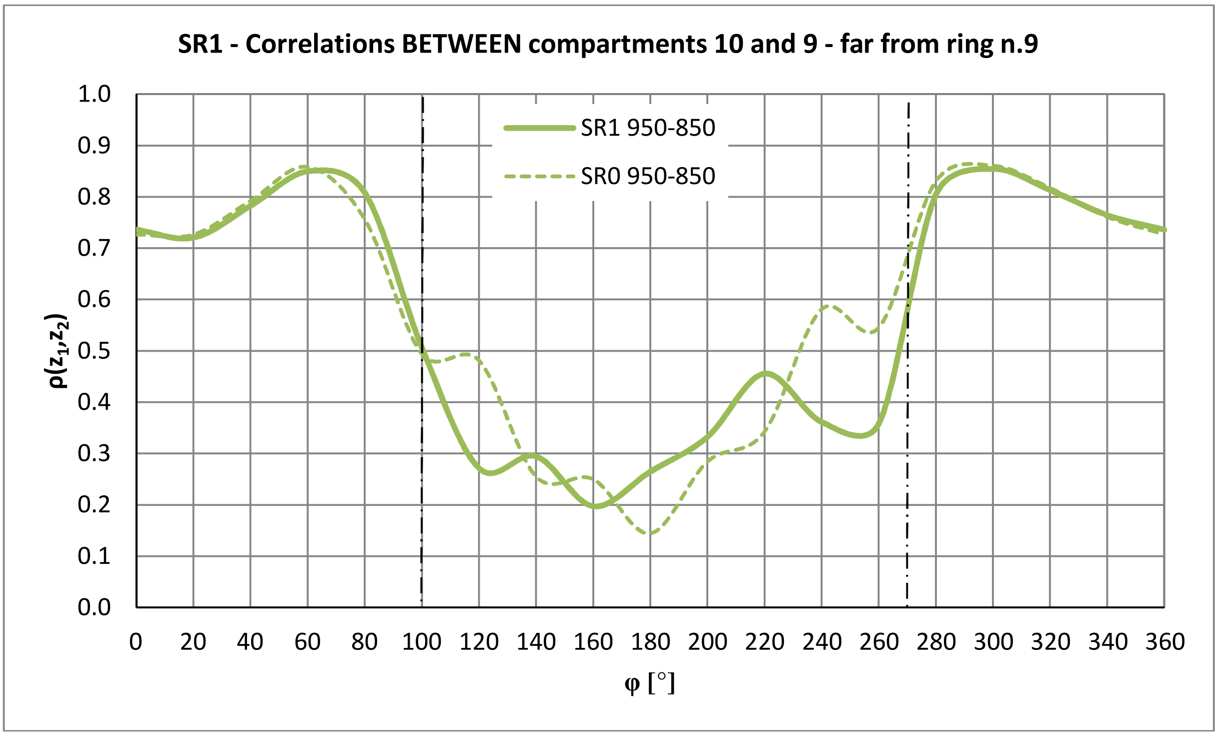

Figure 5.24 Cross-correlations of C_p between two levels
10 rings (continuos line SR1), without rings (dashed line SR0):
$z_1 = 950$ *mm*, $z_2 = 850$ *mm (WiSt, T1-SR1/SR0-R1-EF0)*

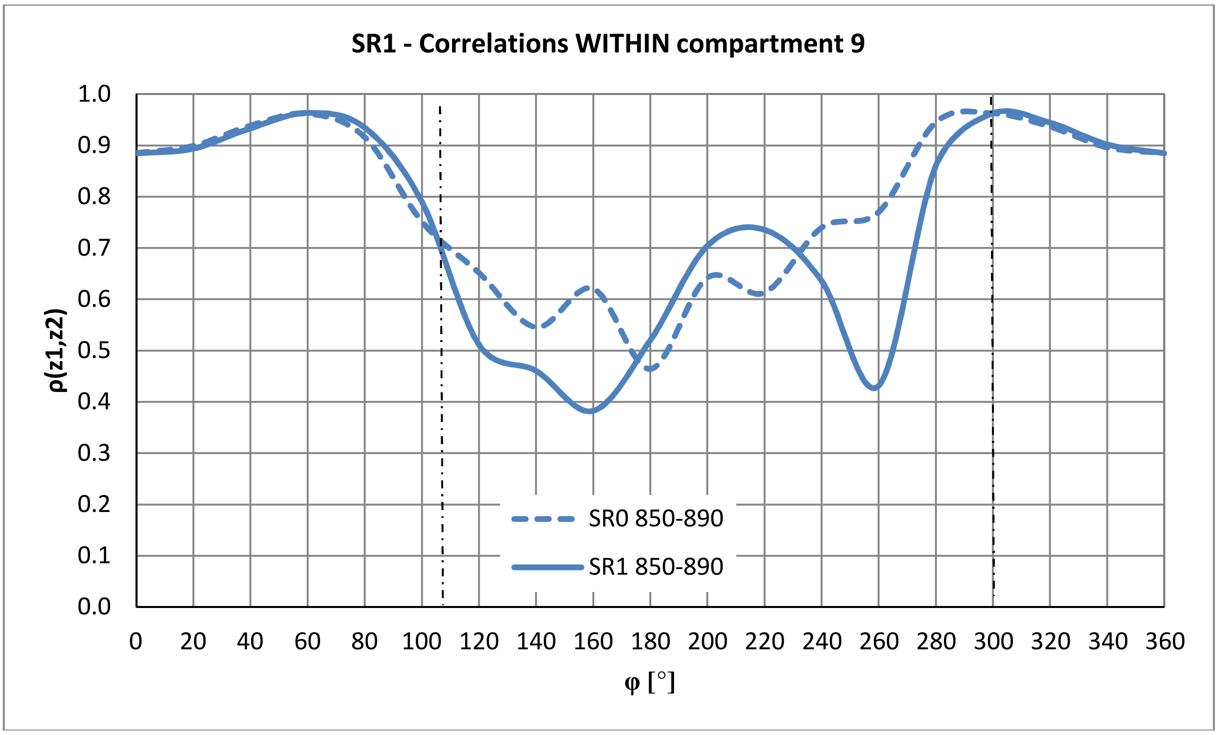

Figure 5.25 Cross-correlations of C_p between two levels 10 rings (continuos line), without rings (dashed line): z_1 = 850 mm, z_2 = 890 mm (WiSt, T1-SR1/SR0-R1-EF0)

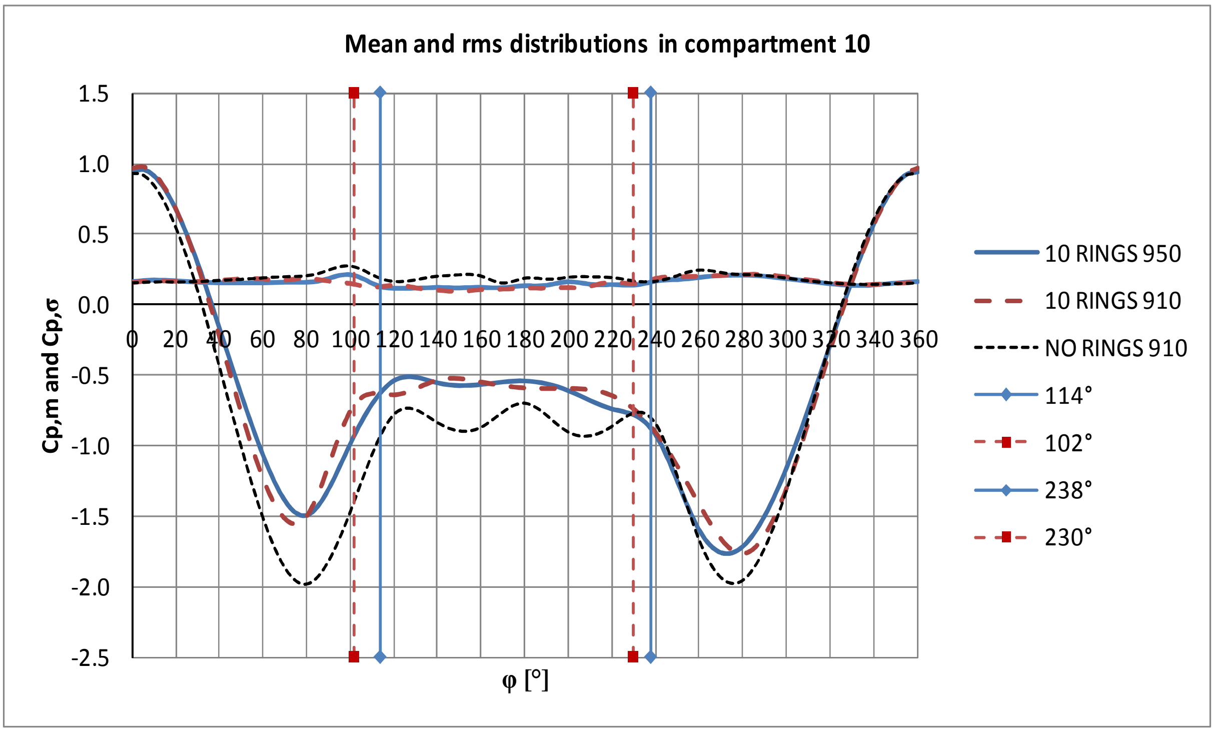

Figure 5.26 Angles of separation in the compartment n.10 (WiSt, T1-SR1/SR0-R1-EF0)

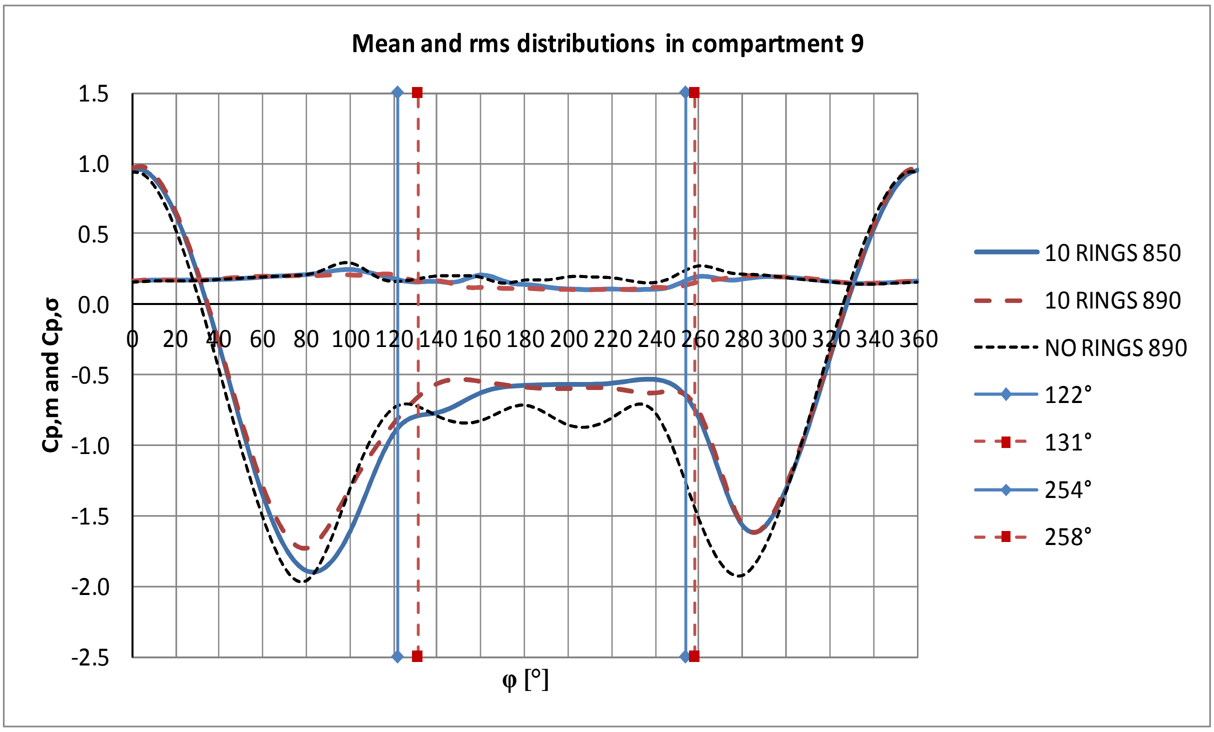

Figure 5.27 Angles of separation in the compartment n.9
(WiSt, T1-SR1/SR0-R1-EF0)

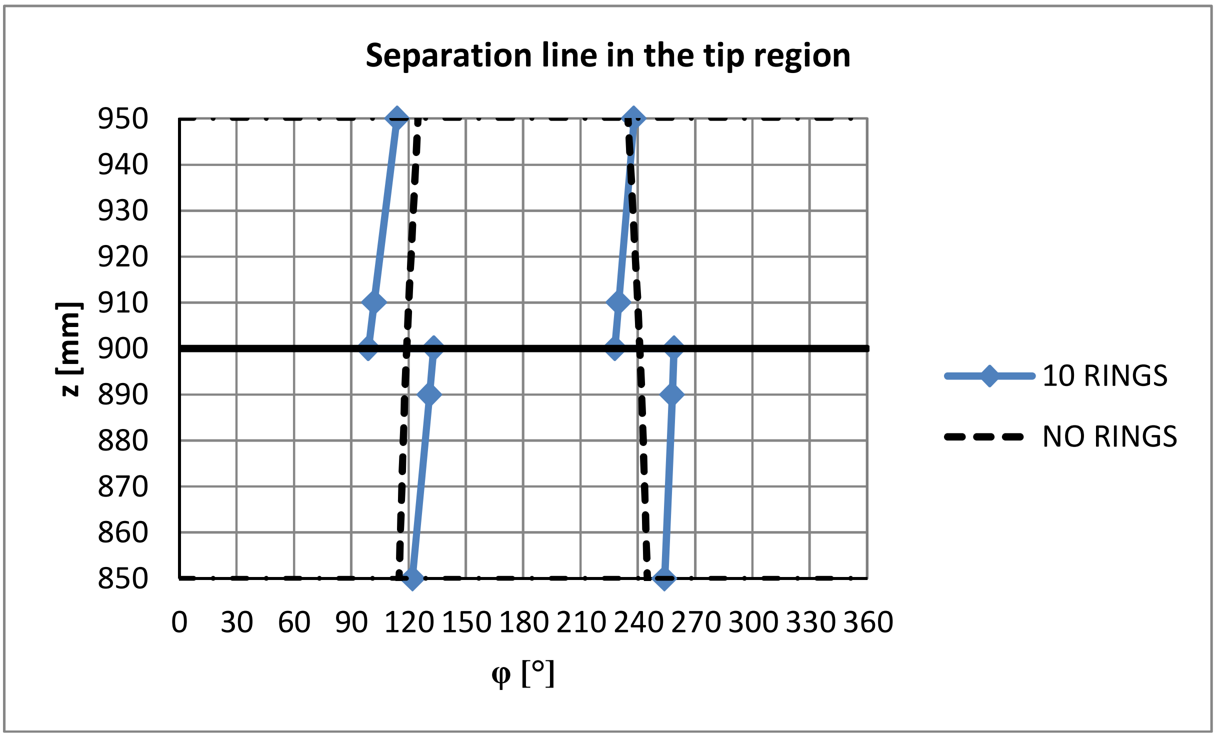

Figure 5.28 Discontinuity of the mean separation line within one state
(WiSt, T1-SR1/SR0-R1-EF0)

A jump between two states produces an inversion of the position of the separation line around the circumference. Then, around the circumference, there is an appreciable movement of the mean position of separation, which can be identified in the pressure measurements. For example at the level 890 mm, the separation point oscillates around two different mean positions, which alternate in time: one is before 120° and one is after that. Therefore, the time history recorded at $\varphi = 120°$ shows two different states of the flow (Figure 5.29): the pressure tap lies once in the attached boundary layer before separation (higher rms) and once in the wake (lower rms).

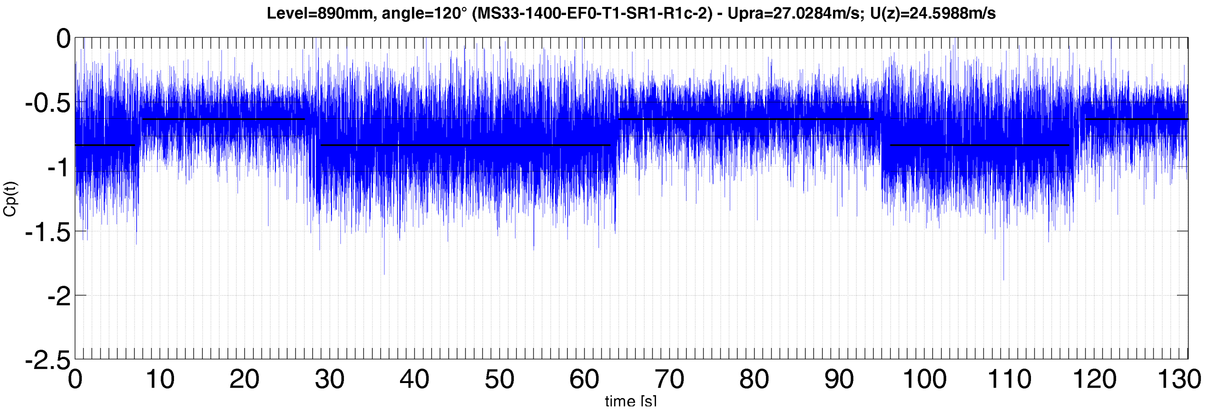

Figure 5.29 Bistability of the flow: movement of mean separation point (WiSt, T1-SR1-R1-EF0)

Figure 5.22 (referring to compartment n. 10) showed an anticipated drop of the cross-correlation coefficients on the side 0°-180° in case of ten rings. The same happened in the compartment below on the side 180°-360° (Figure 5.25). It is now interesting to split up the cross-correlation coefficients between two levels at a certain angle in the frequency domain (Co-spectrum(z_1,φ_1; z_2,φ_1)/$\sigma_1\sigma_2$), in order to indentify the missing contributions with respect to the case without rings. The angle 100° and 260° are chosen as reference in both compartments 10 and 9. In particular, the angle 100° lies on the normal side in compartment 10 and on the bubble side in compartment 9. The opposite holds for the angle 260°. Figure 5.22 and Figure 5.25 show that $\rho(950,910)$ at 260° and $\rho(850,890)$ at 100° (bubble sides) are basically the same both in presence and in absence of rings (SR1 and SR0). It is then surprising that the difference in case of rings is on the so-called normal side. The missing contribution in SR1 can be identified in the frequency domain. It results to be a typical 3D effect of circular cylinders with a free-end. It is a proof that the rings interact, somehow, with the three dimensional flow. In fact, Figure 5.30 a), d) shows that the missing contribution in the co-spectra of C_p on the normal sides (0°-180° in compartment 10 and 180°-360° in compartment 9) are not in the frequency range of Karman vortex shedding (nD/U ≈ 0.2), but at lower frequencies.

In order to understand the phenomenon created by the rings, it is now important to go one step back and investigate deeper the flow around the free-end, even in absence of rings. So far, the effect of the rings has been described as an asymmetric pressure distribution, associated to a fragmented separation line and a misaligned wake of the cylinder. The study of the cross-correlations within the same compartment and in different compartments has suggested that an earlier and a delayed separation develops at the rings. The phenomenon evolves within the compartment as one moves towards the ring; the cross-correlations at middle levels between rings are not affected much longer downstream. The frequency split-up of the cross-correlations at about 100° between different levels allowed to identify the range of frequencies where, in presence of rings, the phenomenon acts. It is not the range of Karman vortex shedding ($S_t \approx 0.2$). Rather, it is a lower range, that results to be – by literature documentation – the frequency range of TAV, tip-associated-vortices (Kitagawa et al., 2001).
Tip-associated-vortices, described in Chapter 3, should not be confused with the longitudinal trailing vortices at the tip of the cylinder, which are created by the interaction between the upwards flow at the flanges and the downwards flow over the tip. The TAV are bigger Karman vortices, at a frequency around one third of the usual Karman frequency at intermediate levels. They are responsible for the variation of the Strouhal number in the tip region which is produced, according to Farivar (1981), by the entrainment in the wake and elongation of the eddy formation region. The tests performed by Kitagawa et al. (2001) constitute, so far, one of the deepest investigations of TAV. Those tests are performed in uniform flow on a H/D = 26 circular cylinder. Therefore, it is not surprising that the TAV are confined at high-levels and do not interact with the Karman vortex shedding at middle height (Figure 3.34c). A different situation and a stronger interaction should be expected on a H/D = 7 circular cylinder. In fact, in our experiments, double-peak spectra – low frequency peak due to TAV and Strouhal peak due to Karman vortex shedding – describe the cross-wind fluctuations at the high levels in SR0. As it will be shown in Chapter 6 by comparison with CRIACIV, the boundary layer influences the either stronger or weaker interaction between the two peaks at different levels. In any case, there is general agreement on the shedding frequency of TAV, about nD/U = 0.07, as confirmed by Kitagawa et al. (2001) and Park&Lee (2000). The results of the present work in SR0 are a further confirmation.

Compartment n. 10 (900-1000 mm):

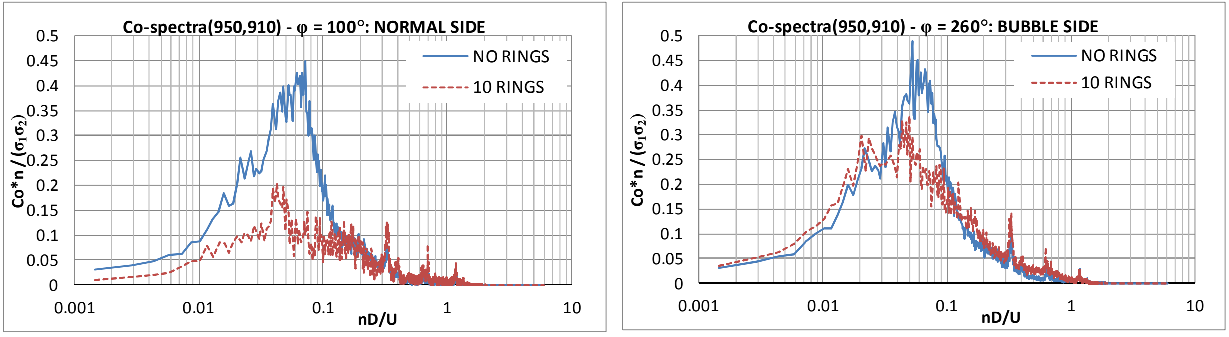

a) *b)*

Compartment n. 9 (800-900 mm):

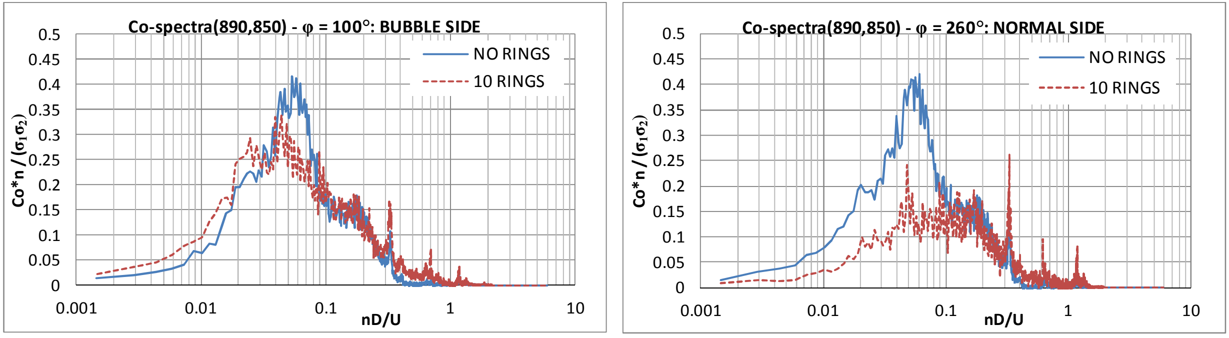

c) *d)*

Figure 5.30 Asymmetry of the of the flow in the frequency domain:
blue line: no rings; red line: 10 rings;
a) Co(950,910) at 100°; b) Co(950,910) at 260°;
c) Co(850,890) at 100°; d) Co(950,890) at 260°;
x-axis: nD/U_{1000}; y-axis = $Co_{Cp}(z_1,z_2)*n/(\sigma_1\sigma_2)$;
(WiSt, T1-SR0/SR1-R1-EF0)

Figure 5.31 shows the strong interaction in absence of spanwise rings between the low-frequency peak at nD/U = 0.062 and $S_t = 0.2$.

The TAV predominate at z/H = 0.95, where the Karman vortex shedding is weak (but not completely absent).

At z/H = 0.85 there is a strong interaction between the two peaks and then the low-frequency peak disappears at $z/H \leq 0.75$. Only a skewness of the spectra remains.

It is also observed (not shown) that in presence of efflux the low-frequency peak disappears. In Chapter 7 the effect of the low-frequency peak on the response will be investigated. It essentially gives a contribution in the quasi-static oscillation, on which Karman resonance is superimposed.

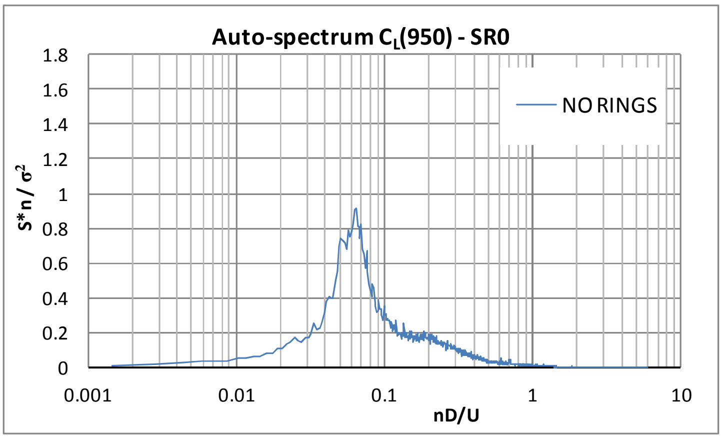

a) z = 950 m

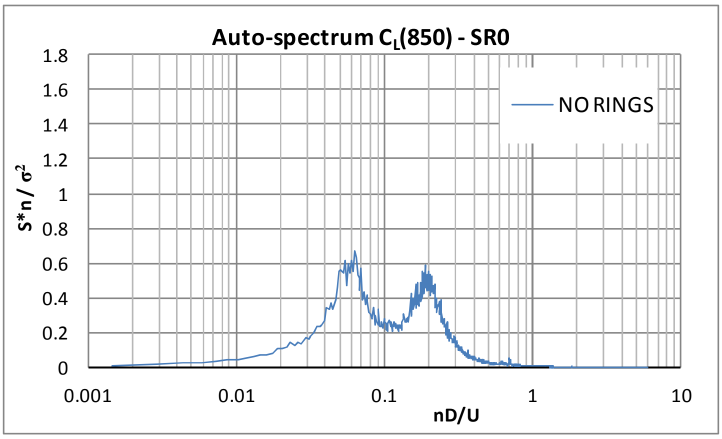

b) z = 850 m

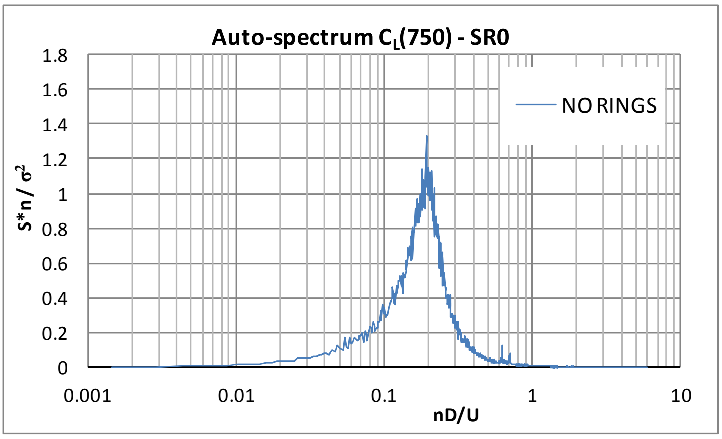

c) z = 750 m

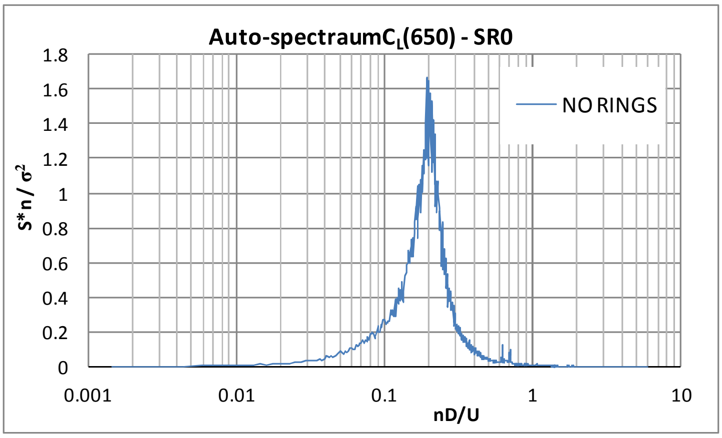

d) z = 650 m

Figure 5.31 Lift spectra along the height without rings (WiSt, T1-SR0-R1-EF0)

In this section, it is interesting to analyze the effect of the rings on the TAV. It is interesting to see in Figure 5.32 that the spectra of lift coefficients in the tip region are not double-peak spectra (as they are in SR0), but they present only one peak at Strouhal number 0.2 (von Karman vortex shedding). Actually, it was for this reason, that the spectral analysis in case of ten rings alone could not say so much, before being compared with the corresponding case without rings. The single-peak lift spectra in SR1 appeared to be perfectly reasonable at first sight. Only the comparison with the results of the circular cylinder without rings highlighted the disappearance of tip-associated-vortices.

In terms of pressures, Figure 5.30 has suggested that the low frequency peak due to tip associated vortices is fragmented on the normal side of the cylinder at each level, while such bigger vortices still remain on the bubble side. These big vortices associated to low frequency contributions, which remain on one side only of the cylinder, are responsible for the delayed separation on the bubble side. This explains also the asymmetry. Moreover, since low frequency tip-associated vortices are fragmented on one side of the cylinder in case of ten rings, they do not produce lift fluctuations: the low-frequency peak in the lift disappears.

Compartment n. 10 (900-1000 mm):

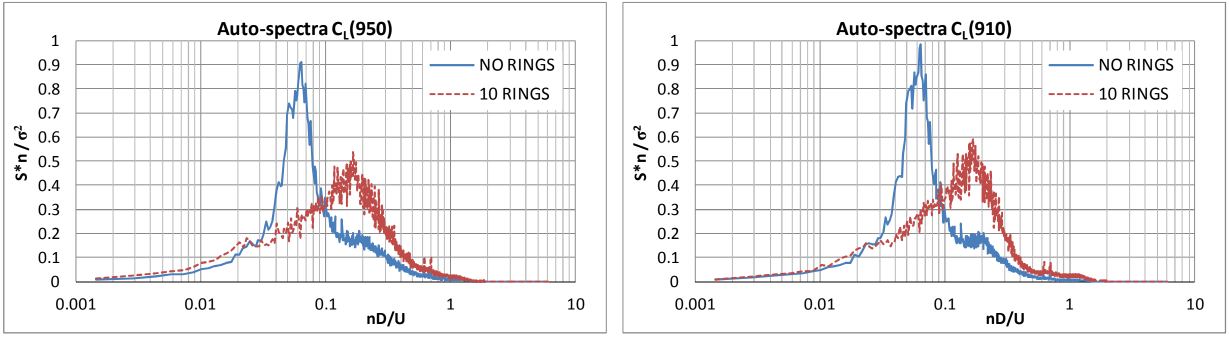

a) *b)*

Compartment n. 9 (800-900 mm):

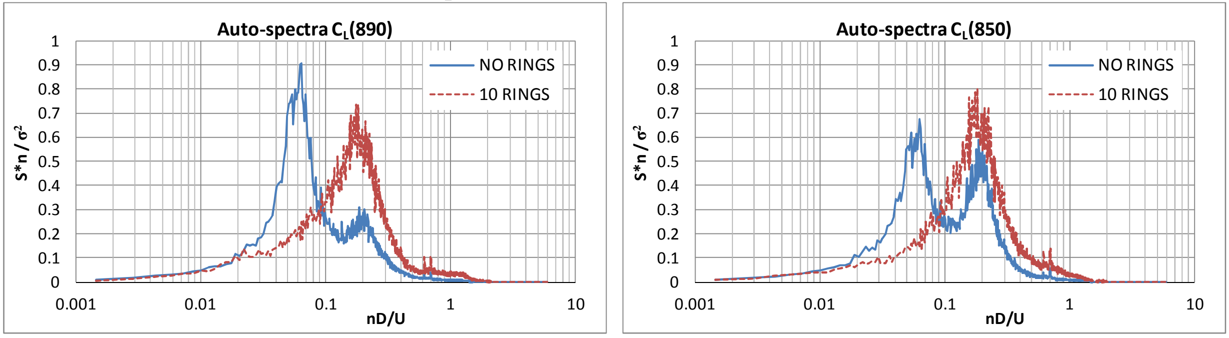

c) *d)*

Figure 5.32 a-d) Lift spectra at 950-910-890-850 mm. $S_{CL}(z_1)*n/\sigma)$ *vs* nD/U_{1000}*;*
(WiSt, T1-SR0/SR1-R1-EF0)

Kitagawa et al. (1999) placed a circular disk (not a ring) on the top of a circular cylinder of finite length and observed the disappearance of tip vortices. The disk had a diameter of 1.6 times the tower diameter. A smaller disk (with a diameter 20% larger than the tower diameter) was not able to suppress the tip vortices, it just reduced their strength. Kitagawa concluded correctly that the tip vortices were produced by the free-end and therefore some modification of the free-end conditions would have altered them. One may then think that the top ring on the solar tower could have, alone, the same effect as the disk placed by Kitagawa, although the diameter of the ring is only 10% larger than the tower diameter, comparatively smaller than what Kitagawa observed. Due to the small dimensions of the ring, such a strong effect would be surprising. In fact, by adding the results of the tests with the five ringed cylinder, a new explanation can be supposed.

Figure 5.33 shows the vertical cross-correlations of lift forces between different compartments. The reference level is 950 mm. A similar picture (Figure 6.15) will also be shown in Chapter 6 as further proof. Figure 5.33 shows that the lift cross-correlations in case of five rings follow the same bahaviour as in SR0 (no rings). The co-spectra divided by the product of the standard deviations, i.e. the split up over frequencies of the cross-correlation coefficients, prove that in case of five rings the tip vortices are not suppressed. It should also be remembered (Figure 5.20) that in case of five rings the flow is neither asymmetric nor bistable. Instead, in case of ten rings, $\rho,C_L(950,850)$ (i.e. ρ,C_L ($\Delta z=100$)) is much lower because the contribution of the tip-associated vortices is missing.

It follows that a certain distribution of rings, at a sufficiently small distance, interacts and kills the bigger vortices in the tip region. It should also be observed that in case of ten rings the distance between them is 10 cm in the scale of the wind tunnel model (i.e. 2/3 of the diameter) and in case of five rings the distance between them is 20 cm (i.e. 4/3 of the diameter). Between 10 and 20 cm, the value 15 cm lies. This is actually the tower diameter. Although so far there is not an experimental proof of it, it can be supposed that the tower diameter could be taken as reference to calibrate the distance between rings, in order not to interact with tip vortices. Even more, it could be supposed that, since the big tip vortices develop only in the tip region, the key feature is the distance between rings only in the tip region and not all along the tower. In this regard, Chapter 8 will mention, among future outlooks, the importance of doing tests where the ring beams are not equally distributed along the heihgt, but they are placed at larger distance (e.g. 4/3D) in the tip region only.

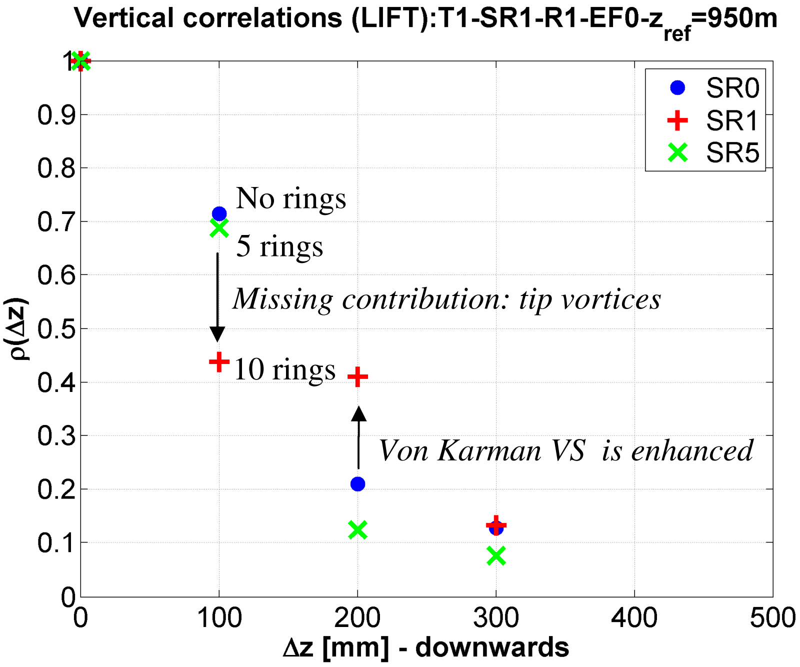

Figure 5.33 Cross-correlation coefficients of C_L without rings (blue), 10 rings (red) and 5 rings (green). z_{ref} = 950 mm (see also Figure 6.15)

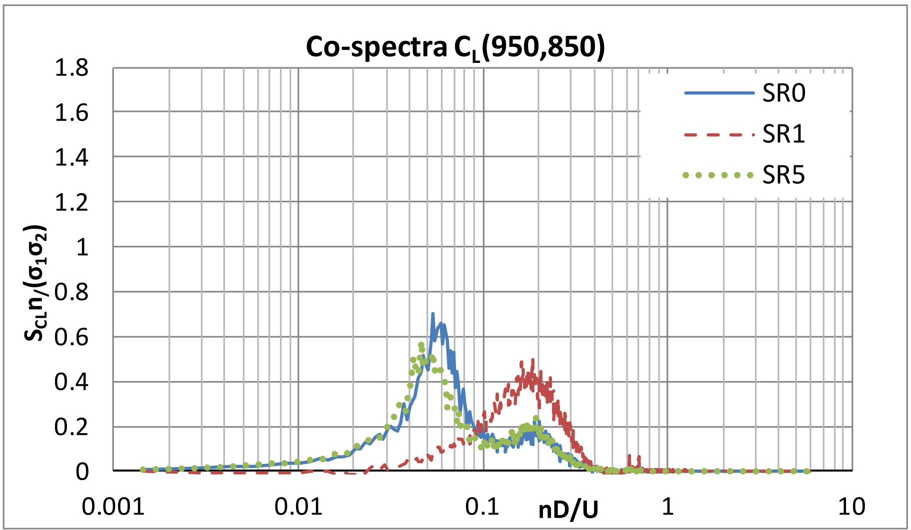

Figure 5.34 Co-spectra of C_L: $S_{CL}(z_1,z_2)*n/\sigma^2$ vs nD/U, z_1 = 950 mm, z_2 = 850 mm; (see also Figure 6.16). (WiSt, T1-SR0/SR1/SR5-R1-EF0)

A further proof that the tip vortices are disturbed by rings placed at a too small distance is given by the experiments with 10 small rings (KR1). In that case, the flow is not able to undergo jumps, but it is asymmetric (Figure 5.20). Figure 5.35 shows that ten rings, at a smaller distance than the diamter (2/3 of it, in this case) are able to suppress tip associated vortices, even if the rings are small. Figure 5.36 proves that the Karman vortex shedding ($S_t \approx 0.2$) is not significantly affected by the rings. The low-frequency contributions in the spectra of SR1-SR5-KR1 represent the oscillations produced in the time histories by the changes of state (e.g. in Figure 6.9 at 650 mm).

The spectra are evaluated separately in each interval of time, the intervals are clearly detectable for example by looking at the time histories of either lift force or pressures in the tip region (see Figure 5.3 and Figure 5.4, the selection of intervals is evident). However, as it will be better explained in Chapter 6 (Figure 6.12), the stability within each state is progressively lost at low levels and even within the same interval of time the frequency of jumps between the two states increases. However, a predominant low frequency peak cannot be identified.

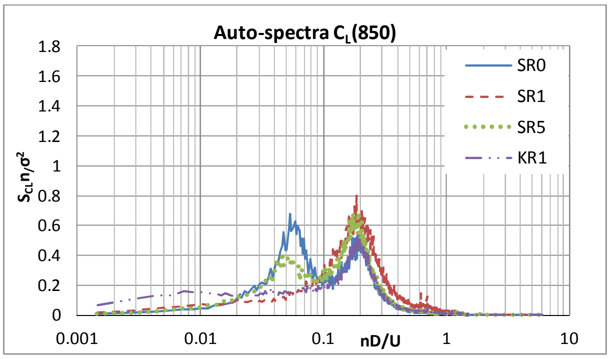

Figure 5.35 Lift spectra at 850 mm. $S_{CL}(z_1)*n/\sigma^2$ vs nD/U_{1000}; (WiSt, T1-SR0/SR1/SR5/KR1-R1-EF0)

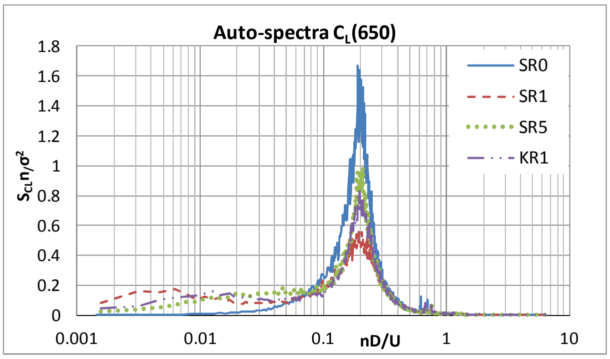

Figure 5.36 Lift spectra at 650 mm. $S_{CL}(z_1)*n/\sigma^2$ vs nD/U_{1000}; (WiSt, T1-SR0/SR1/SR5/KR1-R1-EF0)

The auto-spectra are normalized with respect to the variance, so that the area is one. The following table reports the variances, for the sake of completeness.

Table 5.1 Variances of C_L

C_L,σ^2				
	SR0	**SR1**	**SR5**	**KR1**
950	0.020	0.014	0.053	0.027
850	0.033	0.017	0.034	0.042
750	0.020	0.022	0.053	0.044
650	0.022	0.039	0.030	0.035

The TAV are a typical three dimensional effect due to the free-end: the reason for the lower frequency contribution close to the top is the entrainment of flow in the wake from above the cylinder, as previously said. The numerical simulations in Chapter 6 will clarify that the entrainment of flow in the wake results to be significantly altered by the presence of rings. This motivates not only the disappearance of tip-associated-vortices, but also the asymmetry and the spanwise inversion.

It is straightforward to wonder what it may happen if the entrainment in the wake is prevented, for example by an end-plate. In other words, what would happen in 2D flow? Within this work, it has not been possible to perform experiments in 2D flow, because a new wind tunnel model with two end-plates, as well as a different experimental set-up would have been necessary. However, on the basis of the results obtained, it is inferred that the bistable flow disappears in 2D conditions (Chapter Chapter 8).

5.5 Effect on wind load

In the tip region, where the asymmetric flow is particularly apparent in SR1 (Figure 5.37), the steady lift is enhanced by high suction on the bubble side (that is, in any case, comparable to SR0) and the relatively lower suction on the normal side. However, C_L remains in any case relatively low (about 0.2-0.3), and the resulting bending moment in the cross-wind direction is not significantly high (see section 7.2.2).

The typical second islet of $C_{p,min}$ in the wake of the cylinder (see e.g. Figure 3.23, Figure 3.24, Figure 3.25, Figure 3.29), produced – according to Kawamura et al. (1984) – by the attachment of trailing swirls, is clear in SR0, but it cannot be detected in SR1 (Figure 5.37a). Such a minimum pressure islet in the tip region is responsible, on free-end cylinders, for the increase in drag in the tip region. Therefore, the tip effect is less pronounced in presence of rings (Figure 5.39). Instead, along the height, the drag coefficient is higher in SR1 than in SR0, due to the separation bubble in the wake, as proved by the mean pressure distribution at 650 mm in Figure 5.38.

On the normal side of the cylinder at middle height the mean and rms distributions of C_p (averaged within only one state) resemble the corresponding distributions in absence of rings. On the bubble side, the negative mean pressures decrease after 90° and this increases the drag force. Also the rms values increase on the bubble side. The effect on the response is quantified in sections 7.2.2 and 7.3.4.

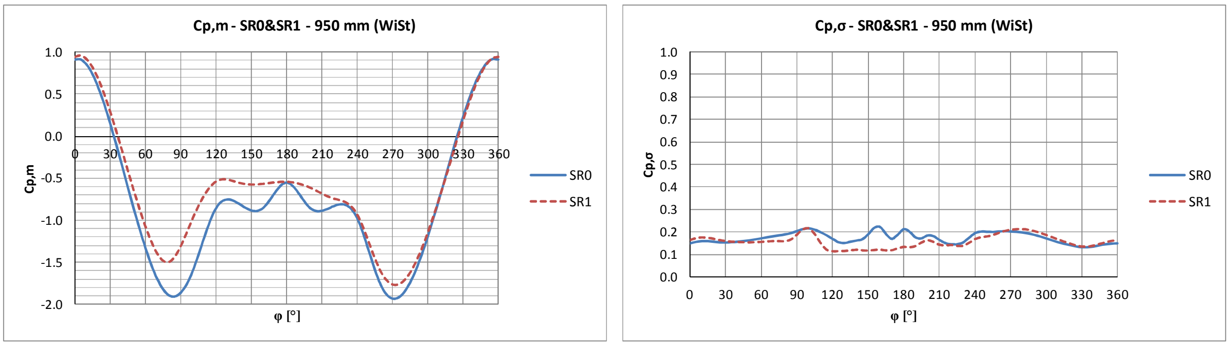

a) *b)*

Figure 5.37 $C_{p,m}$ (a) and $C_{p,\sigma}$ (b) in the tip region with and without rings (WiSt, T1-SR0/SR1-R1-EF0)

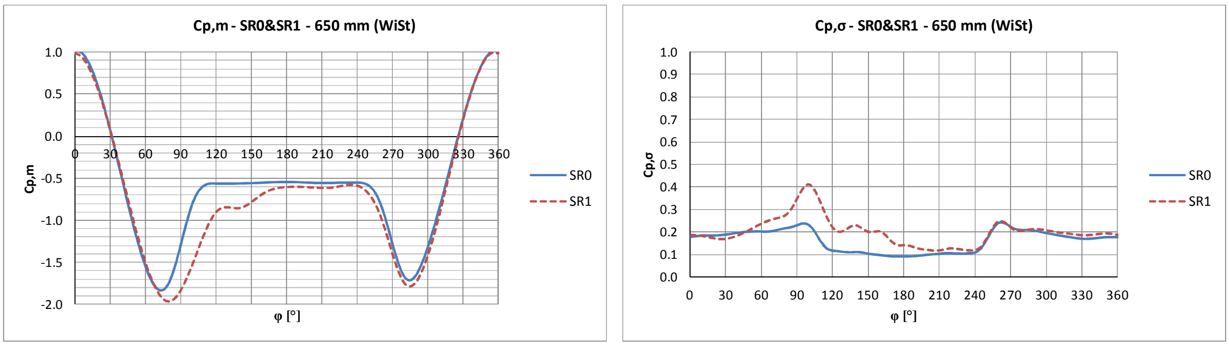

a) *b)*

Figure 5.38 $C_{p,m}$ (a) and $C_{p,\sigma}$ (b) at middle height with and without rings (WiSt, T1-SR0/SR1-R1-EF0)

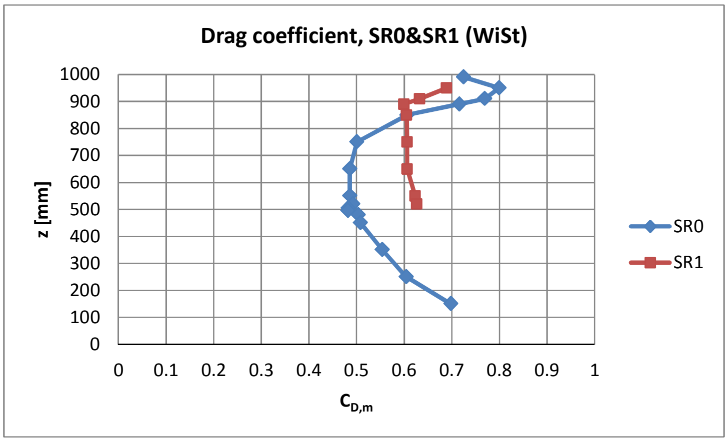

Figure 5.39 $C_{D,m}$ with and without rings (WiSt, T1-SR0/SR1-R1-EF0)

Measurements at low levels (z/H < 0.5) are not available in case of rings at WiSt. However, in order to figure out a three-dimensional distribution of the asymmetric load, the same behaviour as in Figure 5.38 is also hypothesized at lower levels so that, in practice, the presence of rings increases the load on the bubble side. Figure 5.40 and Figure 5.41 plot the resulting $C_{p,m}$ and $C_{p,\sigma}$ distributions, respectively. They are idealized distributions on the safe side, because the two states tend to be mixed as the height decreases (Figure 6.12).

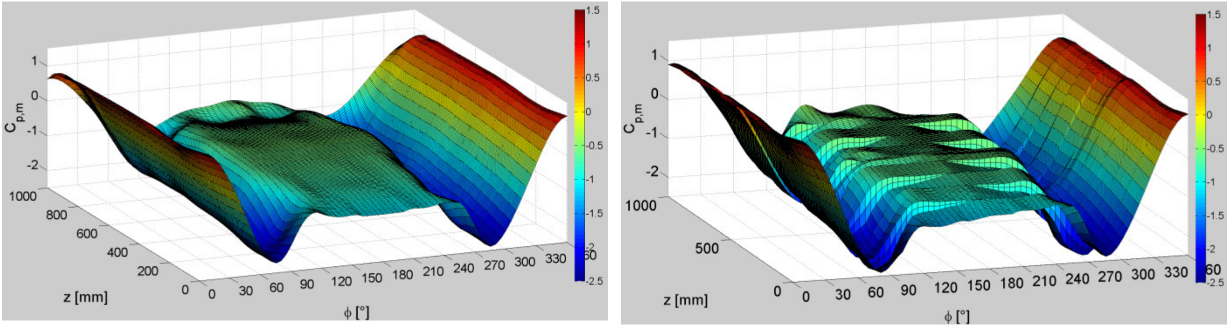

a) *b)*

Figure 5.40 $C_{p,m}$ on the tower: a) without rings; b) with 10 rings (WiSt, T1-SR0/SR1 -R1-EF0)

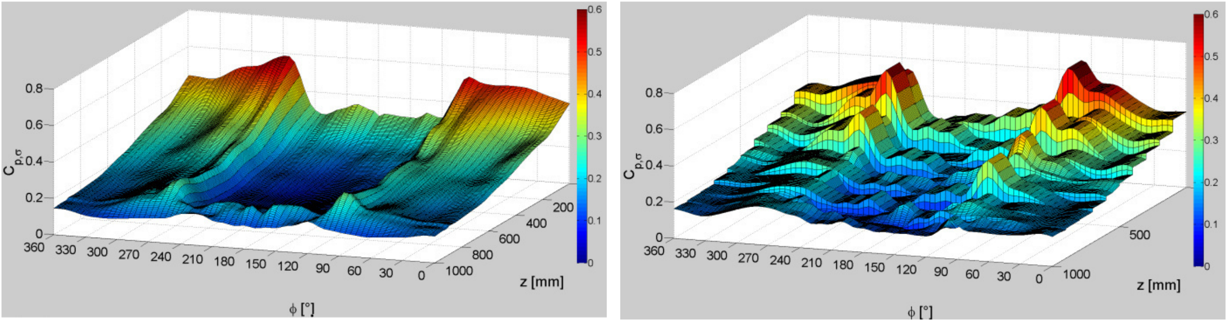

a) *b)*

Figure 5.41 $C_{p,\sigma}$ on the tower: a) without rings; b) with 10 rings (WiSt, T1-SR0/SR1 -R1-EF0)

While in terms of $C_{p,m}$ and $C_{p,\sigma}$ the effect of the rings is a general increase in load, the correlation field is generally reduced.

In terms of horizontal correlations, in case of rings the matrices lose the symmetry with respect to the secondary diagonal, because of the asymmetric conditions between the two sides of the cylinder. Apart from that, the differences are not so relevant. The level z/H = 0.75 is chosen as representative in Figure 5.42, but the same concept applies at the other levels, too. In the case of rings, the correlation field is smoother on the bubble side (180°-360°), where the downstream movement of the separation point, together with the separation bubble, conceal the valley at the separation angle. In the wake, the correlation in case of rings is lower. It consequently decreases the drag force and partly counterbalances the higher Cp_{σ}. However, even though the analysis of the correlation field in SR1 resulted very important for the understanding of the fluid–dynamic phenomenon, structural calculations can safely use the correlation field in SR0 (see Chapter 7).

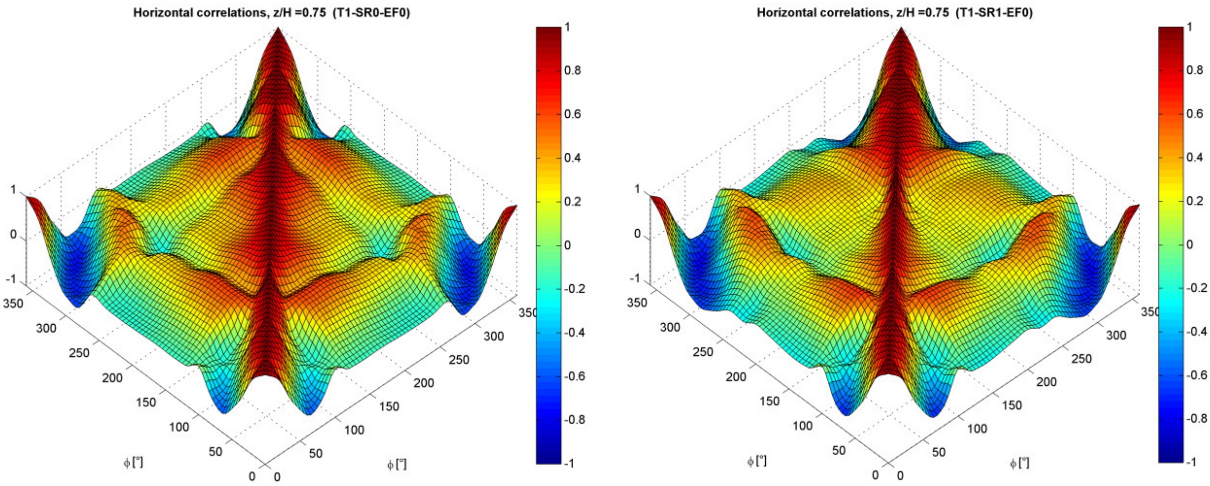

a) *b)*

Figure 5.42 Horizontal correlation field at z/H = 0.75: a) without rings; b) with 10 rings (WiSt, T1-SR0/SR1-R1-EF0)

The vertical cross-correlations are not modified at stagnation and in the frontal region, as motivated in section 5.4. Further downstream, the correlations between levels may show drops in the vicinity of the rings and even at middle levels, as in Figure 5.33. In the wake, there is a reduction of vertical correlations, which is, however, not particularly relevant because the fluctuations in the wake are small.

5.6 Mitigation strategies

After the full investigation, any reason could not be detected which suggested the disappearance of the phenomenon at higher Re. It is then believed – so far, on the basis of this work – that the same phenomenon should also occur in full-scale, whether the same number and size of rings of the experiments are used.

The case of ten big rings, i.e. SR1, represents the upper limit in a design condition. Such big rings may not be necessary. Neverthless, the designer should be aware that an improper use of stiffening rings may produce a negative effect, i.e. the improvement in the structural response can be accompanied by an even more severe load condition.

In the case of rings, the wind load depends on the number, on the size and on the distribution of rings, because different flow structures, like tip-associated vortices and separation bubbles develop in a different way. Therefore, a unified wind load condition for the tower with rings does not exist. The experiments during this work tested several situations and even more are recommended for future research. In chapter 7, a simplified load modelling is provided to the designer. Being unique and being simplified, it cannot include all the load patterns produced by the many different distributions of rings along the height.

Therefore, the aim should be to mitigate, as much as possible, the effect of the rings on the load, in order to design the tower with reference to the design wind load in SR0, that is an established load condition.

Intuitively, small rings at large distance reduce the bistable asymmetric effect. Section 5.3.6 showed that with five rings, even big, the flow is neither bistable nor asymmetric. From the structural point of view, however, it might be preferred to use small rings but more than five. The use of small rings is of course a mitigation strategy, but the tests have shown that e.g. ten rings, even small, still produce an asymmetric flow. In this regard, it is also important to remember that with ten rings, either small or big, the tip-associated vortices are suppressed. Ten rings equally spaced are placed, in this case of study, at a smaller distance than the tower diameter (2/3D). This suggests that a too dense distribution of rings disturbs the tip-associated vortices.

The more pronounced fragmentation of the big vortices on one side of the cylinder produces the not-symmetry, once it is analyzed in the frequency domain. Therefore, rings at a larger distance than one diameter (or, more safely, at 4/3D as it is in SR5) mitigate the effect. If needed, the rings can be placed at larger distance only in the tip region, where the tip-associated vortices are confined.

In any case, it must be remembered that the bistable asymmetric effect is naturally mitigated by the presence of efflux inside the chimney. This is a great advantage, even though out-of-use conditions cannot be neglected.

Chapter 6. **Experimental and numerical evidence**

This chapter confirms and further analyzes the experimental evidence of asymmetric bistable flow at WiSt laboratory, by a cross-checked investigation at CRIACIV wind tunnel and numerical simulations.

6.1 CRIACIV wind tunnel (University of Florence)

6.1.1 Characteristics and instrumentation

The CRIACIV laboratory (Centro di Ricerca Interuniversitario Aerodinamica delle Costruzioni e Ingegneria del Vento, www.criaciv.unifi.it) is an open-circuit wind tunnel located at Polo Universitario Città di Prato, which is a branch of the University of Florence. The total length is about 22 m. The tunnel itself has a length of 11 m, with a slightly divergent shape from the inlet (in order to guarantee a constant pressure along the x-axis) and a test section of 2.4 m in width and 1.6 m in height. A turntable in the test section allows to test different wind directions, if necessary. A honeycomb grid is located at the inlet of the tunnel. Details of the wind tunnel are reported in the Drawing 4 on page 194).

The motor – with a nominal power of 160 kW – and the fan are placed at the end of the wind tunnel, followed by a T-shaped symmetric diffuser. The engine allows to attain a maximum wind speed of about 30 m/s with 1500 rounds per minute of the fan. The variation of the rpm is controlled through an inverter up to 50 Hz. The air flow can also be regulated by adjusting the pitch angle of the ten blades of the fan between 7.7 and 15.4. The experiments in this work are performed by setting the frequency of the inverter at either 45 Hz or 50 Hz and the pitch angle at 15.4.

The atmospheric boundary layer profile which is used in these experiments is produced by three bigger "shark-fins" and four smaller spires, followed by roughness panels with wooden cubes (Figure 6.7).

The Prandtl tube allows to measure the static and the dynamic pressure of the incoming flow. During the experiments, only one Prandtl tube, placed above the tower, has been used during pressure measurements on the model. For specific purposes, for example the measurement of the efflux velocity or the mean wind profile at the tower position, a second Prandtl tube is introduced. For the acquisition of these signals, the instruments are connected to a pressure transducer (Setra System, model 239). The signal is then converted by 32-bit NI card and acquired by a PC. A sampling frequency of 500 Hz is used in the experiments with the Setra System.

Figure 6.1 CRIACIV wind tunnel (University of Florence)

The mean wind profile at the tower position was measured during the experiments by using a mobile Prandtl tube. The mean wind velocity has been indirectly calculated from the dynamic pressure, by using Bernoulli equation. The variation of air density due to temperature variation during the experiments is considered. The result, with respect to the velocity at the main Prandtl tube, is plotted in Figure 6.2. In fact, in order to evaluate pressure coefficients from pressure measurements, the velocity pressure itself, and not the velocity, is used in the calculation.

The turbulence intensity and integral length scale of turbulence L_{ux} were previously measured and tabulated in an internal report of the laboratory. Those data, resulting from hot-wire measurements (Figure 6.3 and Figure 6.4) are referred to in this work.

The pressures on the tower are measured using two different types of pressure scanners:

- Type 1: PSI 8400, consisting of four acquisition units having 16 piezoelectric transducers each and two acquisition units having 32 transducers each. A total amount of 128 pressures can be recorded simultaneously at a sampling frequency of 250 Hz[4] and a time duration of 30 s.

- Type 2: DTC-Initium, two acquisition units having 32 piezoelectric transducers each. A total amount of 64 pressures can be recorded simultaneously at a sampling frequency of 500 Hz.

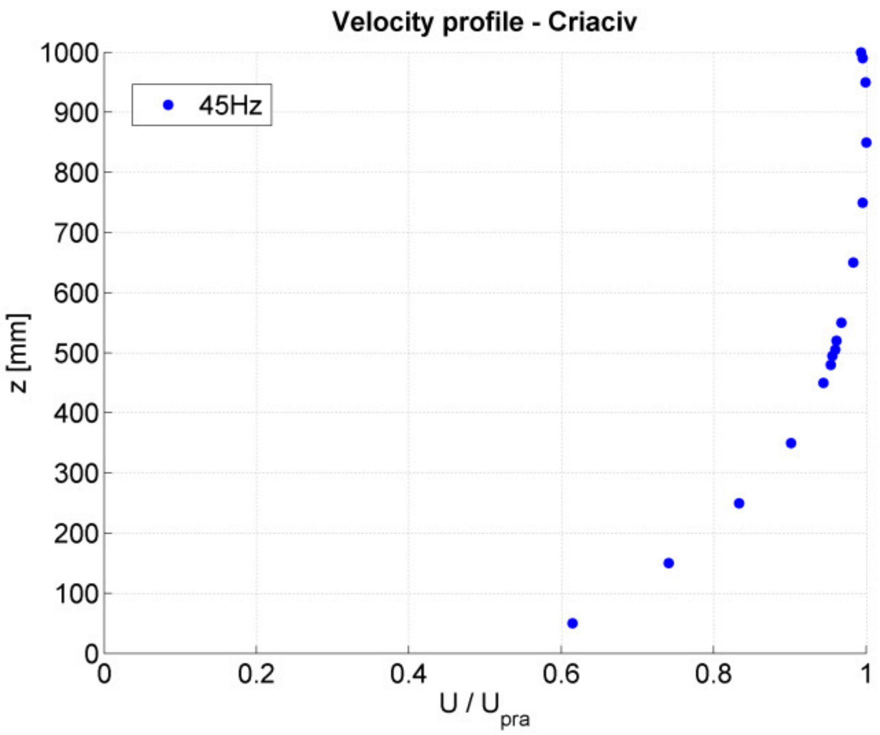

Figure 6.2 Mean wind profile

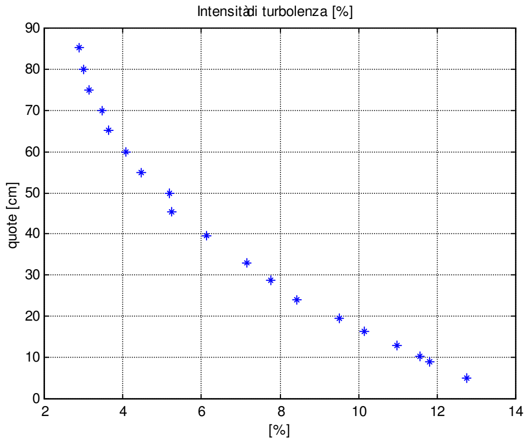

Figure 6.3 Turbulence Intensity Iu (%). (Procino, 2010)

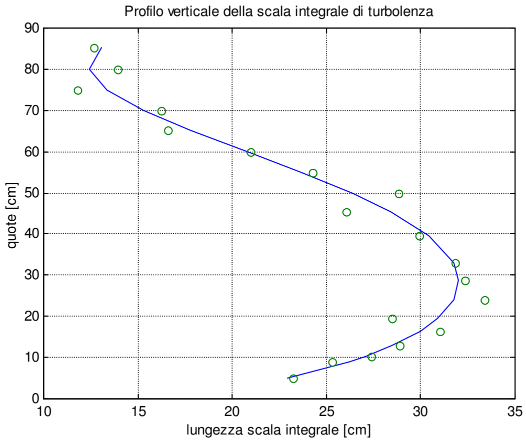

Figure 6.4 Integral length scale L_{ux} (cm). (Procino, 2010)

---

[4] Pressures can be measured with a sampling frequency up to 1 kHz, but the sampling frequency is inversely proportional to the number of channels which are used at the same time. if the maximum number of channels (128) is used simultaneously, the sampling frequency decreases to 250 Hz.

6.1.2 Outline of the experiments

The first purpose of CRIACIV experiments is to confirm the experimental evidence at WiSt laboratory, concerning the bistable and asymmetric flow. In every wind tunnel, it is absolutely common to have some disturbance in the flow. The comparison of results in the two wind tunnels proves that the occurrence of the bistable flow is not induced by some local distortion of a certain laboratory. Furthermore, the wind tunnel tests at CRIACIV allowed to better investigate the bistable flow, also at lower levels.

The two different types of pressure scanners cannot be combined together, therefore the tests are divided into two sets: one with 64 sensor type 2, distributed on three external levels in each measurements, able to measure for a relatively long time (131 s) at high sampling frequency, i.e. 500 Hz; one with 128 sensors type 1, distributed at several levels and able to measure at 250 Hz for a duration of 30 s. The set n.2 aims to attain a global correlation field, but with lower degree of detail.

The tests are repeated by using two wind tunnel velocities: $U_{pra} \approx 28$ m/s (frequency of the wind tunnel inverter = 45 Hz) and $U_{pra} \approx 30$ m/s (frequency of the wind tunnel inverter = 50 Hz). The Reynolds number are: $Re = 2.8*10^5$, $Re = 3.0*10^5$. The first one is more comparable with WiSt; the second one is a further test at a slightly higher Re, but it did not show any additional relevant feature. Therefore, the main study has been based on $Re = 2.8*10^5$.

The following series of measurements, associated to the measure of circumferential levels or vertical lines, are defined. Some of the 128 sensors type 1 were out of use at the time of the measurements. The internal pressures were measured, too, in some of the free channels.

- MS51: levels z = 990-950-910 mm;
- MS52: levels z = 910-890-850 mm;
- MS53: levels z = 850-750-650 mm;
- MS54: levels z = 650-550-520 mm;
- MS55: levels z = 520-505-495 mm;
- MS56: levels z = 495-480-450 mm;
- MS57: levels z = 450-350-250 mm;
- MS58: levels z = 250-150-50 mm;
- MS59: verticals at 0°, 20°, 40°;
- MS60: verticals at 60°, 80°, 100°;
- MS61: verticals at 120°, 140°, 160°;
- MS62: verticals at 180°, 200°, 220°;

- MS63: verticals at 240°, 260°, 280°;
- MS64: verticals at 300°, 320°, 340°;
- MS65: levels z = 950-850-750-650-550(only 9 taps)-450(only 9 taps)-50 mm;
- MS67: levels z = 950-850-750-650-550-450-350-250-150-50 mm (only 9 taps at each level);

The experimental campaign was articulated in the following two sets:

Set n.1 (March 2012):
Pressure scanners type 2
Turbulence setting: T5
Rings: SR1
Efflux: EF0/EF1
Surface roughness: R1
Wind tunnel velocity (Hz): 45/50
Measurement series: MS51/52/53/54/55/56/57/58/59/60/61/62/63/64;

Set n.2 (April 2012):
Pressure scanners type 1
Turbulence setting: T5
Rings: SR0/SR1/SR5/SR7
Efflux: EF0/EF1
Surface roughness: R1
Wind tunnel velocity (Hz): 45/50
Measurement series: MS65/67.

The efflux inside the tower is calibrated at a velocity about one half of U_{pra} (Figure 6.5). In order to adapt the model to the facilities of the laboratory, it was decided to simplify the installation (Drawing 3 on page 126, at WiSt) and remove the ventilator. In fact, a suitable opening below the model was enough to guarantee the proper efflux capacity and velocity (Figure 6.8).

However, as previously explained, the most interesting results referred to the condition without efflux.

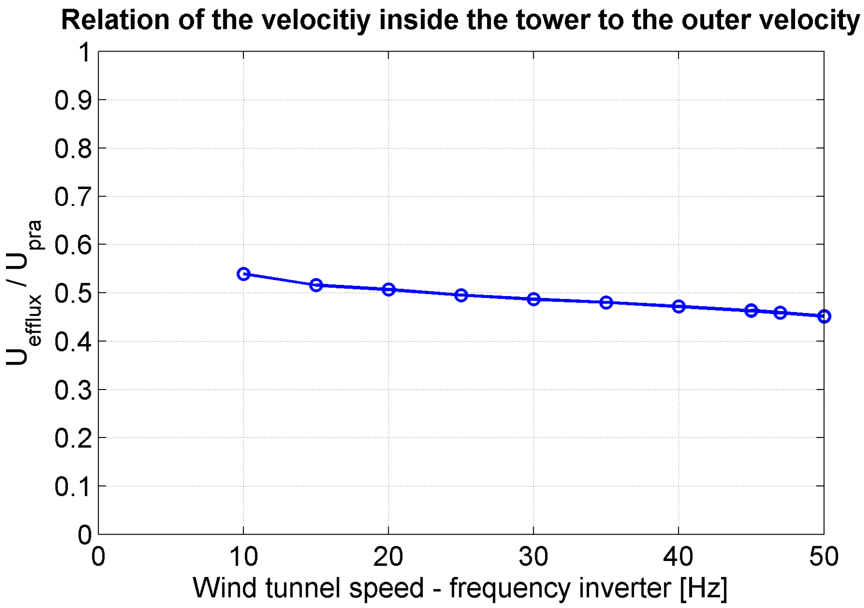

Figure 6.5 Efflux velocity

The model for the experiments is the same as in Bochum. A picture of it in CRIACIV wind tunnel is reported below (Figure 6.6). The smooth collector roof was not placed during these tests. In fact, it was seen that its presence did not affect significantly the substance of the results.

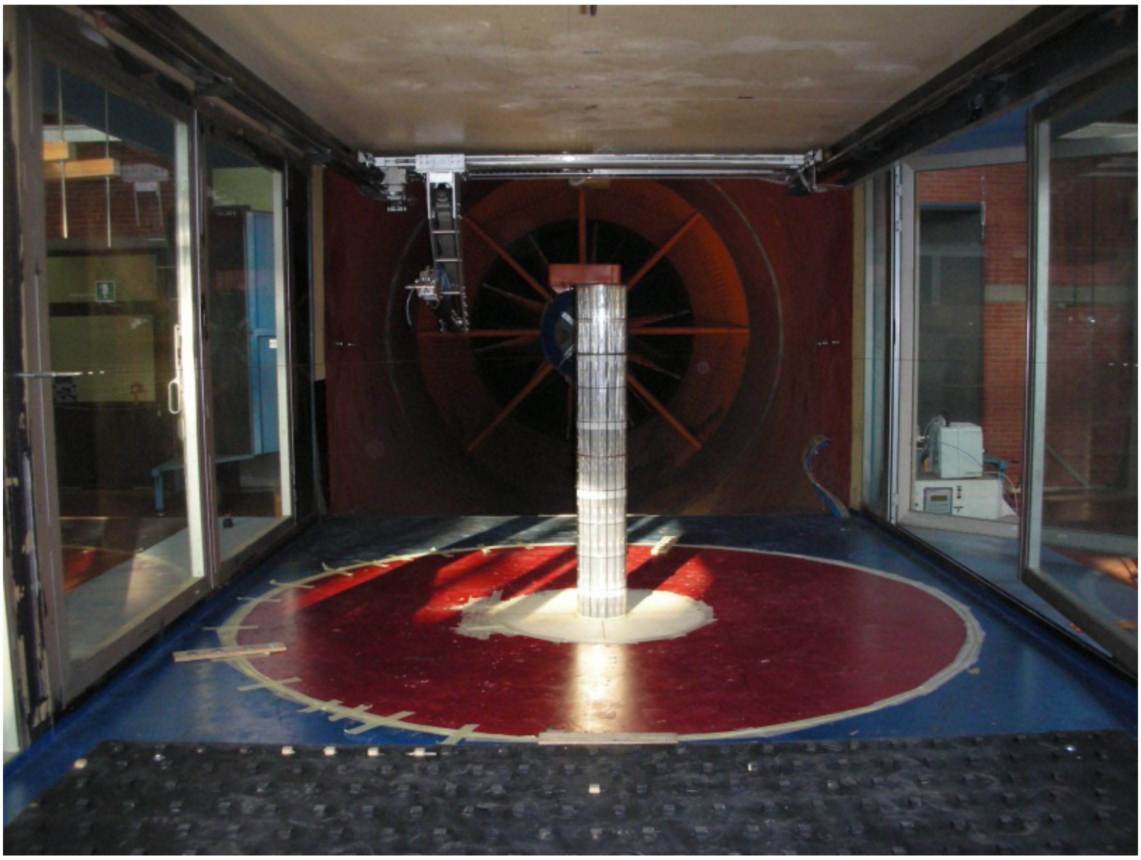

Figure 6.6 Solar tower at CRIACIV wind tunnel

Figure 6.7 Atmospheric boundary layer facilities at CRIACIV

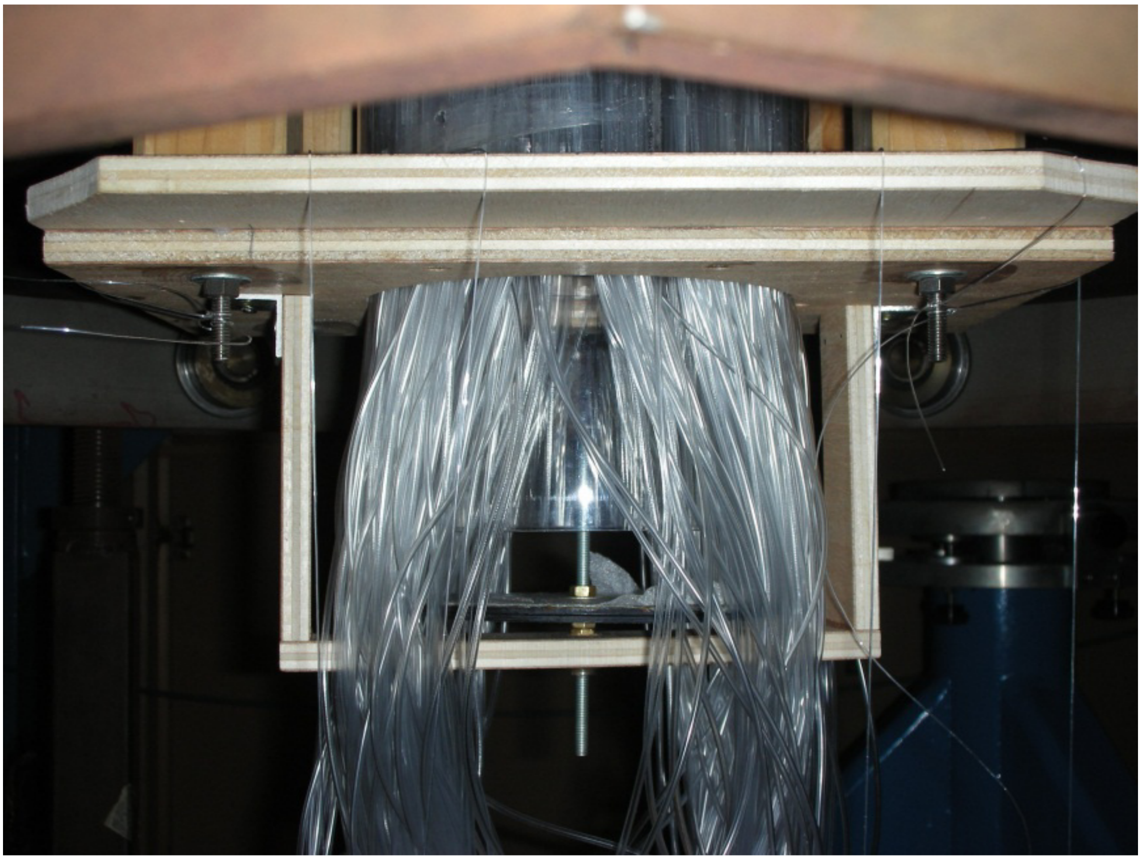

Figure 6.8 Opening below the model for creation of the efflux

DRAWING n.4 CRIACIV Boundary layer wind tunnel University of Florence - PLAN

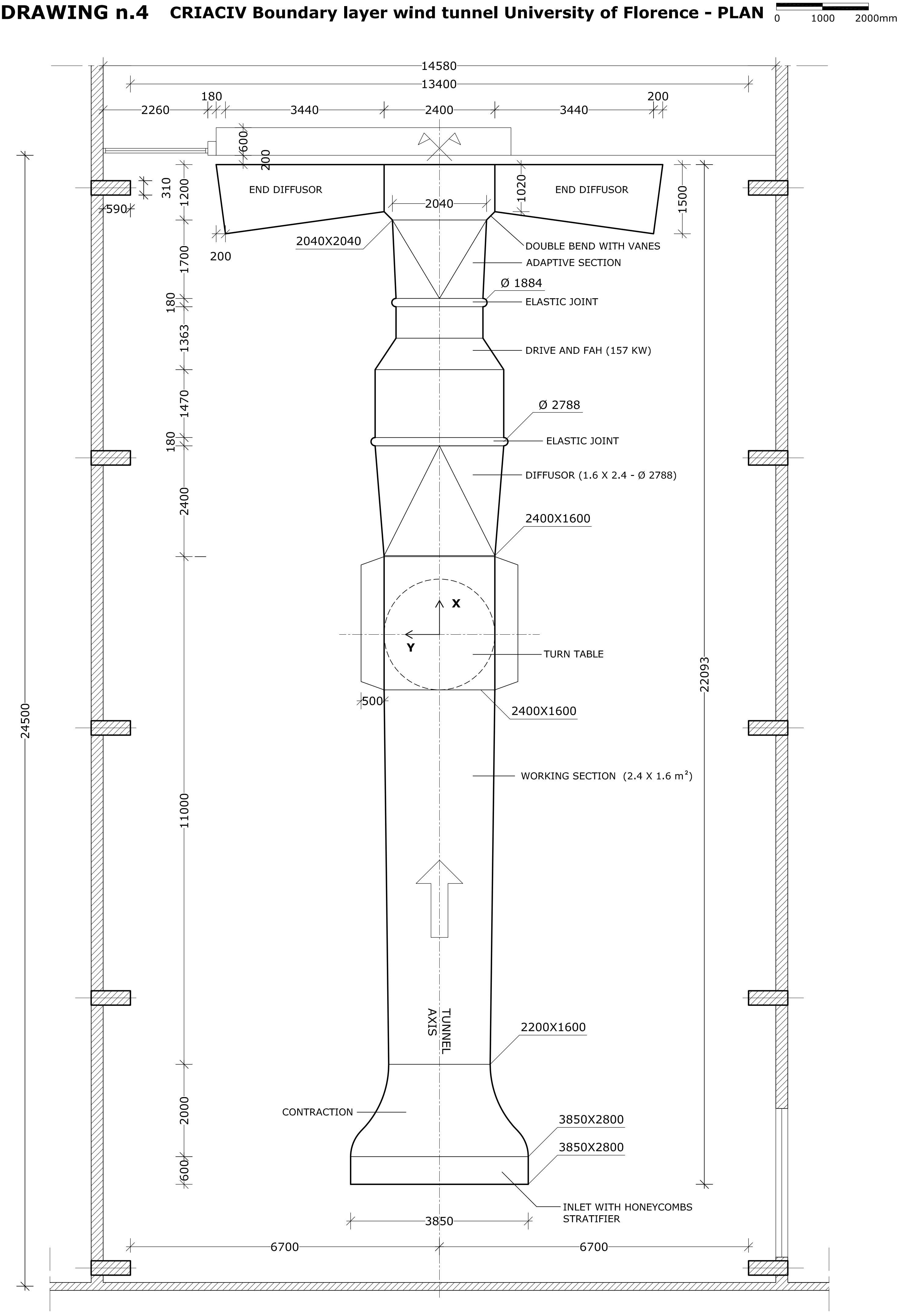

6.2 The bistable flow at CRIACIV

The wind tunnel tests at CRIACIV prove that the bistable flow is a fundamental physical phenomenon, which is not induced by some local distortion of the flow in a given laboratory. Figure 6.9 shows the comparison of pressure coefficients at 100° and at different levels along the height of the tower in the two wind tunnels, in case of ten rings along the height (SR1). The model is the same, therefore any difference between results is only attributable to the flow.

At first sight, it can be seen that the standard deviation of the time histories in each state is different at WiSt and CRIACIV, but this is not surprising, because of the different I_u. The corresponding values of I_u are reported in Table 6.1. Apart from that, the jumps occur in the same manner in the two wind tunnels.

By looking at the time histories, another evidence in the tip region is the existence, in the two wind tunnels, of a predominant state. This lasts longer in every time history. At WiSt, the predominant state in the highest compartment is state 1, i.e. the one which is characterized by positive mean lift in the reference system of the wind tunnel (Drawing 4, page 194). Being the x-axis in the along wind direction, the positive lift in the state 1 is created by a separation bubble on the 180°-360° side of the cylinder. At CRIACIV, the situation is reversed and the predominant state in the highest compartment is state 2, i.e. the one which is characterized by negative mean lift. It means that at CRIACIV the separation bubble in the highest compartment preferably develops on the 0°-180° side, instead of 180°-360° as in WiSt. Then, along the height, the inversion proceeds according to the top condition. In any case, the existence of a predominant state is not due to model imperfections, but to the flow. The question arises about what should be expected in ideal conditions. These cannot be perfectly reproduced in any experiment, but they can be reasonably assumed in a CFD simulation (this issue is addressed in section 6.4).

At a certain level along the height a sort of disruption of the bistable flow starts. The jumps between the two states become more rapid on one side of the cylinder, so that the actual state of the flow is a mixture between the two states. A further insight in this phenomenon will be discussed at the end of this section by using the histograms of pressures along the height until the very low levels. The disruption of the bistable flow starts on the high-suction side of the cylinder, i.e. on the bubble side. This is confirmed in the two wind tunnels by looking in Figure 6.9 at C_p(650mm,100°) in WiSt and C_p(750mm, 100°) in CRIACIV: those pressure taps lie, during the predominant state, on the bubble side. Figure 6.12 clarifies better what occurs at CRIACIV at the levels of disruption on the two sides of the cylinder. It can be seen that the normal side (NS) remains unaffected until a lower level. This explains why the mixture in C_p(750mm, 260°) and C_p(650mm, 100°) in Figure 6.12 is not so evident. In fact, at those levels the separation bubble preferably develop on the other side of the cylinder, as confirmed by C_p(750mm, 100°) and C_p(650mm, 260°). There, instead, the disruption is clear because those pressure taps lie, during the predominant state, on the bubble side.

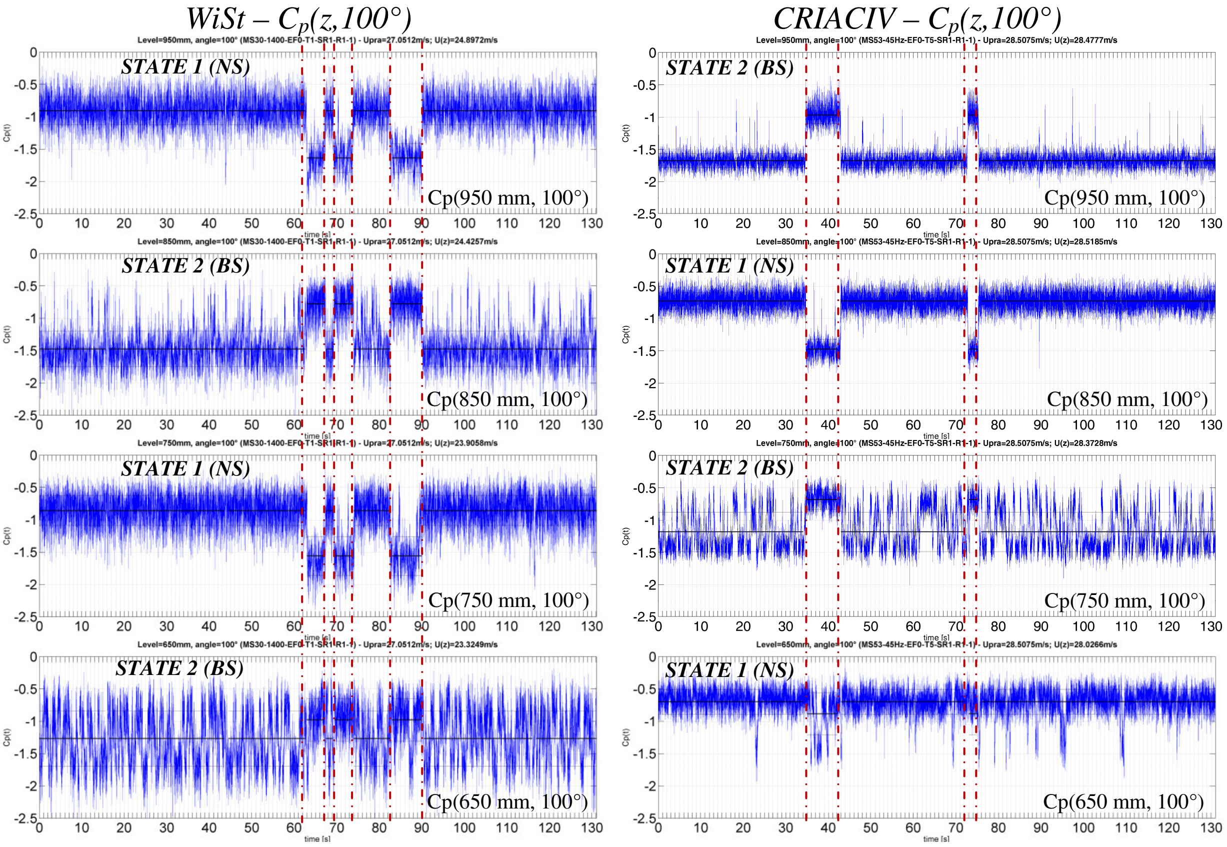

Figure 6.9 The validating result: Wist&CRIACIV (T1/T5-SR1-EF0-R1)
NS = normal side; BS = bubble side (Re = $2.5*10^5$ at WiSt, Re = $2.8*10^5$ at CRIACIV)

Table 6.1 Turbulence intensity at WiSt and CRIACIV

z [mm]	**I_u at WiSt**	**I_u at CRIACIV**
950	0.0794	0.0283
850	0.0823	0.0283
750	0.0863	0.0309
650	0.0925	0.0359

The level at which the bistable flow starts disrupting is different in WiSt and CRIACIV. In particular, at WiSt it starts at 650 mm, while at CRIACIV it starts one compartment above, i.e. at 750 mm. This is not related to I_u, because the value of I_u at

CRIACIV at 750 mm is much lower than the I_u at WiSt, even in the highest compartment (Table 6.1). However, this must be related to the type of atmospheric boundary layer, as it is further proved at WiSt, through the tests in uniform flow (namely T3), shown in Figure 6.13. The figure plots the time histories at levels 550 and 450 mm. The equivalency between the two states is not exactly fulfilled at those levels, but it can be seen that the disruption of the bistable flow, i.e. the more rapid alternation of the two states, starts at level 450 mm on the bubble side. In uniform flow (T3) this happens two compartments lower than in atmospheric boundary layer flow (T1), in the same wind tunnel. Therefore, the spanwise development of the bistable flow must be influenced by the type of atmospheric boundary layer. However, so far it has not been identified a certain property of the boundary layer which is univocally related to the disruption of the bistable flow at a certain level.

The equivalency of the two states, in terms of mean and rms values of the pressure coefficients, is shown in Figure 6.10 and Figure 6.11 (at z = 750 mm), which are comparable to Figure 5.5 and Figure 5.6 at WiSt, respectively.

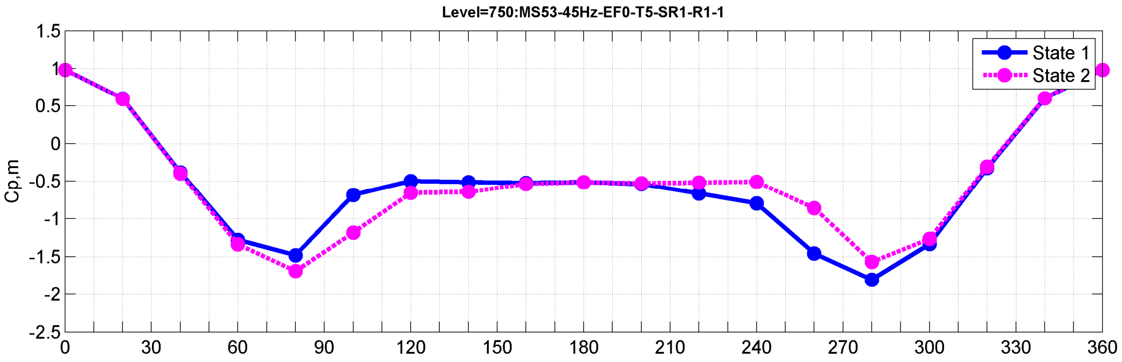

Figure 6.10 $C_{p,m}$ at 750 mm, Re = $2.8*10^5$ (CRIACIV, T5-SR1-EF0-R1)
to be compared with Figure 5.5

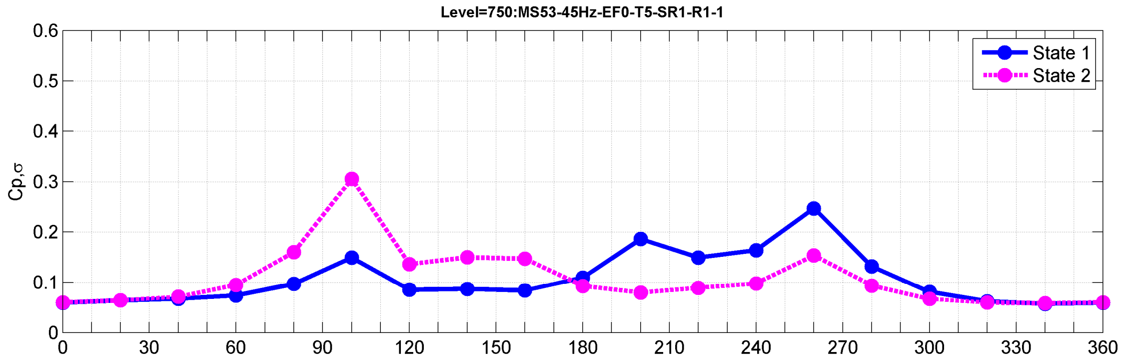

Figure 6.11 $C_{p,\sigma}$ at 750 mm, Re = $2.8*10^5$ (CRIACIV, T5-SR1-EF0-R1)
To be compared with Figure 5.6

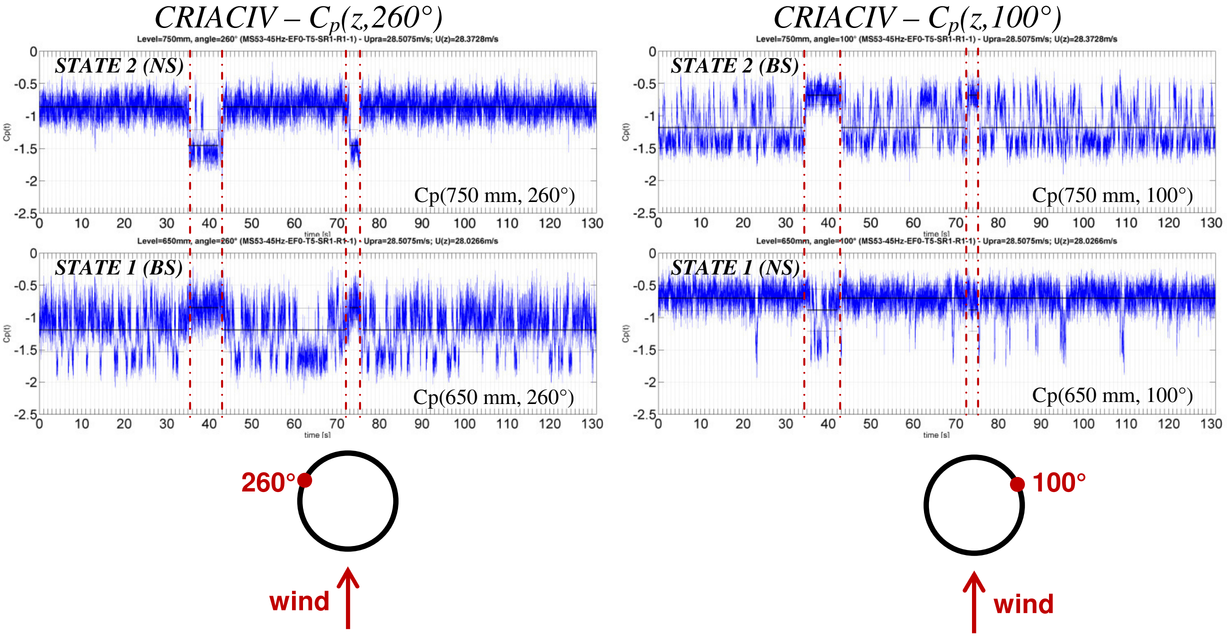

Figure 6.12 The levels of disruption (CRIACIV, T5-SR1-EF0-R1)
NS = normal side; BS = bubble side (Re = $2.8*10^5$, z = 650, 750 mm)

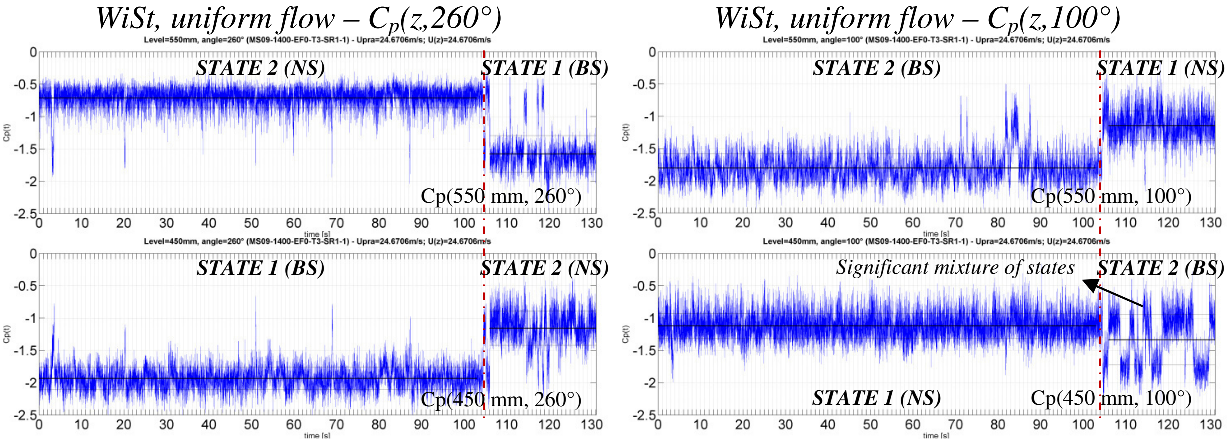

Figure 6.13 Lowering of disruption level in uniform flow (WiSt, T3-SR1-EF0-R1, Re = $2.5*10^5$)

The inversion of the asymmetry along the height of the cylinder is confirmed at CRIACIV, as proved by the previous pictures. It is a sort of cascade effect, which is governed by the tip. Such a spanwise inversion is the result of an interaction between compartments. In order to motivate flow movements between compartments, the pressures and the pressure differences above and below one ring within only one state are plotted in Figure 6.14. The curves of $C_{p,m}$ at 910 and 890 mm are reported in the figure together with the green lines, namely Dp, which represent the difference $C_{p,m}(890) – C_{p,m}(910)$. At WiSt, on the side of the cylinder 0°-180°, the flow moves vertically towards the lower pressure, i.e. towards the compartment with the separation bubble. This results, on the 0°-180° side of the cylinder, in a downwards movement. The opposite occurs on the other side of the cylinder, with an upwards movement, always towards the high-suction, i.e. the bubble-side. All of that is valid during each of the two stable states of the flow. In particular, in Figure 6.14 the results are averaged over the predominant interval. The results at CRIACIV are in wonderful agreement[5].

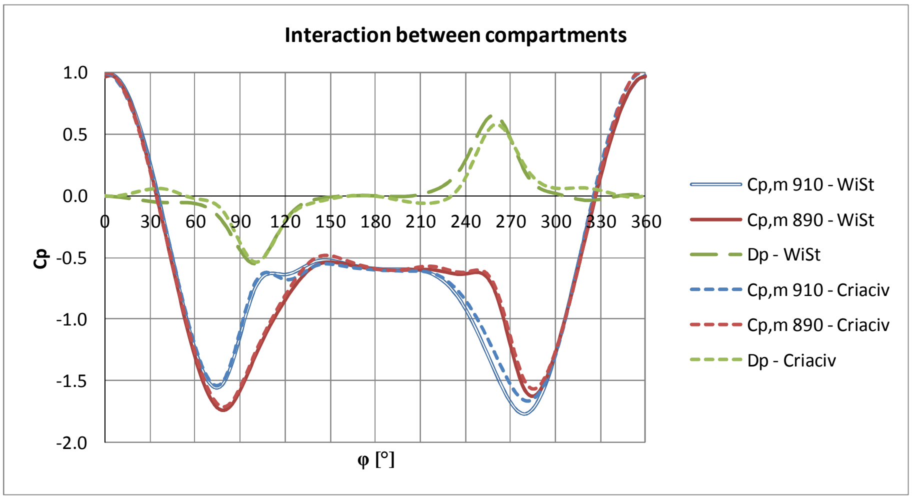

Figure 6.14 Pressures and pressure differences between compartments, above and below the ring n.9 (WiSt&CRIACIV, T1/T5-SR1-EF0-R1)

Figure 5.33 showed the cross-correlations of the lift coefficient at WiSt, with reference height z = 950 mm. In the case of ten rings, a drop of the cross-correlations at Δz = 100 mm due to the missing contribution of the tip-associated vortices was evident. Instead, such a contribution was not disturbed by the presence of only five rings. This is confirmed at CRIACIV in Figure 6.15, both in terms of cross-correlation coefficients and in terms of co-spectra.

In this regard, one comment deserves further attention. The results, so far, have shown:

- the asymmetric flow with spanwise inversion along the height is a cascade effect from the tip (see also section 6.4);
- although it seems to be a free-end effect, it is not merely governed by a modification of the top condition, i.e. by the top ring alone, because the bistable asymmetric flow disappears with five rings.. Rather, the phenomenon seems to be governed by the distribution of rings in the tip region. This conclusion would deserve to be further explored by experiments (Chapter 8).

---

[5] The predominant state at WiSt and Criaciv present separation bubbles on opposite sides. Therefore, in order to compare results in both wind tunnels within the predominant state, results at Criaciv are mirrored.

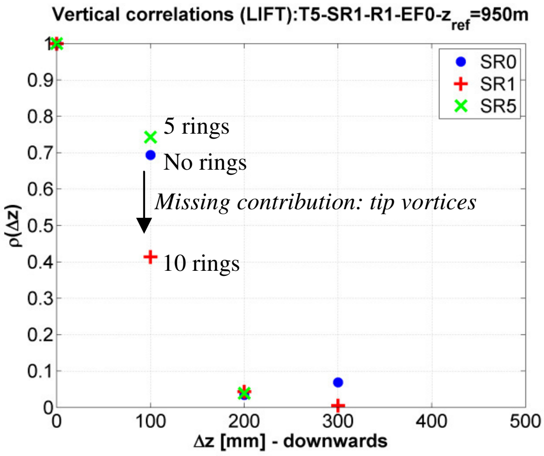

Figure 6.15 *Cross-correlation coefficients of* C_L *without rings (blue), 10 rings (red) and 5 rings (green).* z_{ref} *= 950 mm.*
To be compared with Figure 5.33

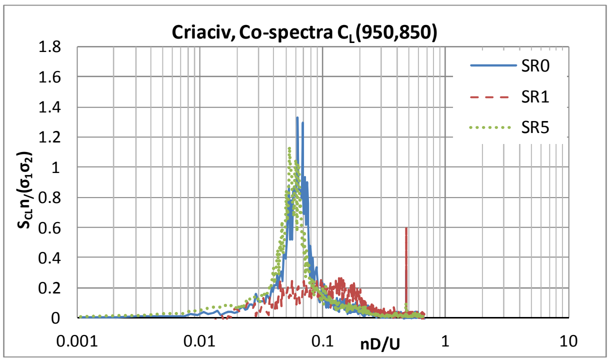

Figure 6.16 *Co-spectra of* C_L: $S_{CL}(z_1,z_2)*n/\sigma^2$ *vs nD/U,* z_1 *= 950 mm,* z_2 *= 850 mm (CRIACIV, T5-SR0/SR1/SR5-EF0-R1).*
To be compared with Figure 5.34

6.3 Influence of the atmospheric boundary layer

The atmospheric boundary layer produces vertical velocity gradients which enhance the flow movement from regions of relatively high pressure to regions of relatively low pressure (Chapter 3). Because of that, differences between results in the two wind tunnels should be expected, even in the mean pressure and force coefficients. In addition, the fluctuating loads are related to the turbulence intensity of the flow and the different length scales influence the load correlation. Chapter 7 takes advantage of the tests in different conditions of the atmospheric boundary layer, in order to model the wind load with regard to the flow properties. In this section, the differences on the circular cylinder without rings are discussed at the beginning, the effect on the bistable flow is commented at the end.

As regards the mean pressure coefficients, the tests in the two wind tunnels on the circular cylinder without rings showed that the most significant differences occurred in the middle region of the tower. It should also be mentioned that below 600 mm in SR0 only 9 measurements per level (instead of 18) were available at CRIACIV. Fitting curves (splines) are used to interpolate data. The available measurements at CRIACIV are highlighted in the graphs in Figure 6.17. The graphs show that the tip effect is perfectly reproduced in the two wind tunnels, without significant influence of the different atmospheric boundary layer. In view of the investigation of the bistable asymmetric flow, this is a great advantage. Instead, lower suction in the wake, as well at the flanges, is apparent at CRIACIV e.g. at 450 mm (Figure 6.17c). The higher pressure at the flanges in CRIACIV may depend on the downstream movement of spanwise flows, produced by the vertical pressure gradients. The mean suction in the wake is related to the steady recirculation region behind the tower and to the length of the eddy formation region. As shown in Chapter 3, the strength of the downwash in the near-wake may be weakened by the boundary layer. This issue is further addressed in the following with regard to the correlation coefficients.

In any case, the two wind tunnels agree in showing higher suction in the wake (and thus higher drag) close to the ground (see $C_{p,m}$ at 150 mm in Figure 6.17). The increase in the drag coefficient also in the lower half of the cylinder, and not only in the tip region was previously commented in Chapter 4, too, concerning preliminary results at WiSt.

Cp_σ is different in the two wind tunnels, due to different I_u. In particular, in Figure 6.17 at 950 mm Cp_σ at stagnation (directly related to I_u) is very small, much smaller than the fluctuations in the wake, which instead are almost the same in WiSt and CRIACIV. These latter are mainly body-induced. This issue, concerning body-induced and turbulence-induced pressure fluctuations, will be addressed in Chapter 7. The different values of Cp_σ (or, similarly, Cp_σ^2) in the two wind tunnels will be related to the corresponding turbulent intensities, in order to quantify the amount of body-induced fluctuations in laminar flow.

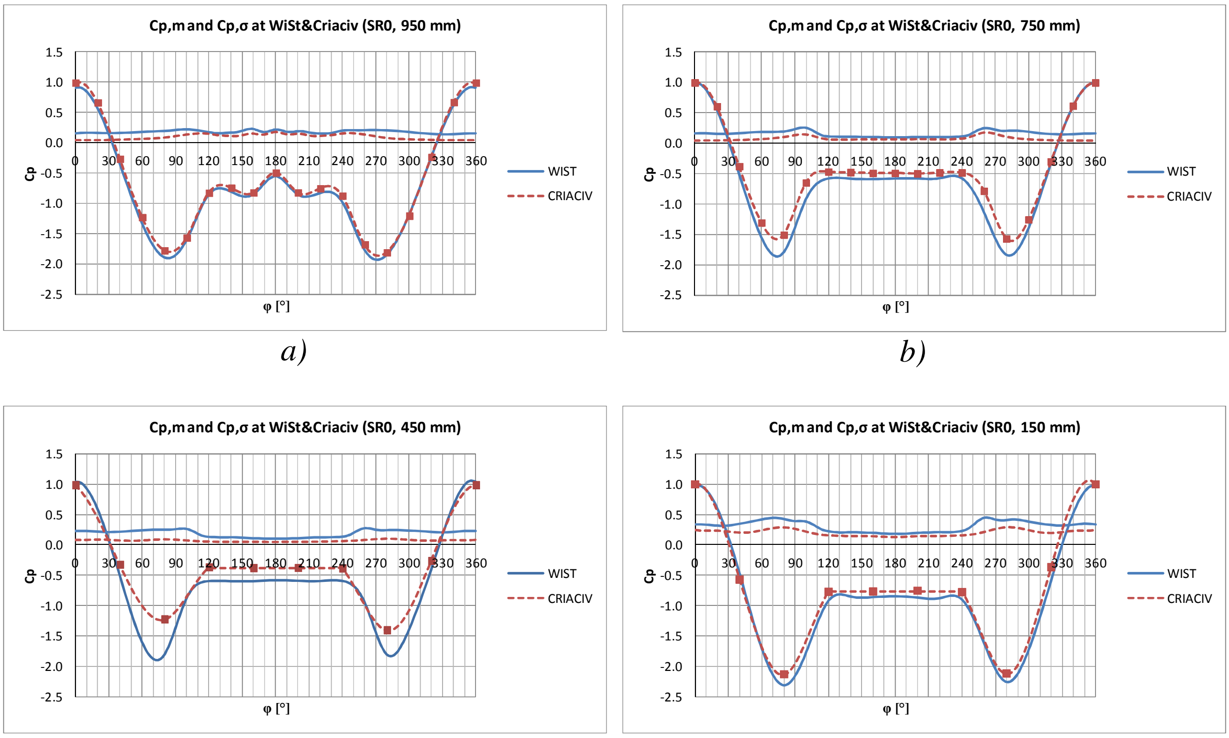

a) *b)*

c) *d)*

Figure 6.17 Mean and rms pressure coefficients at WiSt and CRIACIV (T1/T5-SR0-EF0-R1)

The cross-correlation coefficients and the correlation length L_{pz} depend on the correlation of the flow. In particular, L_{pz} can be related to L_{uz} (see Chapter 7). However, L_{uz} is not available at CRIACIV. In any case, the results at stagnation (where L_{pz} is directly related to L_{uz}) in the two wind tunnels do not show significant differences (Figure 6.18). L_{pz} at CRIACIV is generally lower, likely due to smaller L_{uz}.

The wake structure, instead, shows a certain dependency on the atmospheric boundary layer. As previously said, this is due to the strength of the downwash over the tip and to the formation of steady recirculation bubbles in the near-wake. The near-wake structure can be investigated by looking at the vertical cross-correlations. Representative graphs are shown in Figure 6.19, both in WiSt and in CRIACIV. Due to lack of data, the vertical cross-correlations at WiSt are measured at the angle 180°, while at CRIACIV the values at 160° are reported.

The cross-correlation $\rho(z_{ref}, \Delta z)$, with $z_{ref} = 950$ mm and Δz in the downward direction, shows that at WiSt there is a big steady vortex all along the height. Because of that, the cross-correlations are constant and different from zero even at large distance of separation. This cannot be modeled by a simple negative exponential function. The effect on the response will be quantified in Chapter 7, and it is now anticipated that it is not appreciably big (in the order of a few per cent of the response). In particular, the recirculation bubble at WiSt should arrive shortly above $z = 50$ mm (i.e. $\Delta z = 900$ mm). In CRIACIV, the same happens, but the recirculation bubble is smaller in size: it likely goes from the tip down to 450 mm. At larger distance of separation ($\Delta z > 500$ mm), the cross-correlation is zero. However, the steadiness of the recirculation bubble at CRIACIV is weaker, as shown by the rather low correlations even at small distance of separation, which weakly show a constant level.

In the lower half of the tower ($z/H < 0.5$), i.e. in the region of increase in the drag coefficient due to ground effects (see Chapter 4), a base vortex – maybe of the same type as that mentioned in Chapter 3 among the three-dimensional effects investigated by numerical simulations (Figure 3.18, Figure 3.19, Figure 3.20) – may be identified in the downwards cross-correlations with $z_{ref} = 550$ mm. The vortex can be identified by the still high correlation at $\Delta z = 500$ mm.

Last, but not least, it is interesting to observe that the upwards cross-correlations with $z_{ref} = 50$ mm show the same trend in the two wind tunnels. The base vortex is identified by the hump in the curve, at about $\Delta z = 500$ mm. At larger distances, the cross-correlations drop to zero.

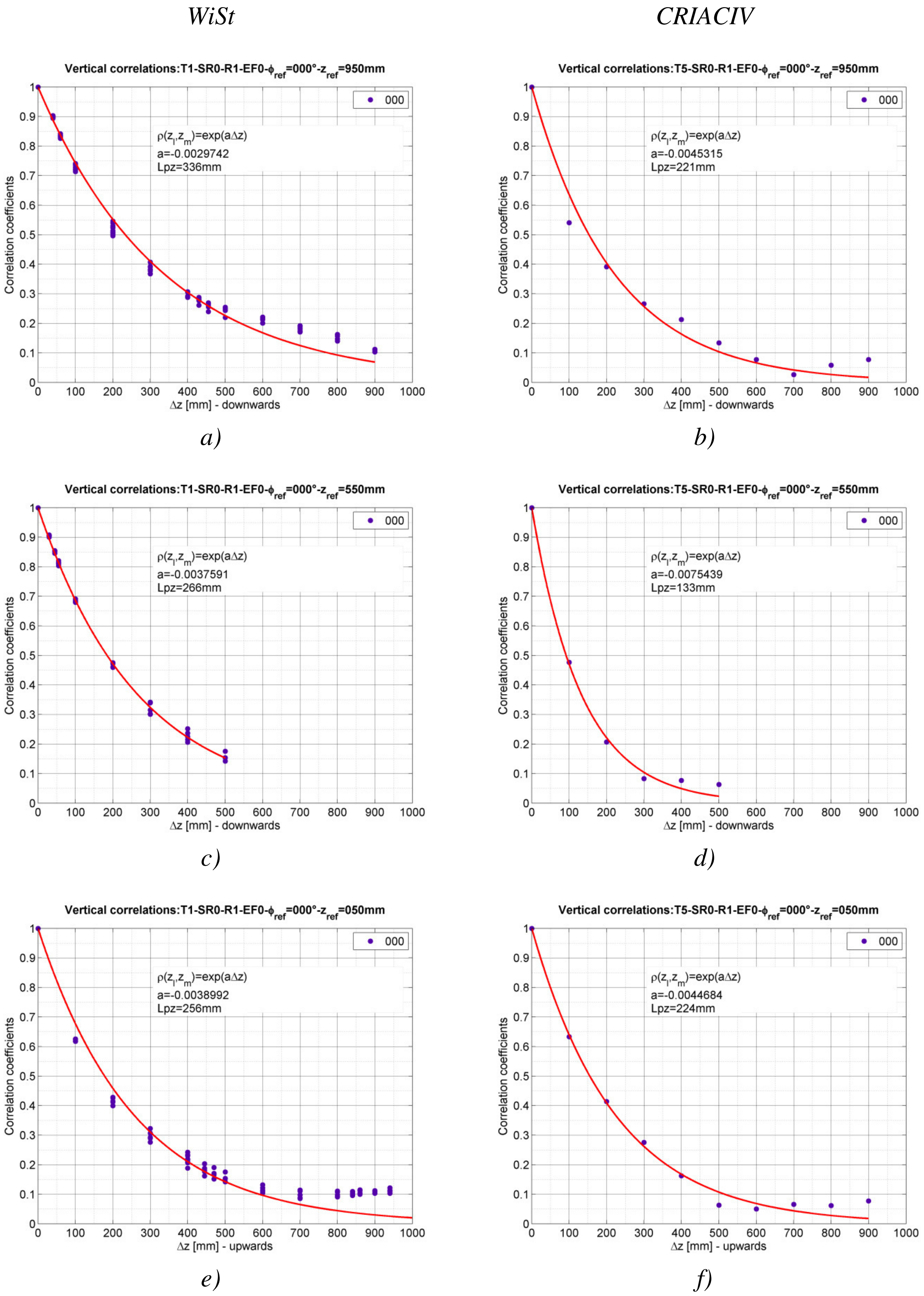

a) *b)*

c) *d)*

e) *f)*

Figure 6.18 Cross-correlation coefficients at stagnation, WiSt and CRIACIV (T1/T5-SR0-EF0-R1)

WiSt *CRIACIV*

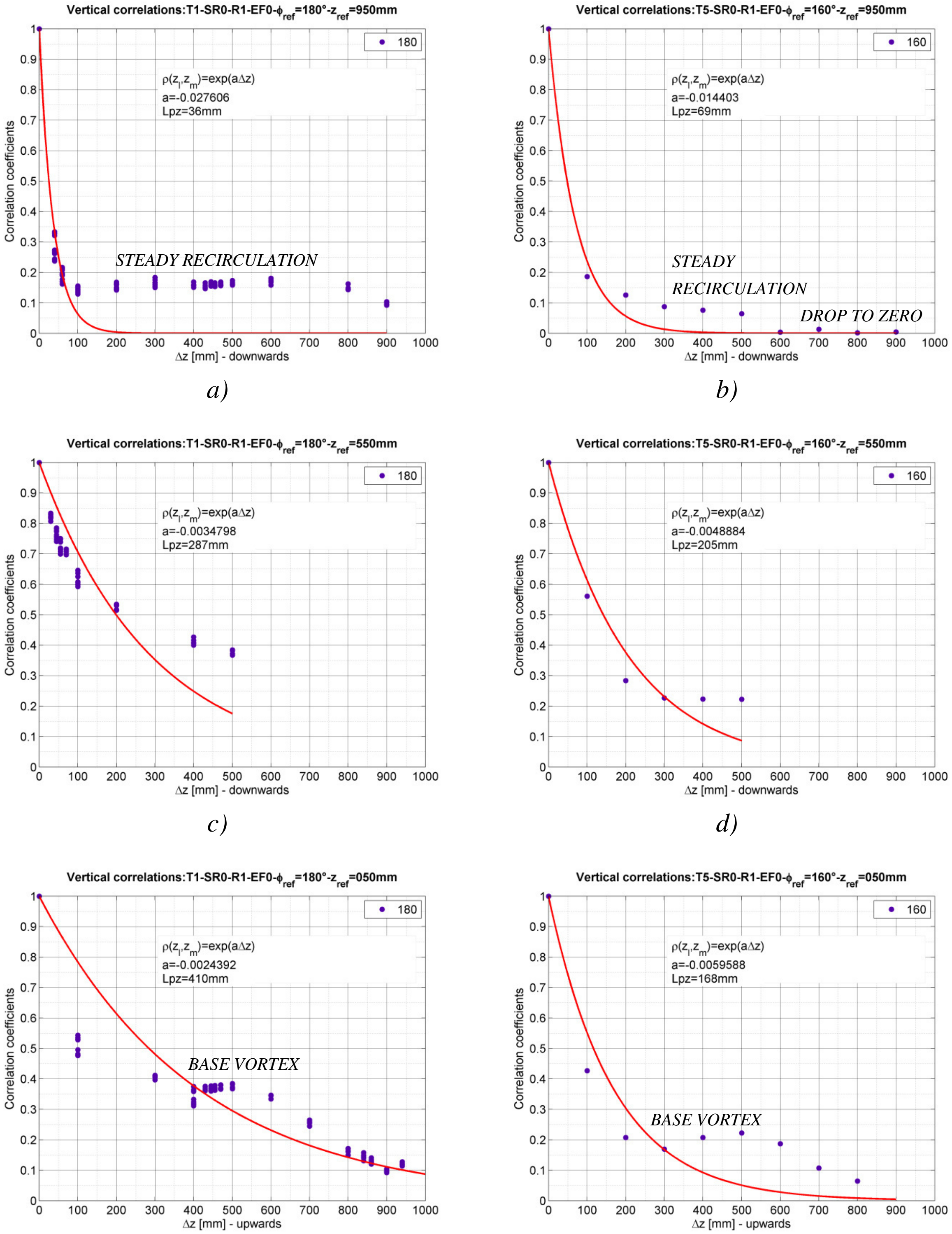

a) *b)*

c) *d)*

e) *f)*

Figure 6.19 Cross-correlation coefficients in the wake, WiSt and CRIACIV (T1/T5-SR0-EF0-R1)

In the tip region of the cylinder, a low frequency peak – around one third of the Strouhal number – appears in the spectra due to the formation of tip-associated vortices.

As reported in literature (Kitagawa et al., 2001; Park&Lee, 2000), the shedding frequency of such big vortices is not deeply influenced by the boundary layer. The wind tunnel tests at CRIACIV, compared to those at WiSt, represent a further confirmation. However, the atmospheric boundary layer does influence the shedding along the height and the interaction between the low-frequency peak and the Karman vortex shedding. In particular, as proved by Figure 6.20, at WiSt the Karman vortex shedding ($S_t = 0.2$) strongly interacts with the tip-associated vortices already at $z/H = 0.85$ and definitely predominates at $z/H = 0.75$. All of that occurs at CRIACIV, too, but at a level which is lower of about 0.1H. In any case, it is confirmed in the spectra that in both wind tunnels the lower non-dimensional shedding frequency is about 0.065.

The explanation regarding the influence of the atmospheric boundary layer on the spanwise variation of the Strouhal number can be indirectly related to the different near-wake structure in the two wind tunnels (Figure 6.19). In fact, the decrease in the Strouhal number in the tip region is due to entrainment of flow over the tip (Farivar, 1981), as explained in the state of the art (Chapter 3). It is a sort of blockage effect, like a splitter plate, which elongates the eddy formation region. At CRIACIV, the atmospheric boundary layer is almost vanished in the tip region (i.e. the shear stress is almost null and the mean wind speed is constant). This can be a realistic situation, especially for the 1.5 km tower. In this condition, the effect is a stronger entrainment in the near-wake at high levels, as also confirmed by Park&Lee (2002) in uniform flow, with respect to boundary layer flow (Figure 3.31). So, at $z/H > 0.75$, the lower frequency peak predominates. Below such a level, the Karman vortex shedding peak arises. The almost constant noise at high frequencies in CRIACIV spectra, especially at $z/H = 0.65$, could be caused by the vibration of the turntable, which could not be completely avoided during the experiments.

It can be concluded that the near-wake structure is different in the two wind tunnels. Since the model is the same, such differences can only depend on the atmospheric boundary layer. In terms of mean wind load, this results in different wake suction (and thus different drag coefficient). In terms of fluctuating load, the spectra show a different interaction along the height between tip-associated vortices and Karman vortices.

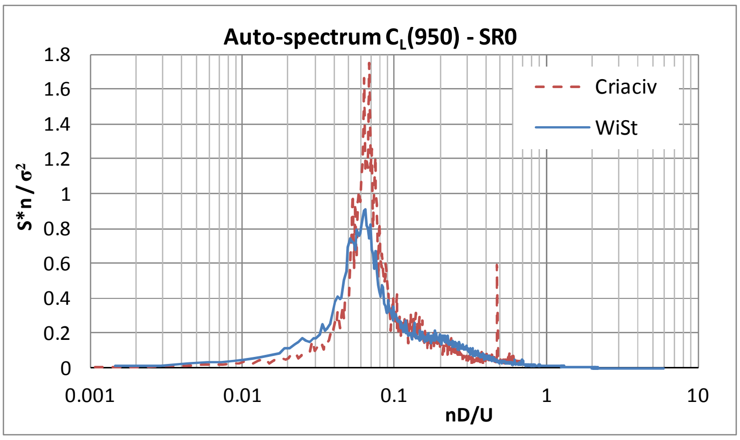

a) z = 950 m

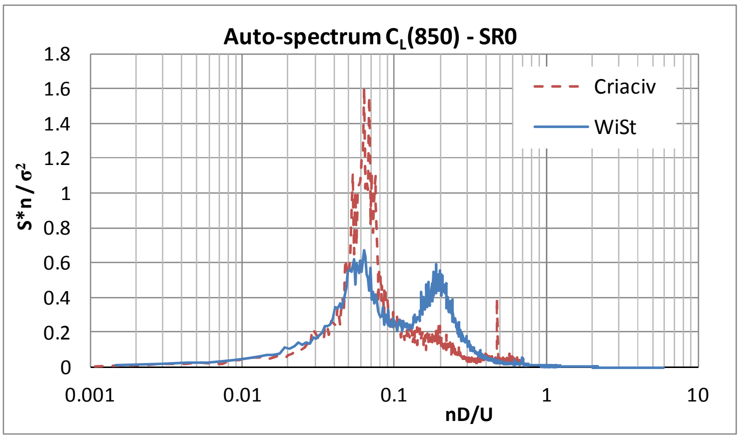

b) z = 850 m

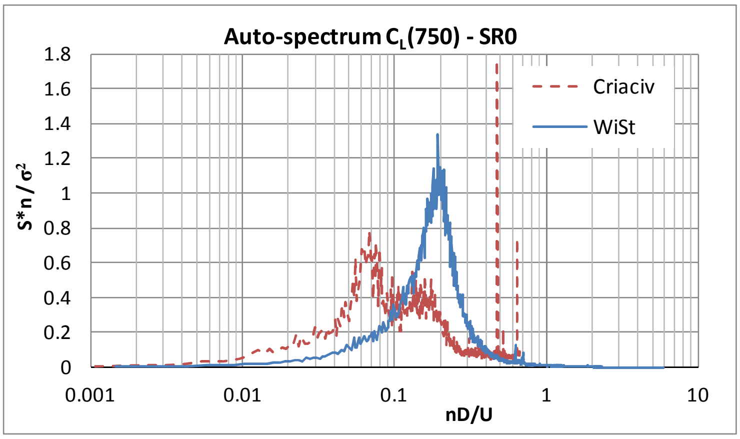

c) z = 750 m

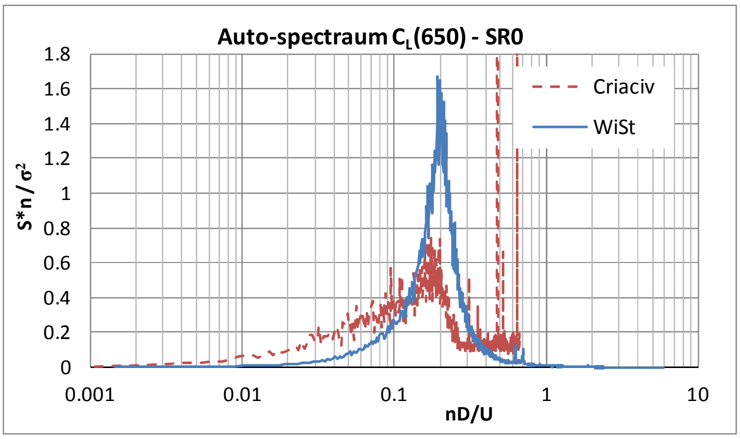

d) z = 650 m

Figure 6.20 a-d) Lift spectra along the height without rings at WiSt and CRIACIV (T1/T5-SR0-R1-EF0)

Last but not least, the atmospheric boundary layer has an influence on the vertical development of the bistable flow. It has been already anticipated that the disruption of the boundary layer starts higher at CRIACIV, with respect to WiSt (Figure 6.9). Unfortunately, measurements at low levels in case of 10 rings were not available at WiSt. They are instead available at CRIACIV and allow to define a complete overview along the height.

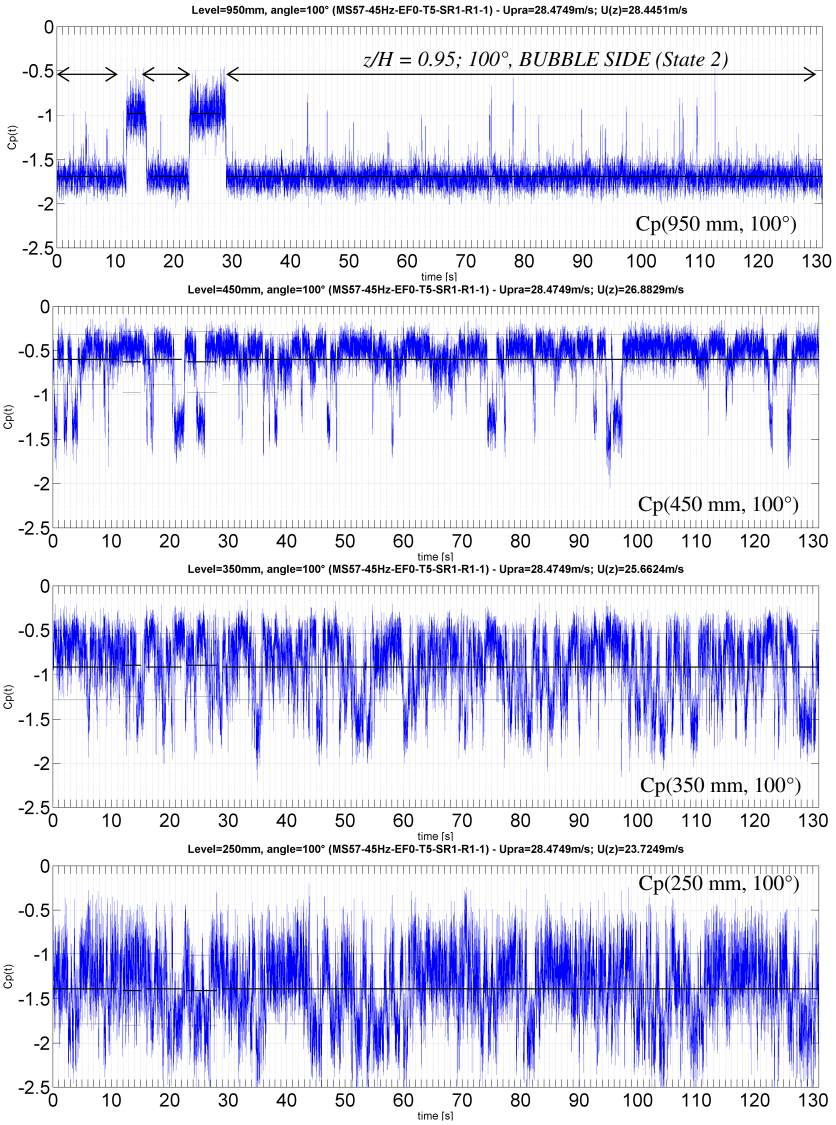

Figure 6.21 Bistability of the flow at low levels, $C_p(z/H,100°)$, simultaneous time histories (CRIACIV T5-SR1-R1-EF0, Re = $2.8*10^5$)

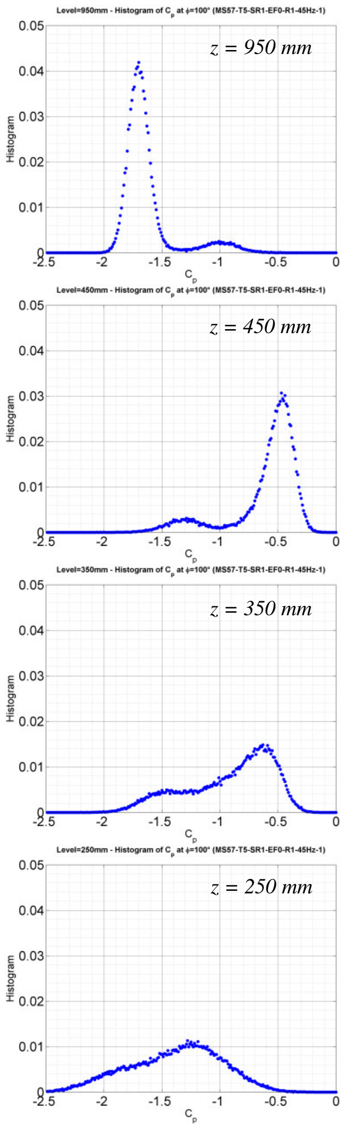

Figure 6.22 Bistability of the flow at low levels, histograms of $C_p(z/H,100°)$ (CRIACIV T5-SR1-R1-EF0)

The measurements along the height show that the flow is purely bistable and asymmetric only in the highest compartments (two at CRIACIV, three at WiSt). Here, bistable pressures produce bistable lift. Then, there is a region of transition (e.g. z =

650-750 mm in Figure 6.12, referring to CRIACIV data), where much more rapid jumps take place on the bubble side of the cylinder. The two states in the transition region are not well organized around the circumference, therefore they do not produce a purely bistable lift force. At lower levels ($z < 500$ mm, Figure 6.21) the time histories of pressures appear as an unstable sequence of states. In fact, the histograms of pressures on the right-hand side of the figure clarify that the pressures still oscillate between two states. Only closer to the ground (e.g. $z = 250$ mm in Figure 6.21), the bistability is substantially lost, not only in the lift but also in the pressures. The turbulence intensity certainly plays a role, although it is not the governing parameter of the bistable flow along the height.

6.4 Asymmetric bi-stable flow in CFD simulations

CFD simulations have been performed on the basis of CRIACIV experiments by the TEE group, Industrial Energy Dept. (formerly known as Energy Engineering Dept. "S. Stecco"), University of Florence (Salvadori&Mattana et al., 2013, unpublished personal communication).

The aim of the simulation is to provide numerical evidence of asymmetric bistable flow, as observed in the experiments. Therefore, the simulation refers to the most representative case: ten rings, no-efflux.

In the following, special attention is paid to those peculiar flow features which correspond to pressure characteristics observed in the experiments and commented up to now. However, the numerical study is only at the very first stage and it was not in the purpose of this work to proceed further. Further studies would be advisable in the future (Chapter 8).

The URANS simulation is performed by using the software Ansys Fluent 14. The incompressible fluid is solved by applying Navier-Stokes equations. The time step is 0.001 s, so about thirty time steps describe one period of vortex shedding. The turbulence model is the Shear Stress Transport (SST) k-ω. This is suitable to describe separated flows on smooth surfaces and adverse pressure gradients.

In order to reproduce the conditions of CRIACIV experiments, the tunnel and also the diffusor downstream of the test section were modelled. However, the presence of the diffusor is not relevant for the simulation and it can be ignored in further studies. Some pictures of the unstructured mesh are reported in Figure 6.23 and Figure 6.24.

The boundary conditions at the inlet are the velocity profile, the turbulence intensity and the turbulent length scale. The boundary conditions at the outlet are the pressure, the turbulence intensity and the turbulent length scale. No slip conditions are set to all the other surfaces. The velocity profile at the inlet is like in Figure 6.2 (with maximum value equal to 28 m/s), while the turbulence intensity and the integral length scale L_{ux} are constant along the height, equal to 1% and 0.0075 m, respectively. These very low values will be increased in future studies, but may be representative in the tip region.

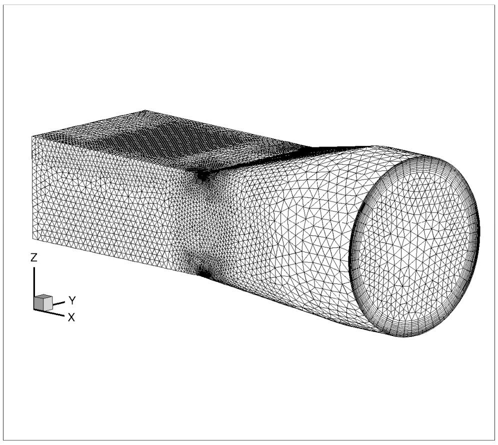

Figure 6.23 CRIACIV boundary layer wind tunnel – mesh (Salvadori&Mattana et al., 2013)

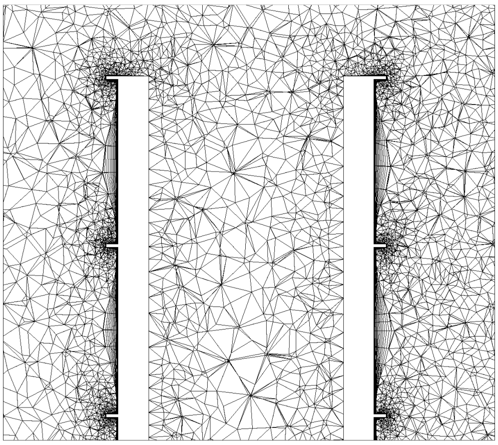

Figure 6.24 Detail of the mesh, transversal cross-section (Salvadori&Mattana et al., 2013)

A peculiar feature of the simulations is the high Re number ($Re = 2.8*10^7$), obtained by reducing the air viscosity of two order of magnitudes ($\nu = 1.5*10^{-7}$ m^2/s). In these transcritical conditions of Re, surface roughness on the cylinder is not necessary. Moreover, differently from wind tunnel experiments, the simulation benefits of ideal test conditions.

The instantaneous flow picture in Figure 6.25 (horizontal cross-section at a representative level, 750 mm), clearly confirms the asymmetry due to a separation bubble on one side of the cylinder. This is consistent with the expectations on the flow, deduced on the only basis of pressure measurements in Figure 5.5 (WiSt) and Figure 6.10 (CRIACIV). The velocity magnitude shows the shift of the wake towards the bubble side. The streamline which separates on the normal side and reattaches on the bubble side motivates the high rms value on the bubble side in the wake. It is especially evident at about 200° in the state 1 (Figure 5.5/WiSt, Figure 6.10/CRIACIV).

Figure 6.26 plots the instantaneous vertical variation of the transversal velocity component, at the same time step as before. The cross-section cuts the cylinder in the across-wind direction Y at 120°-240° (X = 0.0375 m). The figure confirms the alternation between compartments (spanwise inversion), as observed in the experiments. The different colors in the figure on the two sides of the cylinder (i.e. blue on the right-hand side, standing for negative values and red on the left-hand side, standing for positive values) are consistent with expectations: the transversal velocity vectors embrace the cylinder. In fact, what is interesting, and in agreement with the asymmetric phenomenon, is the different intensity of the transversal component on the two sides of the cylinder: in absolute value, the highest transversal velocity components are on the normal side. The differences in the transversal components on the two sides of the cylinder imply that the wake is not symmetrically aligned in each compartment, but it is shifted on one side. The same conclusion was also drawn from the experiments (Figure 5.40b).

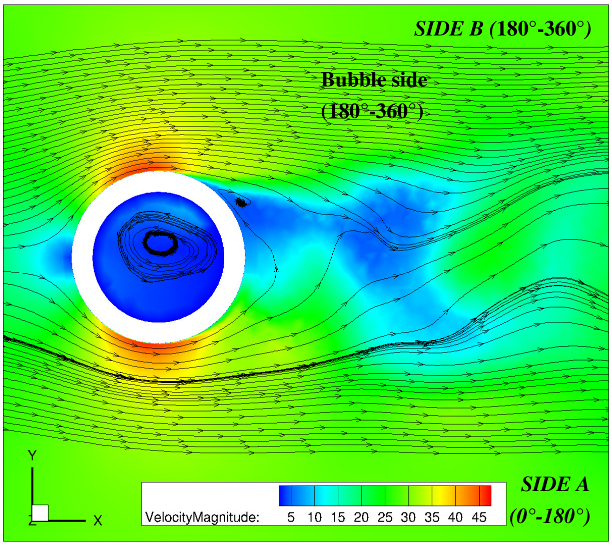

Figure 6.25 Horizontal cross-section, instantaneous flow velocity (magnitude, m/s) at z = 750 mm

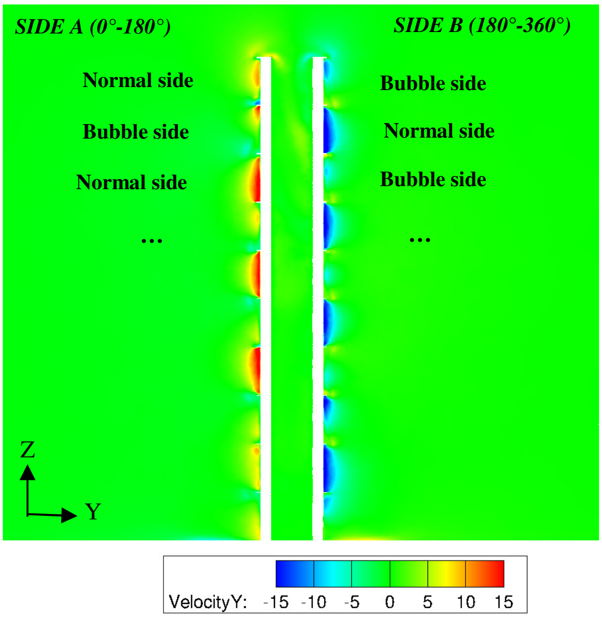

Figure 6.26 Transversal cross-sections, upstream view from the rear, instantaneous flow velocity (Y component, m/s) X = R/2 = 0.0375 m

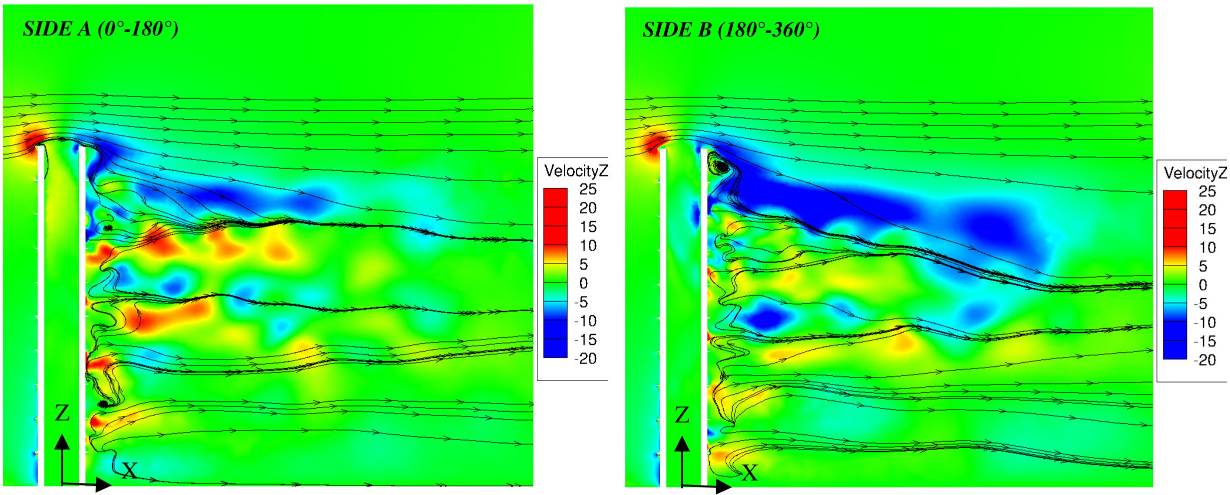

a) *b)*

Figure 6.27 Longitudinal cross-sections, instantaneous flow velocity (Z component, m/s) Y = +/- 0.0257 m (Salvadori&Mattana et al., 2013)

So far, the numerical simulation has provided evidence of the asymmetry around a symmetric structure, due to the formation of a separation bubble on one side of the cylinder. The other fundamental issue which characterizes the phenomenon is the bistability. In order to detect, during the simulation, whether a jump takes place at a certain level, several monitoring probes were placed in the wake of the cylinder. As shown by Figure 6.28, there are two probes on each level for ten levels. The level number 1 is 49 mm above the cylinder, the level number 2 is at the tower top and so on, with a distance between levels of 50 mm. In this way, the probes are placed at each level of the ring and in between two rings, until z/H = 0.6. The probes allow to monitor the absolute pressure during the simulation. It is clear from Figure 6.29, in particular at level 5 (z/H = 0.85), that a jump has taken place at about t = 0.2 s.

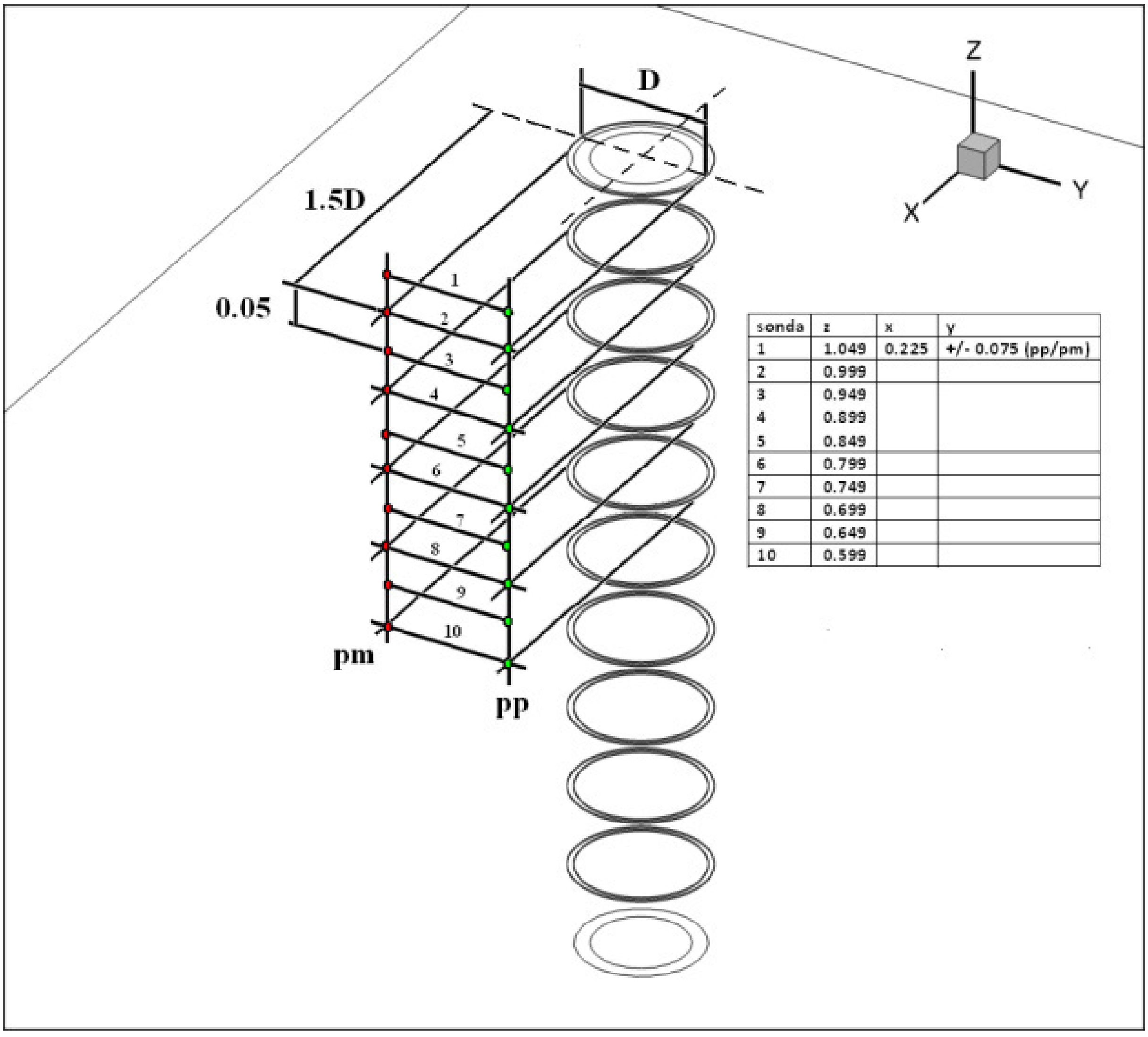

sonda	z	x	y
1	1.049	0.225	+/- 0.075 (pp/pm)
2	0.999		
3	0.949		
4	0.899		
5	0.849		
6	0.799		
7	0.749		
8	0.699		
9	0.649		
10	0.599		

Figure 6.28 Sketch of the probes to monitor flow pressures in the wake (Salvadori&Mattana et al., 2013)

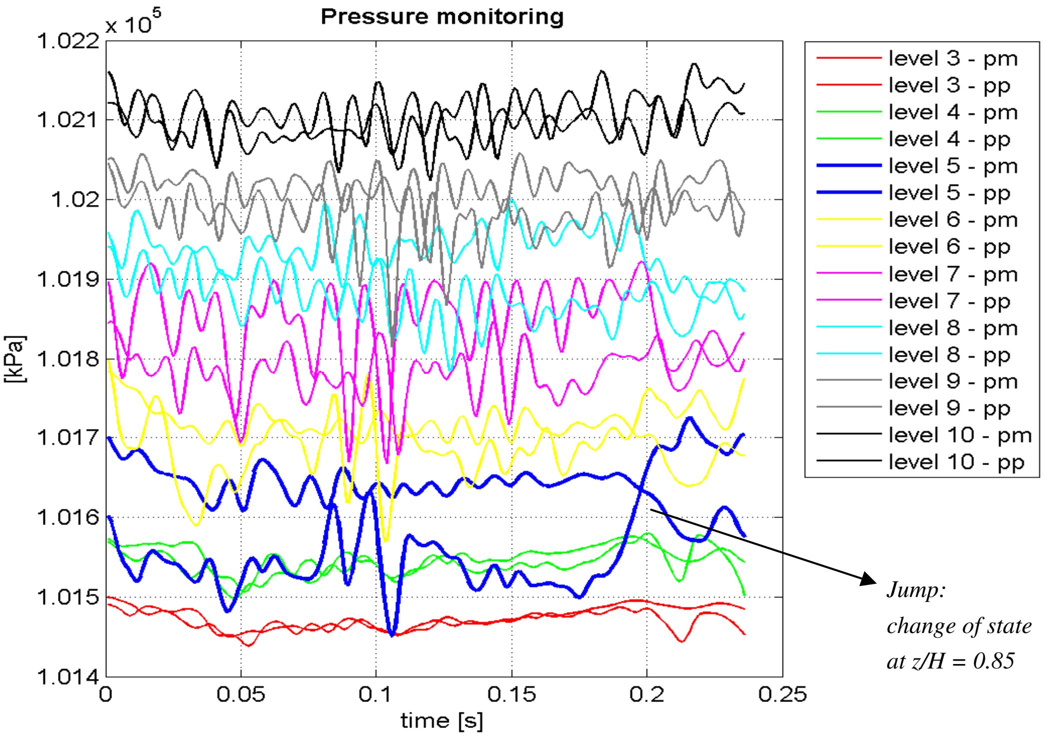

Figure 6.29 Time histories of flow pressures behind the tower (Salvadori&Mattana et al., 2013)

The most representative flow picture which highlights the occurrence of a change of state is the transversal cross-sections at a downstream distance of one radius from the tower in the along-wind direction. Figure 6.30 reports an instantaneous flow picture before a jump, Figure 6.31 reports an instantaneous flow picture once the transition of state is initiated in the tip region.

The simulation shows that the downwash over the tip of the cylinder – the green tongue diverting towards side B in Figure 6.30 and side A in Figure 6.31 – guides the asymmetric flow, with spanwise inversion along the height. Due to the veer of the downwash flow, the sort of “snake” in the wake of the cylinder starts to invert its shape. At the time step in Figure 6.31 (that is the last monitored time step in Figure 6.29), the “snake” keeps the same shape from the ground until about two compartments from the top. There, the transition of state has occurred, as proved by the blue lines at level 5 in Figure 6.29. In fact, the time window of the simulation is relatively short. The experiments provided much longer measurements. Therefore, it cannot be stated whether Figure 6.31 testifies an actual jump, or just an attempt of jump, which is not able to develop along the height. The simulation should then proceed further, but this goes beyond the purpose of this Dissertation and it will be object of future research (Chapter 8).

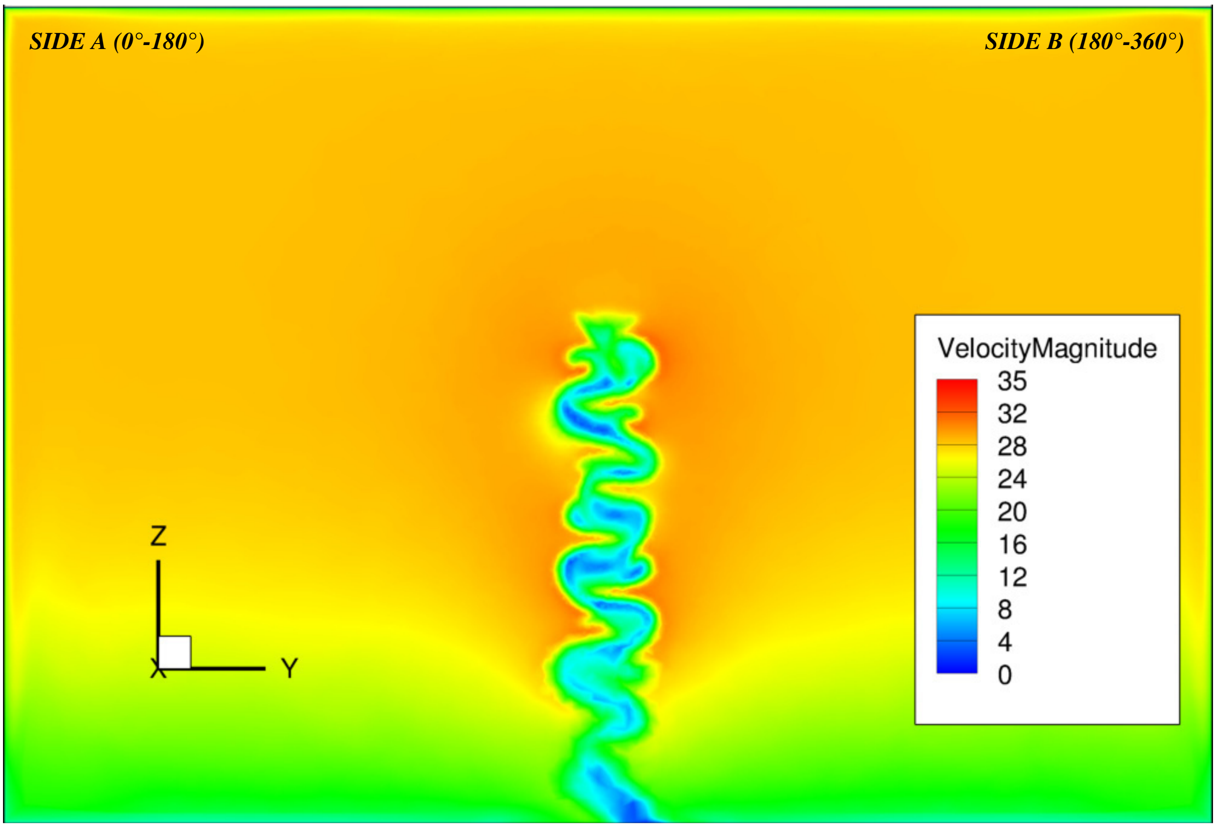

Figure 6.30 Transversal cross section in the wake at X = R from the tower (upstream view). Before the jump (t = 0). (Salvadori&Mattana et al., 2013)

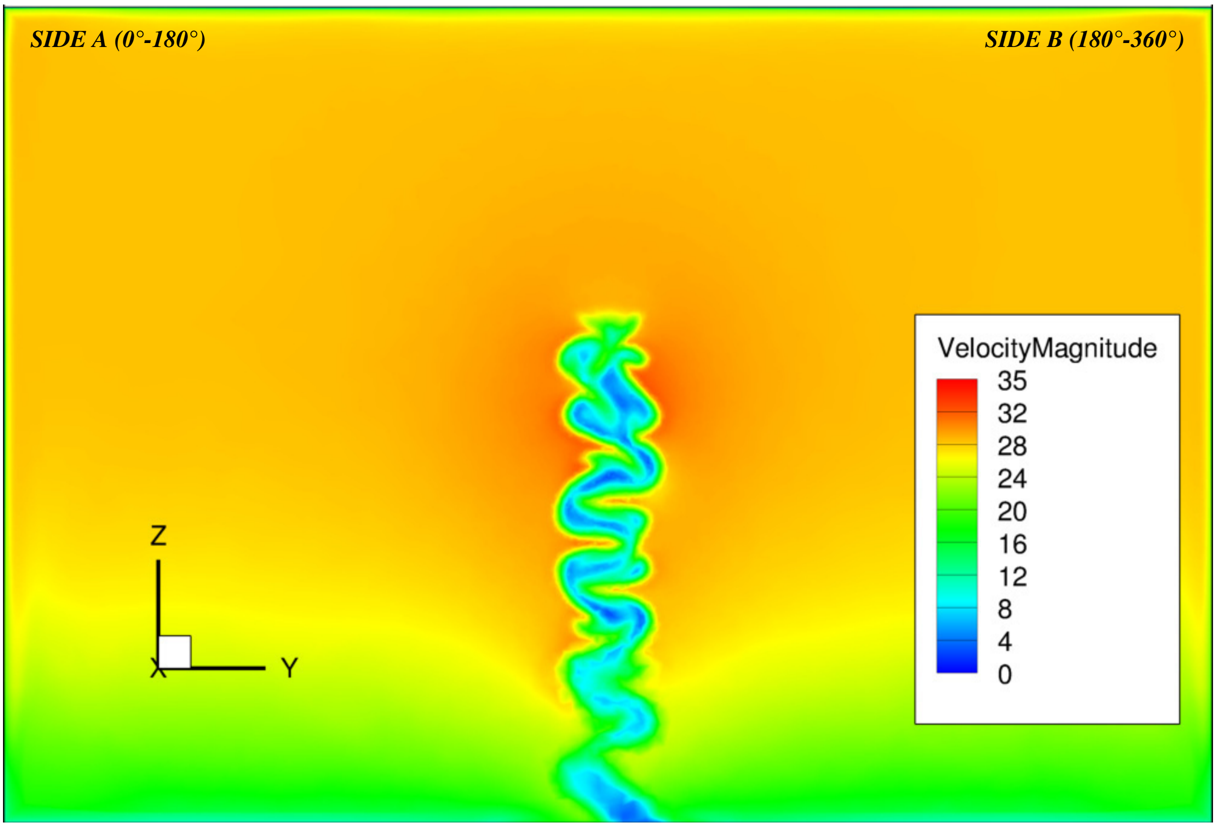

Figure 6.31 Transversal cross section in the wake at X = R from the tower (upstream view). After the jump (t = 0.024 s): transition of state is initiated in the tip region. (Salvadori&Mattana et al., 2013)

6.5 Concluding remarks

The experiments at WiSt and at CRIACIV aimed to discover, prove and understand a new asymmetric and bistable flow condition around circular cylinders, even at moderately high Reynolds numbers. The URANS numerical simulation supports the experimental evidence. However, the numerical study has been just introduced in the Dissertation; it will be the object of future research.

The question of the Reynolds number could not be fully addressed in the wind tunnel, but it had to be limited to the range of Re of the experiments, accompanied by surface roughness on the model. Moreover, experimental conditions in any laboratory are never ideal ones. The existence of any kind of disturbance or local flow distortion can promote asymmetric results. It is, in any case, very unlikely that two different laboratories promote the same asymmetric results due to their own test conditions. However, the cross-check of experiments could not fully answer the question of what would happen in ideal test conditions. This question cannot be addressed experimentally anyhow. From this point of view, the CFD provides the most reliable answer. The proof of existence of an asymmetric effect on a symmetric structure in symmetric flow condition is one of the most important contributions of the CFD simulation. A further contribution is, of course, the occurrence of the jump. Further studies are now necessary to investigate the occurrence of jumps. What can be stated now, is that the occurrence of asymmetric and bistable condition is not a matter of the Re. Moreover, from the experiments it is clear that the stable condition in the highest compartments in the case of ten rings is the asymmetric one, on either side of the cylinder. The CFD is presently too short to confirm the same result. This is an issue which would deserve further attention in the future, especially with regard to the effect of the Reynolds number and ideal test conditions.

The CFD clarified a peculiar feature, also observed in the experiments: the formation of a separation bubble on one side of the cylinder and the misalignment of the wake between different compartments. This is due to the cross-wind component, which predominates on the normal side of the cylinder and diverts the wake towards the bubble side. In particular, the cross-wind component predominates on the side of the cylinder where the vertical downwash is weaker (i.e. on the normal side). This would confirm the key role of the flow over the tip of the cylinder, whose downwash is mainly reversed on the bubble side, where it creates a secondary vortex below the highest ring. For this reason, the presence of efflux inside the cylinder cancels the asymmetric phenomenon. In fact, the downwash flow over the tip is disturbed by the upwards flow out of the tip. It can be then wondered whether it is possible to identify a critical ratio between the Reynolds number of the incoming flow and the Reynolds number of the efflux, which is able to suppress the phenomenon.

Along the height, strips of flow cross each other in neighboring compartments and are responsible for the spanwise inversion. It is reasonable that all these flow movements kill the shedding of tip-associated-vortices. In fact, the lower shedding frequency is due to entrainment in the wake. This is, in case of rings, displaced on either side of the cylinder.

It should also be remembered that the formation of asymmetric separation bubbles disappears if the rings are at a sufficiently large distance (experimental evidence only, CFD not performed). With regard to that, Figure 6.27 shows the effect of ring n.9 (z/H = 0.9) in constraining the recirculation vortex within the highest compartment. Therefore, the role of ring n.9 in the whole phenomenon should be further investigated.

The experimental and numerical evidence of the new phenomenon proposed in this Dissertation is now fully confirmed. It opens the doors to the last step of this work, that is the evaluation of load and response (Chapter 7). In this regard, it is important not to restrict the analysis to the interesting but unique design condition of ten rings along the height. Because of that, the study of the load and the response of the tower is addressed in a wider perspective. But of course, the response to the asymmetric and bistable flow needs to be quantified, too.

Chapter 7. **Load and response**

Wind tunnel experiments performed in different wind tunnels and thus different boundary layers allowed to study the effect of certain atmospheric boundary layer properties on wind forces and pressures. A simple design tool, generalizable to any atmospheric boundary layer flow is then derived by using the results in WiSt and CRIACIV (section 7.1). This model can be applied to calculate the quasi-static response of the tower to the stochastic wind loading process in any design conditions. Basic assumptions are linear structural analysis and quasi-static behaviour.
In sections 7.2 and 7.3 the beam and shell responses are analyzed. The effect of the asymmetric load due to the rings along the height is also quantified.

7.1 Modelling of wind load

The time-averaged mean load and the load covariances (i.e. rms values and correlation coefficients) are the input data to evaluate the quasi-static structural response to the stochastic wind loading process. The breaking-up of the covariances in the frequency domain is not necessary because the mechanical admittance is constant. More sophisticated methods to evaluate the structural response are the spectral method in the frequency domain, which is applicable to linear structures, and the time history method applicable to both linear and non-linear structures.
This section addresses the modelling of the stochastic quasi-static design wind load, with respect to the turbulent properties of the flow, by combining results of both WiSt and CRIACIV wind tunnels. The model refers to the basic configuration (without rings) and has a general application for cylindrical towers of any aspect ratio[6]. It also represents the reference case to evaluate the effect of the rings.

7.1.1 Influence of boundary layer flows on force coefficients

The comparison of experimental data recorded in different wind tunnels – and thus different atmospheric boundary layers – cannot be addressed without considering the properties of the flow in which such data are measured. This approach is pursued in this section with regard to the force coefficients.

---

[6] For low-aspect ratio circular cylinders, i.e. for H/D less than a critical value (which ranges from 1 to 6, depending on the boundary layer thickness) a different flow structure develops in the wake (see section 3.5). The proposed wind load model is thus appropriate for sufficiently slender circular cylinders, e.g. $H/D \geq 6$.

The local mean value of the drag coefficient that results from the experiments (^{EXP}) is calculated by definition as:

$$C_{D,m}^{EXP}(z)=\frac{F_m^{EXP}(z)}{q_m(z)D} \tag{7.1}$$

where $q_m(z)$ is the local velocity pressure, i.e. at the level of the pressure measurement. Similarly, the coefficient can be defined with respect to the velocity pressure at the top of the tower:

$$C_{D,m}^{EXP,H}(z)=\frac{F_m^{EXP}(z)}{q_m(H)D} \tag{7.2}$$

The comparison between results at WiSt and CRIACIV (Figure 7.1a) shows that the local mean force coefficients – calculated according to equation (7.1) – depend on the type of boundary layer. In fact, a certain boundary layer – characterized by its velocity and pressure gradients – may enhance certain flow movements. The time-averaged wake structure may also change, as addressed in section 6.3. While the tip effect is not so sensitive to the characteristics of the boundary layer, lateral and especially wake suction at middle height at CRIACIV are lower than at WiSt. This issue was commented with regard to Figure 6.17, which explains the differences between the two drag curves in Figure 7.1a.

The use of $q_m(H)$ instead of $q_m(z)$ allows to remove the differences due to the boundary layer and the results in the two wind tunnels are in wonderful agreement (Figure 7.1b). However, by using $q_m(H)$, an even more constraining dependency is gained: the one on the aspect ratio. The coefficients in Figure 7.1b are thus only valid for the aspect ratio of the experiments, that is H/D = 6.7.

The rms values of the forces (equation(7.3)) are necessarily different in the two wind tunnels (Figure 7.2), because the turbulence in the flow (σ_u) is different (Figure 7.3).

$$C_{D,\sigma}^{EXP,H}(z)=\frac{F_\sigma^{EXP}(z)}{q_m(z)D} \tag{7.3}$$

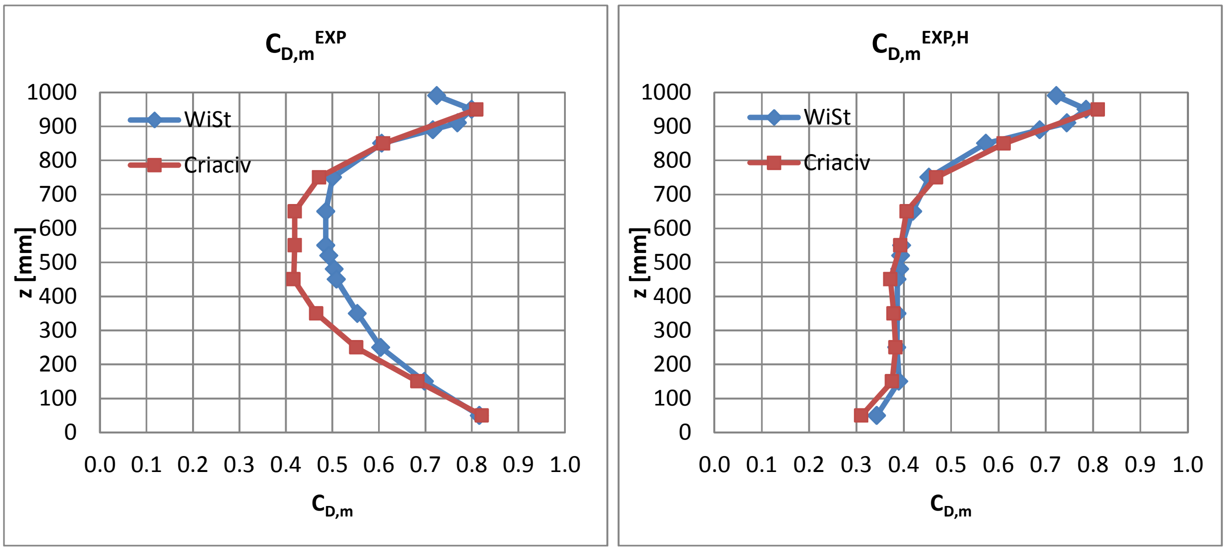

a) b)

Figure 7.1 Mean drag coefficients $C_{D,m}$*: comparison between WiSt and CRIACIV data (EXP) a)* $C_{D,m}$ *by using local velocity pressure* $q_m(z)$*; b)* $C_{D,m}$ *by using velocity pressure on top* $q_m(H)$

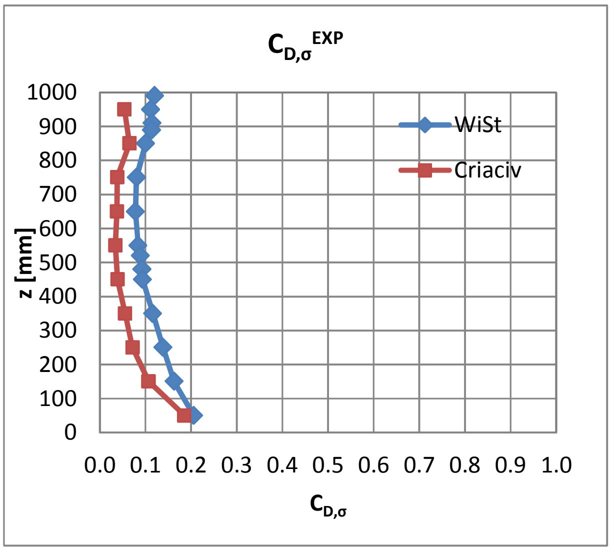

Figure 7.2 Rms drag coefficients $C_{D,\sigma}$*: comparison between WiSt and CRIACIV experimental data (*^{EXP}*)*

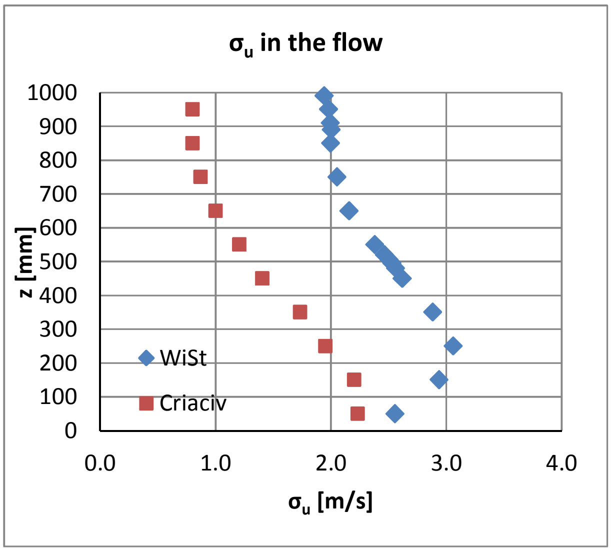

Figure 7.3 Rms values of along wind velocity (σ_u*) at WiSt and CRIACIV*

It is then apparent that, in order to compare results obtained in different boundary layer flows and codify the force coefficients, a more general approach should be used, which includes the mean velocity pressure and the turbulence intensity.

The code approach is based on the peak force coefficient ($C_{D,peak}$), that is the ratio of peak (drag) force and peak velocity pressure (equation (7.4)). The latter is multiplied by D as usual, in order to obtain the dimension of force per unit length. In this way, the results in different boundary layer flows are more comparable even by using the local velocity pressure and not the velocity pressure on top (Figure 7.4). The peak force coefficients are generalizable for load modelling.

$$C_{D,peak}=\frac{F_{peak}}{q_{peak}D}=\frac{F_m^{EXP}+k_F F_\sigma^{EXP}}{q_m\left(1+2k_pI_u\right)D}=\frac{C_{D,m}^{EXP}q_mD+k_FC_{D,\sigma}^{EXP}q_mD}{q_m\left(1+2k_pI_u\right)D}=\frac{C_{D,m}^{EXP}+k_FC_{D,\sigma}^{EXP}}{1+2k_pI_u} \tag{7.4}$$

The peak factors in equation (7.4) are assumed equal to 3.5 for both forces and velocities (k_F and k_p, respectively). The apex (^{EXP}) means resulting from experiments. It should be mentioned, however, that the code definition of the peak force includes the dynamic factor and the size factor. Relying on the experimental data, C_{dyn} = 1 because the model is rigid, C_s is assumed equal to 1, too, although it should take into account the decrease in correlation around the circumference. It could be partially responsible for the differences in the two curves in Figure 7.4.

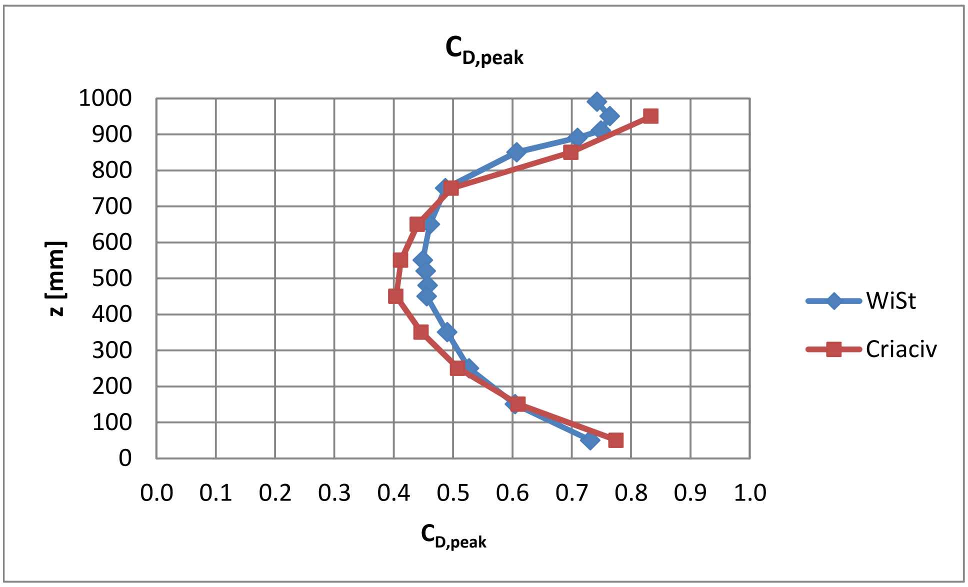

Figure 7.4 Peak drag coefficient $C_{D,peak}$ related to $q_{peak}(z)$

By assuming a quasi-stationary approach (the aerodynamic coefficient is invariant with respect to time) and linearized model (I_u^2<<1), the intensity of force is twice the turbulence intensity and the peak force can be split up into its mean and fluctuating components as follows:

$$F_m = C_{D,peak} q_m D \tag{7.5}$$

$$F_\sigma = C_{D,peak} 2I_u q_m D \tag{7.6}$$

Therefore, the mean and the rms values of the force coefficients to be used in the proposed beam-load model (^{LM}) are:

$$C_{D,m}^{LM} = \frac{F_m}{q_m D} = C_{D,peak} \tag{7.7}$$

$$C_{D,\sigma}^{LM} = \frac{F_\sigma}{q_m D} = C_{D,peak} 2I_u \tag{7.8}$$

The behaviour of the peak drag coefficient along the height resembles the profile of the $C_{D,m}$, which increases both at tower top (tip effect) and at the bottom, as previously commented in sections 3.5 and 4.4.

The main results are reported in the following tables.

Table 7.1 Boundary layer flow at WiSt

	z [mm]	**z/H**	**U [m/s]**	**σ_u**	**$q_m(z)/q_m(H)$**	**I_u**
WiSt: Boundary layer	990	0.99	25.16	1.9431	1.00	0.0772
	950	0.95	24.98	1.9826	0.98	0.0794
	910	0.91	24.79	1.9972	0.97	0.0806
	890	0.89	24.70	2.0041	0.96	0.0811
	850	0.85	24.30	2.0003	0.95	0.0823
	750	0.75	23.78	2.0536	0.91	0.0863
	650	0.65	23.32	2.1580	0.86	0.0925
	550	0.55	22.66	2.3833	0.81	0.1052
	520	0.52	22.43	2.4656	0.80	0.1099
	480	0.48	22.16	2.5621	0.78	0.1156
	450	0.45	21.91	2.6181	0.76	0.1195
	350	0.35	21.01	2.8842	0.70	0.1373
	250	0.25	20.05	3.0614	0.64	0.1527
	150	0.15	18.77	2.9381	0.56	0.1566
	50	0.05	16.28	2.5565	0.42	0.1571

Table 7.2 Drag coefficients at WiSt

	z/H	$\mathbf{C_{D,m}^{EXP}}$	$\mathbf{C_{D,m}^{EXP.H}}$	$\mathbf{C_{D,\sigma}^{EXP}}$	$\mathbf{I_F = C_{D,\sigma}^{EXP}/C_{D,m}^{EXP}}$	$\mathbf{I_F/I_u}$	$\mathbf{C_{D,peak}}$
WiSt: Drag Coeff.	0.99	0.7246	0.7221	0.1198	0.1654	2.1407	0.7425
	0.95	0.7992	0.7853	0.1112	0.1391	1.7528	0.7640
	0.91	0.7693	0.7447	0.1148	0.1492	1.8519	0.7487
	0.89	0.7158	0.6877	0.1134	0.1584	1.9523	0.7096
	0.85	0.6061	0.5732	0.1001	0.1652	2.0073	0.6069
	0.75	0.5007	0.4535	0.0801	0.1601	1.8539	0.4869
	0.65	0.4858	0.4189	0.0781	0.1607	1.7366	0.4606
	0.55	0.4859	0.3956	0.0838	0.1725	1.6401	0.4488
	0.52	0.4924	0.3933	0.0888	0.1804	1.6411	0.4540
	0.48	0.5039	0.3915	0.0922	0.1830	1.5825	0.4568
	0.45	0.5083	0.3863	0.0937	0.1844	1.5430	0.4554
	0.35	0.5540	0.3862	0.1161	0.2095	1.5262	0.4897
	0.25	0.6044	0.3854	0.1386	0.2293	1.5015	0.5266
	0.15	0.6980	0.3899	0.1626	0.2330	1.4879	0.6046
	0.05	0.8160	0.3429	0.2055	0.2519	1.6034	0.7313

Table 7.3 Boundary layer flow at CRIACIV

	z [mm]	**z/H**	**U [m/s]**	$\mathbf{\sigma_u}$	$\mathbf{q_m(z)/q_m(H)}$	$\mathbf{I_u}$
CRIACIV: Boundary layer	950	0.95	28.36	0.8022	1.00	0.0283
	850	0.85	28.40	0.8033	1.00	0.0283
	750	0.75	28.26	0.8731	0.99	0.0309
	650	0.65	27.91	1.0020	0.97	0.0359
	550	0.55	27.47	1.2085	0.94	0.0440
	450	0.45	26.79	1.4070	0.89	0.0525
	350	0.35	25.58	1.7340	0.81	0.0678
	250	0.25	23.65	1.9534	0.70	0.0826
	150	0.15	21.03	2.2015	0.55	0.1047
	50	0.05	17.44	2.2339	0.38	0.1281

Table 7.4 Drag coefficients at CRIACIV

	z/H	$\mathbf{C_{D,m}^{EXP}}$	$\mathbf{C_{D,m}^{EXP.H}}$	$\mathbf{C_{D,\sigma}^{EXP}}$	$\mathbf{I_F = C_{D,\sigma}^{EXP} / C_{D,m}^{EXP}}$	$\mathbf{I_F/I_u}$	$\mathbf{C_{D,peak}}$
CRIACIV: Drag Coeff.	0.95	0.8099	0.8099	0.0539	0.0666	2.3547	0.8337
	0.85	0.6096	0.6113	0.0650	0.1066	3.7681	0.6986
	0.75	0.4717	0.4682	0.0380	0.0806	2.6070	0.4972
	0.65	0.4193	0.4062	0.0375	0.0894	2.4899	0.4400
	0.55	0.4192	0.3932	0.0341	0.0814	1.8498	0.4118
	0.45	0.4164	0.3717	0.0388	0.0931	1.7725	0.4037
	0.35	0.4652	0.3784	0.0552	0.1186	1.7494	0.4465
	0.25	0.5510	0.3831	0.0716	0.1299	1.5729	0.5079
	0.15	0.6830	0.3755	0.1069	0.1564	1.4941	0.6100
	0.05	0.8213	0.3106	0.1852	0.2255	1.7602	0.7748

7.1.2 Mean pressure coefficient distribution

The circumferential distribution of the mean pressure coefficients C_p on the external surface of the tower is described by the following parameters:

- $C_{p,max}$ = maximum pressure coefficient (at stagnation);
- φ_{min} and $C_{p,min}$ = angle and pressure coefficient at maximum lateral suction;
- φ_h and Cp_h = angle of separation and pressure coefficient in the wake;

Depending on the circumferential angle φ, three ranges can be identified along the circumference, as shown in Figure 7.5. The distributions in the three ranges are described by expressions (7.9)-(7.11), derived by studies on cooling towers and codified in the VGB guideline (VGB, 2010).

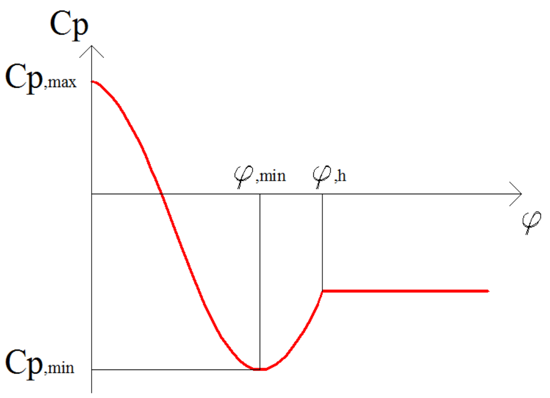

Figure 7.5 Pressure coefficients distribution in the three ranges ($0<\varphi<\varphi_{min}$; $\varphi_{min}<\varphi<\varphi_h$; $\varphi_h<\varphi<180°$)

Range I: $0° \le \varphi \le \varphi_{\min}$

$$C_P(\varphi) = C_{P,\max} - \left(C_{P,\max} - C_{P,\min}\right)\left(\sin\frac{90}{\varphi_{\min}}\varphi\right)^{\varepsilon_{\min}} \tag{7.9}$$

Range II: $\varphi_{\min} \le \varphi \le \varphi_h$

$$C_P(\varphi) = C_{P,\min} - \left(C_{P,\min} - C_{P,h}\right)\left(\sin\frac{90}{\varphi_h - \varphi_{\min}}\left(\varphi - \varphi_{\min}\right)\right)^{\varepsilon_h} \tag{7.10}$$

Range III: $\varphi_h \le \varphi \le 180°$

$$C_P(\varphi) = C_{P,h} \tag{7.11}$$

This model is adapted to the experimental data of the solar tower along the height (WiSt results). The parameter ε_h has been chosen accordingly to the VGB guideline, while the parameter ε_{min} has been calibrated by fitting the measured C_p values and matching the value of the measured drag coefficient. The values are reported in Table 7.5 and plotted in the following graphs. In particular, three spanwise regions can be identified along the height of the cylinder:

- tip region (z' ≤ 2D, i.e. z > 0.7H, as z' starts at z = H in downwards direction);
- normal region (z > 0.5H and z' > 2D);
- low region (z ≤ 0.5H).

Table 7.5 Mean pressure coefficients

	z/H	**Cp max**	**Cp min**	**φ,min [°]**	**Cp,h**	**φ,h [°]**	**ε,min**	**ε,h**	**ΔCp**	**C_D model**	**C_D meas.**
TIP REGION	**0.99**	0.7	-1.40	85	-0.73	130	2.085	2.395	0.68	0.72	0.72
	0.95	0.9	-1.91	85	-0.79	125	2.189	2.395	1.11	0.80	0.80
	0.91	0.9	-1.96	80	-0.82	120	2.390	2.395	1.15	0.77	0.77
	0.89	0.9	-1.95	80	-0.78	118	2.277	2.395	1.16	0.72	0.72
	0.85	1.0	-1.91	75	-0.69	115	2.332	2.395	1.23	0.61	0.61
	0.75	1.0	-1.85	75	-0.58	110	2.395	2.395	1.27	0.50	0.50
NORMAL REGION	**0.65**	1.0	-1.77	75	-0.55	110	2.248	2.395	1.21	0.49	0.49
	0.55	1.0	-1.76	75	-0.54	110	2.238	2.395	1.22	0.49	0.49
LOW REGION	**0.45**	1.0	-1.86	75	-0.59	110	2.261	2.395	1.26	0.51	0.51
	0.35	1.0	-1.94	75	-0.66	110	2.359	2.395	1.28	0.55	0.55

	0.25	1.0	-2.06	75	-0.75	115	2.474	2.395	1.31	0.60	0.60
	0.15	1.0	-2.28	80	-0.86	120	2.256	2.395	1.42	0.70	0.70
	0.05	1.1	-2.28	80	-0.99	110	2.052	2.395	1.29	0.80	0.80

The following figures (Figure 7.6, Figure 7.7, Figure 7.8) plot the circumferential distributions of mean pressure coefficients along the height. The three figures refer to the tip region, the normal region and the low region, respectively. Further variation of the distribution is also present within each region. Modelling according to equations (7.9), (7.10), (7.11) and experimental data are in good agreement.

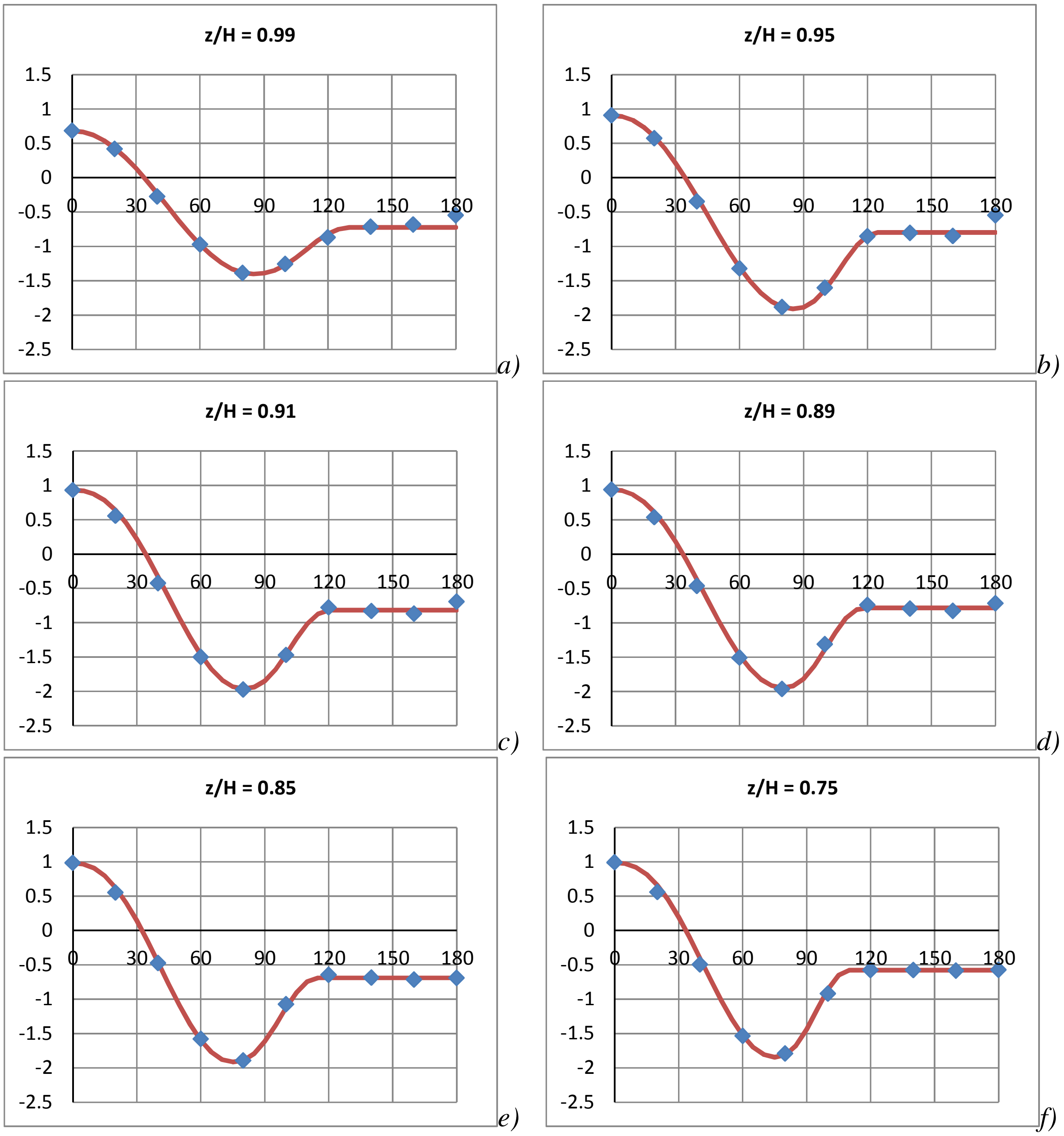

Figure 7.6 e-f) Mean pressure coefficients $C_{p,m}$: proposed model (red) and experimental data (blue) [x-axis = φ (°), y-axis = $C_{p,m}$]. Tip region ($z' < 2D$)

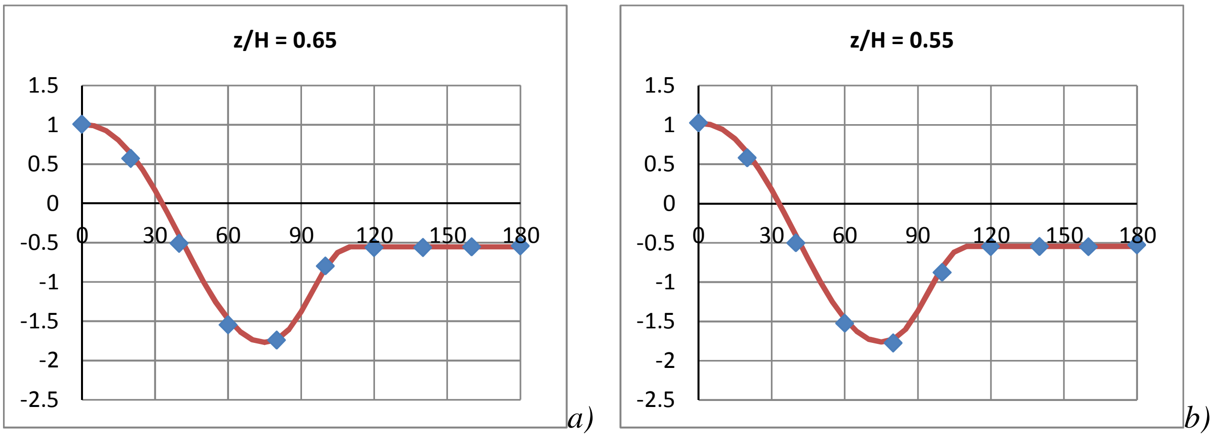

Figure 7.7 a-b) Mean pressure coefficients $C_{p,m}$: proposed model (red) and experimental data (blue) [x-axis = φ (°), y-axis = $C_{p,m}$]. Normal region (z' > 2D; z/H > 0.5)

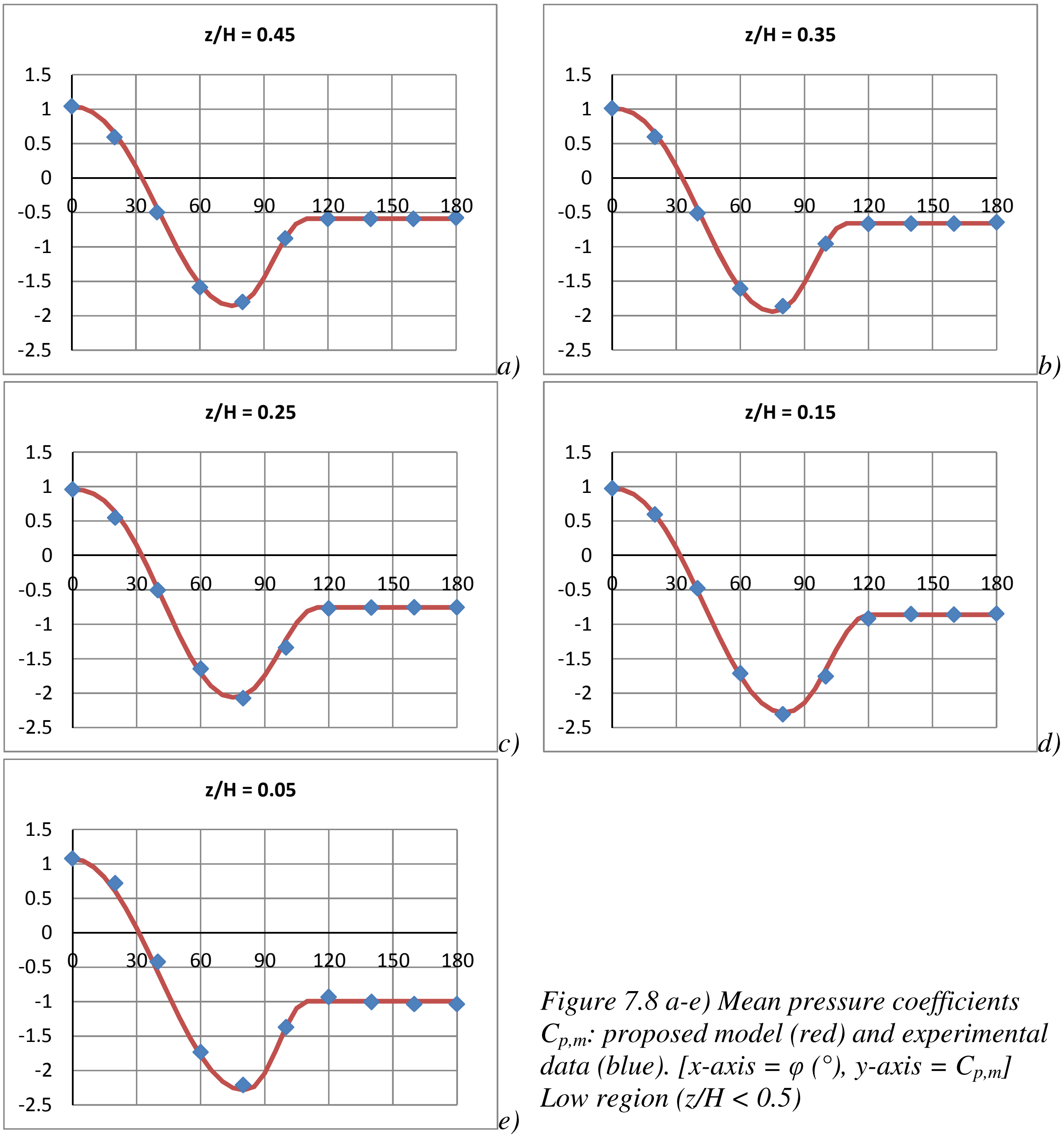

Figure 7.8 a-e) Mean pressure coefficients $C_{p,m}$: proposed model (red) and experimental data (blue). [x-axis = φ (°), y-axis = $C_{p,m}$] Low region (z/H < 0.5)

Finally, Figure 7.9 shows an overview of the distributions of the mean pressure coefficients along the height.

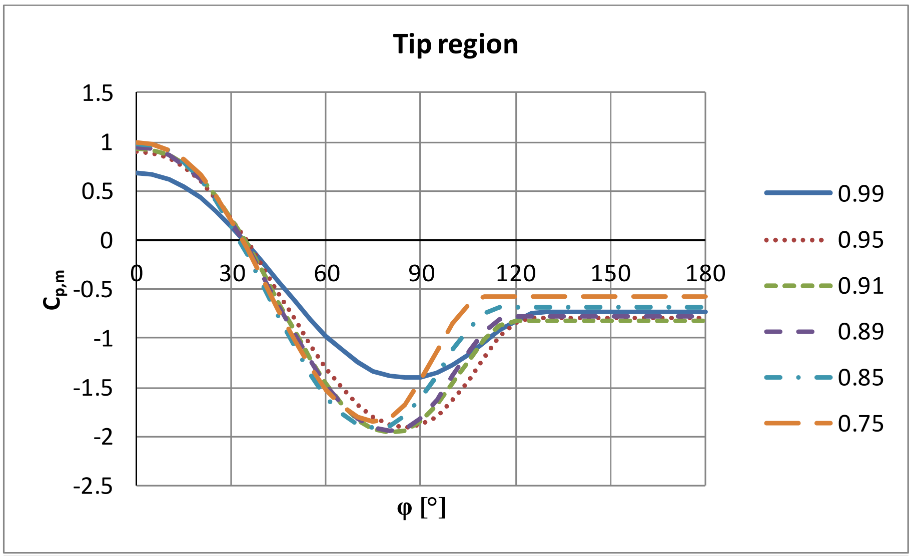

a) *Tip region (z' ≤ 2D)*

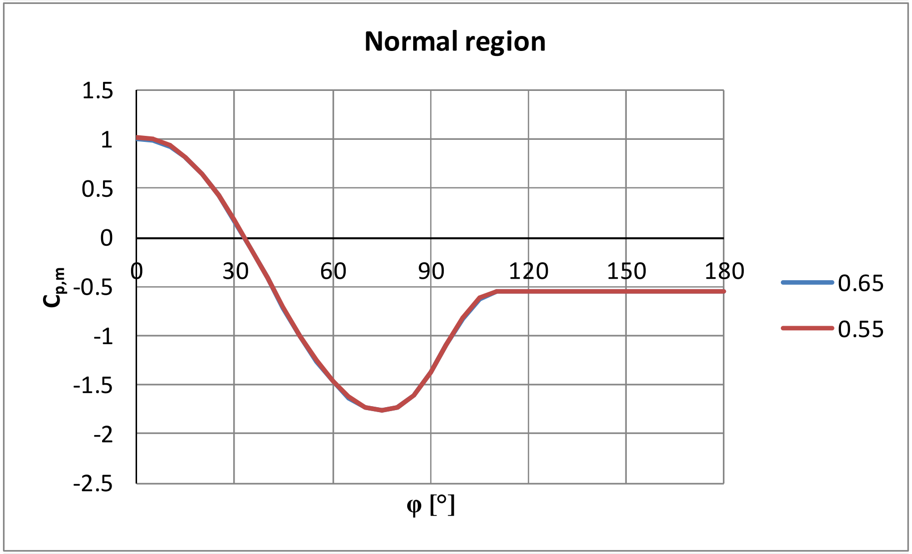

b) *Normal region (z > 0.5H and z' > 2D)*

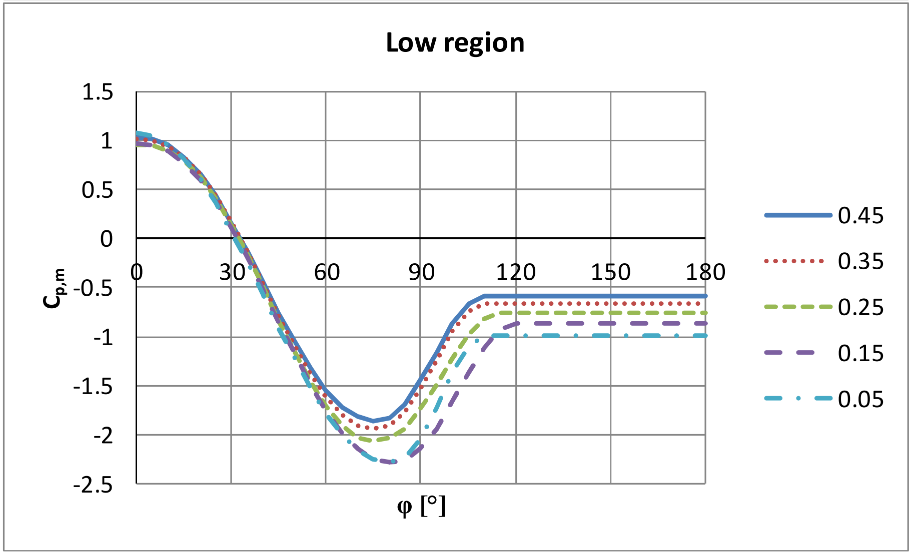

c) *Low region (z ≤ 0.5H)*

Figure 7.9 a-c) Mean pressure coefficients: variation along the height

7.1.3 Rms pressure coefficients: body-induced and turbulence-induced fluctuations

Pressure fluctuations on the shell surface are both body-induced and turbulence-induced. They are due to vortex shedding and to the turbulence of the incoming flow, respectively. In order to model the turbulence-induced fluctuations with regard to the turbulent properties of the boundary layer, the question arises whether it is possible to separate the two contributions. Then, the easiest approach would be to relate the turbulence-induced fluctuations around the circumference to the fluctuation at stagnation, which in turn depends on $I_u(z)$, and to measure the body-induced pressure fluctuations in smooth flow.

The problem cannot be addressed linearly in the rms values, but in the variances. Furthermore, the question is much more complicated because the turbulence of the incoming flow may be responsible for enhancing body-induced fluctuations. However, the simplifying assumption that body-induced pressure fluctuations ($p_{\sigma^2,BI}$) and turbulence-induced pressure fluctuations $p_{\sigma^2,TI}$ are statistically independent finds support in literature (see, for example, the rapid distortion theory by Hunt (1972/1975/1990), section 3.4) and can be accepted as long as I_u is not too high. This assumption is the basis for the model proposed in the following.

If the covariances between body-induced and turbulence-induced fluctuations are assumed to be zero (in view of the statistical independence), it follows that the pressure fluctuation which is measured during an experiment in turbulent flow is just the sum – in terms of variances – of the two contributions, the turbulence-induced one ($_{TI}$) and the body-induced one ($_{BI}$), as follows:

$$p_{\sigma^2} = p_{\sigma^2,TI} + p_{\sigma^2,BI} \tag{7.12}$$

Although it is apparent in the spectra that higher energy content is around the Strouhal peak, the separation of the two contributions is not immediate, especially in high turbulent flow. In terms of variances, the comparison of results in the two wind tunnels (WiSt and CRIACIV) resulted to be helpful. In fact, at CRIACIV the turbulence intensity is very low at high levels and this allows a first good estimation of the body-induced contribution at those levels. Then, extrapolation is made at $I_u = 0$, so that the actual body-induced fluctuations can be estimated all around the circumference. Since equation (7.12) holds in general, the theory can be further extended at low levels.

The validation of this simplified modelling is through comparison of full-scale results on cooling towers (Pröpper, 1977), as explained later on.

In the following, the level z/H = 0.85 is chosen as representative for explanation. At that level, $I_u = 0.028$ at CRIACIV and $I_u = 0.082$ at WiSt.

The circumferential distribution of the total variance of the pressure coefficients ($C_{p,\sigma}^2$) is shown in Figure 7.10. The two sides of the cylinder are not perfectly symmetric due to inhomogeneities of the flow in both wind tunnels. In fact, this is not surprising in experiments in turbulent boundary layer flows. Anyway, the differences between the two sides of the cylinder are small and they do not prevent the development of a model which is, of course, symmetric. Figure 7.10 shows that at stagnation the pressure fluctuations at CRIACIV are very small, resulting from low I_u. At 100° and 260° the fluctuations are instead high and they must be mostly body-induced. An insight in the spectra gives a more clear explanation over frequencies. As can be seen in Figure 7.11, at z/H = 0.85 it is not only the Karman vortex shedding that produces the majority of body-induced contribution, but there is a strong interaction with the tip-associated vortices.

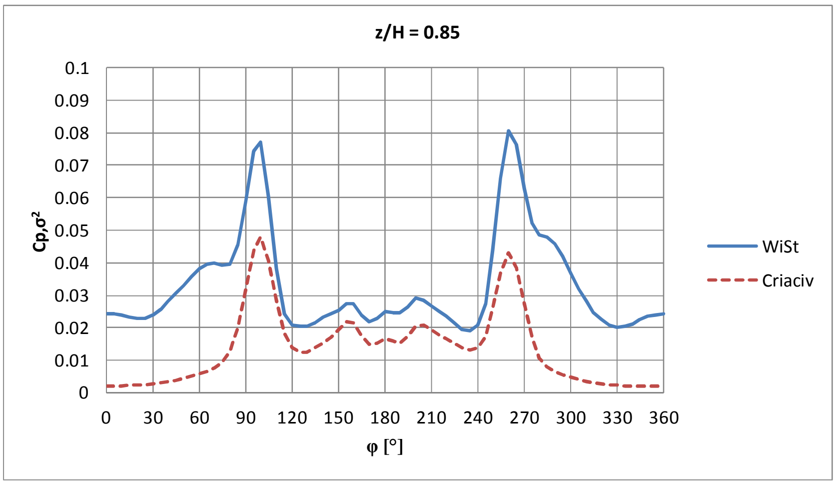

Figure 7.10 Circumferential distribution of the total variance $C_{p,\sigma}^2$ *(body+turb.-induced)*

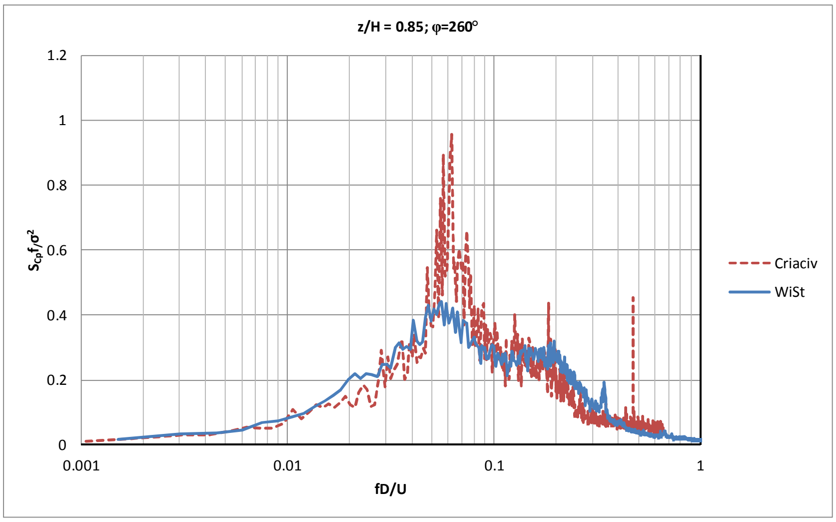

Figure 7.11 Power spectral densities of C_p *at z/H = 0.85, 260°*
$C_{p,\sigma}^2 = 0.0805$ *(WiSt);* $C_{p,\sigma}^2 = 0.0400$ *(CRIACIV)*

In order to separate body-induced and turbulence-induced contributions, the variances measured at CRIACIV (mostly body-induced) are compared to the variances measured at WiSt (mainly, but not only, turbulence-induced). A tentative extrapolation at $I_u = 0$ is proposed in Figure 7.12 and Figure 7.13. Since two experimental points are available at each angle, the extrapolation can only be linear in the plane σ^2, I_u^2. In any case, a linear extrapolation seems to be rather good for several reasons.

First of all, at 0° and up to 60° the body-induced contribution in smooth flow results to be zero and this confirms the expectations: at those angles the pressure fluctuations are mostly induced by the flow fluctuations. Then, moving downstream, the body-induced percentage increases and at 180° the slope of the line is almost flat (Figure 7.13). It means that the fluctuations in the wake are almost completely body-induced and they do not depend significantly on the upwind turbulence. It is also interesting to see that most of the lines in both figures are approximately parallel. It means that the rate of turbulence-induced fluctuations is almost the same at each circumferential angle. This is a further reason to relate the circumferential turbulence-induced distribution to only one reference angle, e.g. the stagnation angle, that can be related to the flow properties.

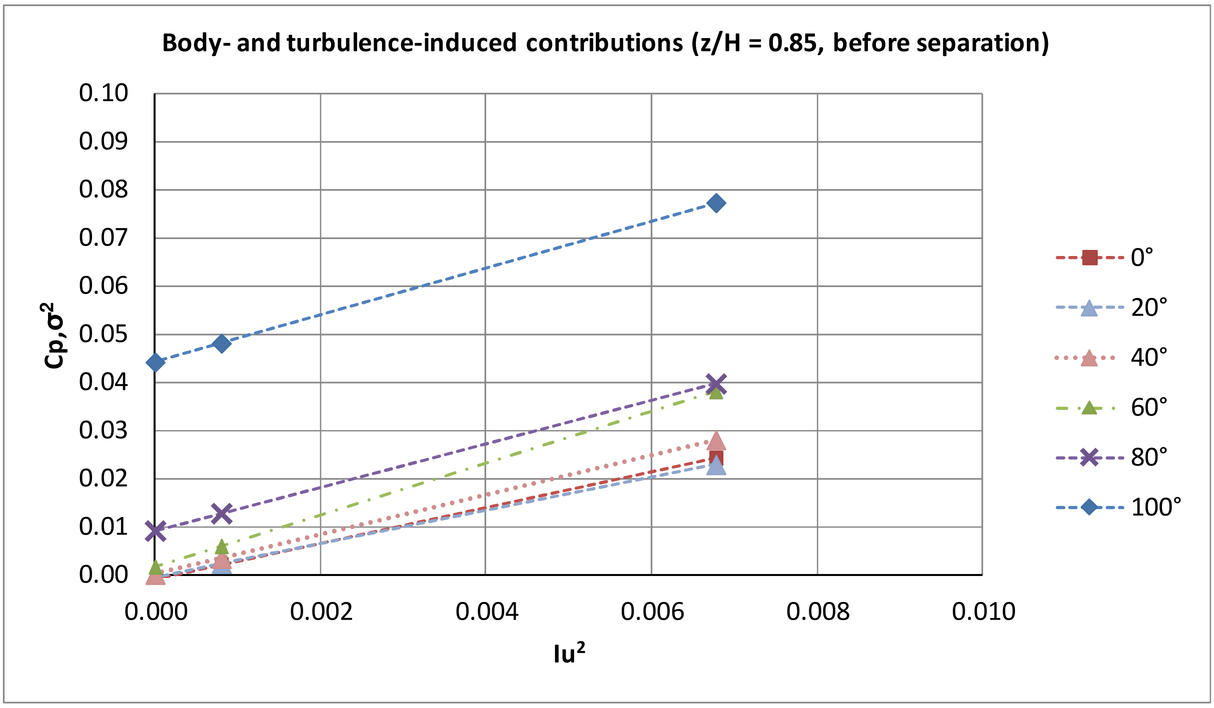

Figure 7.12 Extrapolations of body-induced contributions at angles before separation based on experiments at WiSt ($I_u = 0.082$ at z/H = 0.85) and at CRIACIV ($I_u = 0.028$ at z/H = 0.85)

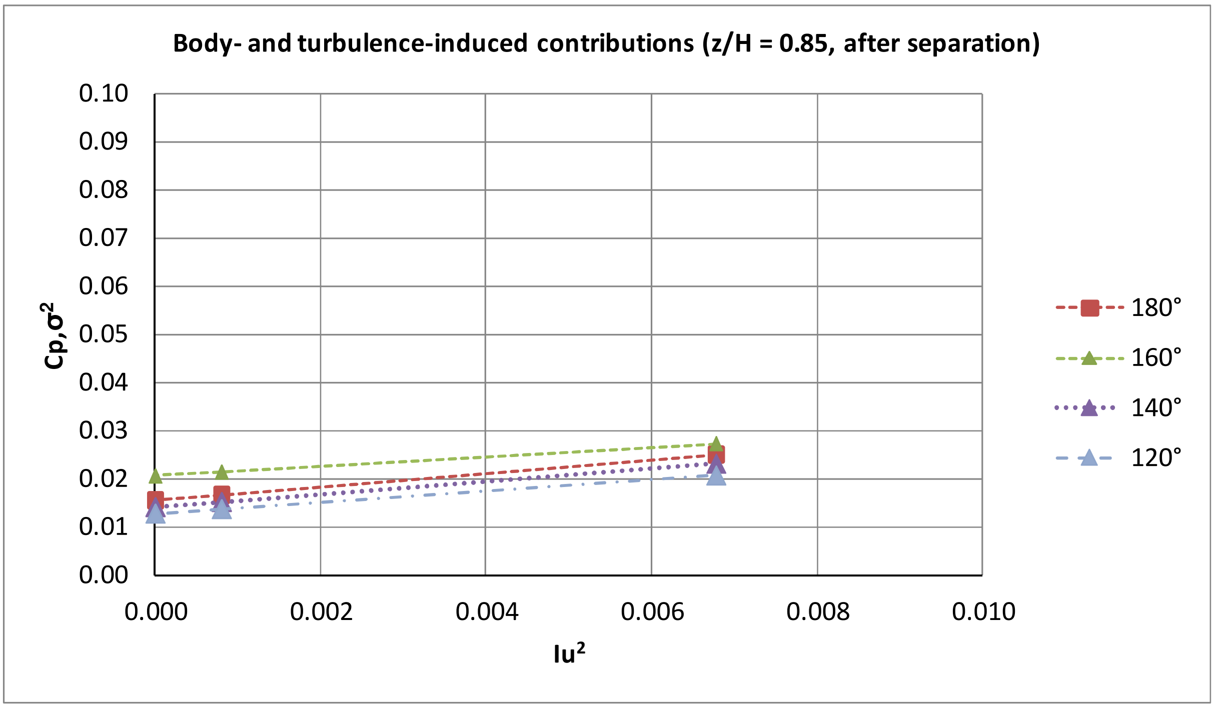

Figure 7.13 Extrapolations of body-induced contributions at angles after separation based on experiments at WiSt (I_u = 0.082 at z/H = 0.85) and at CRIACIV (I_u = 0.028 at z/H = 0.85)

The body-induced contribution extrapolated at $I_u = 0$ is then subtracted by the total variance measured at WiSt tunnel in high turbulent flow. The result represents the turbulence-induced part, which can be modeled around the circumference through the factor a(φ), defined as follows:

$$a^2(\varphi) = \frac{p_{\sigma^2,TI}(\varphi)}{p_{\sigma^2,TI}(0°)} \quad \rightarrow \quad a(\varphi) = \frac{p_{\sigma,TI}(\varphi)}{p_{\sigma,TI}(0°)} = \frac{C_{P,\sigma_{TI}}(\varphi)}{C_{P,\sigma_{TI}}(0°)} \tag{7.13}$$

$p_{\sigma,TI}(\varphi)$ is the standard deviation of the turbulence-induced contribution of the wind pressure; $C_{p,\sigma,TI}(\varphi)$ is the standard deviation of the corresponding pressure coefficient. In particular, at z/H = 0.85 it is:

Table 7.6 Body-induced and turbulence-induced pressure fluctuations (z/H = 0.85)

φ [°]	**$C_{p,\sigma}^2$ (Wist)**	**$C_{p,\sigma}^2$ (CRIACIV)**	**$C_{p,\sigma,BI}^2$**	**$C_{p,\sigma,TI}^2$ (WiSt)**	**$a^2(\varphi)$**	**a(φ)**
0	0.0242	0.0021	0.0000	0.0242	1.0000	1.0000
20	0.0229	0.0023	0.0000	0.0229	0.9428	0.9710
40	0.0280	0.0033	0.0000	0.0280	1.1529	1.0737
60	0.0381	0.0059	0.0016	0.0365	1.5044	1.2265

80	0.0397	0.0127	0.0091	0.0306	1.2602	1.1226
100	0.0772	0.0480	0.0441	0.0331	1.3660	1.1688
120	0.0207	0.0137	0.0128	0.0079	0.3271	0.5719
140	0.0231	0.0152	0.0141	0.0090	0.3720	0.6100
160	0.0273	0.0214	0.0206	0.0067	0.2769	0.5262
180	0.0251	0.0167	0.0155	0.0095	0.3929	0.6268
200	0.0290	0.0204	0.0192	0.0098	0.4043	0.6359
220	0.0237	0.0166	0.0156	0.0081	0.3341	0.5780
240	0.0207	0.0138	0.0129	0.0078	0.3226	0.5680
260	0.0806	0.0431	0.0381	0.0425	1.7527	1.3239
280	0.0486	0.0108	0.0058	0.0428	1.7673	1.3294
300	0.0369	0.0047	0.0004	0.0365	1.5056	1.2270
320	0.0225	0.0027	0.0001	0.0224	0.9254	0.9620
340	0.0212	0.0021	0.0000	0.0212	0.8755	0.9357
360	0.0242	0.0021	0.0000	0.0242	1.0000	1.0000

The same principle is attempted at other levels and the coefficient a(φ) is calculated according to equation (7.13). The results along the height are plotted in Figure 7.14 and in the following ones . The stagnation value is well representative for the turbulence-induced fluctuations around the circumference in the attached region. In the wake the fluctuations drop at around one half. Relying on that, the following simple model $a^{LM}(\varphi)$ can be used to estimate turbulence-induced fluctuations, for any I_u:

$$a^{LM}(\varphi) = \begin{cases} 1 & \varphi \leq \varphi_h \\ 0.5 & \varphi > \varphi_h \end{cases} \qquad (7.14)$$

The apex (^{LM}) stands for load model. According to that, the intensity of pressure fluctuations varies along the circumference: it is constant before separation and drops to 50% in the wake.

The red dotted curve “0.85-tot” in Figure 7.14 represents the ratio $\sigma_p(\varphi) / \sigma_{p,0°}$, where the suffix “tot” means “without subtraction of body-induced fluctuations”. It shows that a considerable contribution of body-induced fluctuations has been removed by the model, although the red curve (namely 0.85) still appears to be higher than 1 before separation. The reason is due to some body-induced contributions which are correlated to turbulent properties of the incoming flow and cannot be removed through tests in smooth flow. These contributions are manly at the flanges of the cylinder. In any case, the departure from 1 is neglected in the proposed simplified model (equation (7.14)).

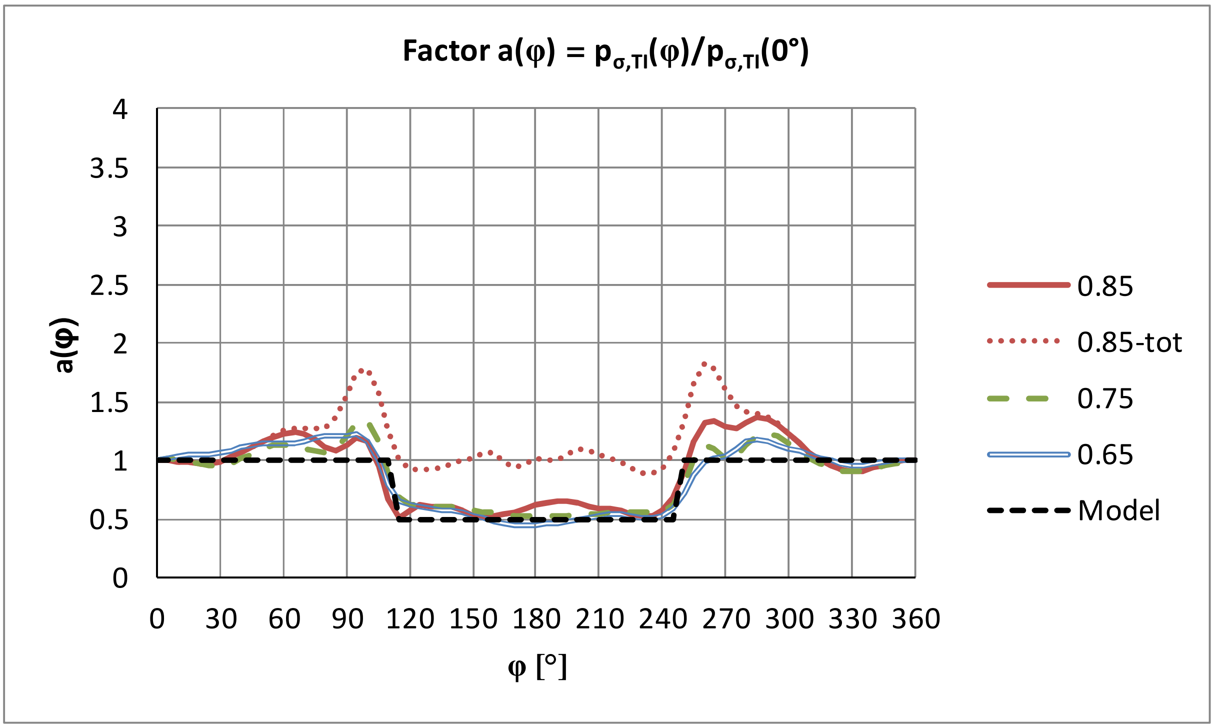

Figure 7.14 Factor a(φ) for modelling turbulence-induced pressure fluctuations (highest levels)

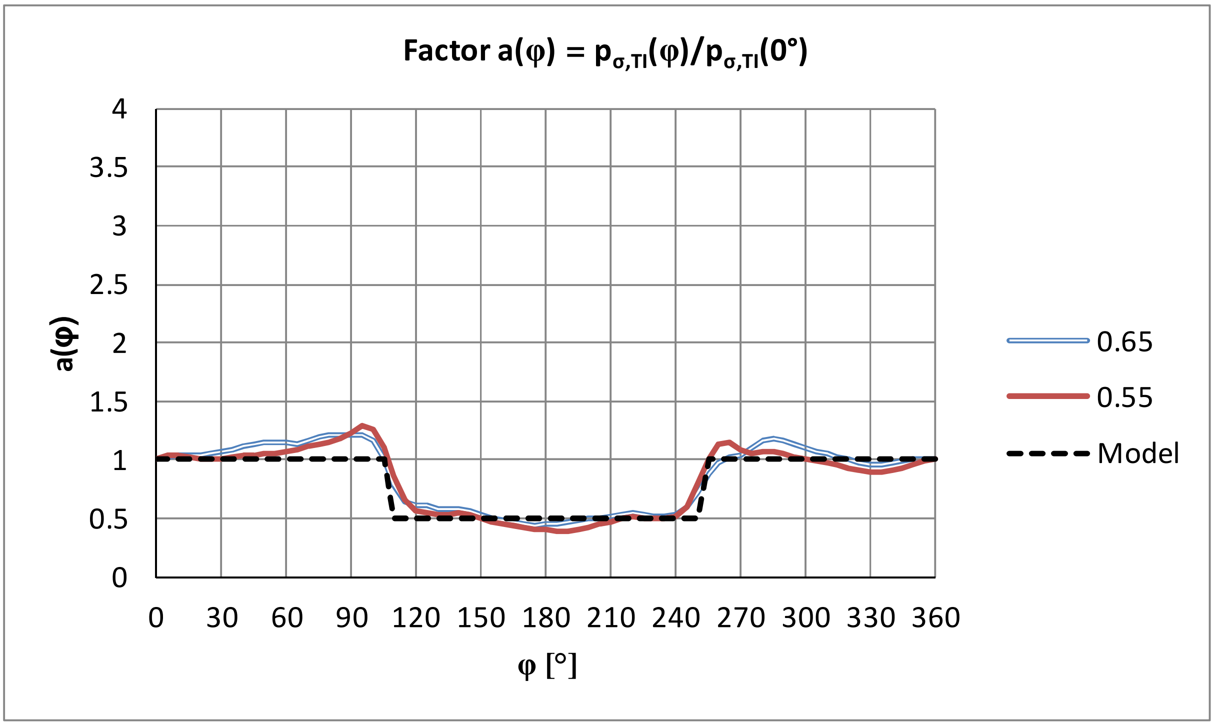

Figure 7.15 Factor a(φ) for modelling turbulence-induced pressure fluctuations (intermediate levels)

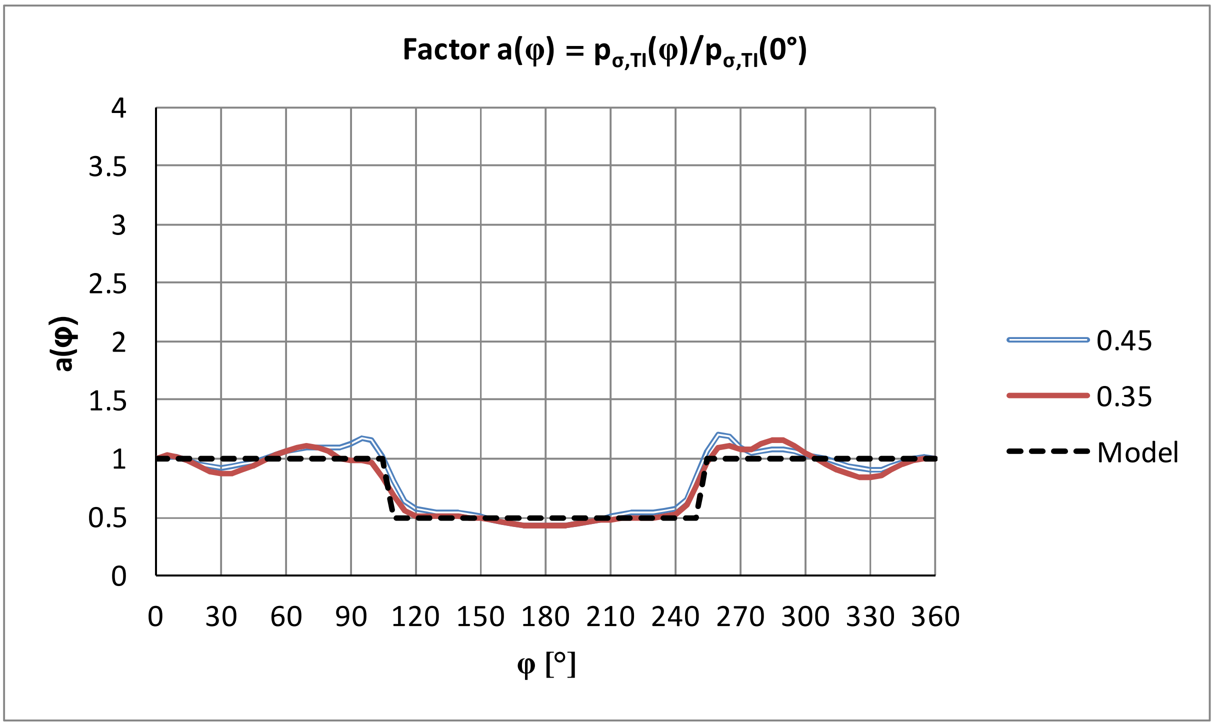

Figure 7.16 Factor a(φ) for modelling turbulence-induced pressure fluctuations (low levels)

The comparison with results in literature is a proof of validity of the model, despite its approximations. In particular, similar results are obtained in full-scale data at transcritical Re by Pröpper (1977, fig. 8.8) on cooling towers. In that case, the contribution of vortex separation is low, so that the predominant contribution is turbulence-induced.

A further comment regards the linear extrapolation of the variances at $I_u^2 = 0$ in Figure 7.12 and Figure 7.13. It was an inevitable choice, since only two points per level at different I_u were available at each angle. However, the choice resulted to be rather reasonable. As a proof, the height-dependent variances at stagnation ($C_p,\sigma^2(z) \approx C_p,\sigma^2{}_{TI}(z)v$ c) are plotted as a function of I_u^2 in Figure 7.17. It shows that a linear relationship, whose extrapolation approximately crosses the origin of axes, is rather correct. The points at the highest turbulence intensity represent pressures on the tower at low levels ($z/H < 0.20$). The reason for which I_u is constant is the presence of the smooth collector roof (Figure 4.8). In any case, at $z/H < 0.20$ the model fails. The reason is that the horseshoe vortex system and the base vortices vary with the free-flow structures and the extrapolation at $I_u = 0$ is strongly non-linear.

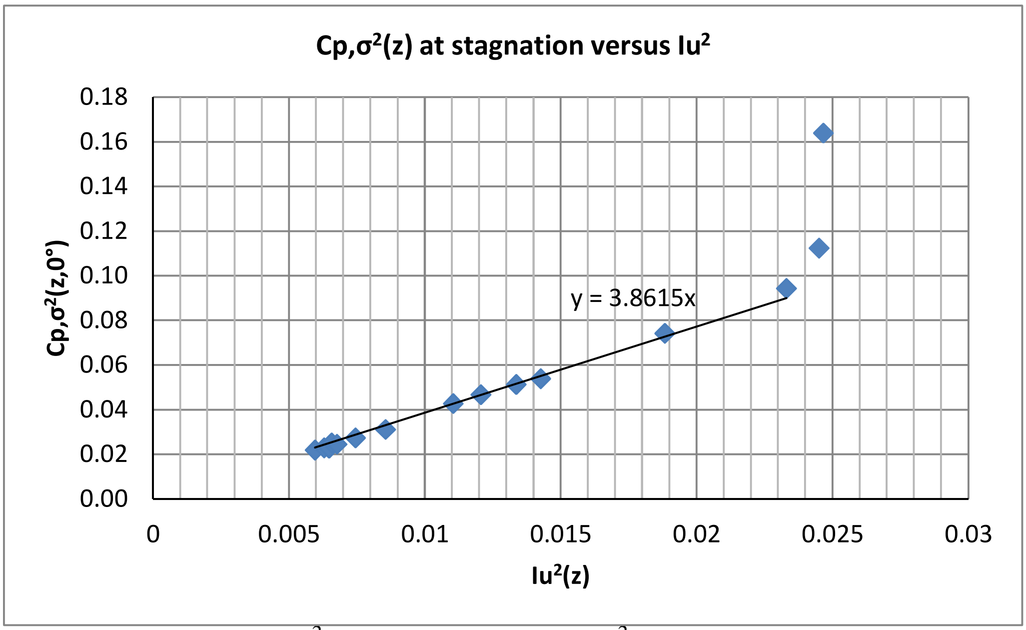

Figure 7.17 Variances C_{p},σ^2 *at stagnation versus* I_u^{2}*: a linear relationship (WiSt data)*

So far, the factor a(φ) has allowed to calculate the turbulence-induced fluctuations around the circumference provided their value at stagnation. Then, the latter can be calculated from the turbulence intensity of the incoming flow. This allows to generalize the model for any boundary layer condition. A first approach has already been proposed in Figure 7.17. A similar approach is based on the factor A(z), which is the ratio between the intensity of pressures at stagnation (the turbulence-induced contribution, namely $I_{P,TI}(z)$) and the intensity of turbulence $I_u(z)$:

$$A(z)=\frac{I_{p,TI}(z)}{I_u(z)} \tag{7.15}$$

The intensity of pressures at stagnation $I_{P,TI}(z)$ is approximately equal to the standard deviation of the pressure coefficient at 0°, being $p_m(z,0°)$ (mean pressure) approximately equal to the mean velocity pressure $q_m(z)$ (because $C_p(z,0°)\approx 1$) and $C_p,\sigma_{TI}(z,0°) \approx C_p,\sigma(z,0°)$, as explained by equation (7.16).

$$\begin{aligned} I_{p,TI}(z) &= \frac{p_{\sigma,TI}(z,0°)}{p_m(z,0°)} = \frac{p_{\sigma,TI}(z,0°)}{C_p(z,0°)q_m(z)} \approx \\ &\approx \frac{p_{\sigma,TI}(z,0°)}{q_m(z)} = C_{P,\sigma,TI}(z,0°) \approx C_{P,\sigma}(z,0°) \end{aligned} \tag{7.16}$$

Therefore:

$$A(z) \approx \frac{C_{P,\sigma}(z,0°)}{I_u(z)} \tag{7.17}$$

The coefficient A(z) calculated on the basis of WiSt results is approximately constant along the height, as shown in Figure 7.18. Its mean value is around 1.93, which is approximately the square root of the slope coefficient of the equation y = 3.8615 in Figure 7.17. Only close to the ground ($z/H \leq 0.20$) is the ratio A(z) higher than twice the turbulence intensity, due to the horseshoe vortex system, as previously mentioned with regard to Figure 7.17. Numerical values are reported in Table 7.7. The value $A^{LM}(z) = 2$, on the safe side, can be assumed by the designer without any significant overestimation (see section 7.3). It means that the intensity of pressure at stagnation is about twice the turbulence intensity of the flow.

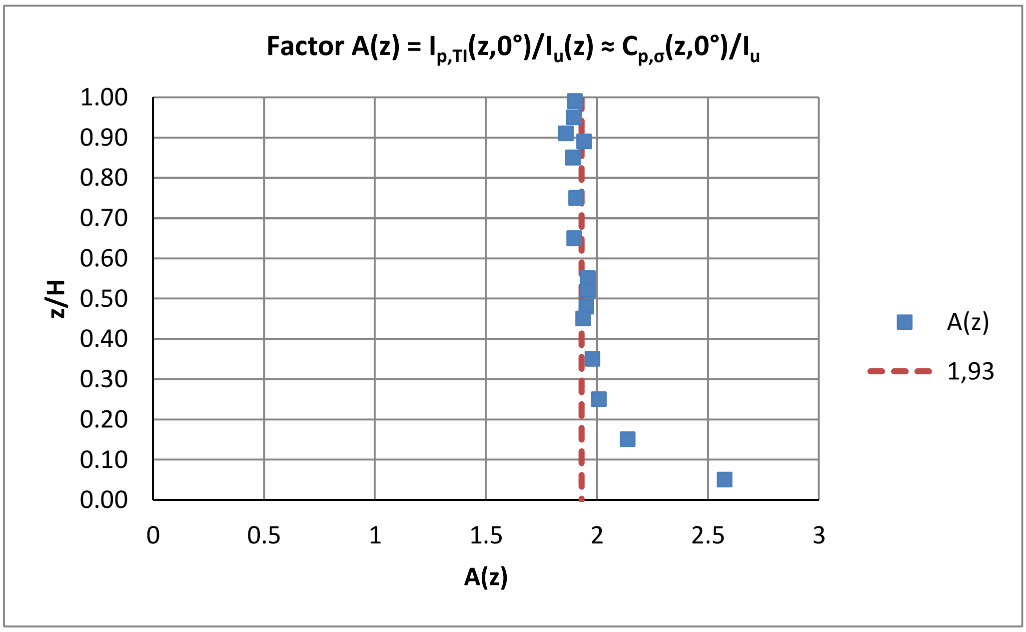

Figure 7.18 Factor A(z)

Table 7.7 Factor A(z) and simplified load modelling $A^{LM}(z)$

	WiSt		
z/H	**I_u**	**$C_{p,\sigma}(z,0°)$**	**$A(z) \approx C_{p,\sigma}(z,0°)/I_u$**
0.99	0.0772	0.1469	1.9016
0.95	0.0794	0.1506	1.8970
0.91	0.0806	0.1499	1.8609
0.89	0.0811	0.1578	1.9443

0.85	0.0823	0.1557	1.8917
0.75	0.0863	0.1646	1.9067
0.65	0.0925	0.1757	1.8985
0.55	0.1052	0.2061	1.9598
0.52	0.1099	0.2154	1.9599
0.48	0.1156	0.2259	1.9532
0.45	0.1195	0.2317	1.9394
0.35	0.1373	0.2719	1.9809
0.25	0.1527	0.3068	2.0095
0.15	0.1566	0.3349	2.1392
0.05	0.1571	0.4046	2.5761
Simplified load modelling: $A^{LM}(z) = 2$			

Under the basic assumption that body-induced fluctuations are statistically independent on turbulence-induced fluctuations (Hunt, 1975), the former can be evaluated by an experiment in smooth flow. The result of the extrapolation at $I_u = 0$ at all levels, based on WiSt and CRIACIV results, as previously described, is plotted in Figure 7.19. Numerical values can be found in the appendix (Table A.1). Differences between the two sides due to experimental asymmetries have been averaged out. The figure highlights three distinct regions: the tip region, with a strong effect of tip-associated vortices; the two-dimensional region, where the strength of Karman vortex shedding is practically absorbed by the stochastic fluctuation (the curves as z/H = 0.55, 0.45, 0.35 are close to zero); the low region with the ground effect.

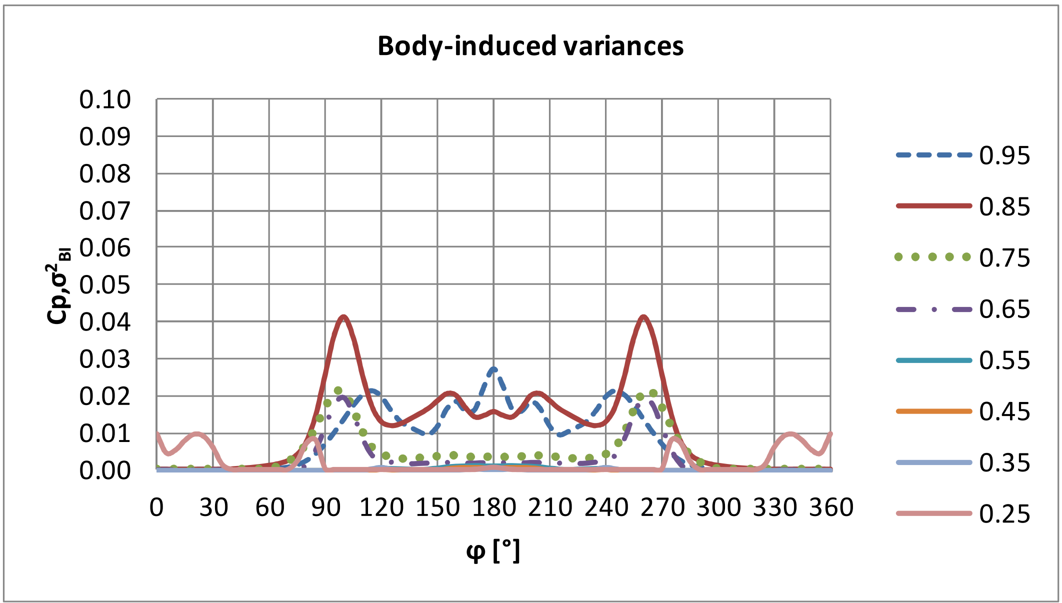

Figure 7.19 Body-induced fluctuations $C_{p,}\sigma^2_{BI}$ all around the tower

7.1.4 Cross-correlation coefficients

The cross-correlation coefficients represent, beside the mean and the rms values, the third piece of information to calculate the quasi-static response of structures to the stochastic wind loading process. They give information about the lack of correlation (size effect). Simple models of cross-correlations of pressure coefficients are proposed in this section, they can be applied for calculation of shell stresses on the solar tower.

The analysis of cross-correlations of pressure coefficients is split up into the vertical and horizontal directions. Their cross product is used to approximate the cross-correlations between points having both horizontal and vertical separation, in case measured data are not available. The goodness of the approximation is discussed at the end of the section and later on in terms of the structural response. This simplification allowed to reduce significantly the total number of simultaneous measurements in the experiments, but a further refinement would be advisable for the future (Chapter 8).

Similarly, since force coefficients are calculated by integration of pressures at each level, the evaluation of their cross-correlations required simultaneous measurements of each level with all the other ones. Simultaneous data of forces at all levels are not available, therefore it is not possible to develop a complete model for cross-correlations of drag and lift coefficients to be used in beam-like calculations. Therefore, cross-correlations of forces are used whenever available for a deeper insight and clarification of pressure cross-correlations.

Vertical cross-correlation coefficients

The vertical correlation of pressures at stagnation depends on the turbulence structure of the incoming flow. As before, it would be important to generalize the results obtained for the specific turbulence condition tested in the wind tunnel to other turbulence conditions. For this purpose, it is mainly referred to results at WiSt, since measurements of both cross-correlations of pressures and velocities are available there. According to Teunissen (1970) the vertical correlation coefficients of wind velocities (along-wind component) in the atmospheric boundary layer have an exponential decay along the height:

$$\rho_u(\Delta z) = e^{-C_{uu}\Delta z} \qquad (7.18)$$

By definition, the vertical integral length scale of turbulence (L_{uz}) is given by integration:

$$L_{uz} = \int_0^{\infty} \rho_u(\Delta z) d(\Delta z) \tag{7.19}$$

Therefore $C_{uu} = 1/L_{uz}$. If also the vertical correlations of pressures ($\rho_p(\Delta z)$) can be described by an exponential curve, then the vertical decay of pressure fluctuations can be related to the vertical decay of turbulence fluctuations. In general, it is:

$$\rho_p(\Delta z) = e^{-C_{pp}\Delta z} \tag{7.20}$$

L_{pz} is the pressure correlation length:

$$L_{pz} = \int_0^{\infty} \rho_p(\Delta z) d(\Delta z) \tag{7.21}$$

Similarly, $C_{pp} = 1/L_{pz}$ and a factor "c" is introduced to describe the relationship between L_{uz} and L_{pz}:

$$\rho_p(\Delta z) = e^{-\Delta z / Lpz} = e^{-c \cdot \Delta z / Luz} \tag{7.22}$$

where:

$$c = \frac{L_{uz}}{L_{pz}} \tag{7.23}$$

However, provided the information regarding the vertical correlation of turbulence (L_{uz}), the relationship between L_{uz} and L_{pz} is in general unknown. It further depends, according to Hunt (1975), on the diameter of the structure. For example, for a circular cylinder ($L_{uz}/D = 0.2 \div 0.5$) Hunt finds $L_{pz}/L_{uz} = 1.5 \div 2.5$ (the factor c is the inverse value). According to him, the correlation length of pressure fluctuations (L_{pz}) is larger than the integral scale of turbulence L_{uz} because the vortices which are smaller than the diameter of the structure pile up at stagnation. This creates more similarity in the pressure fluctuations field.

In the case of the solar tower tested in the WiSt wind tunnel, the vertical integral length scale of the velocity fluctuation varies along the height around 200 mm (see Table 4.2). It is then of the same order of the tower diameter. Two representative levels at small and large heights (z_{ref} = 100 mm, upwards direction; z_{ref} = 700 mm, downwards direction) are reported in Figure 7.20, in view of a direct comparison with the pressure correlations. The vertical cross-correlations of pressures at stagnation are fitted with a negative exponential curve. Figure 7.21 reports L_{pz} at two levels, selected as the most suitable ones for the direct comparison with Figure 7.20.

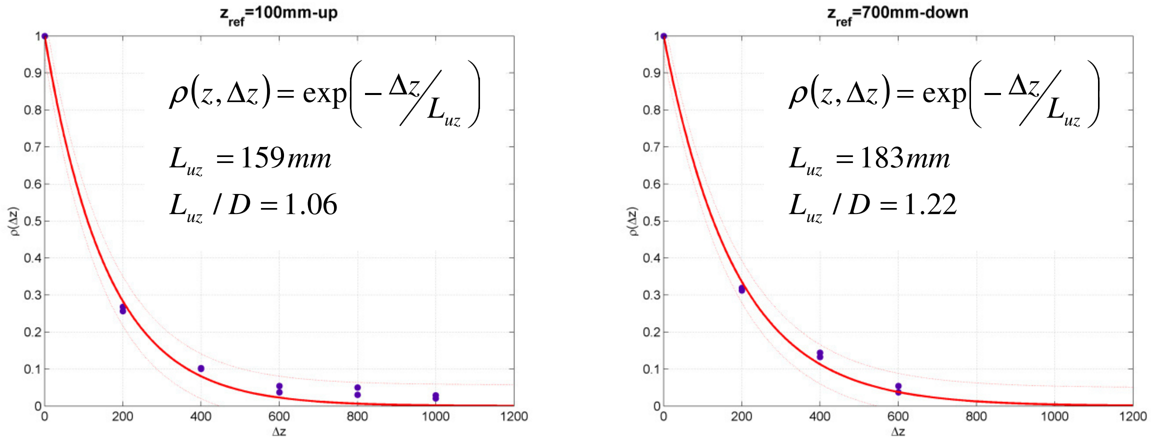

a) *b)*

Figure 7.20 Vertical correlation coefficients of wind velocity (u-component)
a) z_{ref} *= 100 mm (upwards); b)* z_{ref} *= 700 mm (downwards);*

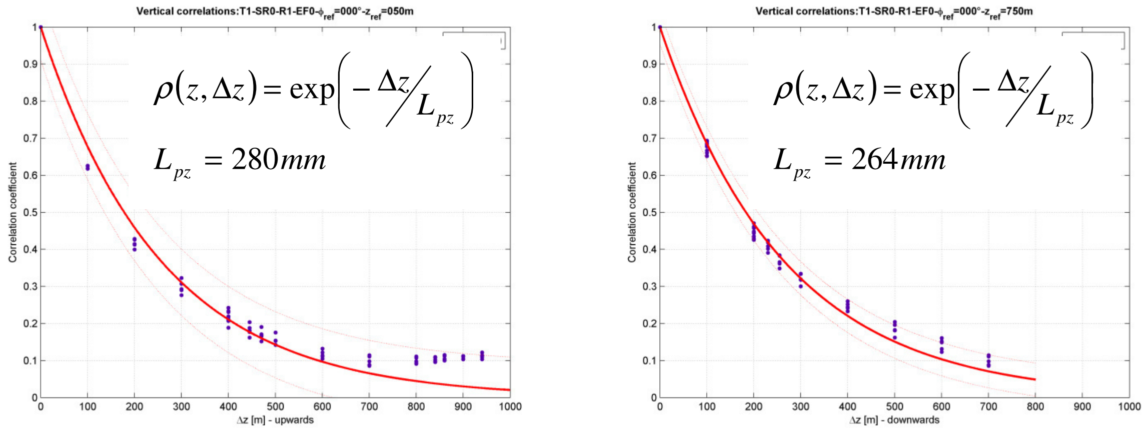

a) *b)*

Figure 7.21 Vertical correlation coefficients of wind pressure at stagnation
a) z_{ref} *= 50 mm (upwards); b)* z_{ref} *= 750 mm (downwards);*

The comparison between Figure 7.20 and Figure 7.21 shows that $L_{pz} > L_{uz}$. It confirms Hunt’s theory of the piling up of vortices at stagnation even for integral length scales of turbulence which are comparable to the tower diameter. Then, in order to develop a general model, a more systematic study is needed at several reference heights and different meridians. It is reported in the following.

In principle, L_{pz} and L_{uz} depend on the direction of movement (Δz upwards, or Δz downwards). However, in view of a simplified model, the correlation coefficients are considered as a function of $|\Delta z|$. Figure 7.22 gives an overview of the pressure correlation lengths in the attached region of the cylinder (i.e. before separation). As said, they are calculated by integration of $\rho(|\Delta z|)$, i.e. assuming independence from the direction of movement. The largest correlation length is the angle $\varphi = 60°$. The figure also plots the integral length scales of the flow L_{uz}. Reference values, averaged along the height, are:

- $L_{uz} \approx 195$ mm (Lux/D = 195/150 = 1.30);
- $L_{pz} \approx 285$ mm at $\varphi = 0°$ ($c(0°) = L_{uz}/L_{pz} = 0.68$);
- $L_{pz} \approx 254$ mm at $\varphi = 20°$ ($c(20°) = L_{uz}/L_{pz} = 0.77$);
- $L_{pz} \approx 341$ mm at $\varphi = 300°$ ($c(300°) = L_{uz}/L_{pz} = 0.57$).

Figure 7.23 shows the experimental height-dependent ratio L_{uz}/L_{pz} (the so-called factor "c", equation (7.23)) at different circumferential angles before separation. The figures shows that the ratio L_{uz}/L_{pz} is different at each angle but it is approximately constant along most of the height.

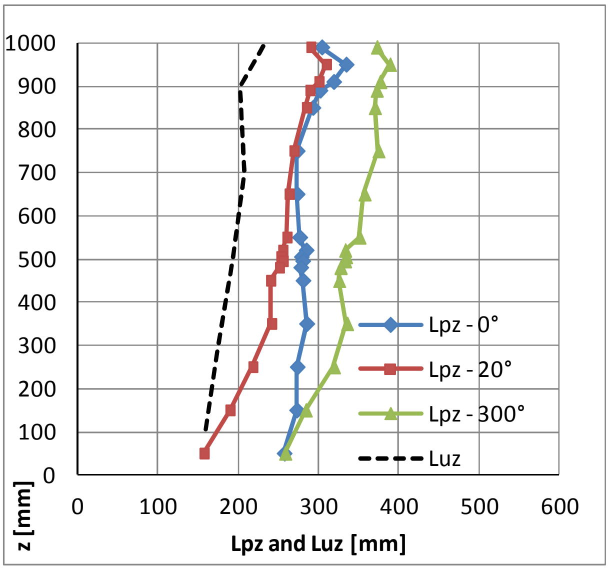

Figure 7.22 L_{pz} and L_{uz} in the attached region before separation, calculated by integration of $\rho(|\Delta z|)$, i.e. assuming independence of direction of movement (WiSt results)

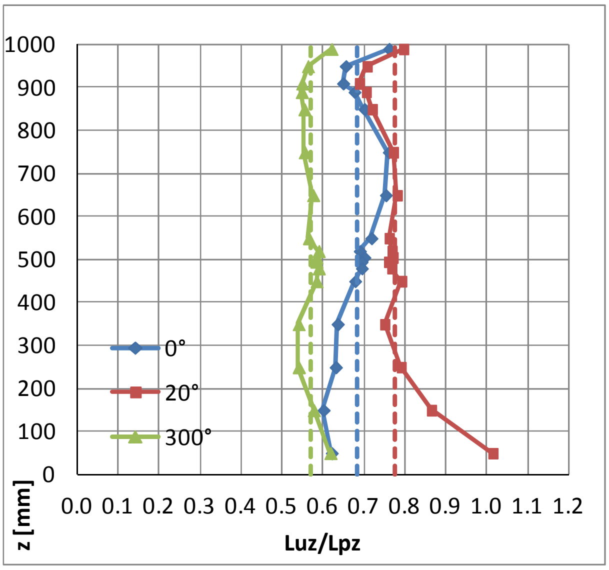

Figure 7.23 Factor $c = L_{uz}/L_{pz}$ (WiSt results)

The cross-correlation coefficients in the wake region drop faster with increasing distance. It would lead to small values of L_{pz}. In fact, at WiSt, the cross-correlation remains almost constant to a non-zero value, around 0.18, at very large distances of separation (Figure 7.24). Such a constant correlation is not present in the undisturbed flow. The physical reason is probably a big steady vortex in the near-wake, due to the recirculating flow, as discussed in section 6.3 in the comparison with CRIACIV data. From a mathematical point of view, the negative exponential function would force the curve rapidly to zero and would not consider this quasi-asymptotic behaviour, leading to an underestimated value of L_{pz}. A double negative exponential function fits better in the wake (Figure 7.24, red curve). However, in this way the integration of the cross-correlation coefficients from zero to ∞ results in an impressively high value. Therefore, it is decided to calculate a so-called "equivalent correlation length" by integration of the double exponential fitting function along the tower height (from zero to $\Delta z = H$). It can then be used to model the correlations according to equation (7.22). The resulting values of the equivalent correlation lengths for the wake region are reported in Figure 7.25. Apart from the departure in the tip region, it can be approximately said that:

- $L_{pz} \approx 260$ mm at $\varphi = 120°$ $\quad$ $(c(120°) = L_{uz}/L_{pz} = 0.75)$;
- $L_{pz} \approx 340$ mm at $\varphi = 180°$ $\quad$ $(c(180°) = L_{uz}/L_{pz} = 0.57)$;

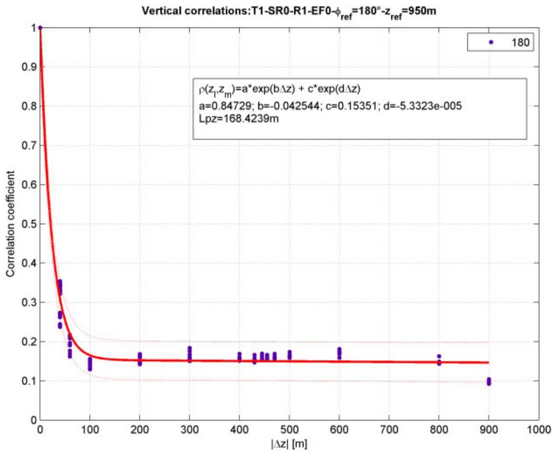

Figure 7.24 ρ(0.95H,|Δz|) double negative exponential fitting curve, in order to fit the almost constant correlation at large distances (WiSt results)

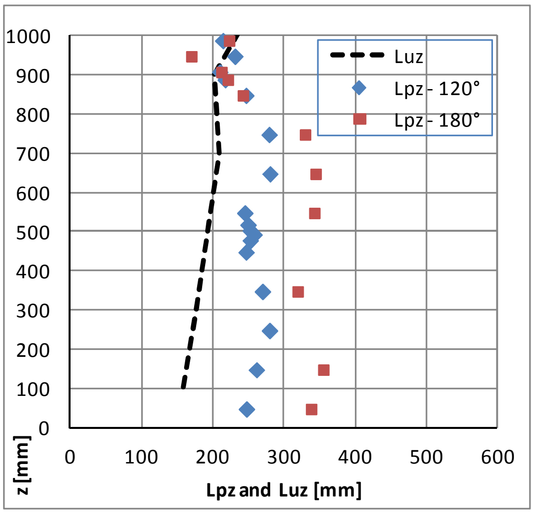

Figure 7.25 Equivalent L_{pz} in the wake region, calculated by integration along the tower height (WiSt results)

It results that around the circumference there is a certain variability of L_{pz}. In any case, provided the values of L_{pz} at different angles, the vertical cross-correlations are easily modelled by applying equation (7.22), i.e. by a negative exponential function.

In order to estimate the goodness of this modelling, Figure 7.26 plots the measured cross-correlations by using the dimensionless x-axis $|\Delta z|/L_{pz}$. The black line is the modeled curve by using a negative exponential function according to equation (7.22). In the dimensionless plane it is just $\rho(|\Delta z|/L_{pz}) = \exp(-1*|\Delta z|/L_{pz})$. It can be seen (Figure 7.26a), that the use of a negative exponential function provides a good estimation of the vertical cross-correlations in the attached region of the cylinder before separation. In the wake region (Figure 7.26b) the scatter is bigger, also because of the quasi-asymptotic behaviour at large distances. In any case, Figure 7.26b, compared to Figure 7.24, shows that this behaviour is partially removed by the use of the "equivalent" L_{pz}, as previously defined. However, at short distances it tends to overestimate the cross-correlations.

In any case, the goodness of the proposed stochastic model for vertical correlations does not depend on the scatter in the approximation of the load, rather on the effect on the response. A beam-like calculation (through the co-variance method) estimated that an even high non-zero drag correlation at large distance (e.g. 0.3) would produce an increase of around 3% of the base peak bending moment. This increase is further reduced by introducing the equivalent (larger) L_{pz}. Therefore, it can be concluded that a simple negative exponential function according to (7.22) can be used without any significant underestimation.

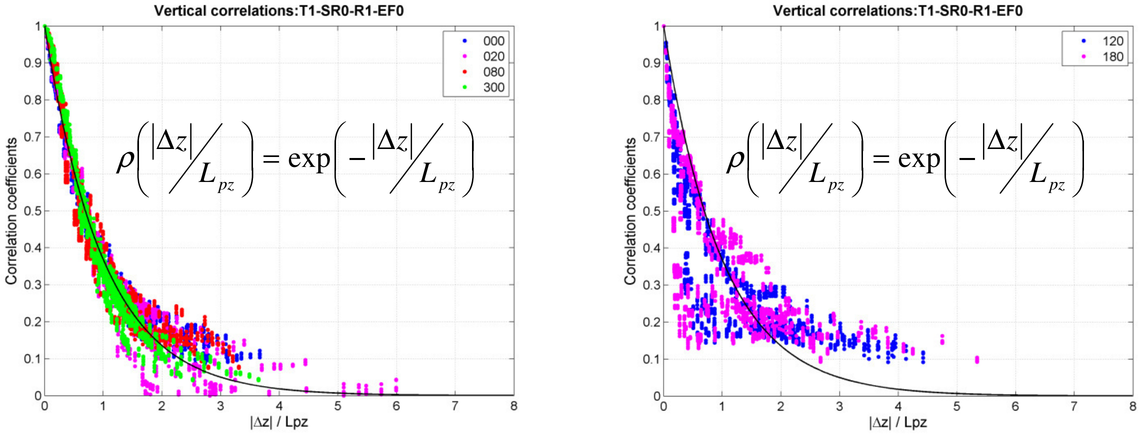

a) *b)*

Figure 7.26 Modelling of vertical cross-correlations by negative exponential function a) attached region before separation; b) wake region

In order to generalize the model to any turbulent boundary layer flow, which is characterized by a certain profile of $L_{uz}(z)$, L_{pz} should be evaluated from L_{uz} by using the factor "c" and equation (7.23). On the basis of WiSt results, such factors around the circumference are summarized in Table 7.8.

A further simplification can be introduced in the load model (^{LM}) by neglecting the circumferential variation of L_{pz}. This is reported in the last row of Table 7.8. Although the load input might be rather approximated, the calculation of the response did not show any significant change. Because of that, the approximation (^{LM}) is recommended.

Table 7.8 The factor "c" to relate L_{pz} and L_{uz}

Luz [mm] - WiSt	φ [°]	L_{pz} [mm] - WiSt	c = L_{uz}/L_{pz}
195	0	285	0.68
	20	254	0.77
	60	341	0.57
	80	296	0.66
	120	260	0.75
	180	340	0.57
(^{LM}) Load Model approx.	0-360		2/3

In conclusion, in the general case the vertical cross-correlations of pressures can be modelled as:

$$\rho_p(z,|\Delta z|) = e^{-\left(\frac{2}{3}\right)\frac{|\Delta z|}{L_{uz}(z)}} \tag{7.24}$$

Horizontal cross-correlation coefficients

The horizontal correlation coefficients around the circumference are governed by the mean flow pattern, while the structure of incoming turbulence is of secondary importance (Pröpper, 1977). Therefore, the first parameter to describe the cross-correlation matrix at a certain level is the separation angle φ_h (see Table 7.5).

By definition, $\rho(\varphi_1; \varphi_2) = \rho(\varphi_2; \varphi_1)$, therefore the correlation matrix is symmetric with respect to the main diagonal, whose values are equal to 1. Moreover, due to the symmetry between the two sides of the cylinder, the matrix is also symmetric with respect to the secondary diagonal. The description of one quarter of the matrix will then contain all the necessary information[7].

---

[7] In case of rings, instead, the presence of a bubble on only one side of the cylinder breaks the symmetry with respect to the secondary diagonal.

The correlation coefficients depend on the reference position and on the direction of movement. The reference position is classified in two groups: points before separation ($\varphi < \varphi_h$) and points after separation ($\varphi \geq \varphi_h$). The direction of movement is either downstream or upstream. The cross-correlations of stagnation and of rear stagnation (i.e. 0° and 180°) are the only ones which are symmetric around the circumference.

The circumferential correlations of the stagnation point with all the other points around the circumference resemble the mean pressure distribution (Figure 7.27). Stagnation and maximum suction have a strong negative correlation; stagnation and wake area have small negative correlations. It means that the fluctuations around the circumference appear to be organized by the mean flow and a considerable portion of them may be understood as a "breathing" of the mean flow.

The correlations of rear stagnation prove that the correlation between points in the wake and points before separation is not equal to zero. There is a relatively strong correlation between the maximum lateral suction and the wake ($\rho(180°,70°) \approx 0.6$) and even at 0° the correlation is not zero: $\rho(180°,0°) = -0.2$. These values are in agreement with Pröpper's results on cooling towers (Pröpper, 1977, figure 8.14). Therefore, Hunt's assumption of statistically independent pressure fluctuations due to incoming turbulence and vortex shedding is not completely confirmed.

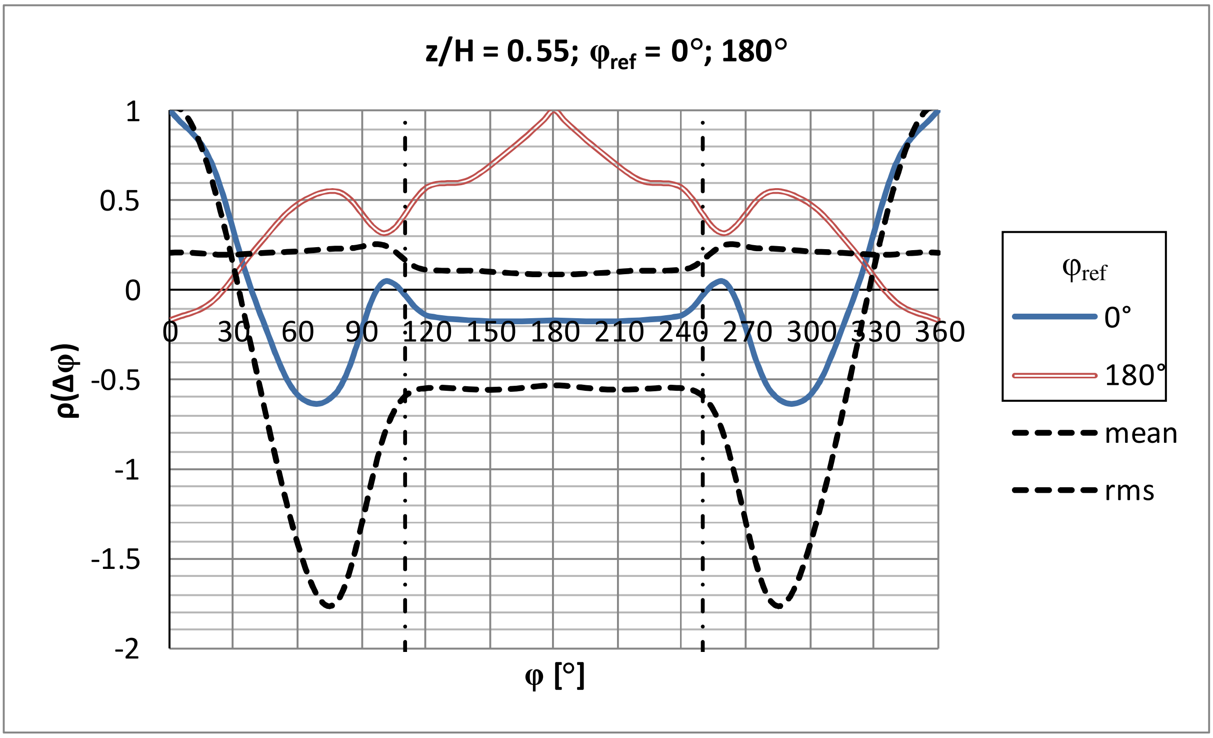

Figure 7.27 Cross-correlation coefficients $\rho(0°,\Delta\varphi)$ and $\rho(180°,\Delta\varphi)$ at z/H = 0.55

Figure 7.28 plots the circumferential cross-correlations at z/H = 0.55 when the reference position (listed in the legend, corresponding to $\rho=1$) is before separation. The downstream movement from the reference position has to be read in the graph from left to right, while the direction towards left refers to the upstream direction of movement. Similarly, Figure 7.29 plots the circumferential cross-correlations at z/H = 0.55 when the reference position is in the wake. All these pieces of information are then synthesized together in the correlation matrix in Figure 7.30.

Let us consider the cross-correlations to a reference angle φ_{ref} before separation (Figure 7.28). A significant difference between going downstream or upstream the cylinder from the reference position is the extension of the range of the negative correlations. In particular, in the downstream direction there is a weak negatively correlated range, which disappears in a positive plateau as the reference position approaches separation. Referring to $\rho(20°,\varphi)$, for example, the negative correlated range lies between $\rho(20°,60°)$ and $\rho(20°,100°)$, i.e. $\Delta\varphi = 40°$. The position $\varphi_{ref} = 60°$ is always positively correlated with the downstream positions. The upstream cross-correlations, instead, drop in a deep negatively correlated area when the two points belong to opposite sides of the cylinder. For example, at $\varphi_{ref} = 20°$ the negative range with circumferential positions on the other side lies between $\rho(20°,340°)$ and $\rho(20°,270°)$, i.e. $\Delta\varphi = 70°$ and the correlation drops till -0.7. The negative correlation between the two sides of the cylinder is marked by the dark blue on the upper right-hand-side corner in Figure 7.30 (or, similarly, the lower left-hand-side corner).

Along the height, the spanwise variation of the circumferential correlations follows the same organization of the mean flow. The following three main regions are detected along the height (Table 7.5):

- tip region (z’ < 2D from the top, i.e. z’ < 0.3H in the case study), Figure 7.31;
- normal region (z/H > 0.5 and z’ > 0.3H), Figure 7.30
- low region (z/H < 0.5), Figure 7.32;

For simplicity, only one correlation matrix is proposed for the low region (Figure 7.32), that is an envelope of values on the safe side. Instead, the tip region can be further subdivided as follows:

- tip region (z’ < 2D): a) z’ < 0.3D (Figure 7.31a)
  b) 0.3D ≤ z’ ≤ 0.5D (Figure 7.31b)

c) 0.5D ≤ z’ ≤ D (Figure 7.31c)
d) D ≤ z’ ≤ 2D (Figure 7.31d)

Numerical values of correlation matrices for calculations are reported in the appendix (section 10.1).

Correlations between points with horizontal and vertical separation

The cross-correlations between points with horizontal and vertical separation ($\Delta\varphi$ and Δz) are approximated by the cross-products (equation (7.25)). The approximation in unavoidable, because the streamlines of the flow descend while flowing round the body. These movements are even enhanced by the velocity gradients in shear flow. Therefore, it is generally not possible to split the correlation into a height-dependent and a circumferential distribution. The topic is also addressed in Kasperski&Niemann (1988). However, the three dimensional correlation field has not been completely measured in the experiments on the tower. Because of that, the use of approximation (7.25) cannot be avoided. Further tests are advisable in the future for refinement of this model.

$$\rho(z_1,\varphi_1;z_2,\varphi_2) \cong \rho(z_1;z_2)\cdot\rho(\varphi_1;\varphi_2) \tag{7.25}$$

Equation (7.25) can be applied in two ways: the vertical correlation can be evaluated at $\varphi = \varphi_1$ and the horizontal correlation at $z=z_2$ or viceversa. Numerically, the results are different, but a general rule does not exist. Therefore, in this work the cross-product was calculated in both ways and the safest result was considered. Whenever measured, $\rho(\varphi_1,z_1;\ \varphi_2,z_2)$ is compared to its approximated modelling. The modelling results to be mostly on the safe side. Only the cross-correlations in the wake might be underestimated.

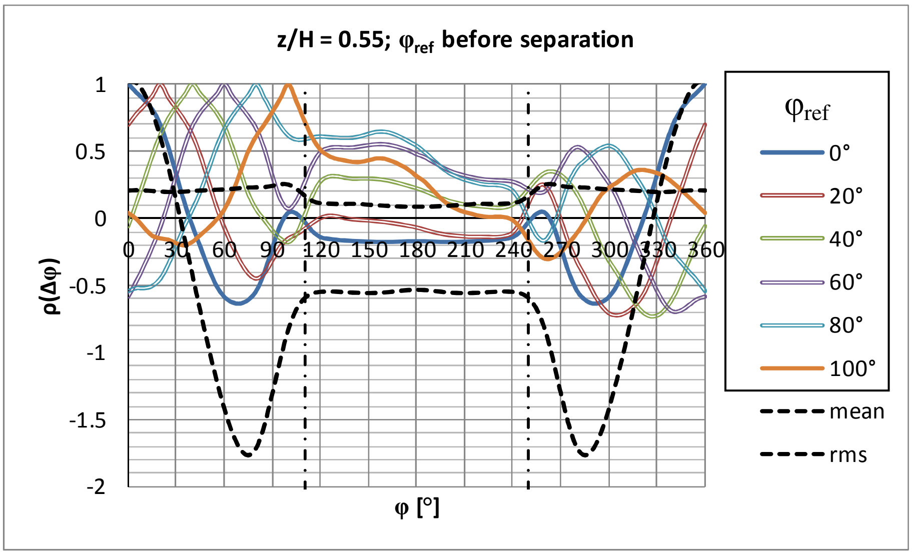

Figure 7.28 Horizontal cross-correlation coefficients at z/H = 0.55; φ_{ref} before separation

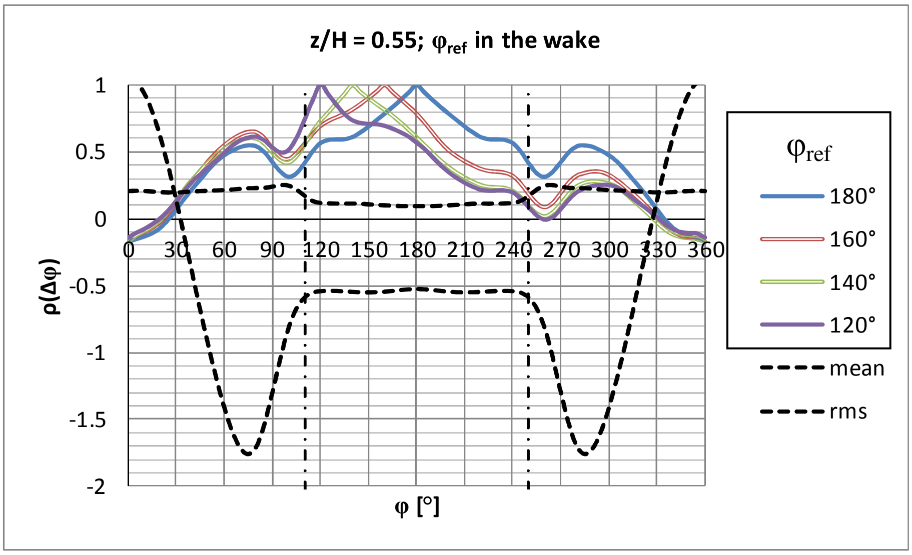

Figure 7.29 Horizontal cross-correlation coefficients at z/H = 0.55; φ_{ref} in the wake

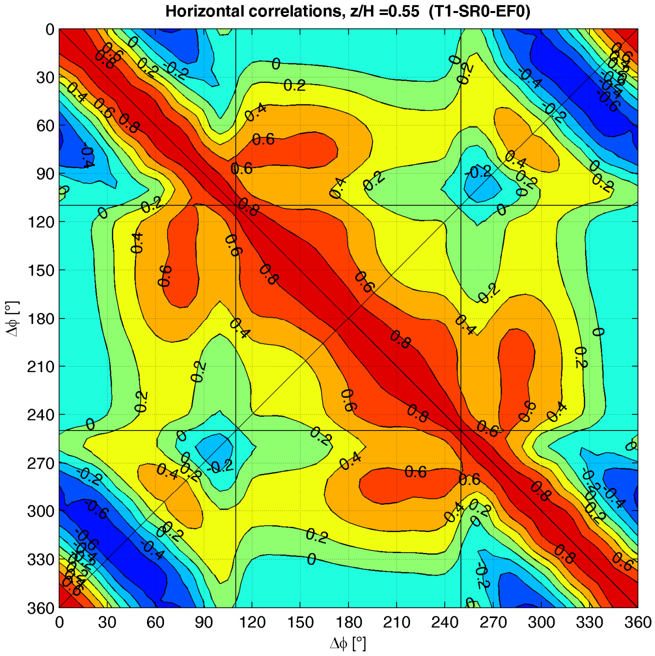

Figure 7.30 Horizontal cross-correlation coefficients at z/H = 0.55

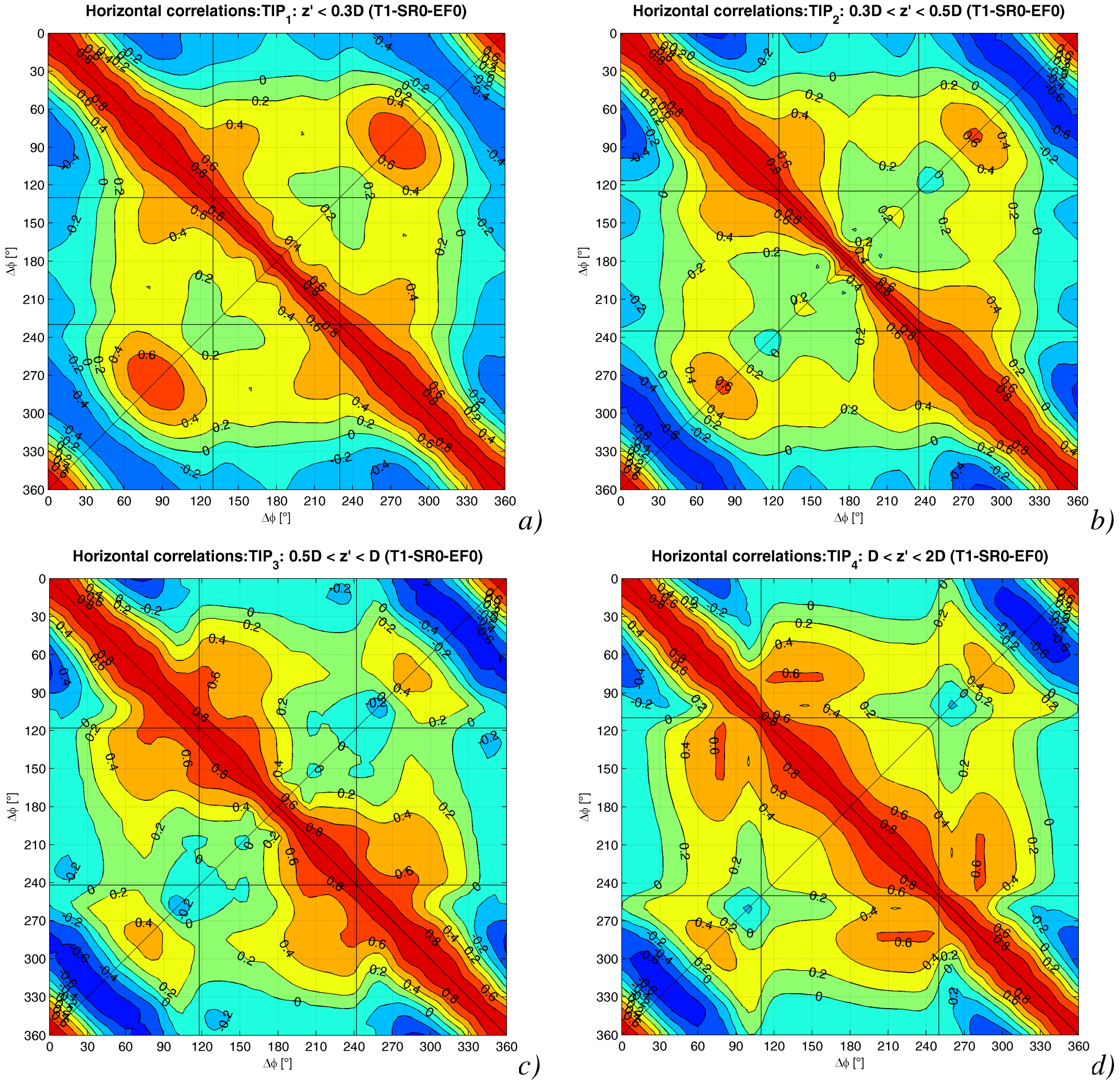

Figure 7.31 a-d) Horizontal cross-correlation coefficients in the tip region (z' < 2D)

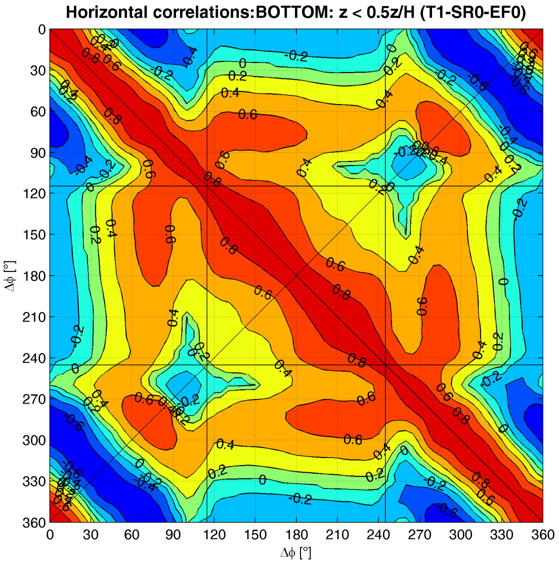

Figure 7.32 Horizontal cross-correlation coefficients in the low region (z/H < 0.5)

7.2 The beam response

The beam response of the solar tower is governed by the first natural vibration mode (n_1 = 0.17 Hz, Figure 2.20). Being $S_t \approx 0.2$ (Chapter 4), the critical velocity for vortex resonance is about $n_1D/\ S_t = 0.17*150/0.2 = 127$ m/s. This is much higher than the design velocity U(1000) ≈ 55 m/s (Deaves&Harris model, Figure 2.4), so that resonance between the Strouhal frequency and the (transversal) vibration frequency is not expected. In these conditions, the design is led by the drag force, even though the cross-wind response remains an important contribution.

This section addresses both the along- and the across-wind beam response to the stochastic wind loading process. The background contribution is at first evaluated by the covariance method. Then, it is split up in the frequency domain by using time histories and influence coefficients. This calculation is then repeated by using the software Ansys, including inertial and damping forces. The first sub-section (7.2.1) considers the reference load condition, i.e. without any load modification produced by the rings. The effect of the rings is estimated in the second sub-section (7.2.2).

7.2.1 Quasi-static and dynamic beam response

The beam response of the tower is evaluated in this section by using the reference load condition, i.e. the effect of the rings on the load is not considered. This load configuration corresponds to the experimental results SR0.

At first, the background response to the drag force (σ_B^2), i.e. the response to the excitation that is transmitted without resonant amplification, is estimated without any split into frequencies through the covariance method (Niemann et al., 1996). This method uses statistical averages obtained from measured time series rather than the time series themselves.

$$\sigma_B^2 = \boldsymbol{\eta}^T \cdot \mathbf{cov}_D \cdot \boldsymbol{\eta} \qquad \text{and } \mathbf{cov}_D = diag[F_\sigma] \cdot \boldsymbol{\rho}_D \cdot diag[F_\sigma] \tag{7.26}$$

The matrix $\mathbf{cov}_D$ contains the covariances between drag forces at different levels and the vector $\boldsymbol{\eta}$ contains the influence coefficients for a certain effect at a certain cross-section. The covariances can be further split up into the product between rms values and correlation coefficients. The peak value of the bending moments ($M_{D,peak}$) is defined as:

$$M_{D,peak}(z) = M_{D,m}(z) + k_p M_{D,\sigma}(z) \qquad \text{where } k_p = 3.5. \tag{7.27}$$

The load data ($C_{D,m}$, $C_{D,\sigma}$ and ρ_D) in the basic load configuration (without rings) and the results are listed in the appendix (Table A.8, Table A.9, Table A.10). A synthetic summary is reported here in Table 7.9 and plotted in Figure 7.33.

The base peak bending moment results in the order of $8.7*10^7$ kNm. The calculation does not include the quasi-asymptotic contribution due to the steady recirculation region in the near-wake (Figure 7.24 showed such a contribution in terms of pressure correlations at 180°). This would result in non-zero values of the cross-correlations of drag force at large distance. However, it has been estimated that even high asymptotic correlation in the drag to the constant value 0.3 instead of 0 would imply an increase in the base peak bending moment of only 3% (i.e. $M_{peak,base} = 9.01*10^7$ kNm). It is then negligible.

Table 7.9 Quasi-static beam response to drag force (effect of the rings on the load not included)

z [m]	**$M_{D,m}$ [kNm]**	**M_{D,σ^2} [kNm]^2**	**$M_{D,peak}$ [kNm]**
0	6.45E+07	4.26E+13	8.74E+07
650	9.90E+06	1.45E+12	1.41E+07
750	5.42E+06	4.64E+11	7.80E+06
850	2.06E+06	7.17E+10	3.00E+06
950	2.14E+05	1.25E+09	3.38E+05

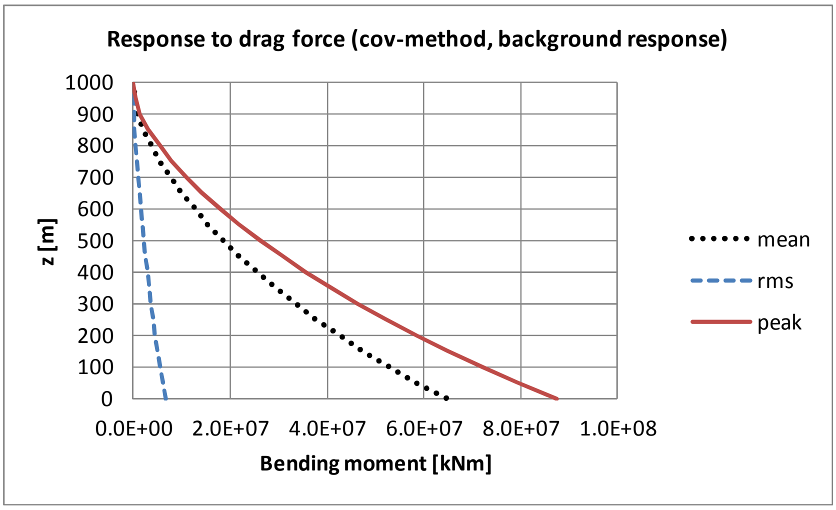

Figure 7.33 Quasi-static along-wind beam response (effect of rings on the load not included)

Then, the across and the along wind beam responses are calculated in the time domain. The background response to the stochastic process is evaluated by the use of measured time histories and influence coefficients, i.e. it is “manually” calculated by applying statically at each time step the influence coefficients of forces along the height. The influence coefficients for the bending moment at the base are just the heights of the forces. The full dynamic response is calculated with the software Ansys by integration of the dynamic equations of motion (including damping and mass forces) and it shows the dynamic amplification at the first two vibration modes. Simultaneous time histories have to be used in the calculation. They have been measured at four levels (950-850-750-650 m) and - for the purpose of this analysis - all the other time histories are considered fully correlated with them.

The spanwise variation of the tower diameter (Figure 1.13) has been included in the calculation, in order not to underestimate the mass of the structure. The data in the wind tunnel ($_{WT}$) are transferred into full-scale ($_{FS}$) by scale factors applied on the length ($\lambda_L = L_{FS}/L_{WT}$), on the velocity ($\lambda_U = U_{FS}/U_{WT}$) and consequently on the frequency ($\lambda_F = \lambda_V/\lambda_L$) and on the time ($\lambda_T = 1/\lambda_F$), as explained in section 4.1.2. The reference length scale is the scale of the model (1:1000), because the tower diameter enters the Strouhal number. It is then assumed that the boundary layer in the wind tunnel is scaled similarly.

The main input data of the analyses are:

- $D_{FS}(H) = 150$ m; $D_{WT}(H) = 0.15$ m $\rightarrow \lambda_L = 1000$;
- U_{FS} (H) = 51.31 m/s (H&D model, $V_b = 25$ m/s, II terrain cat.); U_{WT} (H) = 25.07 m/s $\rightarrow \lambda_V = 2.05$;
- $\lambda_F = 1/488$; $\lambda_T = 488$; it is not too far from the time scale that would have been obtained by comparing T_{ux} in the wind tunnel and T_{ux} in full-scale, even though T_{ux} in full-scale is an uncertain parameter (see section 4.1.2).

In addition, the time domain analysis includes damping and inertial forces (full-transient analysis, Ansys):

- Integration time step = 0.244 s = $(1/n_{sampl})^*\lambda_T = (1/2000)^*488 < 1/20n_1 = 1/(20^*0.17) = 0.29$;
- Rayleigh damping: $[D] = \alpha[M] + \beta[K]$. The coefficients are calculated assuming modal damping ratios ξ_i equal to 0.01 (corresponding to a logarithmic decrement $\delta = 2\pi\xi \approx 0.06$) at $n_1 = 0.17$ Hz (beam bending mode) and $n_3 = 0.65$ Hz (beam mode with two nodes), according to the formula $\xi_i = \alpha/2\omega_i + \beta\omega_i/2$, where $\omega_i = 2\pi n_i$.

Tapered elements “beam188” in Ansys library have been used in the finite element model of the tower.

Figure 7.34 shows the spectrum of the loading process in the across-wind direction (S_{CL}). Figure 7.35 and Figure 7.36 show the quasi-static and the dynamic responses, respectively, in the across-wind direction. Since the methods and the tools of calculations are different, the good agreement of results is a further proof of validity. Instead, Figure 7.37, Figure 7.38, Figure 7.39 refer to the along-wind direction. In this regard, it is interesting to note the similarities to the undisturbed flow fluctuations (Figure 4.11).

Figure 7.34 shows the typical two-peaks lift spectra, due to tip-associated vortices. They are shed only in absence of ring beams (basic load configuration), that is the one considered in this section. The critical wind speed for the lower Strouhal number (around 0.07) is very high, so resonance between the structural mode the low-frequency peak will not occur[8]. On the other hand, there will be a quasi-static low frequency oscillation on which the Karman resonance is superimposed. It is then important to quantify the response contribution of the tip-associated vortices.

In the background response, the contribution of the low frequency peak in the bending moment at the base is around 7% (Figure 7.35). If resonance is included (Figure 7.36), the tip-associated vortices increase the variance of the total response of only 3%[9]. Therefore, the contribution of tip vortices in the total response is not so significant. Moreover, Figure 7.36 highlights the dynamic amplification at the base due to the structural vibration modes. The first mode ($n_1 = n_2 \approx 0.17$; $n_1D/U \approx 0{,}50$) is the beam bending mode, typical of the solar tower (see section 2.4). The filtering effect of the structure at higher frequencies (mechanical transmittance) is also evident in the graph: the black spectrum goes below the blue one after the resonant peak. The second vibration mode ($n_3 \approx 0.65$; $n_3D/U \approx 1{,}9$) is a beam mode with two nodes of inversion in the shape. It is typical for beams but its frequency is not the same as in the shell model of the solar tower. In the shell tower, the second beam mode has a much higher frequency. Many shell-like modes precede it. Therefore, the beam FE model does not reproduce faithfully the real structure, which is not, in fact, a beam. In any case, the vibration frequency of the second beam mode is high and it lies in a frequency range which is not reproduced accurately even in the load. In fact, as explained in section 4.1.3, the damping effect of 1.5m pressure tubes predominates at n > 200 Hz (wind tunnel scale), that is nD/U > 1.2. This is the cut-off frequency for the spectra.

---

[8] In this work, non-linear geometrical effects arising from low frequencies of excitation are not considered, as well as the reduced stiffness due to concrete cracking. Further investigation in the non-linear behaviour is a future outlook.

[9] In Figure 7.36 the spectra do not seem to decrease to zero as n→0. This is a matter of the log plot and Δn. For example, in the “0-qs” curve the first point has coordinate (nD/U = ΔnD/U = 0,00146074 ; Sn = 3,57E+11). The ordinate is more than two orders smaller than the highest magnitude. Moreover, the ordinate is a very small number close to zero once it is divided by the variance, as it is in the dimensionless plot ($3{,}57E{+}11/1{,}61E{+}14 = 2.2 \cdot 10^{-3}$).

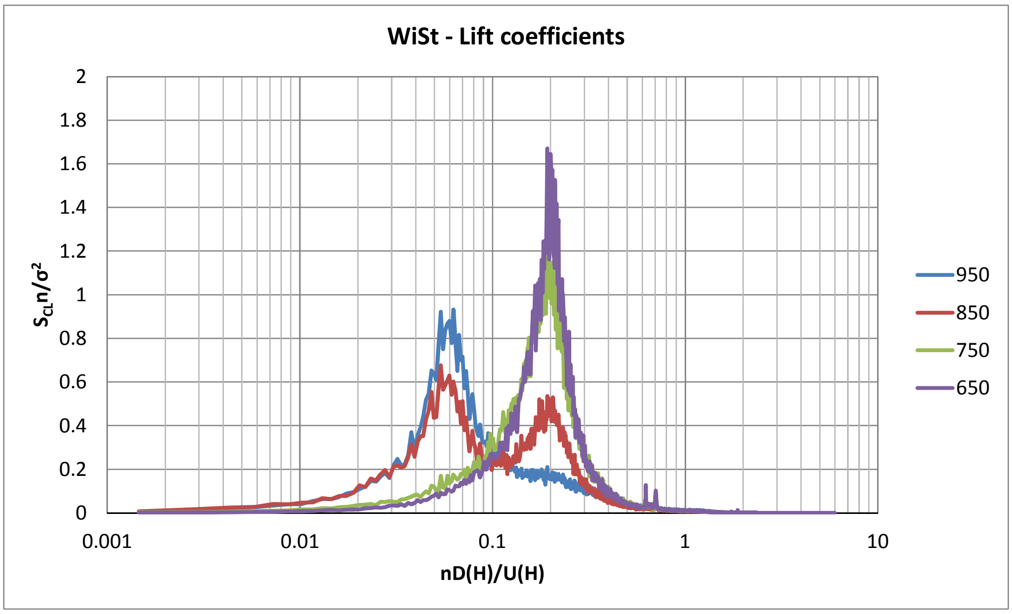

Figure 7.34 Spectra along the height of lift coefficient

(SR0, effect of the rings on the load not included, WiSt data)

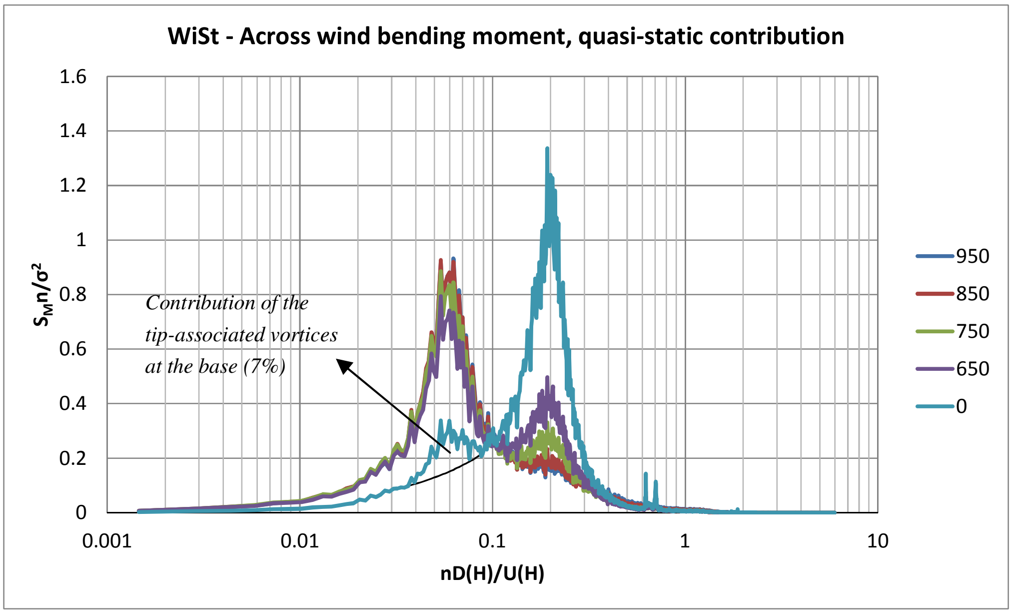

Figure 7.35 Structural response in the across-wind direction. Resonance not included.

(SR0, effect of the rings on the load not included, WiSt data)

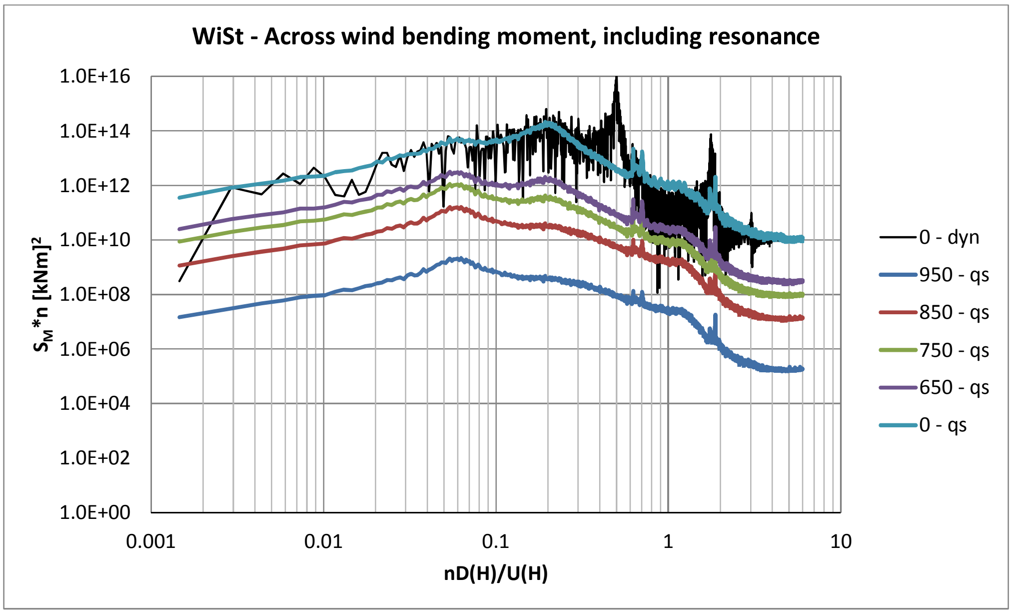

Figure 7.36 Structural response in the across-wind direction. Resonance included.

(SR0, effect of the rings on the load not included, WiSt data)

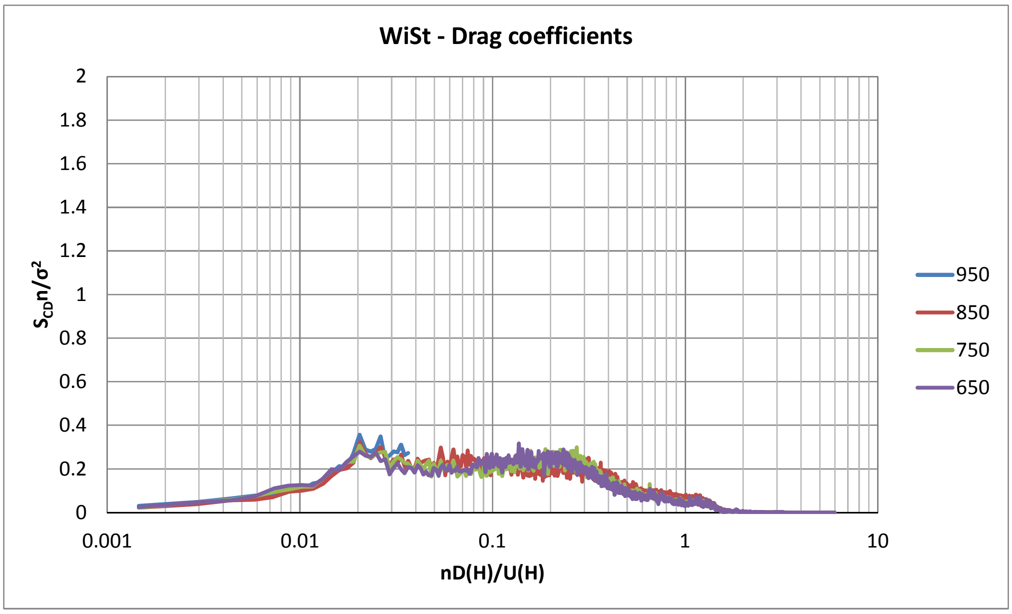

Figure 7.37 Spectra along the height of drag coefficient

(SR0, effect of the rings on the load not included, WiSt data)

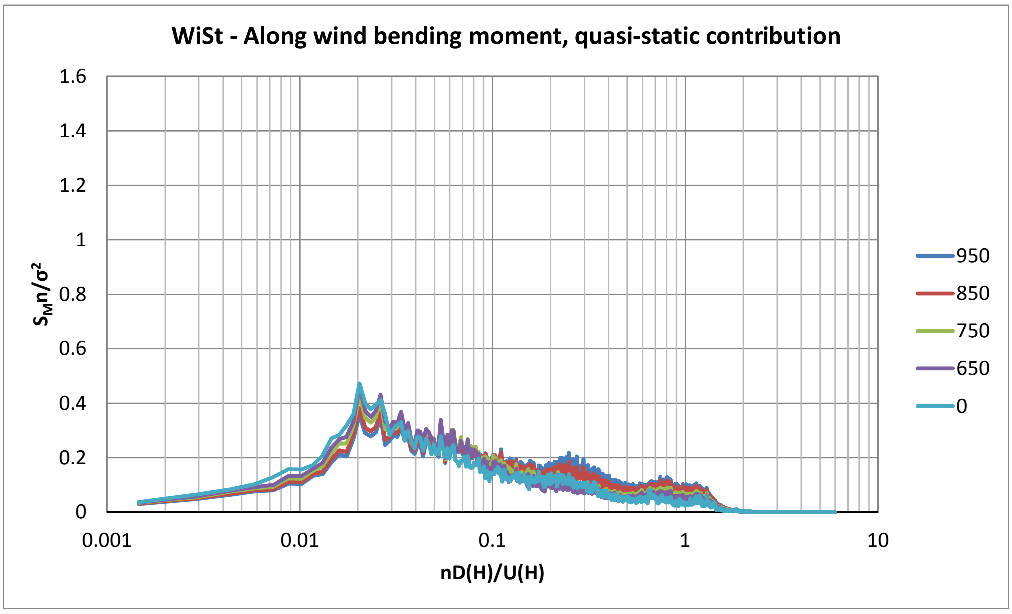

Figure 7.38 Structural response in the along-wind direction. Resonance not included.

(SR0, effect of the rings on the load not included, WiSt data)

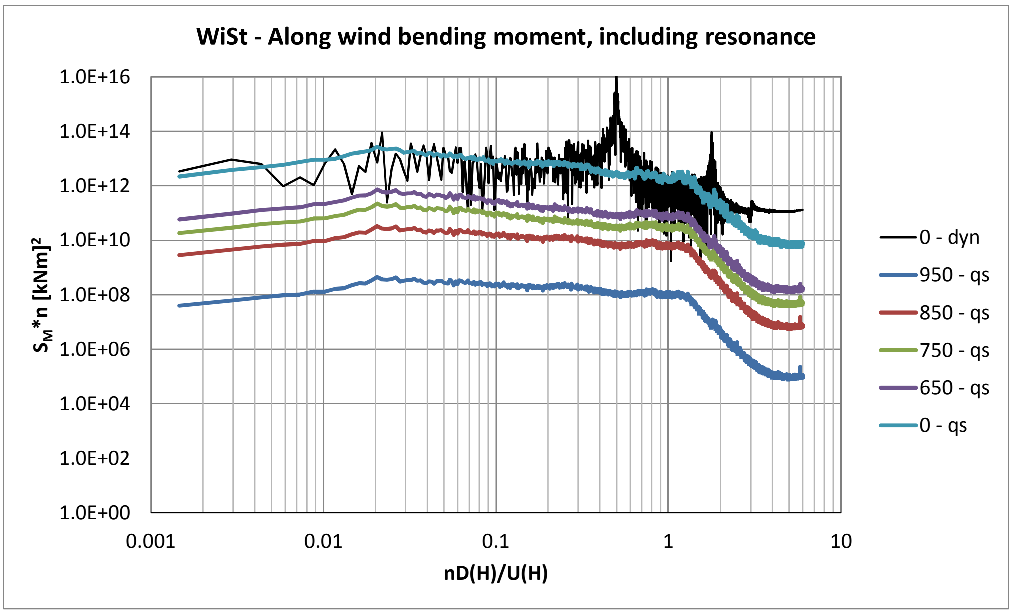

Figure 7.39 Structural response in the along-wind direction. Resonance included.

(SR0, effect of the rings on the load not included, WiSt data)

Table 7.10 summarizes the results of the quasi-static and dynamic beam response. Results are separated in the along wind and across wind direction. The variance of the response in the across-wind direction is higher than in the along-wind direction. This can be explained by looking at Figure 4.13. At sufficiently high frequencies, the energy contribution of the v-component of wind speed is higher than the energy contribution of the u-fluctuations.

The effects in the two directions need to be combined in the resultant bending moment, which is a function of the along- and across-wind bending moments:

$$\mathrm{M}_{\mathrm{res}} = g\left(M_D, M_L\right) \rightarrow \mathrm{M}_{\mathrm{res}} = \sqrt{M_D^2 + M_L^2} \tag{7.28}$$

The resultant bending moment can be linearized with Taylor expansion around the middle value; in general it is:

$$\begin{aligned}\mathrm{M}_{\mathrm{res}} \cong\ & g\left(M_{D,m}, M_{L,m}\right) + \\ & + \left.\frac{\partial g}{\partial M_D}\right|_{\left(M_{D,m}, M_{L,m}\right)} \left(M_D - M_{D,m}\right) + \\ & + \left.\frac{\partial g}{\partial M_L}\right|_{\left(M_{D,m}, M_{L,m}\right)} \left(M_L - M_{L,m}\right)\end{aligned} \tag{7.29}$$

Therefore, the mean and the variance of the resultant bending moment are:

$$\mathrm{M}_{\mathrm{res,m}} = g\left(M_{D,m}, M_{L,m}\right) = \sqrt{M_{D,m}^2 + M_{L,m}^2} \tag{7.30}$$

$$\begin{aligned}\mathrm{M}_{\mathrm{res},\sigma^2} \cong\ & \left(\frac{\partial g}{\partial M_D}\right)^2 \mathrm{M}_{\mathrm{D},\sigma^2} + \left(\frac{\partial g}{\partial M_L}\right)^2 \mathrm{M}_{\mathrm{L},\sigma^2} + \\ & + \left(\frac{\partial g}{\partial M_D}\right)\left(\frac{\partial g}{\partial M_L}\right) \mathrm{M}_{\mathrm{D},\sigma} \mathrm{M}_{\mathrm{L},\sigma} \rho\left(M_D, M_L\right)\end{aligned} \tag{7.31}$$

Where the derivatives are taken at the mean value of the independent variables. If $M_{L,m}$ = 0, by linearizing at the first order it results that $M_{res},\sigma^2 \approx M_D,\sigma^2$.

By combining the effects at each time step in the time domain (equation (7.32)), the variance can be exactly evaluated by the resulting time history. It is reported in Table 7.10 and it allows to quantify the approximation by linearization. It can be seen that in the dynamic calculation $M_{res},\sigma_B^2+\sigma_R^2$ and $M_D,\sigma_B^2+\sigma_R^2$ differ of only 6% at z/H = 0. The difference is higher in the quasi-static calculation (M_{res},σ_B^2 compared to M_D,σ_B^2).

$$\mathrm{M}_{\mathrm{res}}(t)=\sqrt{M_D^2(t)+M_L^2(t)} \qquad (7.32)$$

The dynamic amplification at the base (z/H = 0) is 22%, calculated according to equation (7.33):

$$dyn=\frac{M_{res,\,peak,\,B+R}}{M_{res,\,peak,\,B}}=\frac{M_{D,m}+k_p M_{res,\,\sigma,\,B+R}}{M_{D,m}+k_p M_{res,\,\sigma,\,B}} \qquad (7.33)$$

Table 7.10 [10] *Beam response without and with resonance*
(effect of the rings on the load not included, WiSt results)

z	950	850	750	650	0	m		
$\mathbf{C_D,\sigma^2}$	0.013	0.010	0.007	0.006	0.006		drag coeff.	variance
$\mathbf{C_L,\sigma^2}$	0.024	0.036	0.021	0.020	0.020		lift coeff.	variance
$\mathbf{M_D,m}$	2.14E+05	2.06E+06	5.42E+06	9.90E+06	6.45E+07	kNm	along wind	mean
$\mathbf{M_D,\sigma_B^2}$	1.25E+09	8.65E+10	5.20E+11	1.61E+12	5.75E+13	$[kNm]^2$	along wind	background
$\mathbf{M_D,\sigma_B^2+\sigma_R^2}$	2.98E+10	5.93E+11	2.94E+12	8.53E+12	1.80E+14	$[kNm]^2$	along wind	with resonance
$\mathbf{M_L,\sigma_B^2}$	2.31E+09	1.75E+11	1.28E+12	4.06E+12	1.58E+14	$[kNm]^2$	across wind	background
$\mathbf{M_L,\sigma_B^2+\sigma_R^2}$	4.24E+10	9.10E+11	4.75E+12	1.40E+13	3.28E+14	$[kNm]^2$	across wind	with resonance
$\mathbf{M_{res},\sigma_B^2}$	1.82E+09	1.02E+11	6.06E+11	1.85E+12	6.32E+13	$[kNm]^2$	tot. response	background

---

[10] The mean response in Table 7.10 is evaluated by using the same load distribution as in Table 7.9. Instead, the background and the dynamic responses reported in Table 7.10 are evaluated by using simultaneous time histories measured in the wind tunnel. Since only four levels of simultaneous measurements were available (z/H = 0.95; 0.85; 0.75; 0.65, 18 pressure taps at each level), for the purpose of this analysis all the other time histories at other levels are considered fully correlated with them. Consequently, a higher value of the stochastic response is obtained. Even from the dynamic point of view, the fact that the time histories are fully correlated at lower levels is an overestimation on the safe side, because the first vibration mode does not have inversions of shape along the height.

$M_{res},\sigma_B^2+\sigma_R^2$	3.06E+10	6.17E+11	3.09E+12	9.02E+12	1.92E+14	[kNm]^2	tot. response	with resonance

In the dynamic calculation, time histories of around 80 minutes (full-scale time, based on the previously mentioned scale factor $\lambda_T = 488$) were applied as input in Ansys. This time window corresponds to 10 s in the acquisition of wind tunnel data. A zoom on a time window of 0.5 s (in the wind tunnel scale), which corresponds to 244 s in full scale, is plotted in Figure 7.40 and in the following ones. The aim of these figures is to study, in the time domain, the vortex separation and the structural vibration, both in the stochastic loading process and in the structural response.

The full-scale period of vortex separation is around 15 s ($S_tD/U \approx 0.2*51/150 = 0.068$ Hz). It corresponds to about 0.03 s in the wind tunnel. Therefore, about 16 vortex shedding periods occur in the time window of Figure 7.40. This oscillation is evident in the time history of the loading process (Figure 7.40), superimposed to the stochastic contribution due to turbulence fluctuations. In order to highlight vortex separation, the time histories have been filtered with a passband filter around the Strouhal peak (nD/U between 0.18 and 0.22). The blue lines represent the filtered time histories.
In particular, Figure 7.40 plots the lift coefficient at a representative level (z = 650 m). Figure 7.41 plots the corresponding effect, i.e. the across-wind bending moment, at the same level, both without and with filtering around Strouhal (magenta and blue lines, respectively). The magenta line highlights, in the response, the dominant oscillation at the frequency of the structural vibration: the structure is, itself, a filter. While the vortex shedding period is about 0.03 s in the wind tunnel scale, the structure vibrates with a shorter period, about 0.01 s ($1/n1/\lambda_T = 1/0.17/488$). It results that about 40 cycles occur in the time window of Figure 7.41 (that is 0.5 s).

It is interesting to analyze the response that there would be in conditions of resonance between vortex separation and structural vibration frequency (Figure 7.42). This is not a design condition, resonance has been imposed just for the purpose of this analysis by reducing the Young modulus of the material and increasing the wind speed. Resonant conditions are obtained at $U_H = 74$ m/s and reduced stiffness so that $n_1 = 0.10116$ Hz ($n_1D/U = 0.20 = S_t$). Figure 7.42 proves that in this condition stochastic properties of the load are completely filtered out in the response by the resonant vibration. The magnitude of amplitudes is also much higher (one order of magnitude, if compared to Figure 7.41). The cross-correlation functions in the resonant condition assume a value close to 1 along the whole height and decrease slowly in time.

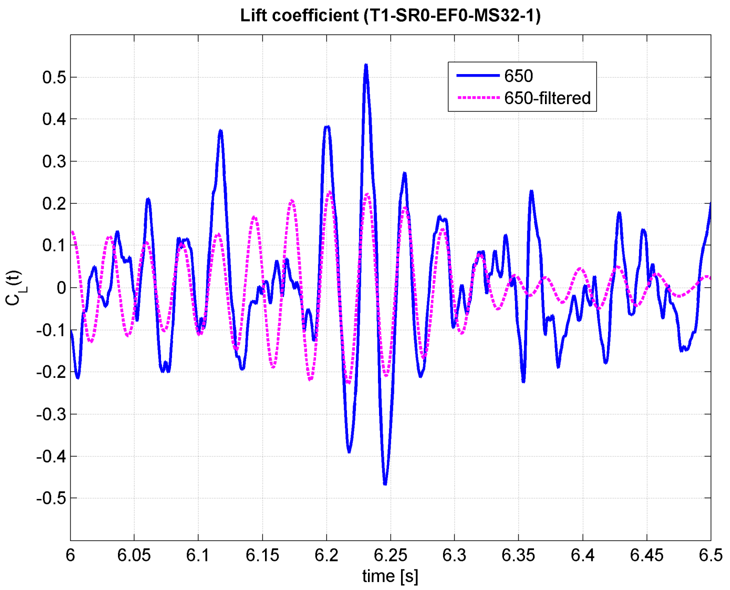

Figure 7.40 Stochastic loading process: time history of C_L, level 650 m. (SR0, effect of the rings on the load not included, WiSt data)
Blue line: bandpassfilter around S_t (0.18-0.22)
x-axis in wind tunnel scale

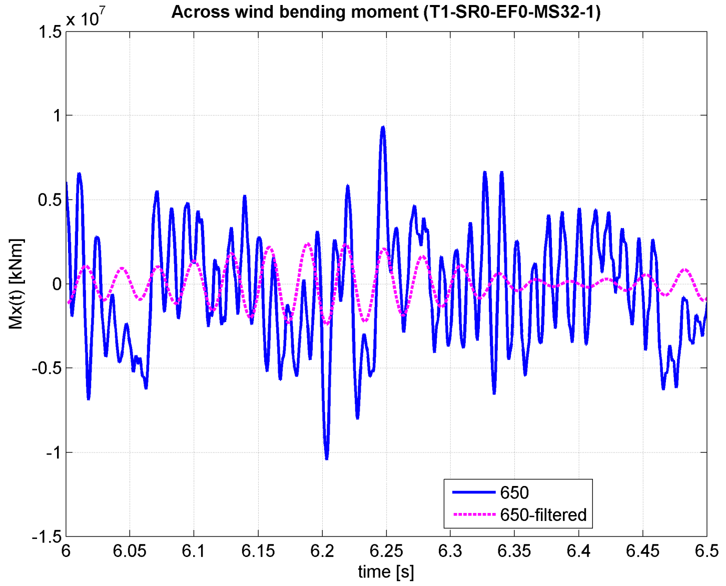

Figure 7.41 Structural response to the stochastic process: across wind bending moment, level 650 m.
$S_t = 0.2$; $n_1D/U = 0.5$
Blue line: bandpassfilter around S_t (0.18-0.22)
x-axis in wind tunnel scale

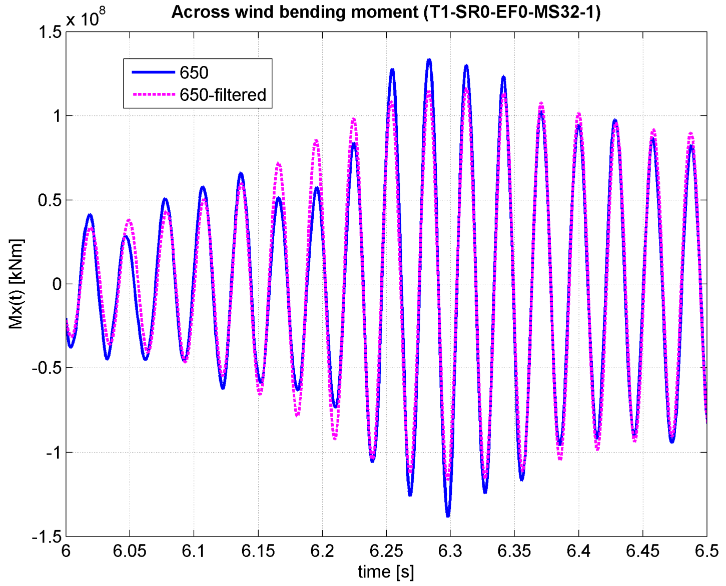

Figure 7.42 Across wind bending moment, level 650 m. Resonant conditions: $S_t = n_1D/U = 0.2$
Blue line: bandpassfilter around S_t (0.18-0.22)
[The y-axis is one order of magnitude larger than in Figure 7.41]
x-axis in wind tunnel scale

Another important issue is the correlation along the height of the lift force and across-wind response.

The cross-correlations of the lift coefficients (z_{ref} = 650 m) are plotted in Figure 7.43. The correlation length of the “total” lift (i.e. unfiltered) is small, around one diameter (L_{LIFT} = 154 m), because of the stochastic effect of turbulence. The correlation length of the filtered time histories (so-called vortex shedding lift) is higher because the stochastic effect is largely removed. Nevertheless, it is still small (L_{VS} = 262 m), less than two diameters. However, the correlation of the response is much higher, being the structure itself, with its vibration frequency, a filter. In the time domain, this effect was clearly evident in Figure 7.41, where the structural oscillation governs the magenta line. In fact, the across-wind response is almost fully correlated along the whole height: Figure 7.44 shows ρ(950,Δz) and proves that ρ(950,1000) is more than 0.8.

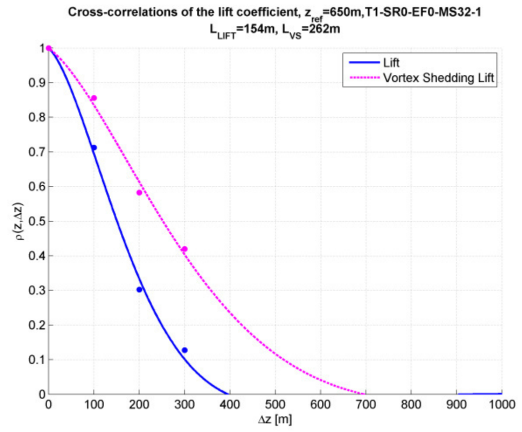

Figure 7.43 Cross-correlation coefficients of lift and vortex shedding lift (z_{ref} = 650 m)

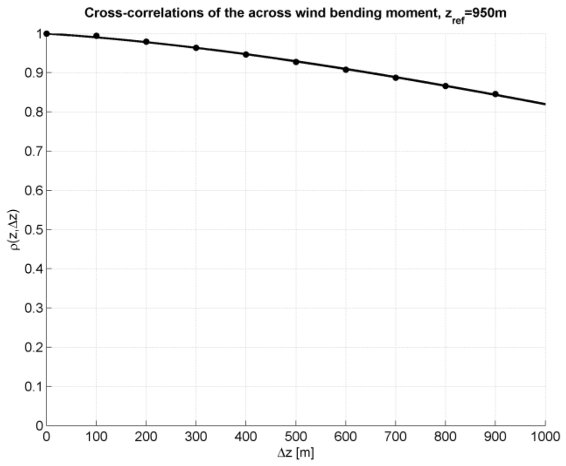

Figure 7.44 Cross-correlation coefficients of the response (across wind bending moment, z_{ref} = 950 m)

The spanwise correlation of the lift force and of the across-wind response is further analyzed in Figure 7.45, Figure 7.46, Figure 7.47. Two levels, 650 and 950 m, are chosen as representative. Load and response at these two levels are compared. Even if the fluctuations at 950 m are small, these levels are selected because simultaneous time histories were available at the largest separation distance (Δz = 300 m). Moreover, Figure 7.44 proves that, even if the fluctuations at 950 m are small, their correlation is high all along the tower, so that even this high level is representative.

Figure 7.45 shows that in the stochastic process the load correlation due to vortex separation is strongly diminished by turbulence (ρ = 0.1273). Once the time histories are filtered around the Strouhal peak (Figure 7.46), the cross-correlation is expectedly higher (ρ = 0.4197).

The modulation in amplitude of the filtered time histories is due to the beats phenomenon. It is produced by vortex shedding frequencies which are very close to each other, so that when the different waves are out of phase they tend to cancel each other and the resulting amplitude is small. Instead, when they are in phase they sum up and the resulting amplitude of oscillation is higher. This enhances the cross-correlation between different levels, too.

Figure 7.46 shows the correlation of the response at z_1 = 950 m and z_2 = 650 m. Consistently with Figure 7.44, the response has a much stronger correlation. The predominant oscillation is the bending vibration mode. The cross-correlation between the responses at the two levels is still close to 1 (ρ = 0.9638), although the two levels are at a distance of 300 m.

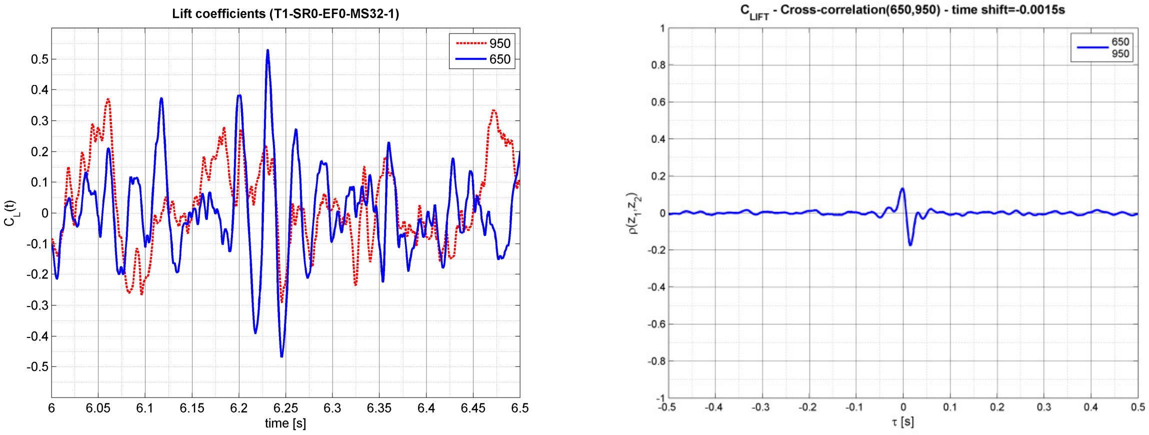

a) *b)*

Figure 7.45 Lift coefficients at z = 650 and 950 m
a) time histories; b) cross-correlation function. ρ(650,950) = 0.1273

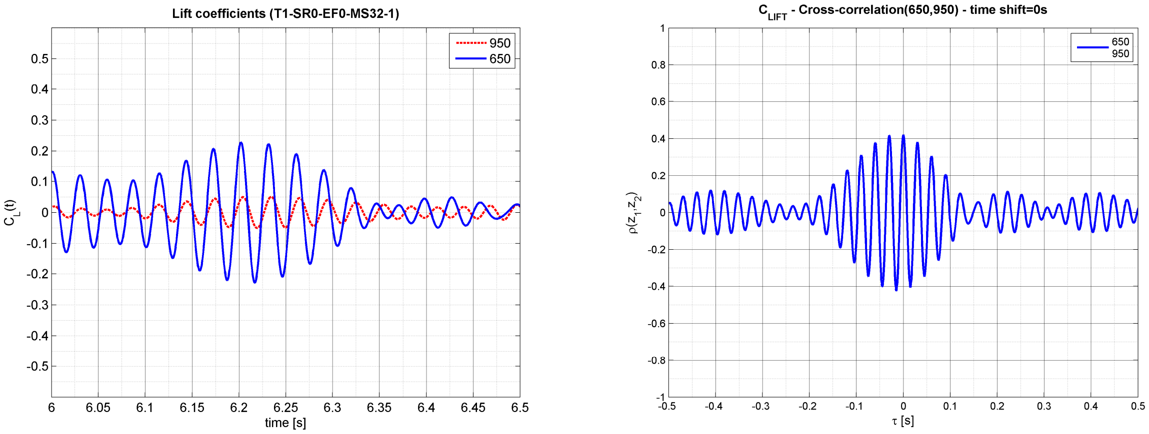

a) *b)*

Figure 7.46 Lift coefficients at z = 650 and 950 m: filtered time histories, bandpass filter around Strouhal (0.18-0.22).
a) time histories; b) cross-correlation function. ρ(650,950) = 0.4197

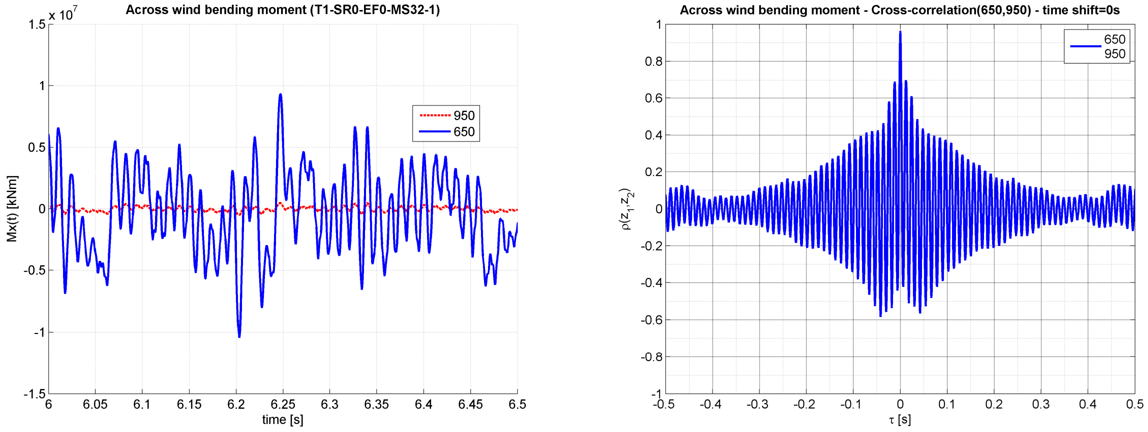

a) b)

Figure 7.47 Cross-wind response at z = 650 and 950 m: a) time histories; b) cross-correlation function. ρ(650,950) = 0.9638

7.2.2 The structural response to the asymmetric load

The mean asymmetric load created by the rings is characterized by higher drag (Figure 5.39) and mean steady lift. $C_{L,m}$ is in any case considerable smaller than $C_{D,m}$. Moreover, the effect of the steady lift at the base is partially balanced by the inversion of the force along the height. In case of rings, the force coefficients (obtained by pressure integration) were not measured all along the height, therefore some approximation has been introduced in the calculation.

Relying on the measurements, a suitable resulting load model is plotted in Figure 7.48, together with its structural response in Figure 7.49. Numerical values are reported in the appendix (Table A.11, Table A.12).

At z = 0:

NO RINGS: $M_{D,m} = 6.45*10^7$ kNm (along wind, mean response)
$M_{res,m} = M_{D,m} = 6.45*10^7$ kNm
10 RINGS: $M_{D,m} = 7.01*10^7$ kNm (along wind, mean response)
$M_{L,m} = 3.14*10^6$ kNm (across wind, mean response)
$M_{res,m} = (M_{D,m}^2 + M_{L,m}^2)^{0.5} = 7.02*10^7$ kNm

Globally, in case of 10 rings, an increase in the mean bending moment at the base is estimated of about 9%:

$M_{res,m}$(10 rings) / $M_{res,m}$(no rings) $= 7.02*10^7/6.45*10^7 = 1.09$

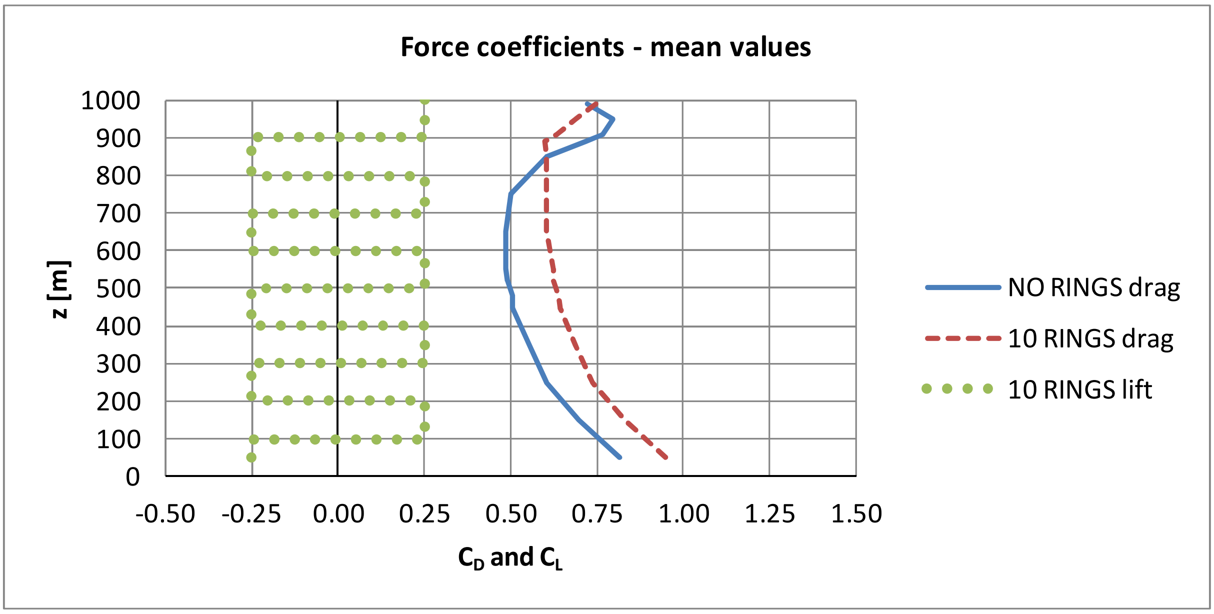

Figure 7.48 Effect of asymmetric flow due to ring beams: mean load

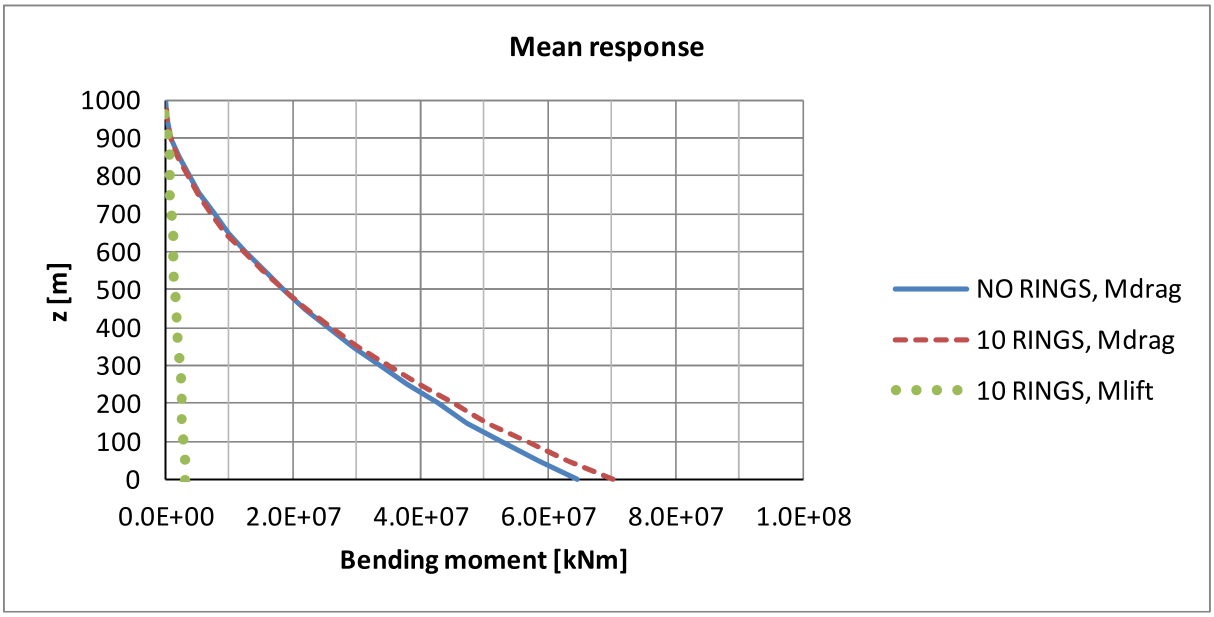

Figure 7.49 Effect of asymmetric load due to ring beams: mean response

Then, the effect on the response is evaluated by applying simultaneous time histories in a quasi-static and a dynamic calculation. The calculation is performed like in section 7.2.1. Results are reported in Table 7.11.

Table 7.11 Beam response (along and across wind bending moment) without and with resonance (load configuration with 10 rings, WiSt data)

z	**950**	**850**	**750**	**650**	**0**	**m**		
C_D,σ^2	0.101	0.095	0.095	0.104	0.104		drag coeff.	variance
C_L,σ^2	0.014	0.017	0.022	0.039	0.039		lift coeff.	variance
M_D,σ_B^2	9.24E+08	6.39E+10	3.92E+11	1.28E+12	6.59E+13	$[kNm]^2$	along wind	background

$M_D, \sigma_B^2+\sigma_R^2$	4.08E+10	8.12E+11	4.08E+12	1.20E+13	2.60E+14	$[kNm]^2$	along wind	with resonance
M_L, σ_B^2	1.37E+09	9.56E+10	6.24E+11	2.20E+12	1.66E+14	$[kNm]^2$	across wind	background
$M_L, \sigma_B^2+\sigma_R^2$	4.20E+10	8.50E+11	4.37E+12	1.32E+13	3.60E+14	$[kNm]^2$	across wind	with resonance
M_{res}, σ_B^2	1,30E+09	7,19E+10	1,36E+12	1,36E+12	7,19E+13	$[kNm]^2$	tot. response	background
$M_{res}, \sigma_B^2+\sigma_R^2$	3,88E+10	7,82E+11	3,97E+12	1,18E+13	2,69E+14	$[kNm]^2$	tot. response	with resonance

Finally, through the comparison of Table 7.10 and Table 7.11, it can be quantified that the increase in the peak response at the base in case of ten rings is about 13% (Table 7.12, Table 7.13). It is basically an effect in the along-wind direction; in fact, the contribution given by the steady lift is one order of magnitude lower. Therefore, the effect of the rings on the beam response is not dramatic. Furthermore, the results presented here represent the highest limit, i.e. many rings (ten) and rather big.

Table 7.12 Across and along wind beam response (including resonance) without and with rings:

	Along wind response (at z = 0)			**Across wind response (at z = 0)**		
	$M_{D,m}$ [kNm]	**$M_{D,\sigma}$ [kNm]**	**$M_{D,peak}$ [kNm]**	**$M_{L,m}$ [kNm]**	**$M_{L,\sigma}$ [kNm]**	**$M_{L,peak}$ [kNm]**
SR0	6.45E+07	1.34E+07	1.12E+08		1.81E+07	6.34E+07
SR1	7.01E+07	1.61E+07	1.27E+08	3.14E+06	1.90E+07	6.96E+07
SR1/SR0	1.09	1.20	1.13		1.05	1.10

SR0 = load modification due to the rings not included;
SR1 = load modification due to 10 rings included

Table 7.13 Resultant beam response (including resonance) without and with rings

	Resultant response (at z = 0)		
	$M_{res,m}$ [kNm]	**$M_{res,\sigma}$ [kNm]**	**$M_{res,peak}$ [kNm]**
SR0	6.45E+07	1.39E+07	1.13E+08
SR1	7.02E+07	1.64E+07	1.28E+08
SR1/SR0	1.09	1.18	1.13

SR0 = load modification due to the rings not included;
SR1 = load modification due to 10 rings included

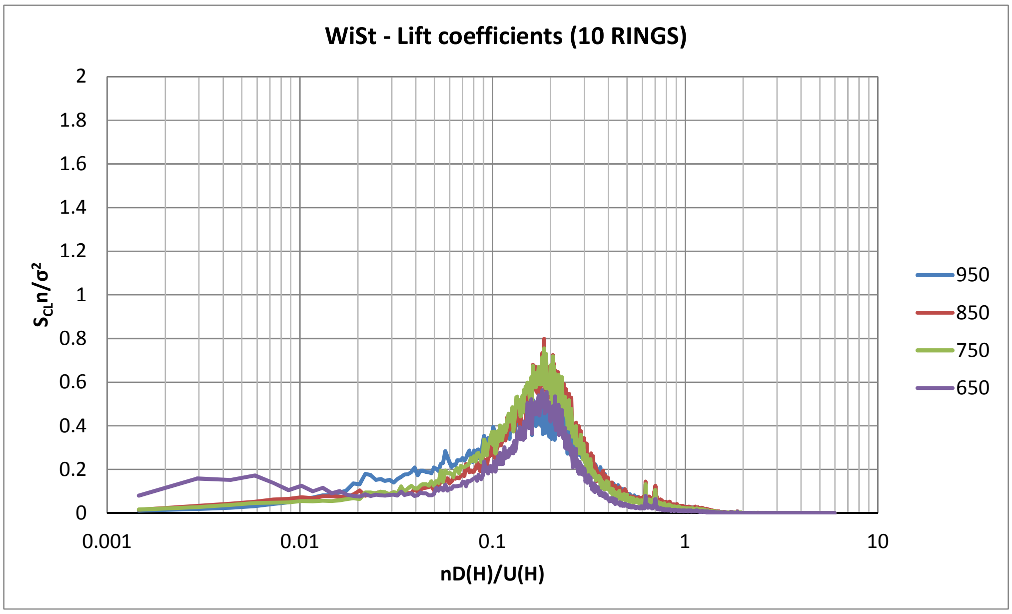

Figure 7.50 Spectra along the height of lift coefficient

(SR1, effect of 10 rings on the load included, WiSt data)

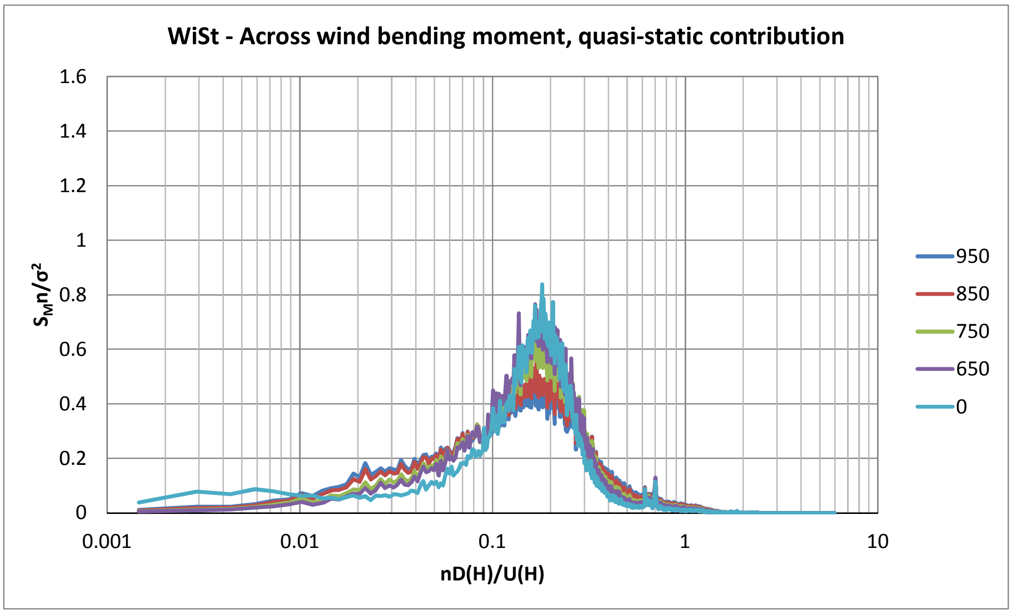

Figure 7.51 Structural response in the across-wind direction. Resonance not included.

(SR1, effect of 10 rings on the load included, WiSt data)

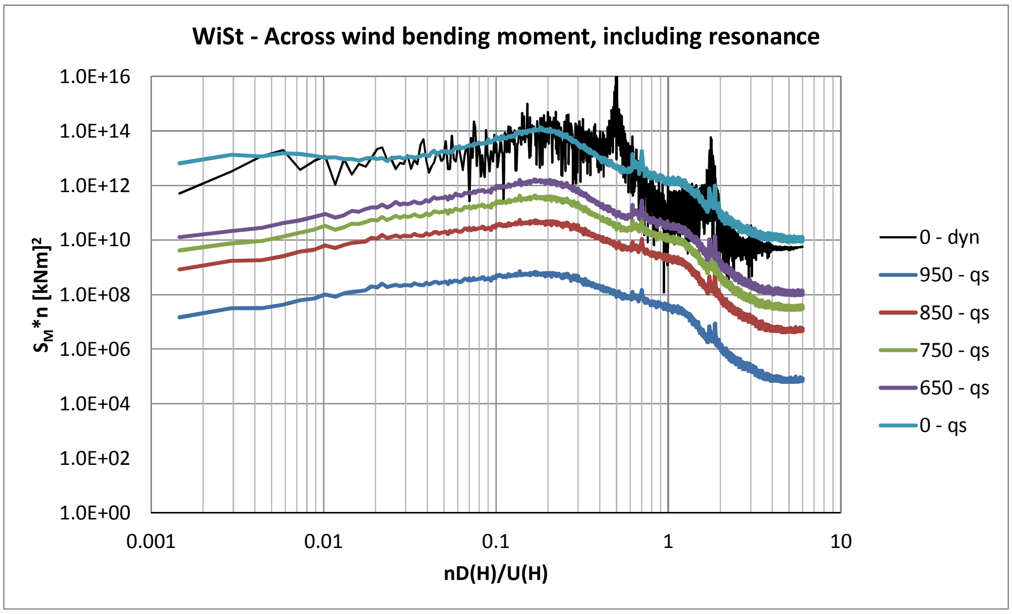

Figure 7.52 Structural response in the across-wind direction. Resonance included.

(SR1, effect of 10 rings on the load included, WiSt data)

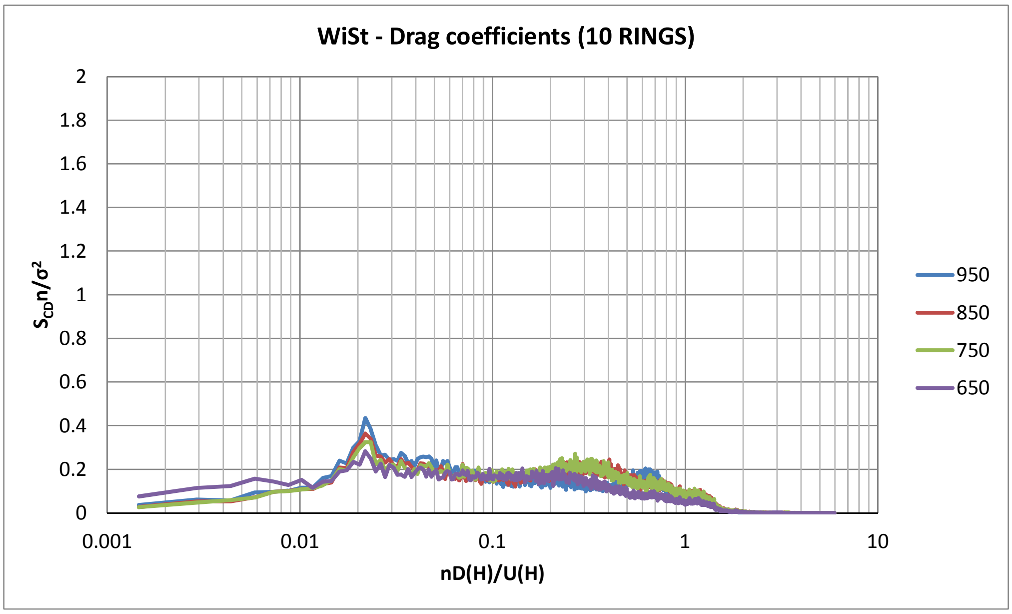

Figure 7.53 Spectra along the height of drag coefficient

(SR1, effect of 10 rings on the load included, WiSt data)

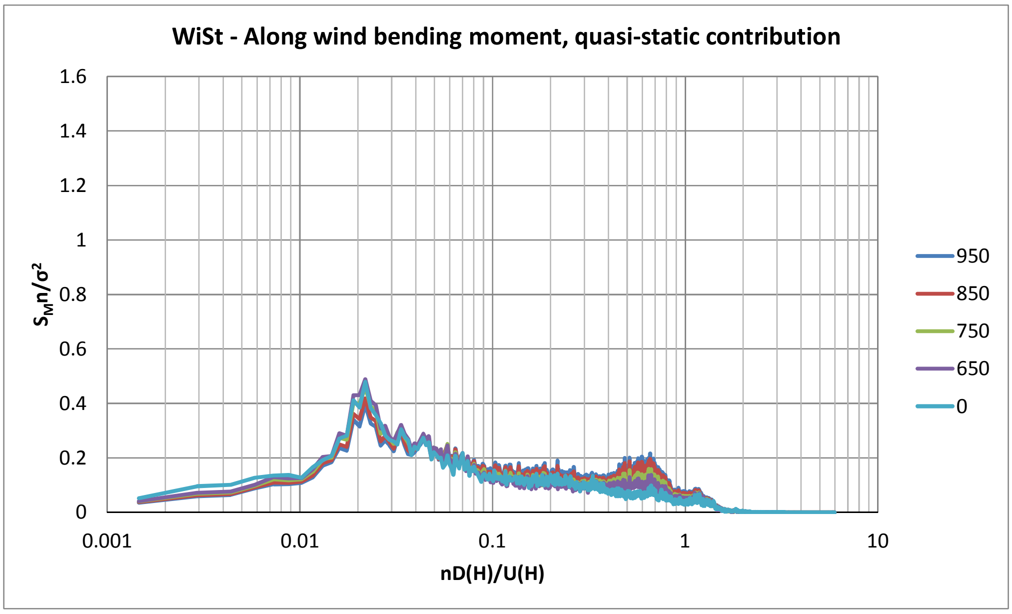

Figure 7.54 Structural response in the along-wind direction. Resonance not included.

(SR1, effect of 10 rings on the load included, WiSt data)

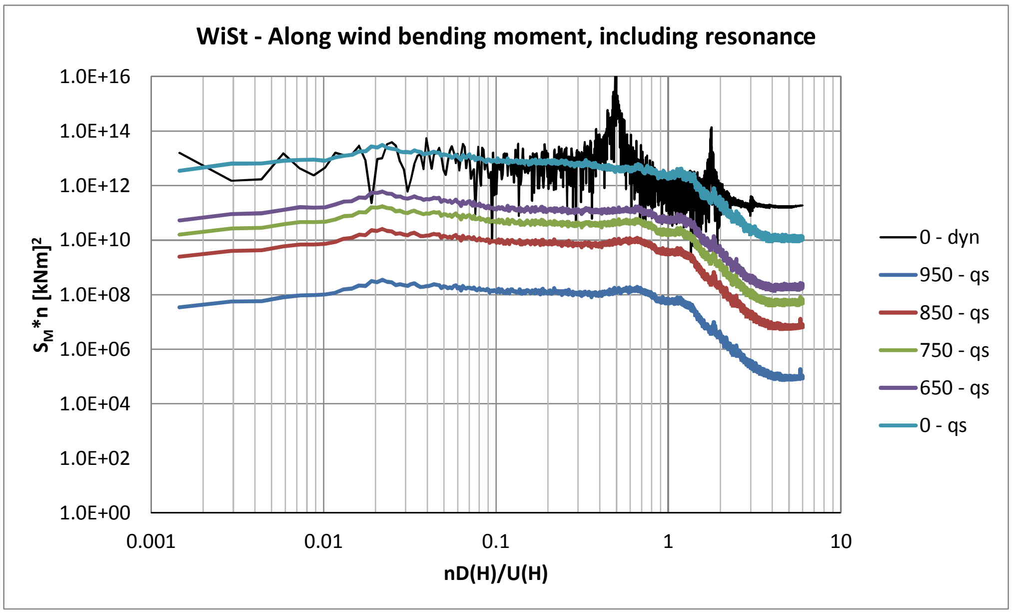

Figure 7.55 Structural response in the along-wind direction. Resonance included.

(SR1, effect of 10 rings on the load included, WiSt data)

7.3 The shell response

The shell response to the stochastic wind loading process is at first investigated through the covariance method. It is a quasi-static calculation (resonance not included) and it allows to consider the wind effect due to correlation of pressure. Input data are $C_{p,m}$, $C_{p,\sigma}$, $\rho(\Delta z, \Delta\varphi)$. They are all available by the experiments[11]. Then, dynamic calculations which include inertial and damping forces are performed on the tower by the software Ansys. The structural calculations always assume the presence of stiffening rings along the height (see Figure 1.13 and Figure 1.14 for the reference tower geometry), while the modification the rings create on the load is included only if specified.

In section 7.1 the big amount of experimental data has been simplified in a few parameters, which are of general application by the designer in any design condition. This simplified model is now validated through comparison of responses by applying either the experimental load data (directly measured) or the simplified load model. Results of the simplified model turn to be well representative of the experimental situation, so they can be extended in further applications to different boundary layer flows (and to structures of different aspect ratios). They allow to calculate the background response to the stochastic process in case of linear structural behaviour.

The wind load model derived from the wind tunnel investigation is then applied to a codified design wind profile for a certain location and terrain category. The local effects in the vicinity of the ring beams represent the substantial difference which is not included in the beam model presented before.

As the wind load is influenced by the actual number and size of rings, the quantification of the expected increase in stresses in the response due to the rings is another object of this section (see 7.3.4).

7.3.1 Validation of the simplified wind load model

The stochastic wind load model proposed in section 7.1 is suitable for being used in the quasi-static calculations through the covariance method (Niemann et al., 1996). The input data which are required are: $C_{p,m}$, $C_{p,\sigma}$, $\rho(\Delta\varphi)$ and $\rho(\Delta z)$. They have been modelled in section 7.1 with regard to the flow properties (especially I_u and L_{uz}) and summarized in the appendix (section 10.1).

---

[11] For locations where $\rho(\Delta z, \Delta\varphi)$ is not measured, it is substituted by the product between $\rho(\Delta z)$ and $\rho(\Delta\varphi)$.

In this section, the structural response of the tower is evaluated through the covariance method, both under the experimental data (directly measured at WiSt tunnel) and the simplified load model, applied to the same flow condition (the one at WiSt wind tunnel). The results are compared in order to identify to which extent the simplifying assumptions on the stochastic load in section 7.1 may affect the response. The aim is to validate the general use of the simplified stochastic load model for any atmospheric boundary layer flow. The wind load model (proposed in section 7.1) introduced the following approximations:

- the cross-correlations between points with horizontal and vertical separation are modeled as a product of $\rho(\Delta\varphi)$ and $\rho(\Delta z)$;
- $A(z) = 2$ constant along the height is a value on the safe side only at $z/H > 0.2$ (section 7.1.3) because it does not include horseshoe and base vortices;
- the body-induced fluctuations (Figure 7.19) are extrapolated at $I_u = 0$, through the assumption that they are not correlated to turbulence-induced fluctuations, although the wake fluctuations show a certain correlation with points before separation (Figure 7.27);
- the vertical correlations refer to the unified value around the circumference $L_{pz} = (3/2)L_{uz}$ (Table 7.8) and the constant almost asymptotic correlation at large distances, due to a large recirculation bubble in the near-wake, is neglected.

These approximations are accepted in view of the following results. Only the first simplifying assumption cannot be completely assessed because of the lack of the complete three dimensional correlation field; further experiments would be necessary (Chapter 8). The lack of a three dimensional correlation field might be one of the main reasons for the differences in the standard deviation of the stresses. In the following figures, the blue lines represent the effect that result from the experimental data, the red dots/lines from the simplified stochastic model applied to the same flow condition.

The stochastic model underestimates of about 10% the rms values of internal forces. As regards the bending moments, the differences are less than 1 kNm/m. Moreover, the approximation is strongly reduced once the peak values are considered, so that the model can be accepted (Figure 7.56). The peak values of the structural response (S = either n_{11}, n_{22}, m_{11} or m_{22}, i.e. circumferential or meridional forces and bending moments (direction 1 is circumferential, 2 is meridional)) are calculated as follows:

$$\begin{aligned} S_p &= S_m + 3.5\sigma_s \qquad if \;\; S_m \geq 0 \\ S_p &= S_m - 3.5\sigma_s \qquad if \;\; S_m < 0 \end{aligned} \tag{7.34}$$

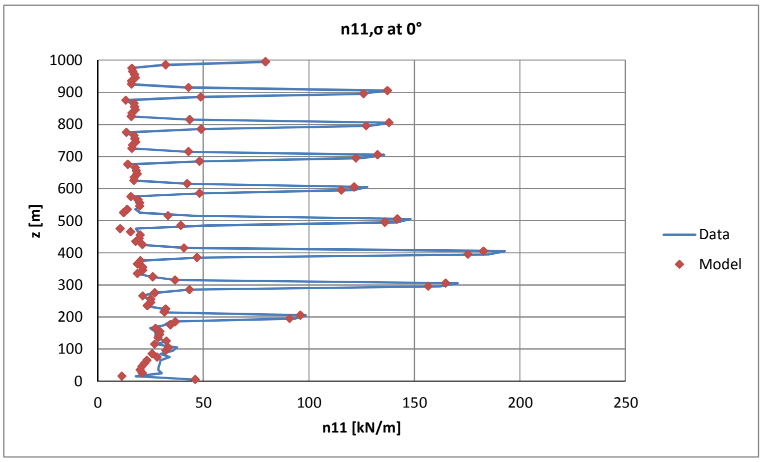

Figure 7.56 a) Circumferential force, rms values. (continued)

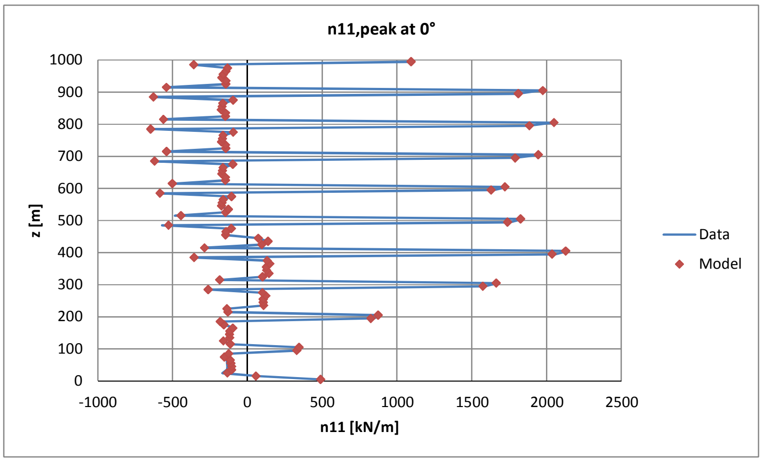

Figure 7.56 b) Circumferential force, peak values. (continued)

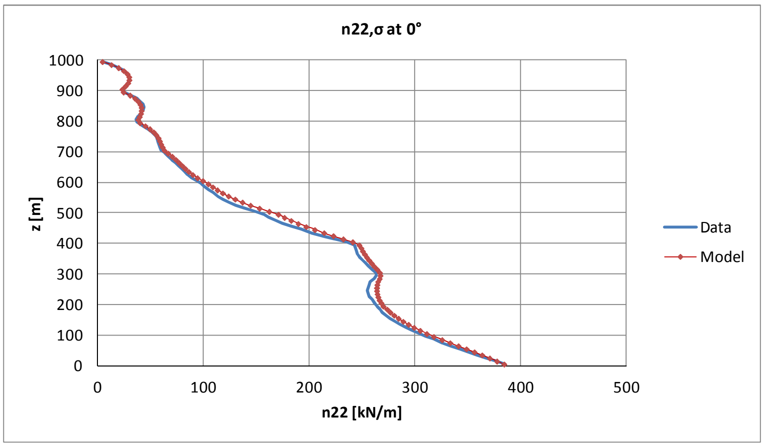

Figure 7.56 c) Meridional force, rms values (continued)

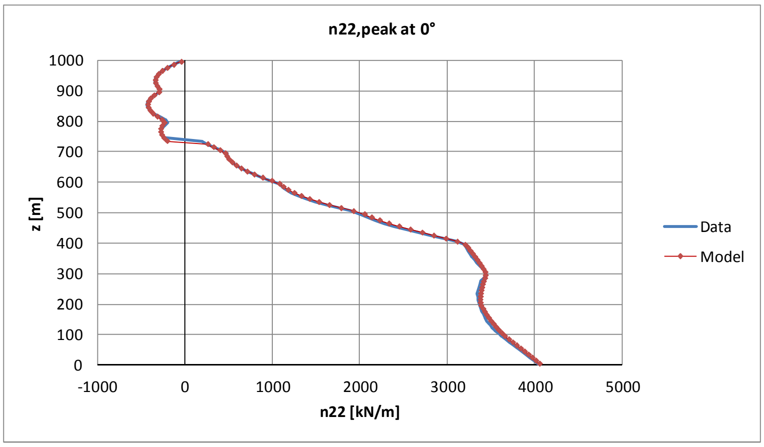

Figure 7.56 d) Meridional force, peak values (continued)

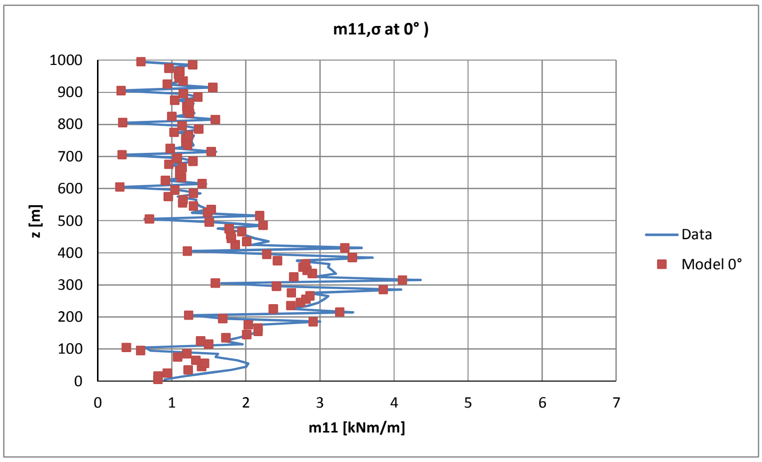

Figure 7.56 e) Circumferential bending moment, rms values (continued)

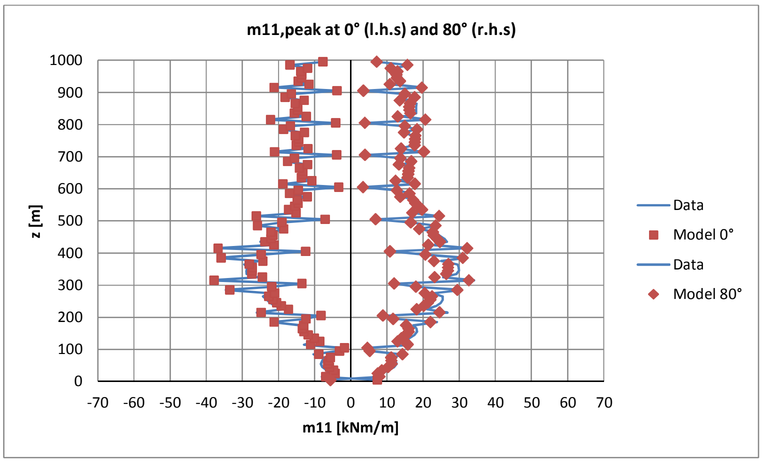

Figure 7.56 f) Circumferential bending moment, peak values (continued)

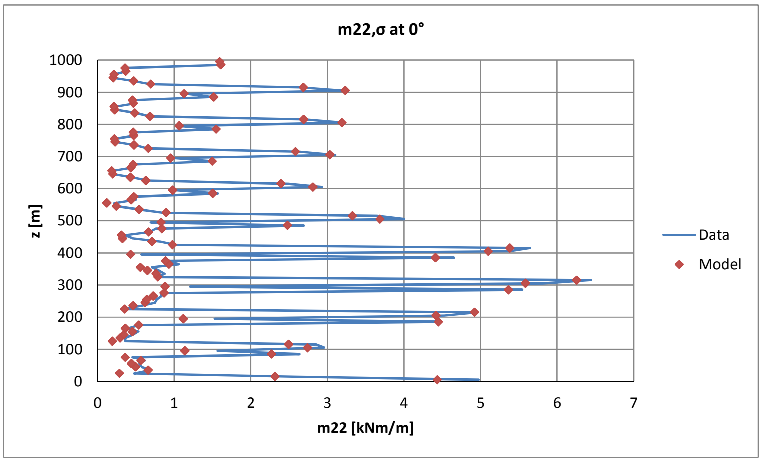

Figure 7.56 g) Meridional bending moment, rms values (continued)

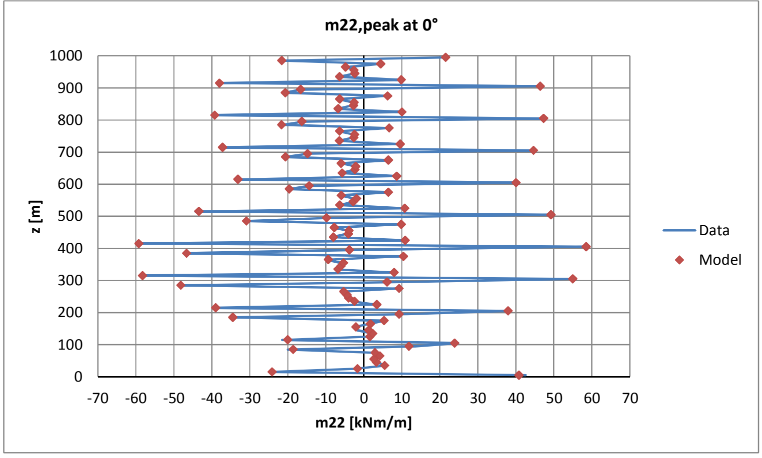

Figure 7.56 h) Meridional bending moment, peak values (continued)

Figure 7.56 Structural response along the height at significant angles, comparison by using experimental load data (blue lines) and proposed stochastic load model (red dots). Validation of the model. Resonance not included; effect of the rings on the load not included.

7.3.2 Local effects in the vicinity of the stiffening rings

The stiffening rings were originally introduced in the design (Goldack, 2004; Backström et al., 2008) in order to reduce ovalizations of the shell. A certain number of rings, properly stiffened, can guarantee a beam-like behaviour at the first eigenmode. As a result, the distribution of internal forces under the wind action is improved and the peaks of tension at the windward side are reduced. By increasing the stiffness and/or the number of rings, the circumferential distribution of meridional forces changes from a cosines-like distribution (typical for shells) to a linear distribution crossing zero at 90°, that is typical for beams (Lupi, 2009). With ten rings, such a beam-like distribution is achieved in the cylindrical shell at middle height (Figure 7.57, black curve). Ovalizations of the shell at the windward side in the upper part of the tower are responsible for the negative values of n_{22} at stagnation and lateral tension at the flanges, as it occurs for example at 850 m in the figure.

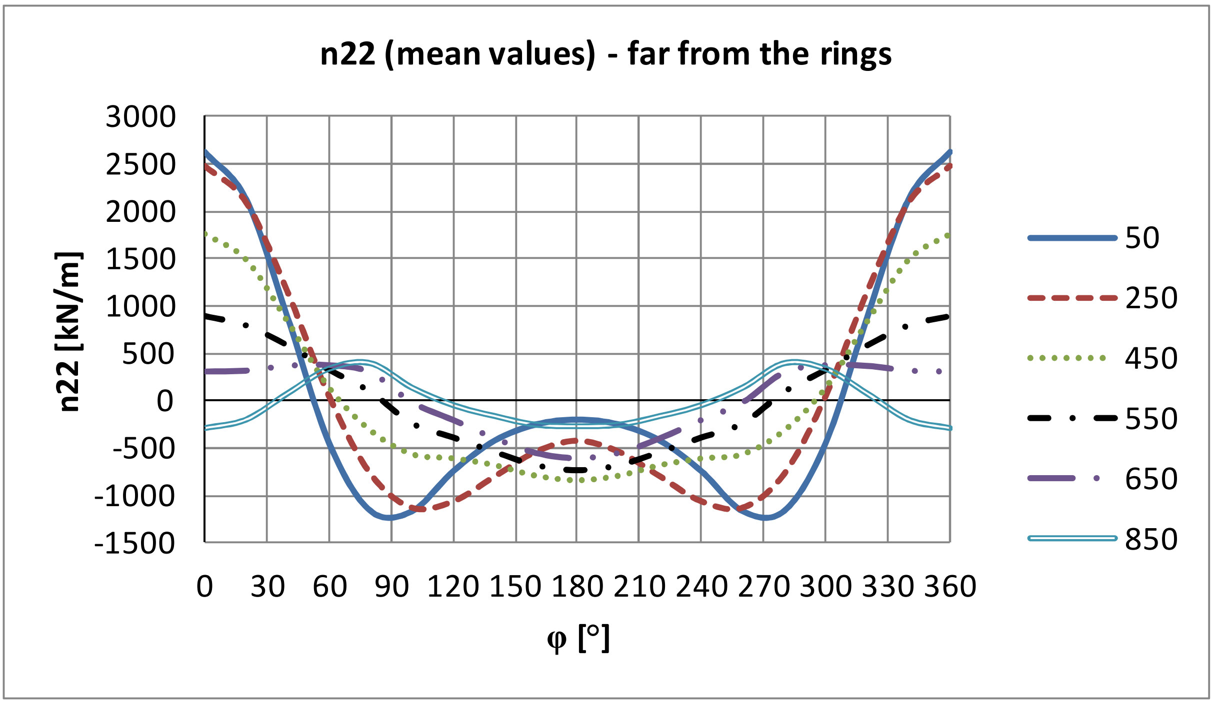

Figure 7.57 Circumferential distribution of meridional stresses – mean response

Even though the stiffening rings guarantee a global beam-like behaviour, evaluation of local effects in the vicinity of the ring beams requires the application of a shell-like model. The magnitude of such local effects – due to ovalization of the cross-section, especially because of the constraining effect of the rings – confirms what was stated in section 2.4 by equation (2.50): a Solar Tower cannot be fully designed by using the beam theory.

The design of the tower is governed by the stresses in the half of the shell which is exposed to the wind. The meridians at stagnation and at 80° (maximum suction) have the highest tension stresses. The stresses at stagnation are reported in the following figures. The calculation is done by the covariance method (resonance not included). The stochastic wind load model results from wind tunnel investigation; this is now applied to the following design properties of the atmospheric boundary layer:

- terrain category II ($z_0 = 0.05$ m), $V_b(10m) = 25$ m/s, latitude = 23°;
- mean wind profile: according to H&D model;
- turbulence intensity: according to the H&D model;
- integral length scale: according to Eurocode;

All these profiles are plotted in Figure 2.4, Figure 2.5, Figure 2.6.
The H&D model would suggest a much larger integral length scale. The approach of the Eurocode is preferred in this calculation, but the designer should bear in mind that a larger integral length scale would imply higher background response.

The following figures show that the structural effect of the rings on the response has an extension in the shell of around 20 m both above and below each ring. In that region both positive and negative peaks of n_{11}, m_{11} and m_{22} arise, due to the constraining effect to the ovalization of the shell exerted by the rings.

Another issue, which is not addressed in this work, but it should be investigated in view of the design, is the correlation of peak effects. In particular, the design of the shell reinforcement should result from combination of axial force and bending moment. The highest limit, if their peaks are fully correlated, is their sum, while the lowest limit in case of zero correlation is the square root of the sum of single square values.

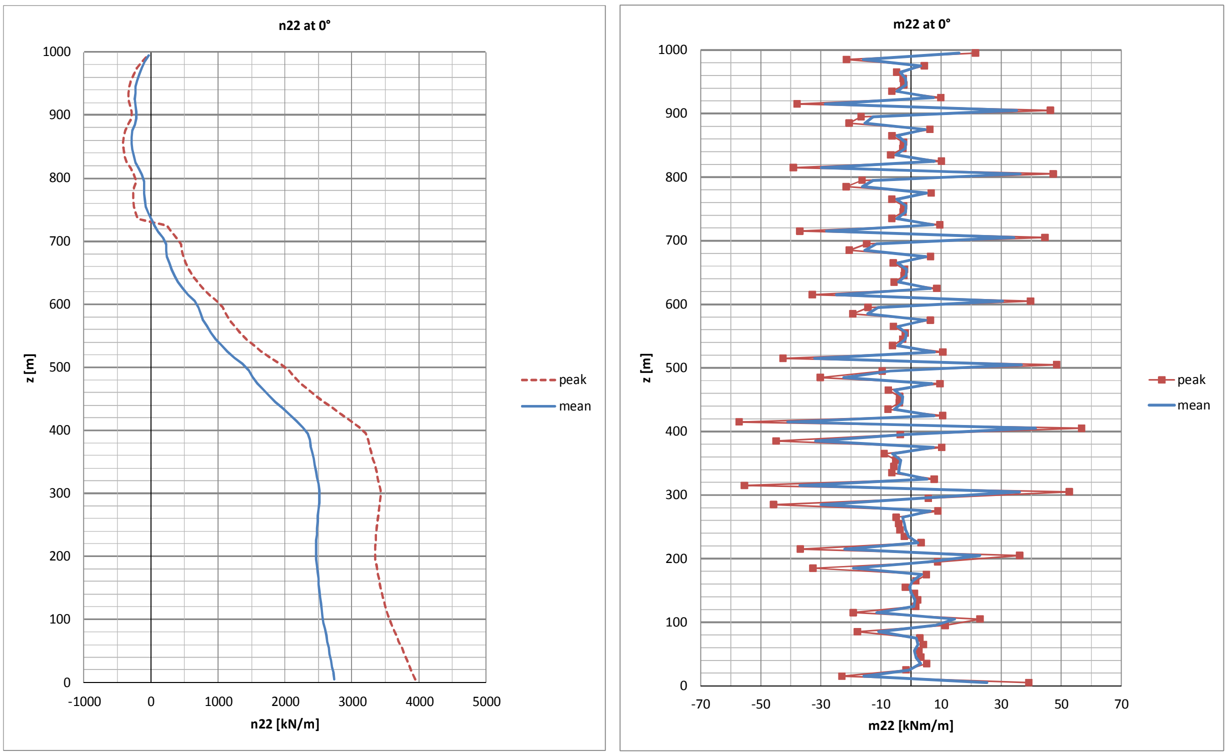

a) b)

Figure 7.58 Shell response in a design condition: meridional force n_{22} (fig. a) and bending moment m_{22} (fig. b) at 0° (resonance not inlcuded, effect of the rings on the load not included)

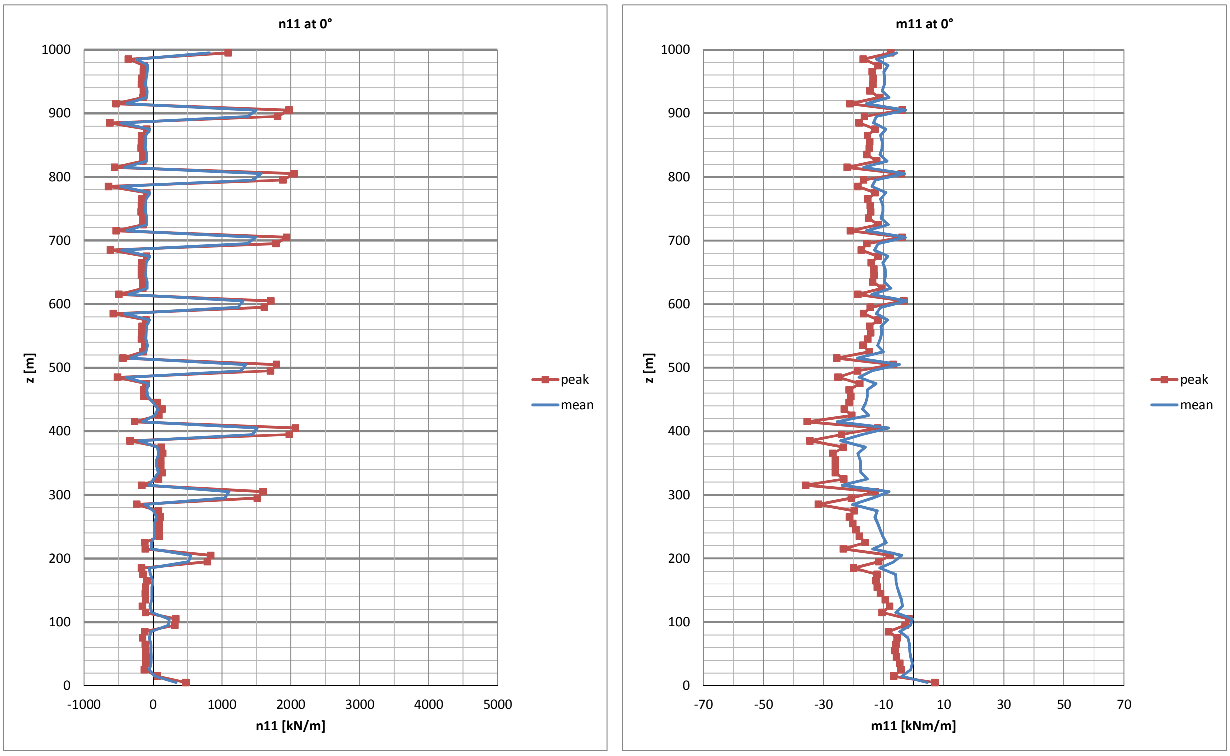

a) b)

Figure 7.59 Shell response in a design condition: circumferential force n_{11} (fig. a) and bending moment m_{11} (fig. b) at 0° (resonance not included, effect of the rings on the load not included)

7.3.3 **Dynamic amplification**

The dynamic amplification is calculated by using the software Ansys. Simultaneous time histories measured in the wind tunnel along the circumference at $z/H = 0.95$; 0.85; 0.75; 0.65 are used for the purpose of this investigation. All the other loads are then fully correlated with them. The result is on the safe side because the predominant contribution is the bending mode, which does not present inversions of shape along the height. However, the result can be only considered as a global effect on the structure. A more sophisticated load condition should be considered in order to investigate dynamic effects in the vicinity of the ring beams. This is, however, beyond the purpose of this work.

The calculation includes mass and damping forces. The Rayleigh damping ($\mathbf{D} = \alpha\mathbf{M} + \beta\mathbf{K}$) is calculated assuming modal damping ratios ξ_i equal to 0.01 (corresponding to a logarithmic decrement $\delta = 2\pi\xi \approx 0.06$) at $n_1 = 0.17$ Hz (beam bending mode) and $n_3 = 0.33$ Hz (shell-like mode with two waves), according to the formula $\xi_i = \alpha/2\omega_i + \beta\omega_i/2$, where $\omega_i = 2\pi n_i$. As in the beam calculation (section 7.2.1), the time factor for transferring data from wind tunnel to full-scale is $\lambda_T = 488$. The integration time step is 0.244 s, as in the beam calculation.

In order to evaluate the dynamic amplification, the results of the dynamic analysis (including mass and damping forces) are compared with the results of a quasi-steady calculation, i.e. a static calculation (not including mass and damping forces) at each time step. The dynamic amplification is the ratio of peak responses, the one at the nominator results from dynamic calculation, the one at the denominator results from the quasi-steady calculation. The mean response is included in the definition of the dynamic amplification. Moreover, only representative results are considered. In fact, the interest of the designer is in the dynamic amplification of those parts of the tower which are especially exposed to the wind action and thus govern the design. In practice, the stagnation line plays the most important role. Since the tower thickness varies along the height, it is important to be aware of the dynamic amplification all along the height, although internal forces are smaller in the tip region. As shown by Figure 7.60, the dynamic amplification is around 10% only at the base of the tower. Along the height, it is much higher than what was expected according to Eurocode calculations (Cd = 1.04 in Lupi, 2009). Further studies are then necessary. The result does not depend significantly on the class of concrete which is selected for the calculation.

These calculations are performed with C50/60 concrete (so that $n_1 = 0.17$ Hz). In fact, the class could be even higher (C70/85) and in this case it would be $n_1 = 0.18$ Hz.

However, as seen in a comparative calculation, this does not change significantly the dynamic response.

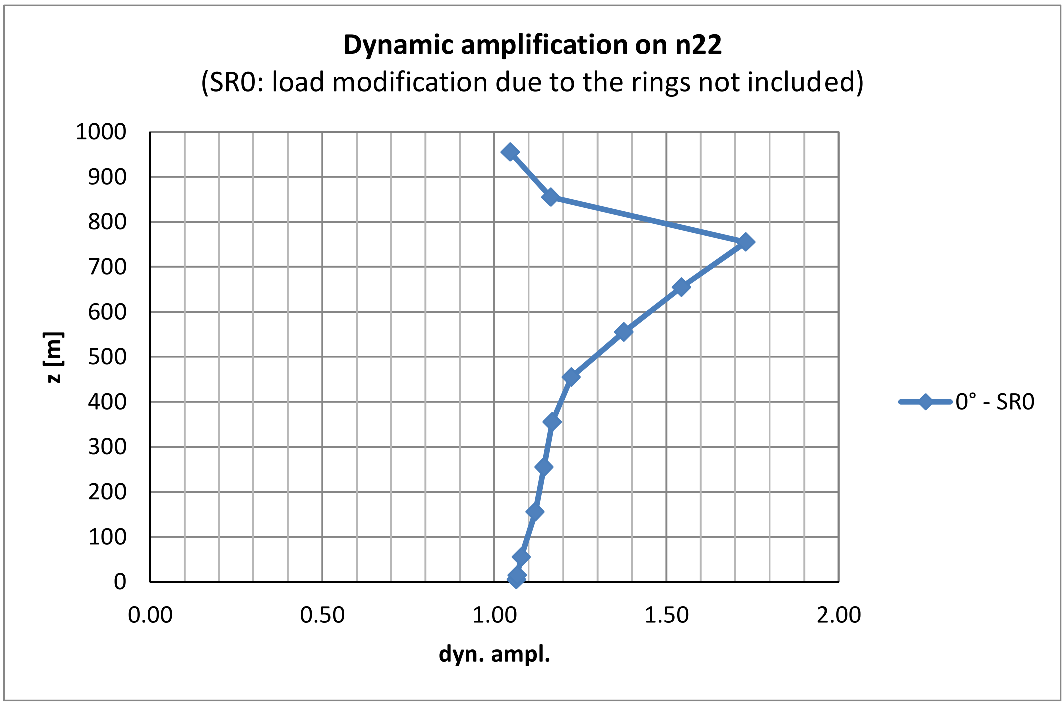

Figure 7.60 Dynamic amplification at stagnation – WiSt results (load modification due to the rings not inclueded)

7.3.4 The shell response under asymmetric wind load (10 ring beams)

The asymmetric response of the tower, due to the load modification induced by the rings (SR1) is analyzed in this section, both in quasi-static and dynamic calculations.

The covariance method is applied to input data that describe the asymmetric load condition, with inversion along the height, created by 10 ring beams (section 5.5). This load condition corresponds to SR1. The response to the SR1 load condition (red lines in the following graphs) is compared to the response in SR0 (load modification due to rings not included, blue lines in the graphs). In any case, the calculation is made on a structure with ten rings (like in Figure 1.13). The flow condition (mean profile, turbulence intensity, integral length scale) is the one in the WiSt tunnel, properly scaled according to the prototype.

The most appreciable effect on the response, due to the load modification induced by the ring beams, is on the meridional forces n_{22} (Table 7.15, Figure 7.63). In particular, the increase in the peak meridional force (n_{22}) at the base is around 10%, comparable to the increase in bending moment in the beam-like model (section 7.2.2).

As regards the circumferential stresses (n_{11}), they are high only close to the rings and the highest ones are at the throat of the hyperboloid. The increase in stresses due to the load modification induced by the rings is less than 10% in the peak response and somewhat higher in the standard deviations (Table 7.14, Figure 7.62).

The bending moments in both meridional and circumferential directions do not present significant variations due to rings; they do not differ more than 5 kNm/m in the peak response.

Numerical values are reported in the appendix (Table A.14, Table A.15, Table A.16).

In any case, these results represent the highest limit in case of ten big rings. Intermediate situations are expected with smaller rings and/or at larger distance. Moreover, the asymmetric load condition all along the height is the worst condition in which the two asymmetric states are never mixed. In fact, the mixture of the two states at low levels tends to weaken the asymmetry towards a mostly symmetric condition at the base, as observed in Chapter 6.

Table 7.14 Effect of load modification due to 10 rings on the quasi-static response (n_{11})
WiSt data; SR0 = load modification due to the rings not included;
SR1 = load modification due to 10 rings included

	n_{11},peak at 0° [kN/m]			**n_{11},m at 0° [kN/m]**			**n_{11},σ at 0° [kN/m]**		
z [m]	**SR0**	**SR1**	**SR1/SR0**	**SR0**	**SR1**	**SR1/SR0**	**SR0**	**SR1**	**SR1/SR0**
5	479	533	1.11	326	347	1.07	45	54	1.20
105	362	370	1.02	232	245	1.05	38	36	0.97
205	890	830	0.93	548	553	1.01	99	80	0.81
305	1672	1681	1.00	1078	1090	1.01	171	169	0.99
405	2144	2269	1.06	1472	1509	1.03	193	218	1.13
505	1841	1966	1.07	1324	1361	1.03	148	174	1.17
605	1737	1824	1.05	1292	1306	1.01	128	148	1.17
705	1945	2007	1.03	1472	1468	1.00	136	154	1.14
805	2039	2084	1.02	1553	1541	0.99	139	155	1.12
905	1965	2012	1.02	1490	1484	1.00	136	152	1.11
995	1090	1096	1.00	817	798	0.98	79	86	1.09

Table 7.15 Effect of load modification due to 10 rings on the quasi-static response (n_{22})
WiSt data; SR0 = load modification due to the rings not included;
SR1 = load modification due to 10 rings included

	n_{22},peak at 0° [kN/m]			**n_{22},m at 0° [kN/m]**			**n_{22},σ at 0° [kN/m]**		
z [m]	**SR0**	**SR1**	**SR1/SR0**	**SR0**	**SR1**	**SR1/SR0**	**SR0**	**SR1**	**SR1/SR0**
5	4039	4442	1.10	2695	2863	1.06	385	451	1.17
105	3581	3973	1.11	2520	2709	1.08	304	362	1.19
205	3364	3683	1.09	2447	2637	1.08	262	299	1.14

305	3440	3608	1.05	2519	2649	1.05	264	275	1.04
405	3100	3117	1.01	2278	2308	1.01	236	232	0.98
505	1893	1814	0.96	1376	1334	0.97	149	137	0.93
605	992	874	0.88	667	580	0.87	93	85	0.90
705	414	337	0.81	204	128	0.62	60	60	1.00
805	-220	-260	1.18	-94	-113	1.20	36	42	1.17
905	-280	-277	0.99	-197	-186	0.95	25	27	1.08
995	-43	-44	1.02	-30	-30	1.03	5	5	1.00

From the dynamic point of view, the calculation is repeated in SR1 as in section 7.3.3. The main difference between SR1 and SR0 is at level 650 m, where the bistable asymmetric flow starts its disruption on the bubble side.

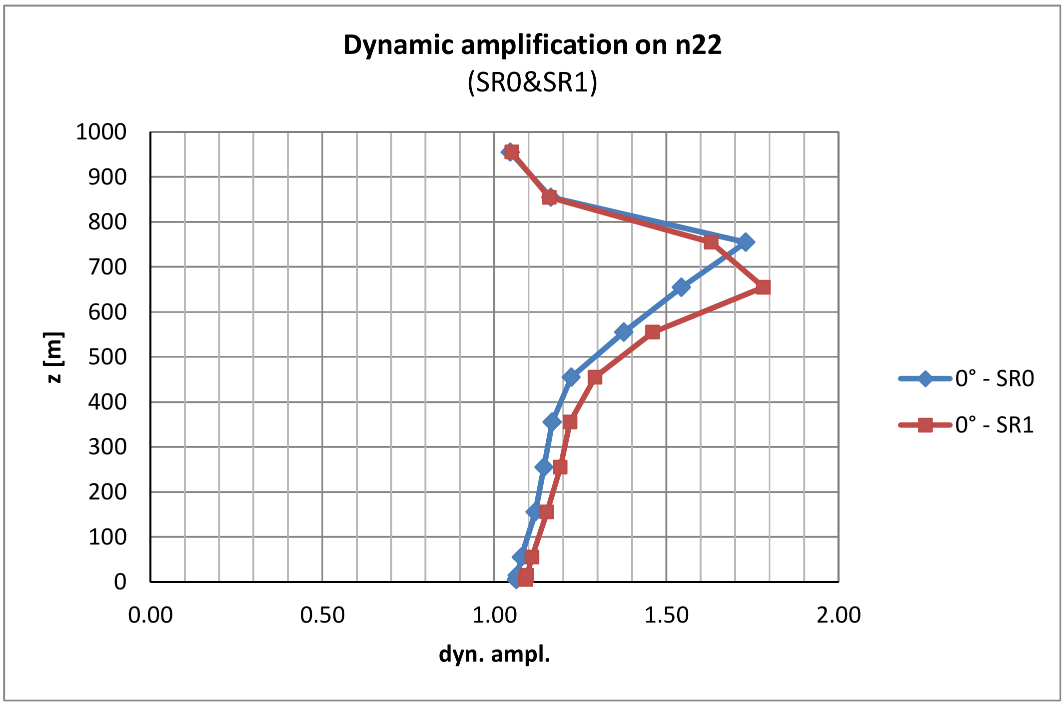

Figure 7.61 Dynamic amplification at stagnation: SR0&SR1– WiSt results

The presence of jumps in the time histories, which mark the transition from state 1 to state 2 or viceversa, should not create severe dynamic problems to the structure. The scale factor λ_T = 488 is applied to the jump reported in Figure 5.10, so that two seconds in the wind tunnel correspond to about 1000 s in full-scale. Figure 7.66 shows that the jump basically occurs between the time steps “d” and “f”. It takes about 10 s, i.e. about twice the natural period of the structure. Nevertheless, the effect of the jump on the response should be further investigated in the future (see Chapter 8), because even in a time period comparable to the natural period of the tower, the load might undergo a steep change.

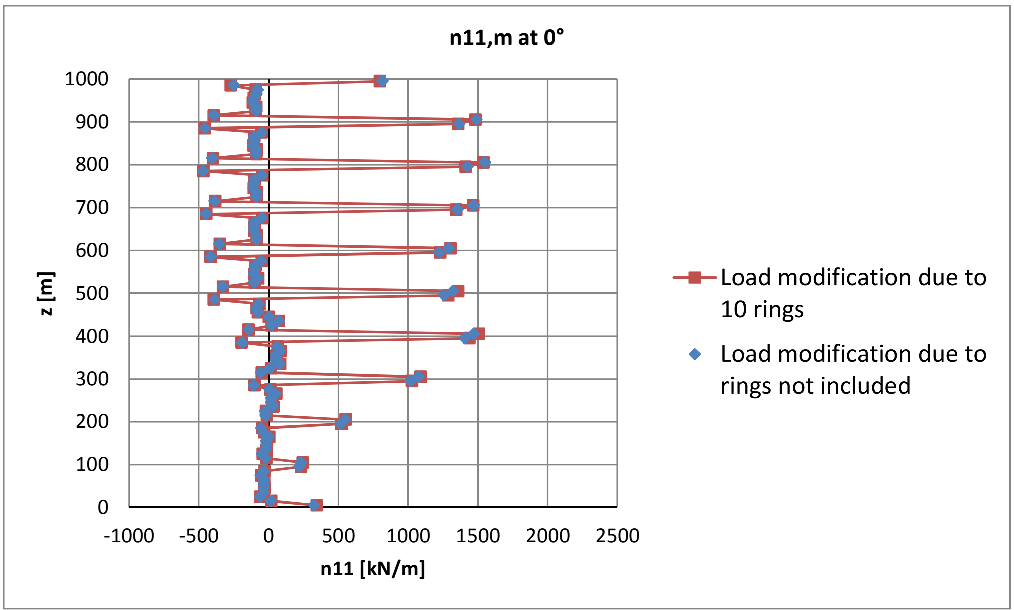

a) mean

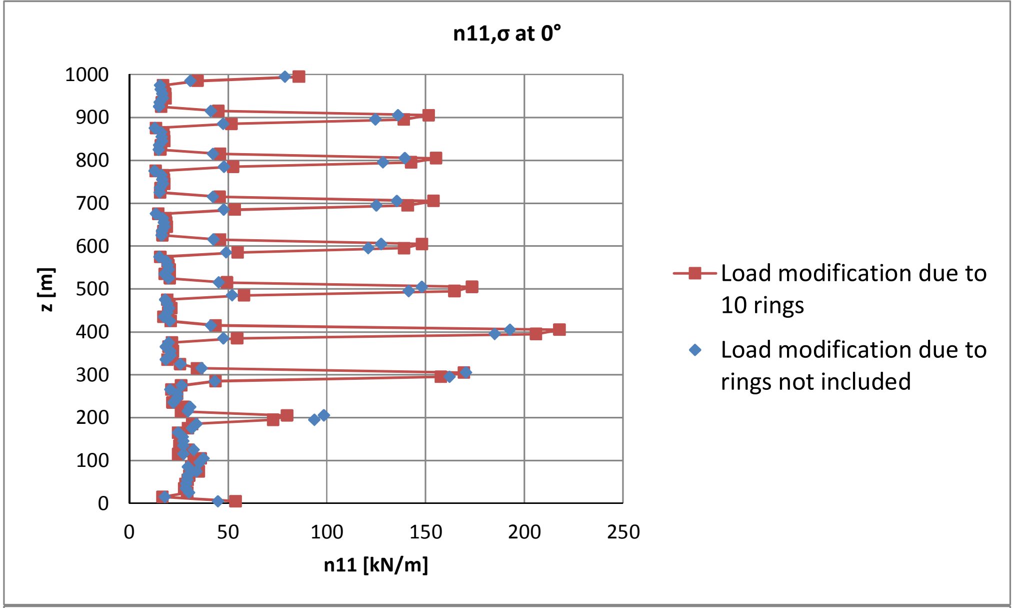

b) rms

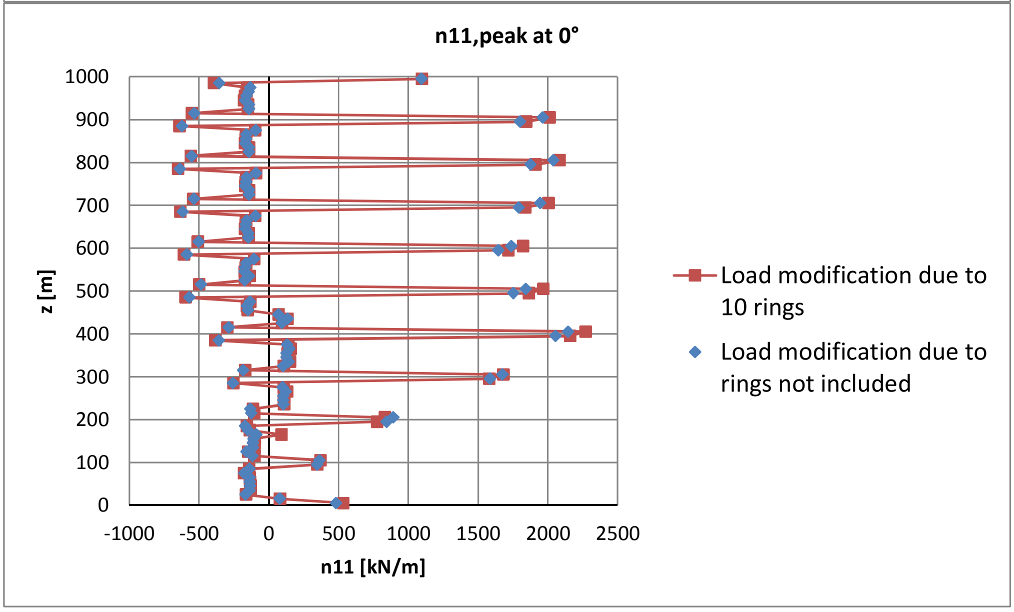

c) peak

Figure 7.62 Effect of the rings on the quasi-static response (n_{11})

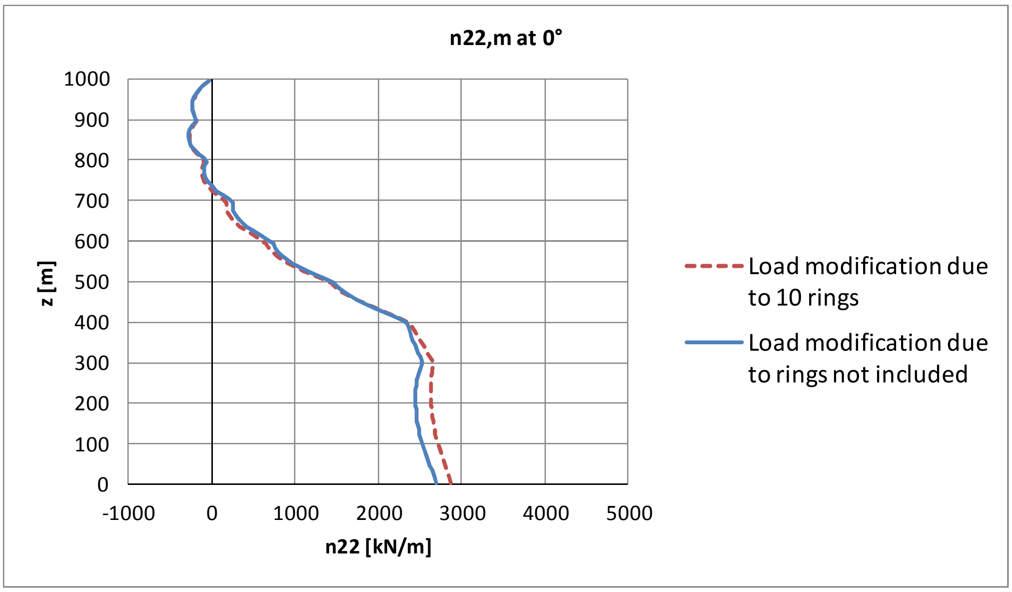

a) mean

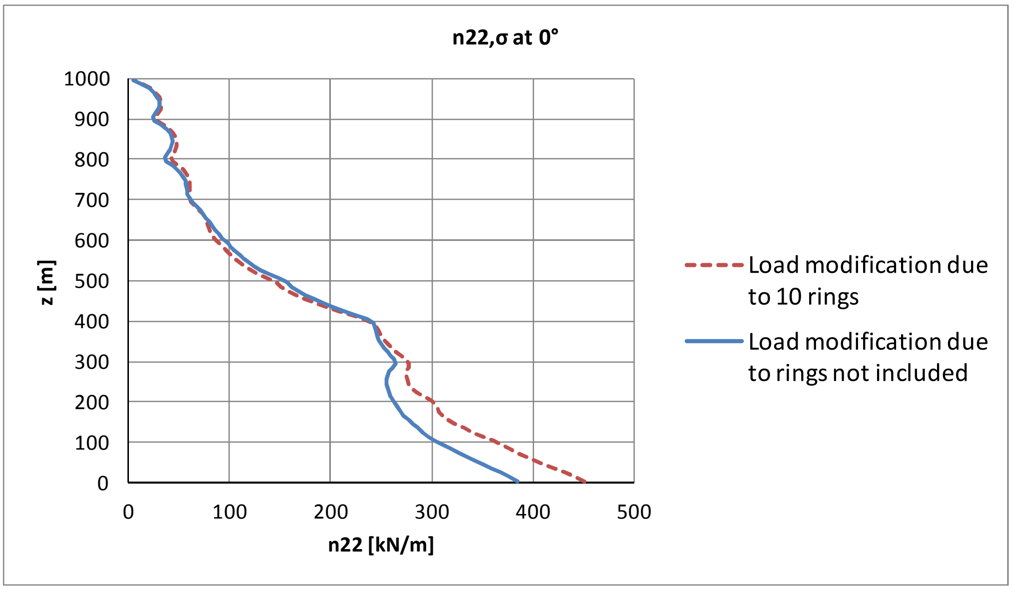

b) rms

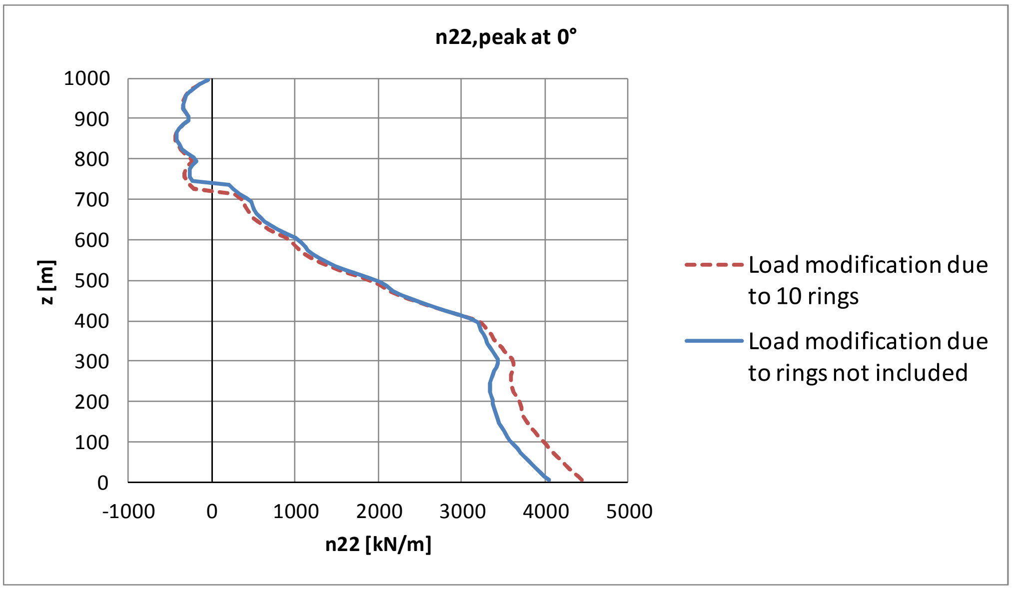

c) peak

Figure 7.63 Effect of the rings on the quasi-static response (n_{22})

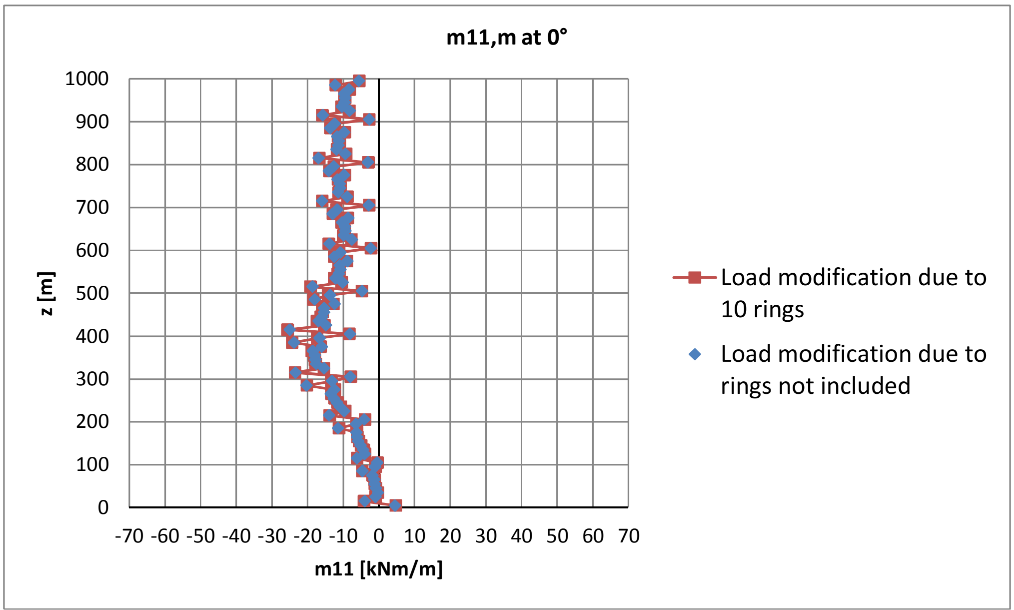

a) mean

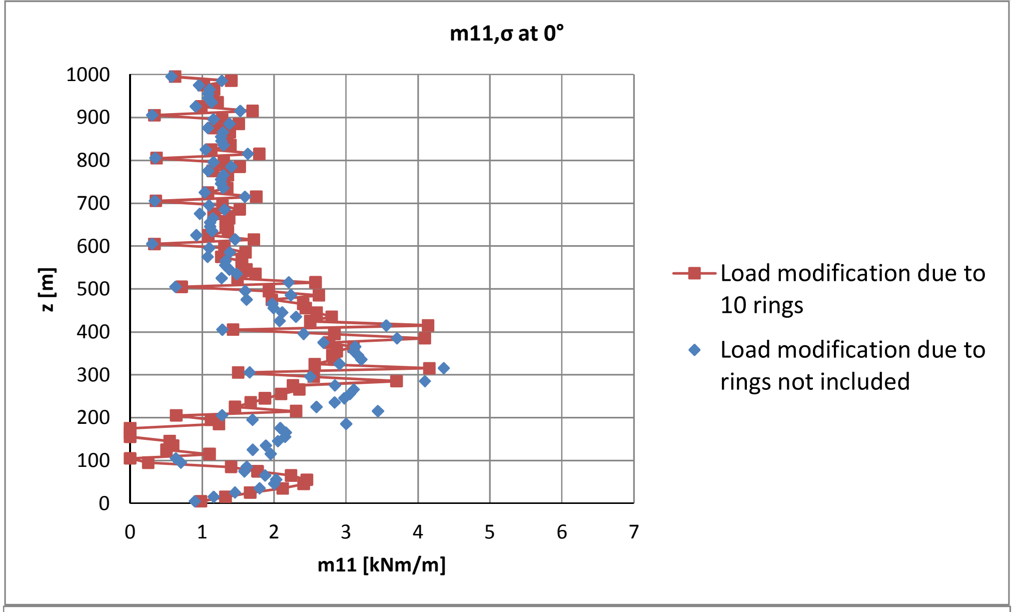

b) rms

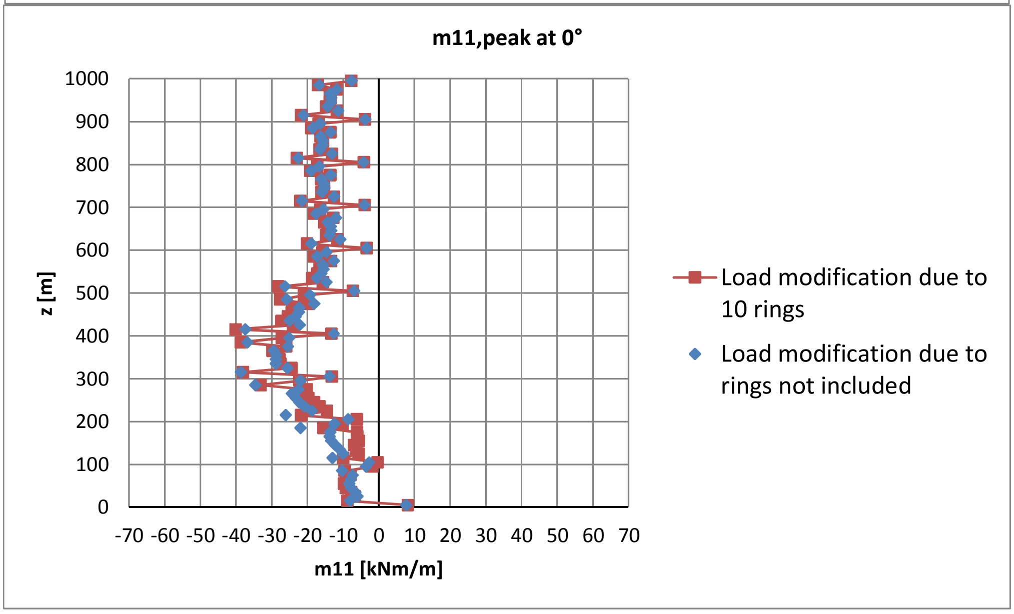

c) peak

Figure 7.64 Effect of the rings on the quasi-static response (m_{11})

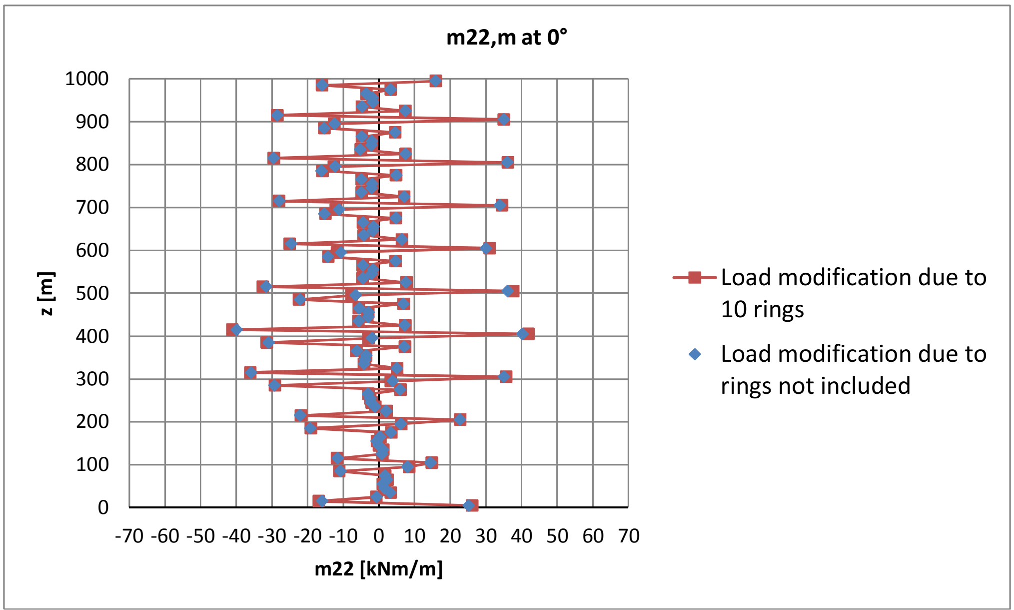

a) mean

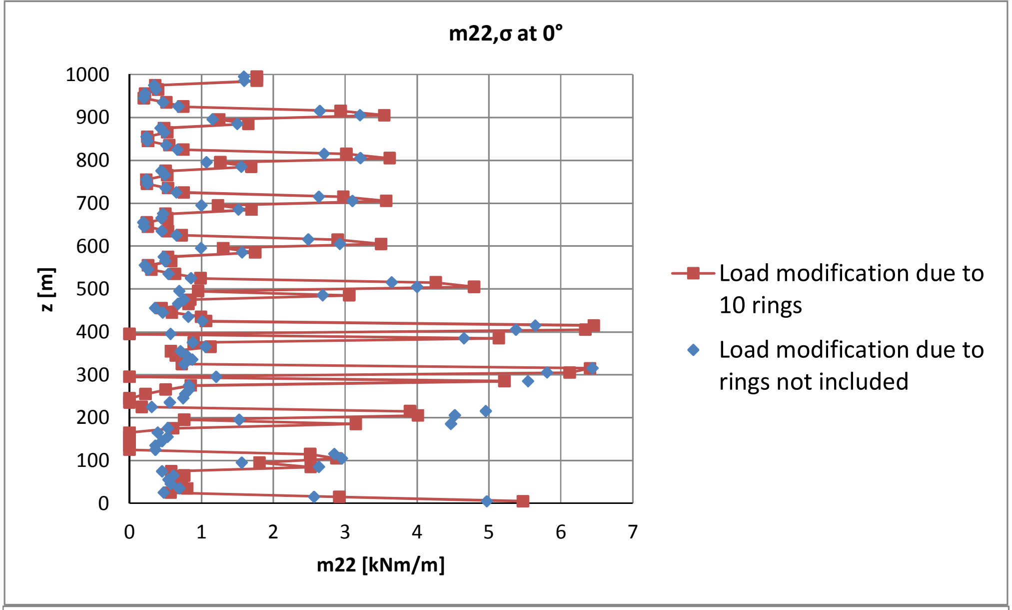

b) rms

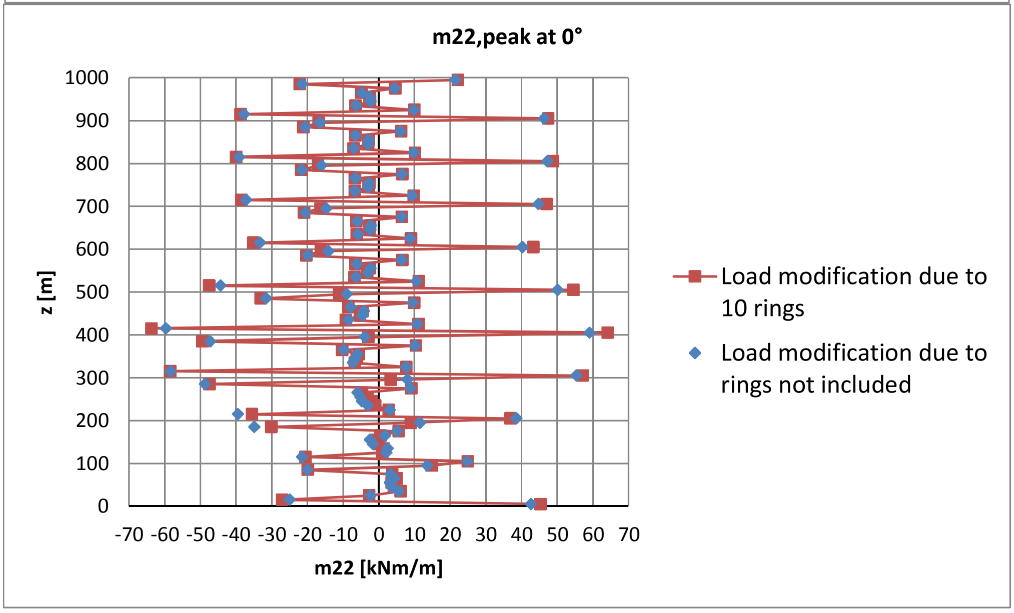

c) peak

Figure 7.65 Effect of the rings on the quasi-static response (m_{22})

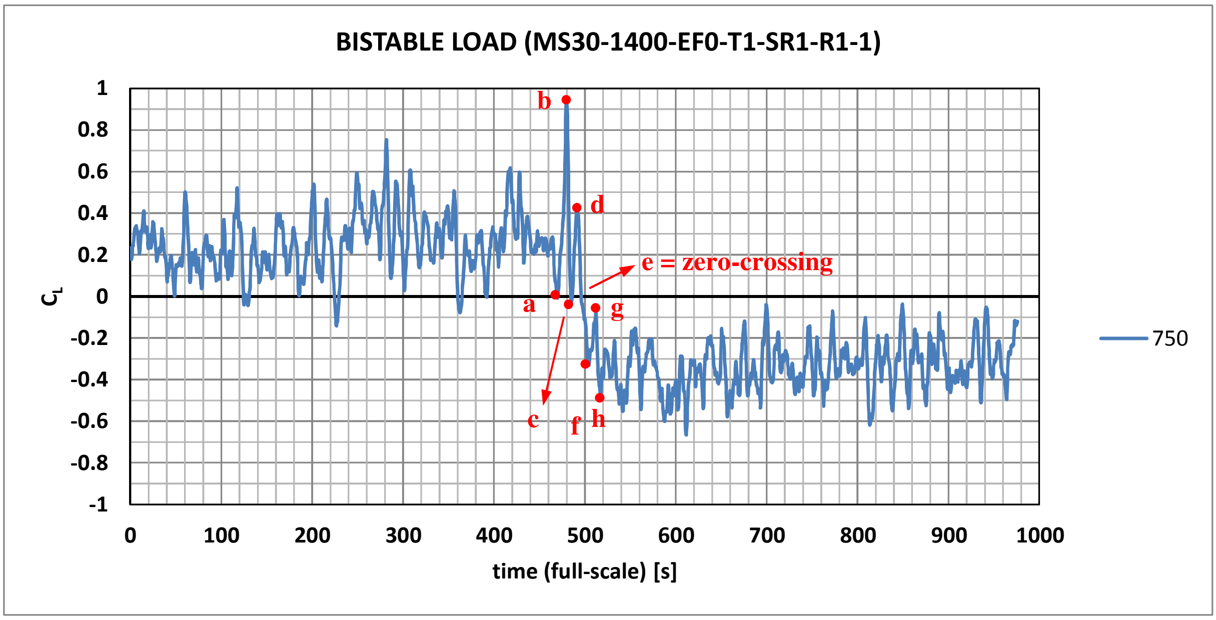

Figure 7.66 Bistable load on the structure: change of state

Chapter 8. **Conclusions and future outlooks**

The dissertation studies the Aeolian risk scenario in the design of ultra-high structures exposed to strong winds in the atmospheric boundary layer. Solar updraft towers represent the main application and constitute the thread of the dissertation.

A deeper knowledge of the natural hazard - the wind action - at large heights and also at small latitudes in the atmospheric boundary layer is addressed in Chapter 2. In the design of ultra-high structures, the coupling between wind engineering and boundary layer meteorology becomes stronger and it cannot benefit of experimental data, which are scarce at large heights and even inexistent in strong wind conditions. Therefore, Chapter 2 approaches the problem at first on theoretical bases, and then outlines the possible experimental and numerical investigations which could support future studies.

Then, the aerodynamic study of the flow around circular cylinders is required for the design of towers with circular cross-section. A large amount of literature has been written on the topic and it is reviewed in Chapter 3. However, the flow around circular cylinders is so sensitive to many either governing or influencing parameters (such as Re, aspect ratio, free-end, characteristics of the boundary layer…), that a unified and systematic investigation is currently not available to the designer.

In Chapter 4, the dissertation investigates the flow around a circular cylinder of finite length through wind tunnel tests at WiSt laboratory (Ruhr-University Bochum). The full understanding of such a reference case study is the basis to interpret the effect of spanwise rings along the height of the tower.

The discovery and the physical interpretation of a new phenomenon around circular cylinders, induced by stiffening rings along the height, is the original contribution of this research. The phenomenon is described in Chapter 5 on the basis of WiSt wind tunnel results. An asymmetric and bistable flow condition establishes around a symmetric structure like a circular cylinder and it does not disappear at moderately high Reynolds numbers, far beyond the Re_{cr}.

The debate between literature and novelty, between similar effects in completely different physical contexts, encouraged the deep investigation of this asymmetric and bistable flow condition. Similar cases of bistable flows are also described in literature.

They are well-known for example on isolated cylinders in the critical range of the Reynolds number, as well as on side-by-side cylinders. But despite the similarities, the physical reasons appeared to be profoundly different. This immediately resulted from the analysis of the conditions of occurrence. The Reynolds numbers at which this new bistable phenomenon occurs are not limited to a small range around Re_{cr}. The effect can also be considered as a sort of interaction phenomenon. However, the interaction is not between wide and narrow wakes, like in the case of side-by-side cylinders, but between the wake in different spanwise compartments along the height. In fact, the peculiar characteristic of the cylinder, which is responsible for the occurrence of the phenomenon, is the presence of spanwise rings at a certain distance along the height of the tower. The contribution of the flow over the tip seems to play a key role, so that the phenomenon is a cascade effect, alternated in different compartments, towards the base of the tower.

In order to confirm and provide experimental evidence of the same asymmetric bistable flow condition even in a different wind tunnel, the experiments are repeated on the same model at CRIACIV wind tunnel at University of Florence and documented in Chapter 6. It is confirmed that the phenomenon does not depend on some local conditions or disturbances of a certain laboratory, but it is induced by the ring beams. It is also confirmed that in the moderately high range of Re which was investigated on the rough cylinder (up to $Re = 3*10^5$), the effect does not disappear. So far, no reason has been identified, which may suggest the disappearance of the phenomenon at higher Reynolds numbers, e.g. in full-scale conditions.

A further proof is provided by numerical simulations (Chapter 6). They have been performed on the basis of CRIACIV experiments by the TEE group, in the Industrial Energy Department at the University of Florence. The CFD simulation reproduces the experimental conditions but it benefits of two additional important aspects: ideal conditions and higher Reynolds numbers (in the order of 10^7, obtained by reduction of air viscosity). Even in this case, the asymmetric bistable phenomenon appears.

Therefore, the thesis can state that under peculiar conditions (the presence of spanwise rings along a circular cylinder of finite length), an asymmetric flow tends to stabilize around a symmetric structure. Random jumps occur in the time histories and reverse the situation. The wind tunnel experiments confirmed that the phenomenon belongs to one of those paradoxical cases where the symmetric flow structure appears to be intrinsically unstable and hence impossible. This was cited by Zdravkovich (2003) concerning side-by-side cylinders, but the concept seems to be perfectly fitting also to the case of an isolated cylinder with spanwise rings.

Furthermore, this type of asymmetric flow is not only an interesting fluid dynamic phenomenon. In fact, the presence of rings along the height of the tower, which are responsible for creating the effect, has an important structural function. In many pre-designs of the solar tower, stiffening rings were introduced in order to reduce the structural vulnerability to the wind action. They enhance a beam-like behaviour and reduce the peaks of tension at the windward side. They also increase the buckling stiffness. The stiffening rings were then considered, for the solar tower, a strategy to mitigate the structural risk. However, the effect of the rings on the load had never been investigated before, so it was not expected that the improvement in the structural behaviour might also be responsible for an even more severe load condition. This increases the structural damage. For this reason, the effect of the fluid dynamic phenomenon had to be quantified in terms of structural response. Fortunately, the increase in internal forces did not result to be dramatic (in the order of 10-15%), but the designer should be aware that reduction of structural vulnerability, by adding stiffening rings, can become a double-edge sword. Because of that, further design conditions (with a different number and/or size of rings), as well as mitigation strategies are also investigated in this work. It resulted that the asymmetric bistable flow tends to disappear as the rings become smaller and/or at larger distance. Moreover, the presence of efflux inside the chimney is a natural rescue.

A further contribution of the research is the development of a stochastic load model to be used in quasi-static calculations of the tower in any atmospheric boundary layer flow. It could be developed thanks to the comparative studies between WiSt and CRIACIV results, which allowed to investigate the dependency of wind forces and pressures on the characteristics of the atmospheric boundary layer. This tool allows the designer to evaluate the structural damage even in the vicinity of the stiffening rings, where the shell-like behaviour predominates and no load model was available before.

The dissertation suggested many interesting aspects and new ideas, which would deserve further investigation in the future.

The asymmetric and bistable flow discovered in this work was completely unknown, so there are many issues which should be further addressed. The results suggested that the bistable asymmetric flow is a three-dimensional phenomenon, related to the flow structures which develop around the free-end. This explains also the disruption along the height. In view of that, experiments in two dimensional conditions are recommended as a further proof. Moreover, it would also be important to test the influence of the aspect ratio of the cylinder. In any case, even if the phenomenon is related to the free-end condition, it is not the top ring alone which initiates the effect. In fact, in the case, for example, of five rings (instead of ten) the top ring is still there but the phenomenon disappears. This suggests to study the distribution of rings in the tip region more in detail. The thesis proved, by experiments, that equally distributed rings at sufficiently large distance mitigate the effect. However, the designer might need rings at smaller distance. Because of that, an important result would be to know whether it is sufficient, in order to mitigate the phenomenon, to outdistance the rings only in the tip region, as supposed in Chapters 5 and 6 on the basis of these results.

The CFD simulations presented in Chapter 6 are just at their first stage. The time window of the URANS is presently too short to be representative. More periods should be investigated. If it is the case, a large eddy simulation could allow to better investigate the bistability of the flow, being the bistability a stochastic effect.

Wind tunnel tests at higher Reynolds numbers on a smooth cylinder in three dimensional conditions would represent a decisive result to confirm what has been stated in this dissertation by using the concept of effective Reynolds number.

Moreover, the three dimensional correlation field should be investigated more extensively in the wind tunnel. This would allow to refine results in Chapter 7. A future aim of the research is to develop a simpler wind load model, e.g. an equivalent static wind load, which could be easily used to evaluate local effects. The approach could be the same as for cooling towers, by using the load response correlation method (Niemann, 1998).

The dynamic response of the solar tower should be further investigated, too. In the case of rings, a dynamic effect could rise within the jump. In this regard, it would be important to characterize the bistable pressure field and model bistable time histories. Moreover, the non-linear behaviour should be included in the analyses.

Chapter 9. **Bibliography**

Achenbach E. (1968). Distribution of local pressure and skin friction around a circular cylinder in cross-flow up to $Re=5\times10^6$. Journal of Fluid Mechanics, 34, 625-639.

Achenbach E. (1971). Influence of surface roughness on the cross-flow around a circular cylinder. Journal of Fluid Mechanics, 46, 321-335.

Achenbach E., Heinecke E. (1981). On vortex shedding from smooth and rough cylinders in the range of Reynolds numbers 6×10^3 to 5×10^6. Journal of Fluid Mechanics, 109, 239-251.

Afgan I., Moulinec C., Prosser R., Laurence D. (2006). Large eddy simulation of turbulent flow for wall mounted cantilever cylinders of aspect ratio 6 and 10. International Journal of heat and fluid flow, 28 (4), 561-574.

Augusti G., Borri C., Niemann H.-J. (2001). Is aeolian risk as significant as other environmental risks? Reliability Engineering and System Safety, 74 (3), 227-237.

Ayoub A., Karamcheti K. (1982). An experiment on the flow past a finite circular cylinder at high subcritical and supercritical Reynolds numbers. Journal of Fluid Mechanics, 118, 1-26.

Backström T.W. von, Fluri T.P. (2006). Maximum fluid power condition for solar chimney power plants – An analytical approach. Solar Energy, 80, 1417-1423.

Backström T.W. von, Harte R., Höffer R., Krätzig W.B., Kröger D.G., Niemann, H.-J., van Zijl, G.P.A.G. (2008). State and Recent Advances of Solar Chimney Power Plant Technology. VGB PowerTech, 88 Vol. 7, 64-71.

Backström T.W. von, Fluri T.P. (2010). Solar chimney turbine layout and design considerations. Proc. 2nd Int. Conf. Solar Chimney Power Technology, 239-246. Ruhr-Universität Bochum and Bergische Universität Wuppertal.

Baker, C.J. (1980). Vortex flow around the bases of obstacles. Dissertation, Cambridge.

Baker, C.J. (1980). The turbulent horseshoe vortex. Journal of Wind Engineering and Industrial Aerodynamics, 6 (1-2), 9-23.

Baker, C.J. (1991). Oscillation of horseshoe vortex systems. Journal of Fluids Engineering, Transactions of the ASME, 113 (3), 489-495.

Banakh V.A., Smalikho I.N., Köpp F., Werner C. (1995). Representativeness of wind measurements with a cw Doppler lidar in the atmospheric boundary layer. Applied Optics, 34 (12), 2055-2067.

Bange J. (2007). Airborne measurement of turbulent energy exchange between the earth surface and the atmosphere. Habilitationsschrift, Technical University Braunschweig, Germany.

Basu, R.I. (1985). Aerodynamic forces on structures of circular cross-section. Part 1. Model-scale data obtained under two-dimensional conditions in low-turbulence streams. Journal of Wind Engineering and Industrial Aerodynamics, 21 (3), 273-294

Basu, R.I. (1986). Aerodynamic forces on structures of circular cross-section. Part 2. The influence of turbulence and three-dimensional effects. Journal of Wind Engineering and Industrial Aerodynamics, 24 (1), 33-59.

Batham J.P. (1973). Pressure distributions on circular cylinders at critical Reynolds numbers. Journal of Fluid Mechanics, 57, 209-228.

Bearman P.W. (1969). On vortex shedding from a circular cylinder in the critical Reynolds number regime. Journal of Fluid Mechanics 37 (3), 577-585.

Bearman P.W., Wadcoc A.J. (1973). The interaction between a pair of circular cylinders normal to a stream. Journal of Fluid Mechanics, 61, 499-511.

Belik L. (1973). The secondary flow around circular cylinders mounted normal to a flat plate. Aero. Quart., 29, 47-54.

Bénard H. (1908). Formation of centres of circulation behind a mmoving obstacle (in French). Comptes Rendus Academie des Sciences, 147, 839-842.

Bendat J.S., Piersol A. (1993). Engineering Applications of Correlation and Spectral Analysis. John Wiley&Sons, Inc.

Bendat J.S., Piersol A. (2000). Random Data, analysis and measurement procedures. John Wiley&Sons, Inc.

Bennett A.R. (1896). An improved differential temperature air motor, adapted for scientific applications, for philosophical toys, for advertising and for other purposes. A.D. 1986, n. 8711. Printed by Darling and Son Ld, London.

Bergermann R., Weinrebe G. (2010). Realization and costs of solar updraft towers. Proceedings of the SCPT 2010 – International Conference on Solar Chimney Power Technology, 63-68. Ruhr-University Bochum and Bergische Universität Wuppertal, Bochum, Germany.

Bernardes M.A.d.S. (2004). Technische, ökonomische und ökologische Analyse von Aufwind-kraftwerken. Dr.-Ing. Thesis, University of Stuttgart.

Bernardes M.A.d.S. (2012). On the heat storage in solar updraft towers collectors. Proc. 3rd Int. Conf. on Solar Updraft Power Technology SUTPT 2012, 13-25. HUST, Wuhan, China.

Bloor M.S., Gerrard J.H. (1966). Measurements on turbulent vortices in a cylinder wake. Proceedings of the Royal Society of London, Series A (Mathematical and Physical Sciences), 294 (1438), 319-342.

Borri C., Pastò S. (2006). Lezioni di Ingegneria del Vento. Firenze University Press.

Borri C., Lupi F., Marino E. (2010). Optimum Shell Design of Solar Updraft Towers. Proc. 2nd Int. Conf. Solar Chimney Power Technology, Ruhr-Universität Bochum and Bergische Universität Wuppertal, 155-162.

Breuer W., Hüwe A (2010). Solar chimney power plants – An economist’s point of view. International Conference on Solar Chimney Power Technology, 55-61. Ruhr-University Bochum and Bergische Universität Wuppertal, Bochum, Germany.

Britter R.E., Hunt J.C.R., Mumford J.C. (1979). The distortion of turbulence by a circular cylinder. Journal of Fluid Mechanics, 92 (2), 269-301.

Buresti G. (1981). The effect of surface roughness on the flow regime around circular cylinders. Journal of Wind Engineering and Industrial Aerodynamics, 8 (1-2), 105-114.

Buresti G. (2012). Elements of Fluid Dynamics. Ed. Imperial College Press.

Cabanyes I. (1903). Las chimeneas solares (Solar chimneys). La ernergia eléctrica. Cited due to Wikipedia.

Canadillas B. (2010). A study of the marine boundary layer by LES-modelling and experimental observations with a focus on offshore wind energy applications. Gottfried Wilhelm Leibniz Universitaet Hannover.

Clobes M., Willecke A., Peil U. (2009). A refined analysis of guyed masts in turbulent wind. Proc. 5th European and African Conference on Wind Engineering, EACWE 5, Florence, Italy.

Clobes M., Willecke A. (2009). On the numerical simulation of gust and vortex excitation of guyed masts. IASS 24th meeting, Helsinki.

Cook N.J. (1985). Designer's Guide to Wind Loading of Building Structures Part 1: Background, Damage Survey, Wind Data&Structural Classification. Department of the Environment Building research establishment.

Cook N.J. (1997). The Deaves and Harris ABL model applied to heterogeneous terrain. Journal of Wind Engineering and Industrial Aerodynamics, 66, 197-214.

Counihan J. (1969). An improved method of simulating an atmospheric boundary layer in a wind tunnel. Atmospheric Environment 3 (2), 197-214.

Couregelongue J. (1929). On the existence of two families of eddies behind immersed solids (in French). Comptes Rendus Academie Sciences, 189, 972-974.

Courtney M., Wagner R., Lindelöw P. (2008). Testing and comparison of lidars for profile and turbulence measurements in wind energy. IOP Conference Series: Earth and Environmental Science, 1.

Crandall S.H., Mark W.D. (1963). Random Vibration in Mechanical Systems. Academic Press, New Yoerk and London.

Csanady G.T. (1967). On the resistance law of a turbulent Ekman layer. Journal of the Atmospheric Sciences, 24 (5), 467-471.

Davies F., Collier C.G., Bozier K.E., Pearson G.N. (2003). On the accuracy of retrieved wind information from Doppler lidar observations. Quart. Journal. Royal. Meteorology. Society. 129, 321-334.

Deaves D.M. (1981). A note on the upper boundary conditions for turbulence models in the neutral atmosphere. Boundary Layer Meteorology, 21 (4), 489-493.

Deaves D.M., Harris R.I (1982). A note on the use of asymptotic similarity theory in neutral atmosphere boundary layers. Atmospheric Environment, 16 (8), 1889-1893.

DIN EN 4133 (2009). German industrial standards: Steel stack / Chimneys built of Steel.

Durbin P.A., Hunt J.C.R. (1980). On surface pressure fluctuations beneath turbulent flow round bluff bodies. Journal of Fluid Mechanics, 100 (1), 161-184.

Dyrbye C., Hansen S.O. (1997). Wind Loads on Structures. John Wiley & Sons.

Eaddy M. (2004). Lift forces on smooth and rough circular cylinders in low and high turbulence flows. Dissertation. Monash University, Victoria.

Eisner F. (1925). Pressure measurements in flow cylinders. Zeitschrift für agewandte Mathematik und Mechanik, 5, 486-489.

Ekman (1905). Influence of the Earth's rotation on ocean currents. Arkiv for Matematik, Astronomioch Fysik, 2 (11), 1-52.

Emeis S., Harris M., Banta R.M. (2007). Boundary-layer anemometry by optical remote sensing for wind energy applications. Meteorologische Zeitschrift, 16 (4), 337-347.

Emeis S. (2010). Surface-Based Remote Sensing of the Atmospheric Boundary Layer. Atmospheric and Oceanographic Sciences Library. Springer.

EN 1990:2001-11, Eurocode - Basis of structural design, CEN 2001.

ESDU 71012, Fluid forces on non-streamline bodies - background notes and description of the flow phenomena, Engineering Sciences Data Unit, London.

ESDU 74030, Characteristics of atmospheric turbulence near the ground. Part I: definitions and general information, Engineering Sciences Data Unit, London.

ESDU 80025, Mean forces, pressures and flow field velocities for circular cylindrical structures: single cylinder with two-dimensional flow, Engineering Sciences Data Unit, London.

ESDU 81017, Mean forces, pressures, and moments for circular cylindrical structures: finite-length cylinders in uniform and shear flow, Engineering Sciences Data Unit, London.

ESDU 82026, Strong Winds in the Atmospheric Boundary Layer. Part 1: Mean hourly wind speeds, Engineering Sciences Data Unit, London.

ESDU 83045, Strong Winds in the Atmospheric Boundary Layer. Part 2: Discrete Gust Speeds, Engineering Sciences Data Unit, London.

ESDU 85020, Characteristics of atmospheric turbulence near the ground. Part II: single point data for strong winds (neutral atmosphere), Engineering Sciences Data Unit, London.

ESDU 86010, Characteristics of atmospheric turbulence near the ground. Part III: variations in space and time for strong winds (neutral atmosphere), Engineering Sciences Data Unit, London.

ESDU 96030, Response of structures to vortex shedding, Engineering Sciences Data Unit, London.

Fage A. (1928). The air flow around circular cylinder in the region where boundary layer separates from the surface. Aeronautical Research Council, Rep&Memo 1179.

Fage A, and Warsap J.H. (1929). The effects of turbulence and surface roughness on the drag of a circular cylinder. Aeronautical Research Council, Rep.&Memo 1253.

Farell C., Blessmann J. (1983). On critical flow around smooth circular cylinders. Journal of Fluid Mechanics, 136, 375-391.

Farivar Dj. (1981). Turbulent uniform flow around cylinders of finite length. AIAA Journal, 19 (3), 275-281.

Fasel H. F. (2012). Fluid dynamics and heat transfer analysis of geometrically scaled models of solar updraft tower plants using CFD. Proc. 3rd Int. Conf. on Solar Updraft Power Technology SUTPT 2012, 126-127. HUST, Wuhan, China.

Ferziger J.H., Peric M. (2002). Computational Methods for Fluid Dynamics. Springer.

Fluri T.P. (2008). Turbine layout for and optimization of solar chimney power conversion units. Ph.D. thesis, University of Stellenbosch.

Fluri T.P., Backström T.W. von (2008). Performance analysis of the power conversion unit of a solar chimney power plant. Solar Energy, 82 (11), 999-1008.

Fox T. A., West G.S. (1990). On the use of end plates with circular cylinders in wind tunnel studies. Research Report Series - University of Queensland, Department of Civil Engineering, CE118, 1-17

Fox T.A., West G.S. (1993). Fluid-Induced Loading of Cantilevered Circular Cylinders in a Low-Turbulence Uniform Flow. Part 1: Mean Loading with Aspect Ratios in the Range 4 to 30. Journal of Fluids and Structures, 7 (1), 1-14.

Fox T.A., West G.S. (1993). Fluid-Induced Loading of Cantilevered Circular Cylinders in a Low-Turbulence Uniform Flow. Part 2: Fluctuationg Loads on a Cantilever of Aspect Ratio 30. Journal of Fluids and Structures, 7, (1), 15-28.

Fox T.A., Apelt C.J. (1993). Fluid-Induced Loading of Cantilevered Circular Cylinders in a Low-Turbulence Uniform Flow. Part 3: Fluctuating Loads with Aspect Ratios 4 to 25. Journal of Fluids and Structures, 7 (4), 375-386.

Fox T.A., Apelt C.J., West G.S. (1993). The aerodynamic disturbance caused by the free-ends of a circular cylinder immersed in a uniform flow. Journal of Wind Engineering and Industrial Aerodynamics, 49 (1-3), 389-399.

Fröhlich J., Rodi W. (2004). LES of the flow around a circular cylinder of finite height. International Journal of Heat and Fluid Flow, 25 (3), 537-548.

Garg R.K., Niemann H.-J. (1995). On three dimensionality of fluctuating aerodynamic forces on circular cylindrical structures. Proc. of the 9th International Conference on Wind Engineering, New Delhi, India.

Gerrard, J.H. (1966). Three-dimensional structure of wake of circular cylinder. Journal of Fluid Mechanics, 25, 143-164.

Gerrard J.H. (1978). The wakes of cylindrical bluff bodies at low Reynolds number. Philosophical Transactions of the Royal Society of London A (Mathematical and Physical Sciences), 288 (1354), 351-382.

Gill A.E. (1968). Similarity theory and geostrophic adjustment. Journal Royal Meteorology Society, 94, 586-588.

Goldack A. (2004). Tragverhalten und Aussteifung hoher Stahlbetonrohren fuer Aufwindkraftwerke (Load-bearing behaviour and stiffening of high-rise RC-tubes for updraft power plants). Dissertation, University of Stuttgart. (in German).

Goldack A. (2011). Natural frequencies and Mode Shapes of Towers for Solar Updraft Power Plants. Proc. 8th Int. Conf. Structural Dynamics, EURODYN 2011, Leuven, Belgium, 3575-3581.

Goliger A. M., Milford R. V. (1998). A review of worldwide occurrence of tornadoes. Journal of Wind Engineering and Industrial Aerodynamics, 74/76, 111-121.

Gould R.W.E., Raymer W.G., Ponsford P.J. (1968). Wind tunnel tests on chimneys of circular section at High Reynolds Number. Proceedings of the Symposium on wind effects on buildings and structures, Loughborough.

Günther H. (1931). In hundert Jahren - Die künftige Energieversorgung der Welt (In hundred years – World’s future energy supply). Kosmos, Franckh'sche Verlagshandlung Stuttgart.

Güven O., Farell C., Patel V.C. (1980). Surface-roughness effects on the mean flow past circular cylinders. Journal of Fluid Mechanics, 98 (4), 673-701

Güven O., Farell C., Patel V.C. (1983). Boundary-layer development on a circular cylinder with ribs. Transactions of the ASME. Journal of Fluids Engineering, 105 (2), 179-184.

Haan F.L., Sarkar P.P., Gallus W.A. (2008). Design construction and performance of a large tornado simulator for wind engineering applications. Engineering Structures, 30, 1146-1159.

Hardesty R.M., Darby L.S. (2005). Ground-based and airborne lidar. Encyclopedia of Hydrologic Sciences. Malcolm G. Anderson (Ed.), Wiley, 697–712.

Harris R.I., Deaves D.M. (1980). The structure of strong winds. Proc. CIRIA Conference. London, Construction Industry Research and Information Association.

Harris R.I. (1986). Longer turbulence length scales. Journal of Wind Engineering and Industrial Aerodynamics, 24 (1), 61-68.

Harris M., Constant M., Ward C. (2001). Continuous wave bistatic laser Doppler wind sensor. Applied Optics, 40, 1501–1506.

Harte R., Graffmann M., Wörmann R. (2010). Progress in the Structural Design of Solar Chimneys. Proc. 2nd Int. Conf. Solar Chimney Power Technology, Ruhr-

Universität Bochum and Bergische Universität Wuppertal, 145-152, Bochum, Germany.

Holmes J.D. (2003). Wind Loading of Structures. Spon Press, Taylor&Francis Group.

Hölscher N., Niemann H.-J. (1993). On the flow around finite circular cylinders in turbulent shear flows. Physics of separated flows – Numerical, experimental and theoretical aspects. Ed.: Kl. Gersten, Notes on numerical fluid mechanics, Vol 40, pp. 216-244.

Hölscher N. (1993). Ein multivariater Ansatz fuer die aerodynamische Uebertragungsfunktion der Winddruecke in atmosphaerischer Grenzschichtstroemung. Dissertation 93-3, Ruhr University Bochum.

Holton J.R. (1979). An introduction to dynamic meteorology. Academic Press, New York.

Houghton J.T. (1977). The physics of the atmospheres. Cambridge University Press.

Hunt J.C.R. (1972). A theory for fluctuating pressures on bluff bodies in turbulent flows. Symposium on flow-induced structural vibrations. Karlsruhe, Germany.

Hunt J.C.R. (1973) A theory of turbulent flow round two-dimensional bluff bodies. Journal of Fluid Mechanics, 61, 625-705.

Hunt J.C.R. (1975) Turbulent velocities near and fluctuating surface pressures on structures in turbulent winds. Proc. International Conference on Wind Effects on Building and Structures.

Hunt J.C.R. (1990). A review of velocity and pressure fluctuations in turbulent flows around bluff bodies. Journal of Wind Engineering and Industrial Aerodynamics, 35, 49-85.

Irwin P. (2009). Wind engineering research needs, building codes and project scientific studies. Proc. 11th American Conference on Wind Engineering. San Juan, Puerto Rico.

Ishigai S., Nishikawa E., Nishimura K., Cho K. (1972). Experimental study on structure of gas flow in tube banks with tube axes normal to flow. Bulletin of the Japan Society of Mechanical Engineers, 15 (86), 949-956.

Isyumov N. (1999). Wind Tunnel Studies of Buildings and Structures. ASCE American Society of Civil Engineers.

Jørgensen Finn E. (2002). How to measure turbulence with hot-wire anemometers - a practical guide. Dantec Dynamics.

Kalash S., Naimeh W., Ajib S. (2012). A simplified analysis of the main parameters affecting the solar updraft power plants. Proc. 3rd Int. Conf. on Solar Updraft Power Technology SUTPT 2012, 101-106. HUST, Wuhan, China.

Karman Th. von, Rubach H. (1912). On the mechanism of resistance in fluids (in German). Physikalische Zeitschrift, 13.

Kasperski M, Niemann H.-J. (1988). On the correlation of dynamic wind loads and structural response of natural-draught cooling towers. Journal of Wind Engineering and Industrial Aerodynamic, 30, 67-75.

Kawamura T. Hiwada M, Hibino T., Mabuchi I., Kumada M. (1984). Flow around a finite circular cylinder on a flat plate. Cylinder height greater than turbulent boundary layer thickness. Bulletin of the Japan Society of Mechanical Engineers, 27 (232), 2142-2151.

Kindler D., Oldroyd A., Macaskill A., Finch D. (2007). An 8 month test campaign of the QinetiQ ZephIR system: preliminary results. Meteorologische Zeitschrift, 16, 463–473.

Kitagawa T., Fujino Y., Kimura K. (1999). Effects of free-end condition on end-cell-induced vibration. Journal of Fluids and Structures, 13 (4), 499-518.

Kitagawa T., Fujino Y., Kimura K., Mizuno Y. (2001). Wind pressures on end-cell-induced vibration of circular tower. Journal of Engineering Mechanics, 127 (11), 1135-1143.

Kitagawa T., Fujino Y., Kimura K., Mizuno Y. (2002). Wind pressures measurement on end-cell-induced vibration of a cantilevered circular cylinder. Journal of Wind Engineering and Industrial Aerodynamics, 90 (4-5), 395-405.

Kovásznay, L. S. G. (1949). Hot-Wire Investigation of the Wake behind Cylinders at Low Reynolds Numbers. Proceedings of the Royal Society of London. Series A, Mathematical and Physical Sciences, 198 (1053), 174-190.

Krajnovic, S. (2011). Flow around a tall finite cylinder explored by large eddy simulation. Journal of fluid mechanics, 676, 294-317.

Krätzig W.B., Harte R., Wörmann R. (2008). Large shell structures for power generation technologies. Proc. 6th Int. Conf. IASS-IACM 2008, Cornell University, Ithaca, NY, USA.

Krätzig W.B., Niemann H.-J., Harte R. and Höffer R. (2009a). Solar Updraft Power Plant with 750 m power towers and collector diameters of 3000 m to 4000 m. Internal manual, Bochum.

Krätzig W.B., Harte R., Montag U., Woermann R., (2009b). From large natural draft cooling tower shells to chimneys of solar upwind power plants. In: A. Domingo, C. Lazaro (eds.), IASS Symposium on Evolutions and Trends in Design, Analysis and Construction of Shells. CD-Rom, University of Valencia.

Krätzig W.B., Harte R., Montag U., Graffmann M. (2010). On Structural Engineering Problems of Solar Updraft Chimneys. Proc. 4th Int. Conf. Structural Engineering, Mechanics and Computation, SEMC 2010, Cape Town, South Africa.

Krätzig W.B., Gould Ph.L., Harte R. (2011). Shell structures for power technology. In: Mungan, I., Abel, J.F. (eds.) Fifty years of progress for shell and spatial structures. International Association for Shell and Spatial Structures (IASS), Madrid, 165-194.

Krätzig W.B. (2012a). Solar updraft power technology, State and advances of low-concentrated thermal solar power generation. VGB PowerTech 92, Vol. 11, 34-39.

Krätzig W.B. (2012b). Physics, Computer Simulation and Optimization of Thermo-fluidmechanical Processes of SUPPs. Proceedings 3rd Int. Conf. on Solar Updraft Power Tower Technology SUTPT 2012, 1-12. HUST Wuhan, China.

Krätzig W.B., Harte R., Graffmann M., Montag U. (2013). Load response and design of Giga-towres. CICIND Report 29 Vol. 1, 55-62.

Kroonenberg van den A. (2009). Airborne Measurement of Small-Scale Turbulence with special regard to the Polar Boundary Layer. Dissertation. Technical University Carolo-Wilhelmina, Braunschweig.

Lee T., Lin C.-L., Friehe C.A. (2007). Large-eddy simulation of air flow around a wall-mounted circular cylinder and a tripod tower. Journal of turbulence, 8 (29), 1-28.

Luo S.C., Gan T.L., Chew Y.T. (1996). Uniform flow past one (or two in tandem) finite length circular cylinder(s). Journal of Wind Engineering and Industrial Aerodynamics, 59 (1), pp. 69-93.

Lupi F. (2009) Structural behaviour, optimization and design of a solar chimney prototype under wind loading and other actions. Master Thesis, University of Florence in cooperation with Ruhr University Bochum.

Lupi F., Borri C., Krätzig W.B., Niemann H.-J., (2011). Solar Updraft Power Plant technology: basic concepts and structural design. In Encyclopedia Online of Life Support Systems (EOLSS) developed under the auspices of the UNESCO, Eolss Publishers, Oxford, UK.

Lupi F., Borri C., Niemann H.-J., Peil U. (2011) Non-conventional wind loading on ultra-high Towers in Solar Updraft Power Plants. International Journal of Shell and Space Structures, 52 (4), 257-264.

Mahbub Alam, Md., Sakamoto, H., Moriya, M. (2003). Reduction of fluid forces acting on a single circular cylinder and two circular cylinders by using tripping rods. Journal of Fluids and Structures 18 (3-4), 347-366.

Mahbub Alam Md., Meyer, J.P. (2011). Two interacting cylinders in cross flow. Physical Review Section E, Statistical Nonlinear and Soft Matter Physics 84 (5).

Mann J., Cariou J.P., Courtney M., Parmentier R., Mikkelsen T., Wagner R., Lindelöw P., Sjöholm M., Enevoldsen K. (2008). Comparison of 3D turbulence measurements using three staring wind lidars and a sonic anemometer. IOP Conference Series: Earth and Environmental Science, 1.

Matsuno T. (1966). Quasi-geostrophical motions in the equatorial area. Journal Meteorol. Jpn,. 44, 25-42.

Mikkelsen T., Mann J., Courtney M., Sjöholm (2008). Windscanner: 3-D wind and turbulence measurements from three steerable Doppler Lidars. Proc. 14th Int. Symposium for the Advancement of Boundary Layer Remote Sensing.

Monin A.S., Yaglom A.M. (1971). Statistical fluid mechanics: mechanics of turbulence, Vol. 1. Mit Press, Cambridge.

Nakamura Y., Tomonari Y. (1982). The effects of surface roughness on the flow past circular cylinders at high Reynolds numbers. Journal of Fluid Mechanics, 123, 363-378.

Neuhaus C. (2009). ZurIdentifikationselbsterregteraeroelastischerKräfte im Zeitbereich. Dissertation. BergischeUniversität Wuppertal, Germany.

Neuhaus C. (2010). Numerische frequenzabhängige Kalibrierung langer Druckmessschlauchsysteme. Internal report, Windingenieurwesen und Strömungsmechanik, Ruhr-Universität Bochum, Germany.

Newland D.E. (1993). An Introduction to Random Vibrations, Spectral & Wavelet Analysis. Dover Publications, Inc, Mineola, New York.

Niemann H.-J., Schräder P. (1981). Konstruktiver Ingenierbau Berichte, Heft 35/36, Gebäudeaerodynamik. DFG-Kolloquium, Ruhr-Universität Bochum, Germany.

Niemann H.-J., Hölscher N. (1990). A review of recent experiments on the flow past circular cylinders. Journal of Wind Engineering and Industrial Aerodynamics, 33 (1-2), 197-209.

Niemann H.-J., Flaga A., Höffer R., Hölscher N., Kasperski M. (1996). Structural response to wind. In: Dynamics of Civil Engineering Structures, Wilfried B. Krätzig & Hans-Jürgen Niemann (Eds.) A.A. Balkema, Rotterdam.

Niemann H.-J. (1998). Wind load modelling in the analysis of very high cooling towers. Proc. Wind effects on buildings and structures, A.A. Balkema.

Niemann H.-J-, Hölscher N., Meiswinkel R. (2007). A probabilistic approach for the determination of extreme actions with respect to the structural design. Proc. of ICAPP 2007, Nice, France.

Niemann H.-J., Höffer R. (2007). Wind loading for the design of the solar tower. Proc. 3rd Int. Conf. SEMC, Cape Town, South Africa.

Niemann H.-J (2008). Prototyp eines Aufwindkraftwerks. Windeigenschaften, winderregte Schwingungen und Windlasten zur Bemessung des Stahlbetonturms. Internal report, Bochum. (in German)

Niemann H.-J., (2009). A Refined Approach to Wind Loading for the Design of the Solar Tower. CICIND Report, 25 (2).

Niemann H.-J., Lupi F., Höffer R., Hubert W., Borri C., (2009). The solar updraft power plant: design and optimization of the tower for wind effects. Proceedings of the 5th European and African Conference on Wind Engineering EACWE5, Florence, Italy.

Niemann H.-J. (2010). Static, quasi-static and resonant wind effects on solar towers. 2nd International Conference on Solar Chimney Power Technology, Ruhr-University Bochum and Bergische Universität Wuppertal, Bochum.

Okamoto S., Yagita M. (1973). The experimental investigation on the flow past a circular cylinder of finite length placed normal to the plane surface in a uniform stream. Bulletin of the Japan Society of Mechanical Engineers, 16 (95), 805-814.

Okamoto S., Yagita M. (1984). Flow past circular cylinder of finite length placed normal to ground plane in uniform shear flow. Bulletin of the Japan Society of Mechanical Engineers. 27 (229), 1454-1459.

Okamoto S., Sunabashiri Y. (1992). Vortex shedding from a circular cylinder of finite length placed on a ground plane. Transactions of the ASME. Journal of Fluids Engineering, 114 (4), 512-521.

Palau-Salvador G., Stoesser T., Fröhlich J., Kappler M., Rodi W. (2010). Large Eddy Simulations and Experiments of Flow Around Finite-Height Cylinders. Flow, Turbulence and Combustion, 84 (2), 239-275.

Park C.-W., Lee S.J. (2000). Free end effects on the near wake flow structure behind a finite circular cylinder. Journal of Wind Engineering and Industrial Aerodynamics, 88, (2-3), 231-246.

Park C.-W., Lee S.J. (2002). Flow structure around a finite circular cylinder embedded in various atmospheric boundary layers. Fluid Dynamics Research, 30 (4), 197-215.

Parsumarthi N., Sherif S.A. (1997). Performance of a Demonstration Solar Chimney Model for Power Generation. Proc. 35th Heat Transfer and Mechanics Conference, 203-240. California State University, School of Engg. and Computer Science. Sacramento.

Peil U., Nölle H. (1990). Measurement of Wind Load and Response of a guyed Mast. Proc. European Conference on Structural Dynamics, Eurodyn '90, Bochum, Germany.

Peil U., Nölle H., (1992). Guyed masts under wind load. Journal of Wind Engineering and Industrial Aerodynamics, 43 (3), 2129-2140.

Peil U.,Nölle H., Wang Z.H. (1996). Dynamic behaviour of guys under turbulent wind load. Journal of Wind Engineering and Industrial Aerodynamics, 65 (1-3), 43-54.

Peil U., Nölle H., (1998). Stress distribution in steel chimneys. CICIND, Proc. 6th International Chimney Conference, 1. Brighton, England.

Plate E.L. (1982). Engineering meteorology. Elsevier Scientific Publishing Company.

Pliefke T. (2010). Public Investments in Disaster Risk Reduction – A Social Cost Benefit Analysis. Dissertation. Technical University of Braunschweig, University of Florence.

Pope S.B. (2000). Turbulent flows. Cambridge University Press.

Prandtl L. (1904). Fluid motion with very small friction (in German). Proc. of the 3rd International Mathemathical Congress, 484-491.

Pretorius J.P., Kröger D.G. (2006). Solar Chimney Power Plant Performance. ASME J. Solar Energy Engineering 128, 302-311.

Pretorius J.P. (2007). Optimization and Control of a Large-Scale Solar Chimney Power Plant, PhD-Thesis, University of Stellenbosch.

Pretorius J.P., Kröger D.G. (2010). Basic theory and numerical simulation of large scale solar updraft power plants. Proc. 2nd Int. Conf. Solar Chimney Power Technology, 45-54. Ruhr-Universität Bochum and Bergische Universität Wuppertal.

Procino L. (2010). Profilo mare. Internal report, CRIACIV.

Pröpper H. (1977) Zur aerodynamischen Belastung groβer Kühltürme. Dissertation 77-3, Ruhr-Universitaet Bochum, Germany.

Raasch S., Etling D. (1991). Numerical simulation of rotating turbulent thermal convention. Beitr. Phys. Atmos. 64, 185-199.

Raasch S., Etling D. (1998). Modelling deep ocean convention: large eddy simulation in comparison with laboratori experiments. Journal of Physical Oceanography, 28, 1786-1802.

Raasch S., Schröter M. (2001). PALM – A large eddy simulation model performing on massively parallel computers. Meteorologische Zeitschrift, 10 (5), 363-372.

Rayleigh L. (1896). The theory of sound.

Rayleigh L. (1915). Aolian tones. Philosophical Magazine, 6th series, 42, 173-176.

Reynolds O. (1883). An experimental investigation of the circumstances which determine whether the motion of water shall be direct or sinuous, and the law of resistance in parallel channels. Philosophical Transactions, 174, 935-982.

Ribeiro D.J.L. (1991). Effects of surface roughness on the two-dimensional flow past circular cylinders I: mean forces and pressures. Journal of Wind Engineering and Industrial Aerodynamics. 37 (3), 299-309.

Ribeiro D.J.L. (1991). Effects of surface roughness on the two-dimensional flow past circular cylinders II: fluctuating forces and pressures. Journal of Wind Engineering and Industrial Aerodynamics. 37 (3), 311-326.

Roshko A. (1954). On development of turbulent wakes from vortex streets. National Advisory Committee for Aeronautics, Reports.

Roshko A. (1954). On the effect of air pressure on Strouhal number. Journal of the Aerospace Sciences, 26 (2), 121.

Roshko A. (1955). On the wake and drag of bluff bodies. Journal of the Aeronautical Sciences, 22 (2), 124-132.

Roshko A. (1961). Experiments on the flow past a circular cylinder at very high Reynolds number. Journal of Fluid Mechanics 10 (3), 345-356.

Rostamy N., Sumner D., Bergstrom D. J., Bugg J. D (2012). Local flow field of a surface-mounted finite circular cylinder. Journal of fluid and structures, 34, 105-122.

Sagaut P. (2006). Large eddy simulation for incompressible flows. Springer, Germany.

Sakamoto H., Arie M. (1983). Vortex shedding from a rectangular prism and a circular cylinder placed vertically in a turbulent boundary layer. Journal of Fluid Mechanics, 126, 147-165.

Salvadori S.&Mattana A., Barbanti G.&Vita G. (2013). CFD simulations on a Solar Updraft Tower on the basis of CRIACIV experiments, personal communication, unpublished.

Sathe A., Mann J., Gottschall J., Courtney M.S. (2011). Can wind lidars measure turbulence? Journal of Atmospheric and Oceanic Technology, 28 (7), 853-868.

Schewe G. (1983). On the forces acting on a circular cylinder in cross-flow from subcritical up to transcritical Reynolds numbers. Journal Fluid Mechanics 133, 265-285.

Schlaich J. (1995). The Solar Chimney, Electricity from the Sun. Edition A. Menges, Stuttgart.

Schlaich J., Bergermann R., Schiel W., Weinrebe G. (2005). Design of Commercial Solar Updraft Tower Systems. ASME J. Solar Energy Engineering, 127, 117-124.

Schlaich J. (2010). Concept and motivation of solar updraft power technology. Proc. 2nd Int. Conf. Solar Chimney Power Technology, 15-18. Ruhr-Universität Bochum and Bergische Universität Wuppertal, Bochum, Germany.

Schlichting, H. (1960). Boundary layer theory. McGraw-Hill.

Schrader P. (1993). Die statistische Stabiltät gemessener integraler Längenmaβe und anderer Windparameter. Dissertation, Ruhr-Universität Bochum, Germany.

Simiu E., Scanlan R.H. (1996). Wind effects on structures - Fundamentals and application to design. John Wiley&Sons, Inc. New York.

Simiu E. (2011). Design of Buildings for Wind. John Wiley&Sons, Inc.

Sjöholm M., Mikkelsen T., Mann J.,Enevoldsen K., Courtney M. (2008). Time series analysis of continuous-wave coherent Doppler Lidar wind measurements. IOP Conference Series: Earth and Environmental Science, 1 (1).

Stull R.B. (1988). An introduction to boundary layer meteorology. Kluwer Academic Publishers, Dordrecht, The Netherlands.

SCPT (2010). Proc. 2nd Int. Conf. on Solar Chimney Power Technology, Ruhr-Universität Bochum and Bergische Universität Wuppertal, Bochum, Germany.

Strømmen E.N. (2010). Theory of Bridge Aerodynamics. Springer.

Sumner D., Heseltine J.L. (2008). Tip vortex structure for a circular cylinder with a free end. Journal of Wind Engineering and Industrial Aerodynamics, 96, 1185-1196.

Sumner, D. (2010). Two circular cylinders in cross-flow: A review. Journal of Fluids and Structures 26 (6), 849-899.

SUTPT (2012). Proc. 3rd Int. Conf. on Solar Updraft Power Technology SUTPT 2012. HUST, Wuhan, China.

Szechenyi E. (1974). Simulation of high Reynolds numbers on a cylinder in wind tunnel tests. Recherche Aerospatiale, 3, 155-164.

Szechenyi E. (1975). Supercritical Reynolds number simulation for two-dimensional flow over circular cylinders. Journal of Fluid Mechanics, 70, 529-542.

Tamura Y., Iwatani Y., Hibi K., Suda K., Nakamura O., Maruyama T., Ishibashi R (2007). Profiles of mean wind speeds and vertical turbulence intensities measured at seashore and two inland sites using Doppler sodars. Journal of Wind Engineering & Industrial Aerodynamics, 95 (6), 411-427.

Taniguchi S., Sakamoto H., Arie M. (1981). Flow around a circular cylinder vertically mounted in a turbulent boundary layer. Bulletin of the Japan Society of Mechanical Engineers, 24 (193), 1130-1136.

Taylor G.I. (1916). Pressure distribution round the cylinder. Advisory Committee of Aeronautics, Rep&Memo.

Teunissen H.W. (1970). Characteristics of the mean wind and turbulence in the planetary boundary layer. UTIAS Review No 32. Institute for Aerospace Studies, University of Toronto.

Thompson N. (1990). Integral length scales of turbulence: a re-analysis including data from non-uniform terrain. ESDU Memorandum n.76.

Uematsu Y., Yamada M. (1994). Aerodynamic forces on circular cylinders of finite height. Journal of Wind Engineering and Industrial Aerodynamics, 51 (2), 249-265.

Verkley W.T.M., van der Velde I.R. (2010). Balanced dynamics in the Tropics. Quarterly Journal of the Royal Meteorological Society, 136 (646), 41-49.

Versteeg H.K., Malalasekera W. (1995). An Introduction to Computational Fluid Dynamics. The Finite Volume Method. Longman Scientific&Technical.

VGB (2005). Structural design of cooling towers. Guideline VGB R 610Ue, VGB PowerTech, Essen.

VGB (2010). Structural design of cooling towers. Guideline VGB R 610e, VGB PowerTech, Essen.

Waechter M., Rettenmeier A., Kuehn M., Peinke, J. (2009). Characterization of short time fluctuations in atmospheric wind speeds by LIDAR measurements. Meteorologischezeitschrift, 18 (3), 277-280.

Wie Y., Wu Z. (2012). Shed absorbability and tower structure characteristics of the Solar Heated Wind Updraft Tower Power. Proc. 3rd Int. Conf. on Solar Updraft Power Technology SUTPT 2012, 126-127. HUST, Wuhan, China.

Weinrebe G. (2000). Technische, ökologische und ökonomische Analyse von solarthermischen Turmkraftwerken. Dissertation, University of Stuttgart.

Zdravkovich M.M. (1987). The effects of interference between circular cylinders in cross flow. Journal of Fluids and Structures, 1 (2), 239-261.

Zdravkovich M. M. (1992). A reflection on two modes of eddy shedding at Re = 180-300. Iutam Symposium, Bluff body wakes, Dynamics and Instabilities, Göttingen, 631-639. Springer, Berlin.

Zdravkovich M. M., Pridden D.L., (1977). Interference between two circular cylinders; Series of unexpected discontinuities. Journal of Wind Engineering and Industrial Aerodynamics, 2 (3), 255-270

Zdravkovich, M. M (1997). Flow around circular cylinders, Vol. 1, Fundamentals. Oxford University Press.

Zdravkovich, M. M (2003). Flow around circular cylinders, Vol. 2, Applications. Oxford University Press.

Chapter 10. **Appendix**

10.1 Modelling of wind load (Chapter 7)

Table A.1 Load data: body-induced pressure fluctuations - variance (SR0, effect of the rings on the load not included)

Cp,σ_B^2 = body-induced pressure fluctuations										
	0	**20**	**40**	**60**	**80**	**100**	**120**	**140**	**160**	**180**
0.95	0	0	0	1.04E-05	0.0023097	0.0136799	0.0198095	0.0102689	0.0184776	0.0273402
0.85	0	0	5.006E-05	0.00103	0.0074486	0.0411091	0.0128124	0.014862	0.0199033	0.0155416
0.75	0	0	0	0.000128	0.0070256	0.0211319	0.0041208	0.0030748	0.0037577	0.0034584
0.65	0	0	0	0	0.0014349	0.0192708	0.0023672	0.0017146	0.0019685	0.0020286
0.55	0	0	0	0	0	0	0.0005087	0.0002179	0.0009585	0.0010654
0.45	0	0	0	0	0	0	0.0001991	0	0.0004456	0.000387
0.35	0	0	0	0	0	0	0.0007821	0	5.383E-05	0.0002192
0.25	0.0099196	0.0097788	0	0	0.0072963	0	0	0	0	0.0006125
0.15	0.0373687	0.0325377	0.0093249	0.016141	0.0453442	0	0.0143486	0.0123303	0.012928	0.0100694
0.05	0	0	0	0	0.0669672	0	0.0596038	0.0943915	0.1293659	0.0646646

Table A.2 Load data: horizontal correlations tip region 1 (SR0, effect of the rings on the load not included)

TIP REGION N.1																			
	0	**20**	**40**	**60**	**80**	**100**	**120**	**140**	**160**	**180**	**200**	**220**	**240**	**260**	**280**	**300**	**320**	**340**	**360**
0	1.00	0.73	0.10	-0.40	-0.54	-0.43	-0.27	-0.28	-0.23	-0.19	-0.23	-0.28	-0.27	-0.43	-0.54	-0.40	0.10	0.73	1.00
20	0.73	1.00	0.64	0.02	-0.36	-0.40	-0.26	-0.22	-0.18	-0.14	-0.15	-0.21	-0.13	-0.24	-0.42	-0.53	-0.31	0.23	0.73
40	0.10	0.64	1.00	0.69	0.19	-0.05	-0.06	0.02	0.03	0.06	0.08	0.03	0.16	0.19	0.02	-0.31	-0.49	-0.31	0.10
60	-0.40	0.02	0.69	1.00	0.77	0.43	0.24	0.30	0.29	0.26	0.32	0.28	0.40	0.57	0.50	0.13	-0.31	-0.53	-0.40
80	-0.54	-0.36	0.19	0.77	1.00	0.79	0.46	0.45	0.43	0.33	0.40	0.37	0.42	0.68	0.75	0.50	0.02	-0.42	-0.54
100	-0.43	-0.40	-0.05	0.43	0.79	1.00	0.69	0.47	0.40	0.26	0.29	0.26	0.27	0.55	0.68	0.57	0.19	-0.24	-0.43
120	-0.27	-0.26	-0.06	0.24	0.46	0.69	1.00	0.62	0.35	0.26	0.15	0.12	0.07	0.27	0.42	0.40	0.16	-0.13	-0.27
140	-0.28	-0.22	0.02	0.30	0.45	0.47	0.62	1.00	0.52	0.36	0.23	0.21	0.12	0.26	0.37	0.28	0.03	-0.21	-0.28
160	-0.23	-0.18	0.03	0.29	0.43	0.40	0.35	0.52	1.00	0.39	0.31	0.23	0.15	0.29	0.40	0.32	0.08	-0.15	-0.23
180	-0.19	-0.14	0.06	0.26	0.33	0.26	0.26	0.36	0.39	1.00	0.39	0.36	0.26	0.26	0.33	0.26	0.06	-0.14	-0.19
200	-0.23	-0.15	0.08	0.32	0.40	0.29	0.15	0.23	0.31	0.39	1.00	0.52	0.35	0.40	0.43	0.29	0.03	-0.18	-0.23
220	-0.28	-0.21	0.03	0.28	0.37	0.26	0.12	0.21	0.23	0.36	0.52	1.00	0.62	0.47	0.45	0.30	0.02	-0.22	-0.28
240	-0.27	-0.13	0.16	0.40	0.42	0.27	0.07	0.12	0.15	0.26	0.35	0.62	1.00	0.69	0.46	0.24	-0.06	-0.26	-0.27
260	-0.43	-0.24	0.19	0.57	0.68	0.55	0.27	0.26	0.29	0.26	0.40	0.47	0.69	1.00	0.79	0.43	-0.05	-0.40	-0.43
280	-0.54	-0.42	0.02	0.50	0.75	0.68	0.42	0.37	0.40	0.33	0.43	0.45	0.46	0.79	1.00	0.77	0.19	-0.36	-0.54
300	-0.40	-0.53	-0.31	0.13	0.50	0.57	0.40	0.28	0.32	0.26	0.29	0.30	0.24	0.43	0.77	1.00	0.69	0.02	-0.40

320	0.10	-0.31	-0.49	-0.31	0.02	0.19	0.16	0.03	0.08	0.06	0.03	0.02	-0.06	-0.05	0.19	0.69	1.00	0.64	0.10
340	0.73	0.23	-0.31	-0.53	-0.42	-0.24	-0.13	-0.21	-0.15	-0.14	-0.18	-0.22	-0.26	-0.40	-0.36	0.02	0.64	1.00	0.73
360	1.00	0.73	0.10	-0.40	-0.54	-0.43	-0.27	-0.28	-0.23	-0.19	-0.23	-0.28	-0.27	-0.43	-0.54	-0.40	0.10	0.73	1.00

Table A.3 Load data: horizontal correlations tip region 2 (SR0, effect of the rings on the load not included)

TIP REGION N.2																			
	0	**20**	**40**	**60**	**80**	**100**	**120**	**140**	**160**	**180**	**200**	**220**	**240**	**260**	**280**	**300**	**320**	**340**	**360**
0	1.00	0.69	-0.05	-0.55	-0.65	-0.38	-0.18	-0.27	-0.21	-0.15	-0.21	-0.27	-0.18	-0.38	-0.65	-0.55	-0.05	0.69	1.00
20	0.69	1.00	0.61	-0.02	-0.39	-0.36	-0.14	-0.17	-0.15	-0.10	-0.12	-0.19	-0.08	-0.18	-0.52	-0.70	-0.55	0.07	0.69
40	-0.05	0.61	1.00	0.73	0.29	-0.02	0.06	0.14	0.07	0.06	0.11	0.08	0.13	0.21	-0.01	-0.37	-0.67	-0.55	-0.05
60	-0.55	-0.02	0.73	1.00	0.82	0.41	0.30	0.38	0.28	0.18	0.29	0.31	0.26	0.44	0.44	0.11	-0.37	-0.70	-0.55
80	-0.65	-0.39	0.29	0.82	1.00	0.78	0.54	0.50	0.40	0.21	0.34	0.39	0.24	0.45	0.63	0.44	-0.01	-0.52	-0.65
100	-0.38	-0.36	-0.02	0.41	0.78	1.00	0.79	0.46	0.41	0.13	0.21	0.23	0.04	0.18	0.45	0.44	0.21	-0.18	-0.38
120	-0.18	-0.14	0.06	0.30	0.54	0.79	1.00	0.56	0.37	0.11	0.11	0.12	-0.04	0.04	0.24	0.26	0.13	-0.08	-0.18
140	-0.27	-0.17	0.14	0.38	0.50	0.46	0.56	1.00	0.48	0.14	0.19	0.21	0.12	0.23	0.39	0.31	0.08	-0.19	-0.27
160	-0.21	-0.15	0.07	0.28	0.40	0.41	0.37	0.48	1.00	0.05	0.18	0.19	0.11	0.21	0.34	0.29	0.11	-0.12	-0.21
180	-0.15	-0.10	0.06	0.18	0.21	0.13	0.11	0.14	0.05	1.00	0.05	0.14	0.11	0.13	0.21	0.18	0.06	-0.10	-0.15
200	-0.21	-0.12	0.11	0.29	0.34	0.21	0.11	0.19	0.18	0.05	1.00	0.48	0.37	0.41	0.40	0.28	0.07	-0.15	-0.21
220	-0.27	-0.19	0.08	0.31	0.39	0.23	0.12	0.21	0.19	0.14	0.48	1.00	0.56	0.46	0.50	0.38	0.14	-0.17	-0.27
240	-0.18	-0.08	0.13	0.26	0.24	0.04	-0.04	0.12	0.11	0.11	0.37	0.56	1.00	0.79	0.54	0.30	0.06	-0.14	-0.18
260	-0.38	-0.18	0.21	0.44	0.45	0.18	0.04	0.23	0.21	0.13	0.41	0.46	0.79	1.00	0.78	0.41	-0.02	-0.36	-0.38
280	-0.65	-0.52	-0.01	0.44	0.63	0.45	0.24	0.39	0.34	0.21	0.40	0.50	0.54	0.78	1.00	0.82	0.29	-0.39	-0.65
300	-0.55	-0.70	-0.37	0.11	0.44	0.44	0.26	0.31	0.29	0.18	0.28	0.38	0.30	0.41	0.82	1.00	0.73	-0.02	-0.55
320	-0.05	-0.55	-0.67	-0.37	-0.01	0.21	0.13	0.08	0.11	0.06	0.07	0.14	0.06	-0.02	0.29	0.73	1.00	0.61	-0.05
340	0.69	0.07	-0.55	-0.70	-0.52	-0.18	-0.08	-0.19	-0.12	-0.10	-0.15	-0.17	-0.14	-0.36	-0.39	-0.02	0.61	1.00	0.69
360	1.00	0.69	-0.05	-0.55	-0.65	-0.38	-0.18	-0.27	-0.21	-0.15	-0.21	-0.27	-0.18	-0.38	-0.65	-0.55	-0.05	0.69	1.00

Table A.4 Load data: horizontal correlations tip region 3 (SR0, effect of the rings on the load not included)

TIP REGION N.3																			
	0	**20**	**40**	**60**	**80**	**100**	**120**	**140**	**160**	**180**	**200**	**220**	**240**	**260**	**280**	**300**	**320**	**340**	**360**
0	1.00	0.67	-0.09	-0.56	-0.61	-0.21	-0.19	-0.20	-0.19	-0.17	-0.19	-0.20	-0.19	-0.21	-0.61	-0.56	-0.09	0.67	1.00
20	0.67	1.00	0.65	0.06	-0.32	-0.22	-0.04	-0.04	-0.08	-0.10	-0.16	-0.19	-0.18	0.03	-0.47	-0.70	-0.63	-0.08	0.67
40	-0.09	0.65	1.00	0.76	0.32	-0.04	0.31	0.30	0.25	0.12	0.05	-0.02	0.00	0.25	0.04	-0.35	-0.69	-0.63	-0.09
60	-0.56	0.06	0.76	1.00	0.82	0.32	0.52	0.49	0.44	0.29	0.21	0.15	0.16	0.30	0.42	0.14	-0.35	-0.70	-0.56
80	-0.61	-0.32	0.32	0.82	1.00	0.71	0.65	0.57	0.54	0.35	0.23	0.19	0.15	0.20	0.52	0.42	0.04	-0.47	-0.61
100	-0.21	-0.22	-0.04	0.32	0.71	1.00	0.71	0.47	0.52	0.22	0.03	0.02	-0.10	-0.28	0.20	0.30	0.25	0.03	-0.21
120	-0.19	-0.04	0.31	0.52	0.65	0.71	1.00	0.75	0.67	0.36	0.01	0.01	-0.06	-0.10	0.15	0.16	0.00	-0.18	-0.19
140	-0.20	-0.04	0.30	0.49	0.57	0.47	0.75	1.00	0.74	0.39	0.08	0.08	0.01	0.02	0.19	0.15	-0.02	-0.19	-0.20
160	-0.19	-0.08	0.25	0.44	0.54	0.52	0.67	0.74	1.00	0.45	0.09	0.08	0.01	0.03	0.23	0.21	0.05	-0.16	-0.19

180	-0.17	-0.10	0.12	0.29	0.35	0.22	0.36	0.39	0.45	1.00	0.45	0.39	0.36	0.22	0.35	0.29	0.12	-0.10	-0.17
200	-0.19	-0.16	0.05	0.21	0.23	0.03	0.01	0.08	0.09	0.45	1.00	0.74	0.67	0.52	0.54	0.44	0.25	-0.08	-0.19
220	-0.20	-0.19	-0.02	0.15	0.19	0.02	0.01	0.08	0.08	0.39	0.74	1.00	0.75	0.47	0.57	0.49	0.30	-0.04	-0.20
240	-0.19	-0.18	0.00	0.16	0.15	-0.10	-0.06	0.01	0.01	0.36	0.67	0.75	1.00	0.71	0.65	0.52	0.31	-0.04	-0.19
260	-0.21	0.03	0.25	0.30	0.20	-0.28	-0.10	0.02	0.03	0.22	0.52	0.47	0.71	1.00	0.71	0.32	-0.04	-0.22	-0.21
280	-0.61	-0.47	0.04	0.42	0.52	0.20	0.15	0.19	0.23	0.35	0.54	0.57	0.65	0.71	1.00	0.82	0.32	-0.32	-0.61
300	-0.56	-0.70	-0.35	0.14	0.42	0.30	0.16	0.15	0.21	0.29	0.44	0.49	0.52	0.32	0.82	1.00	0.76	0.06	-0.56
320	-0.09	-0.63	-0.69	-0.35	0.04	0.25	0.00	-0.02	0.05	0.12	0.25	0.30	0.31	-0.04	0.32	0.76	1.00	0.65	-0.09
340	0.67	-0.08	-0.63	-0.70	-0.47	0.03	-0.18	-0.19	-0.16	-0.10	-0.08	-0.04	-0.04	-0.22	-0.32	0.06	0.65	1.00	0.67
360	1.00	0.67	-0.09	-0.56	-0.61	-0.21	-0.19	-0.20	-0.19	-0.17	-0.19	-0.20	-0.19	-0.21	-0.61	-0.56	-0.09	0.67	1.00

Table A.5 Load data: horizontal correlations tip region 4 (SR0, effect of the rings on the load not included)

TIP REGION N.4																			
	0	**20**	**40**	**60**	**80**	**100**	**120**	**140**	**160**	**180**	**200**	**220**	**240**	**260**	**280**	**300**	**320**	**340**	**360**
0	1.00	0.66	-0.07	-0.55	-0.51	0.00	-0.14	-0.16	-0.15	-0.15	-0.15	-0.16	-0.14	0.00	-0.51	-0.55	-0.07	0.66	1.00
20	0.66	1.00	0.65	0.03	-0.35	-0.19	-0.01	0.00	-0.02	-0.05	-0.10	-0.12	-0.09	0.23	-0.29	-0.68	-0.62	-0.05	0.66
40	-0.07	0.65	1.00	0.73	0.17	-0.18	0.25	0.28	0.25	0.18	0.11	0.09	0.10	0.36	0.18	-0.31	-0.68	-0.62	-0.07
60	-0.55	0.03	0.73	1.00	0.70	0.07	0.47	0.51	0.48	0.40	0.30	0.28	0.26	0.29	0.51	0.20	-0.31	-0.68	-0.55
80	-0.51	-0.35	0.17	0.70	1.00	0.60	0.62	0.61	0.60	0.48	0.34	0.31	0.25	0.01	0.47	0.51	0.18	-0.29	-0.51
100	0.00	-0.19	-0.18	0.07	0.60	1.00	0.48	0.40	0.40	0.29	0.14	0.10	0.04	-0.22	0.01	0.29	0.36	0.23	0.00
120	-0.14	-0.01	0.25	0.47	0.62	0.48	1.00	0.71	0.63	0.49	0.32	0.27	0.23	0.04	0.25	0.26	0.10	-0.09	-0.14
140	-0.16	0.00	0.28	0.51	0.61	0.40	0.71	1.00	0.76	0.55	0.38	0.32	0.27	0.10	0.31	0.28	0.09	-0.12	-0.16
160	-0.15	-0.02	0.25	0.48	0.60	0.40	0.63	0.76	1.00	0.68	0.46	0.38	0.32	0.14	0.34	0.30	0.11	-0.10	-0.15
180	-0.15	-0.05	0.18	0.40	0.48	0.29	0.49	0.55	0.68	1.00	0.68	0.55	0.49	0.29	0.48	0.40	0.18	-0.05	-0.15
200	-0.15	-0.10	0.11	0.30	0.34	0.14	0.32	0.38	0.46	0.68	1.00	0.76	0.63	0.40	0.60	0.48	0.25	-0.02	-0.15
220	-0.16	-0.12	0.09	0.28	0.31	0.10	0.27	0.32	0.38	0.55	0.76	1.00	0.71	0.40	0.61	0.51	0.28	0.00	-0.16
240	-0.14	-0.09	0.10	0.26	0.25	0.04	0.23	0.27	0.32	0.49	0.63	0.71	1.00	0.48	0.62	0.47	0.25	-0.01	-0.14
260	0.00	0.23	0.36	0.29	0.01	-0.22	0.04	0.10	0.14	0.29	0.40	0.40	0.48	1.00	0.60	0.07	-0.18	-0.19	0.00
280	-0.51	-0.29	0.18	0.51	0.47	0.01	0.25	0.31	0.34	0.48	0.60	0.61	0.62	0.60	1.00	0.70	0.17	-0.35	-0.51
300	-0.55	-0.68	-0.31	0.20	0.51	0.29	0.26	0.28	0.30	0.40	0.48	0.51	0.47	0.07	0.70	1.00	0.73	0.03	-0.55
320	-0.07	-0.62	-0.68	-0.31	0.18	0.36	0.10	0.09	0.11	0.18	0.25	0.28	0.25	-0.18	0.17	0.73	1.00	0.65	-0.07
340	0.66	-0.05	-0.62	-0.68	-0.29	0.23	-0.09	-0.12	-0.10	-0.05	-0.02	0.00	-0.01	-0.19	-0.35	0.03	0.65	1.00	0.66
360	1.00	0.66	-0.07	-0.55	-0.51	0.00	-0.14	-0.16	-0.15	-0.15	-0.15	-0.16	-0.14	0.00	-0.51	-0.55	-0.07	0.66	1.00

Table A.6 Load data: horizontal correlations normal region (SR0, effect of the rings on the load not included)

NORMAL REGION																			
	0	**20**	**40**	**60**	**80**	**100**	**120**	**140**	**160**	**180**	**200**	**220**	**240**	**260**	**280**	**300**	**320**	**340**	**360**
0	1.00	0.70	-0.06	-0.59	-0.54	0.07	-0.14	-0.17	-0.18	-0.17	-0.18	-0.17	-0.14	0.07	-0.54	-0.59	-0.06	0.70	1.00
20	0.70	1.00	0.64	-0.03	-0.44	-0.16	-0.01	-0.02	-0.04	-0.07	-0.11	-0.13	-0.09	0.27	-0.29	-0.70	-0.60	-0.02	0.70

40	-0.06	0.64	1.00	0.71	0.12	-0.19	0.27	0.29	0.29	0.23	0.15	0.11	0.12	0.37	0.24	-0.30	-0.68	-0.60	-0.06
60	-0.59	-0.03	0.71	1.00	0.69	0.06	0.50	0.54	0.56	0.48	0.36	0.30	0.28	0.24	0.54	0.26	-0.30	-0.70	-0.59
80	-0.54	-0.44	0.12	0.69	1.00	0.61	0.66	0.65	0.67	0.54	0.36	0.29	0.23	-0.14	0.38	0.54	0.24	-0.29	-0.54
100	0.07	-0.16	-0.19	0.06	0.61	1.00	0.54	0.44	0.45	0.32	0.14	0.07	0.03	-0.30	-0.14	0.24	0.37	0.27	0.07
120	-0.14	-0.01	0.27	0.50	0.66	0.54	1.00	0.75	0.70	0.58	0.38	0.28	0.25	0.03	0.23	0.28	0.12	-0.09	-0.14
140	-0.17	-0.02	0.29	0.54	0.65	0.44	0.75	1.00	0.83	0.64	0.44	0.33	0.28	0.07	0.29	0.30	0.11	-0.13	-0.17
160	-0.18	-0.04	0.29	0.56	0.67	0.45	0.70	0.83	1.00	0.79	0.56	0.44	0.38	0.14	0.36	0.36	0.15	-0.11	-0.18
180	-0.17	-0.07	0.23	0.48	0.54	0.32	0.58	0.64	0.79	1.00	0.79	0.64	0.58	0.32	0.54	0.48	0.23	-0.07	-0.17
200	-0.18	-0.11	0.15	0.36	0.36	0.14	0.38	0.44	0.56	0.79	1.00	0.83	0.70	0.45	0.67	0.56	0.29	-0.04	-0.18
220	-0.17	-0.13	0.11	0.30	0.29	0.07	0.28	0.33	0.44	0.64	0.83	1.00	0.75	0.44	0.65	0.54	0.29	-0.02	-0.17
240	-0.14	-0.09	0.12	0.28	0.23	0.03	0.25	0.28	0.38	0.58	0.70	0.75	1.00	0.54	0.66	0.50	0.27	-0.01	-0.14
260	0.07	0.27	0.37	0.24	-0.14	-0.30	0.03	0.07	0.14	0.32	0.45	0.44	0.54	1.00	0.61	0.06	-0.19	-0.16	0.07
280	-0.54	-0.29	0.24	0.54	0.38	-0.14	0.23	0.29	0.36	0.54	0.67	0.65	0.66	0.61	1.00	0.69	0.12	-0.44	-0.54
300	-0.59	-0.70	-0.30	0.26	0.54	0.24	0.28	0.30	0.36	0.48	0.56	0.54	0.50	0.06	0.69	1.00	0.71	-0.03	-0.59
320	-0.06	-0.60	-0.68	-0.30	0.24	0.37	0.12	0.11	0.15	0.23	0.29	0.29	0.27	-0.19	0.12	0.71	1.00	0.64	-0.06
340	0.70	-0.02	-0.60	-0.70	-0.29	0.27	-0.09	-0.13	-0.11	-0.07	-0.04	-0.02	-0.01	-0.16	-0.44	-0.03	0.64	1.00	0.70
360	1.00	0.70	-0.06	-0.59	-0.54	0.07	-0.14	-0.17	-0.18	-0.17	-0.18	-0.17	-0.14	0.07	-0.54	-0.59	-0.06	0.70	1.00

Table A.7 Load data: horizontal correlations bottom region (SR0, effect of the rings on the load not included)

BOTTOM REGION																			
	0	**20**	**40**	**60**	**80**	**100**	**120**	**140**	**160**	**180**	**200**	**220**	**240**	**260**	**280**	**300**	**320**	**340**	**360**
0	1.00	0.71	-0.14	-0.66	-0.73	0.02	-0.25	-0.31	-0.32	-0.33	-0.32	-0.31	-0.25	0.02	-0.73	-0.66	-0.14	0.71	1.00
20	0.71	1.00	0.66	-0.14	-0.51	-0.44	-0.16	-0.15	-0.16	-0.19	-0.21	-0.21	-0.15	0.24	-0.48	-0.75	-0.67	0.08	0.71
40	-0.14	0.66	1.00	0.73	0.24	-0.29	0.27	0.31	0.29	0.26	0.20	0.18	0.24	0.51	0.33	-0.27	-0.68	-0.67	-0.14
60	-0.66	-0.14	0.73	1.00	0.81	0.23	0.56	0.59	0.57	0.54	0.47	0.44	0.41	0.53	0.71	0.40	-0.27	-0.75	-0.66
80	-0.73	-0.51	0.24	0.81	1.00	0.73	0.69	0.67	0.69	0.63	0.54	0.50	0.38	-0.13	0.79	0.71	0.33	-0.48	-0.73
100	0.02	-0.44	-0.29	0.23	0.73	1.00	0.64	0.52	0.53	0.42	0.29	-0.03	-0.06	-0.35	-0.13	0.53	0.51	0.24	0.02
120	-0.25	-0.16	0.27	0.56	0.69	0.64	1.00	0.78	0.72	0.58	0.36	0.32	0.25	-0.06	0.38	0.41	0.24	-0.15	-0.25
140	-0.31	-0.15	0.31	0.59	0.67	0.52	0.78	1.00	0.84	0.65	0.44	0.39	0.32	-0.03	0.50	0.44	0.18	-0.21	-0.31
160	-0.32	-0.16	0.29	0.57	0.69	0.53	0.72	0.84	1.00	0.78	0.52	0.44	0.36	0.29	0.54	0.47	0.20	-0.21	-0.32
180	-0.33	-0.19	0.26	0.54	0.63	0.42	0.58	0.65	0.78	1.00	0.78	0.65	0.58	0.42	0.63	0.54	0.26	-0.19	-0.33
200	-0.32	-0.21	0.20	0.47	0.54	0.29	0.36	0.44	0.52	0.78	1.00	0.84	0.72	0.53	0.69	0.57	0.29	-0.16	-0.32
220	-0.31	-0.21	0.18	0.44	0.50	-0.03	0.32	0.39	0.44	0.65	0.84	1.00	0.78	0.52	0.67	0.59	0.31	-0.15	-0.31
240	-0.25	-0.15	0.24	0.41	0.38	-0.06	0.25	0.32	0.36	0.58	0.72	0.78	1.00	0.64	0.69	0.56	0.27	-0.16	-0.25
260	0.02	0.24	0.51	0.53	-0.13	-0.35	-0.06	-0.03	0.29	0.42	0.53	0.52	0.64	1.00	0.73	0.23	-0.29	-0.44	0.02
280	-0.73	-0.48	0.33	0.71	0.79	-0.13	0.38	0.50	0.54	0.63	0.69	0.67	0.69	0.73	1.00	0.81	0.24	-0.51	-0.73
300	-0.66	-0.75	-0.27	0.40	0.71	0.53	0.41	0.44	0.47	0.54	0.57	0.59	0.56	0.23	0.81	1.00	0.73	-0.14	-0.66
320	-0.14	-0.67	-0.68	-0.27	0.33	0.51	0.24	0.18	0.20	0.26	0.29	0.31	0.27	-0.29	0.24	0.73	1.00	0.66	-0.14
340	0.71	0.08	-0.67	-0.75	-0.48	0.24	-0.15	-0.21	-0.21	-0.19	-0.16	-0.15	-0.16	-0.44	-0.51	-0.14	0.66	1.00	0.71
360	1.00	0.71	-0.14	-0.66	-0.73	0.02	-0.25	-0.31	-0.32	-0.33	-0.32	-0.31	-0.25	0.02	-0.73	-0.66	-0.14	0.71	1.00

10.2 The beam response (Chapter 7)

Table A.8 Load data: mean and rms drag forces (SR0, effect of the rings on the load not included)

z [m]	U [m/s]	q_m [kN/m^2]	D [m]	Δz [m]	$C_{D.m}$	F_m [kN]	$C_{D.\sigma}$	F_σ [kN]
990	51.22	1.640	150	30	0.725	5346.37	0.120	884.04
950	50.86	1.616	150	40	0.799	7751.58	0.111	1078.48
910	50.48	1.593	150	30	0.769	5513.67	0.115	822.48
890	50.29	1.581	150	30	0.716	5091.11	0.113	806.49
850	49.89	1.556	150	70	0.606	9901.57	0.100	1635.98
750	48.83	1.490	150	100	0.501	11192.00	0.080	1791.60
650	47.64	1.419	150	100	0.486	10337.94	0.078	1661.10
550	46.30	1.340	150	65	0.486	6345.71	0.084	1094.48
520	45.85	1.314	150	22.5	0.492	2183.83	0.089	393.90
505	45.62	1.301	150	12.5	0.483	1177.26	0.090	219.80
495	45.46	1.292	150	12.5	0.482	1167.56	0.092	221.95
480	45.22	1.278	150	22.5	0.504	2173.84	0.092	397.82
450	44.73	1.250	150	65	0.508	6196.09	0.094	1142.33
350	42.83	1.147	158.94	100	0.554	10098.03	0.116	2115.57
250	40.43	1.021	183.15	100	0.604	11306.93	0.139	2592.24
150	38.34	0.919	217.59	100	0.698	13956.99	0.163	3251.36
50	33.26	0.691	258.20	100	0.816	14564.22	0.206	3668.03
$M_{D,m}(z=0)$	6.45E+07	kNm						
$M_{D,\sigma}(z=0)$	6.53E+06	kNm		including lack of correlation				
$M_{D,peak}(z=0)$	8.74E+07	kNm						

Table A.9 Load data: correlation matrix of drag forces (SR0, effect of the rings on the load not included)

Z [m]	990	950	910	890	850	750	650	550	520	505	495	480	450	350	250	150	50
990	1.000	0.683	0.445	0.387	0.357	0.316	0.214	0.129	0.031	0.028	0.026	0.023	0.019	0.009	0.004	0.002	0.001
950	0.683	1.000	0.705	0.614	0.519	0.425	0.341	0.155	0.112	0.104	0.099	0.091	0.078	0.047	0.028	0.017	0.010
910	0.445	0.705	1.000	0.863	0.610	0.393	0.308	0.187	0.117	0.108	0.102	0.094	0.079	0.046	0.026	0.015	0.009
890	0.387	0.614	0.863	1.000	0.710	0.398	0.337	0.205	0.130	0.120	0.114	0.105	0.089	0.051	0.029	0.017	0.010
850	0.357	0.519	0.610	0.710	1.000	0.477	0.365	0.247	0.160	0.148	0.140	0.129	0.109	0.063	0.036	0.021	0.012
750	0.316	0.425	0.393	0.398	0.477	1.000	0.583	0.407	0.329	0.306	0.291	0.271	0.234	0.144	0.089	0.055	0.034
650	0.214	0.341	0.308	0.337	0.365	0.583	1.000	0.610	0.497	0.458	0.433	0.399	0.343	0.202	0.119	0.070	0.041
550	0.129	0.155	0.187	0.205	0.247	0.407	0.610	1.000	0.845	0.775	0.735	0.685	0.613	0.347	0.204	0.120	0.071
520	0.031	0.112	0.117	0.130	0.160	0.329	0.497	0.845	1.000	0.916	0.856	0.806	0.687	0.410	0.240	0.188	0.084
505	0.028	0.104	0.108	0.120	0.148	0.306	0.458	0.775	0.916	1.000	0.945	0.847	0.722	0.444	0.260	0.201	0.091

495	0.026	0.099	0.102	0.114	0.140	0.291	0.433	0.735	0.856	0.945	1.000	0.905	0.763	0.468	0.274	0.210	0.096
480	0.023	0.091	0.094	0.105	0.129	0.271	0.399	0.685	0.806	0.847	0.905	1.000	0.839	0.506	0.297	0.225	0.103
450	0.019	0.078	0.079	0.089	0.109	0.234	0.343	0.613	0.687	0.722	0.763	0.839	1.000	0.606	0.348	0.326	0.121
350	0.009	0.047	0.046	0.051	0.063	0.144	0.202	0.347	0.410	0.444	0.468	0.506	0.606	1.000	0.590	0.431	0.205
250	0.004	0.028	0.026	0.029	0.036	0.089	0.119	0.204	0.240	0.260	0.274	0.297	0.348	0.590	1.000	0.637	0.348
150	0.002	0.017	0.015	0.017	0.021	0.055	0.070	0.120	0.188	0.201	0.210	0.225	0.326	0.431	0.637	1.000	0.590
50	0.001	0.010	0.009	0.010	0.012	0.034	0.041	0.071	0.084	0.091	0.096	0.103	0.121	0.205	0.348	0.590	1.000

Table A.10 Results – covariance method (SR0, effect of the rings on the load not included)

z [m]	$M_{D,m}$ [kNm]	$M_{D,\sigma}$ [kNm]	$M_{D,peak}$ [kNm]
0	6.45E+07	6.53E+06	8.74E+07
50	5.83E+07	5.98E+06	7.93E+07
100	5.28E+07	5.47E+06	7.20E+07
150	4.74E+07	4.98E+06	6.48E+07
200	4.26E+07	4.52E+06	5.84E+07
250	3.78E+07	4.08E+06	5.21E+07
300	3.36E+07	3.67E+06	4.64E+07
350	2.93E+07	3.26E+06	4.07E+07
400	2.56E+07	2.88E+06	3.57E+07
450	2.19E+07	2.51E+06	3.07E+07
500	1.85E+07	2.16E+06	2.61E+07
550	1.54E+07	1.82E+06	2.18E+07
600	1.27E+07	1.51E+06	1.79E+07
650	9.90E+06	1.20E+06	1.41E+07
700	7.66E+06	9.40E+05	1.09E+07
750	5.42E+06	6.81E+05	7.80E+06
800	3.74E+06	4.71E+05	5.39E+06
850	2.06E+06	2.68E+05	3.00E+06
900	9.24E+05	1.28E+05	1.37E+06
950	2.14E+05	3.54E+04	3.38E+05
1000	0.00E+00	0.00E+00	0.00E+00

Table A.11 Load data: mean drag forces (SR1, effect of ten rings on the load included)

z [m]	U [m/s]	q_m [kN/m2]	D [m]	Δz [m]	$C_{D.m}$	$F_{D,.m}$ [kN]
990	51.22	1.640	150	30	0.746	5503.44
950	50.86	1.616	150	40	0.689	6684.68
910	50.48	1.593	150	30	0.633	4533.52
890	50.29	1.581	150	30	0.599	4261.88
850	49.89	1.556	150	70	0.605	9882.94

750	48.83	1.490	150	100	0.606	13548.72
650	47.64	1.419	150	100	0.606	12901.86
550	46.30	1.340	150	65	0.623	8140.94
520	45.85	1.314	150	22.5	0.626	2775.63
505	45.62	1.301	150	12.5	0.616	1502.75
495	45.46	1.292	150	12.5	0.615	1490.81
480	45.22	1.278	150	22.5	0.637	2749.58
450	44.73	1.250	150	65	0.642	7822.83
350	42.83	1.147	158.9367	100	0.687	12530.31
250	40.43	1.021	183.1461	100	0.738	13803.53
150	38.34	0.919	217.5889	100	0.831	16625.38
50	33.26	0.691	258.2017	100	0.949	16946.00

$M_{D,m}$(z=0)	7.01E+07	kNm

Table A.12 Load data: mean lift forces (SR1, effect of ten rings on the load included)

z [m]	U [m/s]	q_m [kN/m2]	D [m]	Δz [m]	$C_{L,m}$	$F_{L,m}$ [kN]
950	50.86	1.616	150	100	0.250	6061.72
850	49.89	1.556	150	100	-0.250	-5834.30
750	48.83	1.490	150	100	0.250	5588.57
650	47.64	1.419	150	100	-0.250	-5320.27
550	46.30	1.340	150	100	0.250	5023.32
450	44.73	1.250	150	100	-0.250	-4688.45
350	42.83	1.147	158.9367	100	0.250	4556.57
250	40.43	1.021	183.1461	100	-0.250	-4677.06
150	38.34	0.919	217.5889	100	0.250	4998.87
50	33.26	0.691	258.2017	100	-0.250	-4461.95

$M_{L,m}$(z=0)	3.14E+06	kNm

10.3 The shell response (Chapter 7)

Table A.13 Shell response (effect of the rings on the load not included)

Response at stagnation - wind tunnel model applied to codified wind profile												
	Mean				**Rms**				**Peak**			
z	**n11**	**n22**	**m11**	**m22**	**n11**	**n22**	**m11**	**m22**	**n11**	**n22**	**m11**	**m22**
[m]	**kN/m**	**kN/m**	**kNm/m**	**kNm/m**	**kN/m**	**kN/m**	**kNm/m**	**kNm/m**	**kN/m**	**kN/m**	**kNm/m**	**kNm/m**
5	335.32	2741.12	4.53	25.22	41.06	342.59	0.74	4.00	479.03	3940.17	7.11	39.21
55	-30.04	2651.49	-1.34	1.15	21.94	311.21	1.40	0.42	-106.83	3740.71	-6.22	2.61
85	-32.06	2597.99	-4.64	-10.72	24.94	291.88	1.06	2.02	-119.36	3619.56	-8.37	-17.80
95	222.23	2578.27	-1.06	8.03	26.92	285.34	0.51	0.96	316.45	3576.95	-2.85	11.40
105	233.55	2565.70	-0.39	14.53	28.21	280.28	0.33	2.41	332.27	3546.68	-1.53	22.97

115	-19.05	2552.11	-5.95	-11.41	25.31	275.53	1.29	2.22	-107.63	3516.45	-10.47	-19.19
155	-14.53	2507.25	-5.47	-0.44	26.56	261.37	1.89	0.40	-107.50	3422.06	-12.07	-1.83
185	-52.93	2477.19	-11.24	-19.16	31.85	255.38	2.50	3.83	-164.39	3371.02	-19.99	-32.58
195	515.17	2464.02	-6.58	5.46	78.50	253.57	1.44	0.97	789.91	3351.50	-11.64	8.86
205	547.41	2464.25	-3.98	22.90	83.14	253.12	1.05	3.79	838.40	3350.19	-7.66	36.16
215	-20.04	2466.68	-13.60	-22.08	26.55	252.82	2.80	4.22	-112.96	3351.54	-23.39	-36.86
255	17.78	2489.23	-11.93	-2.20	20.32	255.18	2.37	0.54	88.90	3382.37	-20.21	-4.08
285	-113.27	2510.73	-20.39	-29.92	34.99	260.08	3.24	4.51	-235.72	3421.00	-31.72	-45.71
295	1042.56	2512.81	-13.65	3.07	134.42	261.51	2.02	0.76	1513.03	3428.08	-20.73	5.75
305	1104.82	2511.19	-8.14	36.11	141.49	261.76	1.33	4.73	1600.02	3427.33	-12.78	52.68
315	-60.21	2497.76	-23.83	-36.98	29.41	260.20	3.46	5.27	-163.16	3408.47	-35.94	-55.41
355	50.31	2431.20	-17.84	-3.42	17.67	253.04	2.34	0.46	112.15	3316.84	-26.03	-5.05
385	-198.04	2369.43	-24.28	-31.75	38.45	248.09	2.92	3.76	-332.62	3237.75	-34.50	-44.89
395	1444.30	2342.28	-17.14	-2.28	152.59	245.97	1.94	0.37	1978.36	3203.19	-23.94	-3.56
405	1511.55	2273.12	-8.37	41.38	158.90	240.11	1.02	4.40	2067.69	3113.48	-11.95	56.80
415	-148.16	2173.71	-25.47	-41.04	33.57	231.74	2.85	4.61	-265.65	2984.78	-35.45	-57.16
455	-76.78	1758.99	-15.40	-2.81	17.09	197.91	1.57	0.27	-136.58	2451.67	-20.89	-3.77
485	-392.97	1516.14	-18.21	-22.41	35.29	177.32	1.98	2.22	-516.49	2136.75	-25.14	-30.18
495	1277.73	1455.16	-13.91	-6.96	122.81	171.26	1.35	0.75	1707.55	2054.56	-18.62	-9.57
505	1344.46	1359.20	-4.69	36.75	128.21	162.70	0.62	3.35	1793.18	1928.64	-6.85	48.47
515	-330.27	1248.70	-18.68	-32.04	29.86	153.43	1.97	3.01	-434.77	1785.70	-25.56	-42.56
555	-101.21	894.46	-10.62	-1.49	18.00	122.97	1.06	0.11	-164.20	1324.87	-14.33	-1.88
585	-418.55	742.47	-12.46	-14.42	45.33	107.04	1.21	1.42	-577.19	1117.09	-16.71	-19.38
595	1235.34	712.97	-10.92	-10.99	109.46	102.66	0.98	0.93	1618.46	1072.27	-14.37	-14.26
605	1306.75	643.71	-2.26	30.44	115.15	97.02	0.28	2.67	1709.76	983.29	-3.24	39.80
615	-354.78	557.16	-13.92	-24.87	40.06	91.46	1.33	2.27	-494.99	877.26	-18.59	-32.81
655	-103.39	305.08	-9.50	-1.47	17.60	75.48	1.06	0.18	-165.00	569.26	-13.22	-2.10
685	-453.16	230.75	-13.02	-15.39	47.03	65.96	1.25	1.46	-617.76	461.60	-17.40	-20.51
695	1368.64	226.78	-11.85	-11.48	119.31	62.18	1.05	0.94	1786.23	444.40	-15.52	-14.77
705	1487.98	178.65	-2.75	34.24	129.29	58.62	0.32	2.97	1940.51	383.82	-3.86	44.62
715	-390.52	111.66	-15.76	-28.18	41.92	56.65	1.50	2.52	-537.24	309.94	-21.00	-37.02
755	-105.66	-73.10	-10.28	-1.64	17.11	50.93	1.17	0.21	-165.53	-251.36	-14.37	-2.39
785	-475.22	-106.82	-13.86	-16.22	48.26	40.81	1.35	1.53	-644.14	-249.65	-18.57	-21.57
795	1444.15	-98.35	-12.73	-12.56	125.93	35.83	1.13	1.06	1884.89	-223.77	-16.67	-16.28
805	1571.51	-131.60	-2.95	36.27	136.62	34.26	0.33	3.17	2049.69	-251.52	-4.11	47.35
815	-408.62	-180.28	-16.64	-29.85	42.90	35.92	1.57	2.66	-558.77	-306.01	-22.14	-39.18
855	-107.58	-285.30	-10.46	-1.75	16.86	37.65	1.19	0.21	-166.61	-417.06	-14.62	-2.49
885	-456.89	-247.49	-13.43	-15.34	48.05	28.52	1.34	1.50	-625.07	-347.32	-18.12	-20.60
895	1371.62	-213.67	-12.38	-12.63	125.25	22.40	1.15	1.13	1810.01	-292.06	-16.40	-16.58
905	1496.61	-214.75	-2.71	35.16	136.46	21.47	0.31	3.22	1974.21	-289.91	-3.79	46.43
915	-390.32	-227.98	-15.79	-28.56	42.26	24.71	1.54	2.67	-538.21	-314.48	-21.18	-37.90
955	-99.88	-205.47	-9.70	-1.83	16.65	26.98	1.08	0.21	-158.17	-299.89	-13.47	-2.57
985	-245.32	-85.10	-12.36	-15.89	31.51	12.33	1.27	1.59	-355.60	-128.25	-16.80	-21.46
995	816.33	-28.47	-5.61	15.96	78.39	4.29	0.58	1.57	1090.70	-43.48	-7.63	21.47

Table A.14 Load modification induced by the rings: effect on the quasi-static response (peak values):
SR0 = load modification due to the rings not included;
SR1 = load modification due to 10 rings included

	n11,peak at 0°		**n22,peak at 0°**		**m11,peak at 0°**		**m22,peak at 0°**	
z	**SR0**	**SR1**	**SR0**	**SR1**	**SR0**	**SR1**	**SR0**	**SR1**
[m]	**kN/m**	**kN/m**	**kN/m**	**kN/m**	**kNm/m**	**kNm/m**	**kNm/m**	**kNm/m**
5	483	535	4042	4443	8	8	43	45
55	-137	-133	3802	4189	-8	-10	3	4
85	-138	-139	3666	4056	-10	-10	-20	-20
95	346	348	3619	4015	-4	-2	14	15
105	363	372	3584	3975	-3	0	25	25
115	-117	-101	3546	3924	-13	-10	-21	-21
155	-110	-101	3434	3766	-13	-6	-2	0
185	-171	-156	3385	3712	-22	-16	-35	-30
195	845	778	3370	3700	-12	-10	12	9
205	893	833	3365	3685	-9	-6	39	37
215	-124	-104	3352	3651	-26	-22	-39	-36
255	104	111	3357	3595	-23	-20	-5	-3
285	-257	-253	3419	3620	-35	-33	-49	-47
295	1587	1581	3442	3626	-22	-22	8	3
305	1675	1683	3442	3610	-14	-13	55	57
315	-183	-169	3408	3564	-39	-38	-58	-59
355	125	135	3287	3390	-29	-28	-6	-6
385	-356	-384	3221	3274	-37	-39	-47	-49
395	2056	2161	3196	3228	-25	-27	-4	-3
405	2147	2272	3103	3119	-13	-13	59	64
415	-286	-297	2958	2964	-37	-40	-60	-64
455	-147	-150	2393	2358	-22	-24	-4	-5
485	-570	-596	2091	2028	-26	-28	-32	-33
495	1754	1865	2020	1946	-19	-21	-9	-11
505	1842	1968	1896	1815	-7	-7	50	55
515	-484	-499	1747	1665	-26	-28	-44	-47
555	-169	-167	1295	1204	-15	-16	-2	-3
585	-586	-608	1113	1003	-17	-18	-20	-20
595	1646	1718	1078	961	-15	-16	-14	-16
605	1739	1825	993	876	-3	-3	40	43
615	-502	-510	885	776	-19	-20	-33	-35
655	-165	-166	581	496	-13	-14	-2	-2
685	-617	-634	483	401	-18	-18	-21	-21
695	1792	1839	475	390	-16	-16	-15	-16
705	1947	2007	415	338	-4	-4	45	47
715	-536	-542	331	268	-22	-22	-37	-38
755	-163	-164	-263	-321	-15	-15	-3	-3

785	-638	-650	-236	-284	-19	-19	-22	-22
795	1877	1912	-194	-239	-17	-17	-16	-17
805	2041	2085	-221	-261	-4	-4	47	49
815	-552	-558	-290	-322	-23	-23	-39	-40
855	-163	-166	-431	-436	-16	-16	-3	-3
885	-622	-639	-346	-344	-19	-19	-21	-21
895	1801	1846	-283	-280	-16	-17	-16	-17
905	1966	2014	-282	-279	-4	-4	46	48
915	-534	-550	-314	-313	-21	-22	-38	-39
955	-160	-170	-311	-316	-13	-13	-3	-3
985	-355	-393	-134	-137	-17	-17	-21	-22
995	1094	1099	-45	-47	-8	-8	21	22

Table A.15 Load modification induced by the rings: effect on the quasi-static response (mean values):
SR0 = load modification due to the rings not included;
SR1 = load modification due to 10 rings included

	n11,m at 0°		**n22,m at 0°**		**m11,m at 0°**		**m22,m at 0°**	
z	**SR0**	**SR1**	**SR0**	**SR1**	**SR0**	**SR1**	**SR0**	**SR1**
[m]	**kN/m**	**kN/m**	**kN/m**	**kN/m**	**kNm/m**	**kNm/m**	**kNm/m**	**kNm/m**
5	326	347	2695	2863	5	5	25	26
55	-34	-30	2603	2782	-1	-1	1	1
85	-34	-29	2551	2737	-5	-5	-11	-11
95	221	233	2533	2720	-1	-1	8	9
105	232	245	2520	2709	0	0	14	15
115	-21	-15	2506	2696	-6	-6	-11	-12
155	-15	-9	2465	2658	-6	-6	-1	0
185	-52	-45	2451	2644	-11	-11	-19	-19
195	517	523	2446	2637	-6	-6	6	6
205	548	553	2447	2637	-4	-4	23	23
215	-20	-12	2445	2631	-14	-14	-22	-22
255	19	26	2462	2630	-13	-12	-2	-2
285	-106	-100	2505	2652	-20	-20	-29	-29
295	1019	1029	2519	2657	-13	-13	4	3
305	1078	1090	2519	2649	-8	-8	35	36
315	-55	-48	2499	2621	-23	-23	-36	-36
355	52	57	2419	2504	-18	-18	-4	-4
385	-189	-193	2367	2419	-24	-24	-31	-31
395	1408	1440	2347	2387	-17	-17	-2	-3
405	1472	1509	2278	2308	-8	-8	40	42
415	-141	-144	2173	2196	-25	-26	-40	-41
455	-76	-76	1752	1747	-15	-16	-3	-3

485	-388	-392	1524	1497	-18	-18	-22	-22
495	1258	1289	1471	1435	-14	-14	-7	-8
505	1324	1361	1376	1334	-5	-5	36	38
515	-326	-326	1259	1215	-19	-19	-32	-33
555	-101	-97	897	837	-11	-11	-2	-2
585	-415	-415	758	680	-12	-13	-14	-14
595	1222	1231	735	651	-11	-11	-11	-12
605	1292	1306	667	580	-2	-2	30	31
615	-353	-349	574	489	-14	-14	-25	-25
655	-104	-101	312	232	-10	-10	-2	-2
685	-450	-447	250	169	-13	-13	-15	-15
695	1354	1346	254	173	-12	-12	-11	-12
705	1472	1468	204	128	-3	-3	34	35
715	-387	-382	127	58	-16	-16	-28	-28
755	-104	-103	-73	-114	-11	-11	-2	-2
785	-470	-466	-85	-112	-14	-14	-16	-16
795	1427	1413	-62	-87	-13	-13	-12	-13
805	1553	1541	-94	-113	-3	-3	36	36
815	-404	-397	-156	-166	-17	-17	-30	-29
855	-106	-104	-281	-272	-11	-11	-2	-2
885	-455	-457	-234	-222	-14	-14	-15	-15
895	1365	1360	-193	-182	-12	-12	-12	-12
905	1490	1484	-197	-186	-3	-3	35	35
915	-389	-393	-220	-211	-16	-16	-28	-28
955	-102	-107	-211	-210	-9	-9	-2	-2
985	-247	-272	-88	-89	-12	-12	-16	-16
995	817	798	-30	-30	-6	-6	16	16

Table A.16 Load modification induced by the rings: effect on the quasi-static response (rms values):
SR0 = load modification due to the rings not included;
SR1 = load modification due to 10 rings included

	n11,σ at 0°		**n22,σ at 0°**		**m11,σ at 0°**		**m22,σ at 0°**	
z	**SR0**	**SR1**	**SR0**	**SR1**	**SR0**	**SR1**	**SR0**	**SR1**
[m]	**kN/m**	**kN/m**	**kN/m**	**kN/m**	**kNm/m**	**kNm/m**	**kNm/m**	**kNm/m**
5	45	54	385	451	0.90	0.98	4.97	5.48
55	29	30	342	402	2.03	2.46	0.55	0.71
85	30	31	318	377	1.62	1.40	2.64	2.52
95	36	33	310	370	0.71	0.25	1.57	1.81
105	38	36	304	362	0.64	0.00	2.96	2.88
115	28	25	297	351	1.95	1.11	2.85	2.52
155	27	26	277	316	2.16	0.00	0.53	0.00

185	34	32	267	305	3.00	1.24	4.47	3.15
195	94	73	264	304	1.70	1.12	1.53	0.76
205	99	80	262	299	1.28	0.64	4.53	4.01
215	30	26	259	291	3.45	2.31	4.96	3.91
255	24	24	256	275	3.06	2.10	0.77	0.22
285	43	44	261	277	4.10	3.70	5.55	5.22
295	162	158	264	277	2.51	2.55	1.21	0.00
305	171	169	264	275	1.67	1.50	5.81	6.13
315	37	34	260	269	4.36	4.16	6.44	6.41
355	21	22	248	253	3.11	2.87	0.71	0.58
385	48	55	244	244	3.71	4.10	4.66	5.14
395	185	206	243	241	2.42	2.84	0.57	0.00
405	193	218	236	232	1.28	1.44	5.38	6.34
415	41	44	224	220	3.56	4.14	5.65	6.46
455	20	21	183	175	2.00	2.44	0.36	0.44
485	52	58	162	152	2.23	2.63	2.69	3.06
495	142	165	157	146	1.60	1.93	0.69	0.96
505	148	174	149	137	0.63	0.72	4.00	4.79
515	45	49	139	129	2.21	2.58	3.65	4.26
555	19	20	114	105	1.32	1.55	0.22	0.26
585	49	55	101	92	1.39	1.60	1.57	1.75
595	121	139	98	89	1.10	1.31	0.99	1.31
605	128	148	93	85	0.31	0.34	2.93	3.50
615	43	46	89	82	1.46	1.72	2.49	2.90
655	17	19	77	76	1.11	1.33	0.19	0.24
685	48	53	67	66	1.31	1.53	1.52	1.70
695	125	141	63	62	1.10	1.28	1.00	1.23
705	136	154	60	60	0.34	0.36	3.10	3.58
715	42	46	58	60	1.60	1.76	2.64	2.98
755	17	17	54	59	1.27	1.31	0.24	0.23
785	48	53	43	49	1.41	1.52	1.56	1.70
795	129	143	38	44	1.16	1.30	1.07	1.27
805	139	155	36	42	0.35	0.37	3.22	3.62
815	42	46	38	44	1.64	1.80	2.71	3.02
855	16	17	43	47	1.27	1.35	0.24	0.25
885	48	52	32	35	1.38	1.51	1.50	1.66
895	125	139	26	28	1.16	1.28	1.16	1.25
905	136	152	25	27	0.31	0.34	3.21	3.55
915	41	45	27	29	1.53	1.70	2.65	2.94
955	17	18	28	30	1.09	1.14	0.22	0.22
985	31	35	13	14	1.28	1.41	1.60	1.77
995	79	86	5	5	0.58	0.63	1.59	1.77

The number of decimals after the comma is just a matter of visualization. The values are calculated with higher precision in order to avoid significant truncation errors.

Curriculum Vitae

Personal information

First name / Surname	**Francesca Lupi**
Nationality	Italian
Date of birth	21/04/1984
Place of birth	Prato, Italy
Gender	Female
Mother tongue	Italian
Other languages	English, German

Occupational field — Civil Engineering

Affiliation	DICEA - Department of Civil and Environmental Engineering University of Florence Via di S. Marta 3 50139, Florence Italy
E-mail	francesca.lupi@dicea.unifi.it

Education

Dates	2010 - April 2013
Title of qualification awarded	Dottore di Ricerca / Dr.-Ing. (grade: outstanding) International Research Doctorate on “Mitigation of risk due to natural hazards on structures and infrastructures”
Name of organisation	Università degli Studi di Firenze / Technical University Carolo-Wilhelmina Braunschweig
Dates	February 2010
Title of qualification awarded	Registered Professional Engineer (Civil and Environmental Engineering Sector, Section A)
Name of organisation	Ordine degli Ingegneri della Provincia di Prato, Italy
Dates	2007 - 2009
Title of qualification awarded	Master degree in Civil Engineering, major in Structural Engineering (110/110 cum laude) Thesis: “Structural behaviour, optimization and design of a solar chimney prototype under wind loading and other actions”.
Name of organisation	Università degli Studi di Firenze, Florence, Italy

Dates	February - May 2009
	Erasmus placement
Name of organisation	Niemann&Partner Ingenieurgesellschaft, Bochum, Germany
Dates	2003 - 2007
Title of qualification awarded	Bachelor degree in Civil Engineering (110/110 cum laude)
	Thesis: “Progetto di parcheggio interrato in Piazza Mercatale a Prato” (“Desing of an underground parking in Piazza Mercatale, Prato”)
Name of organisation	Università degli Studi di Firenze, Florence, Italy
Dates	1998 - 2003
Title of qualification awarded	Scientific High School Diploma (100/100)
Name and type of organisation	Liceo Scientifico “Conservatorio San Niccolò”, Prato, Italy

Prizes and Awards

Date	September 2011
	“Outstanding young engineer contribution award” for the paper presented at IABSE-IASS 2011 symposium in London: “Non-conventional wind loading on ultra-high Towers in Solar Updraft Power Plants”.